Contribution to the mathematical analysis and to the numerical solution of an inverse elasto-acoustic scattering problem

Elodie Estecahandy

ACADÉMIE DE BORDEAUX |_|_|_|_|_|_|_|_|_|_|_|_|

THÈSE DE DOCTORAT

Présentée par

Élodie ESTÉCAHANDY

Pour l'obtention du grade de

DOCTEUR DE L'UNIVERSITÉ DE PAU ET DES PAYS DE L'ADOUR

À

L'Université de Pau et des Pays de l'Adour

École doctorale des sciences et leurs applications - ED 211

DOMAINE DE RECHERCHE : Mathématiques Appliquées

Contribution à l'analyse mathématique et à la résolution numérique d'un problème inverse de scattering élasto-acoustique

Directrice de thèse : **Mme Hélène BARUCQ**

Co-direction : **M. Rabia DJELLOULI**

Soutenue le 19 Septembre 2013

Après avis de:

M. Abderrahmane BENDALI	Professeur, Université et INSA Toulouse	Rapporteur
M. Paul MARTIN	Professeur, Colorado School of Mines (USA)	Rapporteur

Devant la commission d'examen formée de:

Mme Hélène BARUCQ	Directrice de Recherche, INRIA	Directrice de thèse
M. Abderrahmane BENDALI	Professeur, Université et INSA Toulouse	Rapporteur
M. Marc BONNET	Directeur de Recherche, CNRS, INRIA, ENSTA ParisTech	Président du Jury
M. Romain BROSSIER	Maître de conférence, Université Joseph Fourier, Grenoble I	Examinateur
M. Henri CALANDRA	Ingénieur de Recherche Expert, Centre CSTJF TOTAL	Examinateur
M. Laurent DEMANET	Assistant professor, MIT (USA)	Examinateur
M. Rabia DJELLOULI	Professeur, California State University Northridge (USA)	Co-directeur de thèse
M. Vladimir TCHEVERDA	Professeur, Russian Academy of Sciences (Russie)	Examinateur

Equipe-Projet INRIA MAGIQUE-3D, Institut National de Recherche en Informatique et en Automatique (INRIA)

Laboratoire de Mathématiques et de leurs Applications de Pau, Unité Mixte de Recherche CNRS-UPPA 5142, Université de Pau et des Pays de l'Adour (UPPA)

Thanks

I want to thank all the people who played a part in this adventure.
First, I am very grateful to all the members of the rich and diverse jury for having participated in my defense and to the reviewers for your great care. It was an honor for me to be examined by a committee composed of scientists of such a calibre and such an international standing. Thank you very much for your kindliness, your interest and encouragement taken in my work.
Thanks a lot to the heads and people from Inria and the University of Pau, and of the Laboratory of Mathematics, who supported me throughout this project and allowed its accomplishment.
Eskerrik asko and Saha to my advisors and coachs Hélène and Rabia too. You gave me the opportunity to work on a topic that I would not have expected at first glance, it was a fortunate and enriching adventure, both on the scientific standpoint and in human terms. Milesker and Merci hèro to Hélène and her family as well for all the moments shared.
I thank the people met during the past years. I really appreciate the Magique-3D team, the dream team. Thanks a lot to my collegues and friends for your dynamism and your support, you have contributed to this happy end.
Last, many thanks to my long-standing friends and family circle for being present. I would like to dedicate this work to my parents and my sister: Maman, Papa, Maïder, Merci pour tout, celà n'aurait pas été possible sans vous.

Contents

Introduction générale: Présentation de la thèse

Contribution à l'analyse mathématique et à la résolution numérique d'un problème inverse de scattering élasto-acoustique

Cette thèse a pour objectif de développer un outil de simulation pour la résolution de problèmes inverses élasto-acoustiques. Elle est organisée en deux parties qui peuvent être lues indépendamment. Chaque partie est composée de deux chapitres et chacun d'eux comporte une introduction faisant référence à une bibliographie que l'on espère complète ainsi qu'une nomenclature. Afin d'éviter les redondances, nous avons choisi, en guise d'introduction, de décrire le contenu de cette thèse sans entrer dans les détails que le lecteur trouvera dans chacun des chapitres.

La détermination de la forme d'un obstacle élastique immergé dans un milieu fluide à partir de mesures du champ d'onde diffracté en présence d'ondes incidentes est un problème d'un vif intérêt dans de nombreux domaines tels que le sonar, le radar, l'exploration géophysique, l'imagerie médicale ou le contrôle non destructif. A cause de son caractère non-linéaire et mal posé, ce problème inverse de l'obstacle (IOP) est très difficile à résoudre, particulièrement d'un point de vue numérique. Le succès de la reconstruction dépend fortement de la quantité et qualité des mesures, notamment des angles d'observations utilisés, et du niveau de bruit. De plus, pour résoudre IOP, la compréhension de la théorie du problème de diffraction direct associé et la maîtrise des méthodes de résolution correspondantes sont fondamentales. Le travail accompli ici se rapporte à l'analyse mathématique et numérique du problème direct de diffraction élasto-acoustique et d'un problème inverse de scattering. Plus précisément, le but de ce travail de recherche est de proposer une méthodologie de résolution d'IOP basée sur une méthode de type Newton régularisée, connue pour être robuste et efficace. Pour atteindre les objectifs que nous nous sommes fixés, nous avons réalisé un travail important sur la résolution du problème direct qui fait l'objet de la première partie de cette thèse. Quant au problème

inverse que nous avons considéré, il est décrit, étudié et mis en oeuvre dans la deuxième partie de la thèse.

La première partie de la thèse est donc consacrée au problème direct. Pour commencer (Chapitre I), nous revisitons la question de l'existence et unicité du système élasto-acoustique en relâchant les hypothèses de régularité qui sont généralement faites sur l'interface fluide-structure. Notre approche repose sur une réécriture du problème, a priori posé dans tout l'espace, en un problème mixte via l'introduction de l'opérateur Dirichlet-to-Neumann (DtoN) de la sphère. On montre alors que cette formulation est équivalente à une formulation du système dans des espaces de Sobolev à poids. On peut ainsi appliquer la théorie de Fredholm et nous établissons que le système est bien posé lorsque le solide est un domaine lipschitzien continu. Nous nous attaquons ensuite à la résolution numérique du problème mixte (Chapitre II) en remplaçant l'opérateur DtoN par une approximation locale. Nous avons fait le choix de mettre en place une méthode de type DG pour résoudre le problème élasto-acoustique. Ce choix est guidé par la volonté, à plus long terme, d'appliquer les travaux de cette thèse à des configurations issues de la géophysique. Il nous est donc apparu pertinent de mettre oeuvre des éléments finis discontinus d'ordre élevé dont le niveau de flexibilité est parfaitement adapté au cas de solides hétérogènes. La méthode que nous avons élaborée permet ainsi de mélanger différents ordres d'approximation et s'adapte ainsi parfaitement à des domaines de calcul composées de régions caractérisées par des vitesses de propagation contrastées. Nous avons validé la méthode DG par comparaison avec des solutions analytiques puis nous avons réalisé une analyse qui illustre d'excellentes performances. Nous montrons en particulier que la méthode DG est très robuste aux effets de pollution numériques. Pour améliorer le niveau de précision des résultats numériques, nous avons enrichi la méthode DG en introduisant des éléments finis courbes sur l'interface fluide-structure. Les calculs numériques que nous présentons illustrent l'intérêt de cet enrichissement qui contribue, quand on l'utilise avec des éléments d'ordre élevé, à limiter l'impact des modes de Jones qui peuvent dans certains cas polluer le champ d'onde dans le fluide. Le solveur est validé tout d'abord en utilisant des solutions analytiques qui s'écrivent comme des développements sur des bases de fonctions spéciales. Les performances de la méthode numérique sont ensuite évaluées en comparant avec des résultats numériques publiés par P. Monk et ses collaborateurs dans le journal Computational and Applied Mathematics, en 2008 et basés sur la méthode ultra-faible.

La deuxième partie de la thèse traite du problème inverse. La méthode de Newton régularisée que nous avons choisie fait intervenir une matrice jacobienne qui doit être évaluée à chaque itération. Nous calculons (Chapter III), dans un premier temps formellement, la différentielle au sens de Fréchet du champ d'onde élasto-acoustique par rapport au bord de l'obstacle. Nous obtenons que

cette dérivée est caractérisée comme la solution du problème élasto-acoustique de départ modulo une modification au niveau des conditions de transmission posées sur l'interface fluide-structure. Les conditions de transmission modifiées sont dans ce cas hétérogènes et le terme hétérogène s'écrit en fonction de traces d'ordre élevé du champ d'onde direct. On montre donc que l'évaluation de la matrice jacobienne passe par la résolution du problème direct avec multi second membre. Avant de poursuivre par la mise en oeuvre numérique du problème inverse, nous essayons de lever le caractère formel de la caractérisation de la dérivée de Fréchet du champ élasto-acoustique. Pour cela, nous avons été confrontés à l'absence de certains résultats de régularité quand l'interface est seulement lipschitzienne. Nous avons cependant obtenu une caractérisation complète de la dérivée de Fréchet quand l'interface est un polygone ou polyèdre curviligne. Dans le cas où la frontière est seulement de classe $\mathcal{C}^{0,1}$, nous n'avons réussi à étendre des résultats établis par Ciarlet et ses collaborateurs et publiés dans les Comptes rendus de l'Académie des Sciences qui donne un sens à la trace de champs dans le domaine du Laplacien. Pour traiter complètement le problème d'interaction fluide-structure, il est nécessaire d'établir des résultats de trace dans le domaine de l'opérateur $\nabla \cdot \sigma$ dont la preuve passe par la construction d'opérateurs de relèvement qui n'est pas triviale. Néanmoins, cette question est en passe d'être résolue. Le cas général d'un domaine Lipschitz soulève encore des questions et est encore loin d'être résolu. Toutefois, nous avons choisi de présenter un résultat de régularité qui nous semble illustrer la difficulté du problème et donner de nombreuses perspectives théoriques à cette thèse. Au dernier chapitre de ce manuscrit (Chapter IV), nous avons mis en oeuvre la méthode de Newton régularisée et nous avons effectué une série de cas tests qui illustrent bien l'intérêt de notre approche.

General Introduction: Presentation of the thesis

Contribution to the mathematical analysis and to the numerical solution of an inverse elasto-acoustic scattering problem

This thesis aims at developing a simulation tool for solving elasto-acoustic inverse problems. It is organized into two parts which can be read independently. Each part consists of two chapters, and each of them has been written with an introduction referring in particular to a bibliography that we hope to be as complete as possible. For each chapter, we also define carefully a nomenclature that should help the reader. In order to avoid a possible redundancy by writing an introduction for the whole document, we begin the document with a general introduction to describe the content of this thesis without going into the details, the reader could find precisions in each chapter.

The determination of the shape of an obstacle immersed in a fluid medium from some measurements of the scattered field in the presence of incident waves is an important problem in many technologies such as sonar, radar, geophysical exploration, medical imaging and nondestructive testing. Because of its nonlinear and ill-posed character, this inverse obstacle problem (IOP) is very difficult to solve, especially from a numerical viewpoint. The success of the reconstruction depends strongly on the quantity and quality of the measurements, especially on the aperture (range of observation angles) and the level of noise in the data. Moreover, in order to solve IOP, the understanding of the theory for the associated direct scattering problem and the mastery of the corresponding solution methods are fundamental. The work accomplished here pertains to the mathematical and numerical analysis of the direct elasto-acoustic scattering problem and of an inverse obstacle scattering problem. More specifically, the purpose of this research work is to propose a solution methodology for the IOP based on a regularized Newton-type method, known to be robust and efficient. To reach our goals, we have

carried out an important work on the solution of the direct problem which is the subject of the first part of this thesis. Next, the inverse problem that we consider here is described, studied and implemented in the second part of the thesis.

The first part of the thesis is thus devoted to the direct problem. First (Chapter I), we revisit the question of the existence and uniqueness of the elasto-acoustic system when relaxing the regularity assumptions that are usually made on the fluid-structure interface. Our approach is based on a rewriting of the problem, a priori set in the whole space, into a mixed boundary value problem via the introduction of the Dirichlet-to-Neumann (DtN) operator of the sphere. We then show that this formulation is equivalent to a formulation of the system in weighted Sobolev spaces. We can therefore apply the Fredholm theory and we establish that the system is well-posed when the solid is a continuous Lipschitz domain. We then tackle the numerical solution of the mixed problem (Chapter II) by replacing the DtN operator by a local approximation. Regarding the numerical solution of the direct problem, we have chosen to implement a DG-type method to solve the elasto-acoustic system. This choice is guided by the wish, in the long term, to apply the works of this thesis to configurations from geophysics. It has therefore seemed to be relevant to implement higher-order discontinuous finite elements because of their high degree of flexibility which is perfectly suited to the case of heterogeneous solids. The method that we have developed is particularly interesting because it allows to mix different orders of approximation, and fits thus perfectly to computational domains composed of regions characterized by highly contrasted propagation velocities. We have validated the DG method by comparison with analytical solutions and then, we have performed an analysis that illustrates excellent performances. We show in particular that the DG method is very robust to the effects of numerical pollution. In order to improve the accuracy of the numerical results, we have enriched the DG method by introducing curved finite elements on the fluid-structure interface. The numerical simulations presented here illustrate the importance of this enrichment which contributes, when employed with higher-order elements, to limit the impact of the Jones modes that may, in some cases, pollute the wave field in the fluid. The solver is first validated by using analytical solutions that can be written as developments on bases of special functions. Regarding the performance of the method, it is assessed by comparison with numerical results published by P. Monk and his collaborators in the journal Computational and Applied Mathematics, in 2008, and based on the ultra-weak method.

The second part of the thesis deals with the inverse problem. The Newton regularized method that we have chosen involves a Jacobian matrix which must be evaluated at each iteration. We compute (Chapter III) the Fréchet derivative of the elasto-acoustic scattered field with respect to the shape

of the obstacle. In order to make the computation of the derivative readable, we have performed it formally and thus the related regularity issues have been first left out. We obtain that this derivative is characterized as the solution to the initial direct elasto-acoustic problem except a change in the transmission conditions set on the fluid-structure interface. The modified transmission conditions are now heterogeneous and the source term involves higher order traces of the direct scattered field. We therefore show that the evaluation of the Jacobian matrix requires the solution of the direct problem with multiple right-hand sides. Then, before proceeding with the numerical implementation of the inverse problem, we have tried to remove the formal character of the characterization of the Fréchet derivative of the elasto-acoustic scattered field. To this end, we have been coped with the absence of some regularity results when the fluid-solid interface is only Lipschitz. However, we have obtained a complete characterization of the Fréchet derivative when the interface is a curvilinear polygon or polyhedron. In the case where the boundary is only of class $\mathcal{C}^{0,1}$, we have not managed to extend results established by Ciarlet and his collaborators, published in the Comptes rendus de l'Académie des Sciences in 2005, which allow to give a sense to the trace for the fields in the domain of the Lapace operator. In order to fully address the fluid-structure interaction problem, it is necessary to establish trace results in the domain of the operator $\nabla \cdot \sigma$ and we tried to tackle this issue before observing that its proof requires non obvious constructions of lifting operators. Nevertheless, this issue is on the way to be solved. The general case of a Lipschitz domain still raises further issues and is still far to be solved. Nevertheless, we have chosen to present a regularity result which seems to illustrate the difficulty of the problem and give numerous theoretical perspectives to this thesis. In the last chapter of this manuscript (Chapter IV), we have implemented the Newton regularized method and we have performed a set of experiments that illustrate the interest of our approach.

Note that the formal characterization established in Chapter III is the subject of an article that has been accepted for publication in Journal of Inverse and Ill-Posed Problems (JIIP). The analysis contained in Chapter I has also been submitted, as well as a reduced version of the work reported in Chapter II.

Part I

The Direct Scattering Problem

Chapter I

On the existence and the uniqueness of a fluid-structure scattering problem

In this chapter, the existence and uniqueness of the solution of a fluid-structure interaction problem is investigated. The proposed analysis distinguishes itself from previous studies by employing the DtN operator properties, and the Fredholm theory. The proposed approach allows to extend the range of validity of the standard existence and uniqueness results to the case where the elastic scatterer is assumed to be only Lipschitz continuous, which is of more practical interest.

I.1 Introduction

The mathematical analysis and the numerical computation of scattered fields by penetrable objects are very important to many real-world applications such as radar and sonar detection, geophysical exploration, structural design, medical imaging, and atmospheric studies. The goal of the proposed study is to investigate the well-posed nature of a class of elasto-acoustic scattering problems that describes the propagation of a scattered field from an elastic bounded object immersed in an infinite domain, representing a fluid medium. This class of problems consists in the coupling of Helmholtz equation with Navier equation.

Helmholtz problems, per se, have been analyzed extensively from both mathematical and numerical viewpoints, and results pertaining to existence and uniqueness can be found in [28, 97, 118, 139], among others. Likewise, elastic scattering problems have been also investigated mathematically and numerically, and results pertaining to their well-posedness can be found in [92, 93, 119, 129]. However, there have been relatively very few mathematical works on problems involving the coupling of Helmholtz and Navier equations. Indeed, to the best of our knowledge, the well-posed nature of the coupling system has been studied first in [104] and then a few years later in [85]. In reference [104], the authors reformulated the considered boundary value problem as an integro-differential system

whose unknowns are defined on the fluid-structure interface Γ. Such a transformation was accomplished using an integral representation of both the fluid pressure and structural displacement fields. In doing this, the authors established existence and uniqueness results assuming the boundary Γ of the scatterer to be $\mathcal{C}^2$, which is a very restrictive condition when considering practical situations. In reference [85], the authors adopted a different approach that relies on the integral representation of the fluid pressure only. Yet, the approach requires also a $\mathcal{C}^2$ regularity on the boundary Γ to establish similar existence and uniqueness results. Note that this formulation has been numerically implemented in [46] for solving the corresponding inverse elasto-acoustic scattering problem. We must point out that the formulation employed in [46] is slightly different than the adopted in [85]. The authors in [46] consider an artificial exterior boundary surrounding the elastic scatterer, on which an exact boundary condition is imposed via the the integral formulation of the fluid pressure.

We propose here to extend the results obtained in [104] and [46] to the case where the wet surface Γ is assumed to be only Lipschitz continuous, which is of more practical interest. The proposed proof employs a weighted Sobolev space framework [64, 76], the Dirichlet-to-Neumann (DtN) operator [66, 73, 135], the Gårding inequality [17, 126, 130], and the Fredholm alternative [17, 126, 130]. More specifically, the proposed proof can be viewed as a four-step approach:

- In step 1, we specify the mathematical framework for the considered boundary value problem (BVP). We construct a weighted Sobolev-like space that naturally incorporates the asymptotic decay of the fluid pressure variable p as well as its outgoing propagation nature.
- Step 2 consists in reformulating the BVP in a bounded domain. Unlike the approach used in [85], we prescribe the exact DtN boundary condition at the exterior spherical-shaped boundary. Note that adopting the weighted Sobolev space framework and the DtN operator allows to rigorously establish the equivalence between both boundary value problems. To the best of our knowledge, the equivalence between the BVP and the formulation in the bounded domain is established rigorously for the first time.
- Step 3 focuses on the boundary value problem formulated in a finite domain. We derive a variational formulation for this problem, and then, using the sign property of the DtN operator, we prove that the Gårding's inequality holds.
- Step 4 consists in applying the Fredholm alternative which allows to prove, under minimal condition on the regularity of the fluid-structure interface Γ, (a) the existence of the solution of the BVP, (b) the uniqueness of the fluid pressure, and (c) the uniqueness of the structural displacement field modulo Jones frequencies [37, 92]. These frequencies may exist only for a particular class of elastic objects, such as spheres [37, 49, 79].

The remainder of the chapter is organized as follows. In Section I.2, we first state the considered mathematical model in the infinite domain. Then, we introduce the weighted Sobolev space formulation and the formulation in a bounded domain. Finally, we prove the equivalence between the two formulations. Section I.3 is devoted to the mathematical analysis of the boundary value problem formulated in a bounded domain. More specifically, we state the variational formulation corresponding to this problem. We then establish the equivalence between the strong and the weak formulations, and then examine the properties of the considered variational problem. In Section I.4, we investigate the existence and the uniqueness of the solution of the variational problem. Using the Fredholm alternative, we prove the existence of the solution. We then prove that the pressure field is unique, whereas the displacement field is unique only modulo Jones frequencies. Furthermore, and for completeness purpose only, we recall in Appendix A.1 some properties of the Hankel spherical functions and the spherical harmonics needed to derive and to study the DtN operator. In Appendix A.2, we perform an analytical study of the uniqueness of the solution of an exterior Helmholtz problem for which the boundary of the scatterer is a sphere. Appendix A.3 is devoted to the construction of the DtN operator.

I.2 The Boundary Value Problem Formulations

I.2.1 Formulation in the infinite domain

Let Ω^s be a bounded domain of $\mathbb{R}^3$ representing an elastic obstacle, and $\Omega^f = \mathbb{R}^3 \setminus \overline{\Omega}^s$ be the homogeneous inviscid (fluid) medium surrounding the elastic domain. Γ is the boundary of Ω^s and is assumed to be Lipschitz continuous.

We consider the scattering of a time-harmonic acoustic wave p^{inc} by the elastic obstacle Ω^s embedded in Ω^f as depicted on Figure I.2.1. The problem is to determine the scattered wave p in the fluid and the transmitted elastic wave u in the scatterer. Note that the time dependence $e^{-\mathrm{i}\omega t}$ is harmonic, that is suppressed throughout, according to the linearity of the considered problem. The corresponding system of equations BVP (1) reads as the coupling of the Helmholtz and Navier equations. This problem can be formulated as follows:

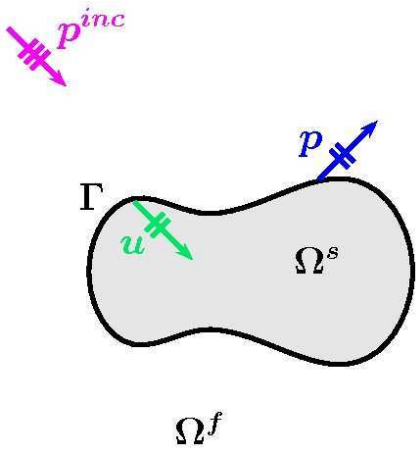

Figure I.2.1 – Problem statement in the infinite domain.

$$\text{BVP (1)} \quad \begin{cases} \Delta p + kp = 0 & \text{in } \Omega^f & \text{(I.2.1)} \\ \nabla \cdot \sigma(u) + \omega^2 \rho_s u = 0 & \text{in } \Omega^s & \text{(I.2.2)} \\ \omega^2 \rho_f u \cdot \nu = \dfrac{\partial p}{\partial \nu} + \dfrac{\partial g}{\partial \nu} & \text{on } \Gamma & \text{(I.2.3)} \\ \tau(u) = -p\nu - g\nu & \text{on } \Gamma & \text{(I.2.4)} \\ \lim\limits_{r \to +\infty} r \left(\dfrac{\partial p}{\partial r} - \mathrm{i}kp \right) = 0 & & \text{(I.2.5)} \end{cases}$$

The pair (p, u) represents the elasto-acoustic scattered field. p is the fluid pressure in Ω^f whereas u is the displacement field in Ω^s. $g = p^{inc} = e^{\mathrm{i}\omega/c_f x \cdot d}$ is the incident plane wave. ω is the circular frequency. c_f is a positive real number representing the sound velocity in the fluid. ρ_f and ρ_s are positive real numbers denoting respectively the densities of the fluid Ω^f and of the scatterer Ω^s. ω and c_f are associated with the wavenumber $k = \dfrac{\omega}{c_f}$. σ is the stress tensor related to the strain tensor ε by Hooke's law:

$$\sigma_{lm} = C_{lmjn} \varepsilon_{jn} \tag{I.2.6}$$

where C_{lmjn} is a fourth order elastic stiffness tensor, bounded from above, symmetric, that is $C_{lmjn} = C_{mljn} = C_{jnlm}$, and such that the coefficients C_{lmjn} satisfy:

$$C_{lmjn} \epsilon_{lm} \epsilon_{jn} \geq \alpha_\sigma \sum_{lm} \epsilon_{lm}^2, \tag{I.2.7}$$

for some positive constant α_σ, for all symmetrical second order tensor ϵ.

Note that, in the case of an isotropic medium, it is invariant under rotations and reflections [93], and reads as:

$$C_{lmjn} = \lambda\delta_{lm}\delta_{jn} + \mu(\delta_{lj}\delta_{mn} + \delta_{ln}\delta_{mj}),$$

where λ, μ are the Lamé coefficients. The strain tensor ε is related to the displacement field u by [93, 120]:

$$\varepsilon(u) = \frac{1}{2}\left(\nabla u + (\nabla u)^t\right).$$

Last, τ denotes the traction vector on the surface of the scatterer Ω^s, that is:

$$\tau(u) = \sigma(u)\nu.$$

The following observations about the linear boundary value problem BVP (1) are noteworthy [85, 104]:

- The viscoelastodynamic displacement field u and the dynamic component of the fluid pressure p satisfy respectively the Navier equation (see Eq. (I.2.2)) and the Helmholtz equation (see Eq. (I.2.1)) under the hypothesis of small amplitude oscillations both in the solid and in the fluid.
- The transmission conditions given by Eqs. (I.2.3)-(I.2.4) are kinematic and dynamic coupling conditions. They represent respectively the equality of normal displacements of the solid and the fluid and the equilibrium of forces.

I.2.2 The Weighted Sobolev Space framework

Specifying the mathematical framework is a pre-requisite for investigating the well-posed nature of BVP (1). Clearly, the standard Sobolev space $W = (H^1(\Omega^s))^3$ is the primary candidate for the displacement variable u, whereas $H^1(\Omega^f)$ is not appropriate for the fluid pressure p. The latter can be easily established by considering the asymptotic behavior of the field ([28, 118] and Eq.(A.2.17) in Appendix A.2):

$$p \sim \frac{e^{ikr}}{r} := f(r); \qquad \text{for } r = \|x\|_2 \text{ large enough}.$$

Indeed, for $D = \{x \in \mathbb{R}^3 | \|x\|_2 > 1\}$, one can show that $\|p\|_{L^2(D)}$ is infinite since we have:

$$\begin{aligned}
\|f\|_{L^2(D)} &= \int_D f\overline{f} dx \\
&= \int_D \frac{e^{\mathrm{i}kr}}{r}\frac{e^{-\mathrm{i}kr}}{r} dx \\
&= \int_D \frac{1}{r^2} dx \\
&= \int_0^{2\pi}\int_0^{\pi}\int_1^{+\infty} \frac{1}{r^2} r^2 \sin\theta dr d\theta d\phi \\
&= 2\pi \int_0^{\pi} \sin\theta d\theta \int_1^{+\infty} 1 dr \\
&= 4\pi \int_1^{+\infty} 1 dr \\
&= +\infty.
\end{aligned}$$

Hence, p is in $H^1_{loc}(\Omega^f)$, which is just a Fréchet space [3]. However, denoting $\rho(r) := 1 + r^2$, we observe that [118]:

$$\frac{p}{\rho^{1/2}} \in L^2(\Omega^f) \quad \text{and} \quad \frac{\nabla p}{\rho^{1/2}} \in (L^2(\Omega^f))^3.$$

Note that, if the origin is not located in Ω^f, then we have $\dfrac{p}{\varrho} \in L^2(\Omega^f)$ and $\dfrac{\nabla p}{\varrho} \in (L^2(\Omega^f))^3$, with $\varrho(r) := r$.

Hence, using the weight function $\dfrac{1}{\rho^{1/2}}$ or $\dfrac{1}{\varrho}$ restores the H^1 property to the pressure field. However, this does not encompass the outgoing nature of the pressure field p, as required by the Sommerfeld condition (see Eq. (I.2.5) of BVP (1)). Not incorporating explicitly such condition will affect the uniqueness of the solution p of BVP (1), since the presence of the eigenfunctions is no longer excluded.

To avoid possible loss of the uniqueness, we construct a more appropriate weighted Sobolev space as follows. First, we consider C_0^∞ the space of all functions that are infinitely differentiable with compact support. We then set:

$$C_0^\infty(\Omega^f) = \{p_{|\Omega^f} : p \in C_0^\infty(\mathbb{R}^3)\}. \tag{I.2.8}$$

We set $\rho(r) := 1 + r^2$. For $p, q \in C_0^\infty(\Omega^f)$, we consider the following inner product:

$$(p,q)_{1,\rho} := \int_{\Omega^f} \left(\frac{\nabla p \cdot \nabla \overline{q} + p\overline{q}}{\rho(r)} + \left(\frac{\partial p}{\partial r} - \mathrm{i}kp\right)\overline{\left(\frac{\partial q}{\partial r} - \mathrm{i}kq\right)} \right) dx. \tag{I.2.9}$$

Consequently, the norm corresponding to this inner product is denoted by $\|\cdot\|_{1,\rho}$, that is, $\|p\|_{1,\rho} = (p,p)_{1,\rho}^{1/2}$.
Then, the weighted Sobolev space $V_\rho = H^1_\rho(\Omega^f)$ of trial functions is defined by completion, as the closure of the space $C_0^\infty(\Omega^f)$ with respect to the norm $\|\cdot\|_{1,\rho}$, i.e., $V_\rho := H^1_\rho(\Omega^f) = \overline{C_0^\infty(\Omega^f)}^{\|\cdot\|_{1,\rho}}$.
Furthermore, since the trial functions are weighted, we need to define a different space for the test functions to derive the variational formulation corresponding to the exterior Helmholtz equation (see Eq. (I.2.1) of BVP (1)). In order to offset the weight of the trial functions, we naturally choose test functions with an inverse weight $1/\rho$. Thus, the weighted Sobolev space of test functions $H^1_{1/\rho}(\Omega^f)$ can be defined properly as the closure of $C_0^\infty(\Omega^f)$ with respect to the norm $\|\cdot\|_{1,1/\rho} := (p,p)_{1,1/\rho}^{1/2}$, i.e., $V_{1/\rho} := H^1_{1/\rho}(\Omega^f) = \overline{C_0^\infty(\Omega^f)}^{\|\cdot\|_{1,1/\rho}}$.

On the other hand, since the structural displacement field is defined inside the bounded obstacle, we consider the classical Hilbert space $W = (H^1(\Omega^s))^3$. We define the inner product for $u, v \in W$ by:

$$(u,v)_W := \int_{\Omega^s} u \cdot v \, dx + \int_{\Omega^s} \nabla u : \nabla v \, dx. \tag{I.2.10}$$

The corresponding norm in W is then given by:

$$\|u\|_W = \left(\|u\|_0^2 + \int_{\Omega^s} \nabla u : \nabla u \right)^{1/2}. \tag{I.2.11}$$

Finally, we define the trial space as $H_\rho = V_\rho \times W$. Consequently, our goal is to study the existence and uniqueness of $(p,u) \in H_\rho = V_\rho \times W$ such that the field (p,u) satisfies BVP (1).

Remark I.2.2.1 *Observe that this setting guarantees that all the integrals of the weak formulation that can be derived from BVP (1) in infinite domain are well defined. Indeed, for $(p,u) \in V_\rho \times W$ and $(q,v) \in V_{1/\rho} \times W$, we have:*

$$\left| \int_{\Omega^f} p\overline{q} dx \right| \;=\; \left| \int_{\Omega^f} \left(\frac{1}{\rho^{1/2}} p \right) (\rho^{1/2}\overline{q}) dx \right|.$$

Using Cauchy-Schwarz inequality and the definition of the weighted norm associated to Eq. (I.2.9), we obtain:

$$\begin{aligned} \left| \int_{\Omega^f} p\overline{q} dx \right| &\leq \| \frac{1}{\rho^{1/2}} p \|_0 \| \rho^{1/2} q \|_0 \\ &\leq \|p\|_{V_\rho} \|q\|_{V_{1/\rho}}. \end{aligned}$$

Similarly, we also have:

$$\begin{aligned}\left|\int_{\Omega^f}\nabla p\overline{\nabla q}dx\right| &= \left|\int_{\Omega^f}\left(\frac{1}{\rho^{1/2}}\nabla p\right)(\rho^{1/2}\overline{\nabla q})dx\right| \\ &\leq \|\frac{1}{\rho^{1/2}}\nabla p\|_0\|\rho^{1/2}\nabla q\|_0 \\ &\leq \|\nabla p\|_{V_\rho}\|\nabla q\|_{V_{1/\rho}}.\end{aligned}$$

Remark I.2.2.2 *For the boundary terms, since the obstacle is enclosed in a sphere of finite radius $r = R$, we observe that, for every point x on Γ, we have $\frac{1}{\rho(r)} \leq 1$ and $\rho(r) \leq 1 + R^2$.*
For all $(p, u) \in V_\rho \times W$ and $(q, v) \in V_{1/\rho} \times W$, we have:

$$\begin{aligned}\left|\int_\Gamma u\cdot\nu\overline{q}ds\right| &= \left|\int_\Gamma\left(\frac{1}{\rho^{1/2}}u\cdot\nu\right)(\rho^{1/2}\overline{q})ds\right| \\ &\leq \left|\int_\Gamma(u\cdot\nu)(\rho^{1/2}\overline{q})ds\right| \\ &\leq \|u\|_{(L^2(\Gamma))^3}\|\rho^{1/2}q\|_{L^2(\Gamma)} \\ &\leq \|u\|_{(H^1(\Omega^s))^3}\|\rho^{1/2}q\|_{H^1(\Omega^f)} \\ &\leq \|u\|_W\|q\|_{V_{1/\rho}}\end{aligned}$$

and

$$\begin{aligned}\left|\int_\Gamma p\nu\cdot\overline{v}ds\right| &= \left|\int_\Gamma\left(\frac{1}{\rho^{1/2}}p\right)(\rho^{1/2}\nu\cdot\overline{v})ds\right| \\ &\leq \left|\sqrt{1+R^2}\int_\Gamma\left(\frac{1}{\rho^{1/2}}p\right)(\nu\cdot\overline{v})ds\right| \\ &\leq \sqrt{1+R^2}\|\frac{1}{\rho^{1/2}}p\|_{L^2(\Gamma)}\|v\|_{(L^2(\Gamma))^3} \\ &\leq \sqrt{1+R^2}\|p\|_{V_\rho}\|v\|_W.\end{aligned}$$

Remark I.2.2.3 *It is easy to verify that, for every bounded domain $K \subset \Omega^f$, the weighted Sobolev space $H^1_\rho(K)$ coincides with the classical Hilbert space $H^1(K)$ and their norms are equivalent. Indeed, since $C^\infty_0(K)$ is dense in $H^1_\rho(K)$, it is sufficient to prove the equivalence of the norms for smooth functions.*

- *First, we have:*

$$\begin{aligned}
\|p\|_{1,\rho}^2 &= \int_K \left(\frac{\nabla p \cdot \nabla \overline{p} + p\overline{p}}{\rho(r)} + \left(\frac{\partial p}{\partial r} - \mathrm{i}kp \right) \overline{\left(\frac{\partial p}{\partial r} - \mathrm{i}kp \right)} \right) dx \\
&= \int_K \left(\frac{|\nabla p|^2 + |p|^2}{\rho(r)} + \left| \frac{\partial p}{\partial r} - \mathrm{i}kp \right|^2 \right) dx \\
&\leq \int_K \left(|\nabla p|^2 + |p|^2 + 2 \left| \frac{\partial p}{\partial r} \right|^2 + 2k^2 |p|^2 \right) dx \quad \left(\textit{using that } \frac{1}{\rho(r)} \leq 1 \right) \\
&= \|p\|_{H^1(K)}^2 + 2 \int_K \left(\left| \frac{x}{\|x\|_2} \cdot \nabla p \right|^2 + k^2 |p|^2 \right) dx \\
&\leq \|p\|_{H^1(K)}^2 + 2 \int_K \left(|\nabla p|^2 + k^2 |p|^2 \right) dx \\
&\leq max(3, 1 + 2k^2) \|p\|_{H^1(K)}^2. \qquad \text{(I.2.12)}
\end{aligned}$$

- *Second, since K is bounded, it can be enclosed in a sphere of radius $0 < R < +\infty$. Therefore, for all $x \in K$, we have: $1 + \|x\|_2^2 = \rho(r) \leq 1 + R^2$.*
  It follows that:

$$|\nabla p|^2 + |p|^2 \leq \frac{1 + R^2}{\rho(r)} \left(|\nabla p|^2 + |p|^2 \right)$$

  Since both sides are positive, integrating over K, we get:

$$\begin{aligned}
\|p\|_{H^1(K)}^2 &= \int_K \left(|\nabla p|^2 + |p|^2 \right) \\
&\leq \int_K \frac{1 + R^2}{\rho(r)} \left(|\nabla p|^2 + |p|^2 \right) \\
&\leq (1 + R^2) \int_K \left(\frac{|\nabla p|^2 + |p|^2}{\rho(r)} \right) \\
&\leq (1 + R^2) \int_K \left(\frac{|\nabla p|^2 + |p|^2}{\rho(r)} + \left| \frac{\partial p}{\partial r} - ikp \right|^2 \right) \\
&\leq (1 + R^2) \|p\|_{1,\rho}^2. \qquad \text{(I.2.13)}
\end{aligned}$$

To conclude, there exists two constants C_1, C_2 depending on k and K, such that:

$$C_1 \|p\|_{H^1(K)} \leq \|p\|_{1,\rho} \leq C_2 \|p\|_{H^1(K)}. \qquad \text{(I.2.14)}$$

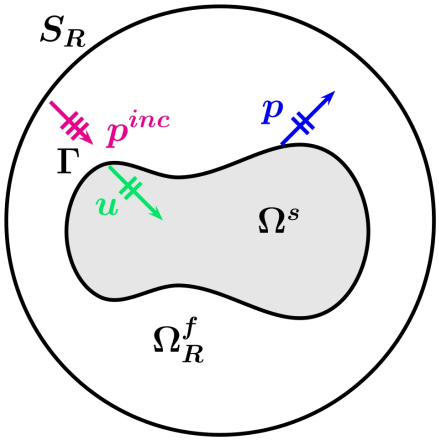

Figure I.2.2 – Problem statement in a bounded domain.

I.2.3 Formulation in a bounded domain

In the following, we reformulate BVP (1) in the bounded domain depicted in Figure I.2.2. Let B_R be the ball of radius $R > 0$ and center 0. We assume R to be large enough so that B_R contains the obstacle, i.e., $\Omega^s \subset B_R$.
The artificial exterior boundary S_R is then given by:

$$S_R = \{x \in \Omega^f / \ \|x\|_2 = R\}. \tag{I.2.15}$$

We then denote by Ω^f_R the domain in the fluid medium bounded by S_R and Γ, and by B^e_R its exterior region, that is to say,

$$\Omega^f_R = \{x \in \Omega^f / \ \|x\|_2 < R\}, \tag{I.2.16}$$

and

$$B^e_R = \mathbb{R}^3 \setminus \overline{\Omega^f_R \cup \Omega^s}. \tag{I.2.17}$$

The Sommerfeld outgoing radiation condition in BVP (1) given by Eq. (I.2.5) can be re-written as follows [28, 118]:

$$\lim_{R\to+\infty} \int_{S_R} \left| \frac{\partial p}{\partial r} - \mathrm{i}kp \right|^2 ds = 0. \tag{I.2.18}$$

Furthermore, the pressure on S_R satisfies the following Robin-type condition [see Appendix A.3]

$$\frac{\partial p}{\partial r} + T_R(p) = 0.$$

where the Dirichlet-to-Neumann operator (DtN) T_R is given by:

$$T_R(p(R,\theta,\phi)) = \sum_{n=0}^{+\infty} \mu_n(k,R) \sum_{m=-n}^{n} p_{mn} Y_{mn}(\theta,\phi), \tag{I.2.19}$$

for $\theta \in [0,\pi]$, $\phi \in [0,2\pi[$, and

- Y_{mn} represents the orthonormalized spherical harmonics of order n, $n \in \mathbb{N}$, $-n \leq m \leq n$;
- $p_{mn} = \int_{S_1} p\overline{Y}_{mn}(\theta,\phi)ds$, and S_1 denotes the unit sphere;
- $\mu_n(k,r) = -k\dfrac{h_n'(kr)}{h_n(kr)}$, and h_n designates the spherical Hankel function of the first kind (see [2] and Appendix A.1).

Note that the Dirichlet-to-Neumann operator T_R is a nonlocal mapping from $H^{1/2}(S_R)$ into $H^{-1/2}(S_R)$, that maps exactly the trace of the radiating solution onto the trace of its radial derivative on the sphere. Given that, we consider the following elasto-acoustic scattering problem defined in a bounded domain:

$$\text{BVP (2)} \quad \begin{cases} \Delta p_R + k p_R = 0 & \text{in } \Omega^f & \text{(I.2.20)} \\ \nabla \cdot \sigma(u_R) + \omega^2 \rho_s u_R = 0 & \text{in } \Omega^s & \text{(I.2.21)} \\ \omega^2 \rho_f u_R \cdot \nu = \dfrac{\partial p_R}{\partial \nu} + \dfrac{\partial g}{\partial \nu} & \text{on } \Gamma & \text{(I.2.22)} \\ \tau(u_R) = -p_R \nu - g\nu & \text{on } \Gamma & \text{(I.2.23)} \\ \dfrac{\partial p_R}{\partial r} + T_R(p_R) = 0 & \text{on } S_R\,. & \text{(I.2.24)} \end{cases}$$

Clearly, the pressure field p_R is in the classical Hilbert space $V = H^1(\Omega_R^f)$. Hence, we define $\|.\|_V$ as being the classical H^1-norm, that is, for $p \in H^1(\Omega_R^f)$, $\|p\|_V = \left(\|p\|_{0,R}^2 + \|\nabla p\|_{0,R}^2\right)^{1/2}$ where $\|\cdot\|_{0,R}^2 = \left(\int_{\Omega_R^f} |\cdot|^2 \, d\mu\right)^{1/2}$.

On the other hand, the displacement component u_R in the scatterer is in $W = \left(H^1(\Omega^s)\right)^3$. We then define the functional space H for both fields as the following product space:

$$H = V \times W = H^1(\Omega_R^f) \times \left(H^1(\Omega^s)\right)^3. \tag{I.2.25}$$

The Hilbert space H is equipped with the standard graph norm,

$$\|(p,u)\|_H = \left(\|p\|_V^2 + \|u\|_W^2\right)^{1/2}; \quad \forall\, (p,u) \in H.$$

In addition, $\langle \cdot,\cdot \rangle_{-1/2,1/2,\Gamma}$ denotes the dual product between $H^{1/2}(\Gamma)$ and $H^{-1/2}(\Gamma)$ or between $(H^{1/2}(\Gamma))^3$

and $(H^{-1/2}(\Gamma))^3$ on Γ.

BVP (2) involves the DtN operator of a sphere. We could have considered any convex regular surface. Indeed, the proof of existence and uniqueness uses properties of the DtN operator that are satisfied when the surface is convex. We have chosen to consider a sphere because we are then able to exhibit such properties by hands, employing special functions. This could be seen as a limitation, but it is nothing like as shown in the following section, the bounded problem is equivalent to the unbounded one formulated in the framework of weighted Sobolev spaces.

I.2.4 Equivalence of the infinite and bounded formulations

Thanks to the construction of the DtN operator in Appendix A.3, we have introduced an exact boundary condition at finite distance, standing for the outgoing Sommerfeld condition, on an artificial spherical boundary S_R. Hence, we have reduced the boundary value problem initially set in the infinite domain to a boundary value problem defined in a finite computational domain $B_R\,(=\Omega_R^f\times\Omega^s)$. The next result states the equivalence between both boundary value problems.

Theorem I.2.4.1 *BVP (1) and BVP (2) are equivalent in the following sense:*

i *If $(p,u)\in H_\rho$ is a solution of BVP (1), then the restriction, denoted (p_R,u_R), of (p,u) to $\Omega_R^f\times\Omega^s$ is a solution of BVP (2).*

ii *If $(p_R,u_R)\in H$ is a solution of BVP (2), then there is a field $(\tilde p,\tilde u)$ given by:*

$$\tilde p=\begin{cases} p_R & \text{in } \overline{\Omega}_R^f\\ p_R^e & \text{in } B_R^e,\end{cases}$$

where p_R^e denotes the Helmholtz solution in the exterior domain B_R^e (see Appendix A.3 for details), and $\tilde u=u_R$, such that $(\tilde p,\tilde u)$ is solution of BVP (1).

Proof The proof of this theorem relies mainly on the properties of the DtN operator T_R (see Appendix A.3)

i Let $(p,u)\in H_\rho$ be a solution of BVP (1) and (p_R,u_R) be the restriction of (p,u) to $\Omega_R^f\times\Omega^s$. Clearly, (p_R,u_R) satisfies the Helmholtz equation in Ω_R^f and the Navier equation, along with the transmission conditions on Γ.
In addition, since p belongs to V_ρ, p is also solution to the exterior Helmholtz problem in B_R^e and p admits an expansion in B_R^e. This allows us to replace the outgoing Sommerfeld condition by the exact boundary condition at finite distance on S_R, such that $p_{|S_R}=p_{R|S_R}$ satisfies

$\frac{\partial p_R}{\partial \nu} = -T_R(p_R)$ on S_R. Hence, (p_R, u_R) is the solution of BVP (2).
Furthermore, since Ω_R^f is a bounded domain, the weighted Sobolev space $H^1_\rho(\Omega_R^f)$ coincide with the classical Hilbert space $H^1(\Omega_R^f)$ (see Remark I.2.2.3). Therefore, the restricted solution (p_R, u_R) belongs to $H = H^1(\Omega_R^f) \times (H^1(\Omega^s))^3$.

ii Conversely, let $(p_R, u_R) \in H$ be the solution to the boundary value problem BVP (2). We define p_R^e as being the solution of the exterior Helmholtz problem in B_R^e with Dirichlet boundary condition $p_R = p_R^e$ on S_R. We know that p_R^e exists and admits a unique series expansion in spherical harmonics in B_R^e (see Appendix A.2). Moreover, p_R^e naturally belongs to $H^1_\rho(B_R^e)$, and by construction of the DtN operator, its expansion satisfies the same exact ABC as p_R on S_R, that is,

$$\frac{\partial p_R^e}{\partial r} + T_R(p_R^e) = 0 \quad \text{on } S_R.$$

Given that and the fact that p_R coincides with p_R^e on S_R, we define $\tilde{p}$ as follows:

$$\tilde{p} = \begin{cases} p_R & \text{in } \overline{\Omega}_R^f \\ p_R^e & \text{in } B_R^e, \end{cases}$$

and $\tilde{u} = u_R$. Since $\tilde{p}$ and its normal derivative are continuous across S_R, it follows that $(\tilde{p}, \tilde{u})$ is the unique solution to the boundary value problem BVP (1). Moreover, we can observe that $(\tilde{p}, \tilde{u})$ belongs to H_ρ. Indeed, $\tilde{u} = u_R$ clearly belongs to W. Next, we prove that $\tilde{p} \in V_\rho$. To this end, we first split the norm into two parts as follows:

$$\begin{aligned} \|\tilde{p}\|_{H^1_\rho(\Omega^f)} &= \|\tilde{p}\|_{H^1_\rho(\Omega_R^f)} + \|\tilde{p}\|_{H^1_\rho(B_R^e)} \\ &= \|p_R\|_{H^1_\rho(\Omega_R^f)} + \|p_R^e\|_{H^1_\rho(B_R^e)}. \end{aligned}$$

Moreover, since Ω_R^f is a bounded domain, the weighted norm in $H^1_\rho(\Omega_R^f)$ is equivalent to the standard norm in $H^1(\Omega_R^f)$. Actually, as shown in Remark I.2.2.3, there is a positive constant C_2, that depends on R, such that:

$$\|\tilde{p}\|_{H^1_\rho(\Omega^f)} \leq C_2 \left(\|p_R\|_{H^1(\Omega_R^f)} + \|p_R^e\|_{H^1_\rho(B_R^e)} \right).$$

Since p_R and p_R^e belong respectively to $H^1(\Omega_R^f)$ and $H^1_\rho(B_R^e)$, both terms in the previous inequality are bounded. Consequently, we have:

$$\|\tilde{p}\|_{H^1_\rho(\Omega^f)} < +\infty,$$

which leads to $\tilde{p} \in V_\rho$, and concludes the proof.

■

I.3 The Variational Formulation

We consider the boundary value problem BVP (2) set in the finite computational domain $B_R\,(= \Omega_R^f \times \Omega^s)$ and its associated variational formulation. Note that the sesquilinear form corresponding to BVP (2) is not strongly elliptic. This prevents us from applying Lax-Milgram lemma. However, using properties of the sign of the DtN operator, we prove that it is continuous and satisfies Gårding's inequality, which in turn allows to apply the Fredholm theory. Note that, for simplicity purpose, we omit in the following the subscript R on the field (p, u) and in the norms.

I.3.1 The Formulation

Consider the following variational problem associated with BVP (2):

$$\text{(VF)} \quad \begin{cases} \text{Find } (p,u) \in H, \text{ such that} \\ a((p,u),(q,v)) = l(q,v); \qquad \text{for all } (q,v) \in H, \end{cases} \tag{I.3.1}$$

where

$$\begin{cases} a((p,u),(q,v)) & = \dfrac{1}{\omega^2 \rho_f} a^f(p,q) + a^s(u,v) \\ & \quad + b((p,u),(q,v)) + b^*((p,u),(q,v)) + \dfrac{1}{\omega^2 \rho_f} c^R(p,q), \end{cases} \tag{I.3.2}$$

$$\begin{cases} l(v,q) & = \dfrac{1}{\omega^2 \rho_f} l_1(q) + l_2(v)\,, \end{cases} \tag{I.3.3}$$

and

$$\begin{cases} a^f(p,q) & = \displaystyle\int_{\Omega_R^f} \nabla p \cdot \nabla \overline{q}\, dx - \frac{\omega^2}{c_f^2} \int_{\Omega_R^f} p\overline{q}\, dx, \\ a^s(u,v) & = \displaystyle\int_{\Omega^s} \sigma(u) : \nabla \overline{v}\, dx - \omega^2 \rho_s \int_{\Omega^s} u \cdot \overline{v}\, dx, \\ b((p,u),(q,v)) & = \langle u \cdot \nu, q \rangle_{-1/2,1/2,\Gamma}, \\ b^*((p,u),(q,v)) & = \overline{b((q,v),(p,u))} \quad \text{(adjoint of } b\text{)}, \\ l_1(q) & = \langle \dfrac{\partial g}{\partial \nu}, q \rangle_{-1/2,1/2,\Gamma}, \\ l_2(v) & = -\langle p\nu, v \rangle_{-1/2,1/2,\Gamma}, \\ c^R(p,q) & = \langle T_R(p), q \rangle_{-1/2,1/2,S_R}. \end{cases} \tag{I.3.4}$$

The following theorem states the equivalence between BVP (2) and the variational problem VF given by Eq. (I.3.1).

Theorem I.3.1.1 *$(p,u) \in H$ is a solution of BVP (2) if and only if (p,u) is a solution of VF given by Eq. (I.3.1).*

Proof

i First, we show that if (p,u) is solution of the BVP (2), then $(p,u) \in H$ is a solution of the variational problem (VF) (I.3.1).
Let (q,v) be a pair of test functions in the space $\mathcal{D}(\bar{\Omega}_R^f) \times (\mathcal{D}(\bar{\Omega}^s))^3$. Integrating Eqs. (I.2.20) and(I.2.21) of BVP (2) on Ω_R^f and Ω^s respectively, we obtain:

$$\int_{\Omega_R^f} \Delta p \overline{q}\, dx + \frac{\omega^2}{c_f^2} \int_{\Omega_R^f} p\overline{q}\, dx = 0,$$
$$\int_{\Omega^s} \nabla \cdot \sigma(u) \overline{v}\, dx + \omega^2 \rho_s \int_{\Omega^s} u \cdot \overline{v}\, dx = 0.$$

Then, applying Green's formula, we deduce that:

$$\begin{aligned} &\int_{\Omega_R^f} \nabla p \cdot \nabla \overline{q}\, dx - \frac{\omega^2}{c_f^2} \int_{\Omega_R^f} p\overline{q}\, dx + \langle \nabla p \cdot \nu, q \rangle_{-1/2,1/2,\Gamma} - \langle \nabla p \cdot \nu, q \rangle_{-1/2,1/2,S_R} = 0, \\ &\int_{\Omega^s} \sigma(u) : \nabla \overline{v}\, dx - \omega^2 \rho_s \int_{\Omega^s} u \cdot \overline{v}\, dx - \langle \sigma(u) \cdot \nu, v \rangle_{-1/2,1/2,\Gamma} = 0. \end{aligned} \tag{I.3.5}$$

Hence, it follows from substituting both transmission conditions Eqs. (I.2.22) and (I.2.23) of

BVP (2) into Eq. (I.3.5), that:

$$\int_{\Omega_R^f} \nabla p \cdot \nabla \overline{q}\, dx - \frac{\omega^2}{c_f^2} \int_{\Omega_R^f} p\overline{q}\, dx + \langle \omega^2 \rho_f u \cdot \nu, q\rangle_{-1/2,1/2,\Gamma} - \langle \nabla p \cdot \nu, q\rangle_{-1/2,1/2,S_R}$$
$$= \langle \frac{\partial g}{\partial \nu}, q\rangle_{-1/2,1/2,\Gamma}, \qquad \text{(I.3.6)}$$

$$\int_{\Omega^s} \sigma(u) : \nabla \overline{v}\, dx - \omega^2 \rho_s \int_{\Omega^s} u \cdot \overline{v}\, dx + \langle p\nu, v\rangle_{-1/2,1/2,\Gamma}$$
$$= -\langle g\nu, v\rangle_{-1/2,1/2,\Gamma}. \qquad \text{(I.3.7)}$$

Note that in spherical coordinates, we have: $\nabla p \cdot \nu = \dfrac{\partial p}{\partial r}$ on S_R.
Furthermore, substituting Eq. (I.2.24) of BVP (2) into Eq. (I.3.6) leads to the following variational formulation, for all $(q, v) \in \mathcal{D}(\bar{\Omega}_R^f) \times (\mathcal{D}(\bar{\Omega}^s))^3$,

$$\int_{\Omega_R^f} \nabla p \cdot \nabla \overline{q}\, dx - \frac{\omega^2}{c_f^2} \int_{\Omega_R^f} p\overline{q}\, dx + \omega^2 \rho_f \langle u \cdot \nu, q\rangle_{-1/2,1/2,\Gamma} + \langle T_R(p), q\rangle_{-1/2,1/2,S_R}$$
$$= \langle \frac{\partial g}{\partial \nu}, q\rangle_{-1/2,1/2,\Gamma}, \qquad \text{(I.3.8)}$$

$$\int_{\Omega^s} \sigma(u) : \nabla \overline{v}\, dx - \omega^2 \rho_s \int_{\Omega^s} u \cdot \overline{v}\, dx + \langle p\nu, v\rangle_{-1/2,1/2,\Gamma}$$
$$= -\langle g\nu, v\rangle_{-1/2,1/2,\Gamma}. \qquad \text{(I.3.9)}$$

Since $\mathcal{D}(\bar{\Omega}_R^f) \times (\mathcal{D}(\bar{\Omega}^s))^3$ is dense into $H^1(\Omega_R^f) \times (H^1(\Omega^s))^3$, the problem can thus be rewritten as follows:

$$\text{(VF)} \quad \begin{cases} \text{Find } (p, u) \in H, \text{ such that} & \\ a^f(p, q) + \omega^2 \rho_f b((p, u), (q, v)) + c^R(p, q) = l_1(q); & \forall\, q \in V, \qquad \text{(I.3.10)} \\ a^s(u, v) + b^*((p, u), (q, v)) = l_2(v); & \forall\, v \in W. \qquad \text{(I.3.11)} \end{cases}$$

Hence, VF given by Eq. (I.3.1) is an immediate consequence of adding Eq.(I.3.10) to Eq.(I.3.11).

ii Conversely, we prove that if $(p, u) \in H$ is the solution of the variational problem VF given by Eq. (I.3.1), then (p, u) is the solution of BVP (2). Indeed, let $(\varphi, \phi) \in \mathcal{D}(\Omega_R^f) \times (\mathcal{D}(\Omega^s))^3$. If $(\varphi, \phi) = (\varphi, 0)$, then we have:

$$a^f(p, \varphi) = 0. \qquad \text{(I.3.12)}$$

Similarly, let $(\varphi, \phi) = (0, \phi)$. Since ϕ vanishes in the neighborhood of Γ, we obtain:

$$a^s(u, \phi) = 0. \qquad \text{(I.3.13)}$$

Hence, we have:

$$\begin{aligned}\int_{\Omega_R^f} \nabla p \cdot \nabla \overline{\varphi}\, dx - \frac{\omega^2}{c_f^2} \int_{\Omega_R^f} p\overline{\varphi}\, dx &= 0, \quad \text{for any } \varphi \in \mathcal{D}(\Omega_R^f),\\ \int_{\Omega^s} \sigma(u) : \nabla \overline{\phi}\, dx - \omega^2 \rho_s \int_{\Omega^s} u \cdot \overline{\phi}\, dx &= 0, \quad \text{for any } \phi \in (\mathcal{D}(\Omega^s))^3.\end{aligned}$$

Therefore, we deduce that, in the distribution sense at least, p and u satisfy:

$$\begin{aligned}\Delta p + \frac{\omega^2}{c_f^2} p &= 0, \quad \text{in } \mathcal{D}'(\Omega_R^f),\\ \nabla \cdot \sigma(u) + \omega^2 \rho_s u &= 0, \quad \text{in } (\mathcal{D}'(\Omega^s))^3.\end{aligned}$$

Moreover, since $p \in H^1(\Omega_R^f)$, $\Delta p \in H^1(\Omega_R^f)$. Similarly, since $u \in (H^1(\Omega^s))^3$, then $\nabla \cdot \sigma(u) \in (H^1(\Omega^s))^3$. It follows that the pair $(p, u) \in H$ and satisfies the Helmholtz and Navier equations in L^2. Consequently, we have:

$$\begin{aligned}\Delta p + \frac{\omega^2}{c_f^2} p &= 0 \quad \text{a.e. in } \Omega_R^f,\\ \nabla \cdot \sigma(u) + \omega^2 \rho_s u &= 0 \quad \text{a.e. in } \Omega^s.\end{aligned}$$

Next, we analyze the behavior of p and u at the boundaries. Let $(\varphi, \phi) \in \mathcal{D}(\overline{\Omega}_R^f) \times (\mathcal{D}(\overline{\Omega}^s))^3$. We set $\phi = 0$. Then,

$$a^f(p, \varphi) + \omega^2 \rho_f b((p, u), (\varphi, \phi)) + c^R(p, \varphi) = l_1(\varphi). \tag{I.3.14}$$

In addition, for $\varphi = 0$, we obtain:

$$a^s(u, \phi) + b^*((p, u), (\varphi, \phi)) = l_2(\phi). \tag{I.3.15}$$

Consequently, we have:

$$\int_{\Omega_R^f} \nabla p \cdot \nabla \overline{\varphi}\, dx - \frac{\omega^2}{c_f^2} \int_{\Omega_R^f} p\overline{\varphi}\, dx + \omega^2 \rho_f \langle u \cdot \nu, \varphi \rangle_{-1/2,1/2,\Gamma} + \langle T_R(p), \varphi \rangle_{-1/2,1/2,S_R} = \langle \frac{\partial g}{\partial \nu}, \varphi \rangle_{-1/2,1/2,\Gamma} \tag{I.3.16}$$

$$\int_{\Omega^s} \sigma(u) : \nabla \overline{\phi}\, dx - \omega^2 \rho_s \int_{\Omega^s} u \cdot \overline{\phi}\, dx + \langle p\nu, \phi \rangle_{-1/2,1/2,\Gamma} = -\langle p\nu, \phi \rangle_{-1/2,1/2,\Gamma}. \tag{I.3.17}$$

Applying again the Green's theorem to Eqs. (I.3.16)-(I.3.17), we obtain:

$$\int_{\Omega_R^f}(\Delta p+\frac{\omega^2}{c_f^2}p)\overline{\varphi}\,dx+\langle\frac{\partial p}{\partial\nu},\varphi\rangle_{-1/2,1/2,\Gamma}-\omega^2\rho_f\langle u\cdot\nu,\varphi\rangle_{-1/2,1/2,\Gamma}-\langle\frac{\partial p}{\partial\nu},\varphi\rangle_{-1/2,1/2,S_R}$$
$$-\langle T_R(p),\varphi\rangle_{-1/2,1/2,S_R}=-\langle\frac{\partial g}{\partial\nu},\varphi\rangle_{-1/2,1/2,\Gamma},\quad\text{for all }\varphi\in\mathcal{D}(\overline{\Omega}_R^f),\quad\text{(I.3.18)}$$
$$\int_{\Omega^s}(\nabla\cdot\sigma(u)+\omega^2\rho_s u)\cdot\overline{\phi}\,dx-\langle\sigma(u)\cdot\nu,\phi\rangle_{-1/2,1/2,\Gamma}-\langle p\nu,\phi\rangle_{-1/2,1/2,\Gamma}$$
$$=\langle p\nu,\phi\rangle_{-1/2,1/2,\Gamma},\quad\text{for all }\phi\in(\mathcal{D}(\overline{\Omega}^s))^3.\quad\text{(I.3.19)}$$

Since p (resp. u) satisfies the Helmholtz (resp. Navier) equation, then it follows from Eqs. (I.3.18)-(I.3.19) that:

$$\langle\frac{\partial p}{\partial\nu},\varphi\rangle_{-1/2,1/2,\Gamma}-\langle\omega^2\rho_f u\cdot\nu,\varphi\rangle_{-1/2,1/2,\Gamma}-\langle\frac{\partial p}{\partial r},\varphi\rangle_{-1/2,1/2,S_R}-\langle T_R(p),\varphi\rangle_{-1/2,1/2,S_R}$$
$$=-\langle\frac{\partial g}{\partial\nu},\varphi\rangle_{-1/2,1/2,\Gamma},\quad\text{for all }\varphi\in\mathcal{D}(\overline{\Omega}_R^f),$$
$$-\langle\sigma(u)\cdot\nu,\phi\rangle_{-1/2,1/2,\Gamma}-\langle p\nu,\phi\rangle_{-1/2,1/2,\Gamma}=\langle p\nu,\phi\rangle_{-1/2,1/2,\Gamma},\quad\text{for all }\phi\in(\mathcal{D}(\overline{\Omega}^s))^3.$$

Finally, taking φ that vanishes on S_R, we obtain the transmission conditions on the Lipschitz fluid-structure interface Γ:

$$\omega^2\rho_f u\cdot\nu=\frac{\partial p}{\partial\nu}+\frac{\partial g}{\partial\nu}\quad\text{in }H^{-1/2}(\Gamma)\qquad\text{(I.3.20)}$$
$$\sigma(u)\cdot\nu=-p\nu-g\nu\quad\text{in }(H^{-1/2}(\Gamma))^3.\qquad\text{(I.3.21)}$$

Next, for ϕ vanishing in a neighborhood of Γ, we obtain the boundary condition on S_R:

$$\frac{\partial p}{\partial r}+T_R(p)=0\quad\text{in }H^{-1/2}(S_R).\qquad\text{(I.3.22)}$$

Since p is in $H^1(\Omega_R^f)$, it follows from the classical trace theorems [18, 30, 35, 70] that $p\in H^{1/2}(\Gamma)$. By multiplying p by the normal vector which is L^∞, we obtain $pn\in L^2(\Gamma)$. Similarly, since $u\in(H^1(\Omega^s))^3$, $u_{|\Gamma}$ exists in $(H^{1/2}(\Gamma))^3$, and its normal trace $u\cdot n$ on Γ is defined in $L^2(\Gamma)$. Using the fact that g is sufficiently regular, and since the fields are linked via the transmission conditions, we thus get that $\nabla p\cdot n$ and $\sigma(u)\cdot n$ have a sense in $L^2(\Gamma)$ and $(L^2(\Gamma))^3$ respectively. Furthermore, in the neighborhood of the smooth spherical artificial boundary S_R, the solution p is $\mathcal{C}^\infty$. Therefore, the normal derivative of p on S_R is at least in $L^2(S_R)$, and thus, $T_R(p)\in L^2(S_R)$. Finally, it follows that Eqs (I.3.20), (I.3.21) and (I.3.22) remain valid in $L^2(\Gamma)$,$(L^2(\Gamma))^3$, $L^2(S_R)$

respectively, that is:

$$\begin{aligned} \rho_f \omega^2 u \cdot \nu &= \frac{\partial p}{\partial \nu} + \frac{\partial g}{\partial \nu} \quad \text{on } \Gamma, \\ \sigma(u) \cdot \nu &= -p\nu - p\nu \quad \text{on } \Gamma, \\ \frac{\partial p}{\partial r} + T_R(p) &= 0 \qquad\quad \text{on } S_R. \end{aligned}$$

In summary, we have proven that $(p, u) \in H$ is the solution of the direct elasto-acoustic problem BVP (2).

■

Remark I.3.1.1 *It is worth noting that the solution is in fact more regular than stated. Indeed, since* $p \in H^1(\Omega_R^f)$*, and* $\nabla p \cdot \nu \in L^2(\Gamma) \cup L^2(S_R)$*, then, according to Jerison-Kenig [90], we have* $p \in H^{3/2}(\Omega_R^f)$*. Similarly, from the results extended to the elastic case [36],* $u \in (H^1(\Omega^s))^3$ *together with* $\sigma(u) \cdot \nu \in (L^2(\Gamma))^3$ *imply that* $u \in (H^{3/2}(\Omega^s))^3$*.*

I.3.2 Mathematical Properties

The goal here is to employ the Fredholm alternative to establish existence and uniqueness results. Our approach relies on the following result [60, 87]:
Assume that the formulation satisfies a Gårding's inequality of the form:

$$Re[a((p,u),(p,u))] + C_U \|(p,u)\|_U^2 \geq \alpha \|(p,u)\|_H^2; \quad \forall\, (p,u) \in H,$$

where the Hilbert space H is compactly embedded in the Hilbert space U. Then, the Fredholm alternative can be applied since the operator $K : H \to H'$ (the dual space of H) defined by $K(p,u) = \|(p,u)\|_U$ is a compact perturbation of the operator corresponding to the sesquilinear form $a(\cdot,\cdot)$. It follows that the uniqueness of the solution (p,u) of the variational problem ensures its existence.
Consequently, all w<e need to show in what follows is that the sesquilinear form $a(\cdot,\cdot)$ given by Eq. (I.3.2) is continuous and satisfies the Gårding's inequality. The latter is established using the sign properties of the real part and imaginary part of the Dirichlet-to-Neumann form $c^R(\cdot,\cdot)$ given by Eq. (I.3.4).

I.3.2.1 Properties of the Dirichlet-to-Neumann operator

First, we establish two fundamental sign properties on the DtN operator.

Lemma 1 *Let k be a positive number and $r \geq R$. Then,*

$$Re\left(\mu_n(k,r)\right) > 0, \quad \forall\, n \in \mathbb{N}. \tag{I.3.23}$$

Proof From the definition of the spherical Hankel functions of the first kind (see Eq. (A.1.5) in Appendix A.1), the coefficients $\mu_n(k,r)$ can be written as:

$$\mu_n(k,r) = -k\frac{j_n'(kr) + \mathrm{i}y_n'(kr)}{j_n(kr) + \mathrm{i}y_n(kr)}. \tag{I.3.24}$$

Taking the real part of Eq. (I.3.24), we obtain:

$$\begin{aligned} Re\left(\mu_n(k,r)\right) &= -k\frac{j_n'(kr)j_n(kr) + y_n'(kr)y_n(kr)}{j_n^2(kr) + y_n^2(kr)} \\ &= -k\frac{\dfrac{1}{2}(m_n^2)'(kr)}{m_n^2(kr)}. \end{aligned} \tag{I.3.25}$$

where

$$m_n^2(kr) = j_n^2(kr) + y_n^2(kr). \tag{I.3.26}$$

On the other hand, we know (see Proposition A.1.1.1) that, $(m_n^2)'(kr) < 0$. Hence, it follows from Eq. (I.3.25) that:

$$Re\left(\mu_n(k,r)\right) > 0, \tag{I.3.27}$$

which concludes the proof of Lemma 1.

■

Lemma 2 *Let k be a positive number and $r \geq R$. Then,*

$$Im\left(\mu_n(k,r)\right) < 0, \quad \forall\, n \in \mathbb{N}. \tag{I.3.28}$$

Proof The proof relies on the properties of the Wronskian (see Appendix A.1).
Taking the imaginary part of Eq. (I.3.24) leads to:

$$Im\left(\mu_n(k,r)\right) = -k\frac{j_n(kr)y_n'(kr) - j_n'(kr)y_n(kr)}{j_n^2(kr) + y_n^2(kr)}. \tag{I.3.29}$$

From the definition of m_n^2 (see Eq. I.3.26)) and Proposition A.1.1.2, we deduce that:

$$Im\left(\mu_n(k,r)\right) = -k\frac{W(j_n(kr), y_n(kr))}{m_n^2(kr)} \quad < \quad 0, \tag{I.3.30}$$

where $W(\cdot,\cdot)$ is the Wronskian defined in Proposition A.1.1.2.

■

Then, we prove the following sign properties on the Dirichlet-to-Neumann form $c^R(\cdot,\cdot)$ given by Eq. (I.3.4).

Proposition I.3.2.1 *Let $c^R(\cdot,\cdot)$ be the sesquilinear form given by Eq. (I.3.4). Then,*

$$Re\left[c^R(p,p)\right] > 0, \qquad \forall\, p \in H^{1/2}(S_R)\setminus\{0\} \tag{I.3.31}$$

$$Im\left[c^R(p,p)\right] < 0. \tag{I.3.32}$$

Proof From the definition of the DtN operator (see Eq. (I.2.19)) and the orthogonality properties of the spherical harmonics Y_{mn} (see, for e.g., [2] or Appendix A.1.2), the sesquilinear form $c^R(\cdot,\cdot)$ (see Eq. I.3.4) can be re-written as follows:

$$c^R(p,q) := \langle T_R(p), q\rangle_{-1/2,1/2,S_R} = \sum_{n=0}^{+\infty}\mu_n(k,R)\sum_{m=-n}^{n} p_{mn}\overline{q_{mn}}, \quad \forall\, p,q \in L^2(S_R). \tag{I.3.33}$$

Hence,

$$c^R(p,p) = \sum_{n=0}^{+\infty}\mu_n(k,R)\sum_{m=-n}^{n}|p_{mn}|^2, \quad \forall\, p \in L^2(S_R). \tag{I.3.34}$$

The result is then an immediate consequence of the definition of $c^R(\cdot,\cdot)$ given by Eq. (I.3.34) and Lemmas 1 and 2.

■

I.3.2.2 Continuity

We prove in this section the following continuity result on the sesquilinear form $a(\cdot,\cdot)$ given by Eq. (I.3.2).

Lemma 3 *The sesquilinear form $a(\cdot,\cdot)$ given by Eq. (I.3.2) is continuous on $H\times H$, that is, there exists a positive constant C_a such that,*

$$|a((p,u),(q,v))| \quad \leq \quad C_a\|(p,u)\|_H\|(q,v)\|_H; \quad \forall\,(p,u)\in H \text{ and } \forall\,(q,v)\in H. \tag{I.3.35}$$

Furthermore, the form $l(\cdot)$ given by Eq. (I.3.3) is a linear form continuous on H.

Proof Let $(p,u),(q,v) \in H$. We can bound each form in $a(\cdot,\cdot)$ defined in Eq. (I.3.2) separately as follows. First, we have:

$$\begin{aligned}
|a^f(p,q)| &= \left| \int_{\Omega_R^f} \nabla p \cdot \nabla \overline{q}\, dx - \frac{\omega^2}{c_f^2} \int_{\Omega_R^f} p\overline{q}\, dx \right| \\
&\leq \left| \int_{\Omega_R^f} \nabla p \cdot \nabla \overline{q}\, dx \right| + \frac{\omega^2}{c_f^2} \left| \int_{\Omega_R^f} p\overline{q}\, dx \right| \\
&\leq \|\nabla p\|_0 \|\nabla q\|_0 + \frac{\omega^2}{c_f^2} \|p\|_0 \|q\|_0 \\
&\leq \max\left(1, \frac{\omega^2}{c_f^2}\right) (\|\nabla p\|_0 + \|p\|_0)(\|\nabla q\|_0 + \|q\|_0) \\
&\leq 2\max\left(1, \frac{\omega^2}{c_f^2}\right) (\|\nabla p\|_0^2 + \|p\|_0^2)^{1/2} (\|\nabla q\|_0^2 + \|q\|_0^2)^{1/2} \\
&\leq 2\max\left(1, \frac{\omega^2}{c_f^2}\right) \|p\|_V \|q\|_V. \qquad \text{(I.3.36)}
\end{aligned}$$

We set

$$C_1 = 2\max\left(1, \frac{\omega^2}{c_f^2}\right). \qquad \text{(I.3.37)}$$

Then, we deduce that:

$$|a^f(p,q)| \leq C_1 \|p\|_V \|q\|_V; \quad \forall\, p,q \in V, \qquad \text{(I.3.38)}$$

which proves the continuity of $a^f(\cdot,\cdot)$ on $V \times V$.

Similarly, we have:

$$\begin{aligned}
|a^s(u,v)| &= \left| \int_{\Omega^s} \sigma(u) : \nabla \overline{v}\, dx - \omega^2 \rho_s \int_{\Omega^s} u \cdot \overline{v}\, dx \right| \\
&\leq \left| \int_{\Omega^s} \sigma(u) : \nabla \overline{v}\, dx \right| + \omega^2 \rho_s \left| \int_{\Omega^s} u \cdot \overline{v}\, dx \right| \\
&\leq \left| \int_{\Omega^s} \sigma(u) : \nabla \overline{v}\, dx \right| + \omega^2 \rho_s \|u\|_0 \|v\|_0. \qquad \text{(I.3.39)}
\end{aligned}$$

On the other hand, the stress tensor σ is related to the strain tensor ε by Hooke's law as follows:

$$\sigma_{lm} = C_{lmjn} \varepsilon_{jn}, \qquad \text{(I.3.40)}$$

Assuming that $C_{lmjn} \in L^\infty(\Omega^s)$, we denote $C_\sigma = \sup_{lmjn} |C_{lmjn}|$. It follows from Eq. (I.3.40) that:

$$\begin{aligned} \left| \int_{\Omega^s} \sigma(u) : \nabla \overline{v}\, dx \right| &= \left| \int_{\Omega^s} \sigma(u) : \varepsilon(\overline{v})\, dx \right| \qquad \text{(I.3.41)} \\ &= \left| \int_{\Omega^s} \sum_{lm} \left(\sum_{jn} C_{lmjn} \varepsilon_{jn}(u) \right) \varepsilon_{lm}(\overline{v}) dx \right| \\ &\leq C_\sigma \left| \int_{\Omega^s} \sum_{lm} \left(\sum_{jn} \varepsilon_{jn}(u) \right) \varepsilon_{lm}(\overline{v}) dx \right| \\ &\leq 9 C_\sigma \|\varepsilon(u)\|_0 \|\varepsilon(v)\|_0. \qquad \text{(I.3.42)} \end{aligned}$$

Substituting Eq. (I.3.42) into Eq. (I.3.39), and using the fact that $\|\varepsilon(u)\|_0 \leq \|\nabla u\|_0$, leads to:

$$\begin{aligned} |a^s(u,v)| &\leq 9 C_\sigma \|\nabla u\|_0 \|\nabla v\|_0 + \omega^2 \rho_s \|u\|_0 \|v\|_0 \\ &\leq 2 \max\left(9 C_\sigma, \omega^2 \rho_s\right) \|u\|_W \|v\|_W. \end{aligned}$$

We set

$$C_2 = 2 \max\left(9 C_\sigma, \omega^2 \rho_s\right). \qquad \text{(I.3.43)}$$

Therefore,

$$|a^s(u,v)| \leq C_2 \|u\|_W \|v\|_W; \quad \forall\, u, v \in W, \qquad \text{(I.3.44)}$$

which proves the continuity of $a^s(\cdot,\cdot)$ on $W \times W$.

Furthermore, using the continuity of the trace mappings [30, 35, 70] from $H^1(\Omega_R^f)$ into $L^2(\Gamma)$, and from $(H^1(\Omega^s))^3$ into $(L^2(\Gamma))^3$ respectively, we obtain that:

$$\begin{aligned} |b((p,u),(q,v))| &= \left| \int_\Gamma u \cdot \nu \overline{q}\, d\sigma \right| \\ &\leq \|u \cdot \nu\|_{L^2(\Gamma)} \|q\|_{L^2(\Gamma)} \\ &\leq \|u\|_{(L^2(\Gamma))^3} \|q\|_{L^2(\Gamma)} \\ &\leq C \|u\|_W \|q\|_V \\ &\leq C \left(\|p\|_V^2 + \|u\|_W^2 \right)^{1/2} \left(\|q\|_V^2 + \|v\|_W^2 \right)^{1/2}, \end{aligned} \qquad \text{(I.3.45)}$$

for some positive constant C. Hence,

$$|b((p,u),(q,v))| \leq C_b\|(p,u)\|_H\|(q,v)\|_H; \quad \forall\,(p,u),(q,v)\in H, \tag{I.3.46}$$

which proves the continuity of $b(\cdot,\cdot)$ on $H\times H$.

Finally, using the continuity of the DtN operator from $H^{1/2}(S_R)$ into $H^{-1/2}(S_R)$, together with the classical trace theorems [70, 101], we obtain that:

$$\begin{aligned} |c^R(p,q)| &= |\langle T_R(p),q\rangle_{-1/2,1/2,S_R}| \\ &\leq \|T_R(p)\|_{H^{-1/2}(S_R)}\|q\|_{H^{1/2}(S_R)} \\ &\leq C\|p\|_{H^{1/2}(S_R)}\|q\|_{H^{1/2}(S_R)}. \\ &\leq C_R\|p\|_V\|q\|_V, \end{aligned} \tag{I.3.47}$$

for some positive constant C_R that depends on R.

To conclude, it follows from Eq. (I.3.38), Eq. (I.3.44), Eq. (I.3.46) and Eq. (I.3.47) that:

$$\begin{aligned} |a((p,u),(q,v))| &\leq \frac{1}{\omega^2\rho_f}C_1\|p\|_V\|q\|_V + C_2\|u\|_W\|v\|_W \\ &\quad +2C_b\|(p,u)\|_H\|(q,v)\|_H + \frac{1}{\omega^2\rho_f}C_R\|p\|_V\|q\|_V \\ &\leq \max\left(\frac{1}{\omega^2\rho_f}(C_1+C_R),C_2\right)(\|p\|_V+\|u\|_W)(\|q\|_V+\|v\|_W) \\ &\quad +2C_b\|(p,u)\|_H\|(q,v)\|_H \\ &\leq 2\max\left(\frac{1}{\omega^2\rho_f}(C_1+C_R),C_2\right)(\|p\|_V^2+\|u\|_W^2)^{1/2}(\|q\|_V^2+\|v\|_W^2)^{1/2} \\ &\quad +2C_b\|(p,u)\|_H\|(q,v)\|_H \end{aligned} \tag{I.3.48}$$

We set

$$C_a = 2\left(\max\left(\frac{1}{\omega^2\rho_f}(C_1+C_R),C_2\right)+C_b\right). \tag{I.3.49}$$

Therefore,

$$|a((p,u),(q,v))| \leq C_a\|(p,u)\|_H\|(q,v)\|_H; \quad \forall\,(p,u),(q,v)\in H, \tag{I.3.50}$$

which proves the continuity of the sesquilinear form $a(\cdot,\cdot)$.
Note that the continuity of the linear form $l(\cdot)$ is an immediate consequence of employing Cauchy-Schwarz inequality.

■

I.3.2.3 Gårding's inequality

The goal here is to prove that $a(\cdot,\cdot)$ satisfies Gårding's inequality on H. First, let U be the following Hilbert space:

$$U = L^2(\Omega_R^f) \times (L^2(\Omega^s))^3,$$

equipped with the standard graph norm. Then, we have: $H \subset U \subset H'$, with dense embeddings and, from Rellich-Kondrachov theorem [3], the compact embedding $H \subset\subset U$. Our goal is to establish the following proposition:

Proposition I.3.2.2 *The sesquilinear form $a(\cdot,\cdot)$ given by Eq. (I.3.2) satisfies Gårding's inequality on H, that is, there are two constants $C_U \geq 0$ and $\alpha > 0$ such that:*

$$Re[a((p,u),(p,u))] + C_U\|(p,u)\|_U^2 \geq \alpha\|(p,u)\|_H^2; \quad \forall\,(p,u) \in H. \tag{I.3.51}$$

Proof Take $(p,u) \in H$. We proceed for each form in $a(\cdot,\cdot)$ defined by Eq. (I.3.2) separately as follows.
For $p \in V$, it follows from Eq. (I.3.4) that:

$$\begin{aligned} a^f(p,p) &= \int_{\Omega_R^f} \nabla p \cdot \nabla \overline{p}\, dx - \frac{\omega^2}{c_f^2}\int_{\Omega_R^f} p\overline{p}\, dx \\ &= \|\nabla p\|_0^2 - \frac{\omega^2}{c_f^2}\|p\|_0^2. \end{aligned}$$

We thus obtain:

$$a^f(p,p) + \frac{\omega^2}{c_f^2}\|p\|_0^2 = \|\nabla p\|_0^2; \quad \forall\, p \in V. \tag{I.3.52}$$

Moreover, since all the terms in Eq. (I.3.52) are real, we conclude that the sesquilinear form $a^f(\cdot,\cdot)$ is V-coercive.
We set

$$C_1 = \frac{1}{\omega^2\rho_f}\left(1 + \frac{\omega^2}{c_f^2}\right) \quad \text{and} \quad \alpha_1 = \frac{1}{\omega^2\rho_f}. \tag{I.3.53}$$

Then,

$$\frac{1}{\omega^2\rho_f} Re\,[a^f(p,p)] + C_1\|p\|_0^2 \;=\; \alpha_1\|p\|_V^2; \quad \forall\, p \in V. \tag{I.3.54}$$

Similarly, take $u \in W$. Using Hooke's law and the property of the stiffness tensor given by Eq. (I.2.6) and Eq. (I.2.7), it follows from Eq. (I.3.4) that:

$$\begin{aligned}
a^s(u,u) &= \int_{\Omega^s} \sigma(u) : \nabla\overline{u}\, dx - \omega^2\rho_s \int_{\Omega^s} |u|^2\, dx \\
&= \int_{\Omega^s} \sigma(u) : \varepsilon(\overline{u})\, dx - \omega^2\rho_s \int_{\Omega^s} |u|^2\, dx \\
&= \int_{\Omega^s} \sum_{lm}\sum_{jn} C_{lmjn}\varepsilon_{jn}(u)\varepsilon_{lm}(\overline{u})\, dx - \omega^2\rho_s \int_{\Omega^s} |u|^2\, dx \\
&\geq \alpha_\sigma \int_{\Omega^s} \sum_{lm} \varepsilon_{lm}(u)\varepsilon_{lm}(\overline{u})\, dx - \omega^2\rho_s \int_{\Omega^s} |u|^2\, dx \\
&\geq \alpha_\sigma \int_{\Omega^s} \varepsilon(u) : \varepsilon(\overline{u})\, dx - \omega^2\rho_s \int_{\Omega^s} |u|^2\, dx.
\end{aligned}$$

We thus deduce:

$$a^s(u,u) \;\geq\; \alpha_\sigma\|\varepsilon(u)\|_0^2 - \omega^2\rho_s\|u\|_0^2, \tag{I.3.55}$$

which proves that $a^s(u,u)$ is a real number.
In addition, since Ω^s has a Lipschitz boundary, the second Korn's inequality ([44, 119]) holds and ensures the existence of a constant $C_k > 0$ such that:

$$\|\varepsilon(u)\|_0^2 + \|u\|_0^2 \geq C_k\|u\|_W^2; \quad \forall\, u \in W. \tag{I.3.56}$$

Combining Eq. (I.3.56) with Eq. (I.3.55), we obtain:

$$\begin{aligned}
Re\,[a^s(u,u)] &\geq \alpha_\sigma C_k\|u\|_W^2 - \alpha_\sigma\|u\|_0^2 - \omega^2\rho_s\|u\|_0^2 \\
&\geq \alpha_\sigma C_k\|u\|_W^2 - (\alpha_\sigma + \omega^2\rho_s)\|u\|_0^2.
\end{aligned}$$

We set

$$C_2 = (\alpha_\sigma + \omega^2\rho_s) \quad \text{and} \quad \alpha_2 = \alpha_\sigma C_k. \tag{I.3.57}$$

Therefore, we have:

$$Re\,[a^s(u,u)] + C_2\|u\|_0^2 \;\geq\; \alpha_2\|u\|_W^2; \quad \forall\, u \in W, \tag{I.3.58}$$

which proves the W-coercivity of $a^s(\cdot,\cdot)$.

Furthermore, since $u \in (H^1(\Omega^s))^3$, then $u \cdot \nu \in L^2(\Gamma)$. In addition, $H^\epsilon(\Gamma)$ is compactly embedded in $L^2(\Gamma)$, for any ϵ such that $0 < \epsilon < 1$. Moreover, the trace theorem given in [30] is valid for Lipschitz domain. Hence, the trace mapping is linear continuous from $H^{1/2+\epsilon}(\Omega)$ into $H^\epsilon(\Gamma)$, for all $0 < \epsilon < 1$. Take $\epsilon = 1/4$. Then,

$$\begin{aligned} |b(p,u),(p,u)| &= \left|\int_\Gamma u\cdot\nu p\right| \\ &\leq \|u\cdot\nu\|_{L^2(\Gamma)}\|p\|_{L^2(\Gamma)} \\ &\leq C\|u\|_{(L^2(\Gamma))^3}\|p\|_{L^2(\Gamma)} \\ &\leq C\|u\|_{(H^{1/4}(\Gamma))^3}\|p\|_{H^{1/4}(\Gamma)} \\ &\leq C\|u\|_{(H^{3/4}(\Omega^s))^3}\|p\|_{H^{3/4}(\Omega_R^f)} \\ &\leq C\|(p,u)\|^2_{(H^{3/4}(\Omega^s))^3\times H^{3/4}(\Omega_R^f)}. \end{aligned} \tag{I.3.59}$$

Furthermore, for any $\delta > 0$, there is a constant C_δ such that:

$$\|(p,u)\|^2_{(H^{3/4}(\Omega^s))^3\times H^{3/4}(\Omega_R^f)} \leq \delta\|(\nabla p,\nabla u)\|^2_U + C_\delta\|(p,u)\|^2_U, \quad \forall\,(p,u)\in H. \tag{I.3.60}$$

Hence, we deduce:

$$\begin{aligned} &|Re\,[b((p,u),(p,u)) + b^*((p,u),(p,u))]| \\ &= |2Re\,[b((p,u),(p,u))]| \\ &\leq C\left(\delta\|(\nabla p,\nabla u)\|^2_U + C_\delta\|(p,u)\|^2_U\right) \\ &\leq C\left(\delta\|(p,u)\|^2_H + C_\delta\|(p,u)\|^2_U\right). \end{aligned}$$

Consequently, we have:

$$Re\,[b((p,u),(p,u)) + b^*((p,u),(p,u))] \geq -C\delta\|(p,u)\|^2_H - CC_\delta\|(p,u)\|^2_U. \tag{I.3.61}$$

Therefore, for any $\delta > 0$, there is a constant $C_b > 0$ such that:

$$Re\,[b((p,u),(p,u)) + b^*((p,u),(p,u))] + C_b\|(p,u)\|^2_U \geq -C\delta\|(p,u)\|^2_H; \quad \forall\,(p,u)\in H. \tag{I.3.62}$$

Last, it follows from Proposition I.3.2.1 that:

$$Re\,[c^R(p,p)] = Re[\langle T_R(p), p\rangle_{-1/2,1/2,S_R}] \geq 0, \quad \forall\, p \in V. \tag{I.3.63}$$

Note that we have chosen $\epsilon = 1/4$. However, one could have used $1/2+\epsilon$ for any $0 < \epsilon < 1/2$.

To conclude, it follows from Eq. (I.3.54), Eq. (I.3.58), Eq. (I.3.62) and Eq. (I.3.63) that, for any $\delta > 0$,

$$\begin{aligned}
&Re\,[a((p,u),(p,u))] + C_1\|p\|_0^2 + C_2\|u\|_0^2 + C_b\|(p,u)\|_U^2 \\
&= \frac{1}{\omega^2\rho_f} Re\,[a^f(p,p)] + Re\,[a^s(u,u)] + Re\,[b((p,u),(p,u)) + b^*((p,u),(p,u))] \\
&\quad + \frac{1}{\omega^2\rho_f} Re\,[c^R(p,p)] + C_1\|p\|_0^2 + C_2\|u\|_0^2 + C_b\|(p,u)\|_U^2 \\
&\geq \alpha_1\|p\|_V^2 + \alpha_2\|u\|_W^2 - C\delta\|(p,u)\|_H^2 \\
&\geq \min(\alpha_1,\alpha_2)(\|p\|_V^2 + \|u\|_W^2) - C\delta\|(p,u)\|_H^2 \\
&\geq \min(\alpha_1,\alpha_2)\|(p,u)\|_H^2 - C\delta\|(p,u)\|_H^2.
\end{aligned}$$

We set

$$\delta = \frac{\min(\alpha_1,\alpha_2)}{2C}, \quad \alpha = \frac{\min(\alpha_1,\alpha_2)}{2} \quad \text{and} \quad C_U = \max(C_1, C_2, C_b). \tag{I.3.64}$$

Then, we deduce that:

$$Re\,[a((p,u),(p,u))] + C_U\|(p,u)\|_U^2 \;\geq\; \alpha\|(p,u)\|_H^2; \quad \forall\,(p,u) \in H. \tag{I.3.65}$$

Eq. (I.3.65) together with the dense and compact embedding $H \subset\subset U$ concludes the proof of Proposition I.3.2.2.

■

I.4 Uniqueness & Existence

For a completeness purpose, we first recall the Fredholm alternative Theorem in the considered mathematical framework. This result can be found, for example, in p.240 of reference [87].

Proposition I.4.0.3 *Consider the following variational problem in the Hilbert space H:*

$$\begin{cases} \text{Find } s \in H, \text{ such that} & \\ a(s,t) = l(t); & \text{for all } t \in H. \end{cases} \tag{I.4.1}$$

Assume that the continuous sesquilinear form $a(\cdot,\cdot)$ satisfies the following Gårding's inequality:

$$Re\,(a(t,t)) + C\|t\|_U^2 \geq \alpha\|t\|_H^2; \quad \forall\, t \in H, \tag{I.4.2}$$

for some a positive constant α and a compact embedding $H \subset\subset U$.
In addition, consider the homogeneous variational problem for a sesquilinear form $a(\cdot,\cdot)$ and its adjoint respectively:

$$\begin{cases} \text{Find } s_0 \in H, \text{ such that} & \\ a(s_0,t) = 0; & \text{for all } t \in H. \end{cases} \tag{I.4.3}$$

$$\begin{cases} \text{Find } t_0 \in H, \text{ such that} & \\ a^*(t_0,s) = \overline{a(s,t_0)} = 0; & \text{for all } s \in H. \end{cases} \tag{I.4.4}$$

Then, we have the following alternative:

i Either (I.4.1) admits exactly one solution $s \in H$ for any given $l \in H^*$.

ii Or the homogeneous problems (I.4.3) and (I.4.4) have finite-dimensional nullspaces of dimension $m > 0$. In addition, the non homogeneous problem (I.4.1) and its adjoint:

$$\begin{cases} \text{Find } t \in H, \text{ such that} & \\ a^*(t,s) = \overline{a(s,t)} = l^*(s); & \text{for all } s \in H. \end{cases} \tag{I.4.5}$$

admit solutions if and only if the following orthogonality conditions are satisfied:

$$l(t_{0(j)}) = 0, \text{ respectively, } l^*(s_{0(j)}) = 0; \qquad \text{for } j = 1, \cdots, m, \tag{I.4.6}$$

where $\{u_{0(j)}\}_{j=1}^m$ spans the eigenspace of (I.4.3), whereas $\{u_{0(j)}\}_{j=1}^m$ spans the eigenspace of (I.4.4).

I.4.1 Announcement of the main results

We are now in a position to apply Proposition I.4.0.3 in order to prove the following theorem in the next sections.

Theorem I.4.1.1 *For any $p^{inc} \in H^1(\Gamma)$, the boundary value problem BVP (2) admits a solution in the space $H = H^1(\Omega^f \cap B_R) \times (H^1(\Omega^s))^3$. This solution is unique modulo Jones resonance frequencies in the elastic scatterer that can exist for certain geometries.*
Moreover, we have the following estimate:

$$\|(p,u)\|_H \leq \|l\|_{H'}. \tag{I.4.7}$$

An immediate consequence of Theorem I.4.1.1 in conjunction with Theorem I.2.4.1 is the following result on the well-posed nature of the boundary value problem BVP (1) in the infinite domain:

Corollary I.4.1.1 *For any $p^{inc} \in H^1(\Gamma)$, the boundary value problem BVP (1) in the infinite domain admits a solution in the space $H_\rho = H^1_\rho(\Omega^f) \times (H^1(\Omega^s))^3$. Moreover, the pressure field p is always unique, whereas the displacement field u is unique up to Jones resonance frequencies that may occur in the elastic scatterer for certain geometries.*

I.4.2 Proof of the uniqueness

We first investigate the uniqueness of the solution of BVP (2) since the existence is a consequence of applying the Fredholm alternative. The uniqueness of the pressure field is established using an analytic continuation argument. However, the uniqueness of the displacement field is not guaranteed. Indeed, there are possible values of the oscillation parameter ω, called Jones frequencies, for which the homogeneous transmission problem has nontrivial solutions, called Jones modes. Therefore, u will be defined up to these vibrating frequencies [104]. Such frequencies can exist for simple geometries (e.g. spheres). Note that Hargé [79] has established that Jones modes do not exist for arbitrarily shaped bodies.

I.4.2.1 Uniqueness of the pressure field

We prove this result by contradiction. Assume the existence of two solutions of the reduced fluid-structure variational problem, denoted by (p_1, u_1) and (p_2, u_2).
We set:

$$p = p_1 - p_2 \quad \text{and} \quad u = u_1 - u_2. \tag{I.4.8}$$

Then, the pair (p, u) is solution of BVP (2) with $g = 0$ and thus satisfies the homogeneous equation:

$$a((p,u),(p,u)) = 0,$$

that is,

$$\frac{1}{\omega^2\rho_f}a^f(p,p) + a^s(u,u) + b((p,u),(p,u)) + b^*((p,u),(p,u)) + \frac{1}{\omega^2\rho_f}c^R(p,p) = 0. \tag{I.4.9}$$

Since $\frac{1}{\omega^2\rho_f}a^f(p,p) + a^s(u,u)$ is a real number, then,

$$Im\left[b((p,u),(p,u)) + b^*((p,u),(p,u))\right] = 0.$$

Hence, we deduce that:

$$Im\left[a((p,u),(p,u))\right] = Im\left[c^R(p,p)\right] = 0. \tag{I.4.10}$$

On the other hand, we know that $Im\left(\mu_n(k,r)\right) < 0,\ \forall\, n \in \mathbb{N}$ (See Lemma 2). Therefore, we must have $p_n = 0,\ \forall\, n \in \mathbb{N}$. Consequently, we obtain:

$$p = 0 \quad \text{on } S_R.$$

Moreover, we also have:

$$T_R(p) = -\frac{\partial p}{\partial r} = -\frac{\partial p}{\partial \nu} = 0 \quad \text{on } S_R.$$

Hence, we can continuously extend the pressure field p by zero in the exterior domain B_R^e. Using the regularity theorems on the Helmholtz operator [74], the extended function $\tilde{p}$ is such that $\tilde{p} \equiv 0$ and belongs to $H^2_{loc}(B_R^e) \cap H^1_{0,loc}(B_R^e)$. Moreover, from the ellipticity of the Helmholtz operator, the function $\tilde{p}$ is analytic. It follows that we can apply the analytic continuation principle, and obtain:

$$p = \tilde{p} = 0 \quad \text{in } \Omega_R^f, \tag{I.4.11}$$

which proves the uniqueness of the pressure velocity.

I.4.2.2 Uniqueness of the displacement field

Let (p,u) be the field given by Eq. (I.4.8) (see Section I.4.2.1). Then, if follows from the uniqueness of the pressure field that:

$$\frac{\partial p}{\partial \nu} = 0 \quad \text{on } \Gamma. \tag{I.4.12}$$

Substituting Eq. (I.4.12) into the transmission conditions on the interface Γ, we obtain:

$$u \cdot \nu = 0 \quad \text{and} \quad \tau(u) = 0 \quad \text{on } \Gamma. \tag{I.4.13}$$

The displacement field u is therefore both traction-free and tangent to the boundary. However, these two homogeneous boundary equations, together with the homogeneous elastodynamic equation, do not necessarily imply that u vanishes in Ω^s. Indeed, as stated by Luke and Martin in [104], for certain geometries and for certain frequencies, some nontrivial solutions to the homogeneous transmission problem exist. More precisely, there is an infinite set of free vibrations of the solid, ω_m, with corresponding displacement modes of vibration, u_m, that satisfies $\tau(u_m) = 0$ on the boundary Γ. If moreover some of these frequencies u_m are such that $u_m \cdot n = 0$ on Γ, such nontrivial solutions u_m are called Jones modes and the associated frequencies ω_m Jones frequencies.
These singularities have been introduced by D. S. Jones [92] in a related context (a thin layer of ideal fluid between an elastic body and a surrounding elastic exterior). Note that Dallas called them in [37] (see p. 7) "complex amplitudes of nonradiating modes". More specifically, according to Lamb and Chree (see § 8.14 in [49]), Jones frequencies exist for simple geometries such as spheres since it can be observed that an elastic sphere could sustain "torsional oscillations", in which the radial component of the displacement is identically zero. Their existence has also been proved in the case of prolate spheroids [125]. Actually, Jones frequencies may occur for any axisymmetric body, because they can sustain torsional oscillations in which only the azimuthal component of displacement is nonzero. Nevertheless, Hargé [79] has proved that we do not expect Jones frequencies to exist for an "arbitrarily-shaped" body.
Note that, as emphasized in [86, 108], these free vibrations are inherent to the physical model that we consider. Indeed, they arise from the absence of constraints on the tangential components of the displacement field u on the fluid-solid interface. This is due to the fact that the fluid is inviscid, and thus can slip freely over the surface of the solid, so that the tangential components are not controlled. Therefore, such free oscillations of the solid do not couple to the fluid, and cannot be precluded by the radiation condition.

I.4.3 Proof of the existence

Because of the possible existence of the Jones frequencies in the elastic medium, we have to distinguish two cases when applying the Fredholm alternative (see Proposition I.4.0.3) to establish the existence of a solution.

First, assume that ω is not a Jones frequency for the elastic scatterer. Then, we have shown in the previous paragraph that the homogeneous problem has only the trivial solution. Hence, we have uniqueness of a solution $(p, u) \in H$ of the boundary value problem BVP (2). In addition, the variational formulation satisfies the Gårding's inequality. Consequently, the existence of the field (p, u) immediately results from applying Fredholm alternative.

Second, suppose that ω is a Jones frequency. Therefore, there is a nonzero displacement field $u \in V$, called Jones mode, such that $(0, u)$ is a solution of the homogeneous variational problem given by Eq. (I.4.3).
Hence, we do not have uniqueness of the displacement field. Therefore, according to the Fredholm alternative (see Proposition I.4.0.3), a solution (p, u) exists if the right-hand side $l(\cdot)$ of Eq. (I.3.1) vanishes for every solution to the homogeneous adjoint problem.
Let $(q^*, v^*) \in H$ be a solution to the homogeneous adjoint equation, that is, (q^*, v^*) satisfies:

$$a^*((q^*, v^*), (s, t)) = 0; \qquad \forall\, (s, t) \in H.$$

Note that $a(\cdot, \cdot)$ is not self-adjoint. Indeed, if $a(\cdot, \cdot)$ was self-adjoint, $a((p, u), (p, u))$ would be real, which is not the case because of the term $c^R(p, p)$ whose imaginary part is strictly negative for $p \neq 0$ (see Section I.3.2.1). By definition of the adjoint operator, we have:

$$a^*((q^*, v^*), (s, t)) \;=\; \overline{a((s, t), (q^*, v^*))}; \qquad \forall\, (s, t) \in H. \tag{I.4.14}$$

Taking the conjugate, we clearly get:

$$a((s, t), (q^*, v^*)) = 0; \qquad \forall\, (s, t) \in H. \tag{I.4.15}$$

Next, we proceed as in Section I.3.1 to derive the boundary conditions satisfied by (q^*, v^*).
Let $(s, t) \in \mathcal{D}(\Omega_R^f) \times (\mathcal{D}(\Omega^s))^3$ be such that $t = 0$. Since s vanishes on Γ and S_R, applying Green's formula, we get:

$$\int_{\Omega_R^f} s(\Delta \overline{q^*} + \frac{\omega^2}{c_f^2} \overline{q^*})\, dx = 0; \quad \forall\, s \in \mathcal{D}(\Omega_R^f),$$

which yields:

$$\Delta q^* + \frac{\omega^2}{c_f^2} q^* = 0 \qquad \text{in } \Omega^f.$$

Similarly, let $(s, t) = (0, t) \in \mathcal{D}(\Omega_R^f) \times (\mathcal{D}(\Omega^s))^3$ and apply Green's theorem. Since t vanishes on Γ,

we obtain:

$$\int_{\Omega^s} t \cdot (\nabla \cdot \sigma(\overline{v^*}) + \omega^2 \rho_s \overline{v^*})\, dx = 0; \quad \forall\, t \in (\mathcal{D}(\Omega^s))^3,$$

that is,

$$\nabla \cdot \sigma(v^*) + \omega^2 \rho_s v^* = 0 \qquad \text{in } \Omega^s.$$

Next, we take $(s,t) \in \mathcal{D}(\overline{\Omega}_R^f) \times (\mathcal{D}(\overline{\Omega}^s))^3$ such that $t = 0$ and s vanishes in a neighborhood of S_R. We apply the Green's formula. We then obtain:

$$\frac{1}{\omega^2 \rho_f} \int_{\Omega_R^f} s(\Delta \overline{q^*} + \frac{\omega^2}{c_f^2} \overline{q^*})\, dx + \frac{1}{\omega^2 \rho_f} \langle s, \frac{\partial q^*}{\partial \nu} \rangle_{-1/2,1/2,\Gamma} - \langle s\nu, v^* \rangle_{-1/2,1/2,\Gamma} = 0.$$

Since q^* satisfies the Helmholtz equation, we obtain:

$$\omega^2 \rho_f v^* \cdot \nu = \frac{\partial q^*}{\partial \nu} \qquad \text{on } \Gamma.$$

For $(s,t) = (0,t) \in \mathcal{D}(\overline{\Omega}_R^f) \times (\mathcal{D}(\overline{\Omega}^s))^3$, the Green's formula allows to obtain:

$$\int_{\Omega^s} t \cdot (\nabla \cdot \sigma(\overline{v^*}) + \omega^2 \rho_s \overline{v^*})\, dx - \langle t, \sigma(v^*) \cdot \nu \rangle_{-1/2,1/2,\Gamma} - \langle t \cdot \nu, q^* \rangle_{-1/2,1/2,\Gamma} = 0$$

Consequently, since v^* satisfies the homogeneous Navier equation, we obtain:

$$\sigma(v^*) \cdot \nu = -q^* n \qquad \text{on } \Gamma.$$

Finally, we take $(s,t) = (s,0) \in \mathcal{D}(\overline{\Omega}_R^f) \times (\mathcal{D}(\overline{\Omega}^s))^3$ such that s vanishes in a neighborhood of Γ. Then, applying again the Green's theorem allows to deduce that:

$$\int_{\Omega_R^f} s(\Delta \overline{q^*} + \frac{\omega^2}{c_f^2} \overline{q^*})\, dx - \langle s, \frac{\partial q^*}{\partial \nu} \rangle_{-1/2,1/2,S_R} - \langle T_R(s), q^* \rangle_{-1/2,1/2,S_R} = 0. \tag{I.4.16}$$

Since q^* satisfies the Helmholtz equation, we necessarily have:

$$\frac{\partial q^*}{\partial r} + T_R^*(q^*) = 0 \qquad \text{on } S_R,$$

where T_R^* stands for the adjoint operator of the DtN operator T_R defined as in Eq. (A.3.14), that is,

$$T_R^*(q) = \sum_{n=0}^{+\infty} \overline{\mu_n(k,R)} q_n.$$

Note that this boundary condition involving T_R^* is an incoming radiation condition, that is,

$$\lim_{r\to+\infty} r\left(\frac{\partial q^*}{\partial r} + \mathrm{i}kq^*\right) = 0.$$

Note that the coefficients $\mu_n(k,R)$ depend in fact on the spherical Hankel functions of the second kind $h_n^{(2)} = \overline{h}_n^{(1)}$.

Let $(\tilde{p},\tilde{u})$ be such that $\tilde{u} = v^*$ and $\tilde{p}$ is a continuous extension of q^* satisfying the exterior Helmholtz equation with incoming radiation condition. Then, the pair $(\tilde{p},\tilde{u})$ is thus solution to the following homogeneous transmission problem:

$$\begin{cases} \Delta\tilde{p} + (-k)^2\,\tilde{p} = 0 & \text{in } \Omega^f \\ \nabla\cdot\sigma(\tilde{u}) + \omega^2\rho_s\tilde{u} = 0 & \text{in } \Omega^s \\ \omega^2\rho_f\tilde{u}\cdot\nu = \dfrac{\partial\tilde{p}}{\partial\nu} & \text{on } \Gamma \\ \tau(\tilde{u}) = -\tilde{p}n & \text{on } \Gamma \\ \dfrac{\partial\tilde{p}}{\partial r} + T_R^*(\tilde{p}) = 0 & \text{on } S_R\,. \end{cases}$$

As established above, this adjoint boundary value problem has a nontrivial solution only if ω is a Jones frequency. Since ω is assumed to be a Jones frequency, we get $\tilde{p}\equiv 0$ and $\tilde{u}$ is a Jones mode with $\tau(\tilde{u})_{|\Gamma}\equiv 0$, $\tilde{u}\cdot n_{|\Gamma}\equiv 0$.

We then deduce that $q^*\equiv 0$ and $\tau(v^*)_{|\Gamma}\equiv 0$, $v^*\cdot n_{|\Gamma}\equiv 0$, and therefore:

$$l(q^*, v^*) = 0.$$

Hence, the right-hand side $l(\cdot)$ of Eq. (I.3.1) vanishes for every solution to the homogeneous adjoint problem. Consequently, there is a solution (p,u) to the reduced direct problem BVP (2). Moreover, the existing pressure field p is unique.

Remark I.4.3.1 *From a numerical view point, the Dirichlet-to-Neumann (DtN) method was employed for the first time in the case of exterior Helmholtz problems by Givoli and Keller in [67, 94]. This was possible using the Fourier series representation of the DtN operator which can be derived in the case of only geometrically simple-shaped exterior boundaries (i.e. circle, ellipse, sphere, ellipsoid). However, this series must be truncated for implementation purposes, but its ability to preclude singular behavior in the finite element solution of the target exterior Helmholtz problem is not affected, as demonstrated in [73, 77]. Nevertheless, since the DtN operator is a non-local mapping*

[67, 94], its application gives rise to a full symmetric sub-matrix associated with the degrees of freedom lying on the artificial boundary. Forming this matrix is reminiscent of integral formulations, and storing it can be prohibitive for three-dimensional high-frequency acoustic scattering problems. However, the DtN approach remains computationally viable when the discrete equations are to be solved by an iterative algorithm that involves essentially matrix-vector products [105]. The latter approach appears nevertheless to be limited to circular- and spherical-shaped boundaries. Given that, various alternative approaches have been suggested to balance between accuracy, stability, and computational efficiency requirements. Examples of such methods include employing approximate boundary conditions, also called absorbing boundary conditions (ABC) (see, for example, [40, 134] as well as the review paper [136] and references therein), the perfectly matched layers formulation (PML), see, e.g., [78], and the so-called infinite elements, see, e.g., [22, 23].

Acknowledgements The authors acknowledge the support by INRIA/CSUN Associate Team Program and by ANR/AHPI research program (Agence Nationale de la Recherche/ Analyse Harmonique et Problèmes Inverses, ANR-07-BLAN-0247-01). They also would like to thank Professor Mohand Moussaoui for enlightening discussions. Any opinions, findings, conclusions or recommendations expressed in this material are those of the authors and do not necessarily reflect the views of ANR, CSUN, or INRIA.

Appendices

Appendix A

Appendices to the Chapter I

A.1 Special functions

The goal of this section is to recall the needed spherical function properties for establishing the sign properties of the Dirichlet-to-Neumann operator. This section is included for completeness only.

A.1.1 The spherical Hankel functions

A.1.1.1 Preliminaries

Let J_n and Y_n be the Bessel functions of the first and second kind [2], and H_n denote the corresponding Hankel function of the first kind defined by:

$$H_n(z) := H_n^{(1)}(z) = J_n(z) + \mathrm{i}Y_n(z). \tag{A.1.1}$$

Then, the spherical Bessel functions of the first and second kind are respectively given by [2]:

$$j_n(z) := \sqrt{\frac{1}{2}\frac{\pi}{z}}J_{n+1/2}(z), \tag{A.1.2}$$

and

$$y_n(z) := \sqrt{\frac{1}{2}\frac{\pi}{z}}Y_{n+1/2}(z). \tag{A.1.3}$$

These special functions satisfy the spherical Bessel differential equation given by:

$$z^2\frac{d^2\,p}{d\,z^2} + 2z\frac{d\,p}{d\,z} + (z^2 - n(n+1))p = 0. \tag{A.1.4}$$

From the classical results of analysis ([132]), it can be shown that the set of solutions of Eq. (A.1.4) is a subspace of dimension 2. Hence, the spherical Hankel functions of the first kind (resp. of the second kind) given by [2]:

$$h_n(z) := h_n^{(1)}(z) = j_n(z) + \mathrm{i}y_n(z) \quad (\text{resp.} \quad h_n^{(2)}(z) = \overline{h}_n^{(1)}(z) = j_n(z) - \mathrm{i}y_n(z)). \tag{A.1.5}$$

also satisfy Eq. (A.1.4).

A.1.1.2 Properties

The two spherical Hankel functions have the following series expansions: [2, 28]:

$$\begin{cases} h_n^{(1)}(kr) = h_n(kr) & = \mathrm{i}^{-n-1}\dfrac{e^{\mathrm{i}kr}}{kr}\sum_{j=0}^{n}\dfrac{(n+j)!}{j!(n-j)!}(-2\mathrm{i}kr)^{-j}, \\ h_n^{(2)}(kr) = \overline{h}_n(kr) & = \mathrm{i}^{n+1}\dfrac{e^{-\mathrm{i}kr}}{kr}\sum_{j=0}^{n}\dfrac{(n+j)!}{j!(n-j)!}(2\mathrm{i}kr)^{-j}. \end{cases}$$

Moreover, for large radius value, the spherical Hankel functions possess the following asymptotic behavior [2, 28]:

$$\begin{cases} h_n^{(1)}(kr) & \sim & (-\mathrm{i})^n\dfrac{e^{\mathrm{i}kr}}{r} & (A.1.6) \\ h_n^{(2)}(kr) & \sim & \mathrm{i}^n\dfrac{e^{-\mathrm{i}kr}}{r}; \quad \text{as } r \to +\infty\,, & (A.1.7) \end{cases}$$

Let M_n be the modulus of H_n, i.e.,

$$M_n^2(z) := J_n^2(z) + Y_n^2(z) \tag{A.1.8}$$

For any $n \in \mathbb{N}$, the function $z \mapsto M_n^2(z)$ is strictly decreasing [135, 138].
Let m_n be the modulus of h_n, i.e.,

$$m_n^2(z) := j_n^2(z) + y_n^2(z). \tag{A.1.9}$$

Then we have:

Proposition A.1.1.1 *For any $n \in \mathbb{N}$, $z \mapsto m_n^2(z)$ is strictly decreasing, that is,*

$$(m_n^2)'(z) < 0. \tag{A.1.10}$$

Proof Indeed, it follows from Eq. (A.1.1)-Eq. (A.1.3) and Eq. (A.1.8)-Eq. (A.1.9) that:

$$m_n^2(z) = \frac{1}{2}\frac{\pi}{z}M_{n+1/2}^2(z). \tag{A.1.11}$$

We thus get, for all $z > 0$,

$$(m_n^2)'(z) = \frac{1}{2}\frac{\pi}{z}(M_{n+1/2}^2)'(z) + \left(-\frac{1}{2}\frac{\pi}{z^2}\right)M_{n+1/2}^2(z).$$

Hence, since $(M_{n+1/2}^2)'(z) < 0$, then $(m_n^2)'(z) < 0$ for all $z \in \mathbb{R}^{+,*}$, and therefore $z \mapsto m_n^2(z)$ is strictly decreasing.

■

Similarly to the approach in [135], let p, q be two solutions of Eq (A.1.4) and define the Wronskian [99] as follows:

$$W(p,q) = pq' - p'q. \tag{A.1.12}$$

Then, in the distribution sense, i.e. $\mathcal{D}'(\mathbb{R}^{+*})$, we have:

$$\begin{aligned}\frac{d\,W(p,q)}{d\,z} &= pq'' - p''q \\ &= -\frac{2}{z}pq' - \frac{1}{z^2}(z^2 - n(n+1))pq + \frac{2}{z}p'q + \frac{1}{z^2}(z^2 - n(n+1))pq \\ &= -\frac{2W(p,q)}{z}.\end{aligned} \tag{A.1.13}$$

Therefore, we obtain:

$$z\frac{dW(p,q)}{dz} + 2W(p,q) = 0. \tag{A.1.14}$$

Consequently, $W(p,q) = \dfrac{C}{z^2}$ for some constant C.
In the particular case where $p = j_n$ and $q = y_n$, we have [2]:

$$W(j_n(z), y_n(z)) = \frac{1}{z^2}. \tag{A.1.15}$$

We deduce the following property of the Wronskian:

Proposition A.1.1.2 *For all* $z \in \mathbb{R}^{+,*}$,

$$j_n(z)y_n'(z) - j_n'(z)y_n(z) > 0. \tag{A.1.16}$$

A.1.2 The spherical harmonics

We recall some definitions and properties of the spherical harmonics. More results can be found in [28, 99], among others.

Let $P_n(t)$ denote the Legendre polynomials, given by the recurrence relations [2] (see Chapter 8, p334):

$$\begin{cases} P_0(t) & = 1, \\ P_1(t) & = t, \\ (n+1)P_{n+1}(t) & = (2n+1)tP_n(t) - nP_{n-1}(t), \end{cases}$$

that is, $P_n(t) = \left(\frac{1}{2^n n!}\right)\frac{d^n(t^2-1)^n}{dt^n}$.
The Legendre polynomial functions satisfy the Legendre equation:

$$(1-t^2)g''(t) - 2tg'(t) + n(n+1)g(t) = 0; \quad n \in \mathbb{N}.$$

We also define the associated Legendre functions P_n^m as follows [2]:

$$P_n^m(t) := (-1)^m(1-t^2)^{m/2}\frac{d^m P_n(t)}{dt^m}; \quad n \in \mathbb{N}, 0 \leq m \leq n.$$

The associated Legendre functions satisfy the associated Legendre differential equation given by [2]:

$$(1-t^2)g''(t) - 2tg'(t) + \left(n(n+1) - \frac{m^2}{1-t^2}\right)g(t) = 0; \quad n \in \mathbb{N}, 0 \leq m \leq n. \tag{A.1.17}$$

Next, we introduce the spherical coordinates (r, θ, ϕ), for $r \in [0, +\infty[$, $\theta \in [0, \pi]$ and $\phi \in [0, 2\pi[$, related to the cartesian coordinates by:

$$x = r\,\sin\theta\,\cos\phi, \quad y = r\,\sin\theta\,\sin\phi, \quad z = r\,\cos\theta.$$

We then define the spherical harmonic functions y_{mn} as follows [28]:

$$y_{mn}(\theta, \phi) := P_n^{|m|}(\cos\theta)e^{\mathrm{i}m\phi}; \quad n \in \mathbb{N}, -n \leq m \leq n. \tag{A.1.18}$$

Note that the spherical harmonics are eigenfunctions of the Laplace operator for r being constant [28].

We recall some properties of these special functions ([28] p. 25)).

Property A.1.2.1

i *For each $n \geq 0$, there exist exactly $2n+1$ linearly independent spherical harmonics y_{mn} of order n; $-n \leq m \leq n$.*

ii *The spherical harmonics are orthogonal with respect to the inner product on $L^2(S_1)$, that is:*

$$\int_{S_1} y_{mn}\overline{y}_{m'n'}ds = 0, \quad \text{if } n \neq n' \text{ or } m \neq m', \tag{A.1.19}$$

and

$$\int_{S_1} |y_{mn}|^2 ds = \frac{4\pi}{(2n+1)}\frac{(n+|m|)!}{(n-|m|)!} := \alpha_{mn}^2. \tag{A.1.20}$$

iii *The functions $Y_{mn}(\theta,\phi) := \dfrac{y_{mn}}{\alpha_{mn}}$; $-n \leq m \leq n$, are called the orthonormalized harmonics and satisfy:*

$$\int_{S_1} Y_{mn}\overline{Y}_{m'n'}ds = \delta_{mm'}\delta_{nn'}, \tag{A.1.21}$$

where $\delta_{mm'}$ are the Kronecker Delta functions.

iv *The set of functions $\{Y_{mn}\}$ forms an orthonormal basis of $L^2(S_1)$. The orthonormal system is complete in $L^2(S_1)$. Hence, every function $f \in L^2(S_1)$ can be expanded into a series of spherical polynomials as follows:*

$$f(1,\theta,\phi) = \sum_{n=0}^{\infty}\sum_{m=-n}^{n} f_{mn}Y_{mn}(\theta,\phi), \tag{A.1.22}$$

where f_{mn} are the Fourier coefficients given by:

$$f_{mn} = \int_{S_1} f(1,\theta,\phi)\overline{Y}_{mn}(\theta,\phi)ds. \tag{A.1.23}$$

Remark A.1.2.1 *Let S_R represent the surface of the ball of radius $r = R$. Then, an element ds_R of S_R is equal to $R^2 ds$, where ds is an element of the surface S_1 of the unit ball .*
Consequently, we deduce that the set of functions Y_{mn}/R forms a basis of $L^2(S_R)$, and a complete orthonormal system in $L^2(S_R)$. It follows that any function $f \in L^2(S_R)$ admits the following series expansion into spherical harmonics

$$f(R,\theta,\phi) = \sum_{n=0}^{\infty}\sum_{m=-n}^{n} f_{mn}Y_{mn}(\theta,\phi),$$

with

$$f_{mn} = \int_{S_1} f(R,\theta,\phi)\overline{Y}_{mn}(\theta,\phi)ds.$$

A.2 The solution to the Helmholtz problem in the domain exterior to a sphere

This section is devoted to the analytical study of the solution of Helmholtz equation outside a sphere. We derive the Fourier series expansion of the solution in terms of the spherical harmonic functions and establish its uniqueness.

A.2.1 Construction of the solution into spherical harmonics

Let B_R be the ball of radius $r = R$, S_R its spherical surface, and B_R^e the exterior domain to $\overline{B_R}$. We consider the Helmholtz problem in the exterior of B_R with Dirichlet boundary condition $g \in L^2(S_R)$, formulated as follows:

$$\begin{cases} \Delta p + k^2 p = 0 & \text{in } B_R^e \quad \text{(A.2.1)} \\ p = g & \text{on } S_R \quad \text{(A.2.2)} \\ \lim\limits_{r\to+\infty} r\left(\dfrac{\partial p}{\partial r} - \mathrm{i}kp\right) = 0, & \quad \text{(A.2.3)} \end{cases}$$

where $r = \|x\|_2$.

The goal is to prove analytically the existence of the solution of the boundary value problem given by Eqs. (A.2.1)-(A.2.3).

Let (r,θ,ϕ) be the system of spherical coordinates, where $r \in [0,+\infty[$, $\theta \in [0,\pi]$ and $\phi \in [0,2\pi[$, related to the cartesian coordinates $x = (x_1,x_2,x_3) \in \mathbb{R}^3$ by:

$$r = \|x\|_2 = \sqrt{x_1^2+x_2^2+x_3^2},\ \theta = arctan(\sqrt{x_1^2+x_2^2}/x_3),\ \phi = arctan(x_2/x_1). \quad \text{(A.2.4)}$$

We recall that the Laplacian in spherical coordinates is given by [89]:

$$\Delta p(r,\theta,\phi) = \frac{1}{r^2}\left[\frac{\partial}{\partial r}\left(r^2\frac{\partial p}{\partial r}\right) + \frac{1}{\sin\theta}\frac{\partial}{\partial\theta}\left(\sin\ \theta\frac{\partial p}{\partial\theta}\right) + \frac{1}{\sin^2\theta}\frac{\partial^2 p}{\partial\phi^2}\right]. \quad \text{(A.2.5)}$$

We set $p(r,\theta,\phi) = f(r)g(\theta)h(\phi)$. Then, Eq. (A.2.1) can be expressed in spherical coordinates as follows:

$$\frac{1}{rf(r)}\frac{\partial}{\partial r}\left(r^2\frac{\partial f(r)}{\partial r}\right) + \frac{1}{r^2}\left[\frac{1}{\sin\theta g(\theta)}\frac{\partial}{\partial\theta}\left(\sin\theta\frac{\partial g(\theta)}{\partial\theta}\right) + \frac{1}{\sin^2\theta h(\phi)}\frac{\partial^2 h(\phi)}{\partial\phi^2}\right] + k^2 = 0. \quad \text{(A.2.6)}$$

We deduce that:

$$\frac{d}{dr}\left(r^2\frac{df(r)}{dr}\right) + (k^2r^2 - a)f(r) = 0, \quad \text{(A.2.7)}$$

$$\sin\theta\frac{d}{d\theta}\left(\sin\theta\frac{dg(\theta)}{d\theta}\right) + (a\sin^2\theta - b)g(\theta) = 0, \quad \text{(A.2.8)}$$

$$\frac{d^2h(\phi)}{d\phi^2} + bh(\phi) = 0, \quad \text{(A.2.9)}$$

for some constants a and b.

Observe that the function f is defined in the exterior domain B_R^e, and must satisfy the outgoing Sommerfeld condition, whereas g and h are defined on S_R.

Since the sphere S_R is a closed surface, we seek for a function h that is periodic in ϕ, i.e., $h(0) = h(2\pi)$. Therefore, Eq. (A.2.9) admits the functions $\{\sin(m\phi)\}, \{\cos(m\phi)\}$ as a set of solutions for $b = m^2$, $m \in \mathbb{N}$.

It follows that:

$$h(\phi) = A_{mn}\sin(m\phi) + B_{mn}\cos(m\phi) \quad \text{(A.2.10)}$$

is solution to (A.2.9).

Next, we set $t = \cos\theta$, and substitute in Eq. (A.2.8). We then obtain:

$$(1-t^2)\frac{d^2g(t)}{dt^2} - 2t\frac{dg(t)}{dt} + \left(a - \frac{m^2}{1-t^2}\right)g(t) = 0. \quad \text{(A.2.11)}$$

For $a = n(n+1)$, for $n \in \mathbb{N}$, Eq. (A.2.11) is in fact the associated Legendre equation (see Eq. (A.1.2) in Appendix A.1), whose solutions are the associated Legendre functions defined in Appendix A.1, Section A.1.2, by:

$$g_{mn}(t) = P_n^m(\cos\theta), \quad 0 \le m \le n. \quad \text{(A.2.12)}$$

It follows that for $n \in \mathbb{N}, 0 \leq m \leq n$, the angular part of the solution is given by:

$$g(\theta)h(\phi) = P_n^m(\cos\theta)(A_{mn}\sin(m\phi) + B_{mn}\cos(m\phi)). \tag{A.2.13}$$

Using Moivre identity, we can re-write Eq. (A.2.13) as follows:

$$g_{mn}(\theta)h(\phi) = c_{mn}P_n^{|m|}(\cos\theta)e^{\mathrm{i}m\phi}, \quad n \in \mathbb{N}, -n \leq m \leq n, \tag{A.2.14}$$

where c_{mn} are complex coefficients.
Using the spherical harmonics y_{mn} (see Eq. (A.1.18) in Appendix A.1) given by:

$$y_{mn}(\theta,\phi) := P_n^{|m|}(\cos\theta)e^{\mathrm{i}m\phi}, \quad n \in \mathbb{N}, -n \leq m \leq n,$$

the angular part of the solution is then expressed in terms of these spherical functions as follows:

$$g_{mn}(\theta)h(\phi) = c_{mn}y_{mn}(\theta,\phi), \quad -n \leq m \leq n.$$

Next, we take $a = n(n+1)$ in Equation (A.2.7), and set $z = kr$. Therefore, Eq. (A.2.7) becomes the Bessel's differential equation given by Eq. (A.1.4). This equation admits the spherical Hankel functions of the first and second kind $h_n^{(1)}$ and $h_n^{(2)}$ as linearly independent solutions, for $n \in \mathbb{N}$.
Using the asymptotic behavior given by Eq. (A.1.6), it follows that only $h_n^{(1)}$ satisfies the outgoing radiating condition.
Therefore, a solution p of the Helmholtz equation in spherical coordinates can be expressed as follows:

$$p(r,\theta,\phi) = \sum_{n=0}^{\infty} h_n(kr) \sum_{m=-n}^{n} c_{mn}y_{mn}(\theta,\phi), \tag{A.2.15}$$

or, using the orthonormalized harmonics (cf. Property A.1.2.1), as follows:

$$p(r,\theta,\phi) = \sum_{n=0}^{\infty} h_n(kr) \sum_{m=-n}^{n} C_{mn}Y_{mn}(\theta,\phi). \tag{A.2.16}$$

for complex coefficients $C_{mn} = \alpha_{mn}c_{mn}$, where α_{mn} are given by Eq. (A.1.20) and c_{mn} are given by Eq. (A.2.14).

Note that the series expansion (A.2.15) converges absolutely and uniformly in every closed and bounded domain contained in the exterior domain of $r > R$ (see [28], p. 34).

Moreover, using the asymptotic behavior of $h_n^{(1)}$ in far-field region, we can see that the solution p depends asymptotically on r as follows [28, 118]:

$$p \sim \frac{e^{\mathrm{i}kr}}{r} \quad \text{as } r \to +\infty. \tag{A.2.17}$$

To determine the expression of the Fourier coefficients C_{mn} in Eq. (A.2.16), we use the boundary condition given by Eq. (A.2.2). From Remark A.1.2.1, the Dirichlet data $g \in L^2(S_R)$ can be expanded into a series of spherical polynomials as follows:

$$g(R,\theta,\phi) = \sum_{n=0}^{\infty} \sum_{m=-n}^{n} g_{mn} Y_{mn}(\theta,\phi), \tag{A.2.18}$$

where

$$g_{mn} = \int_{S_1} g(R,\theta,\phi)\overline{Y}_{mn}(\theta,\phi)ds. \tag{A.2.19}$$

Furthermore, on S_R, p satisfies:

$$p(R,\theta,\phi) = \sum_{n=0}^{\infty} h_n(kR) \sum_{m=-n}^{n} C_{mn} Y_{mn}(\theta,\phi). \tag{A.2.20}$$

Multiplying Eq. (A.2.18) and Eq. (A.2.20) by $\overline{Y}_{mn}$, and integrating over S_1, we obtain by orthogonality of the spherical harmonics that:

$$C_{mn} = \frac{g_{mn}}{h_n(kR)}.$$

It follows that a radiating solution p to the Helmholtz problem in the domain exterior to the sphere S_R with Dirichlet boundary condition admits the following series expansion into spherical harmonics:

$$p(r,\theta,\phi) = \sum_{n=0}^{\infty} \frac{h_n(kr)}{h_n(kR)} \sum_{m=-n}^{n} g_{mn} Y_{mn}(\theta,\phi).$$

Remark A.2.1.1 *Observe that if Eq. (A.2.2) is replaced by a Neumann boundary condition* $\dfrac{\partial p}{\partial \nu} = g$, *we obtain:*

$$\begin{aligned} \frac{\partial p}{\partial r}_{|r=R} &= \sum_{n=0}^{\infty} k h_n'(kR) \sum_{m=-n}^{n} C_{mn} Y_{mn}(\theta,\phi) \\ &= \sum_{n=0}^{\infty} \sum_{m=-n}^{n} g_{mn} Y_{mn}(\theta,\phi). \end{aligned}$$

Consequently, we have:

$$C_{mn} = \frac{g_{mn}}{kh_n(kR)},$$

and therefore, a Neumann radiating solution is given by:

$$p(r,\theta,\phi) = \sum_{n=0}^{\infty} \frac{h_n(kr)}{kh_n(kR)} \sum_{m=-n}^{n} g_{mn} Y_{mn}(\theta,\phi).$$

A.2.2 Uniqueness of the solution

The goal is to prove that the radiating solution into spherical harmonics constructed in Section A.2.1 is the only solution of the exterior Helmholtz problem with Dirichlet or Neumann boundary conditions.

To this end, assume that there exist two solutions $p_1, p_2 \in \mathcal{C}^2(B_R^e)$ to the exterior problem.
Let $p = p_1 - p_2$ denote the difference between these two solutions. Then, p clearly satisfies the Helmholtz equation, the radiation condition at infinity and a homogeneous Dirichlet or Neumann boundary condition on S_R.
Let S_a be the surface of a ball of radius $r = a$ ($> R$) and centered at the origin, enclosing the spherical surface S_R. We denote by $B_R^{e,a}$ the annular domain contained between S_R and S_a.

Applying Green's formula in $B_R^{e,a}$, we first have:

$$\int_{S_a} p\frac{\partial \overline{p}}{\partial \nu} ds = \int_{S_R} p\frac{\partial \overline{p}}{\partial \nu} ds + \int_{B_R^{e,a}} |\nabla p|^2 dx + \int_{B_R^{e,a}} p\Delta\overline{p} dx.$$

Since p satisfies the Helmholtz equation in $B_R^{e,a}$, we obtain:

$$\int_{S_a} p\frac{\partial \overline{p}}{\partial \nu} ds = \int_{S_R} p\frac{\partial \overline{p}}{\partial \nu} ds + \int_{B_R^{e,a}} |\nabla p|^2 dx - k^2 \int_{B_R^{e,a}} |p|^2 dx.$$

Taking the imaginary part of the equation, we get:

$$Im\left(\int_{S_a} p\frac{\partial \overline{p}}{\partial \nu} ds\right) = Im\left(\int_{S_R} p\frac{\partial \overline{p}}{\partial \nu} ds\right). \tag{A.2.21}$$

Moreover, since p satisfies the radiation condition, we obtain:

$$\begin{aligned}\lim_{a\to+\infty}\int_{S_a}\left|\frac{\partial p}{\partial r}-\mathrm{i}kp\right|^2 ds &= \lim_{a\to+\infty}\int_{S_a}\left\{\left|\frac{\partial p}{\partial r}\right|^2+k^2|p|^2+2kIm\left(p\frac{\partial\overline{p}}{\partial\nu}\right)\right\}ds \\ &= 0.\end{aligned} \tag{A.2.22}$$

Substituting Eq. (A.2.21) into Eq. (A.2.22), we deduce that:

$$\lim_{a\to+\infty}\int_{S_a}\left\{\left|\frac{\partial p}{\partial r}\right|^2+k^2|p|^2\right\}ds=-2kIm\left(\int_{S_R}p\frac{\partial\overline{p}}{\partial\nu}ds\right).$$

Since p satisfies a homogeneous Dirichlet (or Neumann) boundary condition on S_R, we conclude that:

$$Im\left(\int_{S_R}p\frac{\partial\overline{p}}{\partial\nu}ds\right)=0, \tag{A.2.23}$$

which yields:

$$\lim_{a\to+\infty}\int_{S_a}\left\{\left|\frac{\partial p}{\partial r}\right|^2+k^2|p|^2\right\}ds=0. \tag{A.2.24}$$

Therefore, we have:

$$\lim_{a\to+\infty}\int_{S_a}|p|^2\,ds=0.$$

Using Rellich's lemma [28], we conclude that $p=0$ in $B_R^{e,a}$, that is, outside a sufficiently large sphere. Furthermore, due to the ellipticity of the Helmholtz operator, the solution p is analytic in $B_R^{e,a}$. Consequently, $p=0$ in the whole exterior domain B_R^e, which concludes the proof of the uniqueness.

Remark A.2.2.1 *Instead of Eq. (A.2.23), assume that the radiating solution to the exterior Helmholtz equation satisfies a boundary condition for which we have the following weaker property:*

$$Im\left(\int_{S_R}p\frac{\partial\overline{p}}{\partial\nu}ds\right)\geq 0.$$

Then, following the previous reasoning, this property is sufficient to lead to:

$$\lim_{a\to+\infty}\int_{S_a}|p|^2\,ds=0.$$

and the application of Rellich's lemma still holds.
For example, the exact boundary condition derived from the Dirichlet-to-Neumann operator T_R, which is defined in the next appendix, satisfies this property. Indeed, this exact boundary condition is given by: $\frac{\partial p}{\partial \nu} + T_R(p) = 0$. As a property of the Dirichlet-to-Neumann operator stated in Proposition I.3.2.1, it is shown that:

$$Im\left(\langle T_R(p), p\rangle_{-1/2,1/2,S_R}\right) < 0, \quad \textit{for all } p \neq 0.$$

Therefore, denoting by T_R^* the adjoint operator of T_R, we get the relaxed property:

$$\begin{aligned} Im\left(\int_{S_R} p\frac{\partial \overline{p}}{\partial \nu} ds\right) &= -Im\left(\langle p, T_R^*(p)\rangle_{-1/2,1/2,S_R}\right) \\ &= -Im\left(\langle T_R(p), p\rangle_{-1/2,1/2,S_R}\right) \\ &\geq 0. \end{aligned}$$

A.3 The Dirichlet-to-Neumann operator

This section is devoted to the construction of the DtN operator on a sphere of radius $r = R$ [89, 94, 135].

Let B_R be the ball of radius $R > 0$ and center 0. We assume R to be large enough so that B_R contains the obstacle, i.e., $\Omega^s \subset B_R$.
We introduce an artificial spherical boundary S_R in the fluid medium, defined as the surface of the ball B_R:

$$S_R = \{x \in \Omega^f / \ \|x\|_2 = R\}. \tag{A.3.1}$$

We then denote by Ω_R^f the domain in the fluid medium bounded by S_R and Γ, and by B_R^e its exterior, i.e.,

$$\Omega_R^f = \{x \in \Omega^f / \ \|x\|_2 < R\}, \tag{A.3.2}$$

and

$$B_R^e = \mathbb{R}^3 \setminus \overline{\Omega_R^f \cup \Omega^s}. \tag{A.3.3}$$

The Sommerfeld outgoing-radiation condition (see Eq. (I.2.24) of BVP (1)) can be rewritten as fol-

lows

$$\lim_{R\to+\infty}\int_{S_R}\left|\frac{\partial p}{\partial r}-\mathrm{i}kp\right|^2 ds=0. \tag{A.3.4}$$

Let p^e be the solution of the Helmholtz equation (see BVP (1)) in B_R^e and $p^e = p$ on S_R given by Eq. (A.3.1). Note that the following construction of the DtN operator holds for all $p \in L^2(S_R)$.
Furthermore, since p^e is given, we can evaluate its normal derivative $\dfrac{\partial p^e}{\partial \nu}$ on S_R.
Hence, we can construct a mapping that maps the Dirichlet trace on S_R onto the Neumann trace on the same boundary as follows:

$$T_R:\ {p^e}_{|S_R}\longrightarrow -\frac{\partial}{\partial\nu}{p^e}_{|S_R}. \tag{A.3.5}$$

The operator T_R is called the Dirichlet-to-Neumann (DtN) operator. It is a pseudo-differential operator of order 1 that characterizes the exact behavior of the solution in the neighborhood of S_R.
This operator is linear and is defined from $H^{1/2}(S_R)$ into $H^{-1/2}(S_R)$ (see, e.g., [7]). Its expression can be determined explicitly ([94]).

Hence, we have:

$$\frac{\partial p^e}{\partial r}+T_R(p^e)=0 \quad \text{on } S_R. \tag{A.3.6}$$

Next, we set explicitly the expression of the DtN operator using the separation of variables procedure employed to derive the analytical expression of the solution of Helmholtz equation.
As shown in Appendix A.2, the outgoing radiating solution p^e in B_R^e admits the following series expansion into spherical harmonics:

$$p^e(r,\theta,\phi)=\sum_{n=0}^{+\infty}h_n(kr)\sum_{m=-n}^{n}C_{mn}Y_{mn}(\theta,\phi). \tag{A.3.7}$$

Therefore, from Remark A.1.2.1 in Appendix A.1, we can expand $p = p^e \in L^2(S_R)$ on the basis of the spherical harmonics on S_R as follows:

$$p^e(R,\theta,\phi)=\sum_{n=0}^{+\infty}\sum_{m=-n}^{n}p_{mn}Y_{mn}(\theta,\phi), \tag{A.3.8}$$

where

$$p_{mn}=\int_{S_1}p(R,\theta,\phi)\overline{Y}_{mn}(\theta,\phi)ds.$$

We can thus identify the expression of the complex coefficients C_{mn} in Eq. (A.3.7) as:

$$C_{mn} = \frac{p_{mn}}{h_n(kR)}. \tag{A.3.9}$$

Consequently, we deduce that:

$$p^e(r,\theta,\phi) = \sum_{n=0}^{+\infty} \frac{h_n(kr)}{h_n(kR)} \sum_{m=-n}^{n} p_{mn} Y_{mn}(\theta,\phi) \quad \text{in } B_R^e. \tag{A.3.10}$$

We derive the expression of the DtN operator by differentiating in the radial direction and taking $r = R$ in Eq. (A.3.10) as follows:

$$\begin{aligned} T_R\left(p(R,\theta,\phi)\right) &= T_R\left(p^e(R,\theta,\phi)\right) \\ &= -\frac{\partial p^e}{\partial r}(R,\theta,\phi) \\ &= -\sum_{n=0}^{+\infty} k \frac{h_n'(kR)}{h_n(kR)} \sum_{m=-n}^{n} p_{mn} Y_{mn}(\theta,\phi). \end{aligned} \tag{A.3.11}$$

We set

$$\mu_n(k,r) = -k\frac{h_n'(kr)}{h_n(kr)} \tag{A.3.12}$$

and

$$p_n(\theta,\phi) = \sum_{m=-n}^{n} p_{mn} Y_{mn}(\theta,\phi), \tag{A.3.13}$$

Then, we can re-write the series expansion of the DtN operator into spherical harmonics as follows:

$$T_R\left(p(R,\theta,\phi)\right) = \sum_{n=0}^{+\infty} \mu_n(k,R) p_n(\theta,\phi). \tag{A.3.14}$$

To conclude, the Dirichlet-to-Neumann operator defines an exact non-reflecting boundary condition on the artificial spherical boundary S_R. Thanks to its exact behavior, the near-field of the initial exterior Helmholtz problem in B_R^e can be exactly determined from the one of the reduced problem. In addition, we notice that, since the evaluation of the coefficients p_{mn} is accomplished by integrating over the whole surface S_R, the DtN operator is a nonlocal operator.

Chapter II

Efficient DG-like formulation equipped with curved boundary edges for solving elasto-acoustic scattering problems

In this chapter, a discontinuous Galerkin based approach is proposed for computing the scattered field from an elastic bounded object immersed in an infinite homogeneous fluid medium. The proposed method possesses two distinctive features. First, it employs higher-order polynomial-shape functions needed to address the high-frequency propagation regime. Second, it is equipped with curved boundary edges to provide an accurate representation of the fluid-structure interface. The most salient benefits resulting from the latter feature, as demonstrated by the numerical investigation, are (a) an improvement by -at least- two orders of magnitude on the relative error, and (b) the disappearance of spurious resonance frequencies in the surrounding fluid medium. In addition, the reported numerical results reveal that using cubic polynomials with less than three elements per wavelength, the proposed DG method computes the scattered field with a relative error below 1% for an elastic scatterer of about 30 wavelengths. This observation highlights the potential of the proposed solution methodology for efficiently solving mid- to high-frequency elasto-acoustic scattering problems.

II.1 Introduction

The development of robust, accurate, and efficient solution methodologies for wave propagation problems is important to many applications. These include radar and sonar detection, geophysical exploration, structural design, medical imaging and atmospheric studies. Although significant progress has been made over the years, the design of reliable and cost-effective numerical methods for mid- and high-frequency wave problems remains a serious challenge due to the presence of the so-called pollution effect [12]. Such a difficulty is clearly visible when solving Helmholtz problem, one of the

simplest mathematical models for time-harmonic scattering phenomena by a rigid object. Indeed, as it has been observed and well-documented (see [89, 134], among others), maintaining a prescribed level of accuracy as the frequency increases, requires, when using classical finite element methods (FEM), a drastic refinement of the mesh and/or the use of higher-order elements leading to prohibitive computational cost since the required hp-refinement incurs the solution of a linear system of equations that can rapidly exceed the available computational capabilities.

A number of new methods have been proposed in recent years to alleviate the pollution effect and improve the unsatisfactory preasymptotic convergence of the standard polynomial finite elements. Many of these approaches employ plane waves as shape functions, since these functions are (a) solution to the homogeneous, free space, Helmholtz equation, and (b) naturally expected to better approximate highly oscillating fields. Examples of such emerging techniques include the partition of unity method [11], the ultra-weak variational method (UWVF) [24], the discontinuous Galerkin method (DGM) [50, 53, 54], the stable discontinuous Galerkin method (SDGM) [6], the least-squares method (LSM) [111], the Trefftz-type wave-based method [38, 62], the plane wave discontinuous Galerkin methods (PWDG) [65, 81, 82], and the local discontinuous Galerkin method for large wave number [55–57]. The first three aforementioned promising methods (see [137] for comparison performance) have been extended to elasto-acoustic problems, in which the scatterer is no longer rigid but elastic, and therefore, the motion of the structure is modeled by the Navier equation for the structural displacements, whereas the acoustic waves in the fluid are modeled by the Helmholtz equation for the fluid pressure [45, 52, 88]. However, all these methods appear to suffer from two major drawbacks. The first one is that they are not applicable to anisotropic (at least inhomogeneous) scatterers as they rely on the knowledge of the exact solution, which limits significantly their application range . The second one is that the use of a higher number of plane waves (which can not be avoided in the mid- and high-frequency regimes) dramatically affects the condition number which in turns has a severe impact on the stability of the method, as observed and reported in [6, 69].

Other attempts have been made to solve efficiently elasto-acoustic scattering [26, 58, 61, 106, 107, 121, 131]. In spite of the tremendous strides, the design of efficient solution methodologies for this class of problems remains a recognized scientific need of pressing importance.

Given that, this chapter aims to propose a discontinuous Galerkin-type formulation for efficiently solving elasto-acoustic problems and to assess its performance. Our purpose is to develop an optimized solver for this direct problem, in the view to next solve the corresponding inverse elasto-acoustic obstacle problem (IOP) by a regularized Newton-type method. Indeed, the computational efficiency of the IOP solver will depend essentially on the efficiency of the solution of a large number

of forward problems that arise at each Newton iteration.

DG methods are of course not new numerical techniques [100, 127]. They have been in recent years among the primary candidates for solving problems involving convection/diffusion terms as well as reaction terms (see, for example, [112, 140] and the references cited therein). These methods received, more recently, a great deal of attention for wave problems, as attested by the various formulations that have been proposed for solving Helmholtz problems [5, 55, 56, 65, 68, 81, 82, 84, 103, 111, 128, 141]. This category of methods is very attractive because of several considerations, chief among them:

- They offer cost-effective procedures for linking separate elements/domains in each of which finite elements, or plane waves, or any expansion series are used for approximation. Indeed, the essence of DG methods lies in the elimination of the Lagrange multipliers, that are used in the domain decomposition framework to accomplish such linking [50–54], so that the total number of variables remains as the sum of those in the individual elements/domains.
- They can easily accommodate heterogeneous media and anisotropic obstacles when using polynomial shape functions, which is very important to many applications.
- They are very flexible for complicated geometries, allowing to consider any scatterer shape.
- They are more versatile since they can easily employ a non uniform mesh, which is very convenient for elasto-acoustic problems in which there are three types of waves (the pressure field in the fluid and the P- and S-waves in the solid) propagating at different speeds. This feature facilitates adaptive mesh implementation.
- The additional cost in p-type representation is proportional to $1/p$ for the interior points and the number of element interfaces. This feature is very important since employing higher-order elements is crucial for a reliable approximation of high frequency scattered fields.

In addition, the proposed DG formulation is equipped, at the element level, with a penalty-type term to preserve the stability of the method. For this reason, we will refer to this method by IPDG (Interior Penalty Discontinuous Galerkin). We must point out that IPDG has been originally designed for solving time-domain wave equation using linear elements [72], and its dispersion properties have been studied in [4]. However, to the best of our knowledge, this formulation has not been employed for solving other wave problems. We propose to tailor IPDG to be applied for solving elasto-acoustic scattering problems. However, the proposed solution methodology possesses two distinctive features. First, it employs high-order polynomial-shape functions that are obviously needed for an accurate approximation of highly oscillating waves. Second, it is equipped with curved boundary edges. Unlike polygonal-shaped approximations, such an accurate representation of the fluid-structure interface provides a very natural setting for better modeling the incoming and outgoing waves, as well as the

surface waves at the wet surface. The importance of an accurate representation of the fluid-structure interface is clearly illustrated by the numerical results obtained in the case of a two-dimensional elasto-acoustic scattering problem with a circular-shaped elastic scatterer. Indeed, these results indicate (a) an improvement on the accuracy level by -at least- two orders of magnitude, and (b) the disappearance of the spurious internal resonances in the fluid that usually occur when the fluid-structure interface is approximated by a "broken" line.

In this chapter, we intend to propose and validate a numerical solution methodology for the direct elasto-acoustic scattering problem. The remainder of the chapter is organized as follows. In Section II.2, we specify the notations adopted throughout this chapter and state the considered mathematical model. Section II.3 is devoted to the description of the proposed IPDG. In Section II.4, we develop two validation test cases for the IPDG method. This first one corresponds to a waveguide-type problem, it assumes that the solutions of the problem can be expressed in terms of simple planes waves. Similarly, the second test case is a radiating-type problem where the solutions are expressed as a Hankel function of the first kind and the gradient or curl of a Bessel function for a fixed mode. These tests allow to observe that we recover and approximate correctly the pressure field and both kind of elastic waves, i.e. the P-waves and the S-waves. Moreover, they allow to show some stability properties of the Discontinuous Galerkin method by performing a modal analysis. In Section II.5, we investigate the numerical performance of IPDG in the case of a two-dimensional homogeneous and isotropic disk-shaped elastic scatterer surrounded by an homogeneous fluid medium. Analytical solutions for the elasto-acoustic scattering problem can only be characterized for simple geometries, such as circles in 2D. Nevertheless, this kind of test is of practical interest and is reasonable for testing the accuracy of the method. We have a look to the resonance phenomenon that can exist in the elastic scatterer with this simple geometry. More specifically, we compute Jones frequencies and compare the results to those obtained with UWVF [88]. We first observe the results obtained with the classical IPDG method without curved boundary edges. They suggest that a particular care is needed for the resonance frequencies. Since a finer mesh on the transmission interface is not sufficient to improve sufficiently the accuracy level, we then equip the method with curved boundary edges and show its salient features. Next, we also examine the sensitivity of the method to the mesh refinement as well as to the frequency regime. More specifically, we assess the effect of using curved boundary edges on the convergence of the method and observe its behavior in the mid and high-frequency regimes. Closing remarks are given in Section II.6. In Appendix B.1, we recall the series expansion of the analytical solution for the disk-shaped elastic scatterer problem considered in Section II.5. The Appendix B.2 addresses a brief analysis on the sensitivity of the Jones frequencies to perturbations of

the scatterer. The last Appendix B.3 provides a sensitivity analysis to the penalization parameter.

II.2 Nomenclature and Problem Statement

II.2.1 Nomenclature

Throughout this chapter, we adopt the following notations and assumptions:

- Ω^s is a bounded domain of $\mathbb{R}^2$ representing an elastic obstacle.
- Ω^f is the bounded fluid medium surrounding the elastic domain.
- Γ is the wet surface of the scatterer Ω^s.
- Σ is the exterior boundary of Ω^f.
- $|\cdot|$ is the Euclidean norm in $\mathbb{R}^2$.
- x is a point of $\mathbb{R}^2$, understood as a column vector and $r = |x|$ is the distance from an origin point to x.
- d is a unit vector representing the propagation direction of the incident plane wave.
- ν is the outward normal to Γ and Σ, $\dfrac{\partial}{\partial \nu}$ is the normal derivative operator.
- ∇ is the gradient operator in $\mathbb{R}^2$.
- $(-e_z) \times \nabla$ defines the curl operator in $\mathbb{R}^2$, where e_z represents the third vector of the canonical basis in $\mathbb{R}^3$.
- $[\cdot]^t$ denotes the transpose matrix.
- M^* denotes the adjoint matrix of M, which is defined as the complex conjugate transpose of M.
- $L^2(E)$ is the standard Lebesgue space and $H^l(E)$ denotes the Sobolev spaces (see, for instance, [3] for definitions and properties).
- $\mathcal{K}_h^f$ and $\mathcal{K}_h^s$ are mesh partitions of the domains Ω^f and Ω^s respectively, composed of triangles K. $\mathcal{K}_h = \mathcal{K}_h^f \cup \mathcal{K}_h^s$ represents the total partition of the computational domain.

- For each element $K \in \mathcal{K}_h$, h_K represents the diameter of K, $h = \min_K h_K$, and d_K represents the diameter of the inscribed circle in K. We assume that there exists a constant $C \geq 1$ such that (see [27]):

$$\frac{h_K}{d_K} \leq C, \quad \forall h, \forall K \in \mathcal{K}_h.$$

This condition prevents the presence of skinny triangles.

- $\mathbb{P}_p(K)$ designates the space of polynomial functions defined on K of degree at most $p \geq 1$.
- The finite element approximation spaces for the pressure and the structural displacement solutions in the fluid and solid media are respectively given by:

$$\begin{aligned} V_h^f &:= \{q \in L^2(\Omega^f) : q_{|K} \in \mathbb{P}_p(K), \forall\, K \in \mathcal{K}_h^f\} \\ V_h^s &:= \{v \in (L^2(\Omega^s))^2 : v_{|K} \in (\mathbb{P}_p(K))^2, \forall\, K \in \mathcal{K}_h^s\}. \end{aligned}$$

  Hence, we consider functions that are piecewise polynomials in each element and whose degrees are less than or equal to p. However, unlike standard finite elements, such functions are not continuous over the computational domain $\Omega^s \cup \Omega^f$. They are only L^2.
- $H^l(\mathcal{K}_h^f) = \{q \in L^2(\Omega^f) : q_{|K} \in H^l(K)\}$, $l \in \mathbb{N}$.
  Hence $V_h^f \subseteq H^l(\mathcal{K}_h^f)$. Similarly, $H^l(\mathcal{K}_h^s)$ is the space for the vectorial displacement field in the solid.
- $\mathcal{E}^f$ and $\mathcal{E}^s$ denote the set of all edges in $\mathcal{K}_h^f$ and $\mathcal{K}_h^s$. $\mathcal{E}_{h,R}^f$ is the set of edges on the exterior boundary Σ, and $\mathcal{E}_{h,tr}^{f,s}$ corresponds to the set of edges on the fluid-structure interface Γ. $\mathcal{E}_{h,int}^f$ and $\mathcal{E}_{h,int}^s$ represent the sets of internal edges in $\mathcal{K}_h^f$ and $\mathcal{K}_h^s$. They are such that $\mathcal{E}_{h,int}^f \cap (\mathcal{E}_{h,R}^f \cup \mathcal{E}_{h,tr}^{f,s}) = \varnothing$ and $\mathcal{E}_{h,int}^s \cap \mathcal{E}_{h,tr}^{f,s} = \varnothing$. It is worth mentioning that the boundary edges on the fluid-solid interface Γ and the exterior fluid surface $\mathcal{E}_{h,R}^f$ are curved and not straight boundary edges (see Fig. II.2.1(b)).

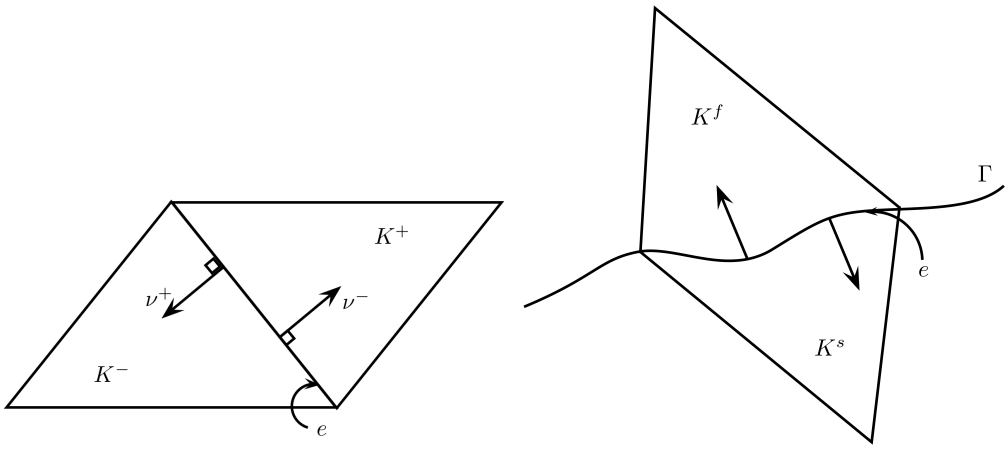

(a) Straight boundary edge for interior triangles (b) Curved boundary edge for triangles at the fluid-structure interface.

Figure II.2.1 – Illustration for two adjacent triangles.

- Note that an edge e in $\mathcal{E}_{h,int}^f$, $\mathcal{E}_{h,int}^s$or $\mathcal{E}_{h,tr}^{f,s}$ is shared by two elements denoted arbitrarily by K^+ and K^-, i.e., $e = \partial K^+ \cap \partial K^-$ (see Figure II.2.1).

- The unit normal vectors to K^+ and K^-, oriented to the exterior direction, are denoted ν^+ and ν^- (see Figure II.2.1).
- For $e \in \mathcal{E}^f_{h,int} \cup \mathcal{E}^s_{h,int}$, we set $d_e = \frac{1}{2}\min\{d_{K^+}, d_{K^-}\}$.
- The traces of a function $q \in H^1(\mathcal{K}^f_h)$ on K^+ and K^- represented by q^+ and q^- exist and belong to $T(\mathcal{E}^f_h) = \prod_{K\in\mathcal{K}^f_h} L^2(\partial K)$. Thus, a function in $T(\mathcal{E}^f_h)$ admits two values on $\mathcal{E}^f_{h,int} \cup \mathcal{E}^{f,s}_{h,tr}$ and one value on $\mathcal{E}^f_{h,R}$. Similar notations can be defined for the trace of a vectorial function $v \in (H^1(\mathcal{K}^s_h))^2 \subseteq (T(\mathcal{E}^s_h))^2$ with $T(\mathcal{E}^s_h) = \prod_{K\in\mathcal{K}^s_h} L^2(\partial K)$.
- The jump and average of $\phi \in T(\mathcal{E}^f_h) \cup T(\mathcal{E}^s_h)$ through an edge are defined by:

$$[\phi] := \phi^+ - \phi^- \quad \text{and} \quad \{\phi\} := \frac{\phi^+ + \phi^-}{2} \quad \text{on } \partial K^+ \cap \partial K^-. \tag{II.2.1}$$

  Note that for an edge on the exterior boundary, it is reduced to:

$$[\phi] := \phi \quad \text{and} \quad \{\phi\} := \phi \quad \text{on } \partial K^+ \cap \Sigma.$$

II.2.2 Problem Statement

Let Ω^s be a bounded domain of $\mathbb{R}^n$ representing an elastic obstacle, and $\Omega^f = \mathbb{R}^n \setminus \overline{\Omega}^s$ be the homogeneous inviscid (fluid) medium surrounding the elastic domain. Γ is the boundary of Ω^s and is assumed to be Lipschitz continuous.
We consider the scattering of a time-harmonic acoustic wave by the elastic obstacle Ω^s embedded in Ω^f as depicted on Figure II.2.2. The corresponding system of equations BVP (1) reads as the coupling

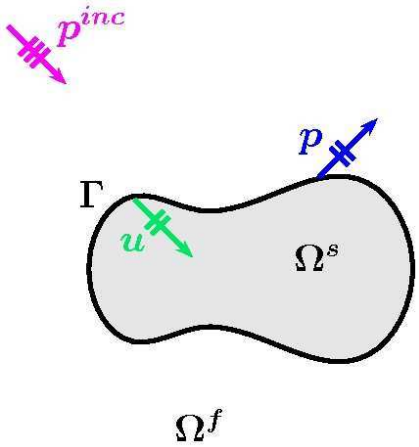

Figure II.2.2 – Problem statement in the infinite domain.

of the Helmholtz and Navier equations. This problem can be formulated as follows:

$$\text{BVP (1)} \quad \begin{cases} \Delta p + k^2 p = 0 & \text{in } \Omega^f \quad \text{(II.2.2)} \\ \nabla \cdot \sigma(u) + \omega^2 \rho_s u = 0 & \text{in } \Omega^s \quad \text{(II.2.3)} \\ \omega^2 \rho_f u \cdot \nu = \dfrac{\partial p}{\partial \nu} + \dfrac{\partial g}{\partial \nu} & \text{on } \Gamma \quad \text{(II.2.4)} \\ \tau(u) = -p\nu - g\nu & \text{on } \Gamma \quad \text{(II.2.5)} \\ \lim\limits_{r \to +\infty} r^{(n-1)/2} \left(\dfrac{\partial p}{\partial r} - \mathrm{i}kp \right) = 0. & \quad \text{(II.2.6)} \end{cases}$$

The pair (p, u) represents the elasto-acoustic scattered field. p is the fluid pressure in Ω^f whereas u is the displacement field in Ω^s. $g = p^{inc} = e^{\mathrm{i}\omega/c_f x \cdot d}$ is the incident plane wave. ω is the circular frequency. c_f is a positive real number representing the sound velocity in the fluid. ρ_f and ρ_s are positive real numbers denoting respectively the densities of the fluid Ω^f and of the scatterer Ω^s. Hence, k represents the wavenumber in the fluid, given by $k = \omega/c_f$. Note that k is the reference frequency for the considered problem.
σ is the stress tensor related to the strain tensor ε by Hooke's law:

$$\sigma_{lm} = C_{lmjn} \varepsilon_{jn},$$

where C_{lmjn} is a fourth order elastic stiffness tensor which is, for an isotropic medium, invariant under rotations and reflections [93]. Therefore, C_{lmjn} is given by:

$$C_{lmjn} = \lambda \delta_{lm} \delta_{jn} + \mu(\delta_{lj}\delta_{mn} + \delta_{ln}\delta_{mj}),$$

where λ, μ are the Lamé coefficients. The strain tensor ε is related to the displacement field u by [93, 120]:

$$\varepsilon(u) = \frac{1}{2} \left(\nabla u + (\nabla u)^t \right).$$

Last, τ denotes the traction vector on the surface of the scatterer Ω^s, that is:

$$\tau(u) = \sigma(u)\nu.$$

The boundary conditions on the wet surface Γ describe the coupling between acoustic and elastic waves. The first one is a kinematic transmission condition, whereas the second one is a dynamic

transmission condition.

The well-posed nature of BVP (1) has been investigated in [46, 85, 87, 104] in the case of isotropic elastic scatterers and in Chapter I. More specifically, it has been established that the solution (u, p) of BVP (1) exists and is unique only in the absence of Jones frequencies. These interior resonance frequencies are usually present in scatterers with axial symmetry such as cylinders and spheres. These frequencies do not exist in the case of arbitrarily-shaped bodies, as demonstrated in [79]. For additional mathematical results, we refer the reader to [43, 79, 92, 93, 104], among other references.

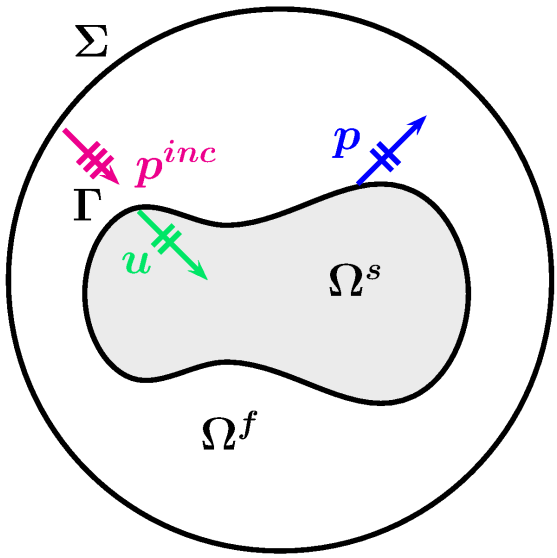

Figure II.2.3 – Prototypical computational domain.

In view of using of a finite element method, we introduce an artificial boundary Σ in the infinite fluid medium to bound the computational domain as depicted on Figure II.2.3. Given that, as described in Chapter I, we consider the following elasto-acoustic scattering problem defined in a bounded domain:

$$\text{BVP (2)} \quad \begin{cases} \Delta p + k^2 p = 0 & \text{in } \Omega^f & \text{(II.2.7)} \\ \nabla \cdot \sigma(u) + \omega^2 \rho_s u = 0 & \text{in } \Omega^s & \text{(II.2.8)} \\ \omega^2 \rho_f u \cdot \nu = \dfrac{\partial p}{\partial \nu} + \dfrac{\partial g}{\partial \nu} & \text{on } \Gamma & \text{(II.2.9)} \\ \tau(u) = -p\nu - g\nu & \text{on } \Gamma & \text{(II.2.10)} \\ \dfrac{\partial p}{\partial \nu} + T_R(p) = 0 & \text{on } \Sigma & \text{(II.2.11)} \end{cases}$$

where T_R denotes the Dirichlet-to-Neumann operator (DtN) operator.

In the following, we use the simplest approximation of the DtN operator, corresponding to a Robin-type condition, given by:

$$\frac{\partial p}{\partial \nu} - ikp = 0 \quad \text{on } \Sigma. \tag{II.2.12}$$

It is worth noting that the low-order absorbing boundary condition given by Eq. (II.2.12) gives rise to spurious reflections, deteriorating the approximation. To improve the accuracy of the solution, it is more interesting to consider at least a first-order absorbing boundary condition involving the mean curvature of Σ. Nevertheless, in the numerical tests that we will consider in this Chapter, this low-order condition will be sufficient. Indeed, the ABC will be taken into account in the expression of the exact solution in order to draw up a suitable analysis.
Recall, that in the case of a circular-shaped artificial boundary, we have proven in Chapter I the existence of a solution to the reduced problem BVP (2), and the result holds when replacing Eq. (II.2.11) by Eq. (II.2.12).

II.3 The Interior Penalty Discontinuous Galerkin Method (IPDG)

II.3.1 The approximation space

In this section, we construct a basis of the spaces V_h^f and V_h^s. To this end, we first introduce the degrees of freedom (d.o.f) of the mesh for such Galerkin Discontinuous finite elements. Let N_h^f (resp. N_h^s) be the number of elements in the fluid (resp. solid) medium, and N be the total number of elements of the mesh, i.e. $N = N_h^f + N_h^s$. For each element K of the mesh, n^K represents the number of degrees of freedom corresponding to the polynomial finite elements $\mathbb{P}_p$. For simplicity, we assume $n^K = m$, that is, we use the same element order in each triangle. In 2D, the dimensions of the $\mathbb{P}_1(K), \mathbb{P}_2(K)$ and $\mathbb{P}_3(K)$ element spaces are respectively given by m equal to 3, 6 and 10. Then, the total number of degrees of freedom in the fluid part used to approximate p_h in V_h^f is equal to $N^f := m \times N_h^f$. We denote by P_i^f the corresponding points, for all $1 \leq i \leq N^f$. Similarly, $N^s := m \times N_h^s$ is the number of unknowns to approximate each component of the displacement field $u_h = (u_{xh}, u_{y_h})$ in V_h^s. The corresponding points are denoted by P_i^s, for all $1 \leq i \leq N^s$. Therefore, the total number of unknowns is equal to $m(N_h^f + 2N_h^s)$, where the factor 2 results from the two components of the displacement field.

Next, consider an element K_l in $\mathcal{K}_h$, with $1 \leq l \leq N_h^f$, and let $(\phi_i^{K_l})_{i=1,\cdots,m}$ be the Lagrange basis functions of degree p in $\mathbb{P}_p(K_l)$. We denote by $G(i, K_l)$ the function allowing to determine the global numbering of the i^{th} degree of freedom of the element K_l on the mesh.
Then, we define $\{\phi_i, 1 \leq i \leq N^f\}$ a basis of the approximation space V_h^f which is of dimension N^f as follows:

$$\begin{cases} \phi_i(P_j^f) = \delta_{ij}, \quad \forall\, i,j = 1,\cdots,N^f, \\ \phi_{i|K_l} \in \mathbb{P}_p(K_l), \quad \forall\, K_l \in \mathcal{K}_h^f,\ \forall\, i = 1,\cdots,N^f. \end{cases}$$

The global basis functions ϕ_i can be expressed in terms of the Lagrange basis functions on K_l as:

$$\begin{cases} \phi_{i|K_l} = \phi_j^{K_l}, \quad \text{with } j \text{ such that } i = G(j,K_l), \quad \text{if } P_i^f \in K_l, \\ \phi_{i|K_l} = 0, \quad \text{if } P_i^f \notin K_l. \end{cases}$$

It follows that any function q_h in V_h^f can be expanded under the following form:

$$q_h(x) = \sum_{j=1}^{N^f} q_j \phi_j(x) = \sum_{l=1}^{N_h^f} \sum_{i=1}^{m} {q_i}^{K_l} \phi_i^{K_l}(x),$$

where the components of q_h in this basis coincide with its degrees of freedom on the mesh, that is $q_j = q_h(P_j^f),\ \forall\, j = 1,\cdots,N^f$.

Regarding the displacement field, we define a basis $\{\psi_i, 1 \leq i \leq 2N_s\}$ of V_h^s of dimension $2N^s$ in the same way. Let (e_x, e_y) be the canonical basis in $\mathbb{R}^2$. We set, for any K_l in $\mathcal{K}_h^s$,

$${\psi_i}^{K_l} = \begin{cases} \phi_i^{K_l} e_x, & \forall\, i = 1,\cdots,m \\ \phi_{i-m}^{K_l} e_y, & \forall\, i = m+1,\cdots,2m. \end{cases}$$

Then, any function of $v_h \in V_h^s$ can be written as follows:

$$\begin{aligned} v_h(x) &= (v_{xh}(x), (v_y)_h(x)) = (\sum_{l=1}^{N_h^s} \sum_{i=1}^{m} v_{x,i}^{K_l} \phi_i^{K_l}(x), \sum_{l=1}^{N_h^s} \sum_{i=1}^{m} v_{y,i}^{K_l} \phi_i^{K_l}(x)) \\ &= \sum_{l=1}^{N_h^s} \sum_{i=1}^{m} v_{x,i}^{K_l} \phi_i^{K_l}(x) e_x + \sum_{l=1}^{N_h^s} \sum_{i=1}^{m} v_{y,i}^{K_l} \phi_i^{K_l}(x) e_y \\ &= \sum_{l=1}^{N_h^s} \sum_{i=1}^{m} \left(v_{x,i}^{K_l} \psi_i^{K_l}(x) + v_{y,i}^{K_l} \psi_{i+m}^{K_l}(x) \right) \end{aligned}$$

$$= \sum_{j=1}^{2N^s} v_j \psi_j(x),$$

where

$$v_j = \begin{cases} v_{xh}(P_j^s), & \forall\, j = 1, \cdots, N^s \\ v_{y_h}(P_j^s), & \forall\, j = N^s + 1, \cdots, 2N^s. \end{cases}$$

II.3.2 The Variational Formulation

In this section, we derive the variational formulation for BVP (2) corresponding to the IPDG method.

Let $(q_h, v_h) \in V_h^f \times V_h^s$. Multiplying by the pair of test functions and integrating Eqs. (II.2.7) and (II.2.8) of BVP (2) on Ω_R^f and Ω^s respectively, we first have:

$$\sum_{K \in K_h^f} \left(\int_K \Delta p \overline{q_h}\, dx + \frac{\omega^2}{c_f^2} \int_K p \overline{q_h}\, dx \right) = 0,$$
$$\sum_{K \in K_h^s} \left(\int_K \nabla \cdot \sigma(u) \overline{v_h}\, dx + \omega^2 \rho_s \int_K u \overline{v_h}\, dx \right) = 0.$$

Applying Green's theorem, we obtain:

$$\begin{aligned} &\sum_{K \in K_h^f} \left(\int_K \nabla p \cdot \nabla \overline{q_h}\, dx - \frac{\omega^2}{c_f^2} \int_K p \overline{q_h}\, dx \right) \\ &- \sum_{e \in \mathcal{E}_{h,int}^f} \left(\int_e (\nabla p^+ \cdot \nu^+ \overline{q_h}^+ + \nabla p^- \cdot \nu^- \overline{q_h}^-) \right) ds + \sum_{e \in \mathcal{E}_{h,tr}^{f,s}} \int_e \nabla p \cdot \nu^+ \overline{q_h}\, ds \\ &- \sum_{e \in \mathcal{E}_{h,R}^f} \int_e \nabla p \cdot \nu^+ \overline{q_h}\, ds = 0, \end{aligned} \tag{II.3.1}$$

$$\begin{aligned} &\sum_{K \in K_h^s} \left(\int_K \sigma(u) : \nabla \overline{v_h}\, dx - \omega^2 \rho_s \int_K u \overline{v_h}\, dx \right) \\ &- \sum_{e \in \mathcal{E}_{h,int}^s} \left(\int_e (\sigma(u)^+ \cdot \nu^+ \overline{v_h}^+ + \sigma(u)^- \cdot \nu^- \overline{v_h}^-) \right) ds \\ &- \sum_{e \in \mathcal{E}_{h,tr}^{f,s}} \int_e \sigma(u) \cdot \nu^+ \overline{v_h}\, ds = 0. \end{aligned} \tag{II.3.2}$$

Substituting both transmission conditions Eqs. (II.2.9)-(II.2.10) into Eqs. (II.3.1)-(II.3.2), it follows

that:

$$\sum_{K\in K_h^f}\left(\int_K \nabla p\cdot\nabla\overline{q_h}\,dx-\frac{\omega^2}{c_f^2}\int_K p\overline{q_h}\,dx\right)$$
$$-\sum_{e\in\mathcal{E}_{h,int}^f}\left(\int_e(\nabla p^+\cdot\nu^+\overline{q_h}^+ +\nabla p^-\cdot\nu^-\overline{q_h}^-\right)ds+\sum_{e\in\mathcal{E}_{h,tr}^{f,s}}\int_e\omega^2\rho_f u\cdot\nu^+\overline{q_h}\,ds$$
$$-\sum_{e\in\mathcal{E}_{h,R}^f}\int_e\nabla p\cdot\nu^+\overline{q_h}\,ds=\sum_{e\in\mathcal{E}_{h,tr}^{f,s}}\int_e\nabla g\cdot\nu^+\overline{q_h}\,ds, \tag{II.3.3}$$
$$\sum_{K\in K_h^s}\left(\int_K\sigma(u):\nabla\overline{v_h}\,dx-\omega^2\rho_s\int_K u\overline{v_h}\,dx\right)$$
$$-\sum_{e\in\mathcal{E}_{h,int}^s}\left(\int_e(\sigma(u)^+\cdot\nu^+\overline{v_h}^+ +\sigma(u)^-\cdot\nu^-\overline{v_h}^-\right)ds+\sum_{e\in\mathcal{E}_{h,tr}^{f,s}}\int_e p\nu^+\overline{v_h}\,ds=$$
$$-\sum_{e\in\mathcal{E}_{h,tr}^{f,s}}\int_e g\nu^+\overline{v_h}\,ds. \tag{II.3.4}$$

Substituting the absorbing boundary condition Eq. (II.2.12) on Σ into Eq. (II.3.3), and multiplying the Eq. (II.3.3) by $1/\rho_f$, we obtain the following discretized problem: for all $(q_h,v_h)\in V_h^f\times V_h^s$,

$$\sum_{K\in K_h^f}\left(\int_K\frac{1}{\rho_f}\nabla p\cdot\nabla\overline{q_h}\,dx-\frac{1}{\rho_f}\frac{\omega^2}{c_f^2}\int_K p\overline{q_h}\,dx\right)$$
$$-\sum_{e\in\mathcal{E}_{h,int}^f}\int_e(\frac{1}{{\rho_f}^+}\nabla p^+\cdot\nu^+\overline{q_h}^+ +\frac{1}{{\rho_f}^-}\nabla p^-\cdot\nu^-\overline{q_h}^-)\,ds+\sum_{e\in\mathcal{E}_{h,tr}^{f,s}}\int_e\omega^2 u\cdot\nu^+\overline{q_h}\,ds$$
$$-\sum_{e\in\mathcal{E}_{h,R}^f}\mathrm{i}\int_e\frac{\omega}{\rho_f c_f}p\overline{q_h}\,ds=\sum_{e\in\mathcal{E}_{h,tr}^{f,s}}\int_e\frac{1}{\rho_f}\nabla g\cdot\nu^+\overline{q_h}\,ds, \tag{II.3.5}$$
$$\sum_{K\in K_h^s}\left(\int_K\sigma(u):\nabla\overline{v_h}\,dx-\omega^2\rho_s\int_K u\overline{v_h}\,dx\right)$$
$$-\sum_{e\in\mathcal{E}_{h,int}^s}\int_e(\sigma(u)^+\cdot\nu^+\overline{v_h}^+ +\sigma(u)^-\cdot\nu^-\overline{v_h}^-)\,ds+\sum_{e\in\mathcal{E}_{h,tr}^{f,s}}\int_e p\nu^+\overline{v_h}\,ds$$
$$=-\sum_{e\in\mathcal{E}_{h,tr}^{f,s}}\int_e g\nu^+\overline{v_h}\,ds. \tag{II.3.6}$$

Moreover, we observe that:

$$\frac{1}{{\rho_f}^+}\nabla p^+\cdot\nu^+\overline{q_h}^+ +\frac{1}{{\rho_f}^-}\nabla p^-\cdot\nu^-\overline{q_h}^- \;=\; \left(\frac{1}{{\rho_f}^+}\nabla p^+\cdot\nu^+ +\frac{1}{{\rho_f}^-}\nabla p^-\cdot\nu^-\right)\left(\frac{\overline{q_h}^+ +\overline{q_h}^-}{2}\right)$$

$$
\begin{aligned}
&+\frac{1}{2}\left(\frac{1}{{\rho_f}^+}\nabla p^+ + \frac{1}{{\rho_f}^-}\nabla p^-\right)\left({\overline{q_h}}^+\nu^+ + {\overline{q_h}}^-\nu^-\right)\\
=\;& \left(\frac{1}{{\rho_f}^+}\nabla p^+\cdot\nu^+ + \frac{1}{{\rho_f}^-}\nabla p^-\cdot\nu^-\right)\left(\frac{{\overline{q_h}}^+ + {\overline{q_h}}^-}{2}\right)\\
&+\frac{1}{2}\left(\frac{1}{{\rho_f}^+}\nabla p^+ + \frac{1}{{\rho_f}^-}\nabla p^-\right)\nu^+\left({\overline{q_h}}^+ - {\overline{q_h}}^-\right)\\
=\;& \left[\frac{1}{\rho_f}\nabla p\cdot\nu\right]\{\overline{q_h}\} + \{\frac{1}{\rho_f}\nabla p\}\nu^+[\overline{q_h}].
\end{aligned}
$$

and

$$
\begin{aligned}
\sigma(u)^+\nu^+\cdot{\overline{v_h}}^+ + \sigma(u)^-\nu^-\cdot{\overline{v_h}}^- &= \left(\sigma(u)^+\nu^+ + \sigma(u)^-\nu^-\right)\left(\frac{{\overline{v_h}}^+ + {\overline{v_h}}^-}{2}\right)\\
&\quad+\frac{1}{2}\left(\sigma(u)^+\nu^+ - \sigma(u)^-\nu^-\right)\left({\overline{v_h}}^+ - {\overline{v_h}}^-\right)\\
&= \left(\sigma(u)^+\nu^+ + \sigma(u)^-\nu^-\right)\left(\frac{{\overline{v_h}}^+ + {\overline{v_h}}^-}{2}\right)\\
&\quad+\frac{1}{2}\left(\sigma(u)^+ + \sigma(u)^-\right)\nu^+\cdot\left({\overline{v_h}}^+ - {\overline{v_h}}^-\right)\\
&= [\sigma(u)\nu]\{\overline{v_h}\} + \{\sigma(u)\}\nu^+\cdot[\overline{v_h}].
\end{aligned}
$$

Substituting the latter expressions into Eqs. (II.3.5)-(II.3.6) leads to the following variational formulation:

$$
\begin{cases}
a^f(p,q_h) + b((p,u),(q_h,v_h)) + c^R(p,q_h) = f_1(q_h),\\
a^s(u,v_h) + b^*((p,u),(q_h,v_h)) = f_2(v_h),
\end{cases}
\qquad \forall\,(q_h,v_h)\in V_h^f\times V_h^s \tag{II.3.7}
$$

where

$$
\begin{aligned}
a^f(p,q_h) &= \sum_{K\in K_h^f}\left(\int_K \frac{1}{\omega^2}\frac{1}{\rho_f}\nabla p\cdot\nabla\overline{q_h}\,dx - \frac{1}{\rho_f}\frac{\omega^2}{c_f^2}\int_K p\overline{q_h}\,dx\right) \qquad \text{(II.3.8)}\\
&\quad-\sum_{e\in\mathcal{E}_{h,int}^f}\frac{1}{\omega^2}\int_e\left(\left[\frac{1}{\rho_f}\nabla p\cdot\nu\right]\{\overline{q_h}\} + \{\frac{1}{\rho_f}\nabla p\}\nu^+[\overline{q_h}]\right)ds\\
b((p,u),(q_h,v_h)) &= \sum_{e\in\mathcal{E}_{h,tr}^{f,s}}\int_e u\cdot\nu^+\overline{q_h}\,ds \qquad \text{(II.3.9)}\\
c^R((p,u),(q_h,v_h)) &= -\sum_{e\in\mathcal{E}_{h,R}^f}\frac{\mathrm{i}}{\omega^2}\int_e\frac{\omega}{\rho_f c_f}p\overline{q_h}\,ds \qquad \text{(II.3.10)}
\end{aligned}
$$

$$f_1(q_h) = \sum_{e\in\mathcal{E}_{h,tr}^{f,s}} \frac{1}{\omega^2}\int_e \frac{1}{\rho_f}\nabla g\cdot\nu^+\overline{q_h}\,ds, \tag{II.3.11}$$

$$a^s(u,v_h) = \sum_{K\in K_h^s}\left(\int_K \sigma(u):\nabla\overline{v_h}\,dx - \omega^2\rho_s\int_K u\overline{v_h}\,dx\right) \tag{II.3.12}$$

$$- \sum_{e\in\mathcal{E}_{h,int}^{s}}\int_e([\sigma(u)\nu]\{\overline{v_h}\} + \{\sigma(u)\}\nu^+\cdot[\overline{v_h}])\,ds$$

$$f_2(v_h) = -\sum_{e\in\mathcal{E}_{h,tr}^{f,s}}\int_e g\nu^+\overline{v_h}\,ds. \tag{II.3.13}$$

(II.3.14)

Next, we proceed to some arrangements to obtain the IPDG formulation that will be an approximation of Eq. (II.3.7). First, the solution (p,u) of the transmission problem BVP (2) has to satisfy the following weak continuity constraints:

$$[\frac{1}{\rho_f}\nabla p\cdot\nu] = 0 \quad \text{and} \quad [\sigma(u)\nu] = 0. \tag{II.3.15}$$

Therefore, we remain consistent writing:

$$\frac{1}{{\rho_f}^+}\nabla p^+\cdot\nu^+\overline{q_h}^+ + \frac{1}{{\rho_f}^-}\nabla p^-\cdot\nu^-\overline{q_h}^- = \{\frac{1}{\rho_f}\nabla p\}\nu^+[\overline{q_h}] \tag{II.3.16}$$

and

$$\sigma(u)^+\nu^+\cdot\overline{v_h}^+ + \sigma(u)^-\nu^-\cdot\overline{v_h}^- = \{\sigma(u)\}\nu^+\cdot[v_h]. \tag{II.3.17}$$

Observe that the terms are not hermitian. We then enforce the weak continuity of the solution through each interior element of the mesh, by seeking a solution such that:

$$[p] = 0 \quad \text{and} \quad [u] = 0. \tag{II.3.18}$$

Consequently, we remain consistent when re-writing Eq. (II.3.16)-(II.3.17) as :

$$\frac{1}{{\rho_f}^+}\nabla p^+\cdot\nu^+\overline{q_h}^+ + \frac{1}{{\rho_f}^-}\nabla p^-\cdot\nu^-\overline{q_h}^- = \{\frac{1}{\rho_f}\nabla p\}\nu^+[\overline{q_h}] + \{\frac{1}{\rho_f}\nabla\overline{q_h}\}\nu^+[p]. \tag{II.3.19}$$

and

$$\sigma(u)^+\nu^+\cdot\overline{v_h}^+ + \sigma(u)^-\nu^-\cdot\overline{v_h}^- = \{\sigma(u)\}\nu^+[\overline{v_h}] + \{\sigma(\overline{v_h})\}\nu^+[u]. \tag{II.3.20}$$

In addition, to guarantee the stability, we must ensure the coercivity of the formulation. To this end, we add the following interior penalty terms in the fluid and solid parts respectively:

$$\frac{\gamma_f c^f_{max}}{d_e}[p][\overline{q_h}] \quad \text{and} \quad \frac{\gamma_s c^s_{max}}{d_e}[u][\overline{v_h}], \tag{II.3.21}$$

where

- γ_f and γ_s are two real penalty parameters that depend on the polynomial order [4];
- $c^f_{max} = \max(\frac{1}{\rho_f{}^+}, \frac{1}{\rho_f{}^-})$
- $c^s_{max} = \max(C_{K^+}, C_{K^-})$, where $C_{K^+} = \max\limits_{ijkl} |C_{ijkl}|$.

Note that, instead of d_e, one could have used $h_e = \min(h_{K^+}, h_{K^-})$. Moreover, observe that this formulation allows to consider heterogeneous media. However, in the following we will only consider homogeneous media. Therefore, both coefficients c^f_{max} and c^s_{max} are fixed equal to $\frac{1}{\rho_f}$, and $\max_{ijkl} |C_{ijkl}|$ respectively.

Given that, combining Eqs. (II.3.19)- (II.3.21), we deduce an approximation of the bilinear forms $a^f(\cdot,\cdot)$ and $a^s(\cdot,\cdot)$ (see Eq. (II.3.7)). The proposed IPDG approach consists in formulating BVP (2) as the following variational problem:

$$\text{(VF)} \quad \begin{cases} \text{Find } (p_h, u_h) \in V_h^f \times V_h^s \text{ such that} \\ a_h^f(p_h, q_h) + b_h((p_h, u_h), (q_h, v_h)) + c_h(p_h, q_h) = f_1(q_h), \quad \forall\, (q_h, v_h) \in V_h^f \times V_h^s \\ a_h^s(u_h, v_h) + b_h^*((p_h, u_h), (q_h, v_h)) = f_2(v_h), \end{cases} \tag{II.3.22}$$

where a_h^f and a_h^s are two sesquilinear and hermitian forms given by:

$$\begin{aligned} a_h^f(p_h, q_h) \;=\; & \sum_{K \in K_h^f} \frac{1}{\omega^2} \left(\int_K \frac{1}{\rho_f} \nabla p_h \cdot \nabla \overline{q_h}\, dx - \frac{1}{\rho_f} \frac{\omega^2}{c_f^2} \int_K p_h \overline{q_h}\, dx \right) \\ & - \sum_{e \in \mathcal{E}^f_{h,int}} \frac{1}{\omega^2} \int_e \left(\{\frac{1}{\rho_f} \nabla p_h\} \nu [\overline{q_h}] + \{\frac{1}{\rho_f} \nabla \overline{q_h}\} \nu [p_h] \right) ds \\ & + \sum_{e \in \mathcal{E}^f_{h,int}} \frac{\gamma_f}{\omega^2 d_e} \int_e c^f_{max} [p_h][\overline{q_h}]\, ds, \end{aligned} \tag{II.3.23}$$

$$a_h^s(u_h, v_h) \;=\; \sum_{K \in K_h^s} \left(\int_K \sigma(u_h) : \nabla \overline{v_h}\, dx - \omega^2 \rho_s \int_K u_h \cdot \overline{v_h}\, dx \right) \tag{II.3.24}$$

$$- \sum_{e \in \mathcal{E}^s_{h,int}} \int_e (\{\sigma(u_h)\}\nu \cdot [\overline{v_h}] + \{\sigma(\overline{v_h})\}\nu \cdot [u_h])\ ds$$
$$+ \sum_{e \in \mathcal{E}^s_{h,int}} \frac{\gamma_s}{d_e} \int_e c^s_{max}[u_h] \cdot [\overline{v_h}]\, ds;$$

c_h and b_h are two sesquilinear forms given by:

$$c_h(p_h, q_h) = - \sum_{e \in \mathcal{E}^f_{h,R}} \frac{\mathrm{i}}{\omega^2} \int_e \frac{\omega}{\rho_f c_f} p_h \overline{q_h}\, ds, \tag{II.3.25}$$

$$b_h((p_h, u_h), (q_h, v_h)) = \sum_{e \in \mathcal{E}^{f,s}_{h,tr}} \int_e u_h \cdot \nu \overline{q_h}\, ds; \tag{II.3.26}$$

f_1 and f_2 are complex-valued linear forms given by:

$$f_1(q_h) = \sum_{e \in \mathcal{E}^{f,s}_{h,tr}} \frac{1}{\omega^2} \int_e \frac{1}{\rho_f} \nabla g \cdot \nu \overline{q_h}\, ds, \tag{II.3.27}$$

$$f_2(v_h) = - \sum_{e \in \mathcal{E}^{f,s}_{h,tr}} \int_e g\nu \cdot \overline{v_h}\, ds. \tag{II.3.28}$$

In summary, VF (II.3.22) results from a local variational formulation of the continuous equations (see BVP (2)) at each element K of the domain partition. The four first integrals in a^f_h and the three first terms in a^s_h result classically from the application of the Green formula while taking into account the jump across the interior element edges. Observe that the sesquilinear forms a^f_h and a^s_h are hermitian. This property has been enforced by adding a continuity constraint on the jumps, via the second to last terms in each form. Moreover, the stability of each local variational form is enforced by incorporating interior penalty terms giving rise to the two penalty parameters γ_f and γ_s in the fluid and solid parts respectively. Note that in the case of the second-order wave equation, it has been suggested in [4] that the values of these two penalty parameters should be greater than $\frac{1}{4}p(p+1)$, where p is the order of the considered finite elements. For an even order approximation, the optimal choice for the penalty parameter is exactly equal to $\frac{1}{4}(p+1)(p+2)$.

Remark II.3.2.1 *We can verify that the added fluxes are consistent and conservative, and thus, the resulting bilinear forms are coercive, and consistent. Indeed, as regards the consistency, for all* $(q_h, v_h) \in V^f_h \times V^s_h$ *and for any* $(p, u) \in V^f_h \times V^s_h$ *satisfying the boundary conditions, we have:*

$$\begin{cases} a^f_h(p, q_h) = a^f(p, q_h) \\ a^s_h(u, v_h) = a^s(u, v_h). \end{cases}$$

II.3.3 The Algebraic Formulation

Thanks to the expression of the functions in the finite element basis described in Section II.3.1, the variational problem VF (II.3.22) can be expressed at the algebraic level as follows:

$$\begin{pmatrix} \boldsymbol{A^f} + \boldsymbol{C} & \boldsymbol{B} \\ \boldsymbol{B^*} & \boldsymbol{A^s} \end{pmatrix} \begin{pmatrix} P \\ U \end{pmatrix} = \begin{pmatrix} F_1 \\ F_2 \end{pmatrix}. \tag{II.3.29}$$

where A^f is a symmetric matrix given by:

$$\boldsymbol{A^f} = \frac{1}{\omega^2} \left(\boldsymbol{K^f} - k^2 \boldsymbol{M^f} - \boldsymbol{J^f} + \gamma_f \boldsymbol{S^f} \right), \tag{II.3.30}$$

and

- $\boldsymbol{K^f}$ is the block diagonal stiffness matrix associated to the pressure field.
- $\boldsymbol{M^f}$ is the block diagonal mass matrix associated to the pressure field.
- $\boldsymbol{J^f}$ is the matrix that contains the jump terms. The entries of this matrix are defined over the interior edges.
- $\boldsymbol{S^f}$ is the mass-like matrix defined over the interior edges in the fluid resulting from the penalty term.

$\boldsymbol{C}$ is the complex-valued damping matrix. It is a mass-like matrix, whose entries are all zeros except for the elements located at the exterior boundary Σ. The matrix $\boldsymbol{A^f} + \boldsymbol{C}$ is symmetric, but non-hermitian, and thus non-positive-definite.
The symmetric matrix $\boldsymbol{A^s}$ is given by:

$$\boldsymbol{A^s} = \boldsymbol{K^s} - \omega^2 \rho_s \boldsymbol{M^s} - \boldsymbol{J^s} + \gamma_s \boldsymbol{S^s}, \tag{II.3.31}$$

and

- $\boldsymbol{K^s}$ is the block diagonal elastic stiffness matrix related to the displacement field.
- $\boldsymbol{M^s}$ is the block diagonal mass matrix related to the displacement field.
- $\boldsymbol{J^s}$ is the matrix that contains the jump terms. The entries of this matrix are defined over the interior edges.
- $\boldsymbol{S^s}$ is the mass-like matrix defined over the interior edges in the solid resulting from the penalty term.

Note that the matrix $\boldsymbol{A^s}$ is positive-definite up to the Jones frequencies, thanks to the interior penalty term that compensates the weak ellipticity of the equation operator. $\boldsymbol{B}$ is a mass-like boundary matrix whose entries are defined on the interface edges only, whereas F_1 and F_2 are the source vectors. The

vector P (resp. U) is the fluid pressure (resp. structural displacement) representation in the finite element basis.

More specifically, the unknown vectors P and U are given by:

$$\begin{cases} P &= (p_i)^t_{1\le i\le N^f_h} = ((p_h)(P^f_i))_{1\le i\le N^f} \\ U &= (U_x, U_y)^t = (u_i)^t_{1\le i\le 2N^s} = ((u_x)_h(P^s_i)_{1\le i\le N^s}, (u_y)_h(P^s_i)_{1\le i\le N^s})^t \end{cases}$$

and

$$\begin{aligned} A^f &= \left(\sum_{K\in K^f_h}\frac{1}{\omega^2}\left(\int_K \frac{1}{\rho_f}\nabla\phi_i\cdot\nabla\phi_j\,dx - \frac{1}{\rho_f}\frac{\omega^2}{c_f^2}\int_K \phi_i\phi_j\,dx\right)\right)_{1\le i,j\le N^f} \\ &\quad + \left(-\sum_{e\in\mathcal{E}^f_{h,int}}\frac{1}{\omega^2}\int_e(\{\frac{1}{\rho_f}\nabla\phi_i\}\nu[\phi_j] + \{\frac{1}{\rho_f}\nabla\phi_j\}\nu[\phi_i])\,ds\right)_{1\le i,j\le N^f} \\ &\quad - \left(\sum_{e\in\mathcal{E}^f_{h,R}}\frac{\mathrm{i}}{\omega^2}\int_e\frac{\omega}{\rho_f c_f}\phi_i\phi_j\,ds\right)_{1\le i,j\le N^f} \\ &\quad + \left(\sum_{e\in\mathcal{E}^f_{h,int}}\frac{1}{\omega^2}\int_e\frac{\gamma_f c^f_{max}}{d_e}[\phi_i][\phi_j]\,ds\right)_{1\le i,j\le N^f} \end{aligned} \tag{II.3.32}$$

$$\begin{aligned} A^s &= \left(\sum_{K\in K^s_h}\left(\int_K\sigma(\psi_i):\nabla\psi_j\,dx - \omega^2\rho_s\int_K\psi_i\psi_j\,dx\right)\right)_{1\le i,j\le 2N^s} \\ &\quad \left(-\sum_{e\in\mathcal{E}^s_{h,int}}\int_e(\{\sigma(\psi_i)\}\nu\cdot[\psi_j] + \{\sigma(\psi_j)\}\nu\cdot[\psi_i])\,ds\right)_{1\le i,j\le 2N^s} \\ &\quad \left(+\sum_{e\in\mathcal{E}^s_{h,int}}\int_e\frac{\gamma_s c^s_{max}}{d_e}[\psi_i][\psi_j]\,ds\right)_{1\le i,j\le 2N^s} \end{aligned} \tag{II.3.33}$$

$$B = \left(\sum_{e\in\mathcal{E}^{f,s}_{h,tr}}\int_e\psi_i\cdot\nu\phi_j\,ds\right)_{1\le i\le 2N^s, 1\le j\le N^f} \tag{II.3.34}$$

$$F_1 = \left(\sum_{e\in\mathcal{E}^{f,s}_{h,tr}}\frac{1}{\omega^2}\int_e\frac{1}{\rho_f}\nabla g\cdot\nu\phi_j\,ds\right)_{1\le j\le N^f} \tag{II.3.35}$$

$$F_2 = \left(- \sum_{e \in \mathcal{E}_{h,tr}^{f,s}} \int_e g\nu \cdot \psi_j \, ds \right)_{1 \le j \le 2N^s} . \tag{II.3.36}$$

(II.3.37)

II.3.4 The Computational Complexity

Let N_h^f (resp. N_h^s) be the number of elements in the fluid (resp. solid) medium, and n^K represents the number of degrees of freedom on an element K. For simplicity, we assume $n^K = m$, that is, we use the same element order in each triangle. Therefore, the total number of unknowns is equal to $m(N_h^f + 2N_h^s)$, where the factor 2 results from the two components of the displacement field. Next, consider an element K_l in $\mathcal{K}_h^f$, with $1 \le l \le N_h^f$ and let $\phi_i^{K_l}$ be a basis function in V_h^f associated to some degree of freedom i, $1 \le i \le m$, on the element K_l. Let $\phi_j^{K_s}$ be an arbitrary basis function of V_h^f in a triangle K_s, with $1 \le j \le m$, $1 \le s \le N_h^f$. Then, $a_h^f(\phi_i^{K_l}, \phi_j^{K_s})$ is nonzero only if $\phi_i^{K_l}$ and $\phi_j^{K_s}$ are basis functions belonging to the same element, i.e. $l = s$, or if K_s is a neighbour element of K_l. Since each triangle K_l has at most 3 neighbours, it is sufficient to store four blocks of size $m \times m$, one block for the internal interactions within the element K_l and 3 for its interactions with its neighbours. Following the same reasoning for the remaining terms of the variational formulation VF (II.3.22), this leads roughly to about $4 \times m \times m \times (N_h^f + 2N_h^s)$ nonzero entries in the global matrix. Moreover, we can also make use of the general symmetry of the terms constituting the matrices to minimize the storage. It is then almost halved, that is about $2 \times m \times m \times (N_h^f + 2N_h^s)$ nonzero terms. For illustration purpose, let us consider an elastic circle of radius a embedded in a fluid medium delimited by a circle of radius b. Let N be the number of elements per wavelength λ. Then, we obtain the computational configuration referenced in Table II.3.1. The linear system given by Eq. (II.3.29) is thus composed

e	♯ points		♯ elements		Total ♯ d.o.f	♯ nonzero terms
(m)	Γ	Σ	N_h^s in Ω^s	N_h^f in Ω^f		
$h = \frac{\lambda}{N}$	$\frac{2\pi a}{h}$	$\frac{2\pi b}{h}$	$\frac{2\pi a^2}{h^2}$	$\frac{2\pi(b^2 - a^2)}{h^2}$	$m\left(\frac{2\pi(a^2+b^2)}{h^2}\right)$	$2m^2\left(\frac{2\pi(a^2+b^2)}{h^2}\right)$

Table II.3.1 – Computational complexity of IPDG.

of sparse matrices whose symmetry property allows for an optimized storage. This system is solved with an LU factorization procedure developed for sparse systems and incorporated in the open-source program suite, MUMPS [1]. An illustrative example of a sparse structure of the DG matrix stored within MUMPS is depicted in Figure II.3.1. This illustration has been obtained for the case of a mesh composed of 18 triangles in the solid and 48 in the fluid part. The number of unknowns is thus equal

to 252 using a linear polynomial approximation, and the matrix contains 1998 nonzero elements.

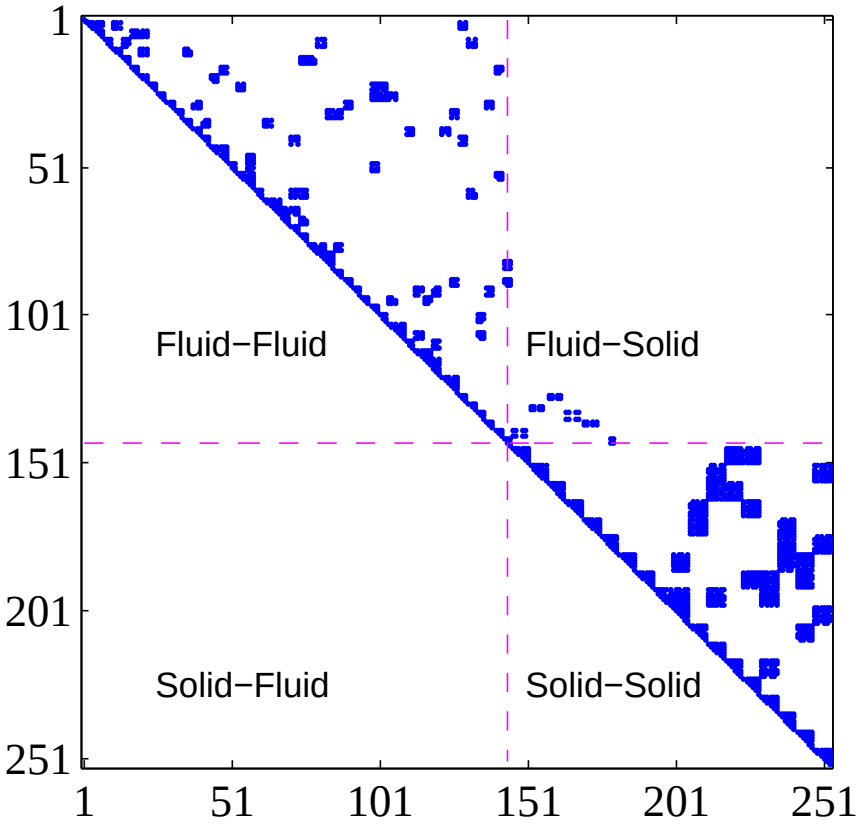

Figure II.3.1 – Illustrative example of the structure of the IPDG matrix given by Eq. (II.3.29): upper triangular storage for a 252×252 matrix. Total number of nonzero entries: 1998.

Note that in the low and mid-frequency regimes, the sparse implementation allows the procedure to run the numerical experiments on a personal computer. However, due to the size of the resulting system in the high-frequency regime, parallel computing platforms have been used to perform the numerical simulations. More specifically, we used the Cluster of the University of Pau consisting of an INTEL type CPU (64bit) with 8 nodes composed of 2×6 cores, and 48 Go RAM.

II.3.5 Brief remark on the curved boundary edges

In this work, we will also make use of curved boundary edges on the fluid-solid interface, as well as on the exterior boundary. This implies some important changes regarding the numerical implementation. Indeed, the transformation from an arbitrary element to the reference element is not the same as for straight finite elements.

Let K be an element of the mesh whose coordinates of the vertices S_i are denoted $(x_i, y_i)_{i=1,\cdot,3}$. We denote by $\hat{K}$ the reference element triangle defined by the vertices $S_1(0,0)$ $S_2(1,0)$, $S_3(0,1)$. Then, there exists an affine transformation F which transforms $\hat{K}$ in K. For straight elements, the transformation can be written as follows:

$$F(\hat{x},\hat{y}) = \begin{pmatrix} x_1 \\ y_1 \end{pmatrix} + \begin{bmatrix} x_2 - x_1 & x_3 - x_1 \\ y_2 - y_1 & y_3 - y_1 \end{bmatrix} \begin{pmatrix} \hat{x} \\ \hat{y} \end{pmatrix}.$$

In the case of curved boundary edges, the transformation is expressed as:

$$F(\hat{x},\hat{y}) = \sum_{i=1}^{m} \phi_i(\hat{x},\hat{y}) P_i,$$

where P_i represents the coordinates of the degrees of freedom on K.
A similar remark can be done for the edge transformation.

As a computational implication, the Jacobian of the transformation is no longer constant. It follows that, by change of variable in the reference element, the determinant must be computed under the integral. In addition, the normal vector to the edge also varies.

II.4 Numerical validation

Our objective here is to validate our numerical implementation of the IPDG method. To this end, we propose to define toy problems for which analytical solutions are available.

We assume the elastic obstacle to be homogeneous, which means the Lamé coefficients are independent of x. Observing that $\nabla \cdot u = tr(\nabla u) = tr(\varepsilon(u))$, the tensor $\sigma(u)$ can be expressed as follows:

$$\sigma(u) = \lambda(\nabla \cdot u) I_3 + 2\mu\varepsilon(u). \tag{II.4.1}$$

Because $\nabla \cdot tr(\varepsilon(u) I_3) = \nabla(\nabla \cdot)$ and $2\nabla \cdot (\varepsilon(u)) = \nabla \cdot (\nabla u) + \nabla \cdot (\nabla u^t) = \Delta u + \nabla(\nabla \cdot u)$, we then have:

$$\nabla \cdot \sigma(u) = (\lambda + \mu)\nabla(\nabla \cdot u) + \mu \Delta u. \tag{II.4.2}$$

Therefore, we obtain that the Navier equation (see Eq. (II.2.2)) can be rewritten as follows:

$$(\lambda + \mu)\nabla(\nabla \cdot u) + \mu \Delta u + \omega^2 \rho_s u = 0, \tag{II.4.3}$$

or, equivalently, since $\Delta u = \nabla(\nabla \cdot u) - \nabla \times (\nabla \times u)$,

$$(\lambda + 2\mu)\nabla(\nabla \cdot u) - \mu \nabla \times (\nabla \times u) + \omega^2 \rho_s u = 0. \tag{II.4.4}$$

From the latter expression of the Navier equation given by Eq. (II.4.4), we can dissociate two types of solutions: those which are curl free, and the others which are divergence free, as follows.

- On the hand, assuming $\nabla \times u = 0$, Eq. (II.4.4) becomes:

$$(\lambda + 2\mu)\Delta u + \omega^2 \rho_s u = 0. \tag{II.4.5}$$

  We recognize a vectorial Helmholtz equation, with wavenumber $k_p = \dfrac{\omega}{c_p}$, where the velocity c_p is equal to $c_p = \sqrt{\dfrac{\lambda + 2\mu}{\rho_s}}$.
  The solutions of this equation correspond to the pressure waves, called P-waves (or primary waves).

- On the other hand, assuming $\nabla \cdot u = 0$, Eq. (II.4.4) becomes:

$$\mu \Delta u + \omega^2 \rho_s u = 0. \tag{II.4.6}$$

  We also find a vectorial Helmholtz equation, with wavenumber $k_s = \dfrac{\omega}{c_s}$, where the velocity is given by $c_s = \sqrt{\dfrac{\mu}{\rho_s}}$.
  The solutions of the latter equation are called S-waves for shear waves (or secondary waves).

Then, it results from Eq. (II.4.4) that the displacement field u can be split into its curl-free component and its divergence-free component. More specifically, u can be expressed in terms of a P-wave scalar potential ϕ and S-wave vector potential ψ as follows:

$$u = \nabla\phi + \nabla \times \psi. \tag{II.4.7}$$

Given that, we have transformed the initial equations into a waveguide-type problem and a radiating-type problem. The fluid-solid interaction problem into consideration is then the following boundary

value problem:

$$\text{BVP (3)} \quad \begin{cases} \Delta p + k^2 p = 0 & \text{in } \Omega_R^f \\ \nabla \cdot \sigma(u) + \omega^2 \rho_s u = 0 & \text{in } \Omega^s \\ \omega^2 \rho_f u \cdot \nu = \dfrac{\partial p}{\partial \nu} + g_1 & \text{on } \Gamma \\ \sigma(u)\nu = -p\nu + g_2 & \text{on } \Gamma \\ \dfrac{\partial p}{\partial \nu} = g_R & \text{on } \Sigma\,. \end{cases} \tag{II.4.8}$$

where the expressions of the right-hand sides g_1, g_2 and g_R will be specified for each numerical test. For these simulations, the domain of computation is an elastic circle Ω^s of radius $a = 1$ m surrounded by an acoustic domain Ω_R^f, whose external boundary is a circle of radius $a_R = 3$ m.

The circular frequency is $\omega = 10$. We will employ polynomial elements of order 1 to 3. Therefore, due to the typical oscillatory character of the solution of scattering problems, we use about 7.5 elements per wavelength for $ka = 6.7$. The corresponding mesh composed of 5374 elements is depicted in Figure II.4.1. The material properties of the considered elastic configuration are reported in Table II.4.1. Note that they correspond to Lamé coefficients $\lambda = 8$ and $\mu = 4$.

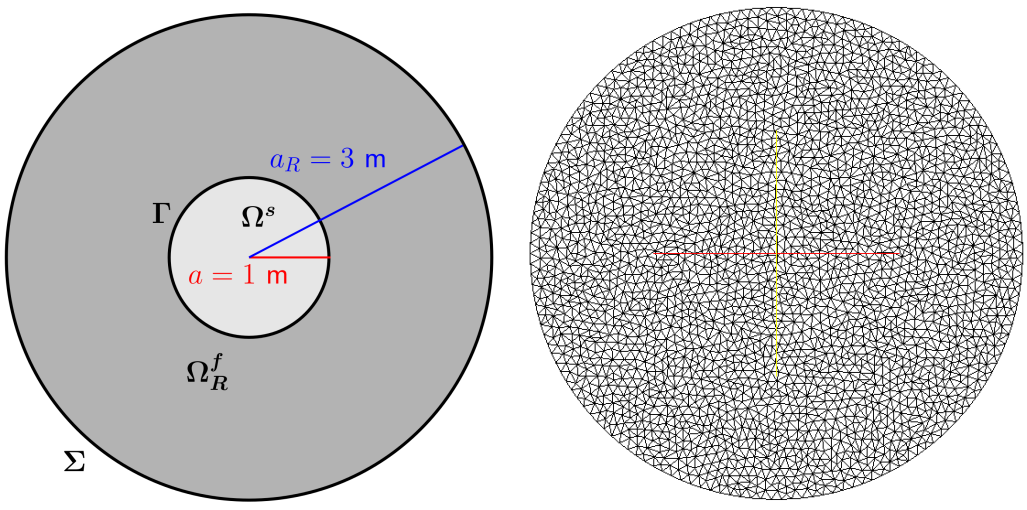

(a) Computational domain (b) Mesh

Figure II.4.1 – Configuration for the waveguide-type problem and radiating-type problem.

Properties / Medium	Density ρ (kg/m^3)	Propagation velocity c_P (m/s)	c_S (m/s)
Fluid	2	1.5	–
Solid	1	4	2

Table II.4.1 – Material properties of the considered fluid-structure medium.

II.4.1 First validation test: a waveguide-type problem

For this first validation test, we assume that the pressure field and both potentials ϕ, ψ exist as plane waves, that is:

$$\begin{cases} p = e^{\mathrm{i}\frac{\omega}{c_f} x\cdot d_1}, & \text{(II.4.9)} \\ \phi = e^{\mathrm{i}\frac{\omega}{c_p} x\cdot d_2}, & \text{(II.4.10)} \\ \psi = e^{\mathrm{i}\frac{\omega}{c_s} x\cdot d_2}, & \text{(II.4.11)} \end{cases}$$

with $d_1 = (\cos\theta, \sin\theta)$, $d_2 = (\cos\alpha, \sin\alpha)$.
We will consider the cases where the displacement is curl free and then where it is divergence free. In particular, these experiments will allow us to verify that we recover correctly both kinds of elastic waves, i.e., P-waves and S-waves.

II.4.1.1 Curl-free displacement

In this first set of experiments, the curl-free displacement u can be expressed as follows:

$$u = \nabla\phi, \tag{II.4.12}$$

The potential ϕ and the pressure field p are plane waves given by Eqs. (II.4.9) and (II.4.10). We can therefore compute explicitly the exact values of p and u for each degree of freedom.
The right-hand sides of BVP (3) are given by:

$$\begin{aligned} g_R &= \nabla e^{\mathrm{i}\frac{\omega}{c_f} x\cdot d_1}\cdot\nu & \text{(II.4.13)} \\ g_1 &= \omega^2\rho_f \nabla e^{\mathrm{i}\frac{\omega}{c_p} x\cdot d_2}\cdot\nu - \frac{\partial e^{\mathrm{i}\frac{\omega}{c_f} x\cdot d_1}}{\partial\nu} & \text{(II.4.14)} \\ g_2 &= \sigma(\nabla e^{\mathrm{i}\frac{\omega}{c_p} x\cdot d_2})\nu + e^{\mathrm{i}\frac{\omega}{c_f} x\cdot d_1}\nu. & \text{(II.4.15)} \end{aligned}$$

They correspond to the particular case where p, ϕ and ψ given by Eqs. (II.4.9), (II.4.10) and (II.4.11) are solution to the problem. We take the following penalty parameters: $\gamma_f = \gamma_s = 3$, $\gamma_f = \gamma_s = 15$

and $\gamma_f = \gamma_s = 60$ for linear, quadratic and cubic elements respectively. We consider the physical material properties defined in the beginning of the Section in Table II.4.1. Moreover, the angles of the plane waves are given by: $\theta = \alpha = 0°$.

First, we compare the results obtained with different approximation orders going from 1 to 3. The error results are reported in Tables II.4.2 to II.4.4. In Figure II.4.2(a)-(b), we show the real parts of the pressure field p and the displacement component u_x for both approximate and exact solutions obtained using cubic elements. Since the component u_y is zero in this case, we do not represent it. Fig. II.4.2(c) illustrates the absolute error between both solutions. The following observations are noteworthy:

- IPDG delivers a very poor accuracy level when using linear elements as indicated in Table II.4.2. We observe that there is three orders of magnitude improvement on the relative error when going from linear to quadratic elements. Employing higher-order (cubic) elements, there is a one order of magnitude improvement on the relative error associated to the displacement field, and a two orders of magnitude improvement on the relative error corresponding to the pressure field. Note that the error associated to the pressure field is poorer than the errors corresponding to the displacement field. This is due to the fact that the wavelength in the fluid is smaller than the wavelengths in the solid. Indeed, we have $k < k_s < k_p$. To improve the accuracy when employing the lowest-order elements, it is necessary to refine the mesh in the fluid part. For example, halving the triangle edges two times successively everywhere, we obtain a relative error of 6.7% for the pressure field using linear polynomial elements.
- In Fig. II.4.2 (a)-(b), we recognize the band structure of the plane waves. Moreover, we observe the difference of wavelengths between the two media. The dominant blue color for the error representation in Fig. II.4.2(c) illustrates the good approximation of the exact solution by the proposed method when employing higher-order elements.

Fields	p	u_x	u_y
L_∞-norm exact solution	1.000	2.500	0.000
L_∞-norm approximate solution	9.717	2.688	0.184
Absolute error	14.555	0.190	0.191
L^2-relative error (%)	301.866	4.318	Infinity

Table II.4.2 – Waveguide-type problem - Curl-free displacement - Error results using linear polynomial elements ($\theta = \alpha = 0°$).

Second, we want to study the stability with respect to the direction of the pressure plane wave. The angle θ of the direction $d_1 = (\cos(\theta), \sin(\theta))$ varies between 0 and 360° with an increment of

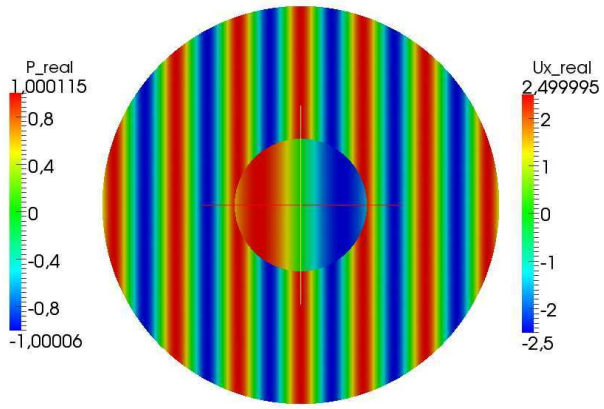

(a) Approximate solution

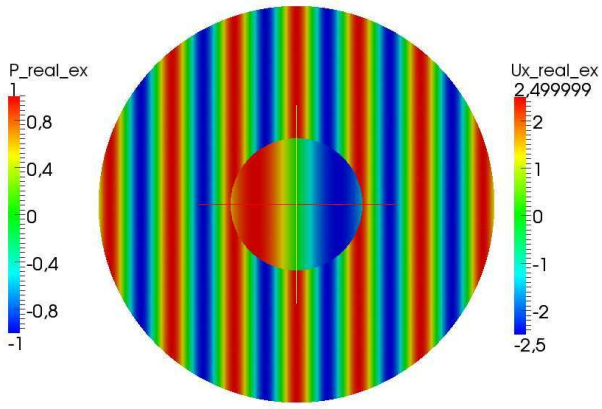

(b) Exact solution

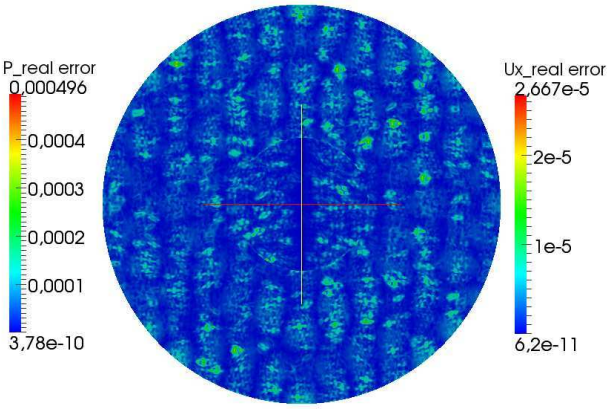

(c) Error between both solutions

Figure II.4.2 – Waveguide-type problem - Curl-free displacement - Figures (a) and (b): Real parts of the pressure field p and displacement component u_x using cubic polynomial elements for the approximate and exact solutions ($\theta = \alpha = 0°$). Figure (c): Absolute error between both solutions.

Fields	p	u_x	u_y
L_∞-norm exact solution	1.000	2.500	0.000
L_∞-norm approximate solution	1.019	2.500	4.391E-004
Absolute error	4.288E-002	2.095E-004	1.932E-004
L^2-relative error (%)	0.856	4.735E-003	Infinity

Table II.4.3 – Waveguide-type problem - Curl-free displacement - Error results using quadratic polynomial elements ($\theta = \alpha = 0°$).

Fields	p	u_x	u_y
L_∞-norm exact solution	1.000	2.500	0.000
L_∞-norm approximate solution	1.000	2.500	6.501E-006
Absolute error	3.777E-004	5.744E-006	2.070E-006
L^2-relative error (%)	7.533E-003	1.298E-004	Infinity

Table II.4.4 – Waveguide-type problem - Curl-free displacement - Error results using cubic polynomial elements ($\theta = \alpha = 0°$).

5°. Given the results obtained previously, we perform the experiments using cubic elements. We take $d_2 = d_1$. We plot both the relative and the absolute errors in Figure II.4.3(a)-(d). We also plot in Fig. II.4.3(e) the condition number of the DG system matrix, as well as the upper bound of the error in the solution, provided by the solver MUMPS. The results indicate the following:

- In Fig. II.4.3 (a)-(c), we observe the well-behavior of the method, we recover the periodicity. The error curves associated to the displacement field is smoother than the error curve corresponding to the pressure field, which is due to the difference of wavelengths between both media. Note that, in Fig. II.4.3 (b), the presence of peaks in the relative error curves associated to the structural displacement field (u_x, u_y) are due to the fact that the displacement components u_x and u_y are zero for $\theta = \pi$ and $\theta = 2 \times \pi$ respectively.
- In Fig. II.4.3) (d), we observe the periodic structure of the condition number.

II.4.1.2 Divergence-free displacement

Similarly to the previous part, the divergence-free component u admits the following representation:

$$u = \nabla \times \psi, \tag{II.4.16}$$

The potential ψ and the pressure field p are plane waves given by Eqs. (II.4.11) and (II.4.9).
As previously, we consider the boundary value problem BVP (3), but the corresponding right-hand

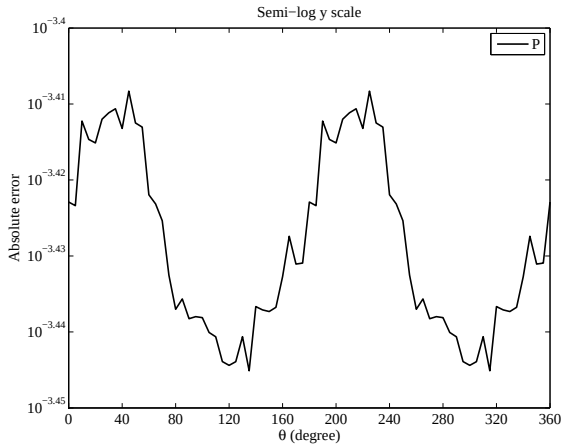

(a) Pressure absolute error

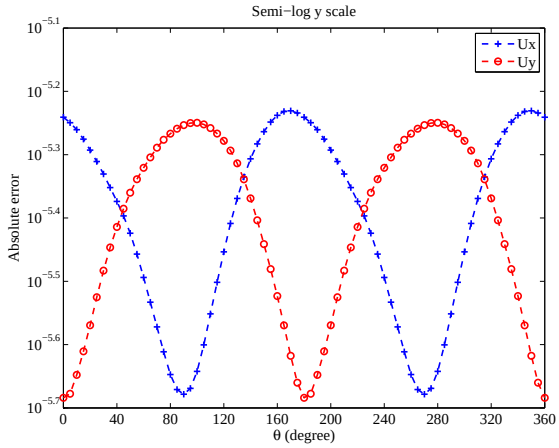

(b) Displacement absolute error

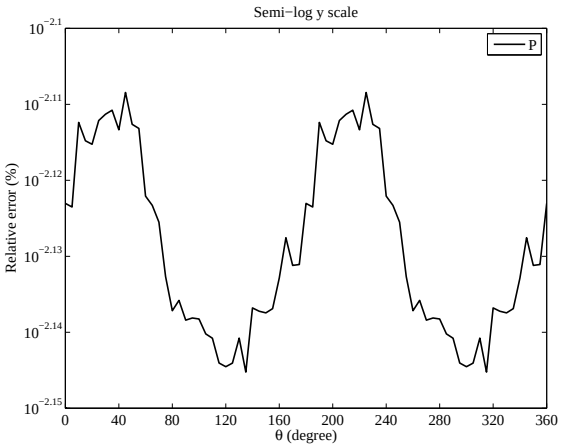

(c) Pressure relative error

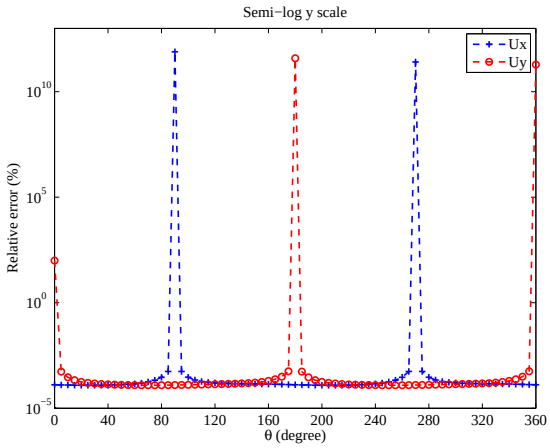

(d) Displacement relative error

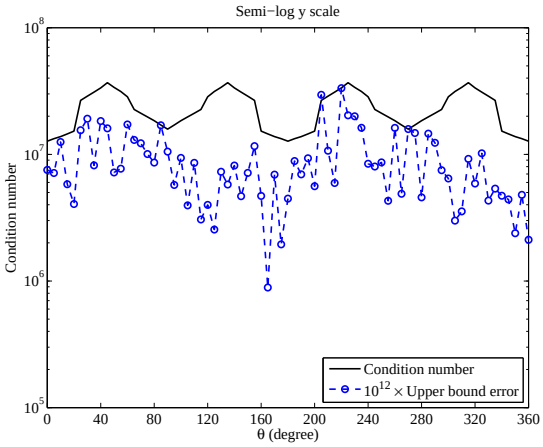

(e) Condition number

Figure II.4.3 – Waveguide-type problem - Curl-free displacement - Figures (a)-(d): Sensitivity of the relative and absolute errors to the angle θ using cubic polynomial elements. Figure (e): Condition number of the system matrix and the upper bound of the error in the MUMPS solution (Semi-log y scale).

sides are now given by:

$$g_R = \nabla e^{\mathrm{i}\frac{\omega}{c_f}x\cdot d_1}\cdot\nu \tag{II.4.17}$$

$$g_1 = \omega^2\rho_f\nabla\times\, e^{\mathrm{i}\frac{\omega}{c_p}x\cdot d_2}\cdot\nu - \frac{\partial e^{\mathrm{i}\frac{\omega}{c_f}x\cdot d_1}}{\partial\nu} \tag{II.4.18}$$

$$g_2 = \sigma(\nabla\times\, e^{\mathrm{i}\frac{\omega}{c_p}x\cdot d_2})\nu + e^{\mathrm{i}\frac{\omega}{c_f}x\cdot d_1}\nu. \tag{II.4.19}$$

Once again, we compute explicitly the exact solutions p and u and compare them to the approximate solution performed with IPDG for linear to cubic polynomial elements. The error results are summarized in Tables II.4.5 to II.4.7. Fig. II.4.4 illustrates the numerical results obtained with cubic polynomial elements. The real parts of the approximate solutions and exact values of p and u_y are represented in Fig. II.4.4(a)-(b), as well as the absolute error between both solutions in Fig. II.4.4(c). Note that, in this case, the component u_x is zero and is not represented. The results reveal the following:

- As before, the use of higher-order elements improve the accuracy, especially for the fluid pressure p.
- Fig. II.4.4 shows the correct recovery of the band structure of the plane waves for both types of media. The errors are poorer than for the P-wave case represented in Fig. II.4.2, this is again due to the fact that $k \leq k_s \leq k_p$.

Fields	p	u_x	u_y
L_∞-norm Exact solution	1.000	0.000	5.000
L_∞-norm Approximate solution	54.459	2.084	5.849
Absolute error	95.221	1.684	1.076
L^2-relative error (%)	1974.802	Infinity	12.424

Table II.4.5 – Waveguide-type problem - Divergence-free displacement - Error results using linear polynomial elements.

Fields	p	u_x	u_y
L_∞-norm Exact solution	1.000	0.000	5.000
L_∞-norm Approximate solution	1.221	1.165E-002	5.009
Absolute error	0.475	7.258E-003	6.597E-003
L^2-relative error (%)	9.471	Infinity	7.455E-002

Table II.4.6 – Waveguide-type problem - Divergence-free displacement - Error results using quadratic polynomial elements.

Fields	p	u_x	u_y
L_∞-norm Exact solution	1.000	0.000	5.000
L_∞-norm Approximate solution	1.002	2.185E-004	5.001
Absolute error	2.092E-003	5.590E-005	2.011E-004
L^2-relative error (%)	4.172E-002	Infinity	2.272E-003

Table II.4.7 – Waveguide-type problem - Divergence-free displacement - Error results using cubic polynomial elements.

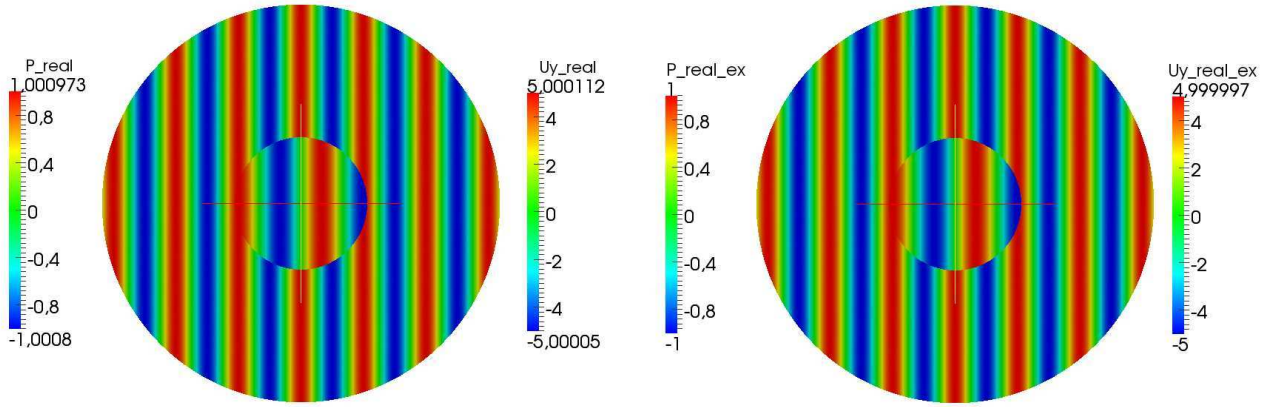

(a) Approximate solution

(b) Exact solution

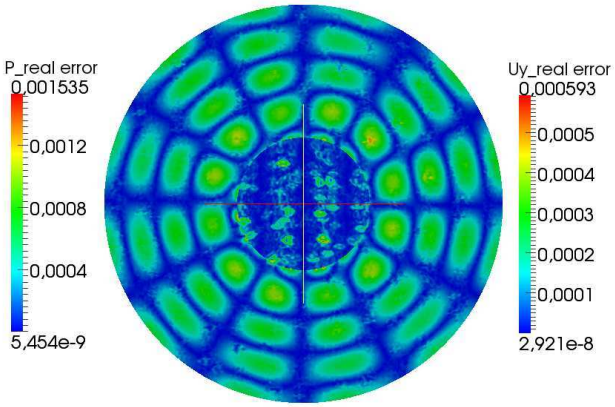

(c) Error between both solutions

Figure II.4.4 – Waveguide-type problem - Divergence-free displacement: Figures (a) and (b): Real parts of the pressure field p and displacement component u_x using cubic polynomial elements for the approximate and exact solutions ($\theta = \alpha = 0°$). Figure (c): Absolute error between both solutions.

To complete this test case, we again study the stability with respect to the direction d_1 of the pressure plane wave. The angle θ of the direction $d_1 = (\cos(\theta), \sin(\theta))$ varies between 0 and 360° with an increment of 5° and d_2 is chosen equal to d_1. We use cubic polynomial elements. In Fig. II.4.5, we represent both absolute and relative errors, and also report the condition number of the system matrix, as well as the upper bound of the error in the solution, provided by the solver MUMPS. As before, we recognize the periodic structure for all the curves. We can observe that the error in pressure is less smooth than the error associated to the structural displacement field. Note that, in Fig. II.4.5 (b), the presence of peaks in the relative error is due to the fact that the displacement components u_x and u_y are zero for $\theta = 2 \times \pi$ and $\theta = \pi$ respectively.

To conclude, both validation cases allow us to ensure that we recover correctly P-waves and S-waves. In particular, the use of high-order finite elements provides accurate results. Moreover, we have observed a stability with respect to the direction of the plane waves.

II.4.2 Second validation test: a radiating-type problem

In this second set of experiments, we propose a test similar to the previous one. We do no longer consider plane waves but the solutions p and u are respectively a Hankel function of the first kind and the gradient or curl of a Bessel function for a fixed mode n.
More precisely, the pressure and the potentials into consideration can be expressed as follows:

$$\begin{cases} p = H_n^{(1)}(kr)\cos(n\theta), & \text{(II.4.20)} \\ \phi = J_n(k_p r)\cos(n\theta), & \text{(II.4.21)} \\ \psi = J_n(k_s r)\sin(n\theta), & \text{(II.4.22)} \end{cases}$$

This test is useful to test the stability of the method.

II.4.2.1 Curl-free displacement

In this first part, the curl-free displacement u is expressed by:

$$u = \nabla\phi, \tag{II.4.23}$$

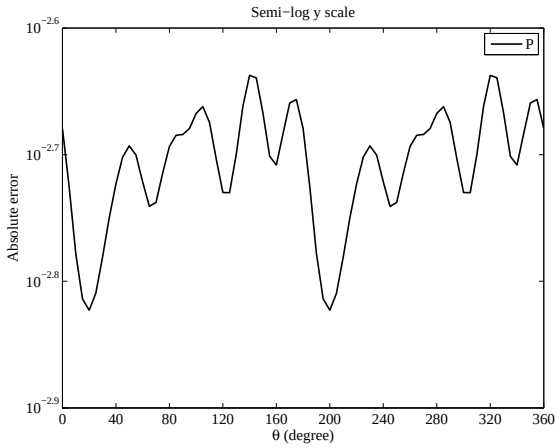

(a) Pressure absolute error

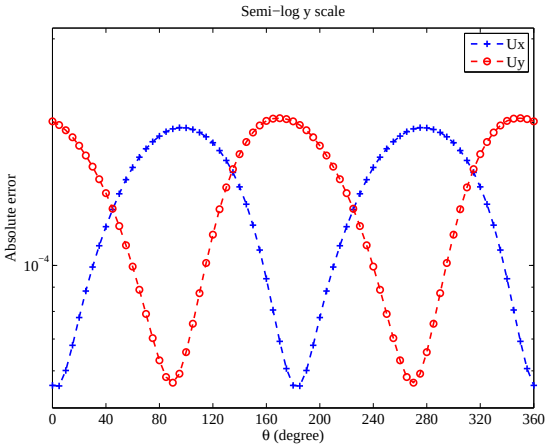

(b) Displacement absolute error

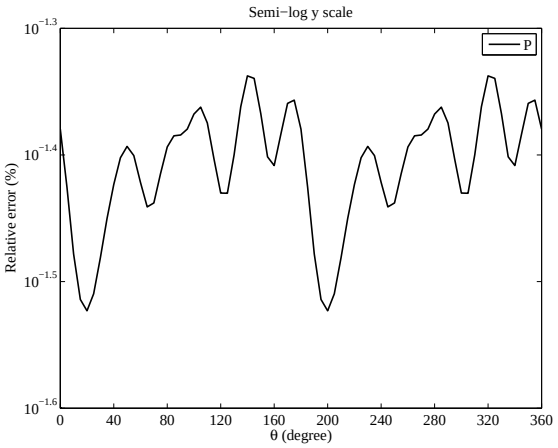

(c) Pressure relative error

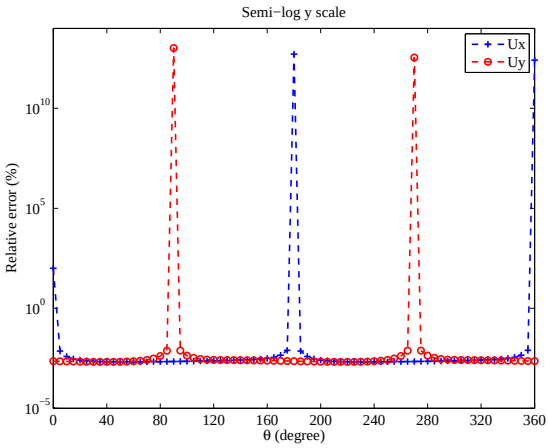

(d) Displacement relative error

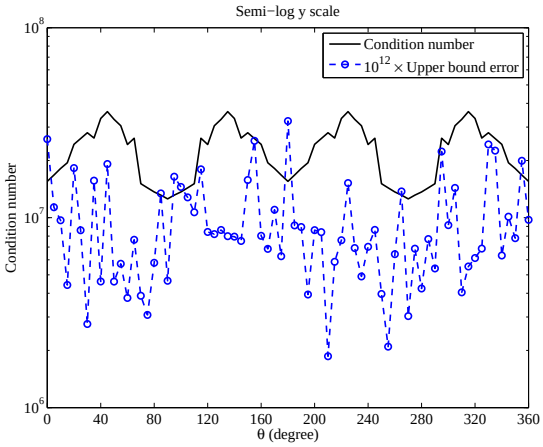

(e) Condition number

Figure II.4.5 – Waveguide-type problem - Divergence-free displacement - Figures (a)-(d): Sensitivity of the relative and absolute errors to the angle θ using cubic polynomial elements. Figure (e): Condition number of the system matrix and the upper bound of the error in the MUMPS solution (Semi-log y scale).

The potential ϕ and the pressure field p are special functions given by Eqs. (II.4.21) and (II.4.20). In order to specify the expression of u, we write the gradient in polar coordinates as follows:

$$\nabla\phi = \frac{\partial\phi}{\partial r}\vec{e}_r + \frac{1}{r}\frac{\partial\phi}{\partial\theta}\vec{e}_\theta. \tag{II.4.24}$$

Let us denote

$$u_r = \frac{\partial\phi}{\partial r} = -k_p J_n'(k_p r)\cos(n\theta) \tag{II.4.25}$$

$$u_\theta = \frac{1}{r}\frac{\partial\phi}{\partial\theta} = -\frac{n}{r}J_n(k_p r)\sin(n\theta). \tag{II.4.26}$$

Then, we obtain:

$$u = u_r\vec{e}_r + u_\theta\vec{e}_\theta. \tag{II.4.27}$$

Since the polar basis vectors are given by $\vec{e}_r = (\cos\theta,\ \sin\theta)^t$ and $\vec{e}_\theta = (-\sin\theta,\ \cos\theta)^t$, it follows that the displacement field can be expressed as:

$$\begin{aligned} u_x &= u_r\cos\theta - u_\theta\sin\theta, \\ u_y &= u_r\sin\theta + u_\theta\cos\theta, \end{aligned}$$

Then, the boundary value problem is still formulated as BVP (3) but with different expressions of the right-hand sides, that is,

$$g_R = \frac{\partial}{\partial r}\left[H_n^{(1)}(kr)\cos(n\theta)\right], \quad r = 3 \tag{II.4.28}$$

$$g_1 = \omega^2\rho_f\frac{\partial}{\partial r}\left[J_n(k_p r)\cos(n\theta)\right] - \frac{\partial}{\partial r}\left[H_n^{(1)}(kr)\cos(n\theta)\right], \quad r = 1 \tag{II.4.29}$$

$$g_2 = \sigma(\nabla\left[J_n(k_p r)\cos(n\theta)\right])\nu + \left[H_n^{(1)}(kr)\cos(n\theta)\right]\nu, \quad r = 1. \tag{II.4.30}$$

We keep the settings defined in the beginning of the section.

First, we consider the mode $n = 2$. We summarize the error results obtained when using linear to cubic polynomial elements in Tables II.4.8 to II.4.10. In Fig. II.4.7 (a)-(b), we depict the real parts of the pressure solution p and the displacement component u_x for both approximate and exact solutions when using cubic elements. Fig. II.4.7 (c) illustrates the absolute error between both solutions. In Figure II.4.6, we represent the imaginary part of the pressure field p and the real part of the displacement component u_y for both approximate and exact solutions when using cubic elements, as well as the absolute error. Since the displacement field is real, we do not represent the zero imaginary part. The

conclusions are similar to those drawn up for the previous test case. More specifically, we observe the following:

- As previously, IPDG delivers a very poor accuracy level when using linear elements. Indeed, we observe that there is a three orders of magnitude improvement on the relative error when going from linear to quadratic elements. However, observe that the use of higher-order elements does not improve the accuracy except for the fluid pressure p.
- In Fig. II.4.7 (a)-(b) and Fig. II.4.6 (a)-(b), we recognize the radiating structure of the solutions. In addition, the difference of wavelengths between both media is again clearly observable.
- The dominant blue color in Fig. II.4.7 (c) and Fig. II.4.6 (c) illustrates the good approximation of the exact solution when using cubic polynomial elements. Note that it seems that the error is concentrated on the transmission interface.

Fields	p	u_x	u_y
L_∞-norm exact solution	0.316	0.636	0.636
L_∞-norm approximate solution	3.770	0.711	0.707
Absolute error	7.130	9.491E-002	9.369E-002
L^2-relative error (%)	949.789	11.471	11.323

Table II.4.8 – Radiating-type problem - Curl-free displacement - Error results using linear polynomial elements ($n = 2$).

Fields	p	u_x	u_y
L_∞-norm exact solution	0.316	0.636	0.636
L_∞-norm approximate solution	0.318	0.636	0.636
Absolute error	4.238E-003	6.002E-005	6.191E-005
L^2-relative error (%)	0.543	7.216E-003	7.443E-003

Table II.4.9 – Radiating-type problem - Curl-free displacement - Error results using quadratic polynomial elements ($n = 2$).

Fields	p	u_x	u_y
L_∞-norm exact solution	0.316	0.636	0.636
L_∞-norm approximate solution	0.316	0.636	0.636
Absolute error	1.731E-004	4.699E-005	4.670E-005
L^2-relative error (%)	2.219E-002	5.649E-003	5.615E-003

Table II.4.10 – Radiating-type problem - Curl-free displacement - Error results using cubic polynomial elements ($n = 2$).

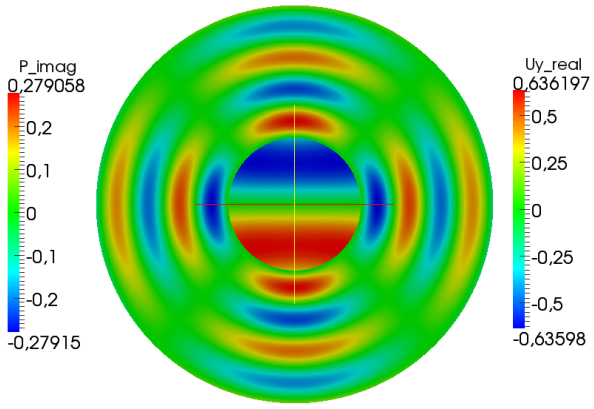

(a) Approximate solution

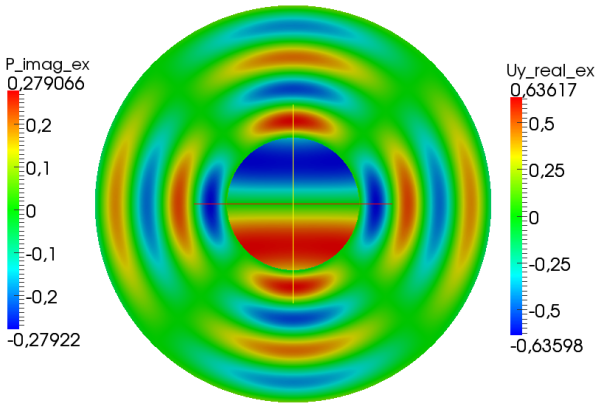

(b) Exact solution

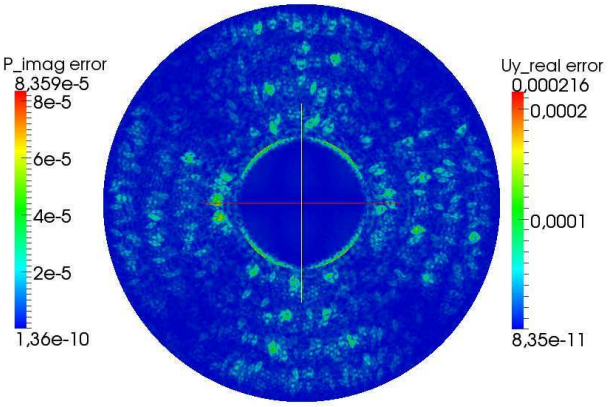

(c) Error between both solutions

Figure II.4.6 – Waveguide-type problem - Curl-free displacement - Figures (a) and (b): Imaginary part of the pressure field p and real part of the displacement component u_y using cubic polynomial elements for the approximate and exact solutions ($n = 2$). Figure (c): Absolute error between both solutions.

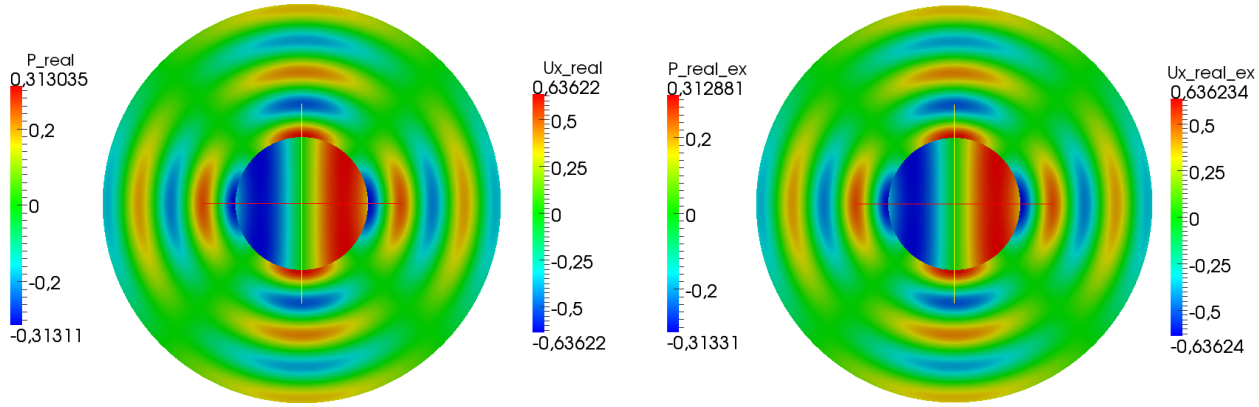

(a) Approximate solution

(b) Exact solution

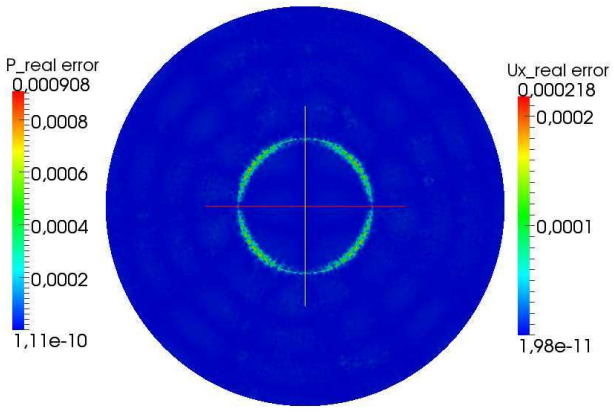

(c) Error between both solutions

Figure II.4.7 – Waveguide-type problem - Curl-free displacement - Figures (a) and (b): Real parts of the pressure field p and displacement component u_x using cubic polynomial elements for the approximate and exact solutions ($n = 2$). Figure (c): Absolute error between both solutions.

Second, we study the stability with respect to the mode n of the special functions. We consider a mode varying from $n = 0$ to $n = 10$. Given the previous observations, we employ cubic polynomial elements. In Figure II.4.8, we depict both absolute and relative errors. We also represent the condition number of the DG matrix, as well as the upper bound of the error in the solution, provided by the solver MUMPS. It seems that there is a relative stability with respect to the mode. Whereas the pressure approximation remains relatively stable, the relative errors corresponding to the structural displacement seem to increase with the mode number. This is due to the fact that the displacement field tends to vanish as the mode number increases, which is observable on the absolute error curves. Last, though we remark that the condition number of the system decreases with n, this is not the case for the error in the Mumps solution.

Remark II.4.2.1 *Later, we will use curved boundary edges on both boundaries Γ and Σ in order to better take into account the geometry of the domain and better modeling the incoming and outgoing waves as well the surface wave at the wet surface. We will see that this can significantly improve the results. However, we can already observe the effect of using curved boundary edges on the accuracy of IPDG for the radiating-type problem into consideration. The preliminary results are reported in Table II.4.11 and Figure II.4.2.1 using cubic polynomial finite elements. Table II.4.11 suggests that there is a gain on both pressure and displacement fields when using curved boundary edges compared to Table II.4.10. Moreover, the error curves depicted in Fig. II.4.2.1 are smoother than the ones in Fig. II.4.8.*

Fields	p	u_x	u_y
L_∞-norm exact solution	0.316	0.636	0.636
L_∞-norm approximate solution	0.316	0.636	0.636
Absolute error	7.735E-005	7.064E-006	7.107E-006
L^2-relative error (%)	9.914E-003	8.480E-004	8.532E-004

Table II.4.11 – Radiating-type problem - Curl-free displacement - Error results using cubic polynomial elements equipped with curved boundary edges ($n = 2$).

II.4.2.2 Divergence-free displacement

In this second part, the divergence-free displacement u is expressed as follows:

$$u = \nabla \times \psi, \tag{II.4.31}$$

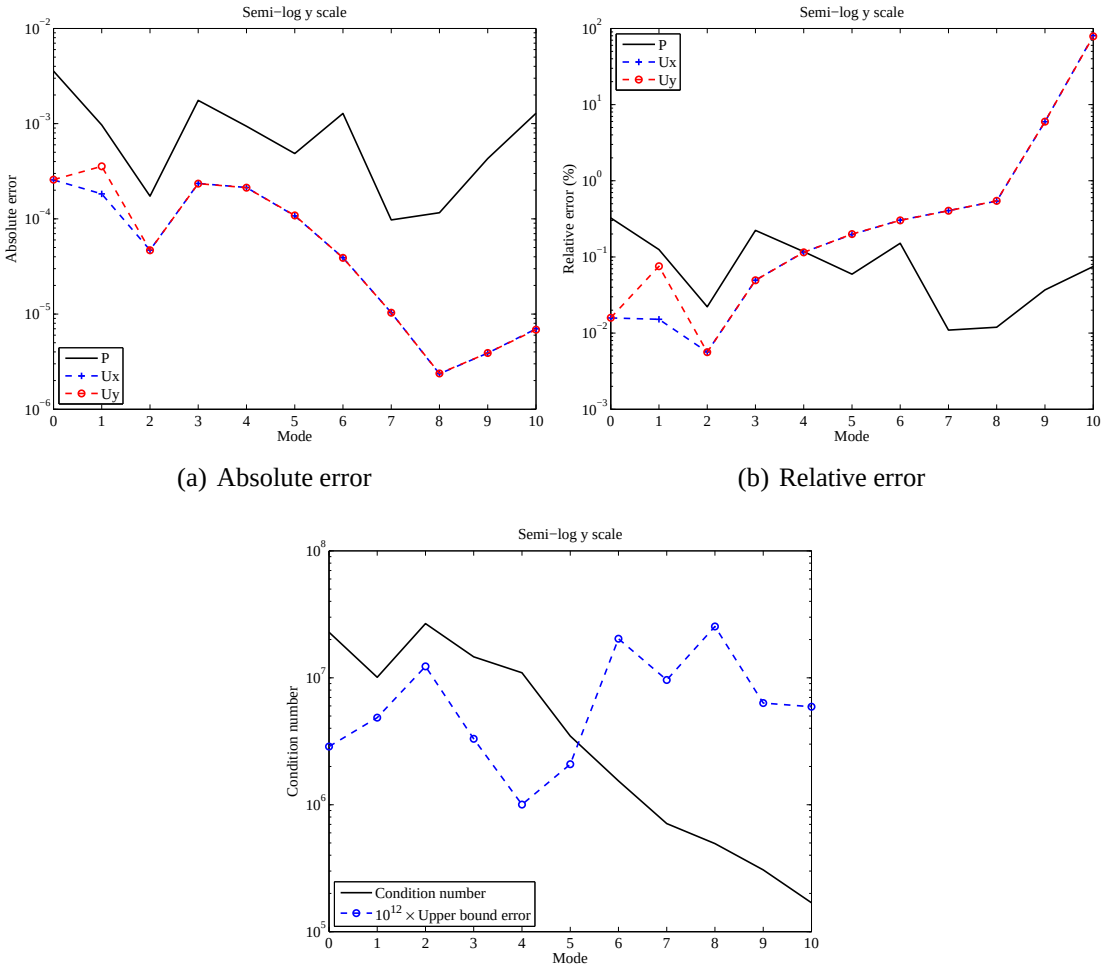

(a) Absolute error

(b) Relative error

(c) Condition number

Figure II.4.8 – Waveguide-type problem - Curl-free displacement - Figures (a)-(b): Sensitivity of the relative and absolute errors to the mode number n using cubic polynomial elements. Figure (c): Condition number of the system matrix and the upper bound of the error in the MUMPS solution (Semi-log y scale).

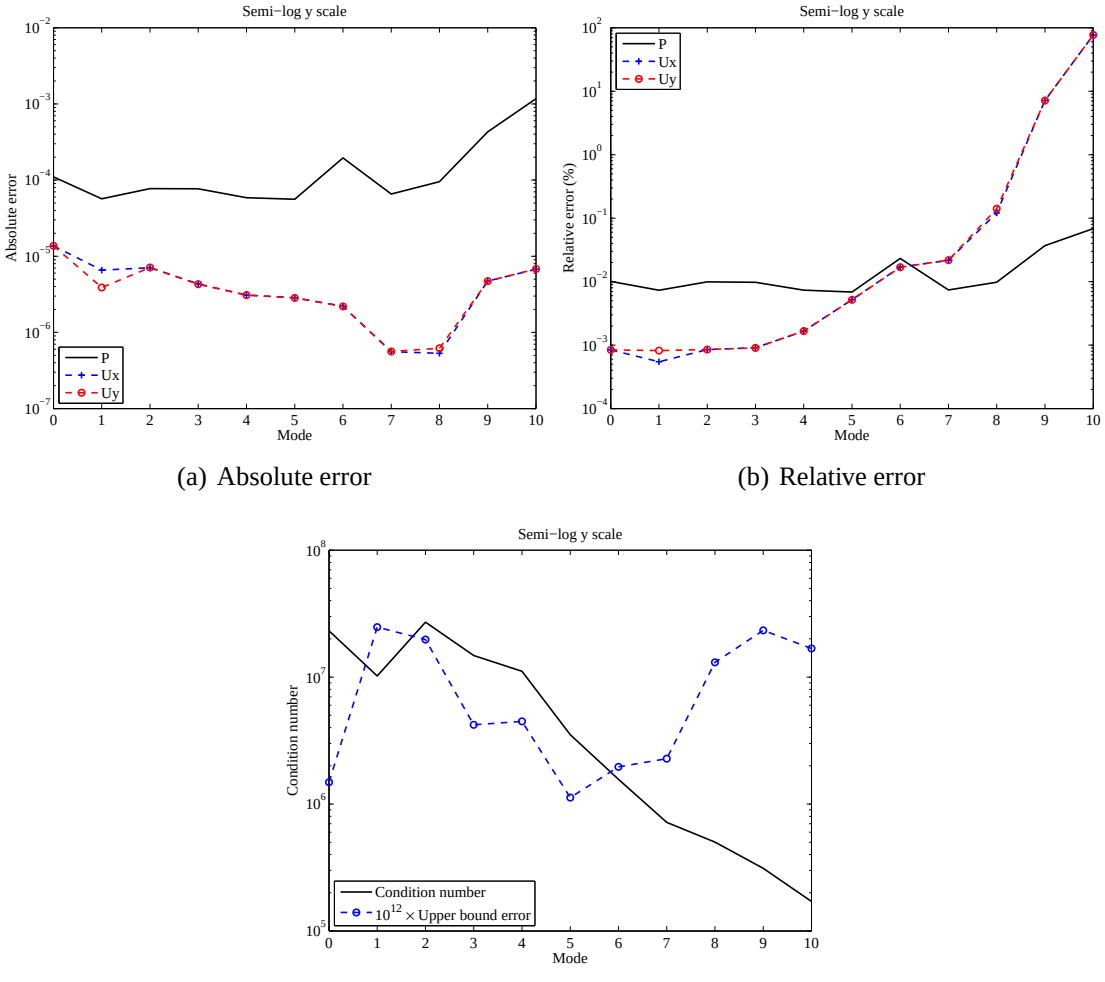

(a) Absolute error

(b) Relative error

(c) Condition number

Figure II.4.9 – Waveguide-type problem - Curl-free displacement - Figures (a)-(b): Sensitivity of the relative and absolute errors to the mode number n using cubic polynomial elements equipped with curved boundary edges. Figure (c): Condition number of the system matrix and the upper bound of the error in the MUMPS solution (Semi-log y scale).

The pressure field p is given by Eq. (II.4.20) and the potential ψ by the Eq. (II.4.22). As above, we expand the form of the solution u. First, we have:

$$\nabla \times \ \psi = \frac{1}{r}\frac{\partial \psi}{\partial \theta}\vec{e}_r - \frac{\partial \psi}{\partial r}\vec{e}_\theta. \tag{II.4.32}$$

Therefore, we obtain:

$$\begin{aligned} u_x &= u_r \cos\theta - u_\theta \sin\theta, \\ u_y &= u_r \sin\theta + u_\theta \cos\theta, \end{aligned}$$

where

$$\begin{aligned} u_r &= \frac{1}{r}\frac{\partial \psi}{\partial \theta} = \frac{n}{r} J_n(k_s r)\cos(n\theta), \\ u_\theta &= -\frac{\partial \psi}{\partial r} = -k_s J_n'(k_s r)\sin(n\theta). \end{aligned}$$

Then, similarly to the previous part, we consider BVP (3) with the following expression for the right-hand sides:

$$g_R = \frac{\partial}{\partial r}\left[H_n^{(1)}(kr)\cos(n\theta)\right], \quad r = 3 \tag{II.4.33}$$

$$g_1 = \omega^2 \rho_f \nabla \times [J_n(k_s r)\sin(n\theta)] \cdot \nu - \frac{\partial}{\partial r}\left[H_n^{(1)}(kr)\cos(n\theta)\right], \quad r = 1 \tag{II.4.34}$$

$$g_2 = \sigma(\nabla \times [J_n(k_s r)\sin(n\theta)])\nu + \left[H_n^{(1)}(kr)\cos(n\theta)\right]\nu, \quad r = 1. \tag{II.4.35}$$

The parameters are the ones defined in the beginning of the section.
In this case, the mode number is again fixed to $n = 2$. The error results using linear to cubic polynomials are reported in Tables II.4.12 to II.4.14. In Fig. II.4.10 (a)-(b), we represent the real parts of the pressure field p and the displacement component u_x for both approximate and exact solutions when using cubic elements. Fig. II.4.10 (c) depicts the absolute error between both solutions. Fig. II.4.11 gives the representation of the imaginary part of the pressure field p and the real part of the displacement component u_y for both approximate and exact solutions when employing cubic elements, as well as the absolute error. Since the displacement field is real, we only show its real part. The results are similar to those obtained in the case of curl-free displacement. They indicate the following:

- As observed in the curl-free displacement case, there is a three orders of magnitude improvement on the relative error when going from linear to quadratic elements. Furthermore, going from quadratic to cubic elements - once again - does not make a difference, except for the

pressure field (see Tables II.4.12-II.4.14).

- Again, we recover the radiating structure of the solutions (see Fig. II.4.10 and Fig. II.4.11), and can observe the difference of wavelengths between both media.
- The concentration of the error on the fluid-solid interface is again observable on Fig. II.4.10 (c) and Fig. II.4.11 (c).

Fields	p	u_x	u_y
L_∞-norm exact solution	0.316	1.788	1.79
L_∞-norm approximate solution	20.808	2.359	2.344
Absolute error	35.381	0.476	0.471
L^2-relative error (%)	4712.858	32.390	32.06

Table II.4.12 – Radiating-type problem - Divergence-free displacement - Error results using linear polynomial elements ($n = 2$).

Fields	p	u_x	u_y
L_∞-norm exact solution	0.316	1.793	1.797
L_∞-norm approximate solution	0.328	1.794	1.798
Absolute error	5.885E-002	1.02E-003	1.034E-003
L^2-relative error (%)	7.544	6.788E-002	6.884E-002

Table II.4.13 – Radiating-type problem - Divergence-free displacement - Error results using quadratic polynomial elements ($n = 2$).

Fields	p	u_x	u_y
L_∞-norm exact solution	0.316	1.799	1.799
L_∞-norm approximate solution	0.318	1.799	1.799
Absolute error	3.915E-003	6.148E-004	6.182E-004
L^2-relative error (%)	0.502	4.093E-002	4.115E-002

Table II.4.14 – Radiating-type problem - Divergence-free displacement - Error results using cubic polynomial elements ($n = 2$).

To end this study, we analyze the stability with respect to the mode n of the special functions. The mode varies from $n = 0$ to $n = 10$ using cubic elements. The error curves are depicted in Fig. II.4.12, together with the condition number of the DG system matrix, as well as the upper bound of the error in the solution, provided by the solver MUMPS. In Fig. II.4.12 (a)-(b), we observe that the errors on the pressure field remain relatively stable. It is also the case for the displacement approximations. Note that the presence of peaks in the relative errors associated to the displacement components in Fig. II.4.12 (b) for the first mode $n = 0$ is due to the fact the displacement is zero for this mode value,

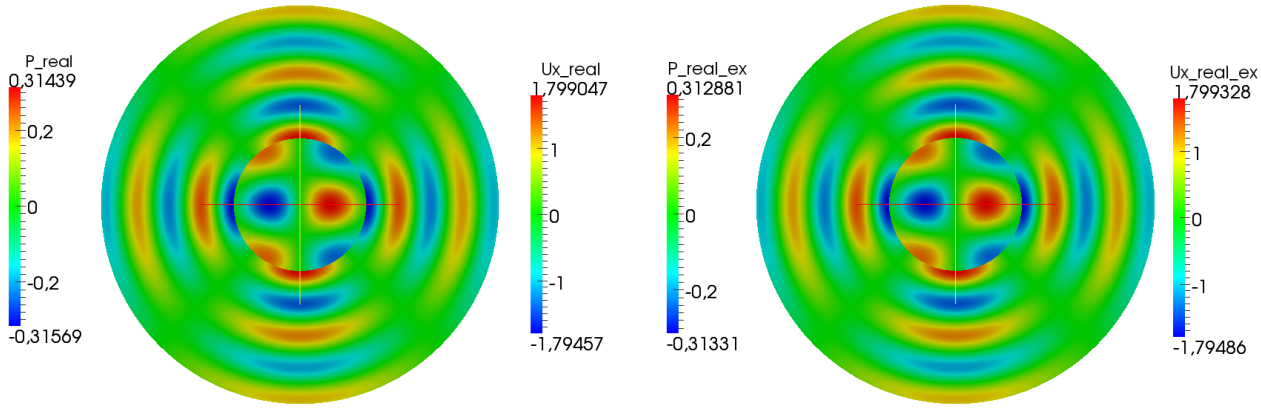

(a) Approximate solution

(b) Exact solution

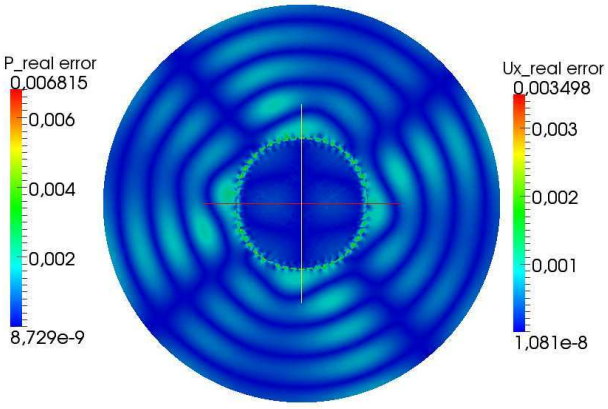

(c) Error between both solutions

Figure II.4.10 – Waveguide-type problem - Divergence-free displacement - Figures (a) and (b): Real parts of the pressure field p and displacement component u_x using cubic polynomial elements for the approximate and exact solutions ($n = 2$). Figure (c): Absolute error between both solutions.

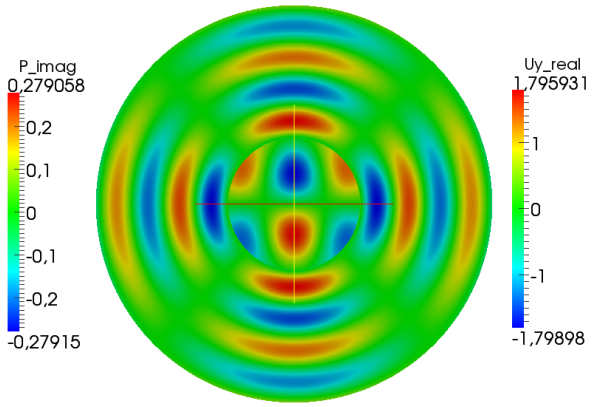

(a) Approximate solution

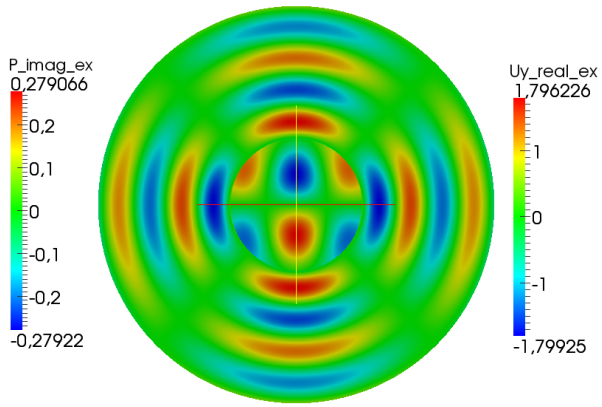

(b) Exact solution

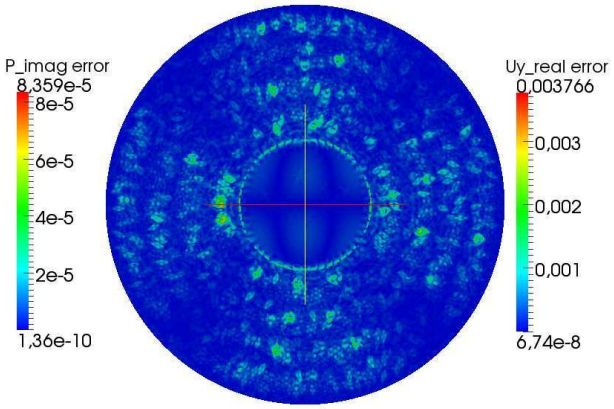

(c) Error between both solutions

Figure II.4.11 – Waveguide-type problem - Divergence-free displacement - Figures (a) and (b): Imaginary part of the pressure field p and real part of the displacement component u_y using cubic polynomial elements for the approximate and exact solution ($n = 2$). Figure (c): Absolute error between both solutions.

as indicated by Fig. II.4.12 (a). As previously, the condition number decreases with the mode number n but not the error in the Mumps solution (see Fig. II.4.12 (c)).

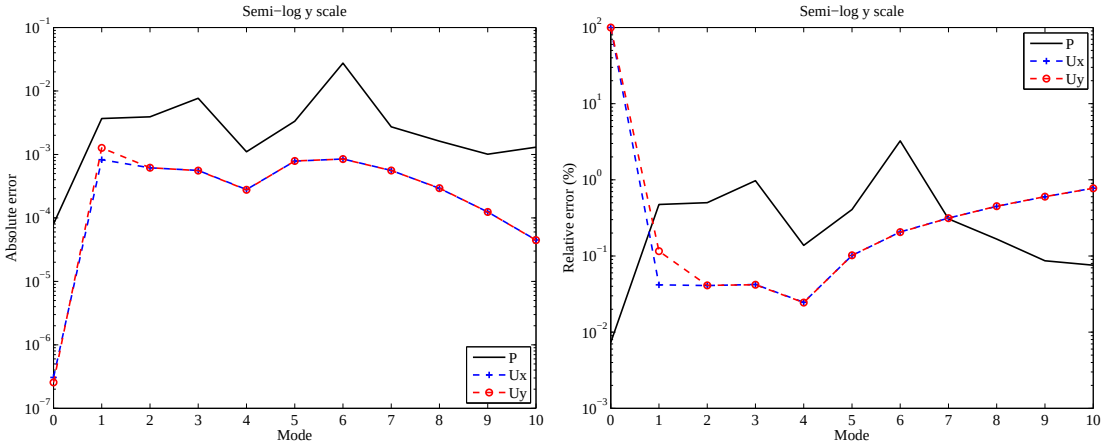

(a) Absolute error (b) Relative error

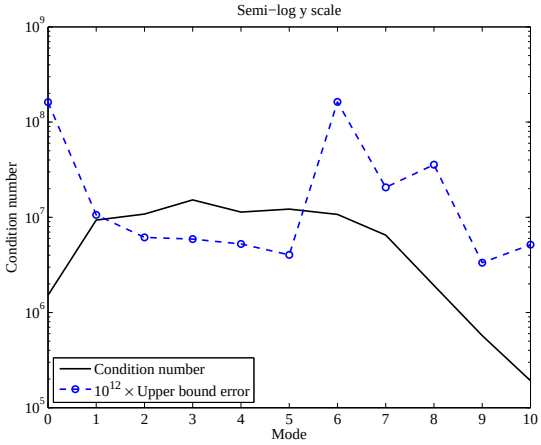

(c) Condition number

Figure II.4.12 – Waveguide-type problem - Divergence-free displacement - Figures (a)-(b): Sensitivity of the relative and absolute errors to the mode number n using cubic polynomial elements. Figure (c): Condition number of the system matrix and the upper bound of the error in the MUMPS solution (Semi-log y scale).

To conclude, it follows from the tests performed on the radiating-type problem that we again recover correctly P-waves and S-waves. The use of high-order (cubic) polynomial elements ensures an accurate approximation. Furthermore, the results seem to show a stability with respect to the mode number of the special functions.

Remark II.4.2.2 *Similarly to Remark II.4.2.1, we address the effect of using curved boundary edges on the approximation for the radiating-type problem in the case of divergence-zero displacement.*

The corresponding results are reported in Table II.4.11 and Fig. II.4.13 using cubic elements. The comparison of these results with Table II.4.10 and Fig. II.4.12 suggests that the curved boundary edges improves the accuracy level delivered by IPDG. We will see a more detailed analysis of the IPDG method equipped with curved boundary edges in the next section.

Fields	p	u_x	u_y
L_∞-norm exact solution	0.316	1.799	1.799
L_∞-norm approximate solution	0.316	1.799	1.799
Absolute error	6.654E-004	7.633E-005	7.613E-005
L^2-relative error (%)	8.529E-002	5.074E-003	5.061E-003

Table II.4.15 – Radiating-type problem - Divergence-free displacement - Error results using cubic polynomial elements equipped with curved boundary edges ($n = 2$).

II.5 Numerical performance

In this Section, we investigate the numerical performance of the proposed IPDG method equipped with curved boundary edges and compare it to the Ultra-Weak Variational Formulation (UWVF) [88]. The principle of the latter method is recalled in the state of the art in the preamble of [69]. As its name indicates, the UWVF method developed by Cessenat-Despré in [24] is constructed in a variational framework. The term "ultra-weak" comes from the fact that the variational problem is obtained after two integrations by parts. The wave field is approximated in a plane-wave basis, which results in in a discontinuous function. The continuity across the interfaces is restored in the weak sense by solving a system whose unknowns are defined on the mesh edges. This reduces the overall computational cost, but auxiliary local problems must be solved before. The discretization of the obtained system leads to a linear system associated with a Hermitian and definite-positive matrix, which nevertheless suffers from ill-conditioning.

To this end, we consider the three-dimensional time-harmonic scattering of acoustic waves by an infinite long aluminum cylinder immersed in water. Note that this configuration has been used in [88] to assess the performance of UWVF for fluid-solid interaction on relatively coarse meshes. In addition, since the axis of the cylinder is z, the problem reduces to a two-dimensional problem in the (x, y)-plane. The considered computational domain is depicted in Figure II.5.1. The solid is a circle Ω^s with radius $a = 0.01$ m surrounded by the fluid Ω^f delimited by the exterior circular-shaped boundary Σ of radius $b = 0.02$ m. The material properties of the considered elastic configuration are reported in Table II.5.1. These are similar to the ones used in [59, 88]. In the following, we consider

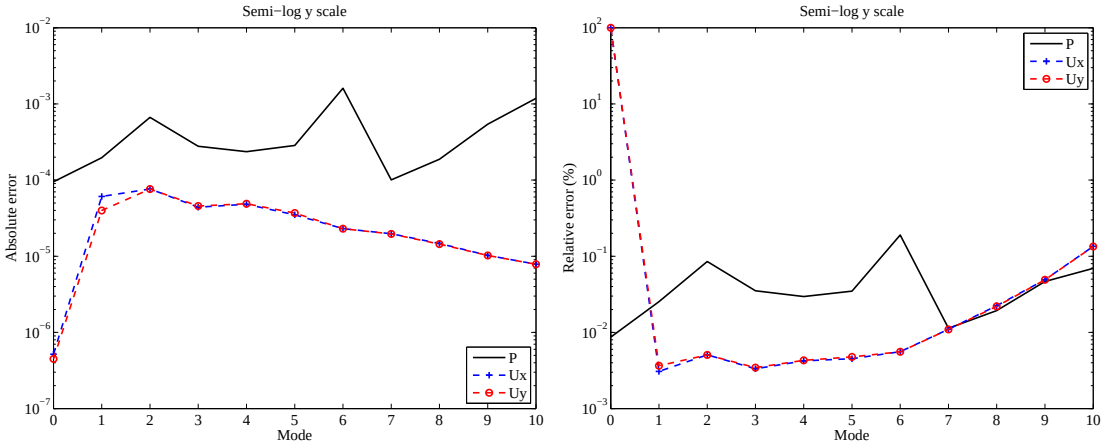

(a) Absolute error (b) Relative error

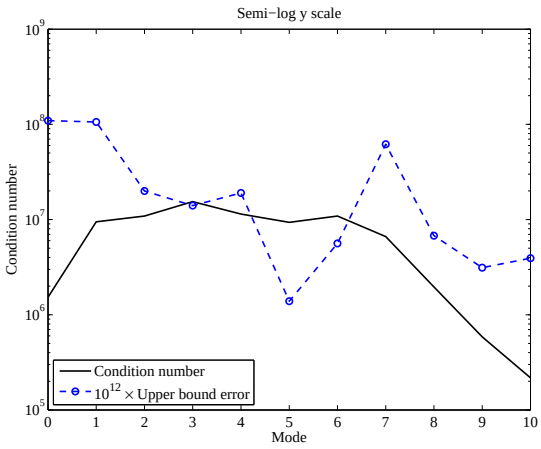

(c) Condition number

Figure II.4.13 – Waveguide-type problem - Divergence-free displacement - Figures (a)-(b): Sensitivity of the relative and absolute errors to the mode number n using cubic polynomial elements equipped with curved boundary edges. Figure (c): Condition number of the system matrix and the upper bound of the error in the MUMPS solution (Semi-log y scale).

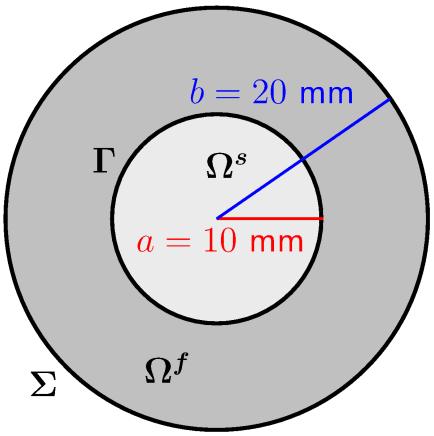

Figure II.5.1 – The computational domain: disk-shaped elastic scatterer Ω^s surrounded by an exterior circular-shaped boundary Σ.

an incident plane wave of the form $p^{inc} = e^{\mathrm{i}kx\cdot d}$ with $d = (1, 0)$. Note that, since the scatterer is isotropic, the fourth-order stiffness tensor reduces to $C_{lmjn} = \lambda\delta_{lm}\delta_{jn} + \mu(\delta_{lj}\delta_{mn} + \delta_{ln}\delta_{mj})$ where $\lambda = \rho_S(c_P^2 - 2c_S^2)$ and $\mu = \rho_S c_S^2$ are positive numbers representing the constant Lamé coefficients defined in terms of the density ρ_S, as well as the pressure and shear velocities c_P and c_S in the solid [93].

Properties / Medium	Density ρ (kg/m^3)	Propagation velocity c_P (m/s)	c_S (m/s)
Water	1000	1500	–
Aluminum	2700	6198	3122

Table II.5.1 – Material properties of the considered fluid-structure medium.

We use an analytical solution for the elasto-acoustic scattering problem existing for simple scatterers, that are circles to derive the method adopted. The construction of the analytical solution in polar coordinates is given in Appendix B.1 by using the separation of variables. Observe that the analytical solution is designed to satisfy the low-order Sommerfeld-type condition and thus the same problem as the approximate solution. By this way, the error between both exact and computed solutions will not be influenced by the radiation condition. As it is well-known, the exact solution of the considered elasto-acoustic problem can be expressed as a Fourier series (see, for example, [88] and Appendix B.1). For completeness purposes, we recall here such an expression. In the fluid domain, the scattered pressure field is expressed as follows [16]:

$$p(r,\theta) = \sum_{n=0}^{+\infty} \left[A_n H_n^{(1)}(kr) + B_n H_n^{(2)}(kr)\right] \cos(n\theta); \quad a < r < b,\ \theta \in [0, 2\pi) \tag{II.5.1}$$

where $H_n^{(1)}$ and $H_n^{(2)}$ denote the Hankel functions of the first and second kind [2], and A_n, B_n are complex numbers. The first term of the series corresponds to the outgoing field. The second term represents the incoming wave due to the presence of the exterior boundary Σ. In the solid obstacle, the scattered displacement field u is expressed using two displacement potentials ϕ and ψ [120]:

$$u = \nabla\phi + (-e_z) \times \nabla\psi. \tag{II.5.2}$$

where these two potentials are given by:

$$\phi(r,\theta) = \sum_{n=0}^{+\infty} C_n J_n(k_p r)\cos(n\theta), \tag{II.5.3}$$

$$\psi(r,\theta) = \sum_{n=0}^{+\infty} D_n J_n(k_s r)\sin(n\theta); \quad 0 \le r < a,\ \theta \in [0, 2\pi). \tag{II.5.4}$$

Here, J_n and Y_n denote the Bessel functions of the first and second kind respectively [2], and $k_p = \dfrac{\omega}{c_p}$, $k_s = \dfrac{\omega}{c_s}$ represent the wavenumbers of the pressure and shear waves in the solid. Moreover, the complex coefficients A_n, B_n, C_n and D_n satisfy the following system [88]:

$$E_n X_n = e_n \tag{II.5.5}$$

where $X_n = (A_n, B_n, C_n, D_n)^t$ and E_n is a 4×4 matrix whose complex-valued entries E_n^{lj} are given by:

$$\begin{aligned}
E_n^{1j} &= kH_n'^{(j)}(ka), \quad j = 1,2 \\
E_n^{13} &= -\omega^2 \rho_f k_p J_n'(k_p a), \\
E_n^{14} &= -\omega^2 \rho_f \frac{n}{a} J_n(k_s a), \\
E_n^{2j} &= H_n^{(j)}(ka), \quad j = 1,2 \\
E_n^{23} &= \frac{2\mu}{a^2}\left[(n^2 + n - \frac{1}{2}k_s^2 a^2)J_n(k_p a) - k_p a J_{n-1}(k_p a)\right], \\
E_n^{24} &= \frac{2\mu}{a^2}\left[n(-(n+1)J_n(k_s a) + k_s a J_{n-1}(k_s a))\right], \\
E_n^{31} &= E_n^{32} = E_n^{43} = E_n^{44} = 0, \\
E_n^{33} &= -\frac{2\mu}{a^2} n\left[-(n+1)J_n(k_p a) + k_p a J_{n-1}(k_p a)\right], \\
E_n^{34} &= -\frac{2\mu}{a^2}\left[(n^2 + n - \frac{1}{2}k_s^2 a^2)J_n(k_s a) - k_s a J_{n-1}(k_s a)\right],
\end{aligned}$$

$$E_n^{4j} = kH_n^{'(j)}(kb) - \mathrm{i}kH_n^{(j)}(kb), \quad j = 1, 2.$$

The right-hand side $e_n \in \mathbb{C}^4$ corresponding to Eq. (B.1.14) is given by:

$$e_n^1 = -\varepsilon_n \mathrm{i}^n k J_n^{'}(ka), \tag{II.5.6}$$
$$e_n^2 = -\varepsilon_n \mathrm{i}^n J_n(ka), \tag{II.5.7}$$
$$e_n^3 = e_n^4 = 0, \tag{II.5.8}$$

where $\varepsilon_0 = 1$ and $\varepsilon_n = 2$ for $n \geq 1$.

We also denote by $E_n^r = (E_n^{jl})_{j=1,2,3;l=1,3,4}$ the reduced matrix in which the effect of the exterior boundary is ignored, whereas $E_n^s = (E_n^{jl})_{j=2,3;l=3,4}$ is the matrix representing the solid Fourier modes.

Recall that the Jones frequencies correspond to frequency values for which the uniqueness of the solution in the elastic medium fails. Such resonance frequencies correspond to the excitation of surface waves on the fluid-solid interface whose integer number of wavelengths fits over the circumference of the interface [88]. Consequently, the determination of these resonance frequencies can be accomplished by monitoring the dependence of these local three matrices E_n, E_n^r and E_n^s with respect to the normalized frequency ka and by determining the values of n that make the corresponding determinants vanish. Note that, omitting the low-order Sommerfeld-type condition term, the determinant associated to E_n^r corresponds to the real unbounded physical problem satisfying the radiation condition. Moreover, observe that, since E_n^s represents the vanishing traction on the surface of the elastic scatterer, the determinant associated to E_n^s naturally coincides with the Jones frequencies.

In all numerical experiments presented here, the exact solution has been evaluated by computing only the first $2kb + 1$ Fourier modes for both the fluid pressure p and the structural displacement u, or less Fourier modes if the relative change due to an additional mode in both acoustic and elastic wave fields is below 10^{-5}. It is worth mentioning that, though this is not necessary, we scale the systems associated to both approximate and exact solutions in order to avoid some instabilities, especially in the high-frequency regime. Indeed, in our numerical experiments, there is a difference of scale of 10^{13} between both acoustic and elastic wave fields, and therefore, the system matrices can suffer from ill-conditioning. Note that, for high frequency values, the analytical solution turns out to be unstable, more particularly the analytical pressure field, and a special care to the mode number precision is required.
We must point out that we have performed this numerical investigation by taking values for the penalty

terms γ_f and γ_s ranging from 0 to 10^6. The obtained results (see Appendix B.3) suggest that one can use any values for γ_f and γ_s without affecting the accuracy of IPDG, provided that these values remain larger than $\frac{1}{4}p(p+1)$, where p is the order of the considered element.

We have performed several numerical experiments and compared the obtained results to those obtained with UWVF [88]. We present here a sample of illustrative results pertaining to (a) the determination of Jones frequencies, (b) the sensitivity to the mesh refinement, and (c) the sensitivity to the frequency regime.

II.5.1 Numerical determination of the Jones frequencies

The objective here is to compute the Jones frequencies of the given problem configuration. To this end, we consider Mesh 1 depicted in Fig. II.5.2(a) and whose characteristics are reported in Table II.5.2. Since ka varies from 4 to 21, the mesh resolution decreases from 20 elements to about 3.9 elements per wavelength. In the first experiment, we consider the case where the boundaries are

	♯ points		♯ elements	
	Γ	Σ	Ω^s	Ω^f
Mesh 1	80	160	1602	4840
Mesh 2	320	160	1956	4244
Mesh 3	44	27	461	184

Table II.5.2 – Disk-shaped elastic scatterer problem - Mesh characteristics.

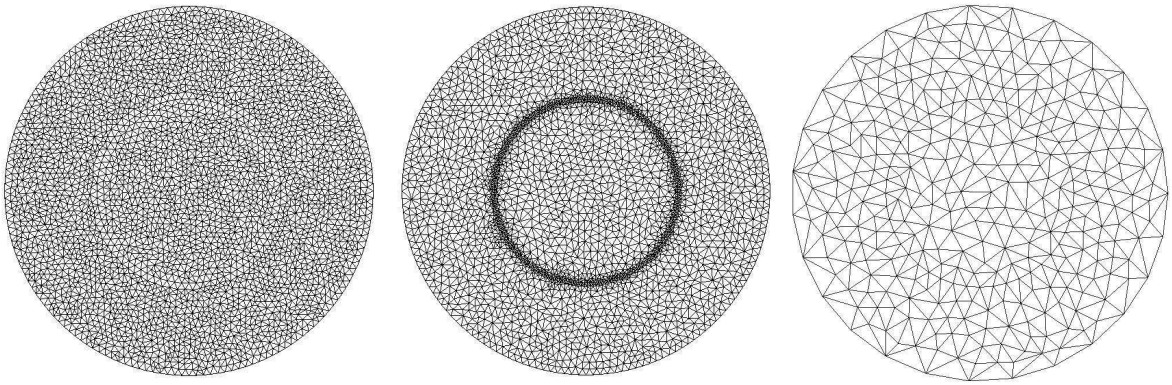

(a) Mesh 1 (b) Mesh 2 (c) Mesh 3

Figure II.5.2 – Disk-shaped elastic scatterer problem.

polygonal-shaped, that is, no curved boundary edges are used, and we employ cubic polynomial functions. The results are reported in Figures II.5.3 to II.5.6. The following observations are noteworthy:

- Except at discrete values of ka, the L^2-relative error remains below 1.5% even when the mesh resolution is as low as 3.9 elements per wavelength, as indicated in Fig. II.5.3 (a).
- Fig. II.5.3 (a) also indicates that the relative error curves associated to the structural displacement field (u_x, u_y) exhibit peaks that correspond to the resonance frequencies, as confirmed in Figure II.5.4 depicting the condition number of the global system given by Eq. (II.3.29).
- The curve corresponding to the L^2-relative error in the fluid pressure also exhibits peaks (see Fig.II.5.3) which is striking since there is no resonance frequency in the fluid. The presence of these spurious frequencies in the fluid medium is due to a poor approximation of the interface fluid/structure Γ, as it will be demonstrated in the next paragraph (see Fig. II.5.18).
- Observe that the highest peak in Fig. II.5.3 is located at the dimensionless frequency $ka = 9.26$, corresponding to the frequency $f_R = 221$ kHz. Fig. II.5.5 reveals that, at this frequency value, the three matrices E_n, E_n^r and E_n^s for the third Fourier mode ($n = 2$) become singular, as observed in Fig. 7, page 178 in [88]. Note that the minimum values of the three determinants are located at the same frequencies, which shows that the resonances for the modal problem are the physically relevant Jones frequencies corresponding to the third type of determinants in Figs. II.5.5-II.5.6. This clearly demonstrates that the frequency value f_R coincides with the Jones frequency associated to the third Fourier mode.

Note that Appendix B.2 addresses a brief analysis on the sensitivity of the Jones frequencies to perturbations of the scatterer.

II.5.2 Towards the IPDG method equipped with curved boundary edges

In this section, we propose a progressive approach towards the IPDG method equipped with curved boundary edges on the transmission interface and exterior boundary as follows. First, we present the results obtained in the neighborhood of the resonance frequency f_R highlighted previously, using straight boundary edges and the globally refined Mesh 1 depicted in Fig. II.5.2(a). Next, we observe the improvements achieved by means of a refinement of the mesh interface, using Mesh 2 depicted in Fig. II.5.2(b), while still employing no curved edges at the boundaries. Second, we come to the IPDG method equipped with curved boundary edges, that will be adopted, using the coarser Mesh 3 depicted in Fig. II.5.2(c).

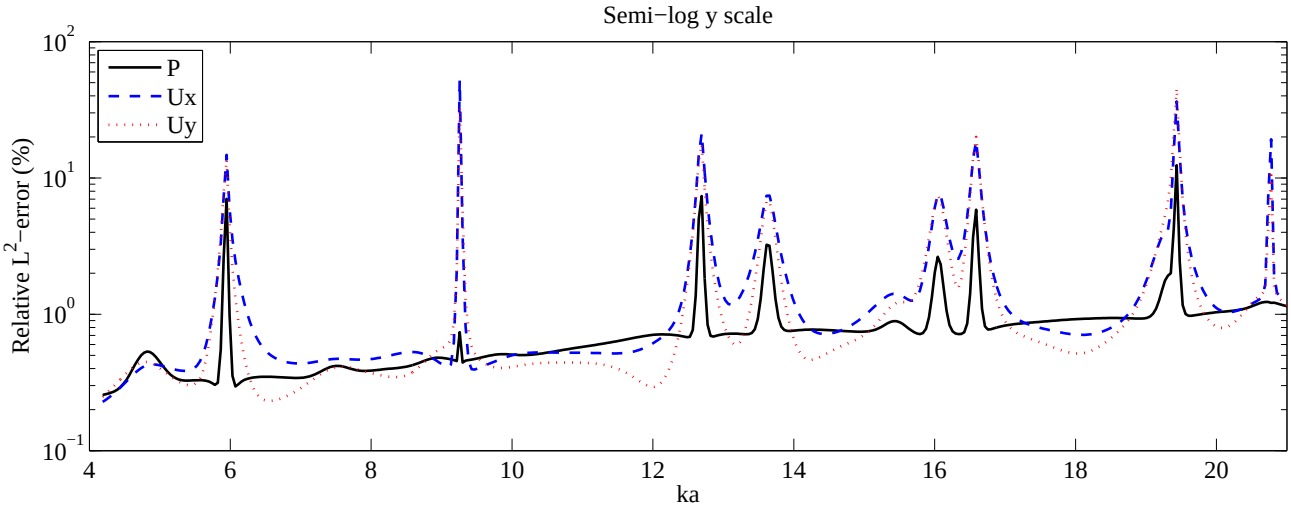

(a) Relative error

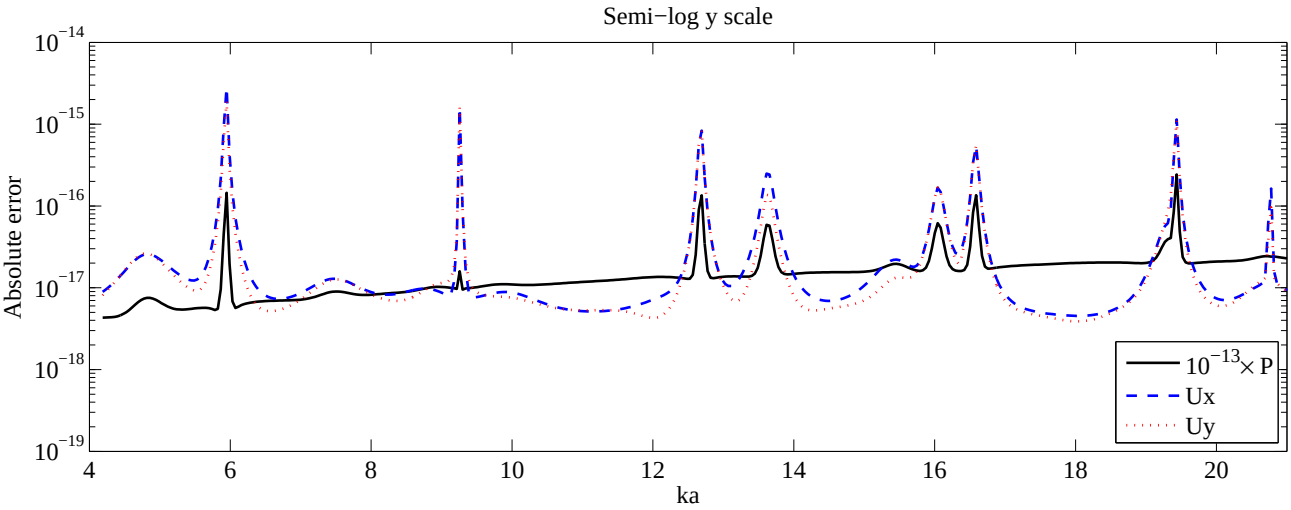

(b) Absolute error

Figure II.5.3 – Sensitivity of the L^2-relative error and of the absolute error to the wavenumber ka when using Mesh 1 and cubic polynomial elements without curved boundary edges.

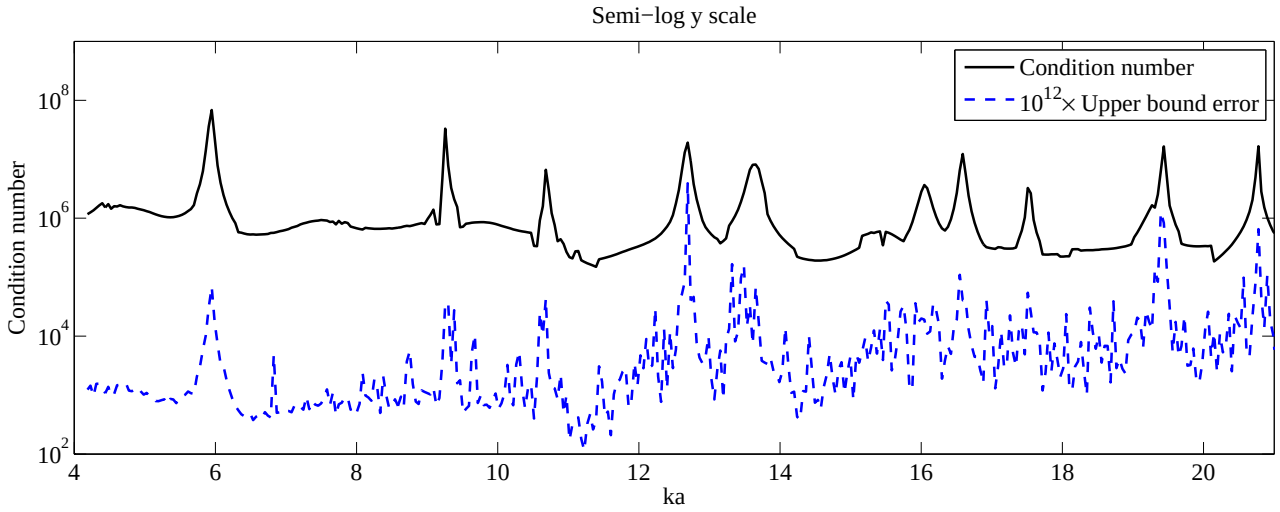

Figure II.5.4 – Sensitivity of the condition number of the system matrix and the upper bound of the error in the MUMPS solution to the wavenumber ka when using Mesh 1 and cubic polynomial elements without curved boundary edges.

II.5.2.1 IPDG method without curved boundary edges

In the following, we analyze the performance of the method in the neighborhood of the resonance frequency f_R highlighted previously. Similarly to [88], we consider the three frequencies $f_1 = 219$ kHz, $f_R = 221$ kHz, and $f_2 = 223$ kHz, corresponding to $ka = 9.1735, 9.2572$, and 9.341 respectively. We have computed the scattered field (p, u_x, u_y) using two meshes: Mesh 1 and Mesh 2 (see Fig. II.5.2(a) and Fig. II.5.2(b)). Note that these two meshes are similar except at the fluid-structure interface in which Mesh 2 is four times finer than Mesh 1, as indicated in Table II.5.2. Moreover, the numerical experiments have been performed using (a) linear polynomials, (b) quadratic polynomials and (c) cubic polynomials. We must point out that no curved edges at the boundaries were employed in these experiments. The obtained L^2-relative errors and absolute errors on the scattered field are reported in Tables II.5.3-II.5.5, Table II.5.6-II.5.5, and Fig. II.5.7. Some illustrations of the numerical results obtained using cubic polynomial elements are depicted in Figs. II.5.8 to II.5.13. The following observations are noteworthy:

- IPDG delivers a very poor accuracy level when using Mesh 1 (see Tables II.5.3-II.5.5) at the Jones frequency f_R. Observe that the use of higher-order elements does not improve the accuracy except for the fluid pressure p. The situation is slightly different for the two other frequencies. Indeed, we observe that there is one order of magnitude improvement on the relative error when going from linear to quadratic elements. However, the error stagnates when using higher-order (cubic) elements (see Table II.5.5).

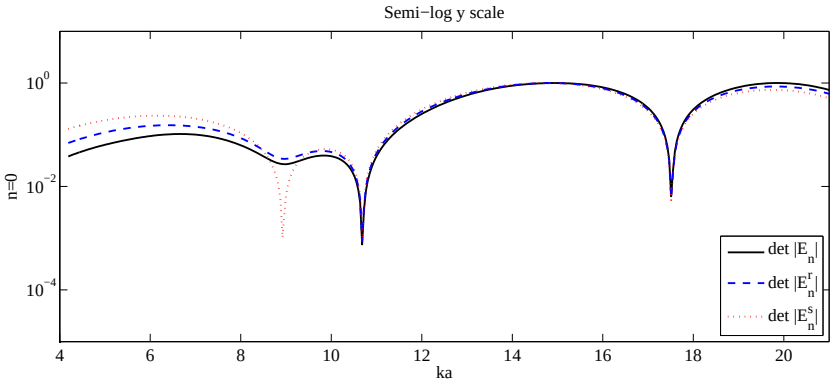

(a) Mode n=0

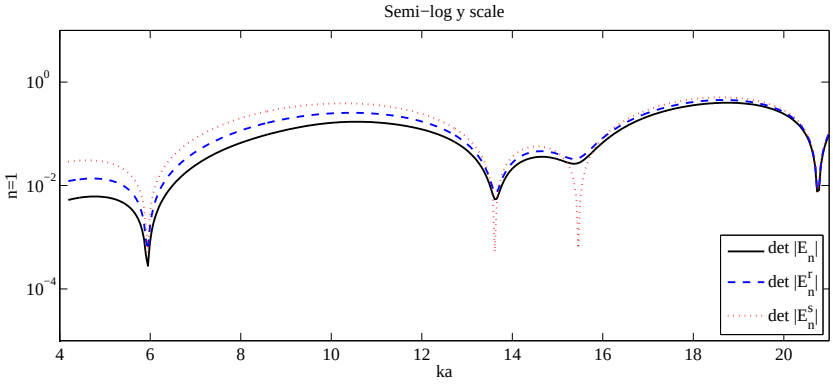

(b) Mode n=1

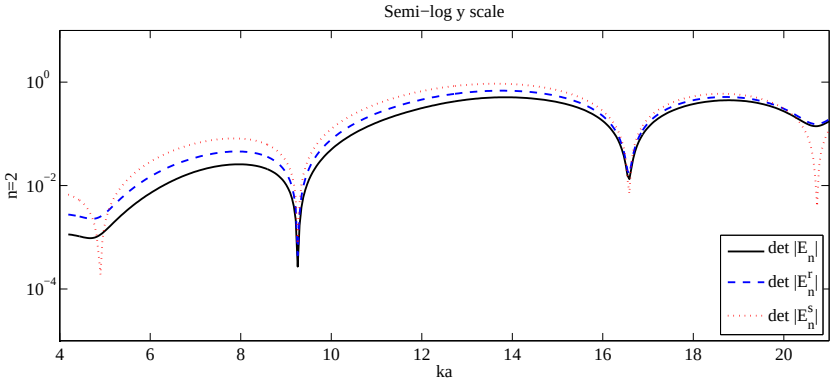

(c) Mode n=2

Figure II.5.5 – Sensitivity of the determinant of the modal matrices to the wavenumber ka. Cases where $n = 0, 1, 2$ (Semi-log y scale).

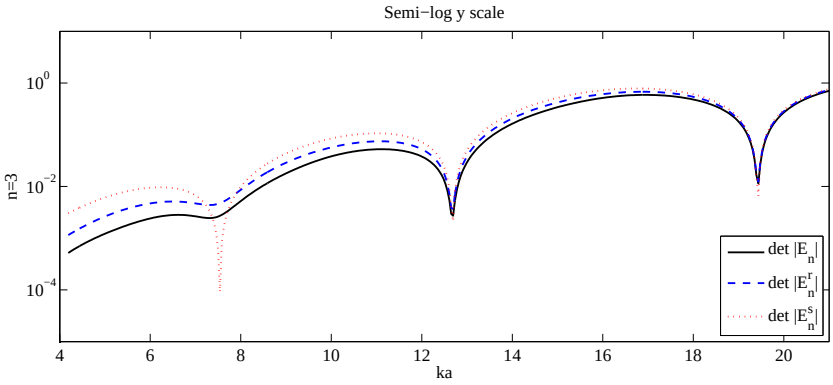

(a) Mode n=3

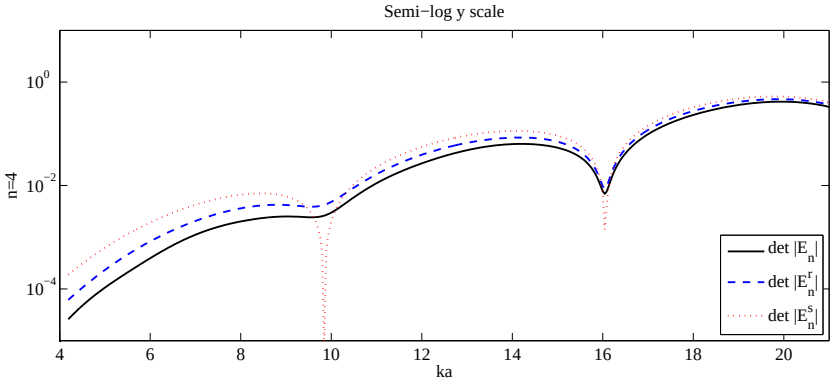

(b) Mode n=4

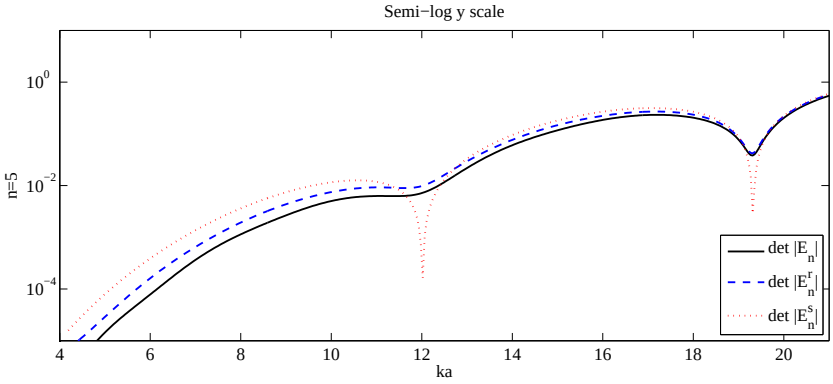

(c) Mode n=5

Figure II.5.6 – Sensitivity of the determinant of the modal matrices to the wavenumber ka. Cases where $n = 3, 4, 5$ (Semi-log y scale).

- The results reported in Tables II.5.6-II.5.8 indicate that a finer mesh on the fluid-structure interface (recall that Mesh 2 is four times finer than Mesh 1 on the interface, as shown in Table II.5.2) improves the accuracy level delivered by IPDG for all three frequencies. These results clearly illustrate the importance of well representing Γ for the accuracy. Yet, the error on the structural displacement at the Jones frequency f_R is about two orders of magnitude higher than the error on the field corresponding to the non-resonant frequencies. Furthermore, going from quadratic to cubic elements - once again - does not make a difference. In addition, the spurious frequencies are still present in the fluid medium, as depicted in Fig. II.5.7.
- Figs. II.5.8- II.5.10, where the pressure modulus and the displacement amplitude field $\sqrt{u \cdot \bar{u}}$ are represented, suggest that the error is due to a poor modeling of the wave transmission through the wet surface. Figs. II.5.11- II.5.13 supports this idea since we can observe a kind of thinning down of the error when considering a finer mesh on the fluid-structure interface.

f (kHz)		p	u_x	u_y
219	L_∞-norm exact solution	1.739	1.98E-013	2.556E-013
	L_∞-norm approximate solution	1.776	2.004E-013	2.427E-013
	Absolute error	2.356E-003	1.201E-016	1.901E-016
	L^2-relative error (%)	11.323	6.464	9.572
221	L_∞-norm exact solution	1.73	4.612E-013	6.346E-013
	L_∞-norm approximate solution	1.757	1.757E-013	2.659E-013
	Absolute error	2.459E-003	3.139E-015	3.247E-015
	L^2-relative error (%)	11.77	102.723	67.206
223	L_∞-norm exact solution	1.706	2.462E-013	2.01E-013
	L_∞-norm approximate solution	1.738	2.615E-013	1.815E-013
	Absolute error	2.483E-003	2.252E-016	2.875E-016
	L^2-relative error (%)	11.931	11.023	17.319

Table II.5.3 – Error results for linear polynomial elements using Mesh 1 and no curved boundary edges.

Remark II.5.2.1 *Before using a refinement of the fluid-structure interface only, we have refined the mesh globally by halving the triangle edges once, which multiplies the number of elements by 4. We have obtained relative errors that are divided by a factor 2.7 in the case of the resonance frequency:* $0.28\%, 19.881\%, 12.594\%$ *for* p, u_x *and* u_y *respectively, when using cubic elements, and similar results when employing cubic elements. Therefore, the global refinement of Mesh 1 only slighty improves the results compared to the benefits obtained using Mesh 2. Moreover, the computational cost is clearly spoiled, and the limitations constituted by the use of polygonal-shaped approximations remain. Note that with Mesh 1, the number of non-zero entries of the system was 1,667,068, whereas on Mesh 2, that admits about the same number of elements as Mesh 1, it becomes 1,756,628, which*

f (kHz)		p	u_x	u_y
219	L_∞-norm exact solution	1.742	1.98E-013	2.556E-013
	L_∞-norm approximate solution	1.743	1.991E-013	2.546E-013
	Absolute error	9.625E-005	1.186E-017	1.763E-017
	L^2-relative error (%)	0.450	0.635	0.881
221	L_∞-norm exact solution	1.736	4.614E-013	6.346E-013
	L_∞-norm approximate solution	1.732	2.671E-013	4.417E-013
	Absolute error	1.612E-004	1.625E-015	1.630E-015
	L^2-relative error (%)	0.751	52.869	33.534
223	L_∞-norm exact solution	1.715	2.462E-013	2.01E-013
	L_∞-norm approximate solution	1.715	2.482E-013	1.994E-013
	Absolute error	9.512E-005	1.703E-017	2.211E-017
	L^2-relative error (%)	0.444	0.829	1.320

Table II.5.4 – Error results for quadratic polynomial elements using Mesh 1 and no curved boundary edges.

f (kHz)		p	u_x	u_y
219	L_∞-norm exact solution	1.744	1.98E-013	2.556E-013
	L_∞-norm approximate solution	1.744	1.991E-013	2.545E-013
	Absolute error	9.880E-005	1.156E-017	1.719E-017
	L^2-relative error (%)	0.462	0.619	0.859
221	L_∞-norm exact solution	1.738	4.622E-013	6.351E-013
	L_∞-norm approximate solution	1.734	2.700E-013	4.446E-013
	Absolute error	1.589E-004	1.599E-015	1.605E-015
	L^2-relative error (%)	0.74	52.045	33.008
223	L_∞-norm exact solution	1.717	2.462E-013	2.01E-013
	L_∞-norm approximate solution	1.718	2.481E-013	1.993E-013
	Absolute error	9.789E-005	1.682E-017	2.167E-017
	L^2-relative error (%)	0.457	0.819	1.294

Table II.5.5 – Error results for cubic polynomial elements using Mesh 1 and no curved boundary edges.

f (kHz)		p	u_x	u_y
219	L_∞-norm exact solution	1.727	1.98E-013	2.556E-013
	L_∞-norm approximate solution	1.839	2.035E-013	2.397E-013
	Absolute error	2.994E-003	1.672E-016	2.456E-016
	L^2-relative error (%)	14.555	9.012	12.371
221	L_∞-norm exact solution	1.723	4.631E-013	6.353E-013
	L_∞-norm approximate solution	1.824	1.891E-013	2.506E-013
	Absolute error	3.098E-003	3.292E-015	3.42E-015
	L^2-relative error (%)	15.010	107.808	70.781
223	L_∞-norm exact solution	1.703	2.462E-013	2.01E-013
	L_∞-norm approximate solution	1.809	2.577E-013	1.864E-013
	Absolute error	3.144E-003	2.691E-016	3.495E-016
	L^2-relative error (%)	15.289	13.186	21.071

Table II.5.6 – Error results for linear polynomial elements using Mesh 2 and no curved boundary edges.

f (kHz)		p	u_x	u_y
219	L_∞-norm exact solution	1.740	1.980E-013	2.556E-013
	L_∞-norm approximate solution	1.740	1.980E-013	2.555E-013
	Absolute error	3.207E-005	1.242E-018	1.836E-018
	L^2-relative error (%)	0.150	6.65E-002	9.173E-002
221	L_∞-norm exact solution	1.735	4.631E-013	6.353E-013
	L_∞-norm approximate solution	1.735	4.338E-013	6.058E-013
	Absolute error	4.330E-005	2.410E-016	2.418E-016
	L^2-relative error (%)	0.202	7.835	4.968
223	L_∞-norm exact solution	1.716	2.462E-013	2.012E-013
	L_∞-norm approximate solution	1.716	2.463E-013	2.010E-013
	Absolute error	3.356E-005	1.546E-018	2.080E-018
	L^2-relative error (%)	0.157	7.517E-002	0.124

Table II.5.7 – Error results for quadratic polynomial elements using Mesh 2 and no curved boundary edges.

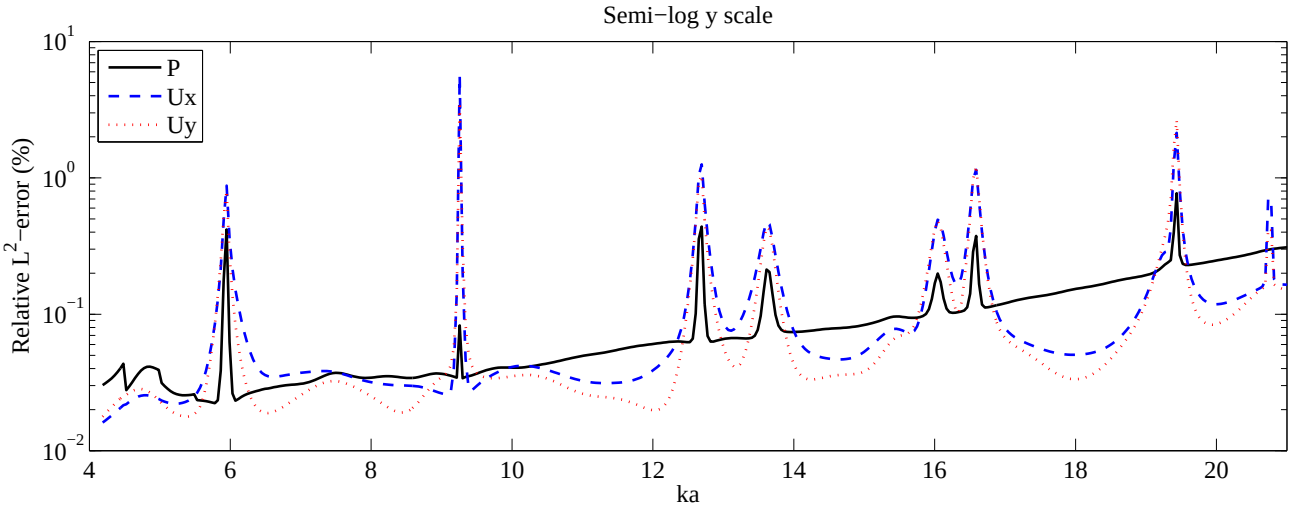

(a) Relative error

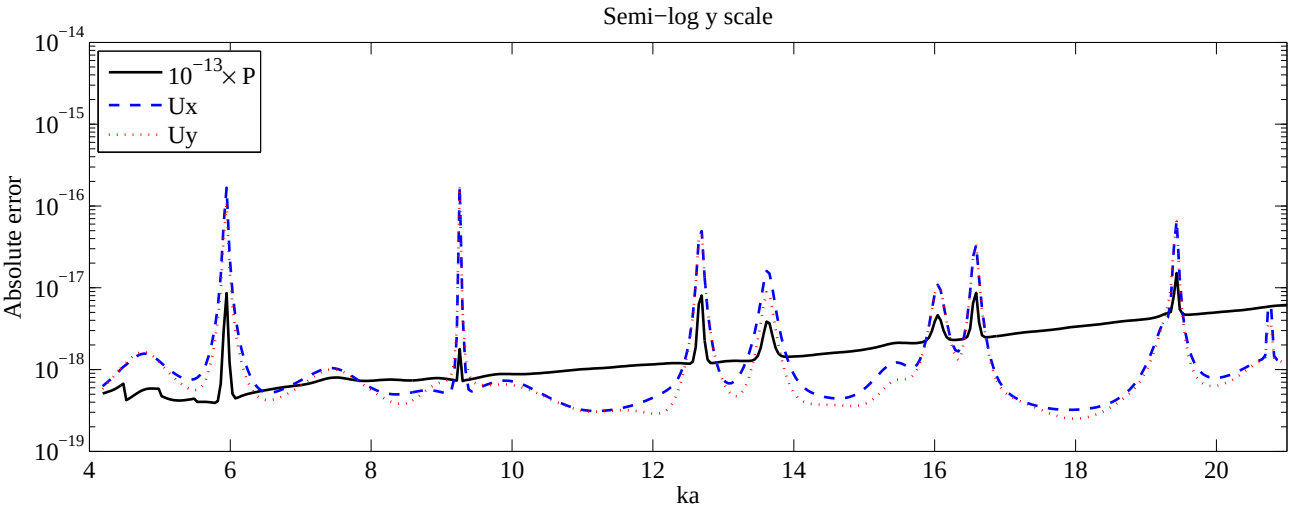

(b) Absolute error

Figure II.5.7 – Sensitivity of the L^2-relative error and of the absolute error to the wavenumber ka when using Mesh 2 and cubic polynomial elements without curved boundary edges.

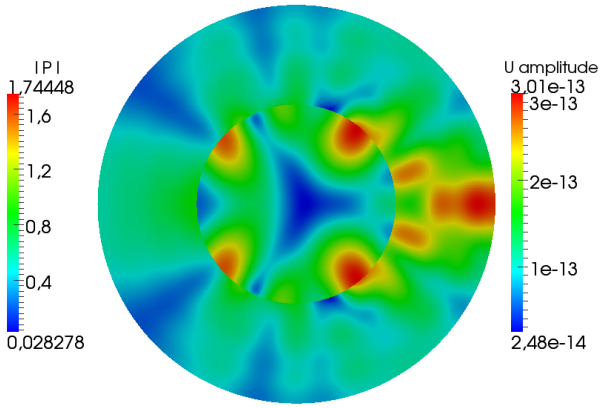

(a) Approximate solution

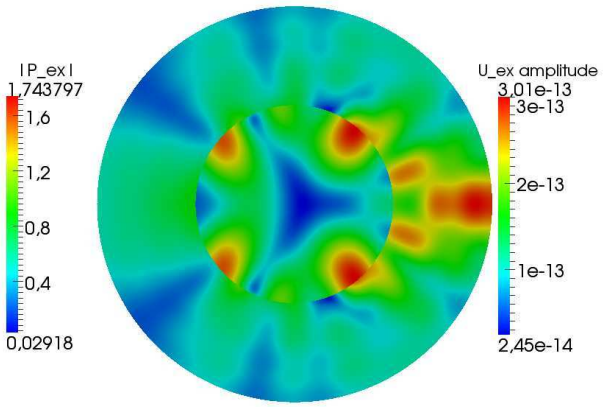

(b) Exact solution

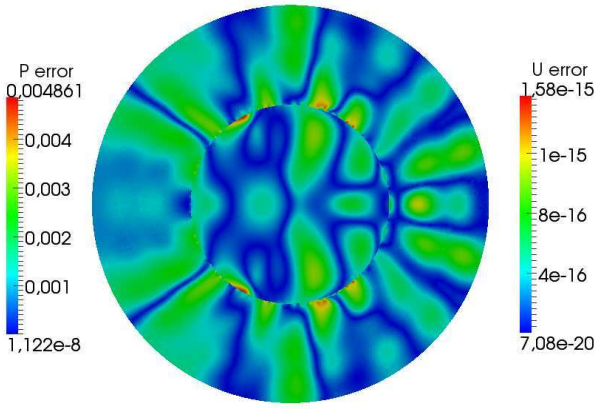

(c) Error between both solutions

Figure II.5.8 – Frequency $f_1 = 219$ kHz using cubic polynomial elements, Mesh 1, and curved boundary edges. Figures (a)-(b): Pressure modulus and displacement amplitude fields. Figure (c): Absolute error between both solutions.

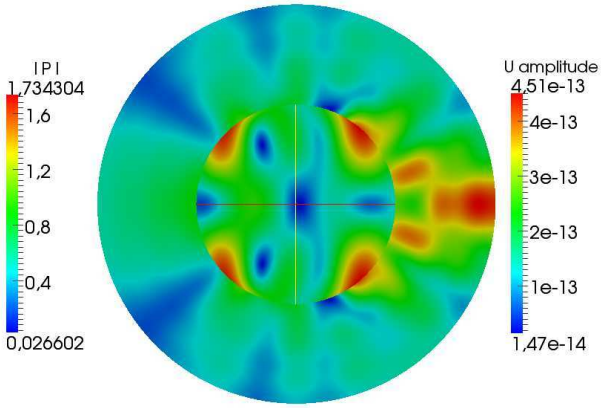

(a) Approximate solution

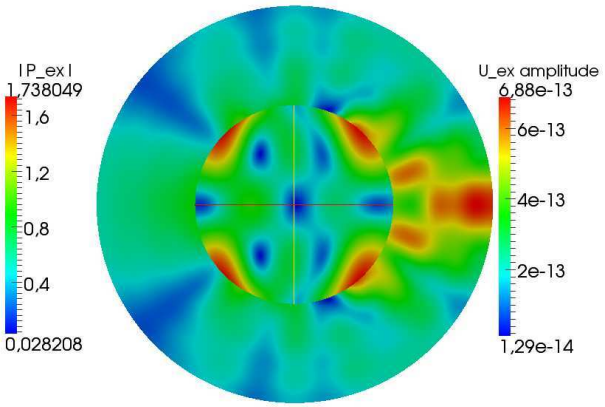

(b) Exact solution

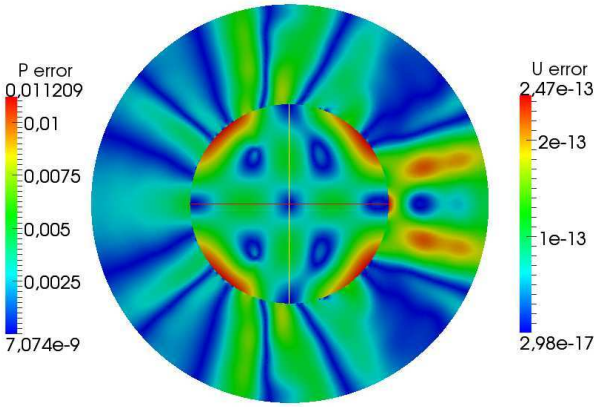

(c) Error between both solutions

Figure II.5.9 – Frequency $f_R = 221$ kHz using cubic polynomial elements, Mesh 1, and curved boundary edges. Figures (a)-(b): Pressure modulus and displacement amplitude fields. Figure (c): Absolute error between both solutions.

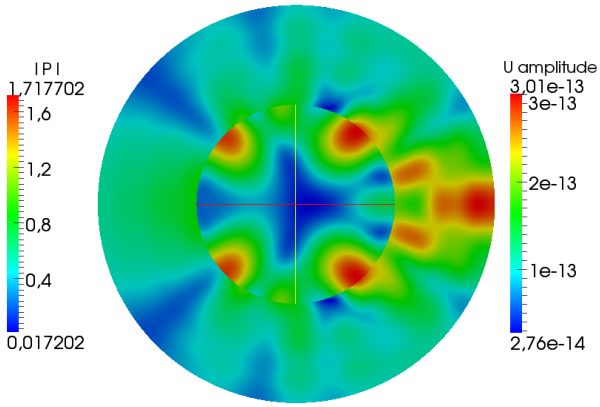

(a) Approximate solution

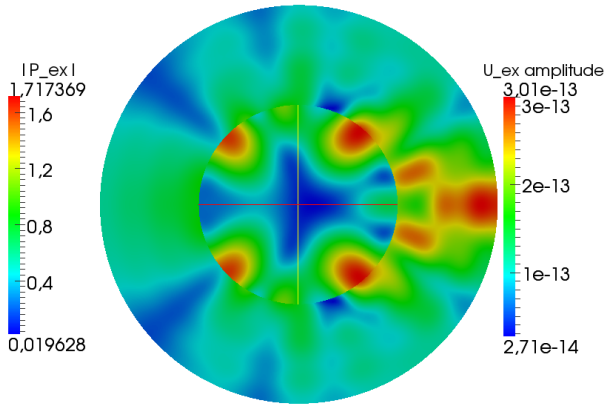

(b) Exact solution

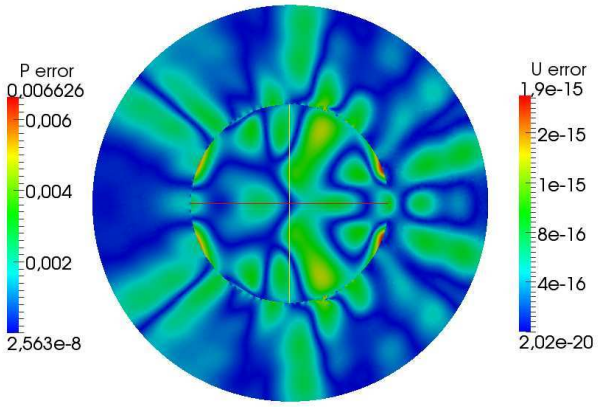

(c) Error between both solutions

Figure II.5.10 – Frequency $f_2 = 223$ kHz using cubic polynomial elements, Mesh 1, and curved boundary edges. Figures (a)-(b): Pressure modulus and displacement amplitude fields. Figure (c): Absolute error between both solutions.

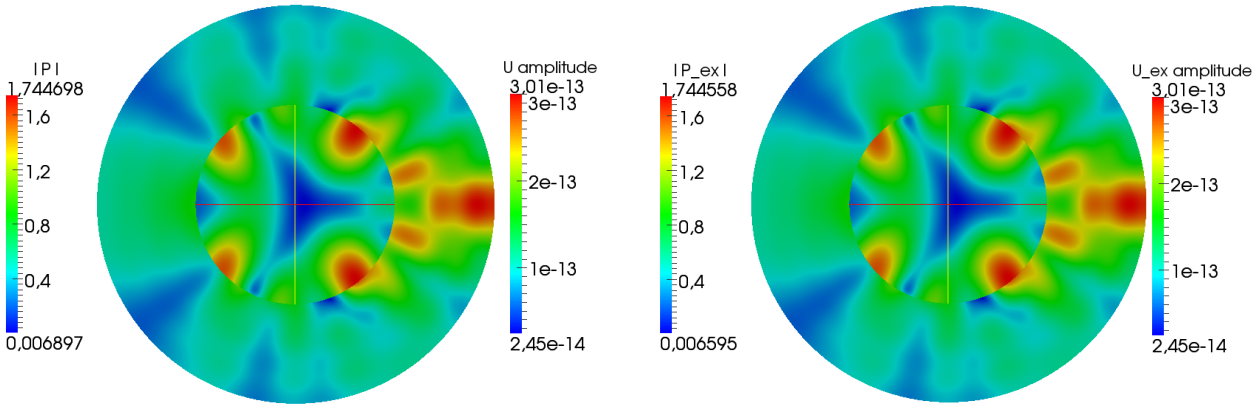

(a) Approximate solution

(b) Exact solution

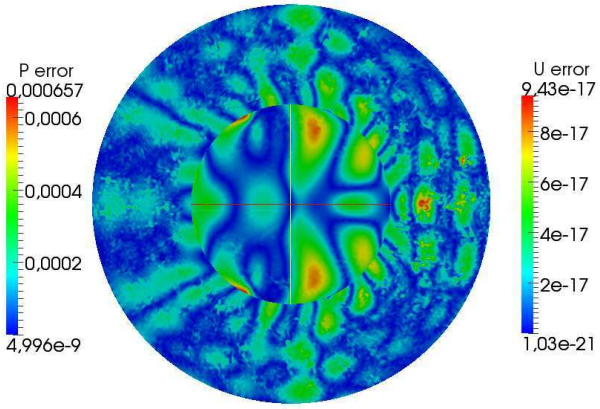

(c) Error between both solutions

Figure II.5.11 – Frequency $f_1 = 219$ kHz using cubic polynomial elements, Mesh 2, and curved boundary edges. Figures (a)-(b): Pressure modulus and displacement amplitude fields. Figure (c): Absolute error between both solutions.

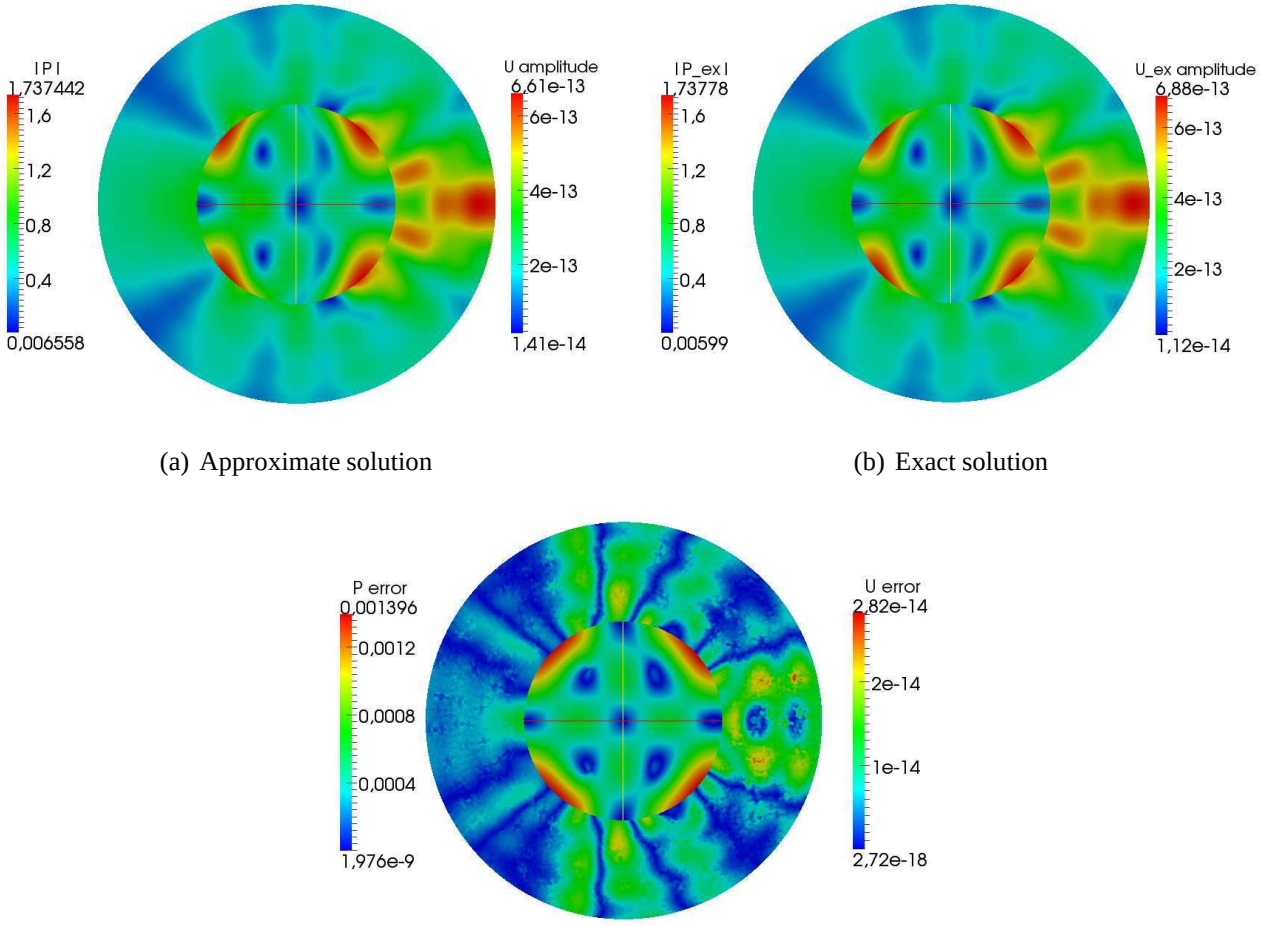

(a) Approximate solution

(b) Exact solution

(c) Error between both solutions

Figure II.5.12 – Frequency $f_R = 221$ kHz using cubic polynomial elements, Mesh 2, and curved boundary edges. Figures (a)-(b): Pressure modulus and displacement amplitude fields. Figure (c): Absolute error between both solutions.

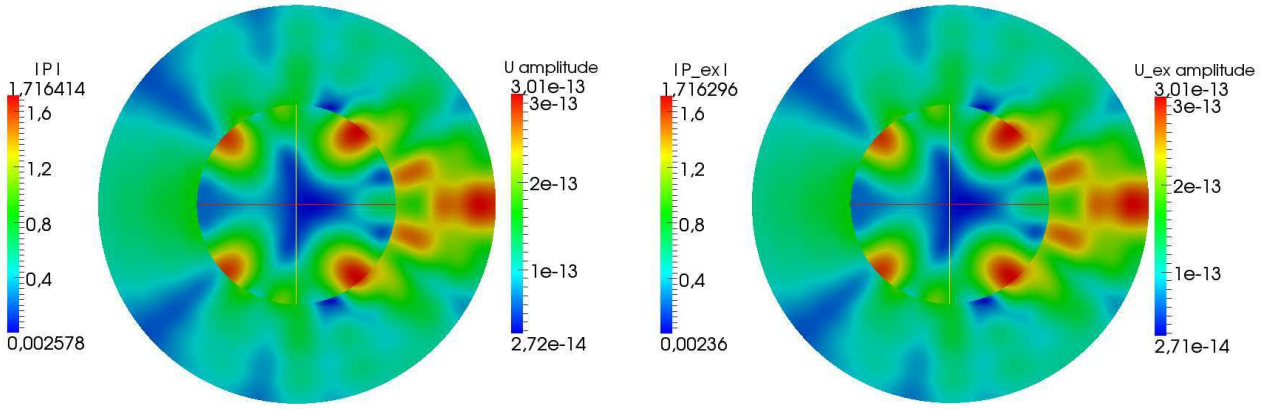

(a) Approximate solution

(b) Exact solution

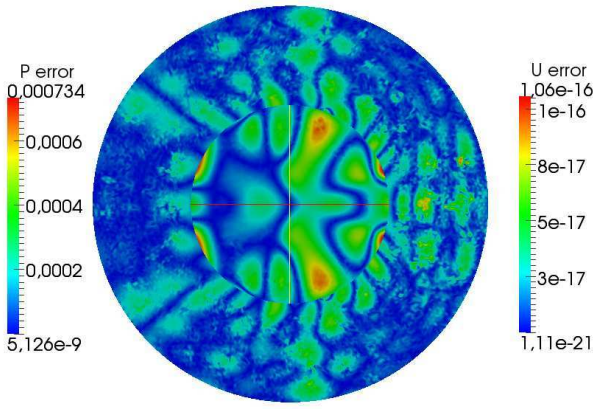

(c) Error between both solutions

Figure II.5.13 – Frequency $f_2 = 223$ kHz using cubic polynomial elements, Mesh 2, and curved boundary edges. Figures (a)-(b): Pressure modulus and displacement amplitude fields. Figure (c): Absolute error between both solutions.

f (kHz)		p	u_x	u_y
219	L_∞-norm exact solution	1.745	1.980E-013	2.556E-013
	L_∞-norm approximate solution	1.745	1.981E-013	2.555E-013
	Absolute error	7.467E-006	7.453E-019	1.147E-018
	L^2-relative error (%)	3.492E-002	3.99E-002	5.73E-002
221	L_∞-norm exact solution	1.738	4.631E-013	6.353E-013
	L_∞-norm approximate solution	1.737	4.417E-013	6.14E-013
	Absolute error	1.779E-005	1.743E-016	1.747E-016
	L^2-relative error (%)	8.284E-002	5.667	3.591
223	L_∞-norm exact solution	1.716	2.462E-013	2.012E-013
	L_∞-norm approximate solution	1.716	2.463E-013	2.011E-013
	Absolute error	7.421E-006	9.709E-019	1.395E-018
	L^2-relative error (%)	3.467E-002	4.722E-002	8.325E-002

Table II.5.8 – Error results for cubic polynomial elements using Mesh 2 and no curved boundary edges.

only represents an increase of 5%.
These results can explain the absence of gain when employing cubic polynomial elements. Indeed, as far as the error is dominated by the volumic error, it is interesting to use higher-order approximations. Nevertheless, as soon as the boundary error represents the main value of the error, to increase the order of approximation does not improve the computations anymore.

Remark II.5.2.2 *Regarding the issue of the choice of the penalty parameters, we have performed a numerical investigation in Appendix B.3. Note that taking the following value for the penalty terms $\gamma_f = 80$ and $\gamma_s = 0$ provides a slight improvement of the results when using cubic elements: $0.724\%, 50.793\%, 32.215\%$ for p, u_x and u_y respectively. Therefore, it seems that, in some situations at least, it can be sufficient to penalize the exterior problem. In fact, in the case of the non-resonance frequencies, the penalty terms ensure the stability, which guarantees the uniqueness that exists on the continuous level in both media. However, in the case of the resonant frequencies, we do not have uniqueness of the displacement field on the theoretical level, which can explain that the penalization is not necessarily relevant inside the obstacle.*

II.5.2.2 IPDG method equipped with curved boundary edges

Given the latter observations, we assess in the following the effect of using curved boundary edges on the accuracy of IPDG. In addition, we compare the obtained results to those obtained with UWVF [88]. To this end, we consider Mesh 3, which is coarser than Mesh 1 and Mesh 2 (see Fig. II.5.2 and Table II.5.2). However, Mesh 3 is comparable to Mesh 2 used in [88]. The latter has about 715 triangles. The results are reported in Tables II.5.9 to II.5.11 and Figures II.5.14 to II.5.20. We provide

some illustrations of the numerical results using cubic polynomial elements in Figs. II.5.14-II.5.16. These results indicate the following:

- The use of curved boundary edges, which is a more precise representation of the boundaries, improves significantly the accuracy of IPDG for all the three frequencies in spite of using a coarse mesh (Mesh 3), as indicated in Tables II.5.9 to II.5.11 and Figs. II.5.14 to II.5.16. Indeed, employing cubic polynomials maintains the relative error on the scattered field below 1% for all the three frequencies (see Table II.5.11). Recall that this is not the case when using polygonal-shaped approximations even with a very fine mesh at the boundary as clearly demonstrated previously in Table II.5.5 and Table II.5.8. Moreover, Figures II.5.14 to II.5.16 illustrate this significant improvement in comparison with the results previously depicted in Figures II.5.11 to II.5.13.
- Figure II.5.17 reveals that the error at the resonance frequency f_R has the same structure as the corresponding resonance mode $n = 2$, which proves again that $f_R = 221$ kHz is indeed the Jones frequency for the third mode ($n = 2$).
- The relative error on the scattered field depicted in Figure II.5.18 is obtained with a mesh resolution of about 6.2 elements per wavelength (for $ka = 4$) to as low as about 1.2 elements per wavelength (for $ka = 21$). The following observations are worth mentioning:
  - The error curve corresponding to the fluid pressure is smooth and the peaks corresponding to the spurious frequencies observed earlier (see Fig. II.5.3) are no longer present. Clearly, this is a direct attribute to the use of curved boundary edges. In addition, this smoothing effect does not remove the peaks from the error curves corresponding to the structural displacement. These physical peaks are clearly apparent which allows an easy determination of the Jones frequencies.
  - Unlike the results presented previously (see Fig. II.5.3), the use of curved boundary edges with cubic polynomials preserves the accuracy level below 5% for all frequency modes in the frequency band $4 \leq ka \leq 15$, even with a mesh resolution as low as 1.7 elements per wavelength.
  - In contrast, the results depicted in Fig.6 p.177 in [88] show that the nonphysical peaks in the fluid pressure error curve delivered with UWVF remain always present. In addition, we observe that the accuracy level deteriorates at and around the resonance frequencies. We must point out that the relative errors computed with UWVF are obtained over the wet surface Γ only, whereas the results depicted in Fig. II.5.18 are obtained over the entire computational domain. The comparison of these results suggests the superiority of IPDG over UWVF. Moreover, in order to maintain the condition number value below 10^8, the UWVF is limited

to the use of a maximum of 15 plane waves, as stated by the authors in [88]. This may constitute a severe limitation, especially when considering high-frequency regime. On the other hand, the use of cubic polynomial elements is sufficient for IPDG equipped with curved boundary edges to deliver an error smaller than 5% for all the modes in the frequency band $4 \leq ka \leq 15$. In addition, the result depicted in Figure II.5.19 tends to indicate that the condition number of IPDG does not suffer dramatically when increasing the order of elements. Indeed, going from linear to cubic polynomials slowly increases the condition number. Last, the UWVF results were obtained using 64 quadrature points to evaluate the integrals over the curved boundary edges, and employing an iterative solver, whereas IPDG uses 8 times less points and a direct solver since the resulting system is relatively small. This last observation also suggests, to some extent, the superiority of IPDG over UWVF in terms of the computational complexity.

f (kHz)		p	u_x	u_y
219	L_∞-norm exact solution	1.679	1.931E-013	2.49E-013
	L_∞-norm approximate solution	1.988	1.862E-013	2.303E-013
	Absolute error	1.209E-002	6.195E-016	8.475E-016
	L^2-relative error (%)	72.436	34.537	44.867
221	L_∞-norm exact solution	1.671	4.621E-013	6.297E-013
	L_∞-norm approximate solution	1.98	1.837E-013	2.247E-013
	Absolute error	1.231E-002	3.158E-015	3.852E-015
	L^2-relative error (%)	73.769	108.271	83.545
223	L_∞-norm exact solution	1.648	2.461E-013	1.983E-013
	L_∞-norm approximate solution	1.971	1.804E-013	2.192E-013
	Absolute error	1.251E-002	9.447E-016	7.65E-016
	L^2-relative error (%)	75.533	48.171	49.02

Table II.5.9 – Error results for linear polynomial elements using Mesh 3 and curved boundary edges.

In view of the overall results and observations, we retain the latter higher-order IPDG method equipped with curved boundary edges. In order to complete the analysis of the method, we examine the sensitivity of the method to the mesh refinement, as well as to the frequency regime, in the forthcoming parts.

Remark II.5.2.3 *In a first time, we have implemented curved finite elements only on the transmission interface Γ and still used straight boundary edges on the exterior boundary Σ. The results obtained are reported in Tables II.5.12 to II.5.14. They indicate the following:*

f (kHz)		p	u_x	u_y
219	L_∞-norm exact solution	1.743	1.979E-013	2.553E-013
	L_∞-norm approximate solution	1.76	1.959E-013	2.510E-013
	Absolute error	1.100E-003	2.292E-017	3.744E-017
	L^2-relative error (%)	5.203	1.227	1.872
221	L_∞-norm exact solution	1.736	4.621E-013	6.346E-013
	L_∞-norm approximate solution	1.749	2.787E-013	4.453E-013
	Absolute error	1.173E-003	1.578E-015	1.597E-015
	L^2-relative error (%)	5.526	51.340	32.836
223	L_∞-norm exact solution	1.714	2.461E-013	2.000E-013
	L_∞-norm approximate solution	1.732	2.459E-013	1.985E-013
	Absolute error	1.152E-003	2.593E-017	4.107E-017
	L^2-relative error (%)	5.446	1.262	2.454

Table II.5.10 – Error results for quadratic polynomial elements using Mesh 3 and curved boundary edges.

f (kHz)		p	u_x	u_y
219	L_∞-norm exact solution	1.738	1.977E-013	2.554E-013
	L_∞-norm approximate solution	1.736	1.977E-013	2.553E-013
	Absolute error	9.794E-005	1.476E-018	1.83E-018
	L^2-relative error (%)	0.457	7.899E-002	9.141E-002
221	L_∞-norm exact solution	1.730	4.621E-013	6.353E-013
	L_∞-norm approximate solution	1.728	4.593E-013	6.322E-013
	Absolute error	1.017E-004	2.578E-017	2.558E-017
	L^2-relative error (%)	0.473	0.838	0.526
223	L_∞-norm exact solution	1.708	2.461E-013	2.012E-013
	L_∞-norm approximate solution	1.705	2.463E-013	2.012E-013
	Absolute error	1.043E-004	1.628E-018	1.936E-018
	L^2-relative error (%)	0.487	7.916E-002	0.116

Table II.5.11 – Error results for cubic polynomial elements using Mesh 3 and curved boundary edges.

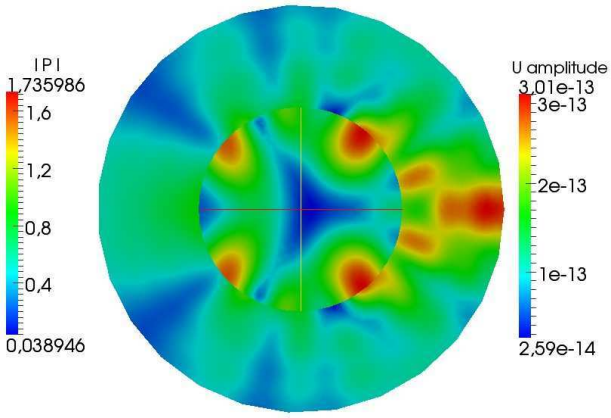

(a) Approximate solution

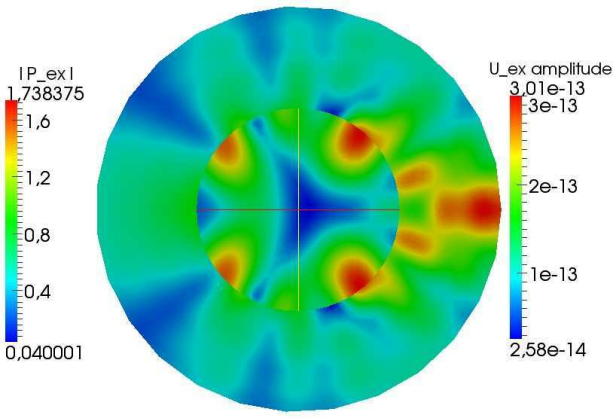

(b) Exact solution

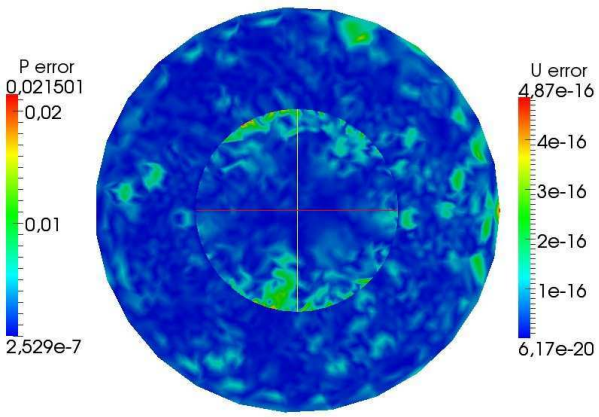

(c) Error between both solutions

Figure II.5.14 – Frequency $f_1 = 219$kHz using cubic polynomial elements, Mesh 3, and curved boundary edges. Figures (a)-(b): Pressure modulus and displacement amplitude fields. Figure (c): Absolute error between both solutions.

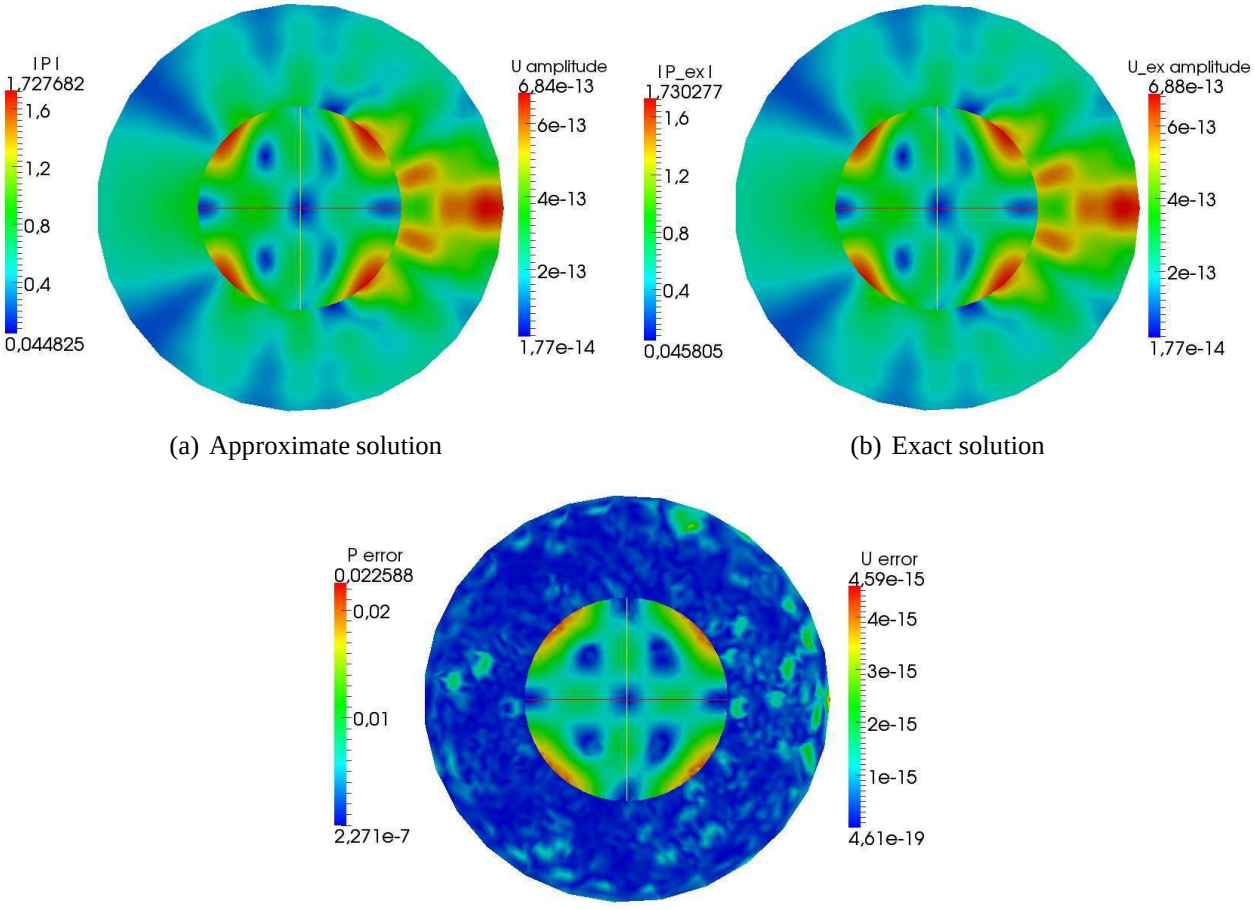

(a) Approximate solution

(b) Exact solution

(c) Error between both solutions

Figure II.5.15 – Frequency $f_R = 221$kHz using Mesh 3, cubic polynomial elements, and curved boundary edges. Figures (a)-(b): Pressure modulus and displacement amplitude fields. Figure (c): Absolute error between both solutions.

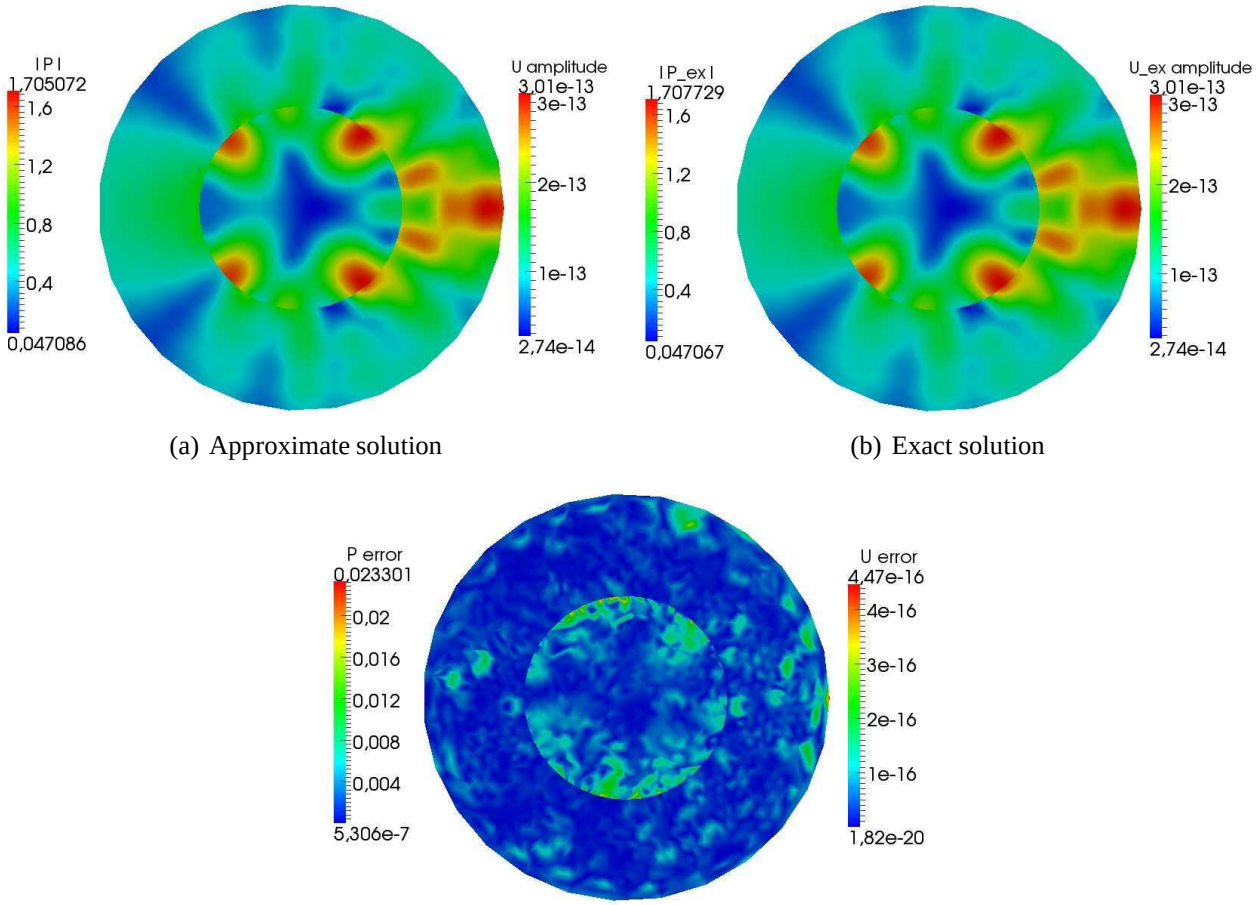

(a) Approximate solution

(b) Exact solution

(c) Error between both solutions

Figure II.5.16 – Frequency $f_2 = 223$kHz using Mesh 3, cubic polynomial elements, and curved boundary edges. Figures (a)-(b): Pressure modulus and displacement amplitude fields. Figure (c): Absolute error between both solutions.

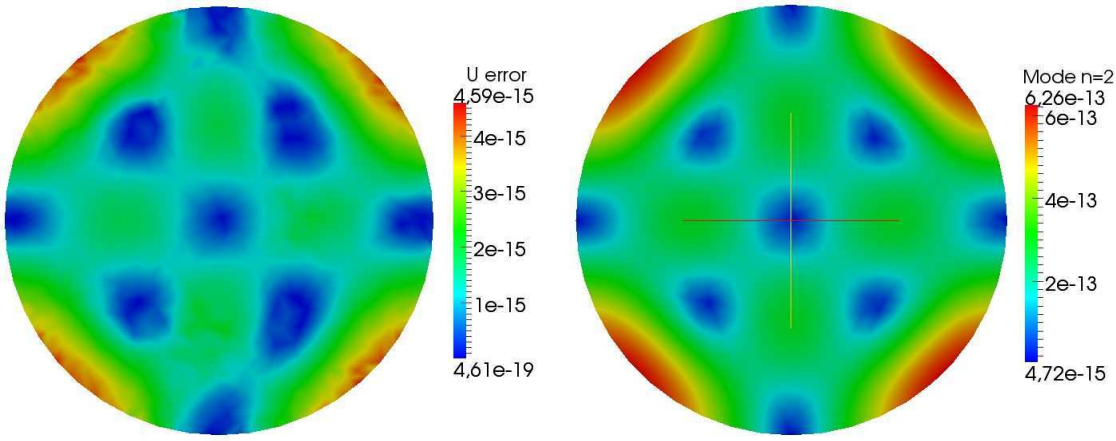

(a) Displacement error (b) Fourier mode $n = 2$

Figure II.5.17 – Comparison between the error in displacement and the third Fourier mode for the resonance frequency $f_{=}$221kHz on Mesh 3 with cubic polynomial elements and curved boundary edges.

- *Globally, we can consider that the results are better than those obtained using polygonal-shaped approximations even with a very fine mesh at the boundary (see Tables II.5.6-II.5.8), since Mesh 3 is clearly coarser than Mesh 2.*
- *When using cubic elements, we observe that employing curved edges on the fluid-solid interface only is sufficient to improve significantly the relative errors on the displacement field for the three frequencies. Indeed, the relative error on the scattered field remains below 1%, even for the resonance frequency.*
- *The use of curved boundary edges on the exterior boundary allows to halve the error associated to the pressure field, as clearly demonstrated previously in Table II.5.11.*

II.5.3 Sensitivity to the mesh refinement

The goal here is to investigate the dependence of the accuracy on the mesh refinement for a fixed frequency and to assess the effect of using curved boundary edges on the convergence of the method. The mesh refinement is performed as follows. The initial mesh is composed of 10 elements on the fluid-structure interface Γ, 20 elements on the exterior boundary Σ, and triangles with a maximum area of 2.10^{-5} m^2 in the domain $\Omega^s \cup \Omega^f$. Hence, this mesh provides about 1 element per wavelength when $ka = 10$. The results presented here are obtained when employing cubic polynomials and for four frequencies. The first three are in the resonance region: $f_1 = 219$ kHz, $f_R = 221$ kHz (the resonance frequency) and $f_2 = 223$ kHz. The fourth one $f_3 = 250$ kHz is considered to be far from the resonance region. These results illustrate the sensitivity to the mesh refinement of (a) the L^2-relative error on the scattered field (see Fig. II.5.21 and Fig. II.5.23), and absolute error (see Fig. II.5.22

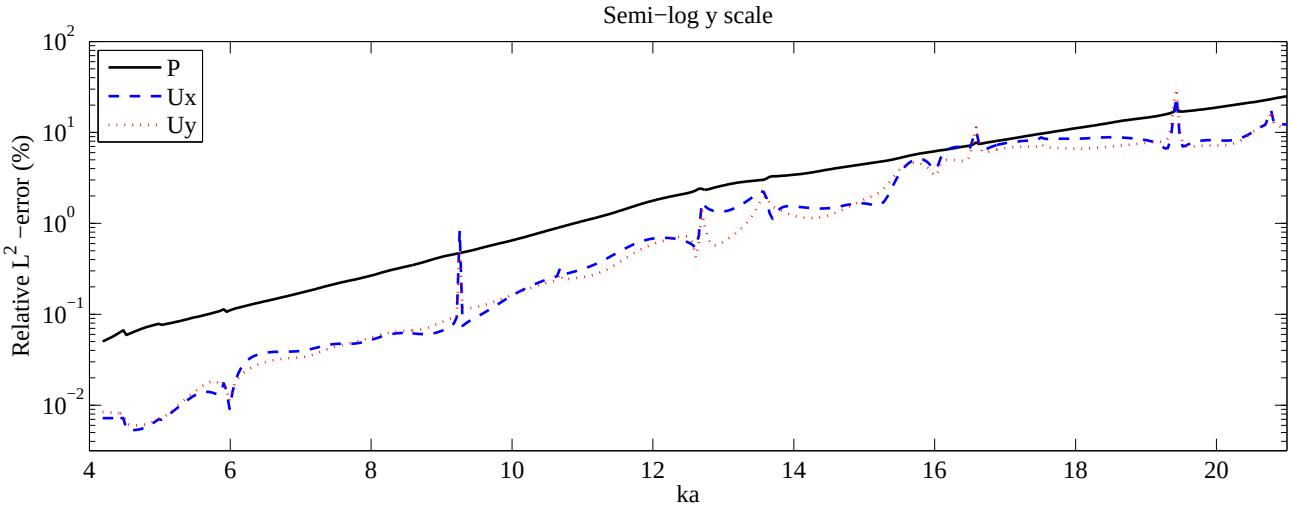

(a) Relative error

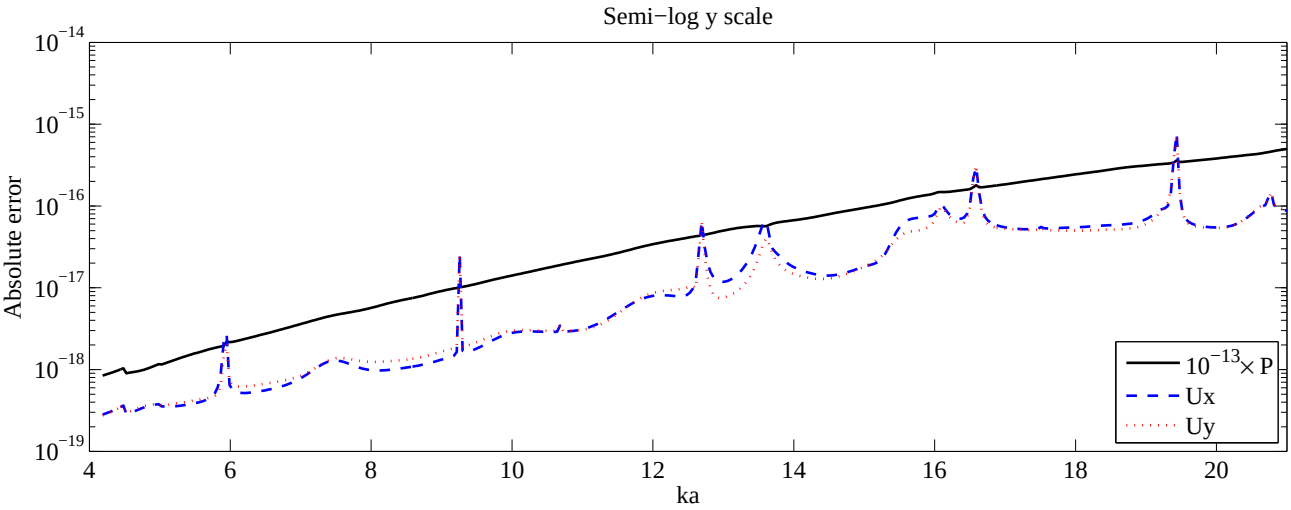

(b) Absolute error

Figure II.5.18 – Sensitivity of the L^2-relative error and of the absolute error to the wavenumber ka using Mesh 3, cubic polynomial elements and curved boundary edges.

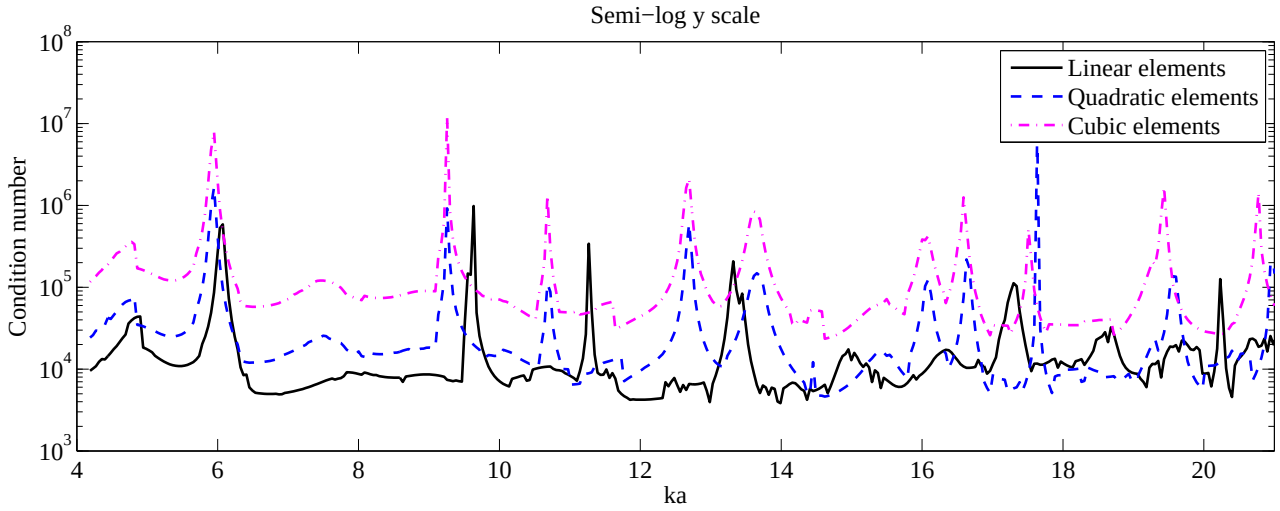

Figure II.5.19 – Sensitivity of the condition number to the wavenumber ka using Mesh 3, and curved boundary edges.

f (kHz)		p	u_x	u_y
219	L_∞-norm exact solution	1.679	1.931E-013	2.49E-013
	L_∞-norm approximate solution	1.988	1.862E-013	2.303E-013
	Absolute error	1.209E-002	6.195E-016	8.475E-016
	L^2-relative error (%)	72.436	34.537	44.867
221	L_∞-norm exact solution	1.671	4.621E-013	6.297E-013
	L_∞-norm approximate solution	1.980	1.837E-013	2.247E-013
	Absolute error	1.231E-002	3.158E-015	3.852E-015
	L^2-relative error (%)	73.769	108.271	83.545
223	L_∞-norm exact solution	1.648	2.461E-013	1.983E-013
	L_∞-norm approximate solution	1.971	1.804E-013	2.192E-013
	Absolute error	1.251E-002	9.447E-016	7.65E-016
	L^2-relative error (%)	75.533	48.171	49.02

Table II.5.12 – Error results for linear polynomial elements and curved elements on the transmission interface only.

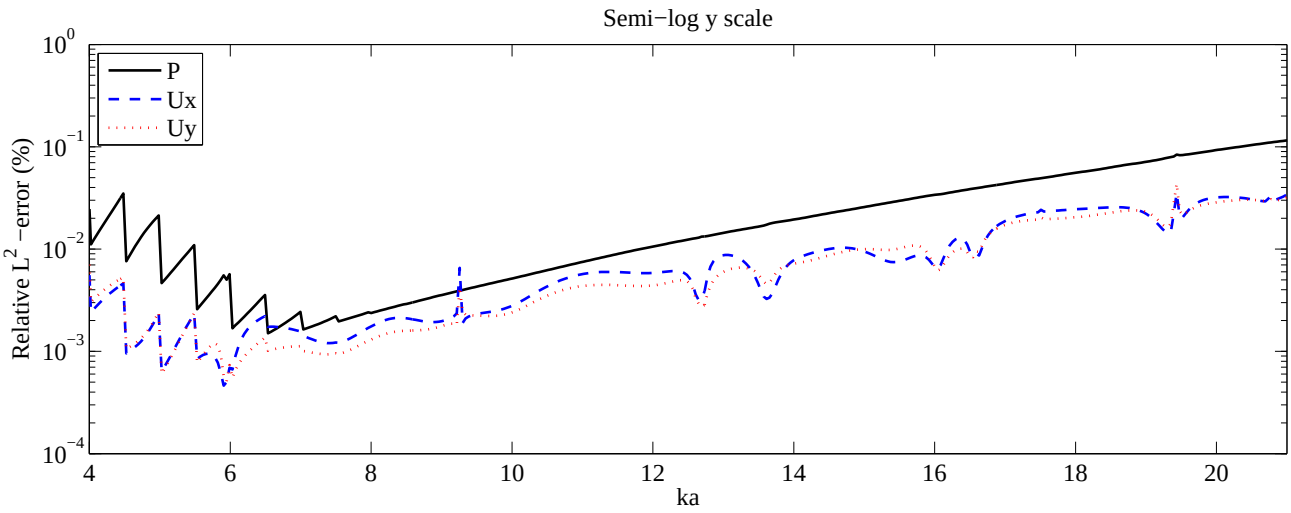

(a) Relative error

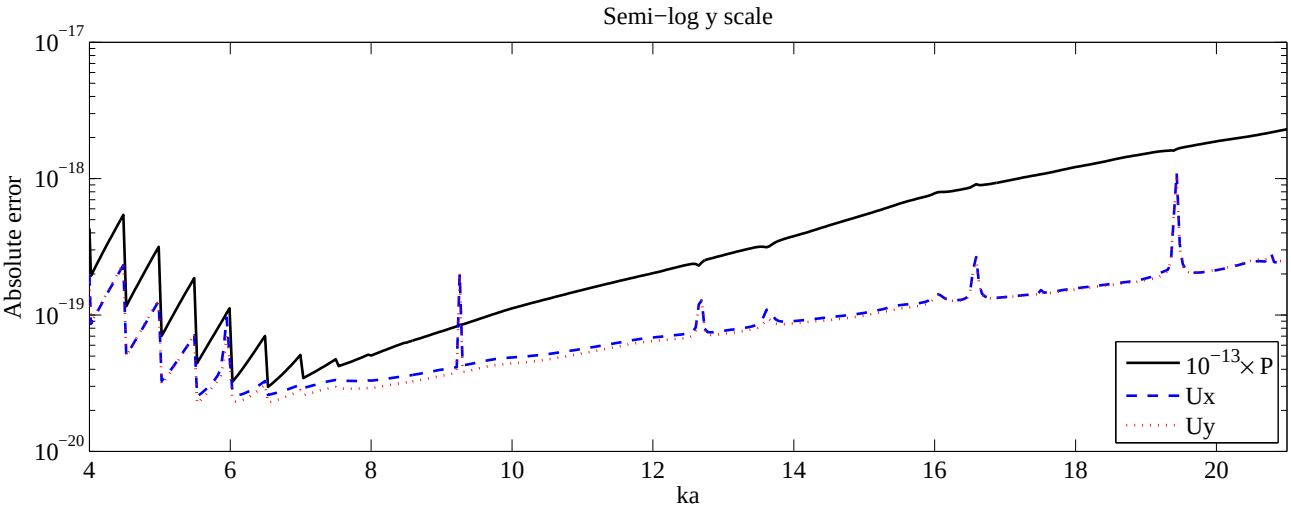

(b) Absolute error

Figure II.5.20 – Sensitivity of the L^2-relative error and of the absolute error to the wavenumber ka using Mesh 1, cubic polynomial elements, and curved boundary edges.

f (kHz)		p	u_x	u_y
219	L_∞-norm exact solution	1.743	1.979E-013	2.553E-013
	L_∞-norm approximate solution	1.761	1.953E-013	2.513E-013
	Absolute error	1.170E-003	2.377E-017	3.773E-017
	L^2-relative error (%)	5.551	1.273	1.887
221	L_∞-norm exact solution	1.736	4.621E-013	6.346E-013
	L_∞-norm approximate solution	1.751	2.788E-013	4.451E-013
	Absolute error	1.23E-003	1.575E-015	1.598E-015
	L^2-relative error (%)	5.811	51.238	32.863
223	L_∞-norm exact solution	1.714	2.461E-013	2.000E-013
	L_∞-norm approximate solution	1.734	2.453E-013	1.981E-013
	Absolute error	1.200E-003	2.687E-017	4.336E-017
	L^2-relative error (%)	5.692	1.308	2.591

Table II.5.13 – Error results for quadratic polynomial elements and curved elements on the transmission interface only.

f (kHz)		p	u_x	u_y
219	L_∞-norm exact solution	1.738	1.977E-013	2.554E-013
	L_∞-norm approximate solution	1.739	1.974E-013	2.557E-013
	Absolute error	2.068E-004	5.684E-018	5.955E-018
	L^2-relative error (%)	0.97	0.304	0.298
221	L_∞-norm exact solution	1.730	4.621E-013	6.353E-013
	L_∞-norm approximate solution	1.731	4.599E-013	6.323E-013
	Absolute error	2.061E-004	2.017E-017	2.373E-017
	L^2-relative error (%)	0.962	0.655	0.488
223	L_∞-norm exact solution	1.708	2.461E-013	2.012E-013
	L_∞-norm approximate solution	1.709	2.459E-013	2.013E-013
	Absolute error	2.059E-004	6.187E-018	6.06E-018
	L^2-relative error (%)	0.965	0.301	0.362

Table II.5.14 – Error results for cubic polynomial elements and curved elements on the transmission interface only.

and Fig. II.5.24), and (b) the condition number of the global system matrix given by Eq. (II.3.29) (see Fig. II.5.27 and Fig. II.5.28). Furthermore, since the sparsity of the global system matrix is a performance indicator that complements the total number of d.o.f., particularly when employing direct methods, as explained in [137], the results depicted in Fig. II.5.25 and Fig. II.5.26 are presented to shed light on this computational efficiency aspect of IPDG. Note that all the reported results are obtained with and without using curved boundary edges. These results clearly demonstrate that employing curved boundary edges improves significantly the performance of the proposed method for all considered frequencies. More specifically, we observe the following:

- In the absence of curved boundary edges, Figure II.5.21 suggests that the convergence order of the method is 2, except at the Jones frequency where it deteriorates to 3/2. On the other hand, there is a gain of two orders when using curved boundary edges, as indicated in Fig. II.5.23). In addition, this convergence order is preserved at the Jones frequency (see Fig. II.5.23(b)).
- A similar observation can be made about the sensitivity of the L^2-relative errors on the scattered field to the total number of nonzero entries of the global system matrix. Indeed, in the absence of curved boundary edges, Fig. II.5.25 suggests that this dependence is $\mathcal{O}(N^{-1})$ for all frequencies, except at the Jones frequency in which it deteriorates to $\mathcal{O}(N^{-3/4})$ (see Fig. II.5.25(b)). On the other hand, there is a one-order gain in the convergence rate when using curved boundary edges, as depicted in Fig. II.5.26. This gain is also preserved at the Jones frequency (see Fig. II.5.26(b)).
- The situation is also similar for the condition number. Fig. II.5.27 suggests that the condition number increases as $\mathcal{O}(h^{-2})$ for all frequencies, except at the resonance frequency, where we notice a dramatic deterioration to $\mathcal{O}(h^{-7/2})$ (see Fig. II.5.27(b)). However, the use of curved boundary edges prevents the deterioration of the condition number for all frequencies, as depicted in Fig. II.5.28.

Before concluding this paragraph, we must point out that we were not able to compare the performance of the proposed method with UWVF since there are no similar results reported in [88], except to some extent the result reported in Fig.3 p.176. Indeed, the result depicted in this figure describes the convergence of UWVF with respect to N for the frequency f_3. However, this dependence is performed when increasing the number of plane waves and not refining the mesh. Recall that the results presented in this paragraph were obtained for a fixed order of elements: cubic polynomial functions.

Remark II.5.3.1 *Further to Remark II.5.2.1, let us observe the results that are obtained with the use of curved boundary edges at the transmission interface only in Figures II.5.29 to II.5.32. In the absence of curved boundary edges on the exterior boundary, the gain is not as significant as in*

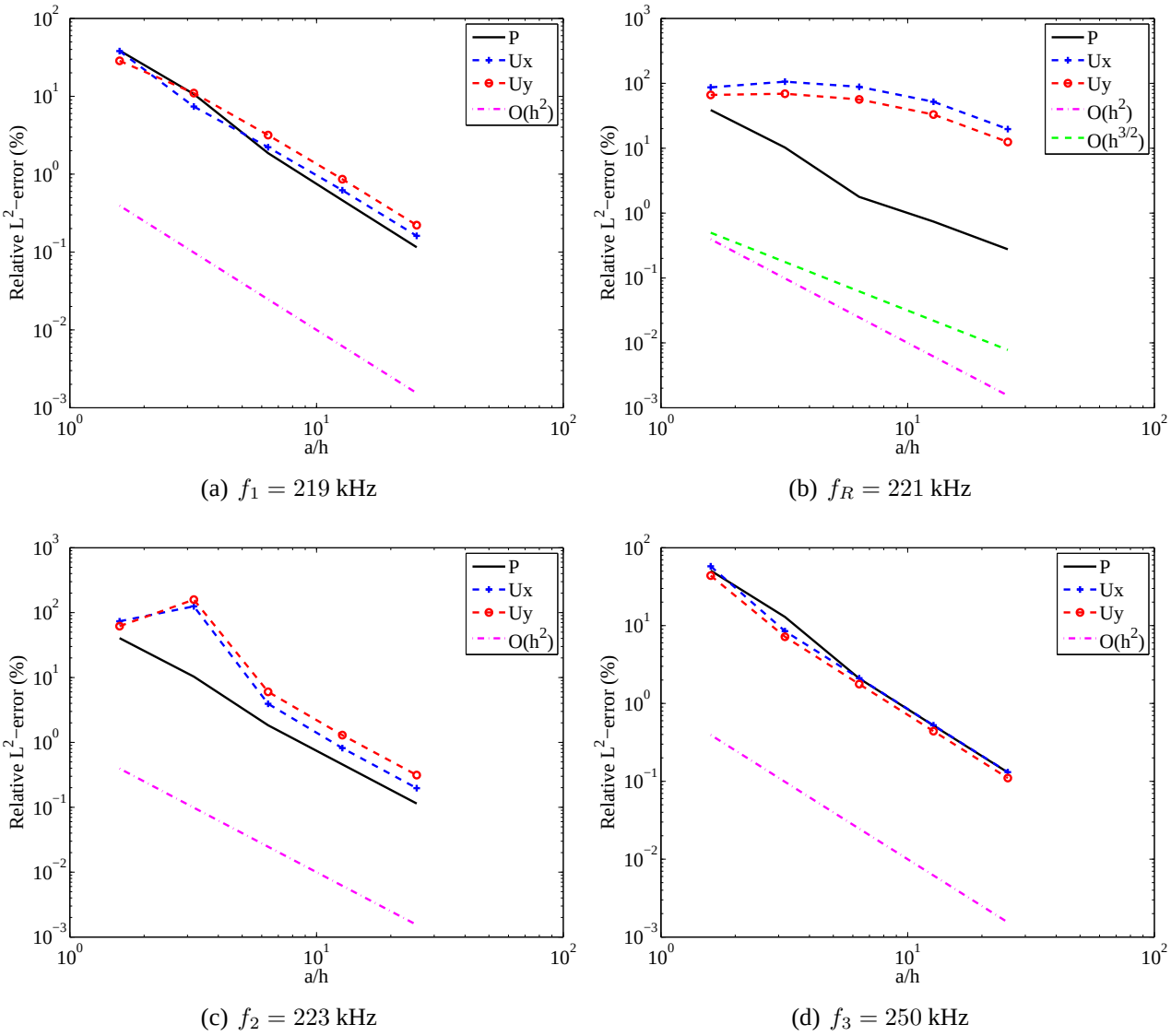

(a) $f_1 = 219$ kHz

(b) $f_R = 221$ kHz

(c) $f_2 = 223$ kHz

(d) $f_3 = 250$ kHz

Figure II.5.21 – Sensitivity of the relative error to the mesh resolution using cubic polynomial finite elements and no curved boundary edges.

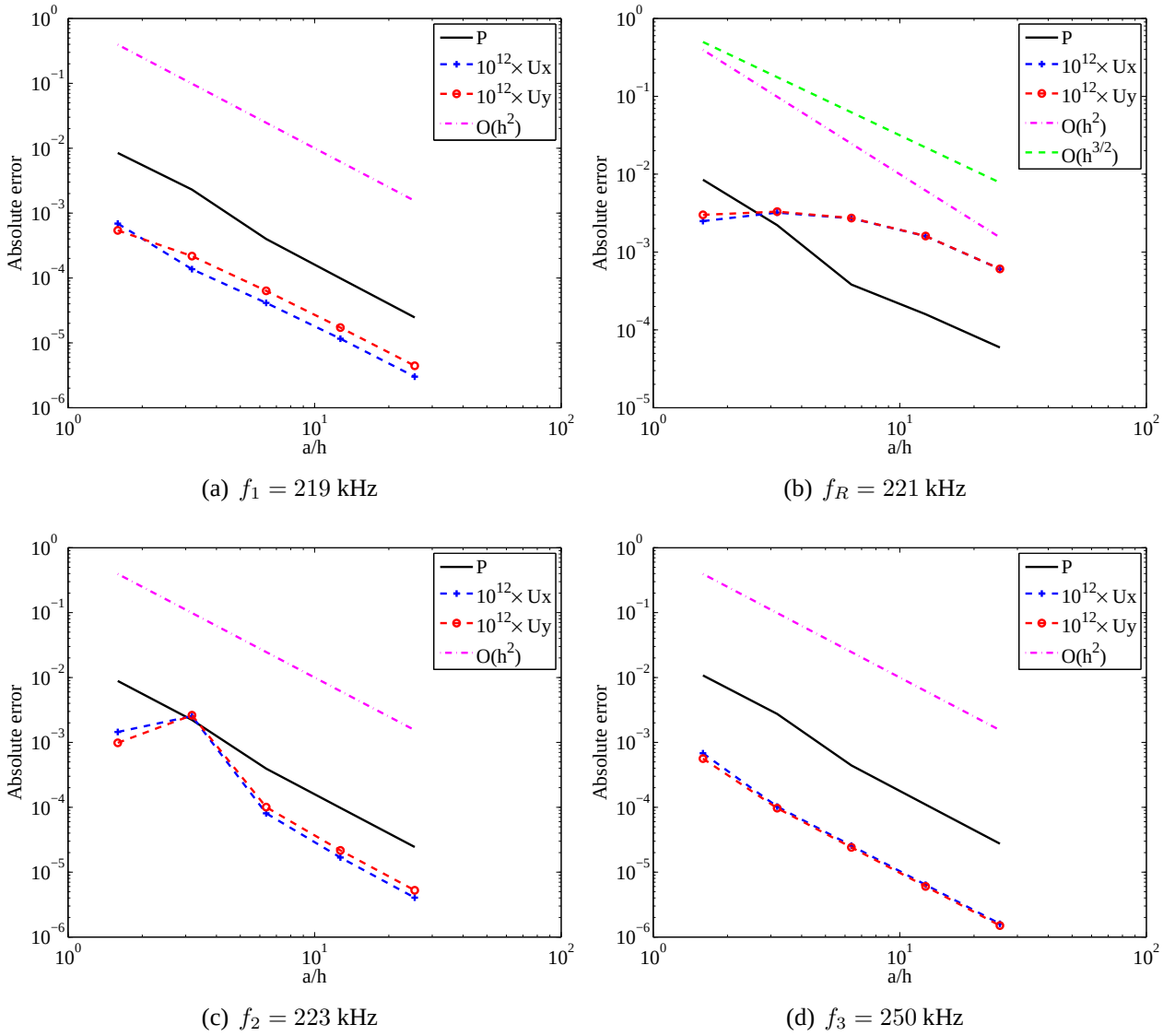

(a) $f_1 = 219$ kHz

(b) $f_R = 221$ kHz

(c) $f_2 = 223$ kHz

(d) $f_3 = 250$ kHz

Figure II.5.22 – Sensitivity of the absolute error to the mesh resolution using cubic polynomial finite elements and no curved boundary edges.

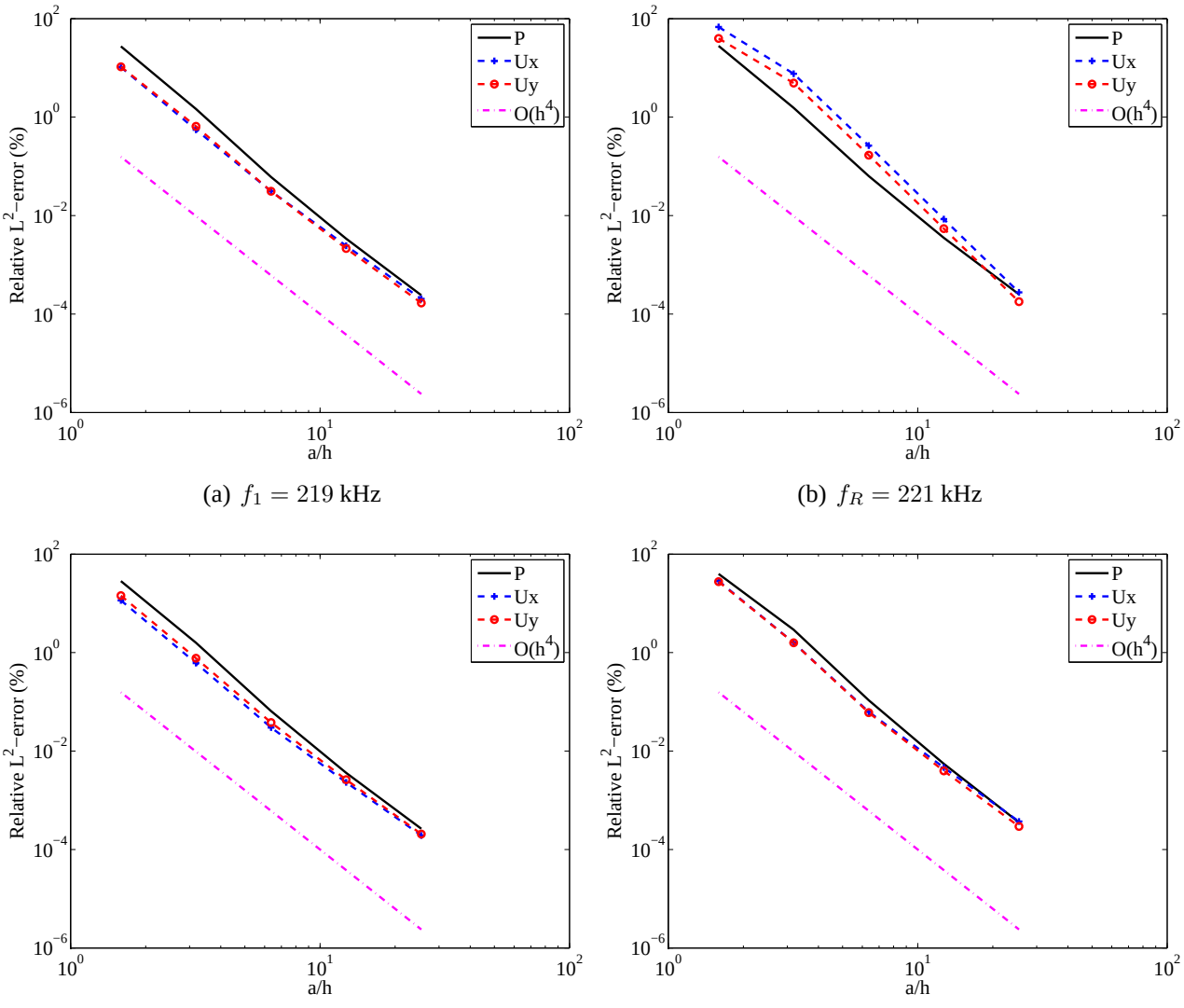

(a) $f_1 = 219$ kHz

(b) $f_R = 221$ kHz

(c) $f_2 = 223$ kHz

(d) $f_3 = 250$ kHz

Figure II.5.23 – Sensitivity of the relative error to the mesh resolution using cubic polynomial finite elements and curved boundary edges.

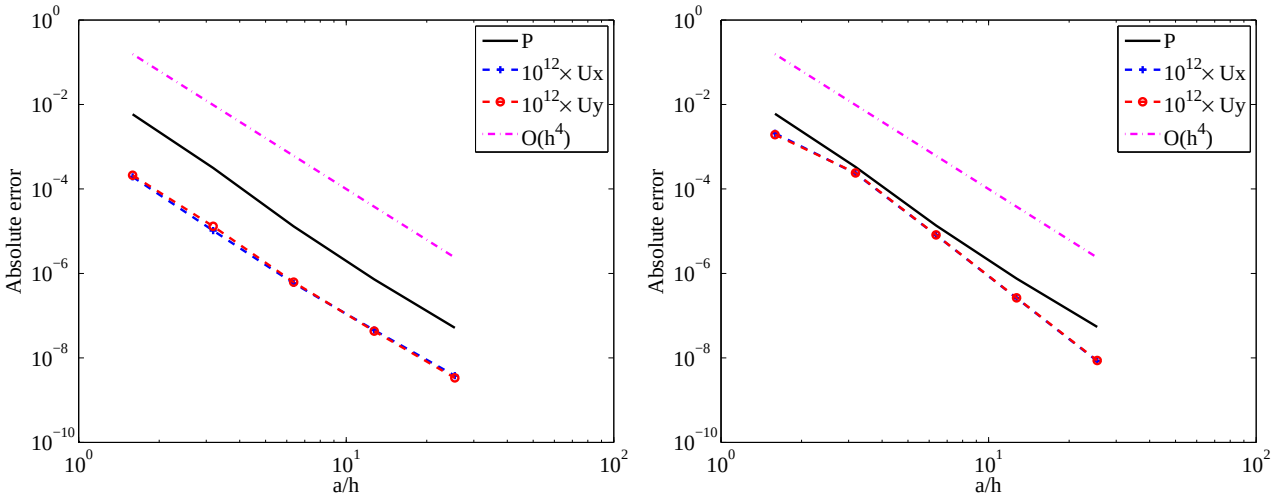

(a) $f_1 = 219$ kHz

(b) $f_R = 221$ kHz

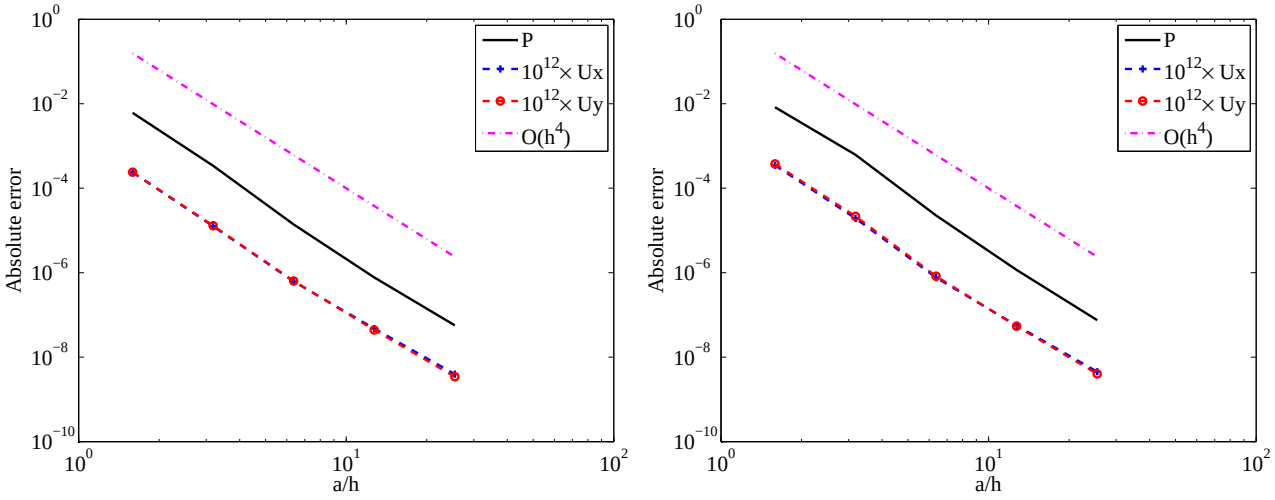

(c) $f_2 = 223$ kHz

(d) $f_3 = 250$ kHz

Figure II.5.24 – Sensitivity of the absolute error to the mesh resolution using cubic polynomial finite elements and curved boundary edges.

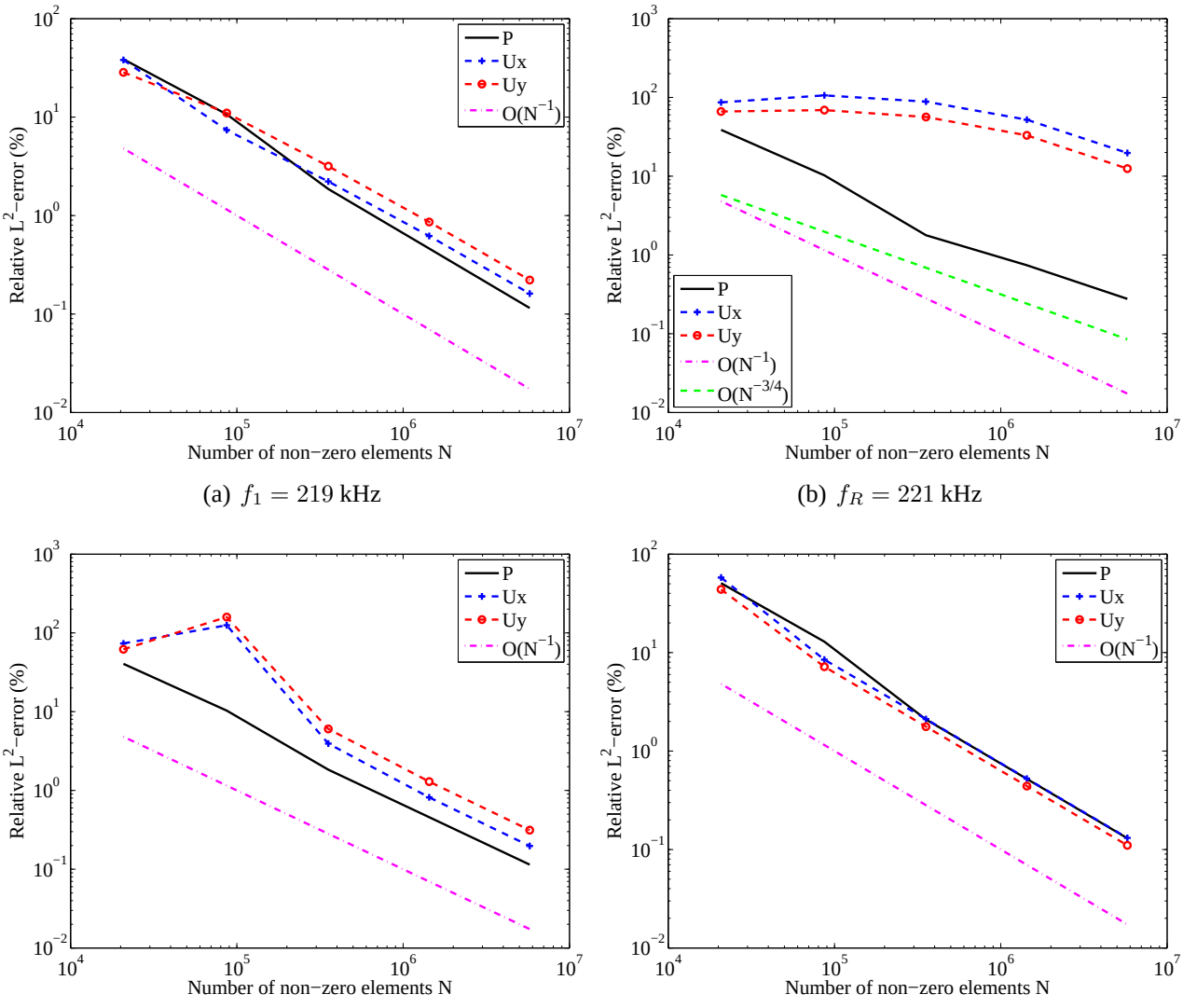

(a) $f_1 = 219$ kHz

(b) $f_R = 221$ kHz

(c) $f_2 = 223$ kHz

(d) $f_3 = 250$ kHz

Figure II.5.25 – Convergence of the relative error as a function of the number N of nonzero entries in the IPDG system matrix using cubic polynomial finite elements and no curved boundary edges.

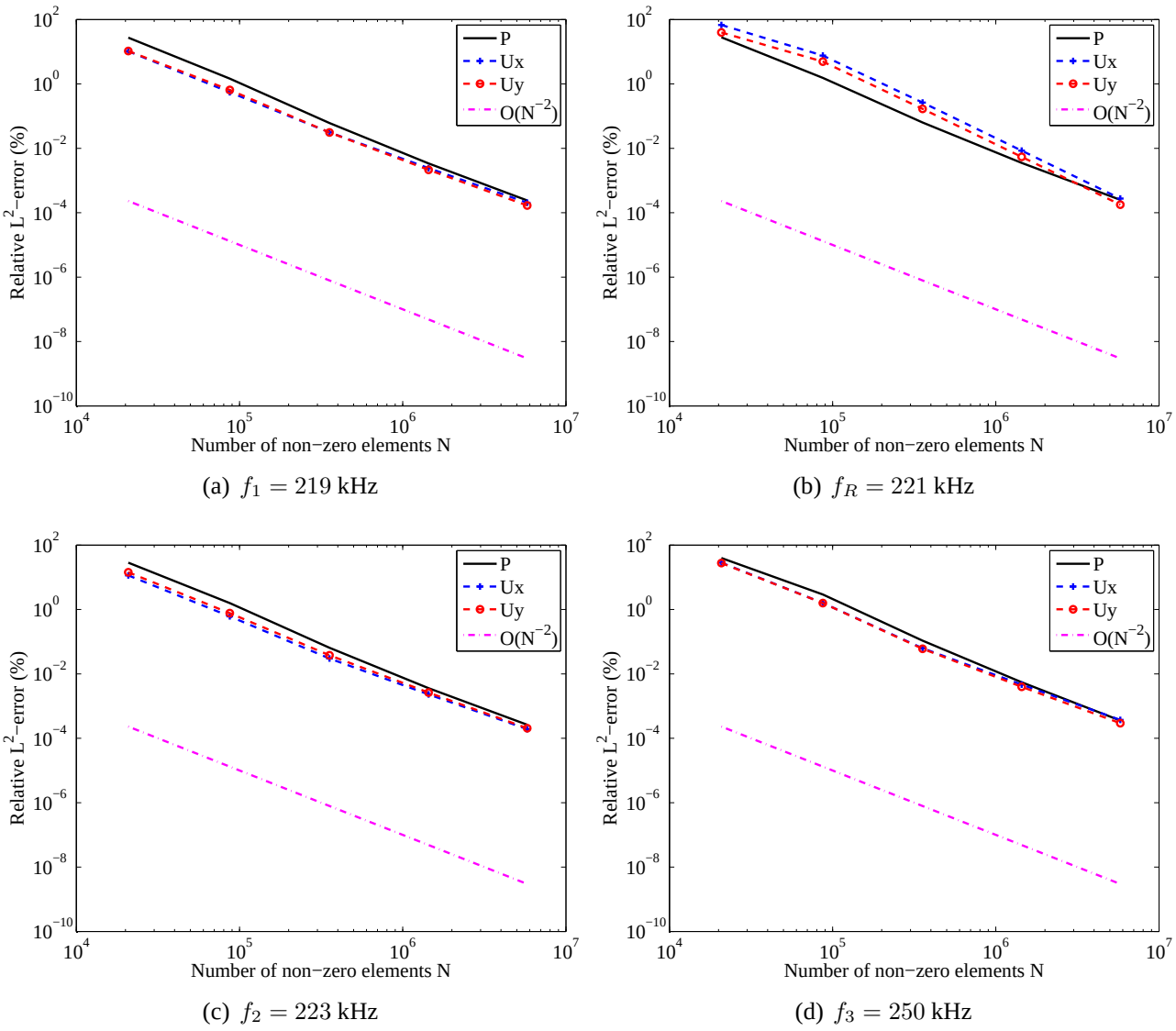

(a) $f_1 = 219$ kHz (b) $f_R = 221$ kHz

(c) $f_2 = 223$ kHz (d) $f_3 = 250$ kHz

Figure II.5.26 – Convergence of the relative error as a function of the number N of nonzero entries in the IPDG system matrix using cubic polynomial finite elements and curved boundary edges.

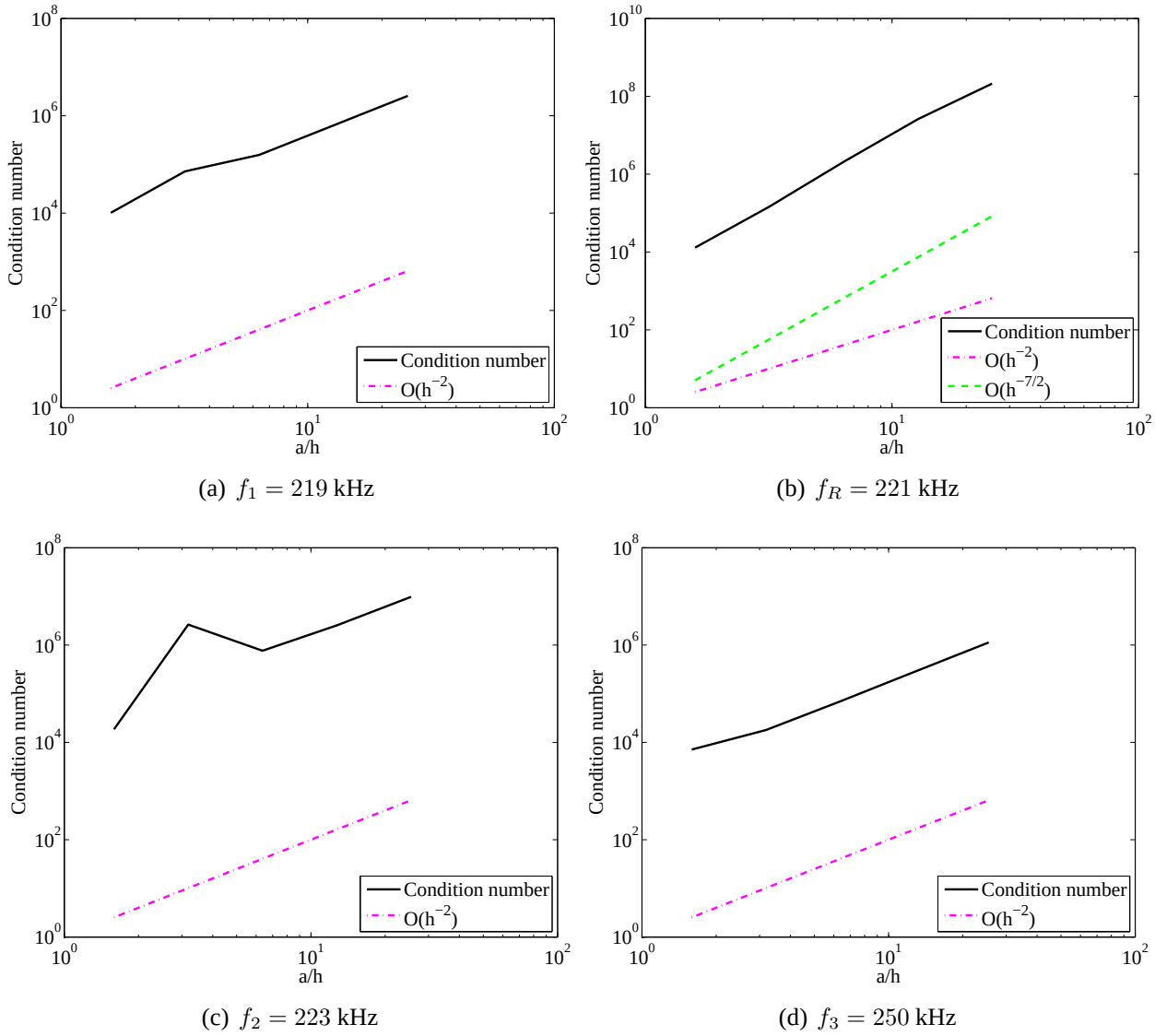

(a) $f_1 = 219$ kHz (b) $f_R = 221$ kHz

(c) $f_2 = 223$ kHz (d) $f_3 = 250$ kHz

Figure II.5.27 – Sensitivity of the condition number to the mesh resolution using cubic polynomial finite elements and no curved boundary edges.

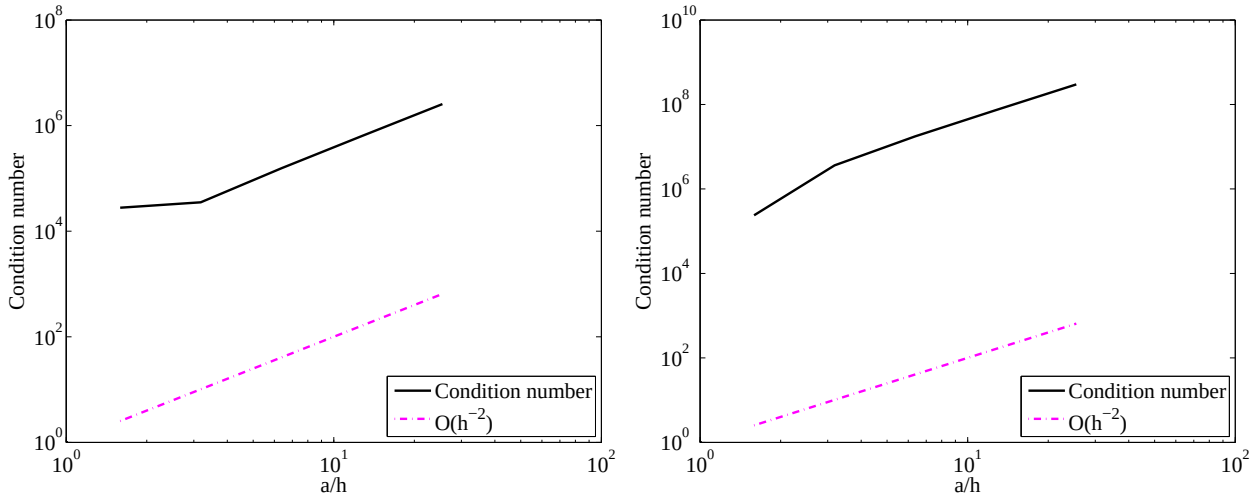

(a) $f_1 = 219$ kHz (b) $f_R = 221$ kHz

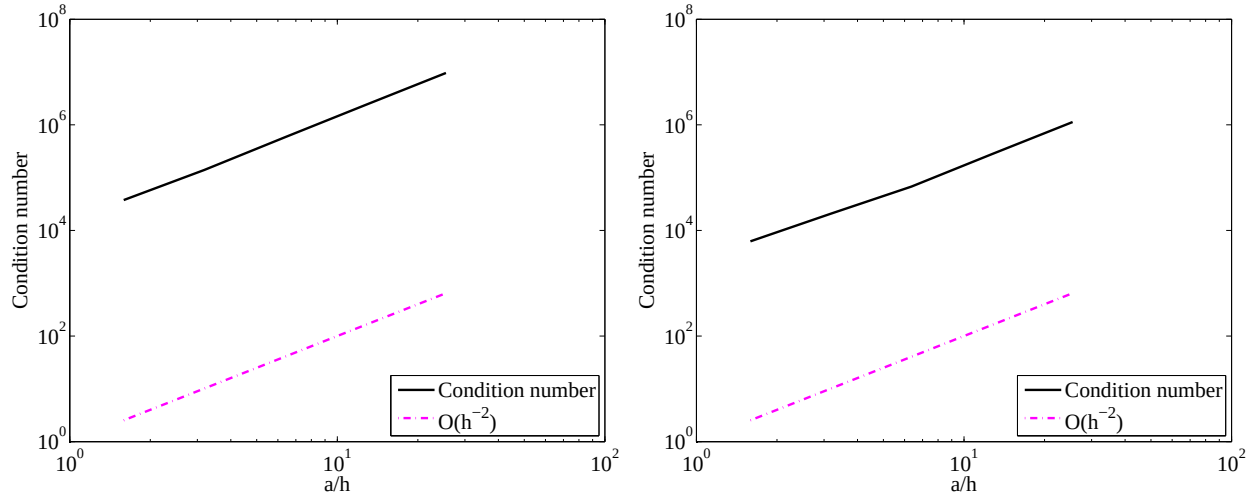

(c) $f_2 = 223$ kHz (d) $f_3 = 250$ kHz

Figure II.5.28 – Sensitivity of the condition number to the mesh resolution using cubic polynomial finite elements and curved boundary edges.

Figs. II.5.23, the convergence order of the method when using curved boundary edges at the wet surface is still 2. Nevertheless, we observe that, unlike polygonal-shaped approximations in Figs. II.5.21, this convergence order is preserved at the Jones frequency. A similar observation can be made about the sensitivity of the L^2-relative errors on the scattered field to the total number of nonzero entries (see Fig. II.5.31), and for the condition number, that does not deteriorate at the Jones frequency (see Fig. II.5.32).

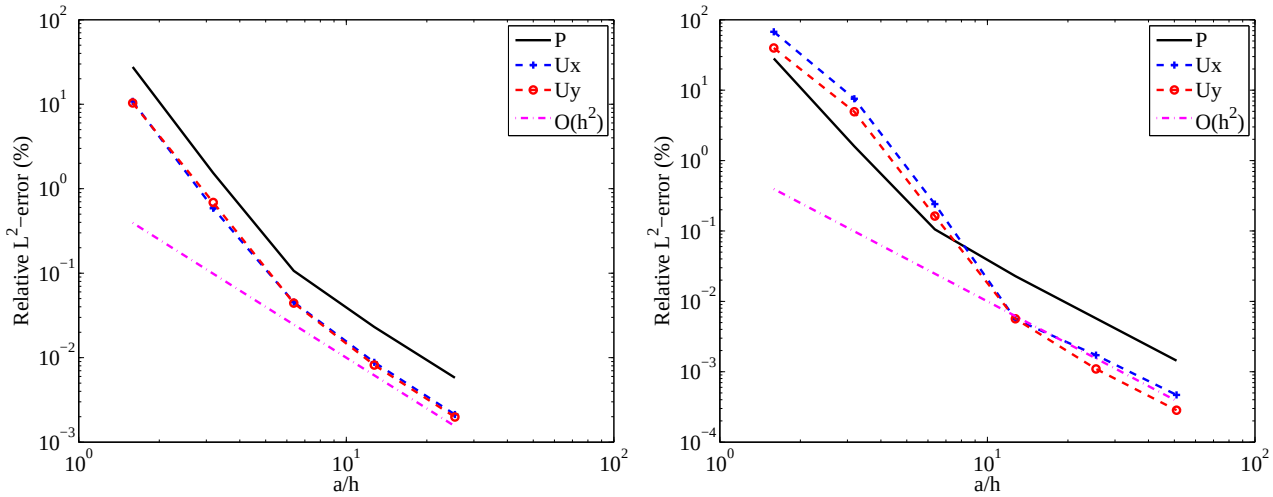

(a) $f_1 = 219$ kHz (b) $f_R = 221$ kHz

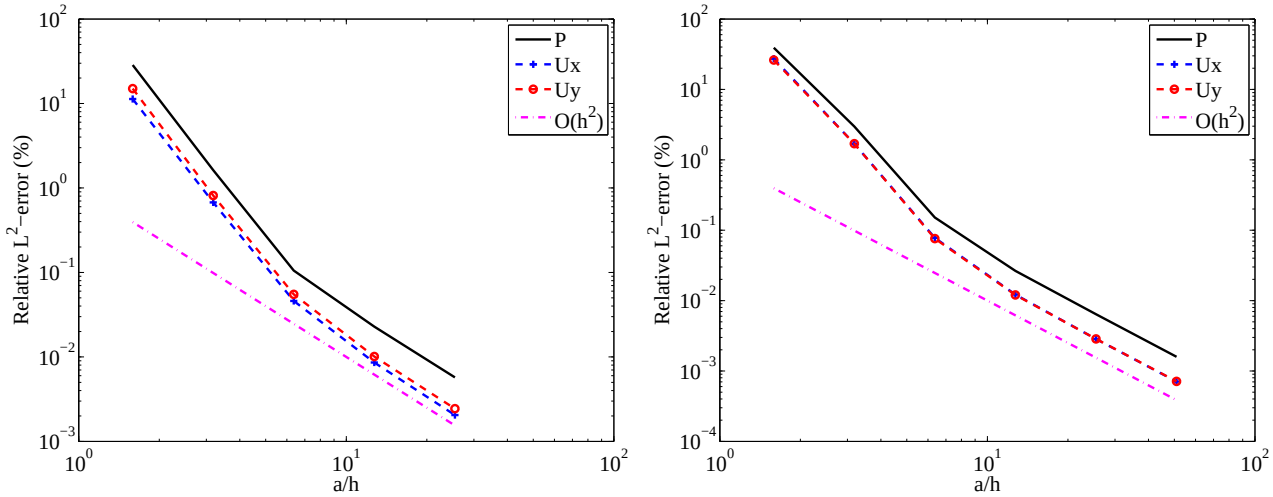

(c) $f_2 = 223$ kHz (d) $f_3 = 250$ kHz

Figure II.5.29 – Sensitivity of the relative error to the mesh resolution using cubic polynomial finite elements and curved boundary edges on the fluid-solid interface only.

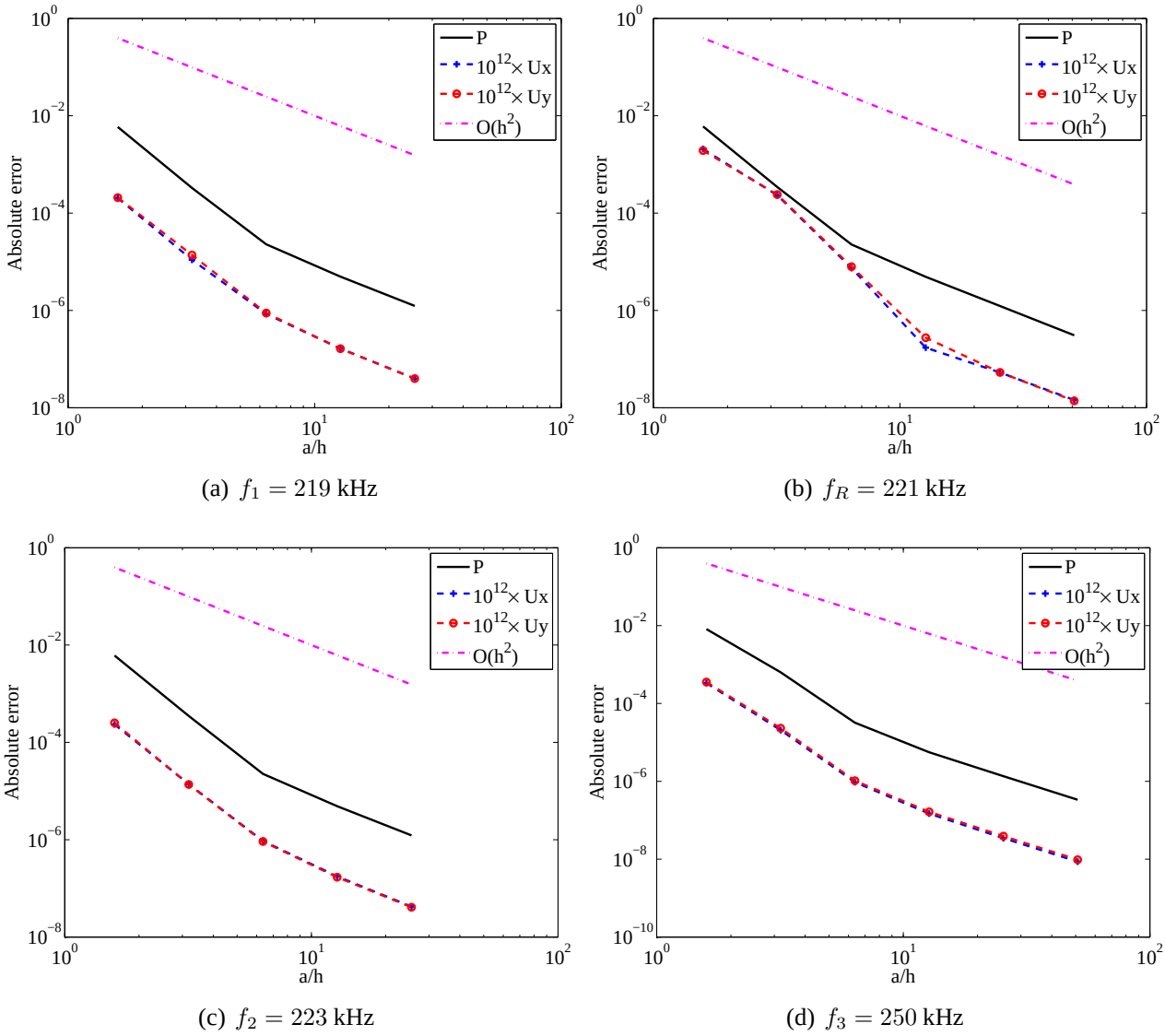

(a) $f_1 = 219$ kHz

(b) $f_R = 221$ kHz

(c) $f_2 = 223$ kHz

(d) $f_3 = 250$ kHz

Figure II.5.30 – Sensitivity of the absolute error to the mesh resolution using cubic polynomial finite elements and curved boundary edges on the fluid-solid interface only.

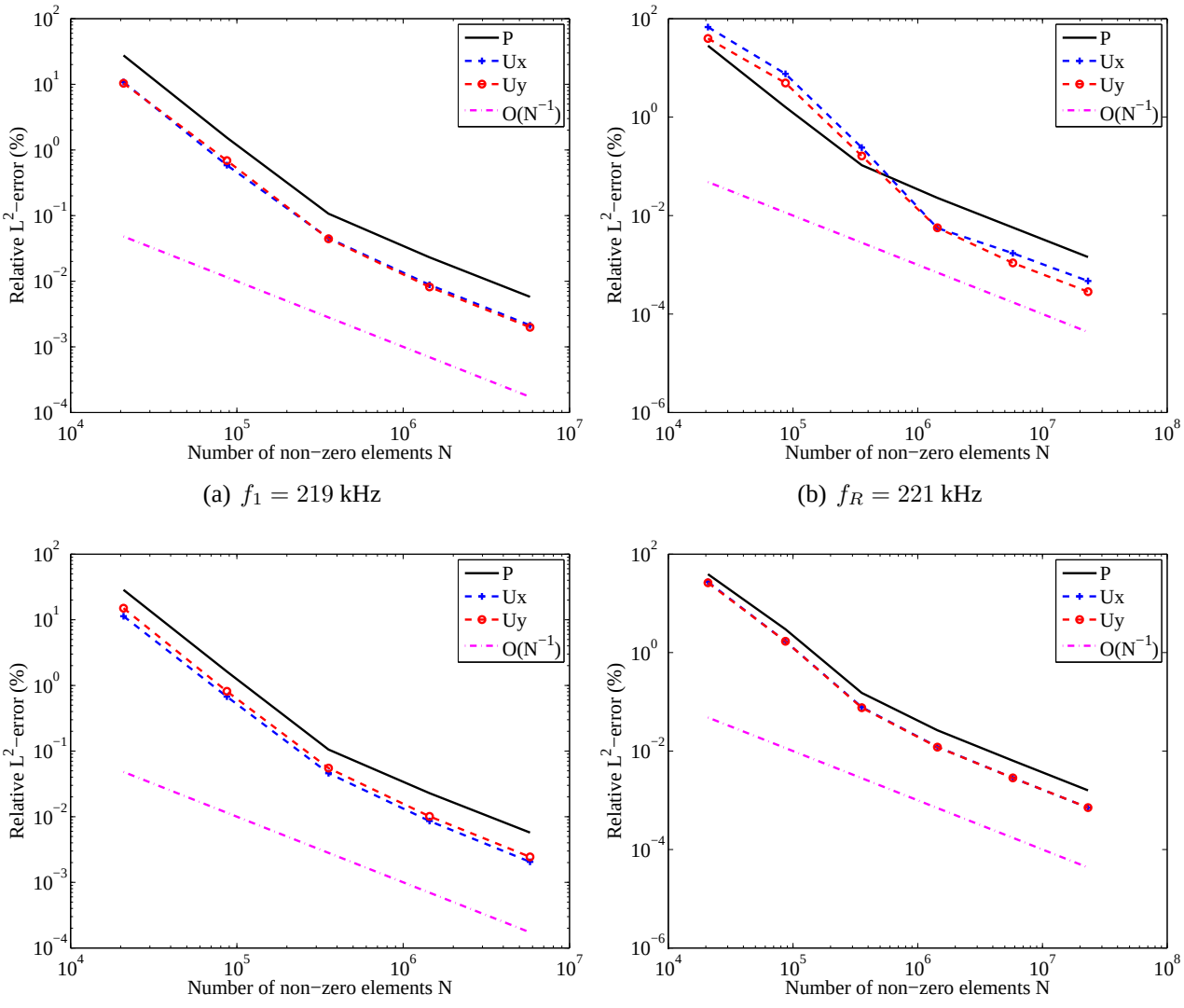

(a) $f_1 = 219$ kHz

(b) $f_R = 221$ kHz

(c) $f_2 = 223$ kHz

(d) $f_3 = 250$ kHz

Figure II.5.31 – Convergence of the relative error as a function of the number N of nonzero entries in the IPDG system matrix using cubic polynomial finite elements and curved boundary edges on the fluid-solid interface only.

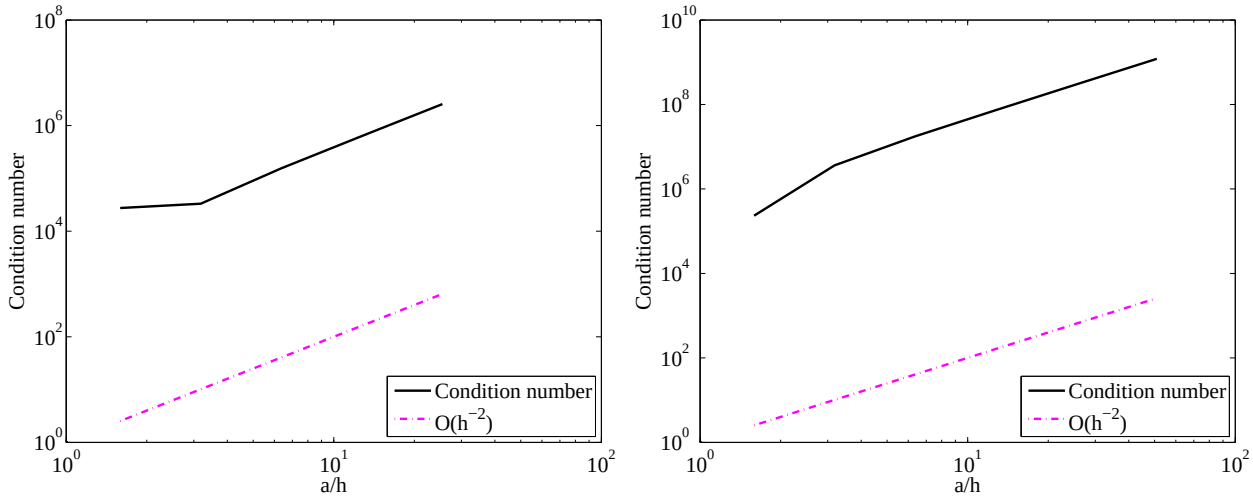

(a) $f_1 = 219$ kHz (b) $f_R = 221$ kHz

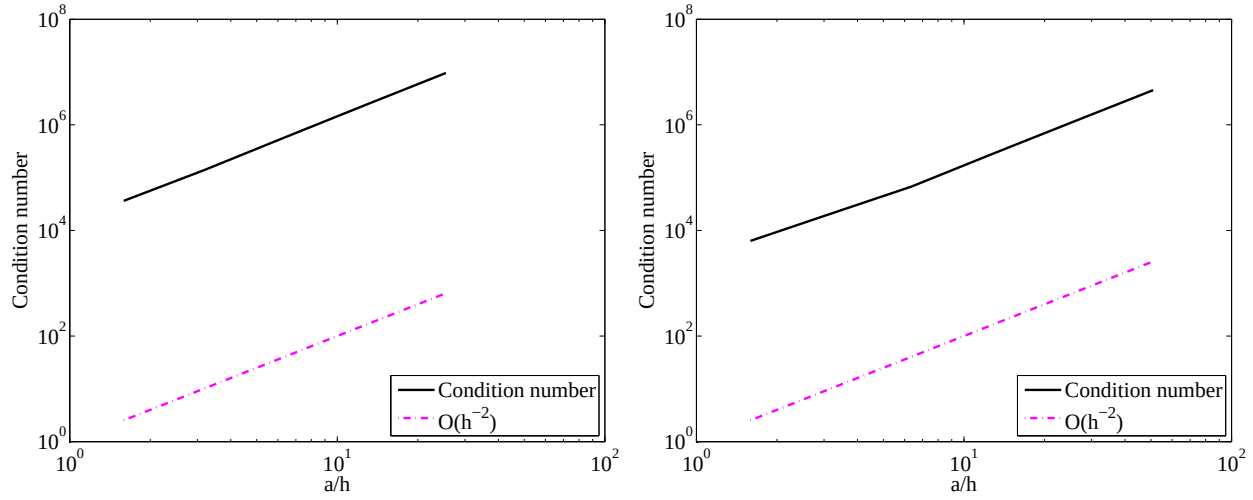

(c) $f_2 = 223$ kHz (d) $f_3 = 250$ kHz

Figure II.5.32 – Sensitivity of the condition number to the mesh resolution using cubic polynomial finite elements and curved boundary edges on the fluid-solid interface only.

II.5.4 Sensitivity to the frequency

The goal of this section is twofold: (i) to determine practical guidelines for achieving a prescribed accuracy level, and (ii) to examine and to assess the pollution effect. To this end, we have investigated the numerical behavior of the L^2-relative error over the computational domain on the elasto-acoustic scattered field as the frequency increases. Two sets of experiments have been performed. In the first set, the mesh is fixed, that is, the resolution degrades as the frequency increases. In the second set, the resolution is maintained fixed, that is, the mesh is refined as the frequency increases. All these experiments are performed with IPDG equipped with curved boundary edges and employing cubic polynomial functions. For illustration purposes, we present a sample of results obtained in the mid- to high-frequency regimes ($10 \leq ka \leq 300$) using four different meshes.

The results depicted in Figures II.5.33 and II.5.34 are obtained using Mesh 1 (see Figure II.5.2 and Table II.5.2) in the frequency band $10 \leq ka \leq 50$ corresponding to 238 kHz $\leq f \leq 1193$ kHz. Hence, the resolution degrades from 8 elements per wavelength to about 1.6 elements per wavelength. The resulting linear system given by Eq. (II.3.29) possesses 80,440 unknowns and 1,667,068 nonzero entries. As stated earlier, we solve this system using an LU factorization. The following observations are noteworthy:

- As anticipated, Fig. II.5.33(a) indicates that the relative error deteriorates as the frequency increases, that is, the resolution degrades. However, Fig. II.5.33(a) also reveals that IPDG delivers an accuracy level of about 1% (resp. 5 %) on the fluid pressure with a resolution of about 2.6 elements per wavelength (resp. 2 elements per wavelength), which corresponds to a frequency $ka \simeq 32$ or $f \simeq 752$ kHz (resp. $ka \simeq 41$, $f \simeq 978$ kHz).
- The error curve corresponding to the fluid pressure (see the solid curve in Fig. II.5.33(a)) is smooth, as already observed in Figure II.5.18, and no peaks corresponding to spurious resonance frequencies are present. Again, as stated earlier, this is a direct effect of using curved boundary edges.
- The error on the fluid pressure is higher than the ones on the structural displacement, except at some resonance frequencies. This is expected since the resolution in the fluid is coarser than the one in the elastic medium.
- The Jones frequencies are clearly located in the structural displacement error curves by the presence of the peaks (see Fig. II.5.33). Observe that the location of these peaks coincides with the ones in the condition number curve (see Fig. II.5.34). We must point out that these peaks are clearly discernible because these results have been computed with a frequency step size of 1 kHz.

- The condition number remains below 10^8 in the considered frequency band $10 \leq ka \leq 50$, that is, 238 kHz $\leq f \leq 1193$ kHz.
- Observe that the location of the peaks in Fig. II.5.33 coincides with the minimum values of the three determinants in Figs. II.5.37-II.5.38, which correspond to the physically relevant Jones frequencies. This suggests that the method does not suffer from numerical resonance in the mid-frequency regime.

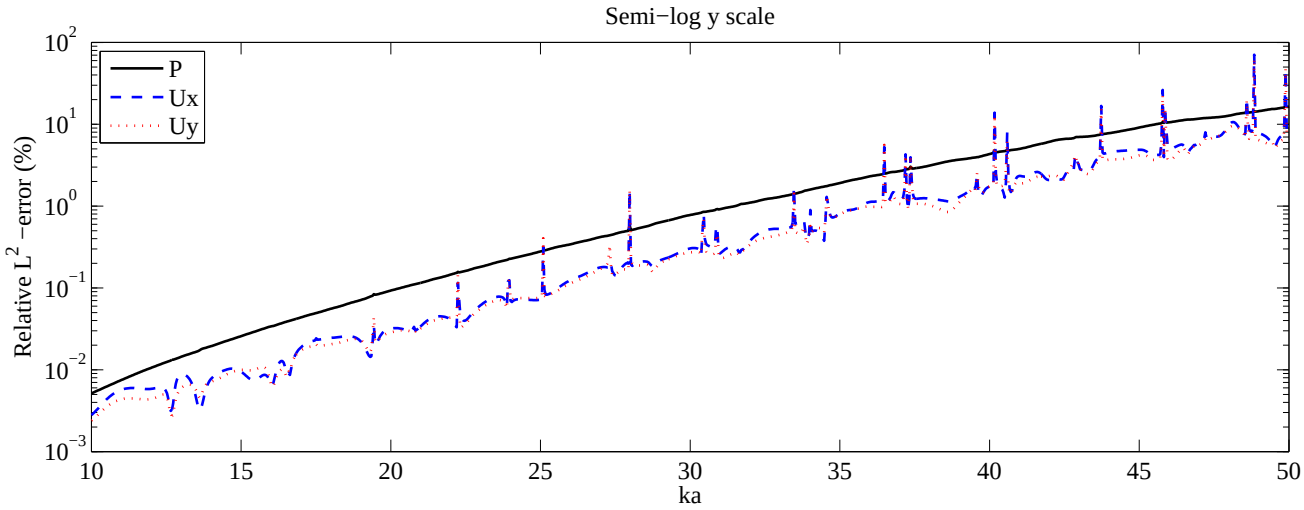

(a) Relative error

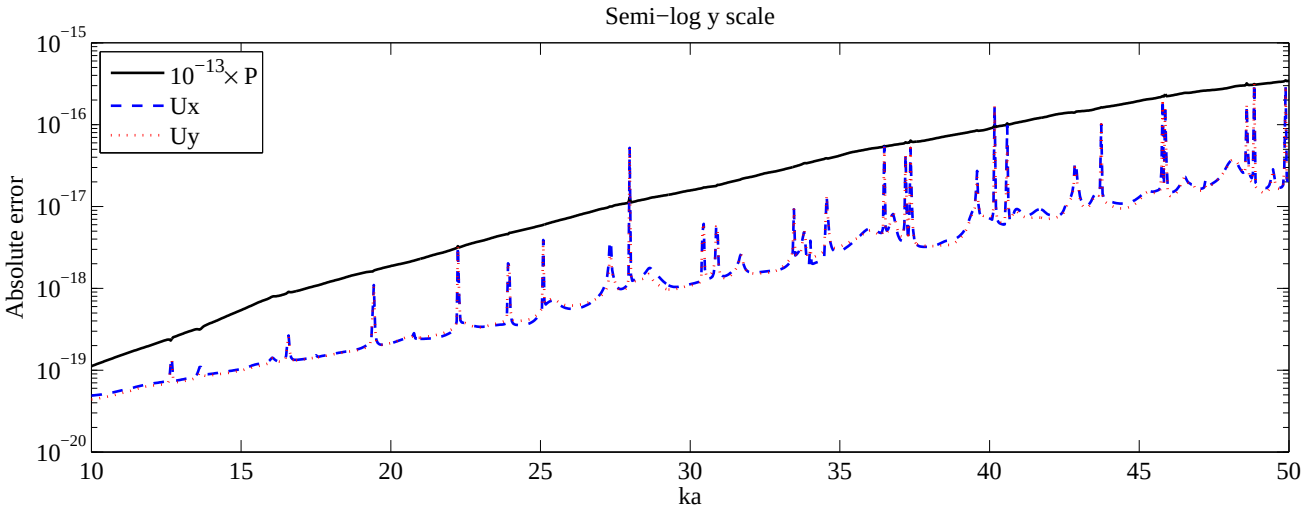

(b) Absolute error

Figure II.5.33 – Sensitivity of the L^2-relative error and absolute error to the frequency ka in the interval $[10, 50]$ when using cubic polynomial finite elements, curved boundary edges, and Mesh 1.

Next, we refine Mesh 1 (see Figure II.5.2 and Table II.5.2) by halving the triangle edges. Hence,

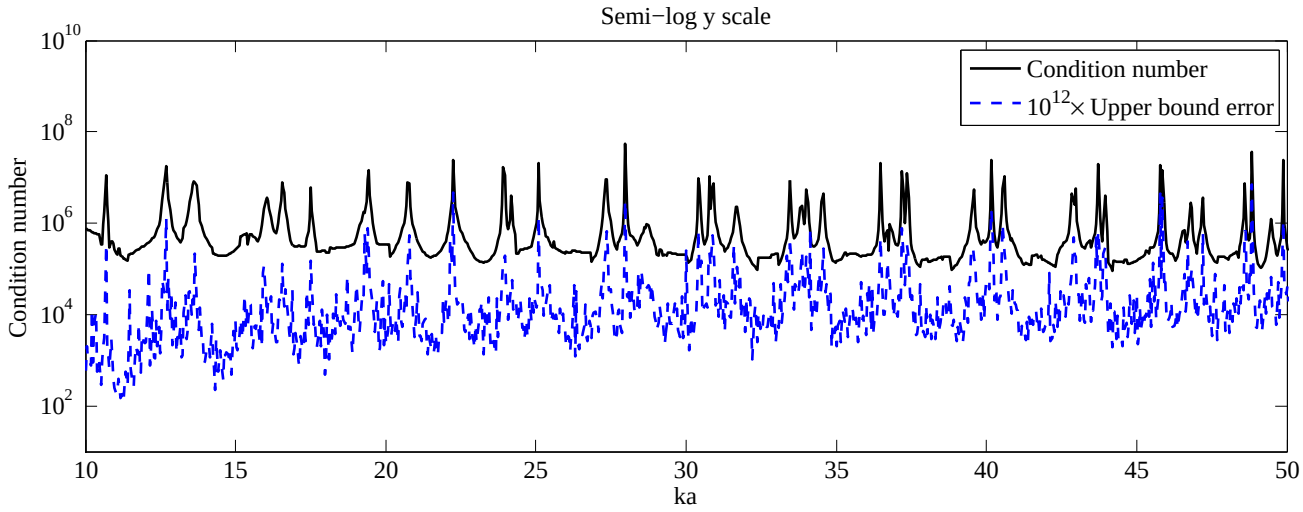

Figure II.5.34 – Sensitivity of the condition number to the frequency ka in the interval $[10, 50]$ when using cubic polynomial finite elements, curved boundary edges, and Mesh 1.

the resulting mesh contains exactly four times more triangles than Mesh 1, and the resulting linear system given by Eq. (II.3.29) possesses 321,760 unknowns and 6,698,992 nonzero entries. We investigate the effect of this mesh refinement for higher frequencies, up to $ka = 100$, corresponding to $f = 2387$ kHz. The results are depicted in Figs. II.5.35 and II.5.36. They indicate the following:

- The relative error remains below 1% (resp. 5 %) up to $ka \simeq 58$ (resp. $ka = 74$) corresponding to a resolution of about 2.8 elements per wavelength (resp. 2.2 elements per wavelength).
- The condition number seems to not suffer from the mesh refinement and remains, as previously, below 10^8 (see Fig. II.5.36).
- Note that the peaks corresponding to the Jones frequencies are again clearly observable in Fig. II.5.35. These results were computed with a frequency step size of 1 kHz.

The next results (see Fig. II.5.39 to Fig. II.5.42) were obtained with a mesh generated from Mesh 1 by halving the triangle edges two times successively. Hence, the resulting mesh contains exactly 16 times more triangles than Mesh 1, and therefore, the linear system given by Eq. (II.3.29) possesses 1,287,040 unknowns and 26,857,408 nonzero entries. The results depicted in Figs. II.5.39 and Fig. II.5.40 are obtained in a frequency band expanded to $ka = 200$ ($f = 4774$ kHz) and computed with a frequency step size of 1 kHz. Figs. II.5.41 and II.5.42 provides a zoom of the behavior in the frequency band $120 \leq ka \leq 140$. Similarly to the previous two results, we observe that the relative error on p remains below 1% (resp. 5 %) with only 3.1 elements per wavelength (resp. 2.4 elements per wavelength) for $ka \leq 105$ (resp. $ka \leq 134$). In addition, the condition number remains stable and always below 10^8 (see Fig. II.5.40) Note that the peaks corresponding to the Jones frequencies are again clearly visible in Fig.II.5.39. This is a consequence of computing these results with a frequency

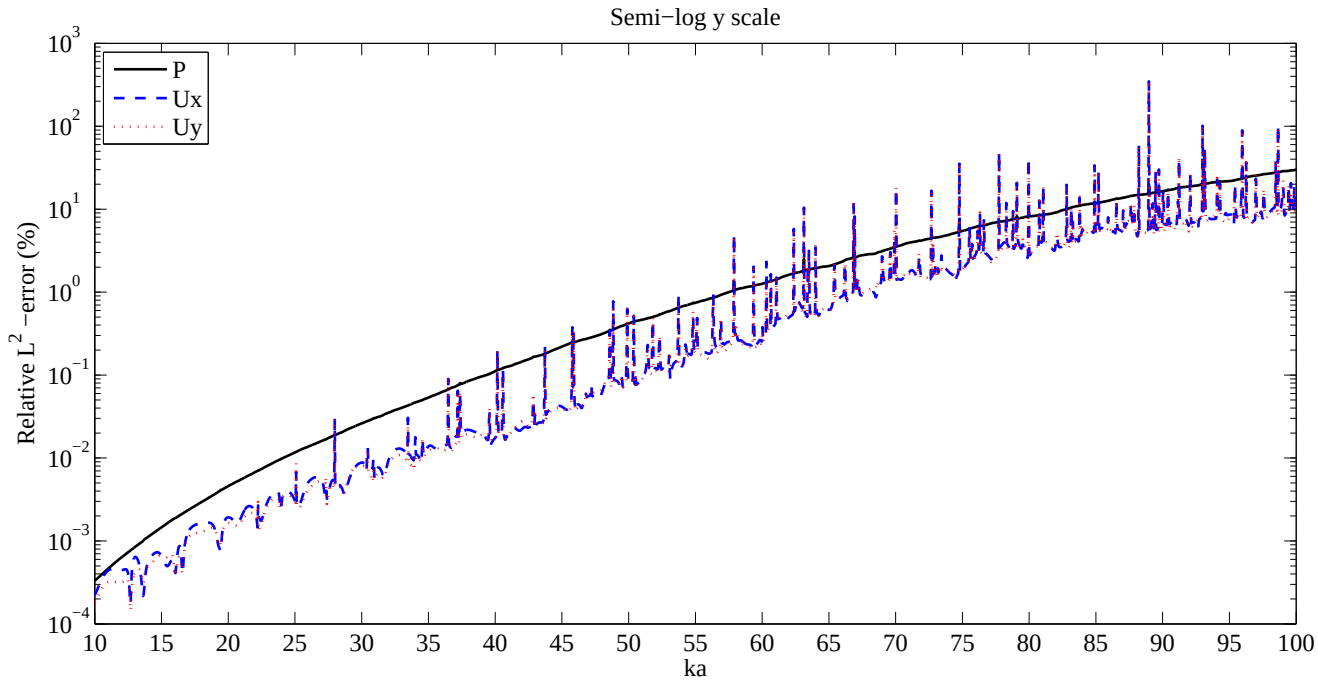

(a) Relative error

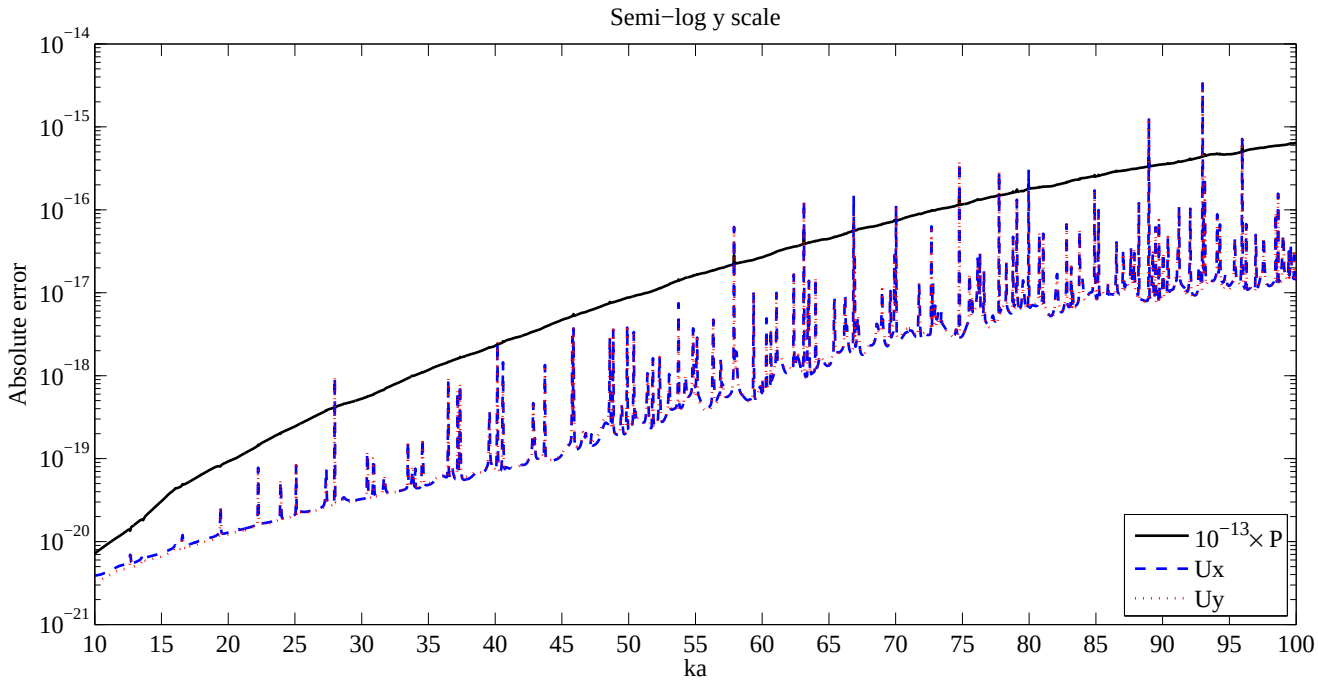

(b) Absolute error

Figure II.5.35 – Sensitivity of the relative error and absolute error to the frequency ka in the interval $[10, 100]$ when using cubic polynomial finite elements, curved boundary edges, and Mesh 1 halved once.

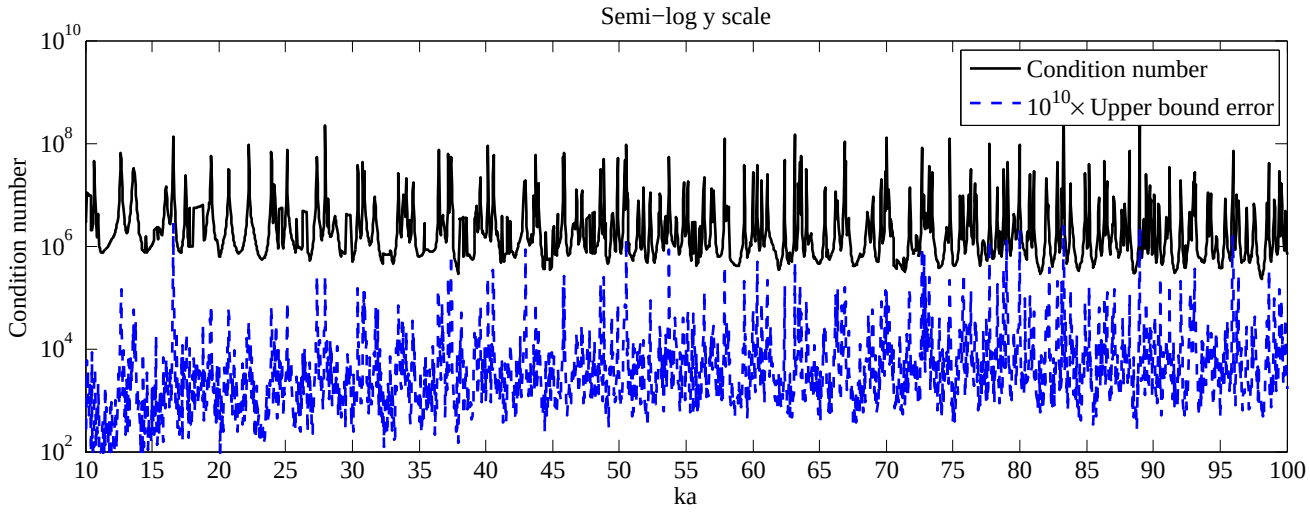

Figure II.5.36 – Sensitivity of the condition number to the frequency ka in the interval $[10, 100]$ when using cubic polynomial finite elements, curved boundary edges, and Mesh 1 halved once.

step size f=1 kHz.

The last results of this set of experiments are reported in Table II.5.15. These results were obtained using a mesh generated from Mesh 1 by halving the triangle edges three times successively. Hence, the resulting mesh contains exactly 64 times more triangles than Mesh 1, and incurs a linear system with 5,148,160 unknowns and 107,552,512 nonzero entries. We assess the effect of this mesh refinement in the frequency band $100 \leq ka \leq 300$ (2387 kHz $\leq f \leq$ 7162 kHz). The results are computed with a frequency step size $ka = 25$. Note that the resolution deteriorates from 6.5 elements per wavelength to about 2.2 elements per wavelength. These results show that IPDG delivers an accuracy level below 1% (resp. 5%) with a mesh resolution as low as 3.7 elements per wavelength (resp. 2.9 elements per wavelength) up to $ka \leq 175$ (resp. $ka \leq 225$). Next, we examine the pollution effect. We set a mesh resolution $kh = 1.94$ corresponding to about 3.2 elements per wavelength and evaluate the L^2-relative error over the computational domain in the frequency band $25 \leq ka \leq 200$ (596 kHz $\leq f \leq 4774$ kHz). The results reported in Table II.5.16 illustrate the behavior of the error as the frequency value doubles while maintaining fixed the resolution. These results reveal that the relative error on p increases linearly from about 0.3% to about 1.4%, whereas the change in the error on the structural displacement is barely noticeable. These results tend to indicate that IPDG exhibits a very little pollution effect in this relatively large frequency band. This observation illustrates the potential of IPDG for solving efficiently high-frequency elasto-acoustic problems.

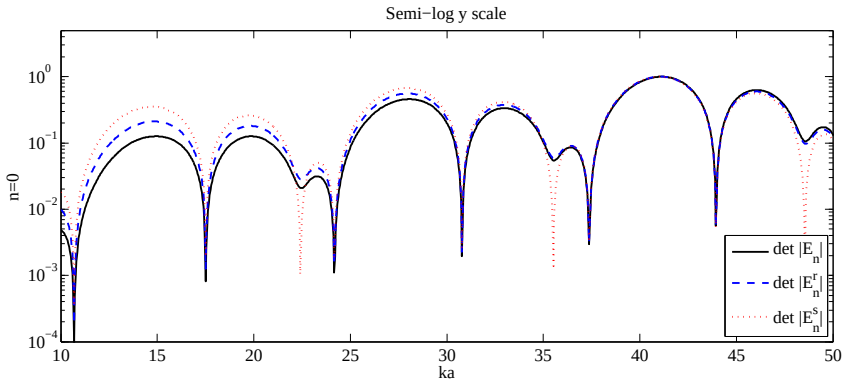

(a) Mode n=0

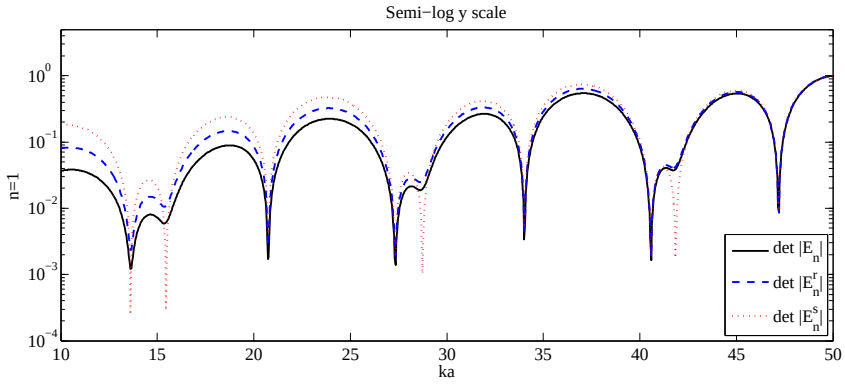

(b) Mode n=1

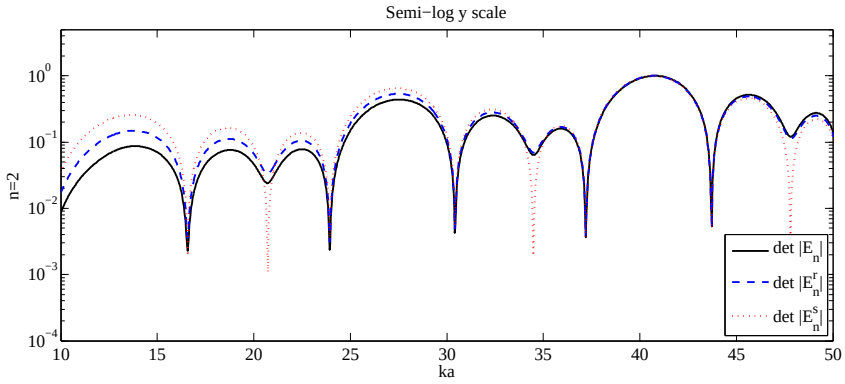

(c) Mode n=2

Figure II.5.37 – Sensitivity of the determinant of the modal matrices to the wavenumber ka. Cases where $n = 0, 1, 2$ (Semi-log y scale).

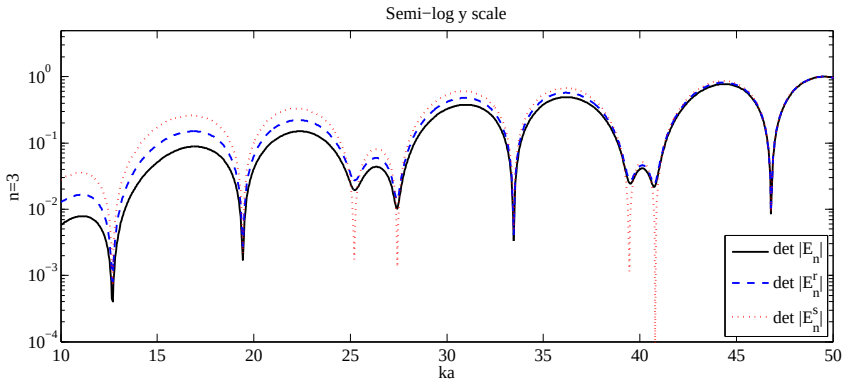

(a) Mode n=3

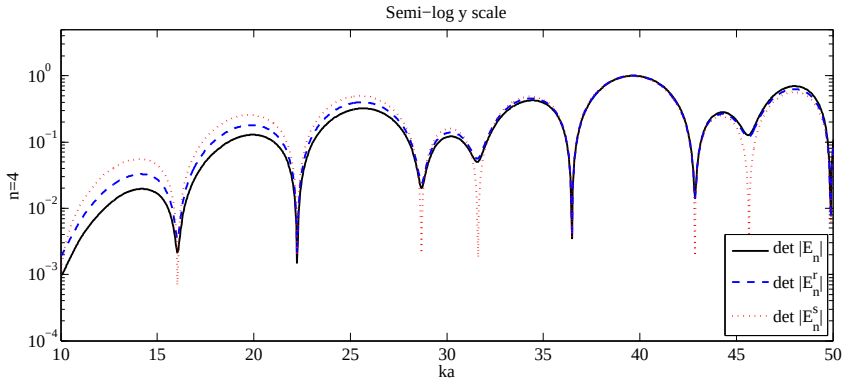

(b) Mode n=4

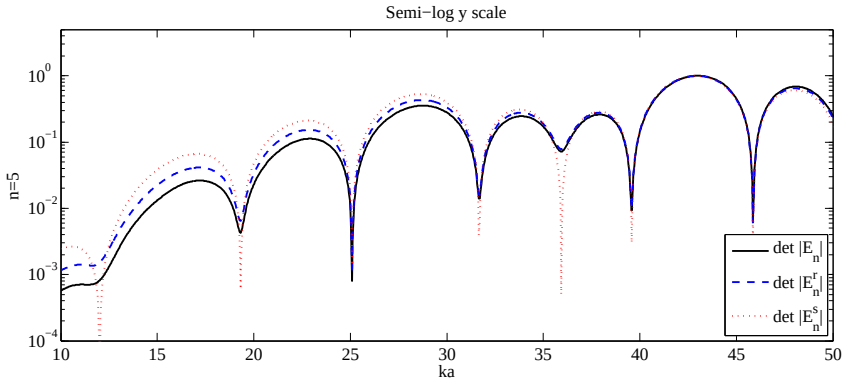

(c) Mode n=5

Figure II.5.38 – Sensitivity of the determinant of the modal matrices to the wavenumber ka. Cases where $n = 3, 4, 5$ (Semi-log y scale).

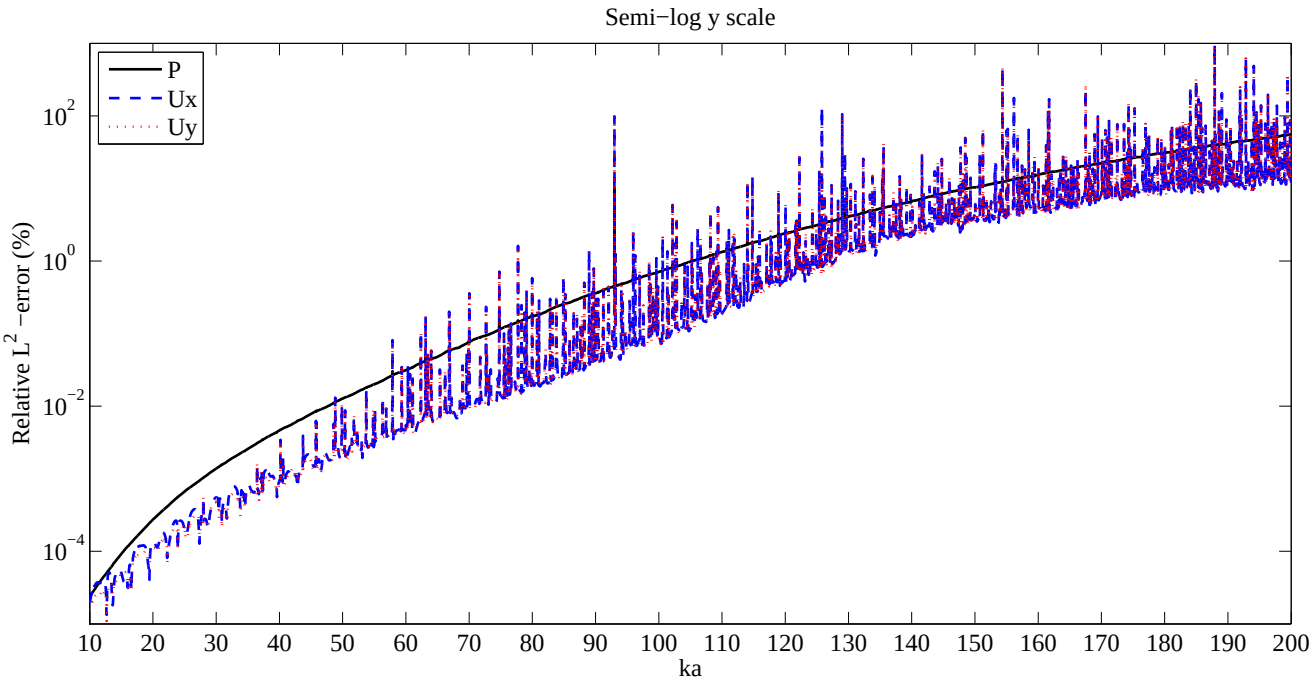

(a) Relative error

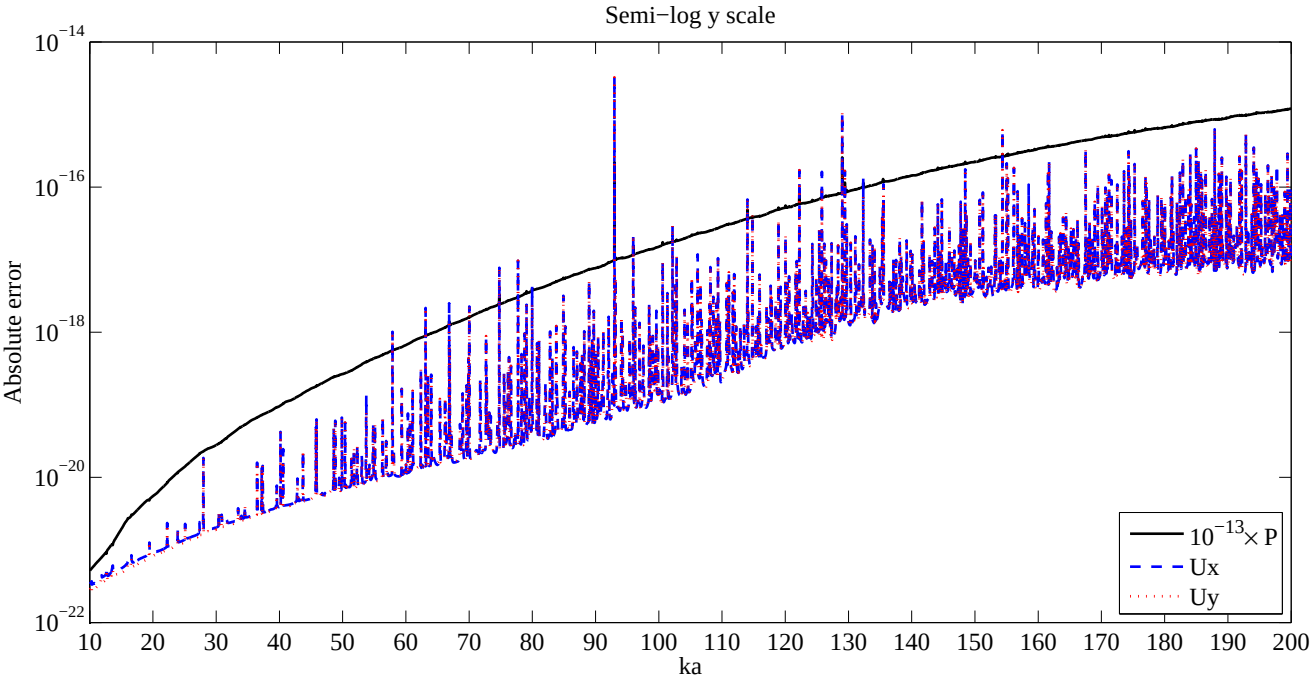

(b) Absolute error

Figure II.5.39 – Sensitivity of the relative error and the absolute error to the frequency ka in the interval $[10, 200]$ when using cubic polynomial finite elements, curved boundary edges, and Mesh 1 halved twice.

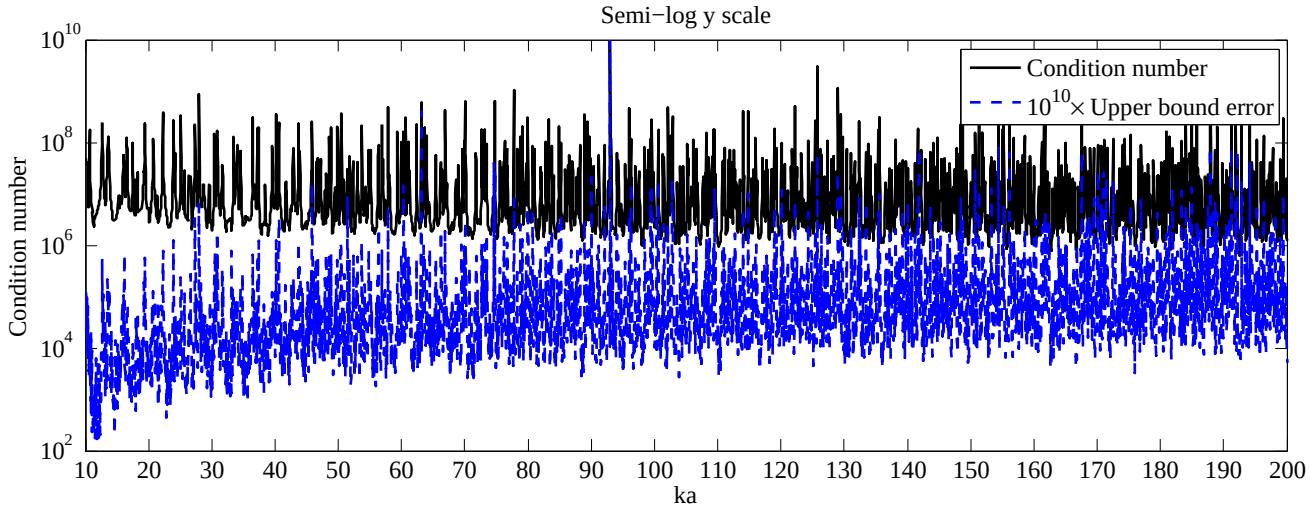

Figure II.5.40 – Sensitivity of the condition number to the frequency ka in the interval $[10, 200]$ when using cubic polynomial finite elements, curved boundary edges, and Mesh 1 halved twice.

ka	p	u_x	u_y
100	0.016	0.002	0.002
125	0.061	0.006	0.007
150	0.201	0.058	0.060
175	0.556	0.039	0.039
200	1.355	0.116	0.115
225	2.971	0.306	0.310
250	6.125	7.408	7.533
275	11.423	4.467	4.422
300	19.878	13.530	13.727

Table II.5.15 – L^2-relative error (%) in the high-frequency regime when using cubic polynomial finite elements, curved boundary edges, and Mesh 1 halved thrice.

	L^2-relative error		
ka	p	u_x	u_y
25	0.279	0.007	0.008
50	0.420	0.009	0.009
100	0.707	0.009	0.009
200	1.355	0.116	0.115

Table II.5.16 – L^2-relative error (%) obtained for $kh = 1.94$ constant with cubic polynomial functions and curved boundary edges.

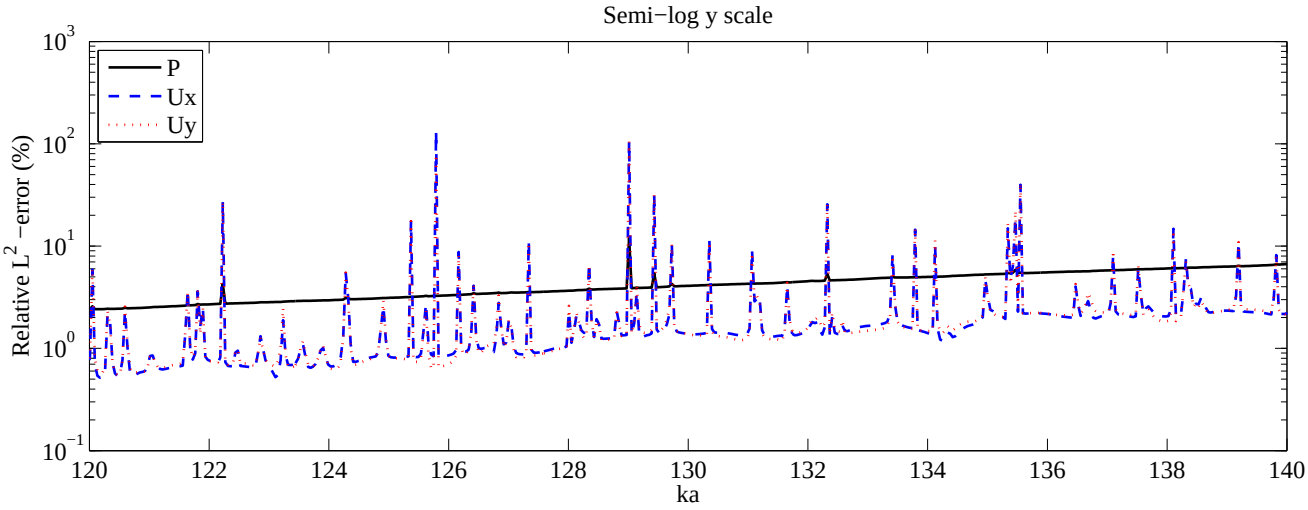

(a) Relative error

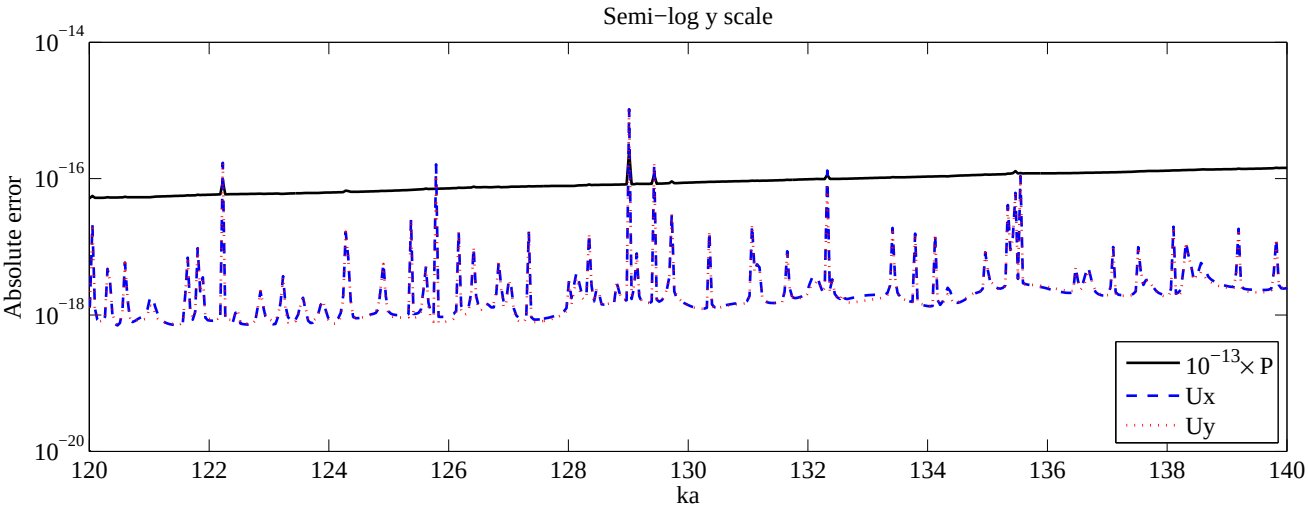

(b) Absolute error

Figure II.5.41 – Zoom on the sensitivity of the relative error and absolute error in the frequency band $120 \leq ka \leq 140$ when using cubic polynomial finite elements, curved boundary edges, and Mesh 1 halved twice.

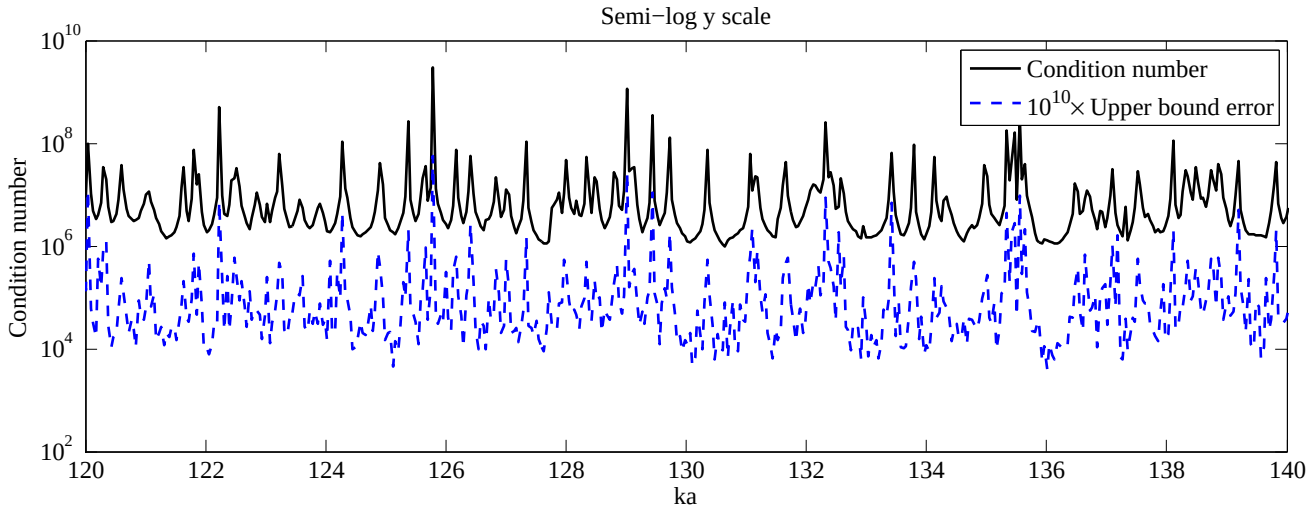

Figure II.5.42 – Zoom on the sensitivity of the condition number in the frequency band $120 \leq ka \leq 140$ when using cubic polynomial finite elements, curved boundary edges, and Mesh 1 halved twice.

II.6 Conclusion

A discontinuous Galerkin method, in which a penalty term is incorporated at the element level for stability purpose, is suggested for solving elasto-acoustic scattering problems. The proposed method, termed IPDG, employs higher-order elements to be employed in the high-frequency regime and curved boundary edges to provide a natural setting for better modeling the incoming and outgoing waves, as well as the surface waves at the wet surface.

On the one hand, the implementation of the method has been validated by means of two test cases: a waveguide-type problem and a radiating-type problem. These numerical experiments show a good approximation of both types of P-waves and S-waves and illustrate some stability properties of the method with respect to the direction of the plane waves, and to the mode number in the case of the waveguide-type problem and of the radiating-type problem respectively.

On the other hand, the numerical investigation performed in the case of an infinite long aluminum cylinder immersed in water reveals that there is a twofold benefit in using curved element boundaries rather than standard polygonal-shaped approximations. First, there is a gain of -at least- two orders of magnitude on the relative error and this improvement is even higher at the Jones frequencies. Second, this formulation prevents spurious resonance frequencies to occur in the fluid medium, which appears to not be possible to achieve if a polygonal-shaped approximation of the interface is used even with a fine mesh and high-order elements. Moreover, the results reported in this chapter illustrate the poten-

tial of IPDG for solving this class of scattering problems in high-frequency regimes. Indeed, IPDG delivers an accuracy level below 3% for $ka \leq 225$ ($f \leq 5371$ kHz) using cubic polynomial elements, and about three elements per wavelength only. Note that such resolution incurs solving a linear system of about 5 million unknowns with about 107 million nonzero entries that is accomplished using a direct method. An interesting prospect remains to study the sensitivity of the method to the mesh refinement, as well as to the frequency regime theoretically.

Acknowledgements The authors acknowledge the support by Inria Carnot Institute and ISIFoR Carnot Institute. Any opinions, findings, conclusions or recommendations expressed in this material are those of the authors and do not necessarily reflect the views of CSUN or INRIA.

Chapter II. Efficient DG-like formulation equipped with curved boundary edges for solving elasto-acoustic scattering problems

Appendices

Appendix B

Appendices to the Chapter II

B.1 Analytical solution for the disk-shaped elastic scatterer problem

It is well-known that the exact solution of the considered elasto-acoustic problem can be expressed as a Fourier series (see, for example, [88]) for a disk-shaped configuration. For completeness purposes, we recall here such an expression. In the fluid domain, the scattered pressure field is expressed as follows [16]:

$$p(r,\theta) = \sum_{n=0}^{+\infty} \left[A_n H_n^{(1)}(kr) + B_n H_n^{(2)}(kr) \right] \cos(n\theta); \quad a \leq r \leq b,\ \theta \in [0, 2\pi) \tag{B.1.1}$$

where $H_n^{(1)}$ and $H_n^{(2)}$ denote the Hankel functions of the first and second kinds [2], and A_n, B_n are complex numbers. The first term of the series corresponds to the outgoing field. The second term represents the incoming wave due to the presence of the exterior boundary Σ. The incident plane wave admits the following Jacobi-Anger expansion [16]:

$$g = p^{inc}(r,\theta) = e^{ikr\cos\theta} = \sum_{n=0}^{+\infty} \varepsilon_n i^n J_n(kr)\cos(n\theta), \tag{B.1.2}$$

where

$$\varepsilon_0 = 1 \quad \text{and} \quad \varepsilon_n = 2;\ \forall\, n > 0.$$

In the solid obstacle, the scattered displacement field u is expressed using two displacement potentials ϕ and ψ [120]:

$$u = \nabla\phi + (-e_z) \times \nabla\psi. \tag{B.1.3}$$

where these two potentials are given by:

$$\phi(r,\theta) = \sum_{n=0}^{+\infty} C_n J_n(k_p r)\cos(n\theta), \tag{B.1.4}$$

$$\psi(r,\theta) = \sum_{n=0}^{+\infty} D_n J_n(k_s r)\sin(n\theta); \quad 0 \le r < a,\ \theta \in [0, 2\pi). \tag{B.1.5}$$

Here, J_n and Y_n denote the Bessel functions of the first and second kind respectively [2], and $k_p = \dfrac{\omega}{c_p}$, $k_s = \dfrac{\omega}{c_s}$ represent the wavenumbers of the pressure and shear waves in the solid.
Let us explicit the Fourier series representation of both components of u. In polar coordinates, we have:

$$\nabla\phi = \frac{\partial\phi}{\partial r}\vec{e}_r + \frac{1}{r}\frac{\partial\phi}{\partial\theta}\vec{e}_\theta \tag{B.1.6}$$

$$(-e_z)\times\nabla\psi = \frac{1}{r}\frac{\partial\psi}{\partial\theta}\vec{e}_r - \frac{\partial\psi}{\partial r}\vec{e}_\theta. \tag{B.1.7}$$

We set

$$u_r = \frac{\partial\phi}{\partial r} + \frac{1}{r}\frac{\partial\psi}{\partial\theta} \tag{B.1.8}$$

$$u_\theta = \frac{1}{r}\frac{\partial\phi}{\partial\theta} - \frac{\partial\psi}{\partial r}. \tag{B.1.9}$$

Then, we obtain:

$$u = u_r\vec{e}_r + u_\theta\vec{e}_\theta. \tag{B.1.10}$$

Since the polar basis vectors are given by $\vec{e}_r = (\cos\theta,\ \sin\theta)^t$ and $\vec{e}_\theta = (-\sin\theta,\ \cos\theta)^t$, it follows that the displacement field can be written in the canonical basis as:

$$\begin{cases} u_x = u_r\cos\theta - u_\theta\sin\theta, \\ u_y = u_r\sin\theta + u_\theta\cos\theta, \end{cases} \tag{B.1.11}$$

where

$$u_r = \sum_{n=0}^{+\infty}\left[C_n k_p J_n'(k_p r) + \frac{n}{r}D_n J_n(k_s r)\right]\cos(n\theta) \tag{B.1.12}$$

$$u_\theta = \sum_{n=0}^{+\infty} -\left[C_n\frac{n}{r}J_n(k_p r) + D_n k_s J_n'(k_s r)\right]\sin(n\theta). \tag{B.1.13}$$

Note that the relationships between the Fourier series displacement potentials and corresponding displacements and tractions are reported in [120].

Moreover, the complex coefficients A_n, B_n, C_n and D_n satisfy the following system [88]:

$$E_n X_n = e_n \tag{B.1.14}$$

where $X_n = (A_n, B_n, C_n, D_n)^t$ and E_n is a 4×4 matrix whose complex-valued entries E_n^{lj} are given by:

$$\begin{aligned}
E_n^{1j} &= kH_n^{'(j)}(ka), \quad j = 1, 2 \\
E_n^{13} &= -\omega^2 \rho_f k_p J_n'(k_p a), \\
E_n^{14} &= -\omega^2 \rho_f \frac{n}{a} J_n(k_s a), \\
E_n^{2j} &= H_n^{(j)}(ka), \quad j = 1, 2 \\
E_n^{23} &= \frac{2\mu}{a^2}\left[(n^2 + n - \frac{1}{2}k_s^2 a^2) J_n(k_p a) - k_p a J_{n-1}(k_p a)\right], \\
E_n^{24} &= \frac{2\mu}{a^2}\left[n(-(n+1)J_n(k_s a) + k_s a J_{n-1}(k_s a))\right], \\
E_n^{31} &= E_n^{32} = E_n^{43} = E_n^{44} = 0, \\
E_n^{33} &= -\frac{2\mu}{a^2} n\left[-(n+1)J_n(k_p a) + k_p a J_{n-1}(k_p a)\right], \\
E_n^{34} &= -\frac{2\mu}{a^2}\left[(n^2 + n - \frac{1}{2}k_s^2 a^2) J_n(k_s a) - k_s a J_{n-1}(k_s a)\right], \\
E_n^{4j} &= kH_n^{'(j)}(kb) - \mathrm{i}kH_n^{(j)}(kb), \quad j = 1, 2.
\end{aligned}$$

The right-hand side $e_n \in \mathbb{C}^4$ of the linear system related to Eq. (B.1.14) is given by:

$$e_n^1 = -\varepsilon_n \mathrm{i}^n k J_n^{'}(ka), \tag{B.1.15}$$

$$e_n^2 = -\varepsilon_n \mathrm{i}^n J_n(ka), \tag{B.1.16}$$

$$e_n^3 = e_n^4 = 0, \tag{B.1.17}$$

where $\varepsilon_0 = 1$ and $\varepsilon_n = 2$ for $n \geq 1$.

The system entries can be determined from the boundary conditions of BVP (2) as follows. Let us consider the first transmission condition given by Eq. (II.2.9) of BVP (2):

$$\omega^2 \rho_f u \cdot \nu = \frac{\partial p}{\partial \nu} + \frac{\partial g}{\partial \nu} \qquad \text{on } \Gamma \tag{B.1.18}$$

Taking the radial component of each mode n gives:

$$\omega^2\rho_f\left(C_n k_p J_n^{'}(k_p a)+D_n\frac{n}{a}J_n(k_s a)\right)=A_n k H_n^{'(1)}(ka)+B_n k H_n^{'(2)}(ka)+\varepsilon_n i^n k J_n^{'}(ka).$$

We therefore infer the first equation of the system (B.1.14).

Next, we consider the second transmission condition given by Eq. (II.2.10) of BVP (2):

$$\tau(u)=-p\nu-g\nu \qquad \text{on } \Gamma.$$

Then, the normal and tangential components of the stress tensor are:

$$\tau(u)\cdot\nu = -p-p^{inc} \qquad \text{on } \Gamma \tag{B.1.19}$$

$$\tau(u)\cdot t = 0 \qquad \text{on } \Gamma, \tag{B.1.20}$$

where t denotes the tangential vector.

In polar coordinates, we have: $\tau(u)\cdot\nu=\sigma_{rr}$ and $\tau(u)\cdot t=\sigma_{r\theta}$. We thus have:

$$\sigma_{rr} = -p-p^{inc} \qquad \text{on } \Gamma \tag{B.1.21}$$

$$\sigma_{r\theta} = 0 \qquad \text{on } \Gamma. \tag{B.1.22}$$

Now, we express σ_{rr} and $\sigma_{r\theta}$ as functions of ϕ and ψ. For that purpose, we set:

$$\sigma_{rr} = \sigma_{rr}^{\phi}+\sigma_{rr}^{\psi} \tag{B.1.23}$$

$$\sigma_{r\theta} = \sigma_{r\theta}^{\phi}+\sigma_{r\theta}^{\psi} \tag{B.1.24}$$

and using [120], we obtain:

$$\sigma_{rr}^{\phi} = \lambda\Delta\phi+2\mu\frac{\partial^2\phi}{\partial r^2} \tag{B.1.25}$$

$$\sigma_{rr}^{\psi} = 2\mu\left[\frac{\partial}{\partial r}\left(\frac{1}{r}\frac{\partial\psi}{\partial\theta}\right)\right] \tag{B.1.26}$$

$$\sigma_{r\theta}^{\phi} = 2\mu\left[\frac{1}{r}\frac{\partial^2\phi}{\partial\theta\partial r}-\frac{1}{r^2}\frac{\partial\phi}{\partial\theta}\right] \tag{B.1.27}$$

$$\sigma_{r\theta}^{\psi} = \mu\left[\frac{1}{r^2}\frac{\partial^2\psi}{\partial\theta^2}-r\frac{\partial}{\partial r}\left(\frac{1}{r}\frac{\partial\psi}{\partial r}\right)\right]. \tag{B.1.28}$$

Observe that ϕ satisfies the following scalar Helmholtz equation with wavenumber $k_p = \frac{\omega}{c_p}$:

$$\Delta\phi \;=\; -k_p^2\phi.$$

This yields:

$$\Delta\phi \;=\; \sum_{n=0}^{+\infty} C_n \left(-\frac{1}{r^2}(k_p^2 r^2) J_n(k_p r)\right)\cos(n\theta).$$

By some calculations, we obtain:

$$\begin{aligned}
\frac{\partial^2\phi}{\partial r^2} &= \sum_{n=0}^{+\infty} C_n k_p^2 J_n^{''}(k_p r)\cos(n\theta) \\
&= \sum_{n=0}^{+\infty} C_n \frac{1}{r^2}\left(-k_p r J_{n-1}(k_p r) + (n^2+n-k_p^2 r^2) J_n(k_p r)\right)\cos(n\theta), \\
\frac{\partial\phi}{\partial\theta} &= \sum_{n=0}^{+\infty} -C_n n J_n(k_p r)\sin(n\theta), \\
\frac{\partial^2\phi}{\partial\theta\partial r} &= \sum_{n=0}^{+\infty} -C_n n k_p J_n^{'}(k_p r)\sin(n\theta) \\
&= \sum_{n=0}^{+\infty} -C_n \frac{n}{r}\left(k_p r J_{n-1}(k_p r) - n J_n(k_p r)\right)\sin(n\theta),
\end{aligned}$$

and

$$\begin{aligned}
\frac{\partial\psi}{\partial\theta} &= \sum_{n=0}^{+\infty} D_n n J_n(k_s r)\cos(n\theta), \\
\frac{\partial^2\psi}{\partial\theta^2} &= \sum_{n=0}^{+\infty} -D_n n^2 J_n(k_s r)\sin(n\theta), \\
\frac{\partial\psi}{\partial r} &= \sum_{n=0}^{+\infty} D_n k_s J_n^{'}(k_s r)\sin(n\theta) \\
&= \sum_{n=0}^{+\infty} D_n \frac{1}{r}\left(k_s r J_{n-1}(k_s r) - n J_n(k_s r)\right)\sin(n\theta), \\
\frac{\partial^2\psi}{\partial r^2} &= \sum_{n=0}^{+\infty} D_n k_s^2 J_n^{''}(k_s r)\sin(n\theta) \\
&= \sum_{n=0}^{+\infty} D_n \frac{1}{r^2}\left(-k_s r J_{n-1}(k_s r) + (n^2+n-k_s^2 r^2) J_n(k_s r)\right)\sin(n\theta),
\end{aligned}$$

$$\begin{aligned}\frac{\partial^2\psi}{\partial r\partial\theta} &= \sum_{n=0}^{+\infty} D_n n k_s J_n^{'}(k_s r)\cos(n\theta)\\ &= \sum_{n=0}^{+\infty} D_n \frac{n}{r}\left(k_s r J_{n-1}(k_s r) - n J_n(k_s r)\right)\cos(n\theta).\end{aligned}$$

In addition, since $k_p^2(\lambda+2\mu) = k_s^2\mu$, we obtain: $\lambda = \frac{k_s^2}{k_p^2}\mu - 2\mu$. It follows that:

$$\begin{aligned}\sigma_{rr}^{\phi} &= \lambda\Delta\phi + 2\mu\frac{\partial^2\phi}{\partial r^2}\\ &= \sum_{n=0}^{+\infty} C_n\{\left(\frac{k_s^2}{k_p^2}\mu - 2\mu\right)\left[-\frac{1}{r^2}(k_p^2r^2)J_n(k_pr)\right]\\ &\quad +2\mu\frac{1}{r^2}\left(-k_pr J_{n-1}(k_pr) + (n^2+n-k_p^2r^2)J_n(k_pr)\right]\}\cos(n\theta)\\ &= \sum_{n=0}^{+\infty} C_n\frac{2\mu}{r^2}\left[(n^2+n-\frac{1}{2}k_s^2r^2)J_n(k_pr) - k_pr J_{n-1}(k_pr)\right]\cos(n\theta).\\ \sigma_{rr}^{\psi} &= \frac{2\mu}{r^2}\left[r\frac{\partial^2\psi}{\partial r\partial\theta} - \frac{\partial\psi}{\partial\theta}\right]\\ &= \sum_{n=0}^{+\infty} D_n\frac{2\mu}{r^2}\left[n\left(k_sr J_{n-1}(k_sr) - nJ_n(k_sr)\right) - nJ_n(k_sr)\right]\cos(n\theta)\\ &= \sum_{n=0}^{+\infty} D_n\frac{2\mu}{r^2}\left[nk_sr J_{n-1}(k_sr) - n(n+1)J_n(k_sr)\right]\cos(n\theta).\end{aligned}$$

Combining σ_{rr}^{ϕ}, σ_{rr}^{ψ}, along with Eq. (B.1.21) and Eq. (B.1.23) at $r = a$ leads to the second equation of the system (B.1.14).

On the other hand, regarding $\sigma_{r\theta}$, we have:

$$\begin{aligned}\sigma_{r\theta}^{\phi} &= 2\mu\left[\frac{1}{r}\frac{\partial^2\phi}{\partial\theta\partial r} - \frac{1}{r^2}\frac{\partial\phi}{\partial\theta}\right]\\ &= \sum_{n=0}^{+\infty} C_n\frac{-2\mu}{r^2}\left[nk_pr J_{n-1}(k_pr) - n(n+1)J_n(k_pr)\right]\sin(n\theta).\end{aligned}$$

Moreover, for the ψ-term, we obtain:

$$\begin{aligned}\sigma_{r\theta}^{\psi} &= \mu\left[\frac{1}{r^2}\frac{\partial^2\psi}{\partial\theta^2} - r\frac{\partial}{\partial r}\left(\frac{1}{r}\frac{\partial\psi}{\partial r}\right)\right]\\ &= \mu\left[\frac{1}{r^2}\frac{\partial^2\psi}{\partial\theta^2} + \frac{1}{r}\frac{\partial\psi}{\partial r} - \frac{\partial^2\psi}{\partial r^2}\right]\end{aligned}$$

$$
\begin{aligned}
&= \sum_{n=0}^{+\infty} D_n \mu \frac{1}{r^2}\{-n^2 J_n(k_s r) + (k_s r J_{n-1}(k_s r) - n J_n(k_s r)) \\
&\quad - \Big(k_s r J_{n-1}(k_s r) + (n^2 + n - k_s^2 r^2) J_n(k_s r)\Big)\} \sin(n\theta) \\
&= \sum_{n=0}^{+\infty} -D_n \frac{2\mu}{r^2} \left[\left[n^2 + n - \frac{1}{2} k_s^2 r^2\right] J_n(k_s r) - k_s r J_{n-1}(k_s r)\right] \sin(n\theta).
\end{aligned}
$$

Combining $\sigma_{r\theta}^{\phi}$, $\sigma_{r\theta}^{\psi}$ with Eq. (B.1.22) and Eq. (B.1.24) at $r = a$, we deduce the third equation of the system (B.1.14).

Finally, the absorbing boundary condition given by Eq. (II.2.10) of BVP (2):

$$
\frac{\partial p}{\partial r} - ikp = 0 \qquad \text{on } \Sigma
$$

easily yields the last equation of the system (B.1.14) as follows:

$$
A_n(kH_n'^{(1)}(kb) - ikH_n^{(1)}(kb)) + B_n(kH_n'^{(2)}(kb) - ikH_n^{(2)}(kb)) = 0.
$$

B.2 Issue on the Jones modes

In this Appendix, we are interested in the following issue: Assume that ka is not a resonance frequency for an initial configuration of the obstacle. When applying a deformation to the scatterer, can ka become a Jones frequency for the perturbed boundary value problem?
This amounts to study the dependence between the frequency ka and a perturbation of the obstacle. To this end, we assume that the scatterer is a circle to which we apply a deformation in the radial direction, so that the perturbed obstacle remains a circle. For a fixed normalized frequency ka, the radius delimiting the fluid domain is fixed to $b = 20$ mm whereas the radius of the elastic obstacle a varies.
Consider the matrix E_n of the linear system (B.1.14) giving the coefficients of the exact Fourier series solution (cf Appendix B.1). We denote by $E_n^r = (E_n^{jl})_{j=1,2,3;l=1,3,4}$ the reduced matrix in which the effect of the exterior boundary is ignored, whereas $E_n^s = (E_n^{jl})_{j=2,3;l=3,4}$ is the matrix representing the solid Fourier modes. Recall that the Jones frequencies correspond to frequency values for which the uniqueness of the solution in the elastic medium fails. In order to identify the resonance mode, we monitor the dependence of these local three matrices E_n, E_n^r and E_n^s with respect to the obstacle radius a, and determine the values that make the corresponding determinants vanish. We consider the three frequencies in a resonance region: $f_1 = 219$ kHz, $f_R = 221$ kHz (the resonance frequency) and $f_2 = 223$ kHz, corresponding to $ka = 9.1735, 9.2572$, and 9.341 respectively. The results obtained for mode number $n = 0, \cdots, 5$ are depicted in Figures B.2.1 to B.2.6.

In light of the results, the answer seems positive. Indeed, the following observations are noteworthy:

- In Figure B.2.3 (c), we recognize the vanishing determinant for the frequency $f_R = 221$ associated to the mode $n = 2$ at the radius $a = 10$ mm , which corresponds to the resonance mode highlighted in our study in Section II.5. This value of the frequency does not remain a resonance frequency associated to the third Fourier mode for perturbed configurations of the obstacle in the neighborhood of $a = 10$ mm, but it is again a Jones frequency at $a = 18$ mm. Moreover, the others curves in Figures B.2.3-B.2.4 reveals that f_R can be a Jones frequency associated to another modes at some other exceptional values of a (e.g. at $a = 0.012$ for the first mode).
- As regards the case of the other frequencies f_1 and f_2 depicted in Figures B.2.1, B.2.2, B.2.5 and B.2.6, a similar observation can be made. Indeed, both frequencies are non-resonance frequencies at $a = 10mm$, but they are Jones frequencies associated to the third mode for values of a very close to 10 mm. In addition, the results also indicate that they can be Jones frequencies associated to another mode in another perturbed configuration.

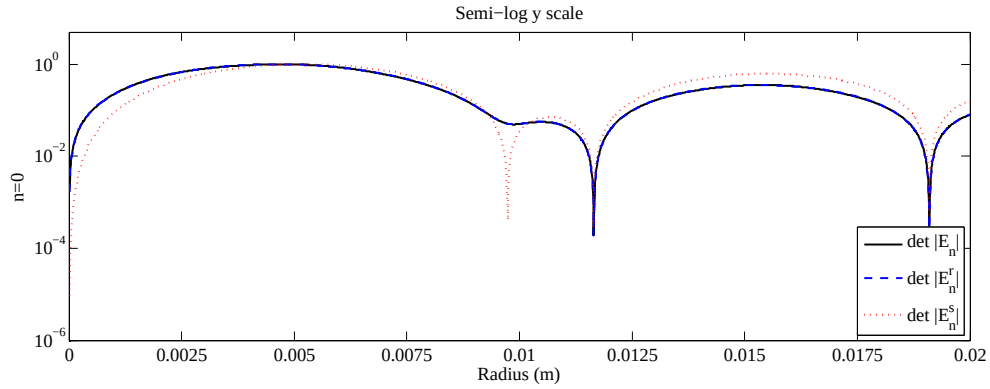

(a) Mode n=0

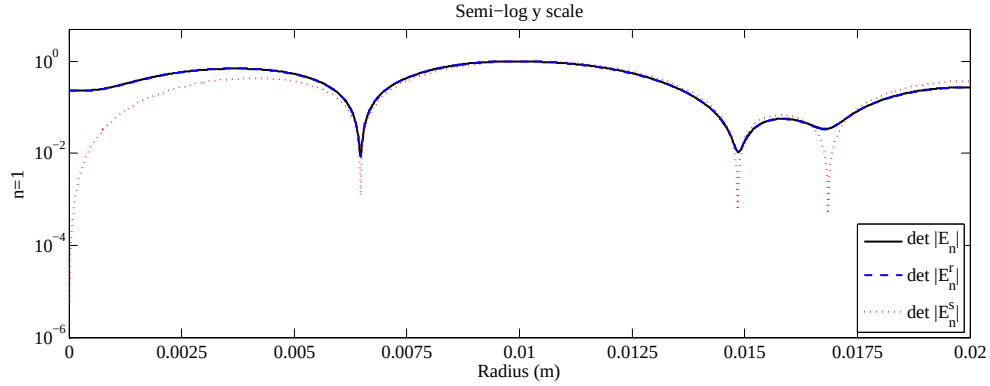

(b) Mode n=1

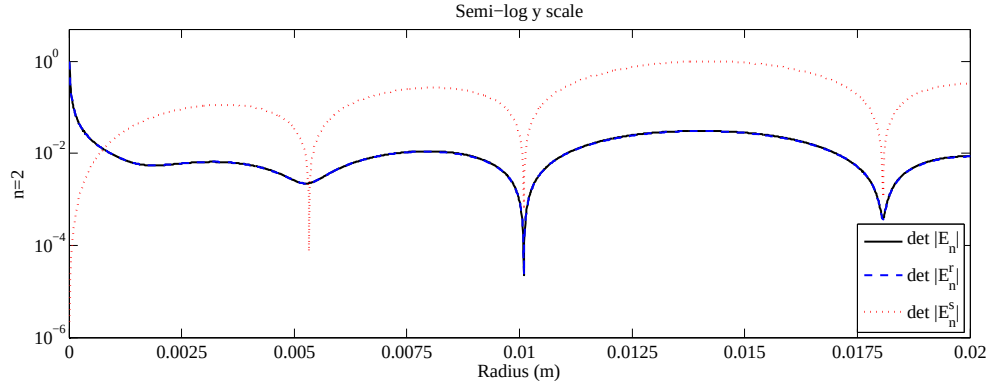

(c) Mode n=2

Figure B.2.1 – Frequency $f_1 = 219$ kHz ($ka = 9.1735$) - Sensitivity of the determinant of the modal matrices to the radius a. Cases where $n = 0, 1, 2$ (Semi-log y scale).

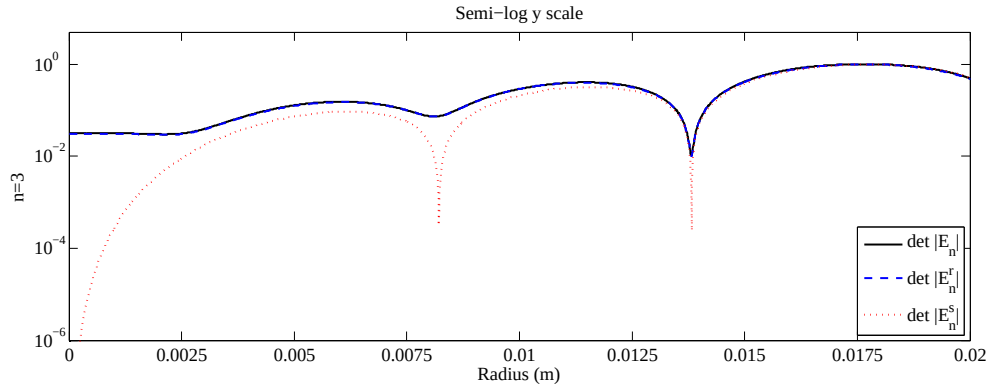

(a) Mode n=3

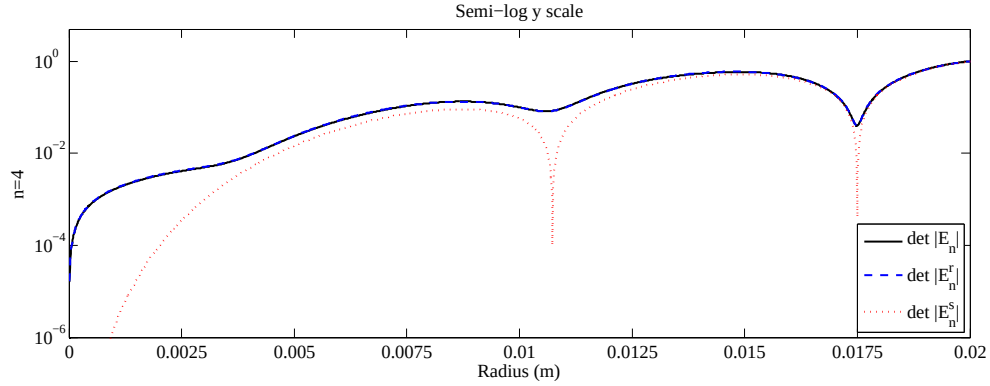

(b) Mode n=4

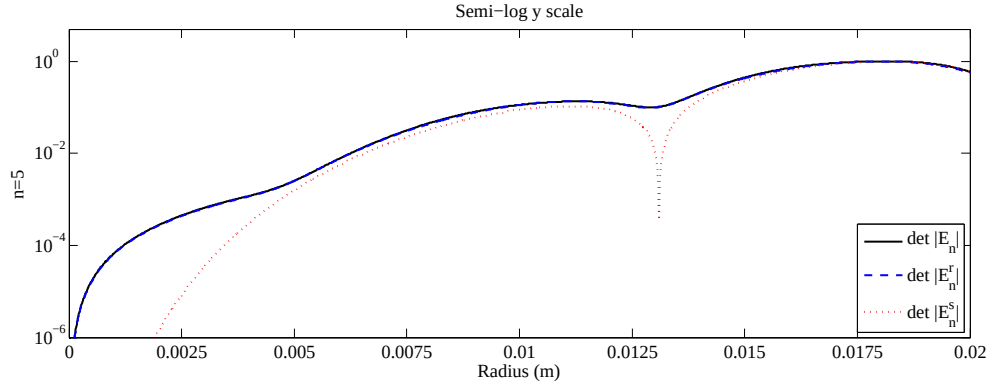

(c) Mode n=5

Figure B.2.2 – Frequency $f_1 = 219$ kHz ($ka = 9.1735$) - Sensitivity of the determinant of the modal matrices to the radius a. Cases where $n = 3, 4, 5$ (Semi-log y scale).

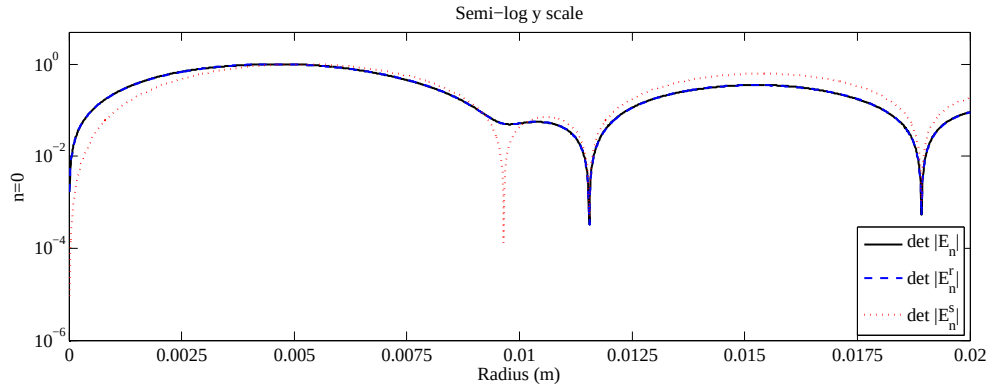

(a) Mode n=0

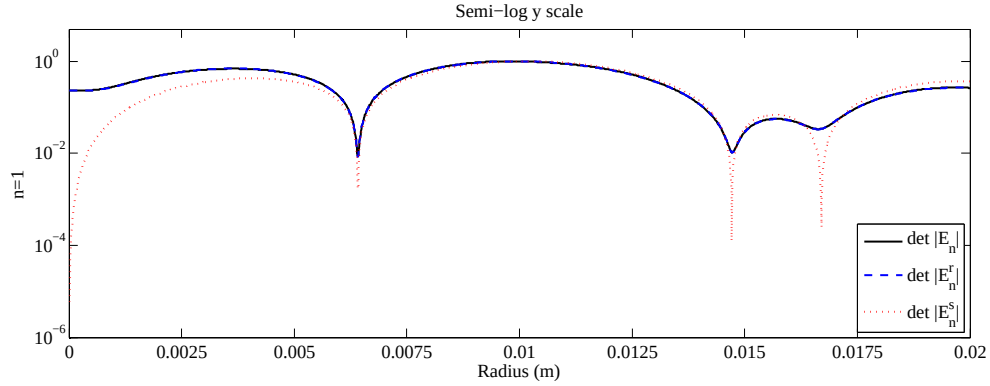

(b) Mode n=1

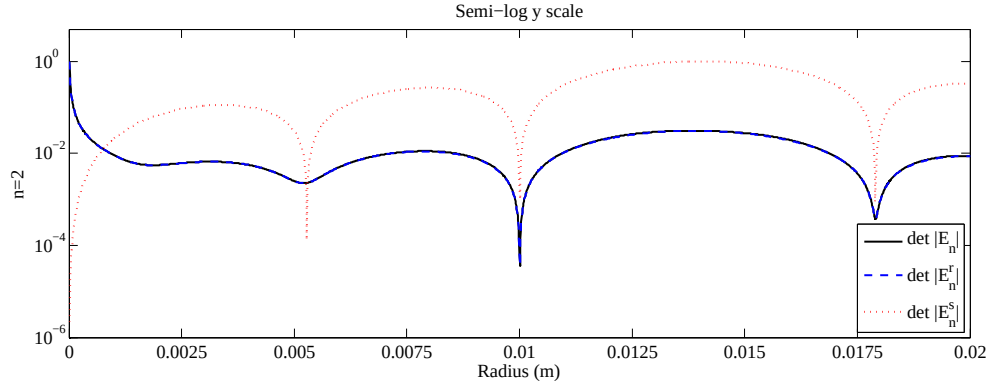

(c) Mode n=2

Figure B.2.3 – Frequency $f_R = 221$ kHz ($ka = 9.2572$) - Sensitivity of the determinant of the modal matrices to the radius a. Cases where $n = 0, 1, 2$ (Semi-log y scale).

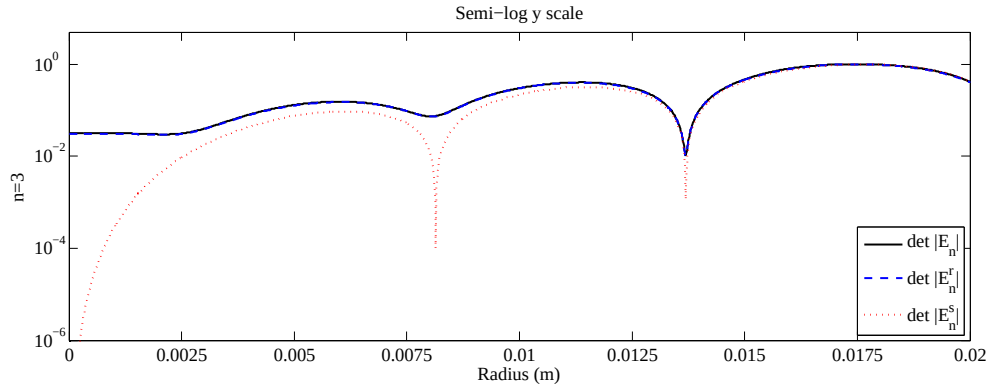

(a) Mode n=3

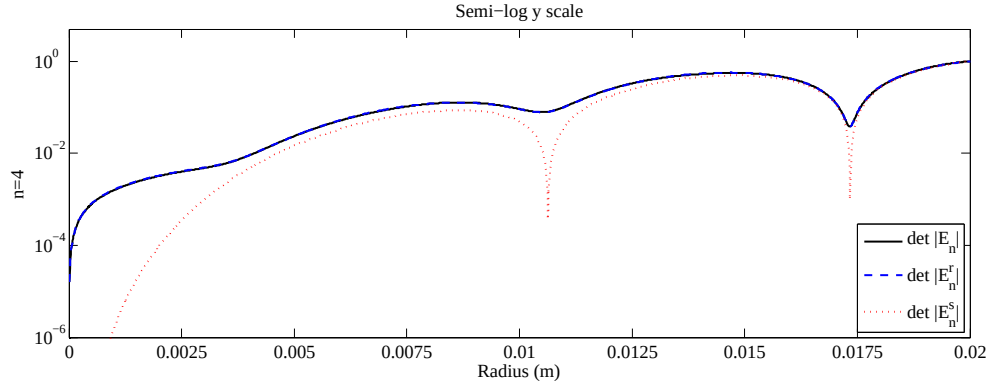

(b) Mode n=4

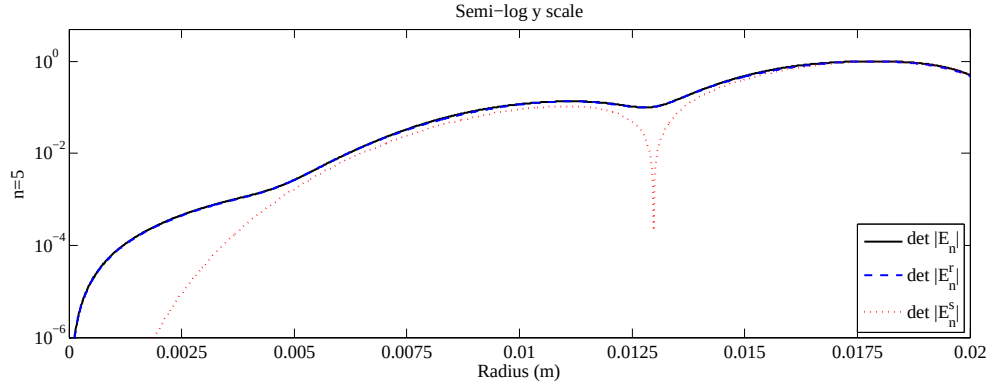

(c) Mode n=5

Figure B.2.4 – Frequency $f_R = 221$ kHz ($ka = 9.2572$) - Sensitivity of the determinant of the modal matrices to the radius a. Cases where $n = 3, 4, 5$ (Semi-log y scale).

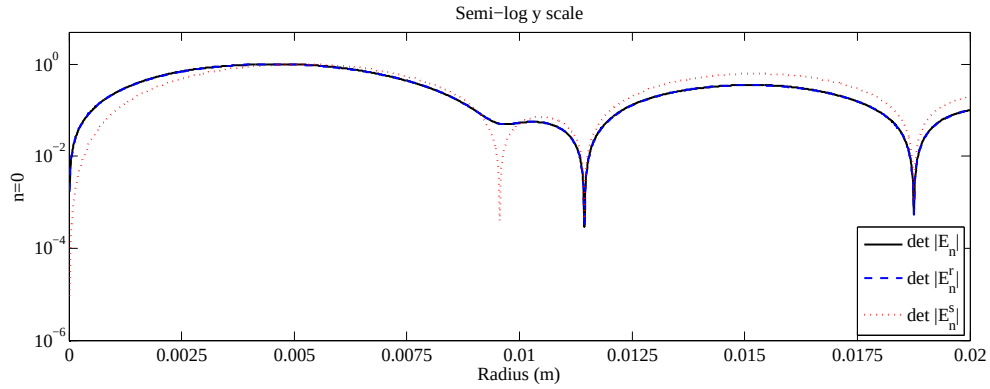

(a) Mode n=0

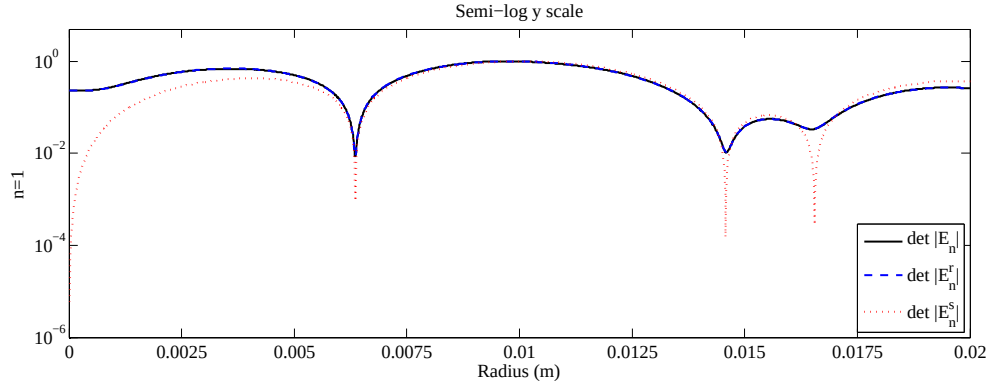

(b) Mode n=1

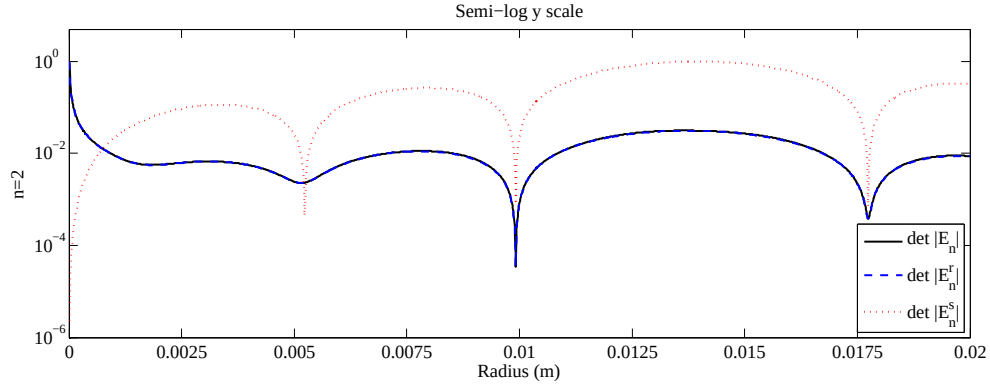

(c) Mode n=2

Figure B.2.5 – Frequency $f_2 = 223$ kHz ($ka = 9.341$) - Sensitivity of the determinant of the modal matrices to the radius a. Cases where $n = 0, 1, 2$ (Semi-log y scale).

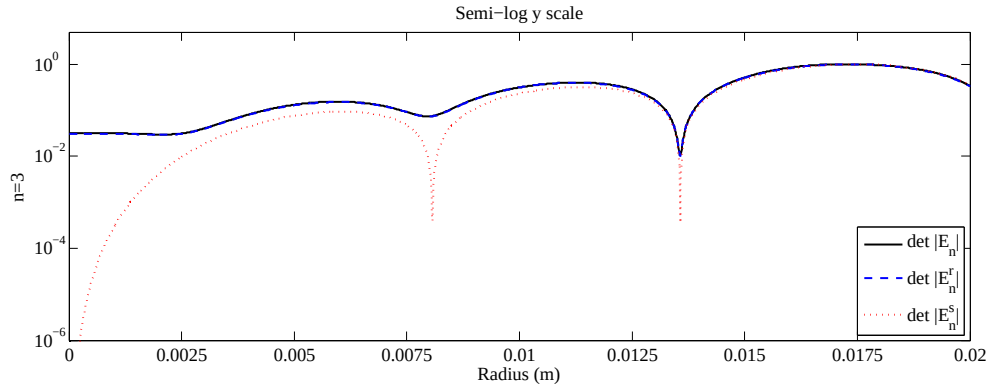

(a) Mode n=3

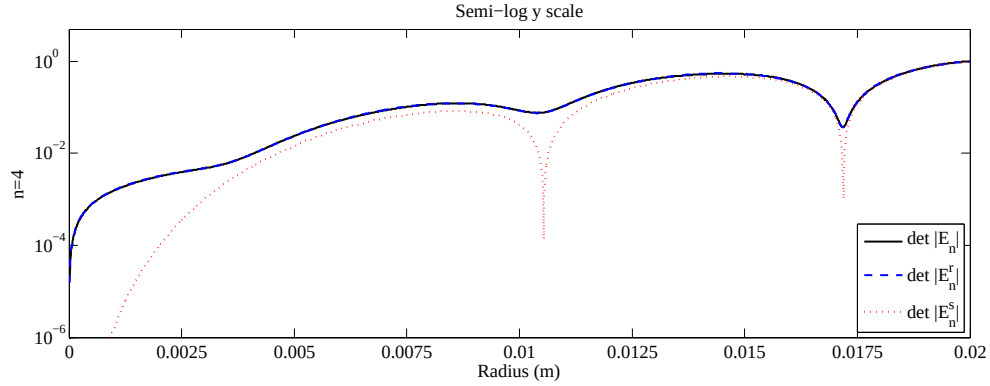

(b) Mode n=4

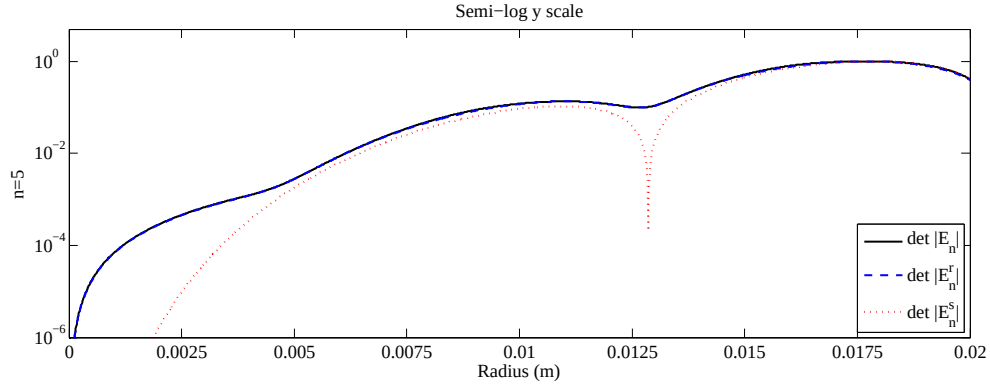

(c) Mode n=5

Figure B.2.6 – Frequency $f_2 = 223$ kHz ($ka = 9.341$) - Sensitivity of the determinant of the modal matrices to the radius a. Cases where $n = 3, 4, 5$ (Semi-log y scale).

B.3 Sensitivity to the penalty parameter

In this appendix, we examine the sensitivity of the relative error to the penalty parameters. First, let us mention that this penalization is important for different reasons, chief among them:

- First, let us observe the case of the Laplace equation. In that situation, we are only semi positive-definite. Then, when writing the formulation with discontinuous basis functions, the jump terms appear and can decomposed into two parts as follows:

$$\begin{aligned}\sum_K \int_K \Delta pq &= \sum_K \int_K \nabla p \nabla q - \sum_e \int_e [\nabla p \cdot \nu q] \\ &= \sum_K \int_K \nabla p \nabla q - \sum_e \int_e [\nabla p \cdot \nu]\{q\} - \sum_e \int_e \{\nabla p\} \nu [q].\end{aligned}$$

  Till then, we remain semi positive-definite. Nevertheless, when we remove the part $[\nabla p \cdot \nu]\{q\}$, though we remain consistent, we lose this property. We thus end up with negative or zero eigenvalues. When we impose the symmetry by adding the negative term $-\sum_e \int_e \{\nabla q\}\nu[p]$, we increase this loss. The interest of the penalization is to raise the spectrum of the eigenvalues as much as possible, so that there are the least possible negative eigenvalues. For Helmholtz problems, it is even worse because of $-k^2$.
- Moreover, the case that we study is a favorable case. The penalty parameter is used to eliminate spurious modes (cf [4]). Since in our case, the resonance Jones modes exist in the solid and must exist, one can take $\gamma_s = 0$ when considering a resonance frequency. However, in the fluid, we have to keep γ_f different from 0.
- Finally, the penalty parameter allows to stabilize the condition number. Without this penalization, some problems may occur. In our small case, this is not necessarily a matter since we can use a direct solver. Nevertheless, for larger simulations, we should go to an iterative solver.

Now, we observe the results obtained for different values of the penalty parameters γ_f and γ_s in three cases: (a) $\gamma_f = \gamma_s$, given in Tables B.3.1 to B.3.8, (b) γ_f vanishes and γ_s varies, summarized in Tables B.3.10 to B.3.18, and (c) γ_f is fixed equal to 10 and γ_s varies, reported in Tables B.3.19 to B.3.27. In each case, we have employed (i) quadratic polynomial elements on Mesh 1, depicted in Fig. II.5.2(a), (ii) cubic polynomial elements on Mesh 1, as well as (iii) cubic elements on Mesh 3 depicted in Fig. II.5.2(c), for the three frequencies f_1, f_R, f_2.

γ_f & γ_s	p	u_x	u_y
0	1.459	0.144	0.129
1	7.645	0.771	0.709
2	9.816E-002	2.448E-002	2.501E-002
3	8.321E-002	2.289E-002	2.536E-002
4	8.042E-002	2.265E-002	2.615E-002
5	8.017E-002	2.274E-002	2.687E-002
6	8.069E-002	2.291E-002	2.747E-002
7	8.143E-002	2.31E-002	2.795E-002
8	8.222E-002	2.329E-002	2.836E-002
9	8.297E-002	2.344E-002	2.869E-002
10	8.368E-002	2.359E-002	2.898E-002
15	8.64E-002	2.414E-002	2.993E-002
30	9.017E-002	2.484E-002	3.103E-002
40	9.130E-002	2.505E-002	3.134E-002
50	9.202E-002	2.518E-002	3.152E-002
60	9.252E-002	2.527E-002	3.165E-002
70	9.289E-002	2.533E-002	3.175E-002
80	9.317E-002	2.538E-002	3.182E-002
90	9.339E-002	2.542E-002	3.187E-002
100	9.357E-002	2.545E-002	3.192E-002
1000	9.508E-002	2.571E-002	3.228E-002
10000	9.523E-002	2.574E-002	3.232E-002
100000	9.525E-002	2.574E-002	3.232E-002
1000000	9.525E-002	2.574E-002	3.232E-002

Table B.3.1 – Disk-shaped elastic scatterer problem - Sensitivity of the L^2-relative error ($\%$) to the penalization parameters γ_f and γ_s using quadratic polynomial elements, curved boundary edges, and Mesh 1 for the frequency f_1 ($ka = 9.1735$).

γ_f & γ_s	p	u_x	u_y
0	1.521	0.449	0.285
1	7.71436	1.342	0.798
2	0.101	0.715	0.455
3	8.659E-002	0.845	0.537
4	8.409E-002	0.918	0.584
5	8.408E-002	0.966	0.614
6	8.476E-002	1.001	0.636
7	8.564E-002	1.027	0.653
8	8.653E-002	1.048	0.666
9	8.737E-002	1.064	0.676
10	8.815E-002	1.078	0.685
15	9.109E-002	1.121	0.712
30	9.510E-002	1.169	0.743
40	6.630E-002	1.182	0.751
50	9.706E-002	1.19	0.756
60	9.759E-002	1.195	0.76
70	9.798E-002	1.199	0.762
80	9.827E-002	1.202	0.764
90	9.850E-002	1.204	0.765
100	9.869E-002	1.206	0.766
1000	0.100	1.221	0.776
10000	0.100	1.222	0.777
100000	0.100	1.222	0.777
1000000	0.100	1.221	0.776

Table B.3.2 – Disk-shaped elastic scatterer problem - Sensitivity of the L^2-relative error ($\%$) to the penalization parameters γ_f and γ_s using quadratic polynomial elements, curved boundary edges, and Mesh 1 for the frequency f_R ($ka = 9.2572$).

γ_f & γ_s	p	u_x	u_y
0	1.668	0.144	0.169
1	7.499	0.840	0.998
2	0.103	2.345E-002	3.019E-002
3	8.727E-002	2.201E-002	3.101E-002
4	8.416E-002	2.182E-002	3.219E-002
5	8.379E-002	2.193E-002	3.318E-002
6	8.426E-002	2.210E-002	3.398E-002
7	8.498E-002	2.228E-002	3.462E-002
8	8.577E-002	2.246E-002	3.515E-002
9	8.653E-002	2.261E-002	3.559E-002
10	8.724E-002	2.275E-002	3.596E-002
15	9.002E-002	2.326E-002	3.718E-002
30	9.39E-002	2.390E-002	3.857E-002
40	9.507E-002	2.409E-002	3.895E-002
50	9.581E-002	2.421E-002	3.918E-002
60	9.633E-002	2.429E-002	3.934E-002
70	9.671E-002	2.435E-002	3.946E-002
80	9.7E-002	2.439E-002	3.955E-002
90	9.723E-002	2.442E-002	3.961E-002
100	9.741E-002	2.445E-002	3.967E-002
1000	9.898E-002	2.469E-002	4.012E-002
10000	9.914E-002	2.471E-002	4.017E-002
100000	9.916E-002	2.472E-002	4.017E-002
1000000	9.916E-002	2.471E-002	4.018E-002

Table B.3.3 – Disk-shaped elastic scatterer problem - Sensitivity of the L^2-relative error ($\%$) to the penalization parameters γ_f and γ_s using quadratic polynomial elements, curved boundary edges, and Mesh 1 for the frequency f_2 ($ka = 9.341$) .

γ_f & γ_s	p	u_x	u_y
0	0.193	6.395E-002	5.722E-002
1	0.121	8.623E-002	8.203E-002
2	0.31	6.147E-002	5.809E-002
3	4.283E-003	2.273E-003	1.802E-003
4	3.948E-003	2.214E-003	1.773E-003
5	3.851E-003	2.194E-003	1.778E-003
6	3.807E-003	2.185E-003	1.785E-003
7	3.783E-003	2.180E-003	1.793E-003
8	3.77E-003	2.178E-003	1.8E-003
9	3.762E-003	2.178E-003	1.806E-003
10	3.758E-003	2.178E-003	1.811E-003
20	3.763E-003	2.187E-003	1.842E-003
30	3.776E-003	2.193E-003	1.855E-003
40	3.786E-003	2.197E-003	1.862E-003
50	3.792E-003	2.2E-003	1.867E-003
60	3.797E-003	2.201E-003	1.87E-003
70	3.801E-003	2.203E-003	1.872E-003
80	3.804E-003	2.204E-003	1.874E-003
90	3.806E-003	2.205E-003	1.875E-003
100	3.808E-003	2.205E-003	1.876E-003
1000	3.826E-003	2.211E-003	1.885E-003
10000	3.828E-003	2.212E-003	1.887E-003
100000	3.828E-003	2.212E-003	1.887E-003
1000000	3.828E-003	2.212E-003	1.887E-003

Table B.3.4 – Disk-shaped elastic scatterer problem - Sensitivity of the L^2-relative error ($\%$) to the penalization parameters γ_f and γ_s using cubic polynomial elements, curved boundary edges, and Mesh 1 for the frequency f_1 ($ka = 9.1735$).

γ_f & γ_s	p	u_x	u_y
0	0.553	4.153E-002	2.537E-002
1	0.129	5.876E-002	3.751E-002
2	0.245	5.125E-002	3.267E-002
3	4.424E-003	3.713E-003	2.409E-003
4	4.08E-003	4.528E-003	2.931E-003
5	3.982E-003	4.964E-003	3.211E-003
6	3.937E-003	5.248E-003	3.392E-003
7	3.913E-003	5.45E-003	3.520E-003
8	3.9E-003	5.601E-003	3.617E-003
9	3.892E-003	5.719E-003	3.692E-003
10	3.888E-003	5.815E-003	3.753E-003
20	3.895E-003	6.250E-003	4.03E-003
30	3.909E-003	6.399E-003	4.124E-003
40	3.919E-003	6.475E-003	4.172E-003
50	3.926E-003	6.520E-003	4.201E-003
60	3.931E-003	6.551E-003	4.221E-003
70	3.935E-003	6.573E-003	4.235E-003
80	3.939E-003	6.589E-003	4.245E-003
90	3.941E-003	6.602E-003	4.253E-003
100	3.943E-003	6.612E-003	4.26E-003
1000	3.961E-003	6.696E-003	4.313E-003
10000	3.963E-003	6.698E-003	4.315E-003
100000	3.964E-003	6.726E-003	4.332E-003
1000000	3.964E-003	6.789E-003	4.370E-003

Table B.3.5 – Disk-shaped elastic scatterer problem - Sensitivity of the L^2-relative error ($\%$) to the penalization parameters γ_f and γ_s using cubic polynomial elements, curved boundary edges, and Mesh 1 for the frequency f_R ($ka = 9.2572$).

γ_f & γ_s	p	u_x	u_y
0	0.459	6.168E-002	7.235E-002
1	0.138	9.121E-002	0.114
2	0.212	5.616E-002	6.983E-002
3	4.559E-003	2.163E-003	2.206E-003
4	4.201E-003	2.108E-003	2.169E-003
5	4.098E-003	2.089E-003	2.176E-003
6	4.051E-003	2.08E-003	2.186E-003
7	4.027E-003	2.0758E-003	2.196E-003
8	4.013E-003	2.074E-003	2.205E-003
9	4.005E-003	2.073E-003	2.212E-003
10	4.001E-003	2.074E-003	2.219E-003
20	4.008E-003	2.082E-003	2.259E-003
30	4.022E-003	2.088E-003	2.276E-003
40	4.032E-003	2.092E-003	2.285E-003
50	4.04E-003	2.094E-003	2.291E-003
60	4.045E-003	2.096E-003	2.295E-003
70	4.049E-003	2.097E-003	2.298E-003
80	4.052E-003	2.098E-003	2.3E-003
90	4.055E-003	2.1E-003	2.301E-003
100	4.057E-003	2.1E-003	2.303E-003
1000	4.076E-003	2.105E-003	2.315E-003
10000	4.078E-003	2.106E-003	2.316E-003
100000	4.078E-003	2.106E-003	2.316E-003
1000000	4.078E-003	2.106E-003	2.316E-003

Table B.3.6 – Disk-shaped elastic scatterer problem - Sensitivity of the L^2-relative error ($\%$) to the penalization parameters γ_f and γ_s using cubic polynomial elements, curved boundary edges, and Mesh 1 for the frequency f_2 ($ka = 9.341$).

γ_f & γ_s	p	u_x	u_y
0	7.271	1.423	1.512
1	6.208	0.627	0.555
2	7.202	0.484	0.452
3	0.435	6.078E-002	6.509E-002
4	0.418	6.366E-002	7.072E-002
5	0.421	6.602E-002	7.441E-002
6	0.424	6.780E-002	7.701E-002
7	0.427	6.920E-002	7.896E-002
8	0.430	7.032E-002	8.047E-002
9	0.433	7.124E-002	8.17E-002
10	0.435	7.201E-002	8.270E-002
20	0.446	7.589E-002	8.763E-002
30	0.452	7.738E-002	8.946E-002
40	0.454	7.817E-002	9.042E-002
50	0.456	7.865E-002	9.101E-002
60	0.457	7.899E-002	9.141E-002
70	0.458	7.923E-002	9.17E-002
80	0.459	7.941E-002	9.192E-002
90	0.46	7.955E-002	9.209E-002
100	0.460	7.967E-002	9.223E-002
1000	0.464	8.063E-002	9.337E-002
10000	0.464	8.073E-002	9.349E-002
100000	0.465	8.074E-002	9.350E-002
1000000	0.465	8.074E-002	9.350E-002

Table B.3.7 – Disk-shaped elastic scatterer problem - Sensitivity of the L^2-relative error ($\%$) to the penalization parameters γ_f and γ_s using cubic polynomial elements, curved boundary edges, and Mesh 3 for the frequency f_1 ($ka = 9.1735$).

γ_f & γ_s	p	u_x	u_y
0	5.902	0.876	0.573
1	6.225	0.755	0.567
2	6.917	0.549	0.249
3	0.449	0.586	0.374
4	0.431	0.657	0.416
5	0.434	0.694	0.438
6	0.438	0.718	0.453
7	0.441	0.736	0.463
8	0.444	0.749	0.471
9	0.447	0.76	0.478
10	0.449	0.768	0.483
20	0.461	0.808	0.507
30	0.467	0.808	0.516
40	0.47	0.830	0.521
50	0.472	0.835	0.524
60	0.473	0.838	0.526
70	0.474	0.840	0.527
80	0.475	0.842	0.528
90	0.475	0.843	0.529
100	0.476	0.844	0.529
1000	0.480	0.853	0.535
10000	0.480	0.854	0.535
100000	0.481	0.854	0.535
1000000	0.481	0.854	0.535

Table B.3.8 – Disk-shaped elastic scatterer problem - Sensitivity of the L^2-relative error ($\%$) to the penalization parameters γ_f and γ_s using cubic polynomial elements, curved boundary edges, and Mesh 3 for the frequency f_R ($ka = 9.2572$).

γ_f & γ_s	p	u_x	u_y
0	5.041	1.020	1.415
1	6.442	0.617	0.68
2	6.591	0.443	0.560
3	0.461	6.022E-002	7.991E-002
4	0.443	6.392E-002	8.842E-002
5	0.446	6.654E-002	9.355E-002
6	0.45	6.842E-002	9.703E-002
7	0.453	6.984E-002	9.959E-002
8	0.456	7.096E-002	0.102
9	0.459	7.186E-002	0.103
10	0.461	7.261E-002	0.104
20	0.475	7.63E-002	0.111
30	0.480	7.768E-002	0.113
40	0.483	7.841E-002	0.114
50	0.485	7.886E-002	0.115
60	0.487	7.916E-002	0.116
70	0.488	7.938E-002	0.116
80	0.489	7.955E-002	0.116
90	0.489	7.968E-002	0.116
100	0.49	7.979E-002	0.117
1000	0.494	8.066E-002	0.118
10000	0.494	8.075E-002	0.118
100000	0.494	8.076E-002	0.118
1000000	0.494	8.076E-002	0.118

Table B.3.9 – Disk-shaped elastic scatterer problem - Sensitivity of the L^2-relative error ($\%$) to the penalization parameters γ_f and γ_s using cubic polynomial elements, curved boundary edges, and Mesh 3 for the frequency f_2 ($ka = 9.341$).

γ_s	p	u_x	u_y	Condition number
0	1.459	0.144	0.129	40,805
1	1.463	0.64	0.585	52,986
2	1.465	3.650E-002	3.469E-002	49,091
3	1.466	3.540E-002	3.519E-002	55,899
4	1.466	3.514E-002	3.586E-002	62,842
5	1.466	3.511E-002	3.644E-002	69,783
10	1.466	3.542E-002	3.814E-002	95,003
50	1.466	3.619E-002	4.024E-002	369,344
100	1.467	3.633E-002	4.056E-002	712,282
1000	1.467	3.647E-002	4.087E-002	6,885,207

Table B.3.10 – Disk-shaped elastic scatterer problem - Sensitivity of the L^2-relative error ($\%$) to the penalization parameter γ_s for $\gamma_f = 0$ using quadratic polynomial elements, curved boundary edges, and Mesh 1 for the frequency f_1 ($ka = 9.1735$).

γ_s	p	u_x	u_y	Condition number
0	1.521	0.449	0.285	1,812,797
1	1.518	1.310	0.838	2,091,925
2	1.521	0.691	0.441	3,137,660
3	1.521	0.825	0.526	4,338,652
4	1.521	0.900	0.574	5,557,654
5	1.521	0.95	0.605	6,729,608
10	1.521	1.064	0.678	12,864,800
50	1.521	1.178	0.751	60,848,613
100	1.521	1.195	0.761	120,826,088
1000	1.521	1.21	0.771	1,200,414,954

Table B.3.11 – Disk-shaped elastic scatterer problem - Sensitivity of the L^2-relative error ($\%$) to the penalization parameter γ_s for $\gamma_f = 0$ using quadratic polynomial elements, curved boundary edges, and Mesh 1 for the frequency f_R ($ka = 9.2572$).

γ_s	p	u_x	u_y	Condition number
0	1.668	0.144	0.169	67,516
1	1.669	0.668	0.805	80,149
2	1.663	3.636E-002	4.525E-002	113,470
3	1.662	3.539E-002	4.597E-002	151,916
4	1.662	3.518E-002	4.677E-002	191,533
5	0.162	3.518E-002	4.742E-002	231,202
10	1.661	3.552E-002	4.926E-002	429,561
50	1.661	3.629E-002	5.144E-002	2,016,444
100	1.661	3.643E-002	5.177E-002	4,000,050
1000	1.661	3.656E-002	5.209E-002	39,704,974

Table B.3.12 – Disk-shaped elastic scatterer problem - Sensitivity of the L^2-relative error ($\%$) to the penalization parameter γ_s for $\gamma_f = 0$ using quadratic polynomial elements, curved boundary edges, and Mesh 1 for the frequency f_2 ($ka = 9.341$).

γ_s	p	u_x	u_y	Condition number
0	0.193	6.395E-002	5.722E-002	445,507
1	0.195	9.067E-002	8.624E-002	453,489
2	0.193	6.1E-002	5.758E-002	483,618
3	0.195	2.342E-003	1.878E-003	455,550
4	0.195	2.283E-003	1.849E-003	464,890
5	0.195	2.263E-003	1.853E-003	474,343
10	0.195	2.246E-003	1.884E-003	521,630
50	0.195	2.266E-003	1.937E-003	899,720
100	0.195	2.272E-003	1.947E-003	1,372,300
1000	0.195	2.278E-003	1.956E-003	9,878,652

Table B.3.13 – Disk-shaped elastic scatterer problem - Sensitivity of the L^2-relative error ($\%$) to the penalization parameter γ_s for $\gamma_f = 0$ using cubic polynomial elements, curved boundary edges, and Mesh 1 for the frequency f_1 ($ka = 9.1735$).

γ_s	p	u_x	u_y	Condition number
0	0.553	4.153E-002	2.537E-002	5,765,515
1	0.56	6.220E-002	3.971E-002	5,899,058
2	0.547	4.94E-002	3.144E-002	7,045,859
3	0.557	3.545E-003	2.164E-003	8,403,097
4	0.557	4.296E-003	2.66E-003	9,795,700
5	0.557	4.71E-003	2.930E-003	11,203,404
10	0.557	5.533E-003	3.465E-003	18,544,252
50	0.557	6.228E-003	3.914E-003	77,263,397
100	0.557	6.32E-003	3.973E-003	150,325,266
1000	0.557	6.403-003	4.027E-003	1,476,746,193

Table B.3.14 – Disk-shaped elastic scatterer problem - Sensitivity of the L^2-relative error ($\%$) to the penalization parameter γ_s for $\gamma_f = 0$ using cubic polynomial elements, curved boundary edges, and Mesh 1 for the frequency f_R ($ka = 9.2572$).

γ_s	p	u_x	u_y	Condition number
0	0.46	6.168E-002	7.235E-002	1,044,132
1	0.464	9.496E-002	0.119	1,048,510
2	0.456	5.85E-002	7.278E-002	1,141,767
3	0.462	2.319E-003	2.509E-003	298,285
4	0.463	2.266E-003	2.471E-003	345,565
5	0.463	2.248E-003	2.473E-003	393,420
10	0.463	2.232E-003	2.505E-003	632,658
50	0.463	2.250E-003	2.564E-003	2,550,151
100	0.463	2.255E-003	2.574E-003	4,947,016
1000	0.463	2.261E-003	2.584E-003	48,090,588

Table B.3.15 – Disk-shaped elastic scatterer problem - Sensitivity of the L^2-relative error ($\%$) to the penalization parameter γ_s for $\gamma_f = 0$ using cubic polynomial elements, curved boundary edges, and Mesh 1 for the frequency f_2 ($ka = 9.341$).

γ_s	p	u_x	u_y	Condition number
0	7.271	1.423	1.512	18,744
1	7.784	0.742	0.714	18,655
2	7.647	1.001	0.962	21,859
3	8.076	0.673	0.657	24,156
4	8.124	0.674	0.659	27,687
5	8.152	0.675	0.66	31,316
10	8.21	0.677	0.662	49,830
50	8.260	0.679	0.664	198,010
100	8.267	0.679	0.664	383,304
1000	8.273	0.679	0.664	3,718,738

Table B.3.16 – Disk-shaped elastic scatterer problem - Sensitivity of the L^2-relative error ($\%$) to the penalization parameter γ_s for $\gamma_f = 0$ using cubic polynomial elements, curved boundary edges, and Mesh 3 for the frequency f_1 ($ka = 9.1735$).

γ_s	p	u_x	u_y	Condition number
0	5.902	0.876	0.573	687,947
1	6.305	0.98	0.586	679,513
2	6.119	0.851	0.501	808,510
3	6.530	0.934	0.568	916,839
4	6.569	0.981	0.599	1,061,190
5	6.592	1.007	0.616	1,208,776
10	6.641	1.061	0.652	1,951,396
50	6.684	1.11	0.684	7,946,735
100	6.69	1.117	0.689	15,433,598
1000	6.695	1.123	0.693	15,0199,166

Table B.3.17 – Disk-shaped elastic scatterer problem - Sensitivity of the L^2-relative error ($\%$) to the penalization parameter γ_s for $\gamma_f = 0$ using cubic polynomial elements, curved boundary edges, and Mesh 3 for the frequency f_R ($ka = 9.2572$).

γ_s	p	u_x	u_y	Condition number
0	5.041	1.020	1.415	24,604
1	5.335	0.545	0.699	24,652
2	5.253	0.715	0.941	28,754
3	5.484	0.461	0.608	33,057
4	5.509	0.463	0.61	38,107
5	5.524	0.464	0.611	43,249
10	5.555	0.466	0.615	69,098
50	5.583	0.469	0.618	276,180
100	5.587	0.469	0.618	535,062
1000	5.591	0.469	0.618	5,194,998

Table B.3.18 – Disk-shaped elastic scatterer problem - Sensitivity of the L^2-relative error (%) to the penalization parameter γ_s for $\gamma_f = 0$ using cubic polynomial elements, curved boundary edges, and Mesh 3 for the frequency f_2 ($ka = 9.341$).

γ_s	p	u_x	u_y	Condition number
0	6.728E-002	0.14	0.125	47,165
1	7.456E-002	0.640	0.585	49,224
2	7.935E-002	2.496E-002	2.533E-002	55,267
3	8.09E-002	2.337E-002	2.566E-002	62,090
4	8.178E-002	2.302E-002	2.638E-002	69,073
5	8.236E-002	2.301E-002	2.703E-002	76,074
10	8.368E-002	2.359E-002	2.898E-002	111,080
50	8.497E-002	2.486E-002	3.14E-002	393,590
100	8.515E-002	2.509E-002	3.177E-002	747,630
1000	8.532E-002	2.531E-002	3.213E-002	7,094,191

Table B.3.19 – Disk-shaped elastic scatterer problem - Sensitivity of the L^2-relative error (%) to the penalization parameter γ_s for $\gamma_f = 10$ using quadratic polynomial elements, curved boundary edges, and Mesh 1 for the frequency f_1 ($ka = 9.1735$).

The following observations are noteworthy:

- Outside the resonance frequency f_R, we improve the results by penalizing both the pressure and displacement fields. On Mesh 1, since the error is around 1% (resp. 0.1%) when employing quadratic (resp. cubic) approximations, the choice of $\gamma_f = \gamma_s = 0$ can be sufficient (see Tables B.3.1 and B.3.3 and Tables B.3.4 and B.3.6). Nevertheless, on the coarser Mesh 3, the error is about 5% for the pressure field when using $\gamma_f = 0$ (see Tables B.3.7 and B.3.9). In the presence of penalty terms, there is about one order of magnitude improvement. It seems that the results using cubic polynomial elements with penalization on the coarser Mesh 3 (see Tables B.3.7 and B.3.9) are as accurate as those obtained using cubic polynomial elements without penalization on Mesh 1 (see Tables B.3.4 and B.3.6). Let us consider another example

γ_s	p	u_x	u_y	Condition number
0	6.983E-002	0.462	0.292	1,839,643
1	7.942E-002	1.304	0.829	2,120,642
2	8.244E-002	0.705	0.448	3,171,656
3	8.445E-002	0.839	0.534	4,378,867
4	8.561E-002	0.914	0.581	5,604,164
5	8.638E-002	0.964	0.613	6,782,234
10	8.815E-002	1.078	0.685	12,949,177
50	8.992E-002	1.192	0.758	61,183,482
100	9.017E-002	1.209	0.768	121,474,079
1000	9.040E-002	1.224	0.778	1,206,699,127

Table B.3.20 – Disk-shaped elastic scatterer problem - Sensitivity of the L^2-relative error ($\%$) to the penalization parameter γ_s for $\gamma_f = 10$ using quadratic polynomial elements, curved boundary edges, and Mesh 1 for the frequency f_R ($ka = 9.2572$).

γ_s	p	u_x	u_y	Condition number
0	7.018E-002	0.139	0.163	48,623
1	7.782E-002	0.684	0.826	84,503
2	8.266E-002	2.402E-002	3.201E-002	117,987
3	8.43E-002	2.254E-002	3.239E-002	156,939
4	8.523E-002	2.223E-002	3.317E-002	196,784
5	8.584E-002	2.222E-002	3.387E-002	236,681
10	8.724E-002	2.275E-002	3.596E-002	436,180
50	8.861E-002	2.391E-002	3.851E-002	2,032,184
100	8.88E-002	2.412E-002	3.890E-002	4,027,192
1000	8.898E-002	2.432E-002	3.927E-002	39,937,348

Table B.3.21 – Disk-shaped elastic scatterer problem - Sensitivity of the L^2-relative error ($\%$) to the penalization parameter γ_s for $\gamma_f = 10$ using quadratic polynomial elements, curved boundary edges, and Mesh 1 for the frequency f_2 ($ka = 9.341$).

γ_s	p	u_x	u_y	Condition number
0	3.692E-003	6.452E-002	5.771E-002	87,290
1	3.729E-003	8.677E-002	8.254E-002	88,131
2	3.734E-003	6.223E-002	5.879E-002	94,304
3	3.741E-003	2.273E-003	1.801E-003	102,107
4	3.747E-003	2.214E-003	1.773E-003	110,885
5	3.751E-003	2.194E-003	1.777E-003	118,816
10	3.758E-003	2.178E-003	1.811E-003	161,473
50	3.764E-003	2.2E-003	1.867E-003	501,608
100	3.765E-003	2.205E-003	1.876E-003	925,953
1000	3.766E-003	2.211E-003	1.886E-003	8,557,984

Table B.3.22 – Disk-shaped elastic scatterer problem - Sensitivity of the L^2-relative error (%) to the penalization parameter γ_s for $\gamma_f = 10$ using cubic polynomial elements, curved boundary edges, and Mesh 1 for the frequency f_1 ($ka = 9.1735$).

γ_s	p	u_x	u_y	
0	3.803E-003	4.220E-002	2.575E-002	5,785,296
1	3.854E-003	5.916E-002	3.778E-002	5,918,825
2	3.848E-003	5.169E-002	3.295E-002	7,065,615
3	3.866E-003	3.689E-003	2.390E-003	8,363,171
4	3.875E-003	4.511E-003	2.918E-003	9,815,347
5	3.879E-003	4.952E-003	3.201E-003	112,22,999
10	3.888E-003	5.815E-003	3.753E-003	18,563,504
50	3.897E-003	6.535E-003	4.212E-003	77,280,349
100	3.898E-003	6.629E-003	4.272E-003	150,339,536
1000	3.899E-003	6.715E-003	4.327E-003	1,476,711,637

Table B.3.23 – Disk-shaped elastic scatterer problem - Sensitivity of the L^2-relative error (%) to the penalization parameter γ_s for $\gamma_f = 10$ using cubic polynomial elements, curved boundary edges, and Mesh 1 for the frequency f_R ($ka = 9.2572$).

γ_s	p	u_x	u_y	Condition number
0	3.93E-003	6.23E-002	7.308E-002	218,662
1	3.971E-003	9.165E-002	0.115	226,762
2	3.977E-003	5.663E-002	7.042E-002	258,315
3	3.982E-003	2.163E-003	2.205E-003	302,655
4	3.989E-003	2.108E-003	2.169E-003	349,933
5	3.993E-003	2.089E-003	2.176E-003	397,539
10	4.001E-003	2.074E-003	2.219E-003	637,205
50	4.008E-003	2.094E-003	2.291E-003	2,554,609
100	4.009E-003	2.1E-003	2.303E-003	4,951,364
1000	4.01E-003	2.105E-003	2.315E-003	48,092,949

Table B.3.24 – Disk-shaped elastic scatterer problem - Sensitivity of the L^2-relative error ($\%$) to the penalization parameter γ_s for $\gamma_f = 10$ using cubic polynomial elements, curved boundary edges, and Mesh 1 for the frequency f_2 ($ka = 9.341$).

γ_s	p	u_x	u_y	Condition number
0	0.428	0.582	0.6	25,080
1	0.431	0.331	0.295	25,559
2	0.432	0.320	0.337	29,443
3	0.432	7.007E-002	7.617E-002	34,253
4	0.433	6.99E-002	7.792E-002	39,441
5	0.434	7.029E-002	7.926E-002 -002	44,717
10	0.435	7.201E-002	8.270E-002	71,193
50	0.436	7.454E-002	8.657E-002	284,674
100	0.436	7.496E-002	8.716E-002	551,159
1000	0.436	7.536E-002	8.771E-002	5,347,900

Table B.3.25 – Disk-shaped elastic scatterer problem - Sensitivity of the L^2-relative error ($\%$) to the penalization parameter γ_s for $\gamma_f = 10$ using cubic polynomial elements, curved boundary edges, and Mesh 3 for the frequency f_1 ($ka = 9.1735$).

γ_s	p	u_x	u_y	Condition number
0	0.442	0.507	0.334	838,322
1	0.446	0.657	0.403	848,754
2	0.445	0.462	0.290	992,025
3	0.446	0.617	0.386	1,159,156
4	0.447	0.674	0.422	1,344,199
5	0.448	0.704	0.442	1,532,768
10	0.449	0.768	0.483	2,479,570
50	0.450	0.827	0.520	1,0115,314
100	0.450	0.835	0.526	19,649,383
1000	0.450	0.843	0.530	191,263,135

Table B.3.26 – Disk-shaped elastic scatterer problem - Sensitivity of the L^2-relative error (%) to the penalization parameter γ_s for $\gamma_f = 10$ using cubic polynomial elements, curved boundary edges, and Mesh 3 for the frequency f_R ($ka = 9.2572$).

γ_s	p	u_x	u_y	Condition number
0	0.455	0.563	0.767	28,042
1	0.459	0.301	0.358	28,648
2	0.458	0.314	2.501E-002	33,082
3	0.459	7.021E-002	9.801E-002	38,775
4	0.46	7.036E-002	9.950E-002	44,718
5	0.460	7.084E-002	0.101	50,751
10	0.461	7.261E-002	0.104	81,018
50	0.462	7.503E-002	0.109	323,210
100	0.462	7.542E-002	0.109	625,950
1000	0.463	7.58E-002	0.11	6,075,273

Table B.3.27 – Disk-shaped elastic scatterer problem - Sensitivity of the L^2-relative error (%) to the penalization parameter γ_s for $\gamma_f = 10$ using cubic polynomial elements, curved boundary edges, and Mesh 3 for the frequency f_2 ($ka = 9.341$).

with the non-resonant frequency f_1. In Table B.3.28, we compare the results obtained on Mesh 1 when employing $\gamma_s = \gamma_f = 10$ to those obtained when refining Mesh 1, and using no penalization, i.e. $\gamma_s = \gamma_f = 0$. Table B.3.28 indicates that the error results are better using

Mesh 1 refinement level	γ_f & γ_s	p	u_x	u_y
0	10	7.734E-003	3.95E-002	3.681E-002
1	0	3.758E-003	2.178E-003	1.811E-003

Table B.3.28 – Disk-shaped elastic scatterer problem - Sensitivity of the L^2-relative error (%) to the penalization parameters γ_f and γ_s using cubic polynomial elements, curved boundary edges, and a different refinement level of Mesh 1 for the frequency f_1.

Mesh 1 than its refinement thanks to the use of the penalization. Therefore, to some extent, the penalization appears to be useful in order to avoid a mesh refinement and to get a more reasonable approximation of the scattered fields.

- When considering the Jones frequency, we always improve the accuracy when penalizing the pressure field since we restore the stability in the fluid domain, but we do not gain on the displacement field because the interior problem is anyway ill-posed, as indicated in Tables B.3.2, B.3.5 and B.3.8.
- Tables B.3.10 to B.3.27 support the idea that the presence of the penalty term improves the accuracy for the fluid pressure for all the three frequencies. They also illustrates an accuracy improvement of the error associated to the displacement field in the presence of the elastic penalty term, except at the Jones frequency. The obtained results suggest that one can use any values for γ_f and γ_s without affecting the accuracy of IPDG, provided that these values remain larger than $\frac{1}{4}p(p+1)$.
- Using cubic approximations on the fine Mesh 1, the condition number deteriorates in the absence of the penalty term in the fluid part, i.e. $\gamma_f = 0$, in comparison with the results obtained when $\gamma_f = 10$ for both frequencies f_1 and f_2, as indicated in Tables B.3.13 and B.3.15 and Tables B.3.22 and B.3.24. However, this remark seems not to be observable neither for quadratic elements on Mesh 1 (see Tables B.3.10 and B.3.12 and Tables B.3.19 and B.3.21), nor for the results obtained on the coarser Mesh 3 (see Tables B.3.16 and B.3.18 and Tables B.3.25 and B.3.27). In the case of the resonance frequency f_R, the penalization of the pressure field does not change the condition number, it is as spoiled in the absence as in the presence of the penalty term (see Tables B.3.14 and B.3.23). Note that a too large penalty parameter can lead to a significant deterioration of the condition number in all cases.

Part II

The Inverse Obstacle Problem

Chapter III

Characterization of the Fréchet derivative of the elasto-acoustic field with respect to Lipschitz domains

In this chapter we establish the continuous Fréchet differentiability of the elasto-acoustic field with respect to Lipschitz continuous deformation of the shape of an elastic scatterer. We then characterize the derivative as a solution of a direct elasto-acoustic-type problem. The proof only assumes the boundary to be Lipschitz continuous and therefore can include sharp corners. We then characterize the derivative of the elasto-acoustic scattered field as a solution of a direct elasto-acoustic-type problem. The proof of this characterization is rigorously given for smooth scatterers of class $\mathcal{C}^2$, as well as for curvilinear polygonal or polyhedral domains of class $\mathcal{C}^{1,1}$. We point out the issues that occur when considering classes of more general Lipschitz domains. Such a characterization has the potential to advance the state-of-the-art of the solution of inverse elasto-acoustic scattering problems.

III.1 Introduction

The determination of the shape of an obstacle from its effects on known acoustic or electromagnetic waves is an important problem in many technologies such as sonar, radar, geophysical exploration, medical imaging and non destructive testing. This inverse scattering problem is difficult to solve, especially from a numerical point of view because it is ill-posed and nonlinear. Its investigation requires as a prerequisite the fundamental understanding of the theory for the associated direct scattering problem, and the mastery of the corresponding numerical solution methods. The solution of this problem by regularized Newton-like methods incurs, at each iteration, the solution of a linear system whose entries are the Fréchet derivatives of the elasto-acoustic field with respect to the

parameters representing the surface of the scatterer. Ensuring the stability, fast convergence and computational efficiency of these iterative methods calls for computing these Fréchet derivatives with a greater robustness and a higher level of accuracy than possible with finite differences. To this effect, it is noted that the Fréchet derivative of the acoustic scattered field with respect to the shape of a rigid obstacle can be characterized as the solution of a direct acoustic scattering problem which differs from the direct acoustic scattering problem only in the boundary conditions [39, 41]. Our goal is to employ the techniques used in [39, 41] to extend the sensitivity analysis to the case of penetrable elastic scatterers immersed in a fluid.
The analysis of the dependence of the scattered field with respect to the shape of a given obstacle has received in the past twenty years a great deal of attention by both the mathematicians and the engineers community. Various approaches have been suggested to analyze the case of acoustic problems for rigid (non penetrable) scatterers with different regularity requirements on the shape of the scatterers as well as on the considered perturbations [80, 83, 96, 122, 124]. The case of "pure" elastic problems has been studied by Charalambopoulos [25], whereas the class of electromagnetic problems has been addressed by several authors including Potthast [123], Haddar and Kress [75], and Costabel and Le Louër [33, 34, 98].

In this chapter, we propose to extend the result of [39, 41] to the case of elastic scatterers [93] by analyzing the dependence of the solution of a direct elasto-acoustic scattering problem on the domain of the obstacle. Such a characterization has been done in [41] for the solution of the associated inverse problem, but the whole approach is based on the variational formulation of the boundary value problems involved. In this paper, we first establish the continuous Fréchet differentiability of the elasto-acoustic field with respect to the shape of elastic scatterers. Our proof is based on the implicit function theorem and the standard trace theorems. It assumes the boundary of the considered elastic scatterer to be only continuous Lipschitzian, and therefore can include sharp corners. The relevant perturbations are continuous. Moreover, compared to paper [39], a novelty for the acoustic part lies in the fact that we formulate the problem into a weighted Sobolev space for the pressure field, which is a natural framework for the exterior Helmholtz problem, since it incorporates explicitly the radiation condition. Secondly, we then prove that the Fréchet derivative of the elasto-acoustic scattered field can be characterized as a solution of the same direct elasto-acoustic scattering problem but with different transmission conditions on the surface of the considered scatterer. Such a result is obtained by using of the chain rule of derivation, also valid in the infinite-dimensional spaces. The main drawback in the case of Lipschitz domains is the lack of proof for surjectivity of the trace operators in particular for the elastic field. That is why we have organized our work by considering first regular domains, and then $C^{1,1}$ polyhedra for which we were able to fully characterize the derivative. We then consider the

case of a $C^{0,1}$ polyhedron for which we were able to give a sense to each term related to the pressure field. Nevertheless, even in that case which is more regular than for general Lipschitz domains, we were faced to a lack of surjectivity. In the case of a Lipschitz domain, we have obtained a characterization of a trace of high order but obviously, as in the case of a $C^{0,1}$ polyhedral domain, we did not obtain the full characterization. However, our formal characterization being justified for quite general domains, at least from a numerical point of view where the domain is a mesh, we propose to use it for general Lipschitz domains and postpone a rigorous construction that we hope possible.
The computational implication of this theoretical characterization is that, at each Newton iteration, one need to solve a *single* system of equations with N_p right-hand-sides; N_p being the number of parameters representing the surface of the considered scatterer.
This result has the potential to advance the state-of-the-art of the solution of inverse elasto-acoustic scattering problems. Furthermore, the methodology adopted for characterizing the Fréchet derivatives with respect to the shape of an elastic scatterer can also be applied to analyze the Fréchet differentiability with respect to its material properties. This is relevant to many inverse problems where not only the shape of an obstacle is of interest but also, and often more importantly, its structure.

The remainder of this paper is organized as follows. In Section III.2, we first specify the nomenclature and assumptions used in this work, then formulate the focus elasto-acoustic scattering problem [93]. In Section III.3, we establish in a first part the continuous Fréchet differentiability of the elasto-acoustic scattered field with respect to the domain of the obstacle. In the second part of Section III.3, we state as a theorem the characterization of the derivative of the scattered field with respect to the domain as the solution of a direct elasto-acoustic-type problem. We finally draw our conclusion in Section III.4.

III.2 Problem Statement

III.2.1 Nomenclature and Assumptions

Throughout this paper, we adopt the following notations and assumptions:

- Ω^s is a bounded domain of $\mathbb{R}^n$ representing an elastic obstacle.
- $\Omega^f = \mathbb{R}^n \setminus \overline{\Omega}^s$ is the homogeneous inviscid (fluid) medium surrounding the elastic domain.
- Γ is the boundary of Ω^s and is assumed to be Lipschitz continuous. Nevertheless, some drawbacks may occur in the general Lipschitz domains. In some cases, we will thus restrict our

study to polygonal or polyhedral domains. We will then adopt the notations of Grisvard [70] and Ciarlet et *al* [8–10].

- $|\cdot|$ is the Euclidean norm in $\mathbb{R}^n$.
- x is a point of $\mathbb{R}^n$, understood as a column vector and $r = |x|$ is the distance from an origin point to x.
- d is a unit vector representing the propagation direction of the incident plane wave.
- ν is the outward normal to Γ and $\dfrac{\partial}{\partial \nu}$ is the normal derivative operator.
- $S^1 = \{x \in \mathbb{R}^n | |x| = 1\}$ is the unit sphere in $\mathbb{R}^n$.
- ∇ is the gradient operator in $\mathbb{R}^n$. The gradient of a scalar function is a column vector field. We adopt the notations from Simon-Murat [115] for the Jacobian matrix. The gradient of a column vector field is a matrix, where the partial derivatives are aligned in rows. For a row vector field, we also define the gradient as a matrix, where the partial derivatives are put in columns.
- $\nabla\cdot$ is the divergence operator in $\mathbb{R}^n$.
- Δ is the Laplace operator in $\mathbb{R}^n$.
- $\mathcal{D}(E)$ is the space of infinitely differentiable functions with compact support in E.
- $\mathcal{D}'(E)$ is the standard space of distributions.
- $\mathcal{C}^{0,1}(E)$ is the set of all Lipschitz continuous functions on $E \subset \mathbb{R}^n$, equipped with the norm $\|\phi\|_{\mathcal{C}^{0,1}(E)} = \|\phi\|_{\mathcal{C}^0(E)} + |\phi|_{Lip(E)}$, where $|\phi|_{Lip} = \sup_{x_1 \neq x_2} |\phi(x_1) - \phi(x_2)|/|x_1 - x_2|$.
- $\mathcal{C}^{1,1}(E)$ is the set of all continuous functions ϕ on $E \subset \mathbb{R}^n$, with Lipschitz continuous derivatives ϕ' , equipped with the norm $\|\phi\|_{\mathcal{C}^{1,1}(E)} = \|\phi\|_{\mathcal{C}^1(E)} + |\phi'|_{Lip(E)}$.
- $\mathcal{C}^1(E)$ is the space of functions with continuous derivatives on $E \subset \mathbb{R}^n$.
- $\mathcal{C}^m(E)$ is the space of functions with continuous derivatives up to order m on $E \subset \mathbb{R}^n$, with the maximum norm of all derivatives.
- $L^2(E)$ is the standard Lebesgue space and $H^1(E)$ is Sobolev space [3].
- $L^2_{loc}(E)$ is the space of functions that are in $L^2(D)$ for any open bounded set D in E.
- For some tensor σ, we define $D(\nabla \cdot \sigma, \Omega^s) = \{w; w \in (L^2(\Omega^s))^n \text{ and } \nabla \cdot \sigma(w) \in (L^2(\Omega^s))^n\}$.
- $D(\Delta, \Omega^f) = \{t; t \in L^2_{loc}(\Omega^f) \text{ and } \Delta t \in L^2_{loc}(\Omega^f)\}$.

- $H(\nabla\cdot, E) = \{w; w \in (L^2(E))^n \text{ and } \nabla \cdot w \in L^2(E)\}$, equipped with the norm:

$$\|w\|_{H_\nabla\cdot(E)} = \left(\|w\|^2_{L^2(E)} + \|\nabla\cdot\ w\|^2_{L^2(E)}\right)^{1/2}.$$

- $H_{loc}(\nabla\cdot, E) = \{w; w \in (L^2_{loc}(E))^n \text{ and } \nabla \cdot w \in L^2_{loc}(E)\}$
- Let $\rho(r) := 1 + r^2$. We introduce the weighted Sobolev space:

$$\mathcal{H}(E) = \{t; \frac{t}{\rho^{1/2}} \in L^2(E), \frac{\nabla t}{\rho^{1/2}} \in (L^2(E))^n \text{ and } \frac{\partial t}{\partial r} - ikt \in L^2(E)\}.$$

- The test space associated to the trial space $\mathcal{H}(E)$ is defined as:

$$\mathcal{H}_T(E) = \{t; \rho^{1/2}t \in L^2(E), \rho^{1/2}\nabla t \in (L^2(E))^n \text{ and } \frac{\partial t}{\partial r} - ikt \in L^2(E)\}.$$

  We refer to [118, 130] for the definition of these Banach spaces and their associated dual spaces. Moreover, classical trace theorems, as well as Green's formula, exist in these spaces [130].

- $H^s(\Gamma)$ are the trace Sobolev spaces.
- $I : \mathbb{R}^n \to \mathbb{R}^n$ is the identity mapping or the unitary matrix.
- $\theta : \mathbb{R}^n \to \mathbb{R}^n$ denotes an admissible perturbation in $(\mathcal{C}^1(\mathbb{R}^n))^n$. It is assumed to have a compact support and to be small enough so that $I + \theta$ is bijective in $\mathbb{R}^n$, for example $\|\theta\|_{(\mathcal{C}^1(\mathbb{R}^n))^n} < \frac{1}{2}$.
- $\Omega^\bullet_\theta = (I + \theta)\Omega^\bullet$ is an admissible perturbed configuration of the reference domain $\Omega^\bullet$; $\bullet = s, f$. Note that $\Omega^\bullet_0 = \Omega^\bullet$.
- Γ_θ is the boundary of Ω^s_θ and ν_θ is the outward normal to Γ_θ. Note that $\Gamma_0 = \Gamma$.
- $[\theta']$ is the Jacobian matrix of θ. Hence $[\theta'] = \left(\frac{\partial \theta_l}{\partial x_j}\right)_{1\le l,j\le n}$.
- $[\theta']^t$ is the transpose Jacobian matrix of θ.
- Tr_Γ is the trace operator on Γ.
- D_1, and D_2 are two bounded domains with smooth boundaries, such that

$$\overline{D}_1 \subset \Omega^s \subset \overline{\Omega}^s \subset D_2. \tag{III.2.1}$$

- For normed spaces, the symbol $\hookrightarrow$ denotes continuous injection.

- Furthermore, in this paper we manipulate a couple of functions (u_θ, p_θ) that is defined on open sets that vary with θ. Hence, these functions cannot be differentiated with respect to θ in the classical sense. For this reason, we follow [115, 133] and adopt the following concept of a local derivative. We say that $\theta \mapsto w_\theta$ is locally differentiable if for every open set D strictly included in Ω^s and strictly included in Ω^s_θ the restriction of w_θ to D is differentiable. Similarly, in the unbounded domain, we say that $\theta \mapsto t_\theta$ is locally differentiable if for every open set D strictly included in Ω^f and strictly included in Ω^f_θ the restriction of t_θ to D is differentiable. We denote by $(w', t') = ((\partial w_\theta/\partial\theta)(0)h, (\partial t_\theta/\partial\theta)(0)h)$ the local derivative of (w_θ, t_θ) at $\theta = 0$ and in the direction h, where h is a vector field satisfying $h \in (\mathcal{C}^2(\mathbb{R}^n))^n$.
  More generally, $\mathcal{F}'(f)h$ is the derivative of $\mathcal{F}$ at f in the direction h, and for $\mathcal{F} = \mathcal{F}(f, g)$, $\mathcal{F}'_f(a, b)h$ is the derivative with respect to the argument f at (a, b) in the direction h.

III.2.2 Mathematical Formulation of the Problem

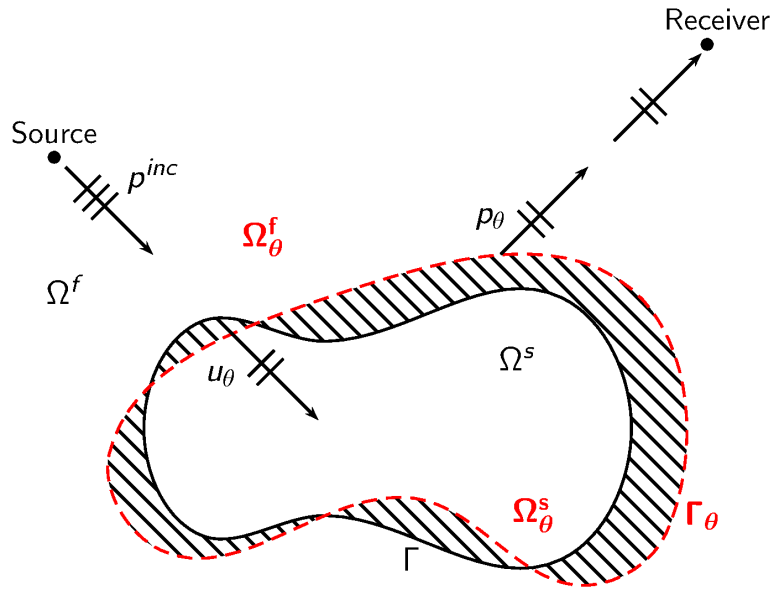

Figure III.2.1 – Problem statement in an admissible perturbed configuration of the reference domain.

The scattering of a time-harmonic acoustic wave by an elastic obstacle Ω^s_θ embedded in a homogeneous medium Ω^f_θ, depicted in Figure III.2.1, can be formulated as the following boundary value

problem [93]:

$$\text{BVP} \quad \begin{cases} \nabla \cdot \sigma(u_\theta) + \omega^2 \rho_s u_\theta = 0 & \text{in } \Omega_\theta^s \quad \text{(III.2.2)} \\ \Delta p_\theta + k^2 p_\theta = 0 & \text{in } \Omega_\theta^f \quad \text{(III.2.3)} \\ \tau(u_\theta) = -p_\theta \nu_\theta - g\nu_\theta & \text{on } \Gamma_\theta \quad \text{(III.2.4)} \\ \omega^2 \rho_f u_\theta \cdot \nu_\theta = \dfrac{\partial p_\theta}{\partial \nu_\theta} + \dfrac{\partial g}{\partial \nu_\theta} & \text{on } \Gamma_\theta \quad \text{(III.2.5)} \\ \lim\limits_{r \to +\infty} r^{(n-1)/2} \left(\dfrac{\partial p_\theta}{\partial r} - \mathrm{i}k p_\theta \right) = 0. & \quad \text{(III.2.6)} \end{cases}$$

where the pair (u_θ, p_θ) represents the elasto-acoustic scattered field, that is p_θ is the fluid pressure in Ω_θ^f whereas u_θ is the displacement field in Ω_θ^s.

$g = p^{inc} = \mathrm{e}^{\mathrm{i}\frac{\omega}{c_f} x \cdot d}$ corresponds to the given incident plane wave.

ω is the circular frequency and c_f is the speed of sound in the fluid Ω_θ^f. ω and c_f are associated with the wavenumber k by $k = \dfrac{\omega}{c_f}$. ρ_f and ρ_s are positive real numbers denoting respectively the density of the fluid Ω_θ^f and that of the scatterer Ω_θ^s.

σ is the stress tensor related to the strain tensor ε by Hooke's law:

$$\sigma_{lm} = C_{lmjn} \varepsilon_{jn} \quad \text{(III.2.7)}$$

where C_{lmjn} is a fourth order elastic stiffness tensor, such that $C_{lmjn} = C_{mljn} = C_{jnlm}$ and $C_{lmjn}\epsilon_{lm}\epsilon_{jn} \geq \alpha \sum\limits_{lm} \epsilon_{lm}^2$ for all symmetrical second order tensor ϵ. Note that, in the case of an isotropic medium, it is invariant under rotations and reflections [93], and reads as:

$$C_{lmjn} = \lambda \delta_{lm} \delta_{jn} + \mu(\delta_{lj}\delta_{mn} + \delta_{ln}\delta_{mj})$$

where λ, μ are the Lamé coefficients.

Recall that the strain tensor ε is related to the displacement field u_θ by:

$$\varepsilon(u_\theta) = \frac{1}{2} \left(\nabla u_\theta + (\nabla u_\theta)^t \right).$$

Last, τ denotes the traction vector on the surface of the scatterer Ω_θ^s, that is,

$$\tau(u_\theta) = \sigma(u_\theta)\nu_\theta.$$

In this paper, we also consider the derivative of the acoustic far-field pattern. We remind the reader that the scattering amplitude $p_{\theta,\infty}$ of the acoustic scattered field p_θ that is the solution of the BVP is defined on the unit sphere S^1 and is obtained from the asymptotic behavior of p_θ [28]: as follows:

$$p_\theta = \frac{\mathrm{e}^{\mathrm{i}kr}}{r^{(n-1)/2}}\left(p_{\theta,\infty}\left(\frac{x}{r}\right) + O\left(\frac{1}{r}\right)\right); \qquad r = \|x\|_2 \to +\infty. \tag{III.2.8}$$

Observe that the direct problem BVP consists in the standard exterior Helmholtz problem Eqs. (III.2.3) and (III.2.6), coupled with the elastodynamic equation Eq. (III.2.2) governing the equilibrium of an elastic scatterer via the transmission conditions Eqs. (III.2.4) and (III.2.5). The first one is a dynamic interface condition whereas the second one is a kinematic interface condition.
This boundary value problem has been investigated mathematically and results pertaining to the existence, uniqueness and regularity can be found in [79, 92, 93, 104], among others, and Chapter I.

III.3 Main results

In this section, we present two main results of this study. The proof of these two results is based on the ideas and the techniques used in [39, 41] for the exterior Helmholtz problems.

III.3.1 Continuous differentiability of the scattered field

In this section, we establish the continuous Fréchet differentiability of the elasto-acoustic scattered field with respect to the domain of the given obstacle.
The main idea is to reformulate the BVP such that the scattered field is a zero of a nonlinear operator in Banach spaces which do not change with the shape deformation θ and then apply the Implicit Function Theorem (cf, e.g., [13]).

III.3.1.1 Transported solution and variational setting

We define the transported solution (v_θ, q_θ) in $\Omega^s \times \Omega^f$ by:

$$(v_\theta, q_\theta) = (u_\theta \circ (I+\theta), p_\theta \circ (I+\theta)) \tag{III.3.1}$$

where (u_θ, p_θ) is a solution to the problem BVP.
We notice that since θ has a compact support, we have $p_\theta(x) = q_\theta(x)$ for all x such that $\theta(x) = 0$. Therefore, q_θ satisfies the Sommerfeld outgoing radiation condition Eq. (III.2.6) in BVP.

Then, the first step consists in the construction of an appropriate variational setting. Our analysis will involve the use of the three following Banach spaces.

- Let the Banach space X be given by

$$X = \{\theta \in \left(\mathcal{C}^1(\mathbb{R}^n)\right)^n \text{ such that } supp\,\theta \subset \overline{D_2} \setminus D_1\}$$

  and equipped with the standard norm in $(\mathcal{C}^1(\mathbb{R}^n))^n$.

  We assume that ω is not a Jones frequency for the set of admissible perturbations X. In other words, we suppose that ω is not a resonance frequency for an initial configuration, and we assume that ω remains a non resonance frequency in the neighborhood of the admissible deformations. Actually, the Jones frequencies are very rare and form a discrete spectrum. Therefore, if the geometry under consideration may admit Jones modes, then the analysis is valid except for at most a discrete set of frequencies. Note that, in that case, we can set onto a slightly perturbed frequency, which would not be a Jones frequency, and then use a continuity argument with respect to frequency.
- We define the Banach space Y that is invariant with respect to shape perturbations θ. This space is defined as a product space $Y = Y_1 \times Y_2$ where

$$\begin{aligned} Y_1 &= \{v \text{ such that } \|v\|_{Y_1} < +\infty\}, \\ Y_2 &= \{q \text{ such that } \|q\|_{Y_2} < +\infty\} \end{aligned}$$

  and

$$\begin{aligned} \|v\|_{Y_1} &= \|v\|_{(H^1(\Omega^s))^n}, \\ \|q\|_{Y_2} &= \|q\|_{\mathcal{H}(\Omega^f)}. \end{aligned}$$

  We notice that this space naturally takes into account the decay condition for the pressure field, given by the Sommerfeld outgoing radiation condition Eq. (III.2.6) in BVP.
- Moreover, the Banach space Z is defined as follows:

$$Z = Z_1 \times Z_2$$

where

$$Z_1 = \{(z_1,\varphi_1), z_1 \in \Big((H^1(\Omega^s))^n\Big)', \quad \varphi_1 \in \Big(H^{-1/2}(\Gamma)\Big)^n\},$$

and

$$Z_2 = \{((z_2,\varphi_2), z_2 \in (\mathcal{H}_T(\Omega^f))', \quad \varphi_2 \in H^{-1/2}(\Gamma)\}.$$

Note that both spaces Z_1 and Z_2 are equipped with the graph norm.

III.3.1.2 Announcement of the first theorem and preliminary lemmas

We next state our first result.

Theorem III.3.1.1 *The mapping $\theta \mapsto (v_\theta, q_\theta)$, where (v_θ, q_θ) is the transported solution (III.3.1) of the BVP, is continuously Fréchet differentiable at $\theta = 0$ from the Banach space X to the Banach space Y.*

The key idea of the proof of this first theorem is to reformulate the boundary problem as an operator equation defined on a Banach space that is invariant with respect to shape perturbations θ, and then apply the Implicit Function Theorem. In order to establish this proof, we thus need to derive some preliminary lemmas.
The first one allows us to rewrite the BVP as an operator equation of the form $\mathcal{F}(\theta, v, q) = 0$.

Lemma 4 *The BVP is equivalent to $\mathcal{F}(\theta, w_\theta) = 0$ where $w_\theta = (v_\theta, q_\theta)$. Moreover, $\mathcal{F} : X \times Y \longrightarrow Z$ is continuous on a neighborhood of $(0, w_0)$ from $X \times Y$ to Z, and its Fréchet derivatives $\mathcal{F}'_\theta$ and $\mathcal{F}'_w$ exist and are continuous on a neighborhood of $(0, w_0)$ in $X \times Y$.*

The proof of this lemma follows the methodology employed in [39] for the exterior Helmholtz problem. It especially makes use of the auxiliary results provided in Appendix A in [39]. This Appendix contains some auxiliary propositions on Fréchet differentiability of operators defined by composition, known as Nemytski operators [95]. It also includes some properties of the transformation of domains with Lipschitz boundary, and the associated change of variable in boundary integral by a Lipschitz continuous mapping.

Proof We assume $\|\theta\|_{(\mathcal{C}^1(\mathbb{R}^n))^n}$ is sufficiently small so that $(I+\theta)^{-1}$ exists and Ω^s_θ has a Lipschitz boundary (see Lemma A.3 in [39]).

Using the variational formulation, we aim at reformulating the coupled problem BVP as an operator equation of the form:

$$\mathcal{F}(\theta, v_\theta, q_\theta) = 0.$$

For simplicity, we omit the complex conjugate notation on the test functions. The weak form of the BVP is:

$$\begin{aligned} \int_{\Omega_\theta^s} \left(\nabla \cdot \sigma(u_\theta) + \omega^2 \rho_s u_\theta\right) \psi \, d\mu = 0 \qquad & \forall \psi \in (\mathcal{D}(\overline{\Omega}_\theta^s))^n \\ \int_{\Omega_\theta^f} \left(\Delta p_\theta + k^2 p_\theta\right) \Psi \, d\mu = 0 \qquad & \forall \Psi \in \mathcal{D}(\mathbb{R}^n \setminus \Omega_\theta^s). \end{aligned}$$

Or, equivalently, by applying Green's formula, for all $(\psi, \Psi) \in (\mathcal{D}(\overline{\Omega}_\theta^s))^n \times \mathcal{D}(\mathbb{R}^n \setminus \Omega_\theta^s)$,

$$\begin{aligned} \int_{\Omega_\theta^s} \sigma(u_\theta) : \nabla \psi \, d\mu - \int_{\Omega_\theta^s} \omega^2 \rho_s u_\theta \psi \, d\mu - \langle \sigma(u_\theta) \cdot \nu_\theta, \psi \rangle_{-1/2,1/2} = 0, \\ \int_{\Omega_\theta^f} \nabla p_\theta \cdot \nabla \Psi \, d\mu - \int_{\Omega_\theta^f} k^2 p_\theta \Psi \, d\mu - \langle \frac{\partial p_\theta}{\partial \nu_\theta}, \Psi \rangle_{-1/2,1/2} = 0. \end{aligned}$$

Then, by plugging the interface conditions into each variational equation, we get the weak formulation, for all $(\psi, \Psi) \in (\mathcal{D}(\overline{\Omega}_\theta^s))^n \times \mathcal{D}(\mathbb{R}^n \setminus \Omega_\theta^s)$,

$$\begin{aligned} \int_{\Omega_\theta^s} \sigma(u_\theta) : \nabla \psi \, d\mu - \int_{\Omega_\theta^s} \omega^2 \rho_s u_\theta \psi \, d\mu + \langle p_\theta \nu_\theta + g \nu_\theta, \psi \rangle_{-1/2,1/2} = 0 \\ \int_{\Omega_\theta^f} \nabla p_\theta \cdot \nabla \Psi \, d\mu - \int_{\Omega_\theta^f} k^2 p_\theta \Psi \, d\mu + \langle \frac{\partial g}{\partial \nu_\theta} - \omega^2 \rho_f u_\theta \cdot \nu_\theta, \Psi \rangle_{-1/2,1/2} = 0 \end{aligned}$$

with

$$\lim_{r \to +\infty} r^{(n-1)/2} \left(\frac{\partial p_\theta}{\partial r} - \mathrm{i} k p_\theta \right) = 0.$$

Moreover, using Hooke's law given by Eq. (III.2.7), we obtain:

$$\int_{\Omega_\theta^s} \sum_{lmjn} C_{lmjn} \varepsilon_{jn}(u_\theta) \frac{\partial \psi_l}{\partial x_m} \, d\mu - \int_{\Omega_\theta^s} \omega^2 \rho_s u_\theta \psi \, d\mu + \langle p_\theta \nu_\theta + g \nu_\theta, \psi \rangle_{-1/2,1/2} = 0 \qquad \text{(III.3.2)}$$

$$\int_{\Omega_\theta^f} \nabla p_\theta \cdot \nabla \Psi \, d\mu - \int_{\Omega_\theta^f} k^2 p_\theta \Psi \, d\mu + \langle \frac{\partial g}{\partial \nu_\theta} - \omega^2 \rho_f u_\theta \cdot \nu_\theta, \Psi \rangle_{-1/2,1/2} = 0 \qquad \text{(III.3.3)}$$

with

$$\lim_{r\to+\infty} r^{(n-1)/2}\left(\frac{\partial p_\theta}{\partial r} - \mathrm{i}kp_\theta\right) = 0.$$

Let $P_\theta = (I+\theta)'$, and e_i be the i^{th} vector of the canonical basis. Using the chain rule (see [133] p. 661), we have for a scalar function f:

$$\frac{\partial f}{\partial x_i} \circ (I+\theta) = e_i^t P_\theta^{-t} \nabla [f \circ (I+\theta)]. \tag{III.3.4}$$

We thus obtain for the transported solution given in Eq. (III.3.1):

$$\nabla p_\theta = P_\theta^{-t} \nabla q_\theta \tag{III.3.5}$$

and

$$\varepsilon_{jn}(u_\theta) = \frac{1}{2}\left(e_n^t P_\theta^{-t} \nabla v_{\theta,j} + e_j^t P_\theta^{-t} \nabla v_{\theta,n}\right) \tag{III.3.6}$$

Consequently, we transport the solution to $\Omega^s \times \Omega^f$, and transform the integrals in Eqs. (III.3.2)-(III.3.3) using the results of change of variable given by Lemmas A.5 and A.6 in [39]. We then have, for all $(\phi, \varphi) \in (\mathcal{D}(\overline{\Omega}^s))^n \times \mathcal{D}(\mathbb{R}^n \setminus \Omega^s)$:

$$\begin{aligned}\int_{\Omega^s} \Big(\sum_{lmjn} C_{lmjn} \frac{1}{2}\left(e_n^t P_\theta^{-t} \nabla v_{\theta,j} + e_j^t P_\theta^{-t} \nabla v_{\theta,n}\right) e_m^t P_\theta^{-t} \nabla \phi_l - \omega^2 \rho_s v_\theta \phi\Big) |\det P_\theta|\, d\mu \\ + \int_\Gamma \left(q_\theta \nu + g(x+\theta(x))\nu\right) \phi J_{\Gamma_\theta}\, d\sigma = 0. \\ \int_{\Omega^f} (P_\theta^{-t} \nabla q_\theta \cdot P_\theta^{-t} \nabla \varphi - k^2 q_\theta \varphi) |\det P_\theta|\, d\mu \\ + \int_\Gamma \left(\frac{\partial g(x+\theta(x))}{\partial \nu} - \omega^2 \rho_f u_\theta \cdot \nu\right) \varphi J_{\Gamma_\theta}\, d\sigma = 0,\end{aligned}$$

The latter equations can be re-written as follows, for all $(\phi, \varphi) \in (\mathcal{D}(\overline{\Omega}^s))^n \times \mathcal{D}(\mathbb{R}^n \setminus \Omega^s)$:

$$\begin{aligned}\int_{\Omega^s} \Big(\sum_{lmjn} C_{lmjn} \frac{1}{2}\left(P_\theta^{-1} e_m e_n^t P_\theta^{-t} \nabla v_{\theta,j} + P_\theta^{-1} e_m e_j^t P_\theta^{-t} \nabla v_{\theta,n}\right) \cdot \nabla \phi_l - \omega^2 \rho_s v_\theta \phi\Big) |\det P_\theta|\, d\mu \\ + \int_\Gamma \left(q_\theta \nu + g(x+\theta(x))\nu\right) \phi J_{\Gamma_\theta}\, d\sigma = 0 \quad \text{(III.3.7)} \\ \int_{\Omega^f} (P_\theta^{-1} P_\theta^{-t} \nabla q_\theta \cdot \nabla \varphi - k^2 q_\theta \varphi) |\det P_\theta|\, d\mu \\ + \int_\Gamma \left(\frac{\partial g(x+\theta(x))}{\partial \nu} - \omega^2 \rho_f u_\theta \cdot \nu\right) \varphi J_{\Gamma_\theta}\, d\sigma = 0 \quad \text{(III.3.8)}\end{aligned}$$

On the one hand, we look at the first equation. For test functions $\phi \in (\mathcal{D}(\Omega^s))^n$, we get that $\mathcal{F}_1^{(1)}(\theta, v_\theta, q_\theta) = 0$, where $\mathcal{F}_1^{(1)}(\theta, v, q) \in (D'(\Omega^s))^n$ denotes the functional

$$\mathcal{F}_1^{(1)}(\theta, v, q) : \phi \mapsto \int_{\Omega^s} (\sum_{lmjn} C_{lmjn} \frac{1}{2} \left(P_\theta^{-1} e_m e_n^t P_\theta^{-t} \nabla v_j + P_\theta^{-1} e_m e_j^t P_\theta^{-t} \nabla v_n \right) \cdot \nabla \phi_l - \omega^2 \rho_s v \phi) |\det P_\theta| \, d\mu.$$

Because $\theta \in (\mathcal{C}^1(\mathbb{R}^n))^n$, $\nabla\theta \in (L^\infty(\mathbb{R}^n))^{n\times n}$, and $\mathcal{F}_1^{(1)}(\theta, v, q)$ is a bounded linear functional on $(H_0^1(\Omega^s))^n$. Therefore we obtain

$$\mathcal{F}_1^{(1)} : X \times (H^1(\Omega^s))^n \times Y_2 \longrightarrow \left((H^1(\Omega^s))^n \right)' .$$

Moreover, regarding the differentiability, we recall that, referring to Lemma A.1 in [39], $\nabla\theta \mapsto |\det P_\theta|$, $\nabla\theta \mapsto P_\theta^{-1} e_m e_n^t P_\theta^{-t} |\det P_\theta|$, and $\nabla\theta \mapsto P_\theta^{-1} e_m e_j^t P_\theta^{-t} |\det P_\theta|$ are continuously Fréchet differentiable in a neighborhood of zero from $(L^\infty(\mathbb{R}^n))^n$ to $L^\infty(\mathbb{R}^n)$, $(L^\infty(\mathbb{R}^n))^{n\times n}$, and $(L^\infty(\mathbb{R}^n))^{n\times n}$ respectively.
In addition, $\mathcal{F}_1^{(1)}(\theta, v, q)$ is given as the sum of trilinear forms of v, $P_\theta^{-1} e_m e_n^t P_\theta^{-t} |\det P_\theta|$ and ϕ, of trilinear form of v, $P_\theta^{-1} e_m e_j^t P_\theta^{-t} |\det P_\theta|$ and ϕ, and of a trilinear form of v, $|\det P_\theta|$ and ϕ, which are bounded on $(H^1(\Omega^s))^n \times (L^\infty(\Omega^s))^{n\times n} \times (H_0^1(\Omega^s))^n$, $(H^1(\Omega^s))^n \times (L^\infty(\Omega^s))^{n\times n} \times (H_0^1(\Omega^s))^n$, and $(H^1(\Omega^s))^n \times L^\infty(\mathbb{R}^n) \times (H_0^1(\Omega^s))^n$ respectively.
The resulting integrand is thus the composition of continuously differentiable mappings, and we conclude that $\mathcal{F}_1^{(1)}$ is continuously Fréchet differentiable in a neighborhood of $(0, v_0, q_0)$ in $X \times (H^1(\Omega^s))^n \times Y_2$.

In order to take into account the boundary integral, we use the density of $(\mathcal{D}(\overline{\Omega}^s))^n$ in $(H^1(\Omega^s))^n$, and then the equation (III.3.7) holds for all $\phi \in (H^1(\Omega^s))^n$.
In addition, there exists an extension operator ξ from Γ, which is linear and continuous from $(H^{1/2}(\Gamma))^n$ to $(H^1(\Omega^s))^n$, and such that $supp\, \xi\Psi \subset \overline{\Omega}^s$, for all $\Psi \in (H^{1/2}(\Gamma))^n$, cf. [117].
Take $\Psi \in (H^{1/2}(\Gamma))^n$. From Eq. (III.3.7) with $\phi = \xi\Psi$, it follows that (v_θ, q_θ) satisfies $\mathcal{F}_1^{(2)}(\theta, v_\theta, q_\theta) = 0$, where $\mathcal{F}_1^{(2)}(\theta, v, q) : (H^{1/2}(\Gamma))^n \to \mathbb{C}$ denotes the functional:

$$\mathcal{F}_1^{(2)}(\theta, v, q) : \Psi \mapsto \int_{\Omega^s} (\sum_{lmjn} C_{lmjn} \frac{1}{2} \left(P_\theta^{-1} e_m e_n^t P_\theta^{-t} \nabla v_j + P_\theta^{-1} e_m e_j^t P_\theta^{-t} \nabla v_n \right) \cdot \nabla (\xi\Psi)_l - \omega^2 \rho_s v \xi\Psi) |\det P_\theta| \, d\mu + \int_\Gamma (q\nu + g\nu) \, \Psi J_{\Gamma_\theta} \, d\sigma.$$

Noting that $\mathcal{F}_1^{(2)}$ is a bounded linear functional on $(H^{1/2}(\Gamma))^n$, for all $(v, q) \in Y$, we find $\mathcal{F}_1^{(2)}(\theta, v, q) \in (H^{-1/2}(\Gamma))^n$.

Since the extension operator ξ is linear continuous from $(H^{1/2}(\Gamma))^n$ to $(H^1(\Omega^s))^n$, the continuous Fréchet differentiability of the volume integral over Ω^s follows from the same argument as for $\mathcal{F}_1^{(1)}$ above.

As regards Fréchet differentiability of the boundary integral, we also observe that it can be written under the form

$$\int_\Gamma N(\theta, v, q)\Psi \, d\sigma.$$

According to [39] (see Lemmas A.1, A.5 and A.7), the mappings $\theta \mapsto \nu = \nu_\theta \circ (I + \theta)$ and $\theta \mapsto J_{\Gamma_\theta}$ are continuously Fréchet differentiable in a neighborhood of zero from $(\mathcal{C}^1(\mathbb{R}^n))^n$ to $(L^\infty(\Gamma))^n$ and $L^\infty(\Gamma)$ respectively.

Moreover, the trace operator $\theta \mapsto Tr_\Gamma \theta$ is linear and bounded from $(\mathcal{C}^1(\mathbb{R}^n))^n$ to $(W^1_\infty(\Gamma))^n$, therefore from Lemma A.2 in [39], the mapping $\theta \mapsto (x \mapsto g(x + \theta(x)) = \mathrm{e}^{ik(x+\theta(x))\cdot d})$ is continuously Fréchet differentiable from $(\mathcal{C}^1(\mathbb{R}^n))^n$ to $W^1_\infty(\Gamma)$.

By embedding theorem, cf. [70, 117], we have $W^1_\infty(\Gamma) \hookrightarrow H^{1/2}(\Gamma)$, thus the mapping $\theta \mapsto (x \mapsto g(x + \theta(x))$ is continuously Fréchet differentiable from $(\mathcal{C}^1(\mathbb{R}^n))^n$ to $H^{1/2}(\Gamma)(\hookrightarrow L^2(\Gamma))$.

Thanks to the regularity of g, the integrand $N(\theta, v, q)$ is therefore the composition of differentiable applications. Combining the above arguments, it ensures that $N(\theta, v, q)$ is continuously Fréchet differentiable for θ in a neighborhood of 0 and all (v, q) in Y, from $(\mathcal{C}^1(\mathbb{R}^n))^n \times (L^2(\Gamma))^n \times Y_2$ into $(L^2(\Gamma))^n$.

Finally, according to the trace theorems ([19, 20, 30, 32, 35, 70, 101, 117]), the trace operator is linear continuous from $(H^1(\Omega^s))^n$ to $(H^{1/2}(\Gamma))^n$. Consequently, it follows that $\mathcal{F}_1^{(2)}$ is continuously Fréchet differentiable in a neighborhood of $(0, v_0, q_0)$ from $X \times Y$ into $(H^{-1/2}(\Gamma))^n$.

To sum up, the first variational equation (III.3.7) is equivalent to the operator equation $\mathcal{F}_1(\theta, v_\theta, q_\theta) = 0$, where $\mathcal{F}_1 = (\mathcal{F}_1^{(1)}, \mathcal{F}_1^{(2)}) : X \times Y \to Z_1$ is continuously Fréchet differentiable in a neighborhood of $(0, v_0, q_0)$ from $X \times Y$ to Z_1.

On the other hand, we deal with the second equation (III.3.8) by analogy.

For test functions $\varphi \in \mathcal{D}(\Omega^f)$, we get that $\mathcal{F}_2^{(1)}(\theta, v_\theta, q_\theta) = 0$, where $\mathcal{F}_2^{(1)}(\theta, v, q) \in \mathcal{D}'(\Omega^f)$ denotes the functional

$$\mathcal{F}_2^{(1)}(\theta, v, q) : \varphi \mapsto \int_{\Omega^f} (P_\theta^{-1} P_\theta^{-t} \nabla q \cdot \nabla \varphi - k^2 q\varphi) |\det P_\theta| \, d\mu.$$

Since $\theta \in (\mathcal{C}^1(\mathbb{R}^n))^n$, $\nabla\theta \in (L^\infty(\mathbb{R}^n))^{n\times n}$.
We can observe that $\mathcal{F}_2^{(1)}(\theta, v, q)$ is a bounded linear functional on $\mathcal{H}_T(\Omega^f)$, therefore, $\mathcal{F}_2^{(1)}(\theta, v, q) \in (\mathcal{H}_T(\Omega^f))'$. Consequently, we have proven that:

$$\mathcal{F}_2^{(1)} : X \times Y_1 \times \mathcal{H}_T(\Omega^f) \longrightarrow (\mathcal{H}_T(\Omega^f))'.$$

Furthermore, regarding the differentiability, it has been shown in [39] that $\nabla\theta \mapsto |\det P_\theta|$ and $\nabla\theta \mapsto P_\theta^{-1}P_\theta^{-t}|\det P_\theta|$ are continuously Fréchet differentiable in a neighborhood of zero from $(L^\infty(\mathbb{R}^n))^n$ to $L^\infty(\mathbb{R}^n)$ and $(L^\infty(\mathbb{R}^n))^{n\times n}$ respectively (see Lemma A.1 in [39]).
Then, we observe that $\mathcal{F}_2^{(1)}(\theta, v, q)$ is given as the sum of a trilinear form of q, $P_\theta^{-1}P_\theta^{-t}|\det P_\theta|$ and φ, and a trilinear form of q, $|\det P_\theta|$ and φ, which are bounded on $\mathcal{H}(\Omega^f) \times (L^\infty(\mathbb{R}^n))^{n\times n} \times \mathcal{H}_T(\Omega^f)$, and $\mathcal{H}(\Omega^f) \times L^\infty(\mathbb{R}^n) \times \mathcal{H}_T(\Omega^f)$ respectively.
The integrand is thus the composition of continuously differentiable applications, and we deduce that $\mathcal{F}_2^{(1)}$ is continuously Fréchet differentiable in a neighborhood of $(0, v_0, q_0)$ in $X \times Y_1 \times \mathcal{H}_T(\Omega^f)$.

Similarly, in order to take into consideration the surface integral, we observe that $\mathcal{D}(\mathbb{R}^n \setminus \Omega^s)$ is dense in $H^1(\Omega^f)$, and thus in $\mathcal{H}_T(\Omega^f)$. Consequently, the equation holds for all $\varphi \in \mathcal{H}_T(\Omega^f)$.
Let D be a bounded domain such that $\overline{\Omega}^s \subset D$. Then, there exists an extension operator ζ from Γ, which is linear and continuous from $H^{1/2}(\Gamma)$ to $\mathcal{H}_T(\Omega^f)$, and such that $supp\,\xi\psi \subset \overline{D}$, for all $\psi \in H^{1/2}(\Gamma)$, cf. [117].
Let $\psi \in H^{1/2}(\Gamma)$. Taking $\varphi = \zeta\psi$ in (III.3.8), we obtain that (v_θ, q_θ) satisfies $\mathcal{F}_2^{(2)}(\theta, v_\theta, q_\theta) = 0$, where $\mathcal{F}_2^{(2)}(\theta, v, q) : H^{1/2}(\Gamma) \to \mathbb{C}$ is defined by

$$\begin{aligned}\mathcal{F}_2^{(2)}(\theta, v, q) : \psi \mapsto \quad & \int_{\Omega^f} (P_\theta^{-1}P_\theta^{-t}\nabla q \cdot \nabla(\zeta\psi) - k^2 q\zeta\psi)|\det P_\theta|\, d\mu \\ & + \int_\Gamma \left(\frac{\partial g}{\partial \nu} - \omega^2 \rho_f u \cdot \nu\right) \psi J_{\Gamma_\theta}\, d\sigma.\end{aligned}$$

We observe that $\mathcal{F}_2^{(2)}$ is a bounded linear functional on $H^{1/2}(\Gamma)$. Thus, for $(v, q) \in Y$, we have $\mathcal{F}_2^{(2)}(\theta, v, q) \in H^{-1/2}(\Gamma)$.
Then, because the extension operator ζ is linear continuous from $H^{1/2}(\Gamma)$ to $\mathcal{H}_T(\Omega^f)$, the continuous Fréchet differentiability of the volume integral over Ω^f follows from the same argument as for $\mathcal{F}_2^{(1)}$ above.
Regarding to the differentiability of the surface integral, we first notice that it is of the form

$$\int_\Gamma K(\theta, v, q)\psi\, d\sigma.$$

Then, it has been proven in [39] (see Lemmas A.1, A.5 and A.7) that the mappings $\theta \mapsto \nu = \nu_\theta \circ (I+\theta)$ and $\theta \mapsto J_{\Gamma_\theta}$ are continuously Fréchet differentiable in a neighborhood of zero from $(\mathcal{C}^1(\mathbb{R}^n))^n$ to $(L^\infty(\Gamma))^n$ and $L^\infty(\Gamma)$ respectively.
Moreover, the trace operator $\theta \mapsto Tr_\Gamma \theta$ is linear and bounded from $(\mathcal{C}^1(\mathbb{R}^n))^n$ to $(W^1_\infty(\Gamma))^n$, therefore from Lemma A.2 in [39], the mapping $\theta \mapsto (x \mapsto g(x+\theta(x)) = \mathrm{e}^{ik(x+\theta(x))\cdot d})$ is continuously Fréchet differentiable from $(\mathcal{C}^1(\mathbb{R}^n))^n$ to $W^1_\infty(\Gamma)$.
By embedding theorem, cf. [70, 117], we have $W^1_\infty(\Gamma) \hookrightarrow H^{1/2}(\Gamma)$, thus the mapping $\theta \mapsto (x \mapsto g(x+\theta(x))$ is continuously Fréchet differentiable from $(\mathcal{C}^1(\mathbb{R}^n))^n$ to $H^{1/2}(\Gamma)(\hookrightarrow L^2(\Gamma))$.
Thanks to the regularity of g, the integrand $K(\theta, v, q)$ is thus the composition of differentiable applications. It follows that $K(\theta, v, q)$ is continuously Fréchet differentiable for θ in a neighborhood of 0 and all (v, q) in Y, from $(\mathcal{C}^1(\mathbb{R}^n))^n \times Y_1 \times L^2(\Gamma)$ into $L^2(\Gamma)$.
Moreover, by trace theorem ([19, 30, 32, 35, 70, 101, 117]), the trace operator is linear continuous from $\mathcal{H}(\Omega^f)$ to $H^{1/2}(\Gamma)$. Therefore, we conclude that $\mathcal{F}_2^{(2)}$ is continuously Fréchet differentiable in a neighborhood of $(0, v_0, q_0)$ from $X \times Y$ into $H^{-1/2}(\Gamma)$.

In summary, the second equation (III.3.8) is equivalent to the operator equation $\mathcal{F}_2(\theta, v_\theta, q_\theta) = 0$, where $\mathcal{F}_2 = (\mathcal{F}_2^{(1)}, \mathcal{F}_2^{(2)}) : X \times Y \to Z_2$ is continuously Fréchet differentiable in a neighborhood of $(0, v_0, q_0)$ from $X \times Y$ to Z_2.

Combining $\mathcal{F}_1$ and $\mathcal{F}_2$, we construct the desired $\mathcal{F}$ as $\mathcal{F} = (\mathcal{F}_1, \mathcal{F}_2) : X \times Y \to Z$, and the proof is completed.

■

In the next step, we require some existence and regularity results about the solution of the elasto-acoustic problem. The following lemma is a consequence of Chapter I. Regarding the uniqueness, there is no difficulty for the pressure field, as a consequence of the Rellich lemma. But it does not imply that u is unique. In fact, u is defined up to Jones modes [92, 104] which can exist for simple geometries such as spheres. Nevertheless, Hargé [79] has obtained results which seem to show that Jones modes do not exist for arbitrarily shaped bodies. In the following, we thus assume that ω is not a Jones frequency for all the set of admissible perturbations.

Lemma 5 *Let $\Omega^s \subset \mathbb{R}^n$ be an elastic domain with Lipschitz boundary embedded in a homogeneous fluid Ω^f. Let $z_1 \in ((H^1(\Omega^s))^n)'$, $z_2 \in (\mathcal{H}_T(\Omega^f))'$, $\varphi_1 \in \left(H^{-1/2}(\Gamma)\right)^n$ and $\varphi_2 \in H^{-1/2}(\Gamma)$.*
Then, there exists a unique $(w, t) \in (H^1(\Omega^s))^n \times \mathcal{H}(\Omega^f)$, up to Jone's frequencies in the elastic

scatterer, solution to the boundary value problem:

$$\begin{cases} \nabla \cdot \sigma(w) + \omega^2 \rho_s w = z_1 & \text{in } \Omega^s \\ \Delta t + k^2 t = z_2 & \text{in } \Omega^f \\ \sigma(w)\nu + t\nu = \varphi_1 & \text{on } \Gamma \\ \omega^2 \rho_f w \cdot \nu - \dfrac{\partial t}{\partial \nu} = \varphi_2 & \text{on } \Gamma \\ \lim\limits_{r \to +\infty} r^{(n-1)/2} \left(\dfrac{\partial t}{\partial r} - \mathrm{i}kt \right) = 0. \end{cases} \tag{III.3.9}$$

Moreover, $\|t\|_{\mathcal{C}^2(\mathbb{R}^n \setminus \overline{D})} < +\infty$ *for any domain* D *such that* $\overline{\Omega}^s \cup supp\, z_2 \subset D$.

Remark III.3.1.1

- *The regularity of the data impacts on the regularity of the solution. In most of the cases, in particular when dealing with scattered fields,* $z_1 = 0$ *and* $\{\varphi_j\}_{j=1,2}$ *is defined from the incident field* p^{inc} *which is regular as a plane wave. It is then interesting to observe that if* $\{\varphi_j\}_{j=1,2} \in L^2(\Gamma)$*, then both* w *and* t *are in Sobolev spaces of order* $3/2$*. Indeed, since* $t \in H^1_{loc}(\Omega^f)$*,* $t_{|\Gamma} \in H^{1/2}(\Gamma)$ *and thus* $t\nu \in (L^2(\Gamma))^n$*. We then deduce that* $\sigma(u)\nu \in (L^2(\Gamma))^n$ *and following Dahlberg-Kenig-Verchota [36], we have that* $w \in (H^{3/2}(\Omega^s))^n$*. The same approach applies to* t*. Indeed, if* $w \in (H^1(\Omega^s))^n$*,* $w \cdot \nu_{|\Gamma} \in L^2(\Gamma)$ *since* $w_{|\Gamma} \in (H^{1/2}(\Gamma))^n$ *and* $\nu \in (L^\infty(\Gamma))^n$*. The transmission condition implies that* $\dfrac{\partial t}{\partial \nu}_{|\Gamma} \in L^2(\Gamma)$ *and following Jerison-Kenig [90], we obtain that* $t \in H^{3/2}_{loc}(\Omega^f)$.

- *The previous observation remains valid when the boundary* Γ *is regular (for instance* $\mathcal{C}^2$*). We then get that* $t \in H^2_{loc}(\Omega^f)$ *and* $w \in (H^2(\Omega^s))^n$*. The gain of regularity comes from the fact that when* Γ *is* $\mathcal{C}^2$*,* ν *is* $\mathcal{C}^1$ *and the normal vector is thus a multiplier of* $H^{1/2}$.

III.3.1.3 Proof of Theorem III.3.1.1

We are now in a position to prove the main theorem. We want to apply the Implicit Function Theorem after checking that the needed conditions are fulfilled.

Let $\mathcal{F}$ be the function constructed at Lemma 4. We proved that $\mathcal{F} : X \times Y \to Z$ is continuous on a neighborhood of $(0, v_0, q_0)$ and its Fréchet derivatives $\mathcal{F}'_\theta$ and $\mathcal{F}'_{v,q}$ exist and are continuous on a neighborhood of $(0, v_0, q_0)$.
Moreover, $\mathcal{F}$ is affine in (v, q) and thus, by differentiation and identification in the distribution sense,

we obtain

$$\mathcal{F}'_{v,q}(0,v,q):(w,t)\mapsto \begin{array}{l}(-\nabla\cdot\sigma(w)-\omega^2\rho_s w, Tr_\Gamma(\sigma(w)\cdot\nu+t\nu+g\nu),\\ \qquad -\Delta t-k^2 t, Tr_\Gamma(\dfrac{\partial t}{\partial\nu}-\omega^2\rho_f w\cdot\nu+\dfrac{\partial g}{\partial\nu})).\end{array}$$

where $\mathcal{F}'_{v,q}$ denotes the derivative of $\mathcal{F}$ with respect to (v,q). We notice that $\mathcal{F}'_{v,q}$ is a bounded bilinear operator from Y to Z and it does not depend on (v,q).

In addition, from Lemma 5, for all $(z_1,\varphi_1,z_2,\varphi_2)$ in Z, there exists a unique $(w,t)\in(H^1(\Omega^s))^n\times\mathcal{H}(\Omega^f)$ such that $\mathcal{F}'_{v,q}(0,v,q)(w,t)=(z_1,\varphi_1,z_2,\varphi_2)$.
Consequently, we have $Z\subset\mathcal{F}'_{v,q}(0,v,q)Y$.
We thus have injectivity and surjectivity of the operator $\mathcal{F}'_{v,q}(0,v,q)$ and its inverse.
It follows that $\mathcal{F}'_{v,q}(0,v,q)$ defines an isomorphism of the Banach spaces Y and Z.

In conclusion, we have three Banach spaces X,Y and Z, in which $\mathcal{F}=\mathcal{F}(\theta,v,q)$ satisfies the following conditions:

- $\mathcal{F}(0,v_0,q_0)=0$;
- By preliminary Lemma 4, $\mathcal{F}$ is continuous on a neighborhood of $(0,v_0,q_0)$ in $X\times Y$ to Z, and the Fréchet derivatives $\mathcal{F}'_\theta$ and $\mathcal{F}'_{v,q}$ exist and are continuous on a neighborhood of $(0,v_0,q_0)$;
- $\mathcal{F}'_{v,q}(0,v_0,q_0)$ admits a bounded inverse on Y.

Consequently, we can apply the Implicit Function Theorem: for every θ in a neighborhood of zero in X, there exists a unique (v_θ,q_θ) in a neighborhood of v_0 in Y such that $\mathcal{F}(\theta,v_\theta,q_\theta)=0$ and the Fréchet derivative of the mapping $\theta\mapsto(v_\theta,q_\theta)$ exists and is continuous on a neighborhood of zero in X.

III.3.1.4 Corollaries to the Theorem III.3.1.1

Finally, we can derive as corollaries the continuous Fréchet differentiability of the scattered field (u_θ,p_θ) solution to the BVP with respect to continuous deformations of the domain of the scatterer.

Corollary III.3.1.1 *For any domain D such that $\overline{D}\subset\Omega^s$, the mapping $\theta\mapsto u_\theta$, where u_θ is the solution of problem BVP, is continuously Fréchet differentiable in a neighborhood of zero from $(\mathcal{C}^1(\mathbb{R}^n))^n$ to $(L^2(D))^n$.*

Proof For a domain D, consider D_1, D_2 such that Eq. III.2.1 is satisfied and

$$\overline{D} \subset D_1.$$

Then, there exists a distribution $\phi \in \mathcal{D}(D_2 \setminus \overline{D_1})$, such that $\phi = 1$ on $\overline{\Omega}^s$.
It follows that $supp\ \phi\theta \subset \overline{D}_2 \setminus D_1$, and the mapping $\theta \mapsto \phi\theta$ is linear and bounded from $(\mathcal{C}^1(\mathbb{R}^n))^n$ to X.
Furthermore, since $\theta = \phi\theta$ in $\overline{\Omega}^s$, we have $\Omega^s_{\phi\theta} = \Omega^s_\theta$.
We can apply the previous theorem with $\phi\theta \in X$. The mapping $\theta \mapsto (p_\theta \circ (I+\theta), u_\theta \circ (I+\theta))$ is continuously Fréchet differentiable in a neighborhood of $\theta = 0$ from $(\mathcal{C}^1(\mathbb{R}^n))^n$ to Y.
From Lemma 2.1 in [133], we deduce that the mapping $\theta \mapsto u_\theta$ is locally continuously Fréchet differentiable in a neighborhood of zero from $(\mathcal{C}^1(\mathbb{R}^n))^n$ to $(L^2(D))^n$.

■

Corollary III.3.1.2 *For any domain D such that $\overline{\Omega}^s \subset D$, the mapping $\theta \mapsto p_\theta$, where p_θ is the solution of problem BVP, is continuously Fréchet differentiable in a neighborhood of zero from $(\mathcal{C}^1(\mathbb{R}^n))^n$ to $L^2_{loc}(\mathbb{R}^n \setminus \overline{D})$.*

Proof For a given domain D, choose D_1, D_2 satisfying Eq. (III.2.1) and

$$\overline{D}_2 \subset D.$$

Then, there exists a distribution $\phi \in \mathcal{D}(D_2 \setminus \overline{D_1})$, such that $\phi = 1$ on $\overline{\Omega}^s$.
It follows that $supp\ \phi\theta \subset \overline{D}_2 \setminus D_1$, and the mapping $\theta \mapsto \phi\theta$ is linear and bounded from $(\mathcal{C}^1(\mathbb{R}^n))^n$ to X.
Furthermore, since $\theta = \phi\theta$ in $\overline{\Omega}^s$, we have $\Omega^s_{\phi\theta} = \Omega^s_\theta$.
We can apply the previous theorem with $\phi\theta \in X$. The mapping $\theta \mapsto (p_\theta \circ (I+\theta), u_\theta \circ (I+\theta))$ is continuously Fréchet differentiable in a neighborhood of $\theta = 0$ from $(\mathcal{C}^1(\mathbb{R}^n))^n$ to Y.
From Lemma 2.1 in [133], we deduce that the mapping $\theta \mapsto p_\theta$ is locally continuously Fréchet differentiable in a neighborhood of zero from $(\mathcal{C}^1(\mathbb{R}^n))^n$ to $L^2_{loc}(\mathbb{R}^n \setminus \overline{D})$.

■

Remark III.3.1.2 *We have proven the continuous Fréchet differentiability of the scattered field with respect to continuous deformations of the shape of the scatterer. According to the analysis carried out in [39], Section 4, we can deduce the continuous Fréchet differentiability of the corresponding acoustic far-field pattern. Indeed, both Corollaries 3.4 and Lemma 4.1 remains valid for the pressure*

field. Therefore, Theorem 4.2, which states that the mapping $\theta \mapsto p_{\theta,\infty}$ at $\theta = 0$ is continuously Fréchet differentiable from $(\mathcal{C}^1(\mathbb{R}^n))^n$ to $\mathcal{C}^m(S^1)$, still holds in our case, along with the stability estimate of Theorem 4.3.

III.3.2 Characterization of the derivative of the elasto-acoustic scattered field

The continuous differentiability of the scattered field being established, it is of interest to characterize the derivative in question. This characterization is the purpose of the result stated in the next theorem. A rigorous proof involves technical tools for constructing traces in Lipschitz domains. To make the readability of the proof easier, we have decided to postpone the regularity issues and to address them later in Section III.3.3.

III.3.2.1 Announcement of the second theorem

Our aim is to prove that the local derivative of the elasto-acoustic scattered field with respect to the boundary of the scatterer is the solution of a boundary value problem that can be viewed as a particular direct elasto-acoustic scattering problem. It is shown to only differ from the initial BVP by the transmission conditions at the interface of the elastic scatterer as follows.

Theorem III.3.2.1 *Let (u', p') be the local derivative at $\theta = 0$ and in a direction $h \in (\mathcal{C}^2(\mathbb{R}^n))^n$ of the solution (u_θ, p_θ) of the problem BVP. Then, (u', p') is the solution of the boundary value problem:*

$$\begin{cases} \nabla \cdot \sigma(u') + \omega^2 \rho_s u' = 0 & \text{in } \Omega^s \\ \Delta p' + k^2 p' = 0 & \text{in } \Omega^f \\ \tau(u') = -p'\nu + F(u,p,h) & \text{on } \Gamma \\ \omega^2 \rho_f u' \cdot \nu = \dfrac{\partial p'}{\partial \nu} + G(u,p,h) & \text{on } \Gamma \\ \lim\limits_{r\to+\infty} r^{(n-1)/2}\left(\dfrac{\partial p'}{\partial r} - \mathrm{i}kp'\right) = 0 \end{cases} \tag{III.3.10}$$

where the functions F and G are given by:

$$F(u,p,h) = -h^t \nabla\sigma(u)\nu - \nabla p^T \cdot h\nu + \sigma(u)[h']^t\nu + p^T[h']^t\nu, \tag{III.3.11}$$

$$G(u,p,h) = -(\omega^2\rho_f \nabla u - \nabla(\nabla p^T))h \cdot \nu + (\omega^2\rho_f u - \nabla p^T)\cdot [h']^t\nu, \tag{III.3.12}$$

and $p^T = p + p^{inc}$. *Here, the notation* $h^t \nabla\sigma(u)\nu$ *stands for* $h^t \nabla\sigma(u)\nu = [h^t \nabla\sigma_l(u)n]_{l=1,\cdots,n}$, *where* σ_l *is the row* l *of the matrix* $\sigma(u)$.

III.3.2.2 Corollary to the Theorem III.3.2.1

From the fact that the mapping $\theta \to p_{\theta,\infty}$ is continuously Fréchet differentiable at $\theta = 0$ in the direction $h \in (\mathcal{C}^2(\mathbb{R}^n))^n$ from $(\mathcal{C}^1(\mathbb{R}^n))^n$ to $(\mathcal{C}^m(S^1))^n$ (see Remark III.3.1.2), we finally deduce the following characterization of the derivative of the far-field pattern $(\partial p_{\theta,\infty}/\partial\theta)(0)h$ (cf. [28]).

Corollary III.3.2.1 *Let* p'_∞ *be the far-field pattern of the solution* p' *of BVP, and let* $(\partial p_{\theta,\infty}/\partial\theta)(0)h$ *be the derivative at* $\theta = 0$ *and in a direction* $h \in (\mathcal{C}^2(\mathbb{R}^n))^n$ *of the far-field pattern* $p_{\theta,\infty}$ *of the solution* p_θ *of BVP. We have*

$$\frac{\partial p_{\theta,\infty}}{\partial\theta}(0)h = p'_\infty. \tag{III.3.13}$$

III.3.2.3 Formal proof of Theorem III.3.2.1

In the following, we omit to precise the suitable functional framework for the characterization because it requires distinguishing different cases related to the regularity of Ω^s. We prove this theorem in five steps, each formulated as a lemma. The use of the chain rule leads to the desired result. More specifically, the first two equations and the Sommerfeld condition are relatively easy to derive, whereas the transmission conditions require a more elaborated and careful work.

We first prove that the local derivative u' at $\theta = 0$ in a direction h of the solution u_θ to the BVP is a solution of the elastodynamic equation.

Lemma 6 *The local derivative* u' *of the elastic scattered field at* $\theta = 0$ *and in a direction* $h \in (\mathcal{C}^2(\mathbb{R}^n))^n$ *satisfies the following elastodynamic equation*

$$\nabla \cdot \sigma(u') + \omega^2 \rho_s u' = 0 \qquad \text{in } \Omega^s \tag{III.3.14}$$

Proof By analogy to Lemma 1 in [41], we define

$$B = \nabla \cdot \sigma + \omega^2 \rho_s I, \tag{III.3.15}$$

and

$$\phi_\theta = B u_\theta. \tag{III.3.16}$$

Then, the elastic scattered field u_θ satisfies the elastodynamic equation Eq. III.2.2 in BVP, i.e.

$$\phi_\theta = 0 \qquad \text{in } \Omega_\theta^s, \tag{III.3.17}$$

and we thus have by transportation on the reference domain

$$\phi_\theta \circ (I+\theta) = 0 \qquad \text{in } \Omega^s. \tag{III.3.18}$$

In addition, B is also a linear and continuous operator from $(H^1(\Omega^s))^n$ into $(\mathcal{D}'(\Omega^s))^n$, B is differentiable at least in the distribution sense, that is, $v \mapsto \langle Bv, \varphi\rangle$ is differentiable for each $\varphi \in \mathcal{D}(\Omega^s)$, and

$$\frac{\partial B}{\partial v} = B. \tag{III.3.19}$$

From Theorem III.3.1.1 and Corollaries III.3.1.1 and III.3.1.2, $\theta \mapsto u_\theta \circ (I+\theta)$ and $\theta \mapsto u_\theta$ are differentiable, therefore, it follows that $\theta \mapsto \phi_\theta \circ (I+\theta)$ and $\theta \mapsto \phi_\theta$ are respectively continuously Fréchet differentiable, and locally continuously Fréchet differentiable - at least in the distribution sense - at $\theta = 0$ and in a direction $h \in (\mathcal{C}^2(\mathbb{R}^n))^n$.
Then, for $\theta \in (\mathcal{C}^1(\mathbb{R}^n))^n$ an admissible perturbation in a neighborhood of zero, we obtain

$$\frac{\partial \phi_\theta}{\partial \theta}(0)h = \frac{\partial}{\partial \theta}(\phi_\theta \circ (I+\theta))(0)h - \nabla\phi(0)h \qquad \text{in } \Omega^s. \tag{III.3.20}$$

Since $Bu = 0$ in Ω^s, we verify $\nabla\phi(0) = \nabla(Bu) = 0$ in Ω^s.
Combining this along with (III.3.18) in (III.3.20), we get

$$\frac{\partial \phi_\theta}{\partial \theta}(0)h = \frac{\partial B}{\partial u}\frac{\partial u_\theta}{\partial \theta}(0)h = 0 \qquad \text{in } \Omega^s. \tag{III.3.21}$$

By definition of B and (III.3.19), we conclude

$$Bu' = \nabla \cdot \sigma u' + \omega^2 \rho_s u' = 0 \qquad \text{in } \Omega^s, \tag{III.3.22}$$

which gives (III.3.14).

■

The next lemma states that the local derivative p' at $\theta = 0$ in a direction h of the solution p_θ satisfies the following Helmholtz equation.

Lemma 7 *The local derivative p' of the acoustic scattered field at $\theta = 0$ and in a direction $h \in (\mathcal{C}^2(\mathbb{R}^n))^n$ satisfies the following Helmholtz equation*

$$\Delta p' + k^2 p' = 0 \qquad \text{in } \Omega^f. \tag{III.3.23}$$

Proof The proof is analogous to the one of Lemma 6 and can be found in [39].

■

Then, we derive the first transmission condition satisfied by (u', p') in the next lemma.

Lemma 8 *Let (u', p') be the local derivative of the scattered field, at $\theta = 0$ and in a direction $h \in (\mathcal{C}^2(\mathbb{R}^n))^n$. Then, it satisfies formally the following boundary equation*

$$\tau(u') = -p'\nu + F(u, p, h) \qquad \text{on } \Gamma. \tag{III.3.24}$$

where F is given by:

$$F(u, p, h) \;=\; -h^t \nabla\sigma(u)\nu - \nabla p^T \cdot h\nu + \sigma(u)[h']^t\nu + p^T[h']^t\nu. \tag{III.3.25}$$

Proof Let θ be an admissible perturbation $\in (\mathcal{C}^1(\mathbb{R}^n))^n$.
The scattered field (u_θ, p_θ) satisfies:

$$\sigma(u_\theta)\nu_\theta = -p_\theta\nu_\theta - g\nu_\theta \qquad \text{on } \Gamma_\theta, \tag{III.3.26}$$

that is

$$(\sigma(u_\theta) + p_\theta + g)\nu_\theta = 0 \qquad \text{on } \Gamma_\theta.$$

We define ϕ_θ by:

$$\phi_\theta = \sigma(u_\theta) + p_\theta + g. \tag{III.3.27}$$

We therefore have

$$\phi_\theta\nu_\theta = 0 \qquad \text{on } \Gamma_\theta. \tag{III.3.28}$$

By transportation, we thus get

$$\phi_\theta \circ (I + \theta)\nu_\theta \circ (I + \theta) = 0 \qquad \text{on } \Gamma \quad \text{a.e.} \tag{III.3.29}$$

Furthermore (see [115], Lemma 4.8), we have:

$$\nu_\theta \circ (I + \theta) = \frac{1}{\|J(\theta)\nu\|_2} J(\theta)\nu \qquad \text{on } \Gamma \quad \text{a.e.}, \tag{III.3.30}$$

where

$$J(\theta) = [(I+\theta)']^{-t} \qquad \text{in } \mathbb{R}^n. \tag{III.3.31}$$

Using (III.3.30) and Eq. III.3.31 in Eq. III.3.29, we get

$$\phi_\theta \circ (I+\theta) J(\theta)\nu = 0 \qquad \text{on } \Gamma \quad \text{a.e.} \tag{III.3.32}$$

In order to differentiate with respect to θ, we then extend the last equation to an open set D containing Γ_θ. Let the extension of the normal vector ν into $(L^\infty(\mathbb{R}^n))^n$ still be denoted by ν. Moreover, the transported solution $(u_\theta \circ (I+\theta), p_\theta \circ (I+\theta))$ is extended into the whole D and its extension is still denoted by $(u_\theta \circ (I+\theta), p_\theta \circ (I+\theta))$.
We can introduce the following auxiliary function φ_θ defined on D by

$$\varphi_\theta = \phi_\theta \circ (I+\theta) J(\theta)\nu \qquad \text{in } D \quad \text{a.e.} \tag{III.3.33}$$

Note that φ_θ satisfies

$$\varphi_\theta = 0 \qquad \text{on } \Gamma \quad \text{a.e.} \tag{III.3.34}$$

Then, we prove that $\theta \mapsto \varphi_\theta$ is differentiable - at least in the distribution sense - at $\theta = 0$ in a direction $h \in (\mathcal{C}^2(\mathbb{R}^n))^n$.
On the one hand, from Theorem III.3.1.1, we have shown that the mappings $\theta \mapsto p_\theta \circ (I+\theta)$ and $\theta \mapsto u_\theta \circ (I+\theta)$ are differentiable at $\theta = 0$ in a direction $h \in (\mathcal{C}^2(\mathbb{R}^n))^n$. Since, $\theta \mapsto g \circ (I+\theta)$ is differentiable, and since the stress tensor operator σ is linear and continuous, it follows that $\theta \mapsto \phi_\theta$ is differentiable - at least in the distribution sense - at $\theta = 0$ in a direction $h \in (\mathcal{C}^2(\mathbb{R}^n))^n$.
Moreover, the mapping $\theta \mapsto J(\theta)$ is differentiable at $\theta = 0$ in a direction $h \in (\mathcal{C}^2(\mathbb{R}^n))^n$, from $(\mathcal{C}^1(\mathbb{R}^n))^n$ into $(\mathcal{C}^1(\mathbb{R}^n))^n$ and we have (see Eq.(44) in [39]),

$$\frac{\partial J(\theta)}{\partial \theta}(0)h = -[h']^t. \tag{III.3.35}$$

Consequently, the mapping $\theta \mapsto \varphi_\theta$ is differentiable - at least in the distribution sense - at $\theta = 0$ in a direction $h \in (\mathcal{C}^2(\mathbb{R}^n))^n$. We then compute the local derivative with respect to θ for each term of φ_θ as follows.
On the one hand, we have

$$\begin{aligned}\frac{\partial}{\partial \theta}\left(p_\theta \circ (I+\theta) J(\theta)\nu\right)(0)h = \quad & \frac{\partial}{\partial \theta}\left(p_\theta \circ (I+\theta)\right)(0) h J(0)\nu \\ & + p_\theta \circ (I+\theta)_{|\theta=0} \frac{\partial J(\theta)}{\partial \theta}(0)h\nu.\end{aligned} \tag{III.3.36}$$

Applying the classical rule of derivation, for θ in a neighborhood of zero, we have

$$\frac{\partial}{\partial\theta}(p_\theta \circ (I+\theta))(0)h = \frac{\partial p_\theta}{\partial\theta}(0)h + \nabla p_\theta(0)\cdot h. \tag{III.3.37}$$

Observe that $J(0) = I$. Combining (III.3.37) and (III.3.35) with (III.3.36), it follows that

$$\frac{\partial}{\partial\theta}\left(p_\theta \circ (I+\theta)J(\theta)\nu\right)(0)h = \left(\frac{\partial p_\theta}{\partial\theta}(0)h + \nabla p_\theta(0)\cdot h\right)\nu - p[h']^t\nu,$$

that is

$$\frac{\partial}{\partial\theta}\left(p_\theta \circ (I+\theta)J(\theta)\nu\right)(0)h = \left(p' + \nabla p\cdot h\right)\nu - p[h']^t\nu. \tag{III.3.38}$$

Similarly, we obtain for g the following local derivative

$$\frac{\partial}{\partial\theta}\left(g \circ (I+\theta)J(\theta)\nu\right)(0)h = \nabla g\cdot h\nu - g[h']^t\nu. \tag{III.3.39}$$

On the other hand, we compute the local derivative $\dfrac{\partial}{\partial\theta}\left(\sigma(u_\theta) \circ (I+\theta)J(\theta)\nu\right)(0)h$.
In order to apply the derivation formula established by Simon-Murat [115] for a scalar function, we use a reasoning component by component on the tensor. Let $\sigma_l(u_\theta)$ be the l^{th} line of the matrix $\sigma(u_\theta)$. We thus have

$$\frac{\partial}{\partial\theta}\left(\sigma(u_\theta) \circ (I+\theta)J(\theta)\nu\right)(0)h = \left[\frac{\partial}{\partial\theta}\left(\sigma_l(u_\theta) \circ (I+\theta)J(\theta)\nu\right)(0)h\right]_{1\le l\le n}. \tag{III.3.40}$$

For $1 \le l \le n$, this leads to

$$\begin{aligned}&\frac{\partial}{\partial\theta}\left(\sigma_l(u_\theta) \circ (I+\theta)J(\theta)\nu\right)(0)h\\ &= \frac{\partial}{\partial\theta}\left(\sigma_l(u_\theta) \circ (I+\theta)\right)(0)hJ(0)\nu + \sigma_l(u_\theta) \circ (I+\theta)_{|\theta=0}\frac{\partial J(\theta)}{\partial\theta}(0)h\nu.\end{aligned}$$

Moreover, using the same rule as in (III.3.37) for each component $\sigma_{lm}(u)$ of the line $\sigma_l(u)$, we have:

$$\begin{aligned}&\frac{\partial}{\partial\theta}\left(\sigma_l(u_\theta) \circ (I+\theta)\right)(0)h\\ &= \left[\frac{\partial}{\partial\theta}\left(\sigma_{lm}(u_\theta) \circ (I+\theta)\right)(0)h\right]_{1\le m\le n}\\ &= \left[\frac{\partial\sigma_{lm}(u_\theta)}{\partial\theta}(0)h + h\cdot\nabla\sigma_{lm}(u_\theta)(0)\right]_{1\le m\le n}\end{aligned}$$

$$= \left[\sigma_{lm} \left(\frac{\partial u_\theta}{\partial \theta}(0)h \right) + h^t \nabla \sigma_{lm}(u) \right]_{1 \le m \le n}.$$

Since $\sigma_l(u)$ is a row vector field, let us denote by $\nabla \sigma_l(u)$ the Jacobian matrix defined as follows $\nabla \sigma_l(u) = [\nabla \sigma_l(u)^{jm}]_{1 \le j,m \le n} = \left[\frac{\partial \sigma_{lm}(u)}{\partial x_j} \right]_{1 \le j,m \le n}$. We thus get

$$\begin{aligned} &\frac{\partial}{\partial \theta} \left(\sigma_l(u_\theta) \circ (I+\theta) J(\theta) \nu \right)(0)h \\ &= \left(\sigma_l \left(\frac{\partial u_\theta}{\partial \theta}(0)h \right) + h^t \nabla \sigma_l(u) \right) \nu - \sigma_l(u)[h']^t \nu. \end{aligned}$$

Consequently, we obtain for $1 \le l \le n$

$$\frac{\partial}{\partial \theta} \left(\sigma_l(u_\theta) \circ (I+\theta) J(\theta) \nu \right)(0)h = \left(\sigma_l(u') + h^t \nabla \sigma_l(u) \right) \nu - \sigma_l(u)[h']^t \nu.$$

Using the notation $h^t \nabla \sigma(u) := [h^t \nabla \sigma_l(u)]_{1 \le l \le n}$, we deduce that

$$\frac{\partial}{\partial \theta} \left(\sigma(u_\theta) \circ (I+\theta) J(\theta) \nu \right)(0)h = \left(\sigma(u') + h^t \nabla \sigma(u) \right) \nu - \sigma(u)[h']^t \nu. \tag{III.3.41}$$

Note that $h^t \nabla \sigma(u) \nu = \left[\sum_{m=1}^{n} h^t \nabla \sigma_{lm}(u) \nu_m \right]_{1 \le l \le n}$.
From Equations (III.3.34), (III.3.38), (III.3.39) and (III.3.41), it follows that

$$\begin{aligned} \frac{\partial \varphi_\theta}{\partial \theta}(0)h \;\; = \;\; & \sigma(u')\nu + h^t \nabla \sigma(u)\nu - \sigma(u)[h']^t \nu \\ & + p'\nu + \nabla p \cdot h\nu - p[h']^t \nu + \nabla g \cdot h\nu - g[h']^t \nu \quad \text{in } D. \end{aligned} \tag{III.3.42}$$

Assuming that Eq. (III.3.42) has a sense on Γ, it follows from both equations (III.3.33) and (III.3.32) that $\frac{\partial \varphi_\theta}{\partial \theta}(0)h = 0$ on Γ and thus:

$$\begin{aligned} & \sigma(u')\nu + h^t \nabla \sigma(u)\nu - \sigma(u)[h']^t \nu \\ & + p'\nu + \nabla p \cdot h\nu - p[h']^t \nu + \nabla g \cdot h\nu - g[h']^t \nu \;\; = 0 \;\text{ on }\; \Gamma. \end{aligned}$$

Rewriting the latter equation, we obtain:

$$\tau(u') = -p'\nu - h^t \nabla \sigma(u)\nu + \sigma(u)[h']^t \nu - \nabla p^T \cdot h\nu + p^T [h']^t \nu, \tag{III.3.43}$$

which completes the proof of Lemma 8.

■

Remark III.3.2.1 *The previous proof is not really complete since we should have given a sense to the derivative of φ_θ. As formerly mentioned, we did not address this issue because it requires non obvious definitions of traces on Γ.*

Next, we specify the second transmission condition satisfied by (u', p') in the following lemma.

Lemma 9 *Let (u', p') be the local derivative of the scattered field, at $\theta = 0$ and in a direction $h \in (\mathcal{C}^2(\mathbb{R}^n))^n$. Then, it satisfies formally the following boundary equation*

$$\omega^2 \rho_f u' \cdot \nu = \frac{\partial p'}{\partial \nu} + G(u, p, h) \qquad \text{on } \Gamma, \tag{III.3.44}$$

where G is given by:

$$G(u, p, h) \;=\; -(\omega^2 \rho_f \nabla u - \nabla(\nabla p^T))h \cdot \nu + (\omega^2 \rho_f u - \nabla p^T) \cdot [h']^t \nu. \tag{III.3.45}$$

Proof Let θ be an admissible perturbation $\in (\mathcal{C}^1(\mathbb{R}^n))^n$.
We use the boundary condition satisfied by (p_θ, u_θ)

$$\omega^2 \rho_f u_\theta \cdot \nu_\theta = \nabla p_\theta \cdot \nu_\theta + \nabla g \cdot \nu_\theta \qquad \text{on } \Gamma_\theta. \tag{III.3.46}$$

Setting

$$\psi_\theta = \omega^2 \rho_f u_\theta - \nabla p_\theta - \nabla g,$$

from (III.3.46) we have

$$\psi_\theta \cdot \nu_\theta = 0 \qquad \text{on } \Gamma_\theta \quad \text{a.e.} \tag{III.3.47}$$

We thus get

$$\psi_\theta \circ (I + \theta) \cdot \nu_\theta \circ (I + \theta) = 0 \qquad \text{on } \Gamma \quad \text{a.e.} \tag{III.3.48}$$

From (III.3.48) and (III.3.30), we thus deduce

$$\psi_\theta \circ (I + \theta) \cdot J(\theta)\nu = 0 \qquad \text{on } \Gamma \quad \text{a.e.} \tag{III.3.49}$$

Before differentiating with respect to θ, we extend the last equation (III.3.49) to an open set D containing Γ_θ. Again, ν denotes an extension of the normal vector ν into $(L^\infty(\mathbb{R}^n))^n$. We also extend the transported solution $(p_\theta \circ (I + \theta), u_\theta \circ (I + \theta))$ in the whole D and still denote its extension by

$(p_\theta \circ (I+\theta), u_\theta \circ (I+\theta))$.

We can thus introduce an auxiliary function Ψ_θ defined on D by

$$\Psi_\theta = \psi_\theta \circ (I+\theta) \cdot J(\theta)\nu \qquad \text{in } D. \tag{III.3.50}$$

It thus satisfies

$$\Psi_\theta = 0 \qquad \text{on } \Gamma \text{ a.e.} \tag{III.3.51}$$

Then, we prove that $\theta \mapsto \Psi_\theta$ is differentiable - at least in the distribution sense - at $\theta = 0$ in a direction $h \in (\mathcal{C}^2(\mathbb{R}^n))^n$.

On the one hand, from Theorem III.3.1.1, we have shown that the mappings $\theta \mapsto p_\theta \circ (I+\theta)$ and $\theta \mapsto u_\theta \circ (I+\theta)$ at $\theta = 0$. Since, $\theta \mapsto g \circ (I+\theta)$ is differentiable, and from the fact that the gradient operator ∇ is linear and continuous, it follows that $\theta \mapsto \psi_\theta \circ (I+\theta)$ is differentiable - at least in the distribution sense - at $\theta = 0$ in a direction $h \in (\mathcal{C}^2(\mathbb{R}^n))^n$.

Let ψ_θ^l denote the l^{th} component of the column vector ψ_θ. Applying the classical rule of derivation for a scalar function from Simon-Murat [115], we then have, for θ in a neighborhood of zero,

$$\frac{\partial}{\partial\theta}(\psi_\theta \circ (I+\theta))(0)h \tag{III.3.52}$$

$$= \left[\frac{\partial}{\partial\theta}(\psi_\theta^l \circ (I+\theta))(0)h\right]_{1\le l\le n} \tag{III.3.53}$$

$$= \left[\frac{\partial\psi_\theta^l}{\partial\theta}(0)h + \nabla\psi_\theta^l(0)h\right]_{1\le l\le n} \tag{III.3.54}$$

$$= \frac{\partial\psi_\theta}{\partial\theta}(0)h + \nabla\psi_\theta(0)h. \tag{III.3.55}$$

We have seen that the mapping $\theta \mapsto J(\theta)$ is differentiable at $\theta = 0$ in a direction $h \in (\mathcal{C}^2(\mathbb{R}^n))^n$, from $(\mathcal{C}^1(\mathbb{R}^n))^n$ into $(\mathcal{C}^1(\mathbb{R}^n))^n$ with

$$\frac{\partial J(\theta)}{\partial\theta}(0)h = -[h']^t. \tag{III.3.56}$$

Therefore, with the use of the chain rule, we can differentiate Ψ_θ with respect to θ, and obtain

$$\begin{aligned}\frac{\partial\Psi_\theta}{\partial\theta}(0)h \;=\; & \frac{\partial}{\partial\theta}(\psi_\theta \circ (I+\theta))(0)h \cdot J(\theta)_{|\theta=0}\nu \\ & + \psi_\theta \circ (I+\theta)_{|\theta=0} \cdot \frac{\partial J(\theta)}{\partial\theta}(0)h\nu \text{ in } D.\end{aligned} \tag{III.3.57}$$

Combining equations (III.3.52), (III.3.56) with (III.3.57), it follows that

$$\frac{\partial \Psi_\theta}{\partial \theta}(0)h = \left(\frac{\partial \psi_\theta}{\partial \theta}(0)h + \nabla \psi_\theta(0)h\right) \cdot J(0)\nu - \psi_\theta(0) \cdot [h']^t \nu \text{ in } D. \tag{III.3.58}$$

We notice that $J(0) = I$ and since $\psi_\theta(0) = \omega^2 \rho_f u - \nabla p - \nabla g$, we have

$$\nabla \psi_\theta(0) = \omega^2 \rho_f \nabla u - \nabla(\nabla p) - \nabla(\nabla g). \tag{III.3.59}$$

where the gradient of the vector field u is defined as $\nabla u = [\nabla u_{lj}]_{1 \le j,l \le n} = \left[\frac{\partial u_l}{\partial x_j}\right]_{1 \le j,l \le n}$.
Furthermore, we also get

$$\frac{\partial \psi_\theta}{\partial \theta}(0)h = \omega^2 \rho_f \frac{\partial u_\theta}{\partial \theta}(0)h - \nabla\left(\frac{\partial p_\theta}{\partial \theta}(0)h\right) - \nabla\left(\frac{\partial g}{\partial \theta}(0)h\right).$$

Hence,

$$\frac{\partial \psi_\theta}{\partial \theta}(0)h = \omega^2 \rho_f u' - \nabla p'. \tag{III.3.60}$$

From Eq. III.3.58 to Eq. III.3.60, we deduce that

$$\begin{aligned} \frac{\partial \Psi_\theta}{\partial \theta}(0)h \;=\; & (\omega^2 \rho_f u' - \nabla p') \cdot \nu + \omega^2 \rho_f \nabla u h \cdot \nu \\ & -\nabla(\nabla p)h \cdot \nu - \nabla(\nabla g)h \cdot \nu \\ & -(\omega^2 \rho_f u - \nabla p - \nabla g) \cdot [h']^t \nu \quad \text{in } D. \end{aligned} \tag{III.3.61}$$

Assuming that (III.3.61) has a sense on Γ, it follows from equation (III.3.51) that:

$$\begin{aligned} & (\omega^2 \rho_f u' - \nabla p') \cdot \nu + \omega^2 \rho_f \nabla u h \cdot \nu \\ & -\nabla(\nabla p)h \cdot \nu - \nabla(\nabla g)h \cdot \nu \\ & -(\omega^2 \rho_f u - \nabla p - \nabla g) \cdot [h']^t \nu = 0 \quad \text{in } \Gamma, \end{aligned}$$

which gives (III.3.44).

■

Remark III.3.2.2 *The previous proof is not really complete since we should have given a sense to the derivative of Ψ_θ. As formerly mentioned, we did not address this issue because it requires non obvious definitions of traces on Γ.*

The last lemma finally shows that the local derivative p' of the scattered field p_θ with respect to an obstacle's domain satisfies the outgoing Sommerfeld condition.

Lemma 10 *The local derivative p' of the acoustic scattered field p_θ, at $\theta = 0$ and in a direction $h \in (\mathcal{C}^2(\mathbb{R}^n))^n$, satisfies the following outgoing radiation equation*

$$\lim_{r\to+\infty} r^{(n-1)/2}\left(\frac{\partial p'}{\partial r} - \mathrm{i}\frac{\omega}{\rho_f}p'\right) = 0. \tag{III.3.62}$$

Proof The proof is given in [39].

■

Lemmas 8 and 9 are necessary for the characterization of the Fréchet derivative (u', p'). Nevertheless, their proof is based on the fact that we can give a sense to $\frac{\partial \varphi_\theta}{\partial \theta}(0)h$ and $\frac{\partial \Psi_\theta}{\partial \theta}(0)h$. We have decided to omit this point in the proof of the Lemmas because it requires to establish regularity results which are not obvious when the boundary Γ is only Lipschitz. In the next section of this chapter, we gather results which form a complete proof of the characterization in some cases. We have also depicted some of the results that were able to prove in the general case of a Lipschitz continuous domain. Unfortunately, we were not able to get a proof in that case. In particular, the proof failed because of the lack of surjectivity of the trace operators.

III.3.3 Mathematical framework for the characterization of the Fréchet derivative

The characterization of the derivative of the elasto-acoustic field exhibits non homogeneous transmission conditions involving traces that are either non standard (like the normal derivative of the pressure gradient) or for fields with a poor regularity. It is thus not obvious to give a sense to these traces, in particular when the solid Ω^s is only Lipschitz. We organize this section by increasing the difficulty level which is related to the regularity of Ω^s.

III.3.3.1 Ω^s is of class $\mathcal{C}^2$

We want to give a sense to the following quantities on Γ:

$$\begin{aligned}\frac{\partial \varphi_\theta}{\partial \theta}(0)h \;=\;& \sigma(u')\nu + h^t\nabla\sigma(u)\nu - \sigma(u)[h']^t\nu \\ & + p'\nu + \nabla p\cdot h\nu - p[h']^t\nu + \nabla g\cdot h\nu - g[h']^t\nu\end{aligned} \tag{III.3.63}$$

and

$$\begin{aligned}\frac{\partial \Psi_\theta}{\partial \theta}(0)h &= (\omega^2\rho_f u' - \nabla p')\cdot\nu + \omega^2\rho_f \nabla u h\cdot\nu \\ &\quad -\nabla(\nabla p)h\cdot\nu - \nabla(\nabla g)h\cdot\nu \\ &\quad -(\omega^2\rho_f u - \nabla p - \nabla g)\cdot[h']^t\nu. \end{aligned} \tag{III.3.64}$$

(i) Let us begin with the terms involved in Lemma 8.

According to Remark III.3.1.1, $u \in (H^2(\Omega^s))^n$, and $p \in H^2_{loc}(\Omega^f)$. We thus have $u' \in (H^1(\Omega^s))^n$ and $p' \in H^1_{loc}(\Omega^f)$. Regarding (III.3.63), we can thus define easily most of the traces from the classical trace theorems [30, 35, 70, 71, 101, 102, 117]:

- $u \in ((H^2(\Omega^s))^n$ implies that $\sigma(u) \in ((H^1(\Omega^s))^{n\times n}$. Since the direction $h \in (\mathcal{C}^2(\mathbb{R}^n))^n$, $h' \in (\mathcal{C}^1(\mathbb{R}^n))^{n\times n}$ which is a multiplier of $(H^{1/2}(\Gamma))^n$. Then, $\sigma(u)_{|\Gamma} \in (H^{1/2}(\Gamma))^{n\times n}$ implies that $\sigma(u)[h']^t_{|\Gamma} \in (H^{1/2}(\Gamma))^{n\times n}$ and so does $\sigma(u)[h']^t_{|\Gamma}\nu \in (H^{1/2}(\Gamma))^n$ since $\nu \in (\mathcal{C}^1(\Gamma))^n$.

- $p \in H^2_{loc}(\Omega^f)$ implies that $p[h']^t\nu$ is defined in $(H^{1/2}(\Gamma))^n$ since $p_{|\Gamma} \in H^{3/2}(\Gamma)$, $[h']^t \in (\mathcal{C}^1(\mathbb{R}^n))^{n\times n}$ and $\nu \in (\mathcal{C}^1(\mathbb{R}^n))^n$.

- $p \in H^2_{loc}(\Omega^f)$ implies that $\nabla p\cdot n_{|\Gamma} \in (H^{1/2}(\Gamma))^n$. Since $h \in (\mathcal{C}^2(\mathbb{R}^n))^n$, we also have $(\nabla p\cdot h)\nu_{|\Gamma} \in (H^{1/2}(\Gamma))^n$ since $\nu \in (\mathcal{C}^1(\Gamma))^n$.

- The terms depending on the datum g do not pose a problem since g is regular, for instance, $g \in H^1(\Gamma)$. We thus have $\nabla g\cdot h\nu_{|\Gamma} \in (L^2(\Gamma))^n$ and $g[h']^t\nu \in (L^2(\Gamma))^n$ too.

- $u' \in (H^1(\Omega^s))^n$ implies that $\sigma(u') \in (H(\nabla\cdot,\Omega^s))^{n\times n}$. The trace $\sigma(u')_{|\Gamma}\nu$ is thus defined in $(H^{-1/2}(\Gamma))^n$.

- $p' \in H^1_{loc}(\Omega^f)$ implies that $p'_{|\Gamma} \in H^{1/2}(\Gamma)$, and $p'\nu \in (H^{1/2}(\Gamma))^n$ since $\nu \in (\mathcal{C}^1(\Gamma))^n$.

- As a consequence, the only term that requires a particular attention seems to be $h^t\nabla\sigma(u)\nu$. Nevertheless, in the case of a regular domain, we know that $u \in (H^2(\Omega^s))^n$, which implies that $\sigma(u) \in (H^1(\Omega^s))^{n\times n}$. Now let us denote by ∂ one of the partial derivatives $\dfrac{\partial}{\partial x_j}$, $1 \le j \le n$. We then have:

$$\nabla\cdot\ \sigma_l(\partial u) + \omega^2\rho_s\partial u_l = 0, \quad \forall\, 1 \le l \le n. \tag{III.3.65}$$

Using that $\partial\sigma_l(u) = \sigma_l(\partial u)$, we can thus deduce that $\partial\sigma_l(u) \in (H(\nabla\cdot, \Omega^s))^n$, which implies that $\partial\sigma_l(u)\nu$ is well-defined in $H^{-1/2}(\Gamma)$. By this way, since the direction $h \in (\mathcal{C}^2(\mathbb{R}^n))^n$, we can define $h^t\nabla\sigma_l(u)\nu$ in $H^{-1/2}(\Gamma)$ also for all $1 \leq l \leq n$.

Collecting each of the previous regularity results, we get that expression (III.3.63) is well-defined in $(H^{-1/2}(\Gamma))^n$ when the solid Ω^s is of class $\mathcal{C}^2$.

(ii) We continue our analysis by focusing on Lemma 9.

- We have $p \in H^2_{loc}(\Omega^f)$ and thus $\nabla p \in (H^1_{loc}(\Omega^f))^n$. We then have $\nabla p_{|\Gamma} \in (H^{1/2}(\Gamma))^n$. The direction vector $h \in (\mathcal{C}^2(\mathbb{R}^n))^n$. Hence, the entries of $[h']$ are in $\mathcal{C}^1(\mathbb{R}^n)$. Knowing that $\mathcal{C}^1(\mathbb{R}^n)$ is a multiplier of $H^{1/2}(\Gamma)$, we then deduce that:

$$[h']\nabla p_{|\Gamma} \in (H^{1/2}(\Gamma))^n$$

  and since $\nu \in (\mathcal{C}^1(\Gamma))^n$, it is a multiplier of $(H^{1/2}(\Gamma))^n$ and we finally obtain:

$$[h']\nabla p \cdot \nu_{|\Gamma} \in H^{1/2}(\Gamma).$$

- We have that $u_{|\Gamma} \in (H^{3/2}(\Gamma))^n$ since $u \in (H^2(\Omega^s))^n$. We then have $[h']u \in (H^{1/2}(\Gamma))^n$ and so does $[h']u \cdot \nu_{|\Gamma}$ which belongs to $H^{1/2}(\Gamma)$.

- Since $u \in (H^2(\Omega^s))^n$, $\nabla u \in (H^1(\Omega^s))^{n\times n}$ and $\nabla uh \in (H^{1/2}(\Gamma))^n$ since $h \in (\mathcal{C}^2(\mathbb{R}^n))^n$. We then deduce that $\nabla uh \cdot \nu_{|\Gamma} \in H^{1/2}(\Gamma)$ at least since $\nabla uh_{|\Gamma} \in (H^{1/2}(\Gamma))^n$ and $\nu \in (\mathcal{C}^1(\mathbb{R}^n))^n$

- Since $u' \in (H^1(\Omega^s))^n$, we have $u'_{|\Gamma} \in (H^{1/2}(\Gamma))^n$, and $\nu \in (\mathcal{C}^1)^n$ is a multiplier of $(H^{1/2}(\Gamma))^n$. We thus have $u' \cdot \nu \in H^{1/2}(\Gamma)$.

- Since $p' \in H^1_{loc}(\Omega^f)$ with $\Delta p' \in L^2_{loc}(\Omega^f)$, we know that $\dfrac{\partial p'}{\partial \nu} \in H^{-1/2}(\Gamma)$.

- As a consequence, the only term that requires a particular care seems to be $\nabla(\nabla p)h \cdot \nu$. Nevertheless, in the case of a regular domain, we know that $p \in H^2_{loc}(\Omega^s)$, which implies that $\nabla p \in (H^1(\Omega^s))^n$. Moreover, we have:

$$\Delta(\nabla p) + k^2\nabla p = 0. \tag{III.3.66}$$

Using that $\Delta(\nabla p) = \nabla \cdot \nabla(\nabla p)$, we can thus deduce that $\nabla(\nabla p) \in (H_{loc}(\nabla\cdot, \Omega^f))^{n\times n}$, which implies that $\nabla(\nabla p)\nu$ is well-defined in $(H^{-1/2}(\Gamma))^n$. By this way, since the direction $h \in (\mathcal{C}^2(\mathbb{R}^n))^n$, we can define $\nabla(\nabla p)h \cdot \nu$ in $H^{-1/2}(\Gamma)$.

Using embedding theorems, we conclude that Eq. (III.3.64) is valid in $H^{-1/2}(\Gamma)$ on Γ.

Remark III.3.3.1 *In the previous proof, we have assumed that h belongs to $\mathcal{C}^2$. In fact, $\mathcal{C}^1$ is sufficient because h only needs to be a multiplier of $H^{1/2}$.*

III.3.3.2 Γ is either a curvilinear polygon or a polyhedron of class $\mathcal{C}^{1,1}$

For these cases, we refer to the books [70, 71] written by Grisvard. We are then able to define the traces locally in the sense that they are defined on each edge (face) and a generalized Green-like formula is available.

We suppose that the boundary Γ of Ω^s is a curvilinear polygon (polyhedron) of class $\mathcal{C}^{1,1}$. Let Γ_j, $1 \leq j \leq N$, be the set of $\mathcal{C}^{1,1}$ curves (faces) defining $\Gamma = \cup_{j=1}^N \Gamma_j$. Let ν_j be a vector of class $\mathcal{C}^{0,1}$ defined in a neighborhood of $\overline{\Omega}^s$ as the unit normal vector outwardly directed to $\overline{\Omega}^s$. Then, $\nu_j = \nu$ a.e on Γ_j, but in general, $\nu_j \neq \nu$ inside Ω^s.

Recall that we want to give a sense to the following quantities on Γ:

$$\begin{aligned}\frac{\partial \varphi_\theta}{\partial \theta}(0)h &= \sigma(u')\nu + h^t\nabla\sigma(u)\nu - \sigma(u)[h']^t\nu \\ &\quad + p'\nu + \nabla p \cdot h\nu - p[h']^t\nu + \nabla g \cdot h\nu - g[h']^t\nu \end{aligned} \tag{III.3.67}$$

and

$$\begin{aligned}\frac{\partial \Psi_\theta}{\partial \theta}(0)h &= (\omega^2\rho_f u' - \nabla p') \cdot \nu + \omega^2\rho_f \nabla u h \cdot \nu \\ &\quad - \nabla(\nabla p)h \cdot \nu - \nabla(\nabla g)h \cdot \nu \\ &\quad - (\omega^2\rho_f u - \nabla p - \nabla g) \cdot [h']^t\nu. \end{aligned} \tag{III.3.68}$$

We will apply a result from [70, 71] which concerns a second order elliptic operator denoted by A with coefficients smooth enough. Let $D(A, \Omega)$ be the maximal domain of A. When $\Omega = \Omega^s$, $D(\nabla \cdot \sigma, \Omega^s)$ is given by:

$$D(\nabla \cdot \sigma, \Omega^s) = \{v \in (L^2(\Omega^s))^n,\ \nabla \cdot \sigma(v) \in (L^2(\Omega^s))^n\}, \tag{III.3.69}$$

and when $\Omega = \Omega^f$,

$$D(\Delta, \Omega^f) = \{q \in L^2_{loc}(\Omega^f),\ \Delta q \in L^2_{loc}(\Omega^f)\}. \tag{III.3.70}$$

Following Grisvard [70, 71], we have (see Theorems 1.5.3.4 and 1.5.3.6, pp. 54 and 57):

Theorem III.3.3.1 *The mapping* $p \mapsto \left(p_{|\Gamma_j}, \dfrac{\partial p}{\partial \nu_j}_{|\Gamma_j}\right)$, *which is defined for* $p \in H^2_{loc}(\Omega^f)$, *has a unique continuous extension as an operator from* $D(\Delta, \Omega^f)$ *into* $H^{-1/2-\varepsilon}(\Gamma_j) \times H^{-3/2-\varepsilon}(\Gamma_j)$ *for any* $\varepsilon > 0$, *for all* $1 \leq j \leq N$.

Theorem III.3.3.2 *The mapping* $u \mapsto \left(u_{|\Gamma_j}, \sigma(u)\nu_{j|\Gamma_j}\right)$, *which is defined for* $u \in (H^2(\Omega^s))^3$, *has a unique continuous extension as an operator from* $D(\nabla\cdot\sigma, \Omega^s)$ *into* $(H^{-1/2-\varepsilon}(\Gamma_j))^n \times (H^{-3/2-\varepsilon}(\Gamma_j))^n$ *for any* $\varepsilon > 0$, *for all* $1 \leq j \leq N$.

Always following [70, 71], it is possible to characterize the traces in the dual space of $\tilde{H}^{1/2}(\Gamma_j)$ and $\tilde{H}^{3/2}(\Gamma_j)$, where $\tilde{H}^s(\Gamma_j)$ denotes the space of functions in $H^s(\Gamma_j)$ such that their continuation by zero to Γ belongs to $H^s(\Gamma)$. By analogy with the classical notations, the dual of $H^s(\Gamma_j)$ is denoted by $\tilde{H}^{-s}(\Gamma_j)$. We then have:

Theorem III.3.3.3 *The mapping* $p \mapsto \left(p_{|\Gamma_j}, \dfrac{\partial p}{\partial \nu_j}_{|\Gamma_j}\right)$ *is defined and continuous from* $D(\Delta, \Omega^f)$ *into* $\tilde{H}^{-1/2}(\Gamma_j) \times \tilde{H}^{-3/2}(\Gamma_j)$, *for all* $1 \leq j \leq N$.
Moreover, let B_R *be the ball with radius* $R > 0$ *large enough to have* $\overline{\Omega}^s \subset B_R$. *Let* $\varphi \in H^2(B_R)$ *such that* $\varphi = 0$ *on* $\partial(B_R \setminus \Omega^s)$ *and* $\partial_\nu \varphi = 0$ *on* ∂B_R. *Then, for any* $p \in D(\Delta, \Omega^f)$,

$$\int_{B_R\setminus\Omega^s} p\Delta\varphi - \int_{B_R\setminus\Omega^s} \Delta p\varphi = \sum_{j=1}^{N} \langle p, \partial_{\nu_j}\varphi\rangle_{\sim,-1/2,1/2,\Gamma_j}. \tag{III.3.71}$$

Let $\psi \in H^2(B_R)$ *such that* $\partial_\nu \psi = 0$ *on* $\partial(B_R \setminus \Omega^s)$ *and* $\psi = 0$ *on* ∂B_R. *Then, for any* $p \in D(\Delta, \Omega^f)$,

$$\int_{B_R\setminus\Omega^s} p\Delta\psi - \int_{B_R\setminus\Omega^s} \Delta p\psi = -\sum_{j=1}^{N} \langle \partial_{\nu_j} p, \psi\rangle_{\sim,-3/2,3/2,\Gamma_j}. \tag{III.3.72}$$

Theorem III.3.3.4 *The mapping* $u \mapsto \left(u_{|\Gamma_j}, \sigma(u)\nu_{j|\Gamma_j}\right)$ *is continuously defined from* $D(\nabla\cdot\sigma, \Omega^s)$ *into* $(\tilde{H}^{-1/2}(\Gamma_j))^n \times (\tilde{H}^{-3/2}(\Gamma_j))^n$, *for all* $1 \leq j \leq N$.
Moreover, let $\varphi \in H^2(\Omega^s)$ *such that* $\varphi = 0$ *on* Γ. *Then, for any* $u \in D(\nabla\cdot\sigma, \Omega^s)$,

$$\int_{\Omega^s} u\nabla\cdot\sigma(\varphi) - \int_{\Omega^s} \nabla\cdot\sigma(u)\varphi = \sum_{j=1}^{N} \langle u, \sigma(\varphi)\nu_j\rangle_{\sim,-1/2,1/2,\Gamma_j}. \tag{III.3.73}$$

Let $\psi \in H^2(\Omega^s)$ such that $\partial_\nu \psi = 0$ on Γ. Then, for any $u \in D(\nabla \cdot \sigma, \Omega^s)$,

$$\int_{\Omega^s} u \nabla \cdot \sigma(\varphi) - \int_{\Omega^s} \nabla \cdot \sigma(u) \varphi = -\sum_{j=1}^{N} \langle \sigma(u)\nu_j, \psi \rangle_{\sim,-3/2,3/2,\Gamma_j}. \tag{III.3.74}$$

Regarding the solution (u, p) to the direct problem, two terms are easy to define using the classical trace theorems [30, 35, 70, 71, 101, 102, 117]. They are as follows:

- $p \in H^{3/2}_{loc}(\Omega^f)$ implies that $p_{|\Gamma} \in H^{1/2}(\Gamma)$. Moreover, because $h \in (\mathcal{C}^2(\mathbb{R}^n))^n$, each entry of its Jacobian matrix $[h']$ is continuous. Since $\nu \in (L^\infty(\Gamma))^n$, the vector $[h']^t\nu$ thus defines a vector of L^∞, which is a multiplier of $L^2(\Gamma)$. We then get: $p[h']^t\nu_{|\Gamma} \in (L^2(\Gamma))^n$.

- $u \in (H^{3/2}(\Omega^s))^n$ implies that $u_{|\Gamma} \in (H^{1/2}(\Gamma))^n$. In addition, we have seen that $[h']^t\nu$ is well-defined on Γ in $(L^\infty(\Gamma))^n$. We thus deduce that $u \cdot [h']^t\nu \in L^2(\Gamma)$.

Next, Theorems III.3.3.3 and III.3.3.4 will help us to define the traces of the elasto-acoustic Fréchet derivative. Indeed, we have:

- $p \in H^{3/2}_{loc}(\Omega^f)$ implies that $p' \in H^{1/2}_{loc}(\Omega^f)$. Since p' satisfies the Helmholtz equation (III.3.23), we thus have $p' \in D(\Delta, \Omega^f)$. Therefore, we can apply Theorem III.3.3.3 to give a sense to $p'_{|\Gamma_j}$ in $\tilde{H}^{-1/2}(\Gamma_j)$. Regarding the transmission condition, we need to define $p'\nu_{j\,|\Gamma_j}$. But we know that ν_j is locally regular. We thus also have $p'\nu_{j\,|\Gamma_j} \in (\tilde{H}^{-1/2}(\Gamma_j))^n$, $1 \leq j \leq N$.

- $u \in (H^{3/2}(\Omega^s))^n$ implies that $u' \in (H^{1/2}(\Omega^s))^n$. Observing that u' is solution to the Navier equation (III.3.14), we thus have $u' \in D(\nabla \cdot \sigma, \Omega^s)$. We can then apply Theorem III.3.3.4, which allows us to define $\sigma(u')\nu_{j\,|\Gamma_j}$ in $(\tilde{H}^{-3/2}(\Gamma_j))^n$.

Moreover we also have:

- $\dfrac{\partial p'}{\partial \nu_j}_{|\Gamma_j} \in \tilde{H}^{-3/2}(\Gamma_j)$, $1 \leq j \leq N$, following Theorem III.3.3.3,

and

- $u'_{|\Gamma_j} \in (\tilde{H}^{-1/2}(\Gamma_j))^n$, $1 \leq j \leq N$, following Theorem III.3.3.4. Observing that ν_j is regular on Γ_j, we then have also that $u' \cdot \nu_j \in \tilde{H}^{-1/2}(\Gamma_j)$, $1 \leq j \leq N$.

Now, we can apply again Theorems III.3.3.3 and III.3.3.4 to give a sense to each of the following terms: $\nabla p \cdot h\nu_{|\Gamma}$, $\nabla p \cdot [h']^t\nu_{|\Gamma}$, $\nabla uh \cdot \nu_{|\Gamma}$, and $\sigma(u)[h']^t\nu_{|\Gamma}$, using similar arguments as for p' and u'.

Indeed, let us denote by ∂ one of the partial derivatives $\dfrac{\partial}{\partial x_j}$, $1 \leq j \leq n$, p' can be replaced by $\dfrac{\partial p}{\partial x_j}$, $1 \leq j \leq n$, and u' by $\dfrac{\partial u}{\partial x_j}$, $1 \leq j \leq n$ as follows.

- Since p satisfies the Helmholtz equation (III.2.3) and using the fact that the partial derivatives of p commutes with the Laplace operator, we have:

$$\Delta(\partial p) + k^2 \partial p = 0. \tag{III.3.75}$$

  Observing that ∂p is in $H^{1/2}_{loc}(\Omega^f)$ because $p \in H^{3/2}_{loc}(\Omega^f)$, we thus obtain that $\partial p \in D(\Delta, \Omega^f)$. Theorem III.3.3.3 then implies that $\partial p_{|\Gamma_j}$ is well-defined in $\tilde{H}^{-1/2}(\Gamma_j)$, and therefore $\nabla p_{|\Gamma_j}$ is well-defined in $(\tilde{H}^{-1/2}(\Gamma_j))^n$. Using that the direction $h \in (\mathcal{C}^2(\mathbb{R}^n))^n$, $\nabla p \cdot h_{|\Gamma_j}$ remains in $\tilde{H}^{-1/2}(\Gamma_j)$. Then, since ν is locally regular, $\nabla p \cdot h \nu_{|\Gamma_j}$ is also in $(\tilde{H}^{-1/2}(\Gamma_j))^n$, for all $1 \leq j \leq N$.

- We have seen that $\nabla p_{|\Gamma_j} \in (\tilde{H}^{-1/2}(\Gamma_j))^n$. Observing that each entry of $[h']$ is in $\mathcal{C}^1(\mathbb{R}^n)$, and using that ν is locally regular, we thus obtain that $\nabla p \cdot [h']^t \nu_{|\Gamma_j}$ is well-defined in $\tilde{H}^{-1/2}(\Gamma_j)$ too, for all $1 \leq j \leq N$.
- Since u satisfies the Navier equation (III.2.2) and using the fact that the partial derivatives of u commutes with the elastodynamic operator, we then have:

$$\nabla \cdot \sigma(\partial u) + \omega^2 \rho_s \partial u = 0. \tag{III.3.76}$$

  Because $\partial u \in H^{1/2}(\Omega^s)$, we get that $\partial u \in D(\nabla \cdot \sigma, \Omega^s)$. It then follows from Theorem III.3.3.4 that $\partial u_{|\Gamma_j}$ is well-defined in $(\tilde{H}^{-1/2}(\Gamma_j))^n$, and therefore $\nabla u_{|\Gamma_j}$ is well-defined in $(\tilde{H}^{-1/2}(\Gamma_j))^{n \times n}$. Using that $h \in (\mathcal{C}^2(\mathbb{R}^n))^n$ and ν is locally regular, we obtain that $\nabla u h \cdot \nu_{|\Gamma_j}$ is also in $\tilde{H}^{-1/2}(\Gamma_j)$, for all $1 \leq j \leq N$.

- We have noticed that $\partial u_{|\Gamma_j} \in (\tilde{H}^{-1/2}(\Gamma_j))^n$. It follows that the trace of the strain tensor $\varepsilon(u)$ is in $(\tilde{H}^{-1/2}(\Gamma_j))^{n \times n}$. Assuming that the coefficients C_{jlmn} of the fourth order elastic stiffness tensor are sufficiently regular, the trace of the stress tensor $\sigma(u)_{|\Gamma_j}$ remains in $(\tilde{H}^{-1/2}(\Gamma_j))^{n \times n}$. Then, since each entry of $[h']$ is in $\mathcal{C}^1(\mathbb{R}^n)$, and ν is locally regular, we deduce that $\sigma(u)[h']^t \nu_{|\Gamma_j}$ is well-defined in $(\tilde{H}^{-1/2}(\Gamma_j))^n$ too, for all $1 \leq j \leq N$.

Now, to complete the characterization, we need to define the following terms involving high-order derivatives: $(\nabla(\nabla p)h) \cdot \nu_{|\Gamma}$, $h^t \nabla \sigma(u) \nu_{|\Gamma}$. We can use the same arguments as for $\dfrac{\partial p'}{\partial \nu}_{|\Gamma}$ and $\sigma(u')\nu_{|\Gamma}$.

- Let us begin with the trace $\nabla(\nabla p)h\cdot\nu_{|\Gamma}$. We have seen that $\partial p\in D(\Delta,\Omega^f)$. Therefore, we can apply Theorem III.3.3.3 and give a sense to $\nabla(\partial p)\cdot\nu_{|\Gamma}$ on each Γ_j in $\tilde{H}^{-3/2}(\Gamma_j)$. It then follows that $\nabla(\nabla p)\nu_{j\,|\Gamma_j}$ can be defined in $(\tilde{H}^{-3/2}(\Gamma_j))^n$. Now, since $h_{|\Gamma_j}\in(\mathcal{C}^2(\Gamma))^n$, we then have :
$$h^t\nabla(\nabla p)\nu_{j\,|\Gamma_j}\in\tilde{H}^{-3/2}(\Gamma_j),\ 1\le j\le N.$$
because $\mathcal{C}^2$ is a multiplier of $\tilde{H}^{3/2}(\Gamma_j)$.

- As regards the last term $h^t\nabla\sigma(u)\nu_{|\Gamma}$, we proceed similarly. We have observed that $\partial u\in D(\nabla\cdot\sigma,\Omega^s)$. Therefore, following Theorem III.3.3.4, $\sigma(\partial u)\nu_{|\Gamma}$ has a sense on each Γ_j in $(\tilde{H}^{-3/2}(\Gamma_j))^n$, which amounts to $\partial\sigma_l(u)\nu_{j\,|\Gamma_j}\in\tilde{H}^{-3/2}(\Gamma_j)$, for all $1\le l\le n$. It then follows that $\nabla\sigma_l(u)\nu_{j\,|\Gamma_j}$ can be defined in $(\tilde{H}^{-3/2}(\Gamma_j))^n$. Consequently, since $h_{|\Gamma_j}\in(\mathcal{C}^2(\Gamma))^n$, we conclude that:
$$(h^t\nabla\sigma_l(u)\nu_{j\,|\Gamma_j})_{1\le l\le n}\in\tilde{H}^{-3/2}(\Gamma_j),\ 1\le j\le N.$$

Remark III.3.3.2 *We can notice the importance of the local regularity of the normal vector to be able to give a sense to the quantities of interest on the boundary Γ, such as, for instance, $p'\nu$, and $u'\cdot\nu$.*

III.3.3.3 Γ is either a linear polygon or a polyhedron of class $\mathcal{C}^{0,1}$

Here, we deal directly with the three dimensional case. We consider the case a polyhedron of class $\mathcal{C}^{0,1}$ using the results from Ciarlet et *al* [8–10].
This case is less regular than the previous one in the sense that the boundary Γ is locally represented by a $\mathcal{C}^{0,1}$ function. Nevertheless, the normal ν_j is regular on each face, but the boundary can admit corners, which was not the case in the previous section.
Using the same notations as in Section III.3.3.2, and following [8–10], we have, for all $1\le j\le N$:

Theorem III.3.3.5

(i) The mapping $p\mapsto p_{|\Gamma_j}$ is linear and continuous from $D(\Delta,\Omega^f)$ to $\tilde{H}^{-1/2}(\Gamma_j)$.

(ii) The following Green formula holds:

$$\int_{\Omega^f}p\Delta q-\int_{\Omega^f}q\Delta p=\sum_j\langle p_{|\Gamma_j},\frac{\partial q}{\partial\nu}_{|\Gamma_j}\rangle_{\sim,-1/2,1/2,\Gamma_j},\ \forall\,(p,q)\in D(\Delta,\Omega^f)\times H^D(\Omega^f).\quad\text{(III.3.77)}$$

(iii) The mapping $p\mapsto\dfrac{\partial p}{\partial\nu}_{|\Gamma_j}$ is linear and continuous from $D(\Delta,\Omega^f)$ to $\tilde{H}^{-3/2}(\Gamma_j)$.

(iv) The following Green formula holds:

$$\int_{\Omega^f} p\Delta q - \int_{\Omega^f} q\Delta p = -\langle \frac{\partial p}{\partial \nu}_{|\Gamma_j}, q_{|\Gamma_j}\rangle_{\sim,-3/2,3/2,\Gamma_j},\ \forall\ (p,q) \in D(\Delta,\Omega^f)\times H_j^N(\Omega^f). \quad \text{(III.3.78)}$$

In the above theorem, $\tilde{H}^s(\Gamma_j)$ is defined as the space of elements φ of $H^s(\Gamma_j)$ such that the continuation of φ by 0 to Γ belongs to $H^s(\Gamma)$. The dual space of $\tilde{H}^s(\Gamma_j)$ is then denoted $\tilde{H}^{-s}(\Gamma_j)$. Moreover, always following [9], the spaces $H^D(\Omega^f)$ and $H_j^N(\Omega^f)$ are given by:

$$\begin{aligned} H^D(\Omega^f) &= H^2_{loc}(\Omega^f)\cap H^1_0(\Omega^f) \\ H_j^N(\Omega^f) &= \{q\in H^2_{loc}(\Omega^f),\ \frac{\partial q}{\partial \nu}_{|\Gamma} = 0,\ q_{|\Gamma_l}=0,\ \forall\ l\neq j\} \end{aligned}$$

The space $\tilde{H}^s(\Gamma_j)$ has been introduced by Grisvard in [70, 71] and also in [14]. Theorem III.3.3.5 provides a generalized Green formula that is of great interest to write the variational formulation of the problem defining (u',p'). In particular, it shows that for the numerical simulations, we define each trace locally on each face Γ_j, which is consistent with the regularity results that we obtain.

Now, recall that we want to give a sense to the following quantities on Γ:

$$\begin{aligned} \frac{\partial \varphi_\theta}{\partial\theta}(0)h &= \sigma(u')\nu + h^t\nabla\sigma(u)\nu - \sigma(u)[h']^t\nu \\ &\quad + p'\nu + \nabla p\cdot h\nu - p[h']^t\nu + \nabla g\cdot h\nu - g[h']^t\nu \end{aligned} \quad \text{(III.3.79)}$$

and

$$\begin{aligned} \frac{\partial \Psi_\theta}{\partial\theta}(0)h &= (\omega^2\rho_f u' - \nabla p')\cdot\nu + \omega^2\rho_f\nabla u h\cdot\nu \\ &\quad -\nabla(\nabla p)h\cdot\nu - \nabla(\nabla g)h\cdot\nu \\ &\quad -(\omega^2\rho_f u - \nabla p - \nabla g)\cdot[h']^t\nu. \end{aligned} \quad \text{(III.3.80)}$$

The terms $p[h']^t\nu_{|\Gamma}$ and $u\cdot[h']^t\nu$, associated with the solution (u,p) to the direct problem, can be defined in $(L^2(\Gamma))^n$ and $L^2(\Gamma)$ respectively, in the same way as in the previous section using the classical trace theorems.

Moreover, as Theorem III.3.3.1 in the previous section, Theorem III.3.3.5 allows to give a sense to the terms $p'\nu_{|\Gamma_j}$, $\nabla p\cdot h\nu_{|\Gamma_j}$, $\nabla p\cdot[h']^t\nu_{|\Gamma_j}$ in $(\tilde{H}^{-1/2}(\Gamma_j))^n$ and $\tilde{H}^{-1/2}(\Gamma_j)$, as well as to $\frac{\partial p'}{\partial\nu}_{|\Gamma_j}$ and $\nabla(\nabla p)h\cdot\nu_{|\Gamma_j}$ in $\tilde{H}^{-3/2}(\Gamma_j)$.

However, regarding the displacement field, we have to extend the results of [9] given in the case of the Laplace operator. Unfortunately, the proof of Theorem III.3.3.5 requires surjectivity results that are not obvious. For instance, we need to prove that for any $\varphi \in (\tilde{H}^{1/2}(\Gamma_j))^n$, there exists $u \in \{v \in (H^2(\Omega^s))^n \cap (H_0^1(\Omega^s))^n, \sigma(u)\nu_{|\Gamma_l} = 0, \text{ for } l \neq j\}$, such that $\sigma(u)\nu_{|\Gamma_j} = \varphi$. At first sight, we were not able to construct such a lifting operator and thus, the question remained open. However, a joint work has been recently initiated with Serge Nicaise, and we think that we are able to define such results in the case of the elastodynamic operator. Once done, this should allow to complete the rigorous justification in the framework of a Lipschitz polyhedron.

III.3.3.4 The general case: Ω^s is a continuous Lipschitz domain

Obviously, this case generates more difficulties than the previous ones. We still aim at giving a sense to the following quantities on Γ:

$$\begin{aligned}\frac{\partial \varphi_\theta}{\partial \theta}(0)h &= \sigma(u')\nu + h^t\nabla\sigma(u)\nu - \sigma(u)[h']^t\nu \\ &\quad + p'\nu + \nabla p \cdot h\nu - p[h']^t\nu + \nabla g \cdot h\nu - g[h']^t\nu \end{aligned} \tag{III.3.81}$$

and

$$\begin{aligned}\frac{\partial \Psi_\theta}{\partial \theta}(0)h &= (\omega^2\rho_f u' - \nabla p') \cdot \nu + \omega^2\rho_f \nabla u h \cdot \nu \\ &\quad -\nabla(\nabla p)h \cdot \nu - \nabla(\nabla g)h \cdot \nu \\ &\quad -(\omega^2\rho_f u - \nabla p - \nabla g) \cdot [h']^t\nu. \end{aligned} \tag{III.3.82}$$

What remains true is that the terms $p[h']^t\nu_{|\Gamma}$ and $u \cdot [h']^t\nu$ can be defined in $L^2(\Gamma)$ and $(L^2(\Gamma))^n$ respectively, using the classical trace theorems as done in Section III.3.3.2.

We tried to get more results but, unfortunately even in the case of the pressure fluid, we were not able to extend the results of [9, 70] to give a sense to p' in particular. Indeed, such a result should be necessary to give a sense to the term p' which belongs to $D(\Delta, \Omega^f)$. More precisely, if one wants to follow the lines of [8, 9], some surjectivity results are required to define the trace theorems in $D(\Delta, \Omega^f)$. The difficulty remains the construction of the suitable lifting operators because of the compatibility condition defining the range of the trace mappings and which depends on the geometry of the domain.

Nevertheless, we obtained a characterization of the traces $\nabla p_{|\Gamma}$, and $\nabla(\nabla p)\nu_{|\Gamma}$. This allows to give a sense to the following terms associated to the pressure field: $\nabla p \cdot h\nu$, $\nabla p \cdot [h'^t]\nu$, and $\nabla(\nabla p)h \cdot \nu$ on the Lipschitz boundary Γ. We proceed as follows.
According to [21], we define the range of the trace mappings $\mathcal{R}$ from H^2-functions on a Lipschitz domain Ω as follows:

$$\mathcal{R} = \{\gamma_0 v, \gamma_1 v, v \in H^2(\Omega)\}. \tag{III.3.83}$$

This is a Hilbert space dense in $H^1(\Gamma) \times L^2(\Gamma)$. It has been characterized in [21] and it is proved that in $\mathcal{R}$, the pair $(\gamma_0 v, \gamma_1 v)$ satisfies a compatibility condition, given in three dimensions by:

$$\mathcal{R} = \{(g_0, g_1) \in H^1(\Gamma) \times L^2(\Gamma) \quad \text{such that } \nabla_\Gamma(g_0) + g_1\nu \in (H^{1/2}(\Gamma))^n\}. \tag{III.3.84}$$

We can view it as a product space $\mathcal{R} = \mathcal{R}_0 \times \mathcal{R}_1$.
It is worth noting that, when considering smooth domains of class $\mathcal{C}^2$ (or $\mathcal{C}^{1,1}$), the range of the trace mappings is exactly characterized, and is equal to $\mathcal{R} = H^{3/2}(\Gamma) \times H^{1/2}(\Gamma)$. As regards polyhedra of $C^{1,1}$ or $C^{0,1}$, without going into the details, the traces are described locally face by face. Because of the boundary singularities, there exists matching conditions at edges and corners [14, 15, 70]. Then, the range of the trace mappings are defined, on each face Γ_j, in the space $\tilde{H}^{1/2}(\Gamma_j) \times \tilde{H}^{3/2}(\Gamma_j)$, whose definition can be found in [8–10, 70] and Section III.3.3.3.

We do not argue about the infinite domain Ω^f. Indeed, we deal with the solution to the Helmholtz equation which is thus regular in the neighborhood of any surface surrounding $\overline{\Omega}^s$. We can thus restrict the proof to the case of a bounded domain that we denote Ω and whose boundary has the same regularity than Γ, and is still denoted by Γ.

Proposition III.3.3.1 *Let us consider the problem in pressure, formulated as follows:*

$$\begin{cases} -\Delta p = ap \in H^1(\Omega) \\ \dfrac{\partial p}{\partial \nu} = c\, u \cdot \nu - \dfrac{\partial g}{\partial \nu} \in L^2(\Gamma) \end{cases} \tag{III.3.85}$$

with $a = \dfrac{\omega^2}{c_f^2}$ *and* $c = \omega^2 \rho_f$.
Then, $(\nabla p_{|\Gamma}, \dfrac{\partial}{\partial \nu}\nabla p_{|\Gamma})$ *is well defined as an element of* $\left(\mathcal{R}_1'\right)^n \times \left(\mathcal{R}_0'\right)^n$.
Moreover, the trace of any element of $H^2(\Omega)/K(\Omega)$ *is in* $(H^1(\Gamma))^n \times (L^2(\Gamma))^n$, *where* $K(\Omega)$ *is given*

by the following closed subspace of $H^2(\Omega)$:

$$K(\Omega) = \{\psi \in H^2(\Omega); \left[\int_\Omega \nabla p \cdot \nabla \frac{\partial \psi}{\partial x} - \int_\Omega \frac{\partial p}{\partial x} \Delta \psi\right] = 0\}. \tag{III.3.86}$$

Proof A natural idea is to do this by means of a process of duality, that is to say in the dual spaces to the trace spaces. The difficulty encountered here comes from the fact that the boundary Γ of Ω^s is only assumed lipschitzian. The classical Sobolev spaces $H^s(\Gamma)$ on Γ are only defined intrinsically for $-1 \leq s \leq 1$.

For a function $q \in H^2(\Omega)$, the classical traces can no longer be well defined as elements of $H^{3/2}(\Gamma) \times H^{1/2}(\Gamma)$, as in the regular case. Moreover, the surjectivity of the trace operators, that we will denote by γ_0, γ_1, from $H^2(\Omega)$ onto $H^{3/2}(\Gamma) \times H^{1/2}(\Gamma)$ is no longer true.

Actually, these traces are in $\mathcal{R}$, defined by Eq.(III.3.83), which is a subspace of $H^1(\Gamma) \times L^2(\Gamma)$, and have to satisfy a compatibility condition that depends on the geometry of Ω, given by Eq.(III.3.84).

The trace spaces of functions of $H^2(\Omega)$ for a lipschitzian domain Ω have been characterized by G. Geymonat and F. Krasucki [63] in two dimensions and by A. Buffa and G. Geymonat in three dimensions [21]. These characterizations extend those accomplished by P. Grisvard [71] in the case of a polygon of $\mathbb{R}^2$ or a polyhedron in $\mathbb{R}^3$.

Using the results of Jerison-Kenig [90, 91], and M. Costabel [31], since $\frac{\partial p}{\partial \nu} \in L^2(\Gamma)$, we easily check that $\gamma_0 p \in H^1(\Gamma)$ and that $p \in H^{3/2}(\Omega)$.

Let x be one of the coordinate variables of $\mathbb{R}^n$. Set $q = \frac{\partial p}{\partial x}$. We want to give a sense to $\frac{\partial q}{\partial \nu}$ on Γ.

We first remark that, in the distribution sense, we have:

$$-\Delta q = aq. \tag{III.3.87}$$

Note that if Ω was regular, and because $q \in L^2(\Omega)$, this would give a sense to $\frac{\partial q}{\partial \nu}$ in $H^{-3/2}(\Gamma)$.

Moreover, we recall that p is solution to the following variational equation:

$$\int_\Omega \nabla p \cdot \nabla v = \int_\Omega apv + \int_\Gamma \frac{\partial p}{\partial \nu} v = \int_\Omega apv + \int_\Gamma l(u)v, \tag{III.3.88}$$

for all $v \in H^1(\Omega)$, with $l(u) = c\,un \cdot \nu - \frac{\partial g}{\partial \nu}$ on Γ.

For $\psi \in H^2(\Omega)$, we take $v = \frac{\partial \psi}{\partial x}$ in (III.3.88) and using Eq. (III.3.87), we obtain:

$$
\begin{aligned}
-\int_\Omega \Delta q\psi &= a\int_\Omega \frac{\partial p}{\partial x}\psi && \text{(III.3.89)}\\
&= -a\int_\Omega p\frac{\partial \psi}{\partial x} + a\int_\Gamma (p\psi)\nu_x && \text{(III.3.90)}\\
&= -\int_\Omega \nabla p\cdot\nabla\frac{\partial\psi}{\partial x} + \int_\Gamma \frac{\partial p}{\partial \nu}\frac{\partial\psi}{\partial x} + a\int_\Gamma (p\psi)\nu_x. && \text{(III.3.91)}
\end{aligned}
$$

This last expression defines a continuous linear form on $H^2(\Omega)$. Therefore, the linear form defined as

$$
L(\psi) = -\int_\Omega \Delta q\psi + \int_\Omega \nabla p\cdot\nabla\frac{\partial\psi}{\partial x} = \int_\Gamma \frac{\partial p}{\partial\nu}\frac{\partial\psi}{\partial x} + a\int_\Gamma (p\psi)\nu_x \qquad \text{(III.3.92)}
$$

is also linear continuous on $H^2(\Omega)$.
At this stage, it should be first noted that, if $\psi \in H_0^2(\Omega)$ (defined as the closure of $\mathcal{D}(\Omega)$ in $H^2(\Omega)$),

then $L(\psi) = 0$.
Thus, L only depends on the traces of ψ. Hence, L is a continuous linear form on $\mathcal{R}$ which, according to [21], is contained in $H^1(\Gamma)\times L^2(\Gamma)$.
Consequently, there exists a pair of $\mathcal{R}'$, dual of $\mathcal{R}$, denoted (L_0, L_1), such that:

$$
L(\psi) = L_0(\gamma_0\psi) + L_1(\gamma_1\psi). \qquad \text{(III.3.93)}
$$

To come down to a standard situation, we set:

$$
L(\psi) = \left[-\int_\Omega \Delta q\psi + \int_\Omega q\Delta\psi\right] + \left[\int_\Omega \nabla p\cdot\nabla\frac{\partial\psi}{\partial x} - \int_\Omega q\Delta\psi\right]. \qquad \text{(III.3.94)}
$$

We denoted by $K(\Omega)$ the following closed subspace of $H^2(\Omega)$:

$$
K(\Omega) = \{\psi\in H^2(\Omega); \int_\Omega \nabla p\cdot\nabla\frac{\partial\psi}{\partial x} - \int_\Omega q\Delta\psi = 0\}. \qquad \text{(III.3.95)}
$$

Then, for all $\psi \in K\Omega)$, we have:

$$
\begin{aligned}
-\int_\Omega \Delta q\psi + \int_\Omega q\Delta\psi &= L_0(\gamma_0\psi) + L_1(\gamma_1\psi) && \text{(III.3.96)}\\
&= \int_\Gamma \frac{\partial p}{\partial\nu}\frac{\partial\psi}{\partial x} + a\int_\Gamma (p\psi)\nu_x. && \text{(III.3.97)}
\end{aligned}
$$

The term $a\int_\Gamma (p\psi)\nu_x$ only depends on $\gamma_0\psi$. For the second one, we proceed as follows.
We consider, for almost every $x\in\Gamma$, a basis (τ_1,τ_2,ν) obtained by atlas. We note (e_1,e_2,e_3) the

canonical basis. For instance, assuming that the chosen variable x is the first one, we have:

$$\frac{\partial \psi}{\partial x} = (\nabla \psi) e_1. \tag{III.3.98}$$

Then, if (a_1, a_2, a_3) are the coordinates of e_1 is the basis (τ_1, τ_2, ν), we have:

$$\frac{\partial \psi}{\partial x} = a_1 \frac{\partial \psi}{\partial \tau_1} + a_2 \frac{\partial \psi}{\partial \tau_2} + a_3 \frac{\partial \psi}{\partial \nu}, \tag{III.3.99}$$

where a_1, a_2, a_3 are $L^\infty(\Gamma)$-functions.

Hence, we can rewrite L as follows:

$$L(\psi) = \int_\Gamma a_3 \frac{\partial p}{\partial \nu} \frac{\partial \psi}{\partial \nu} + \int_\Gamma \frac{\partial p}{\partial \nu} \left[a_1 \frac{\partial \psi}{\partial \tau_1} + a_2 \frac{\partial \psi}{\partial \tau_2} \right] + a \int_\Gamma (p\psi) \nu_x. \tag{III.3.100}$$

It is then clear that:

$$\begin{cases} L_0(\gamma_0 \psi) = \displaystyle\int_\Gamma \frac{\partial p}{\partial \nu} \left[a_1 \frac{\partial \psi}{\partial \tau_1} + a_2 \frac{\partial \psi}{\partial \tau_2} \right] + a \int_\Gamma (p\psi) \nu_x \\ L_1(\gamma_1 \psi) = \displaystyle\int_\Gamma a_3 \frac{\partial p}{\partial \nu} \frac{\partial \psi}{\partial \nu}. \end{cases} \tag{III.3.101}$$

Since $\dfrac{\partial p}{\partial \nu} \in L^2(\Gamma)$, $a_i \in L^\infty(\Gamma)$ for $i = 1, 2, 3$, it immediately follows that:

$$|L_0(\gamma_0 \psi)| \leq C \left(\int_\Gamma |\nabla_T \psi|^2 + |\psi|^2 \right)^{1/2}. \tag{III.3.102}$$

Still according to [21] (see Proposition 4), we get:

$$|L_0(\gamma_0 \psi)| \leq C \|\gamma_0 \psi\|_{H^1(\Gamma)}. \tag{III.3.103}$$

In addition, we obtain, for $\psi \in K(\Omega)$, that:

$$\begin{aligned} -\int_\Omega \Delta q \psi + \int_\Omega q \Delta \psi &= \int_\Gamma a_3 \frac{\partial p}{\partial \nu} \frac{\partial \psi}{\partial \nu} && \text{(III.3.104)} \\ &\quad + \int_\Gamma \frac{\partial p}{\partial \nu} \left[a_1 \frac{\partial \psi}{\partial \tau_1} + a_2 \frac{\partial \psi}{\partial \tau_2} \right] + a \int_\Gamma (p\psi) \nu_x. && \text{(III.3.105)} \end{aligned}$$

This formally gives:

$$\left\{\begin{array}{l} q = a_3 \dfrac{\partial p}{\partial \nu} \\ \dfrac{\partial q}{\partial \nu} = \dfrac{\partial}{\partial \tau_1}\left(a_1 \dfrac{\partial p}{\partial \nu}\right) + \dfrac{\partial}{\partial \tau_2}\left(a_2 \dfrac{\partial p}{\partial \nu}\right) - ap\nu_x \quad \text{on } \Gamma. \end{array}\right. \tag{III.3.106}$$

The latter has a sense in $H^{-1}(\Gamma)$, and $q = a_3 \dfrac{\partial p}{\partial \nu} \in L^2(\Gamma)$.
We deduce that $(L_1(\gamma_1\psi), L_0(\gamma_0\psi))$ is defined as an element of $(\mathcal{R}_1')^n \times (\mathcal{R}_0')^n$, but restricted to the subspace $K(\Omega)$, it is written as

$$L_0(\gamma_0\psi) = -\langle \frac{\partial q}{\partial \nu}, \gamma_0\psi \rangle_{H^{-1}(\Gamma)\times H^1(\Gamma)} \tag{III.3.107}$$

$$L_1(\gamma_1\psi) = \langle q, \gamma_1\psi \rangle_{L^2(\Gamma)\times L^2(\Gamma)}. \tag{III.3.108}$$

Note that because Γ has no boundary, we have $(H^1(\Gamma))' = H^{-1}(\Gamma)$.
Using the same argument for each variable, we finally get the result.

■

Remark III.3.3.3 *Let us consider ψ under the following form:*

$$\psi(x, y, z) = \alpha x + \beta y + \gamma z + \delta$$

with $\alpha \neq 0$.
It is then clear that $\psi \in K(\Omega)$ because $\Delta\psi = 0$ and $\nabla \dfrac{\partial \psi}{\partial x} = 0$. This condition is actually necessary because of the non-uniqueness of the Neumann problem.
Indeed, the Neumann problem formulated as, $-\Delta p = ap$ with $\dfrac{\partial p}{\partial \nu} = l$, gives:

$$\int_\Omega ap\alpha = -\int_\Gamma \frac{\partial p}{\partial \nu}\alpha = -\int_\Gamma \frac{\partial p}{\partial \nu}\frac{\partial \psi}{\partial x}. \tag{III.3.109}$$

Moreover, we have

$$L(\psi) = a\int_\Omega \frac{\partial p}{\partial x}\psi \tag{III.3.110}$$

$$= a\int_\Gamma (p\psi)\nu_x - a\int_\Omega p\alpha \tag{III.3.111}$$

$$= \int_\Gamma \frac{\partial p}{\partial \nu}\frac{\partial \psi}{\partial x} + a\int_\Gamma (p\psi)\nu_x. \tag{III.3.112}$$

We recover the compatibility condition given by Eq. (III.3.109). Therefore, $K(\Omega)$ can be identified (for the three derivatives) as the quotient of $H^2(\Omega)$ by the polynomials of degree 1 (without the unnecessary constraints for our construction).

Remark III.3.3.4

- *Actually, even if $p^{'}$ has a sense in some space $H^s(\Gamma)$, with $s < 0$, the product $p^{'}\nu$ is not meaningful anymore since the normal ν is only L^∞. Therefore, the regularity of $p^{'}$ should be at least $L^2(\Gamma)$ to be able to define such a product globally. This means that p' should be $H^{1/2+\epsilon}_{loc}(\Omega^f)$ and thus would require p to be $H^{3/2+\epsilon}_{loc}(\Omega^f)$ for some $\epsilon > 0$, which is not the case due to the boundary singularities. Otherwise, we might need to restrict ourselves to Lipschitz domain such that ν is piecewise smooth.*

- *Since it appears to be difficult to define such traces in some strong sense on Lipschitz domains, an idea might consist of approaching the Lipschitz boundary Γ with a polyhedron Γ_h. Then, we would have to prove that the solution (u_h, p_h) in $\Omega^s_h \times \Omega^s_h$ and its traces tend to the solution (u, p) and the corresponding traces at least in a very weak sense. Thus, this could ensure that the problem on Lipschitz domains would be well-posed in a very weak sense.*

Remark III.3.3.5 *The general Lipschitz case provides a very challenging theoretical issue but we do not think it defines the real limitations to this work. Indeed, the boundary value problem satisfied by the Fréchet derivative is artificial. It has no real physical meaning, but only a practical one. Moreover, from a numerical viewpoint, these are the cases of polyhedral domains of class $\mathcal{C}^{1,1}$ or $\mathcal{C}^{0,1}$ that interest us, since they would correspond to our computational domain. Consequently, it can be viewed as sufficient to have the rigorous justification for these kinds of domains for our computations.*

III.4 Conclusion

In this paper, we have established the continuous dependence of the scattering amplitude on the shape of the scattering, by proving that both the scattered field and the far-field pattern are differentiable with respect to the domain of the obstacle. Moreover, we have fully characterized the derivative of the elasto-acoustic scattered field with respect to particular Lipschitz domains like $C^{1,1}$ polyhedra. For $C^{0,1}$ polyhedra, we conjecture that the justification can be completed, this is an ongoing work. For general Lipschitz domain, we were not able to complete the proof because of a lack of surjectivity of the trace of the elastic displacement. However, we have formally obtained that the Fréchet derivative is a solution of the same direct elasto-acoustic scattering problem that only differs by the transmission conditions at the interface of the elastic scatterer. This characterization will thus be of

practical interest and has an important potential for reducing the complexity of the solution of inverse scattering problems by Newton-type methods.

Chapter IV

A regularized Newton-type method for the solution of an Inverse Obstacle Problem in fluid-structure interaction

In this chapter, we present some promising results obtained with the proposed solution methodology for solving efficiently inverse two-dimensional elasto-acoustic problems. We observe the behavior of the method using different types of parametrization of the scatterer (polygonal shape, star-like domain, and quadratic B-spline representation).

IV.1 Introduction

The determination of the shape of an obstacle from its effects on known acoustic or electromagnetic waves is an important problem in many technologies such as sonar, geophysical exploration and medical imaging or non-destructive testing. Because of its ill-posed and nonlinear character, this inverse obstacle problem (IOP) is difficult to solve, especially from a numerical viewpoint. Any attempt to its investigation requires the fundamental understanding of the theory for the associated direct scattering problem, and the mastery of the corresponding numerical solution methods.

In this work, we are interested in retrieving the shape of an elastic scatterer from the knowledge of some scattered far-field patterns, and assuming certain characteristics of the surface of the obstacle. We propose a solution methodology based on a regularized Newton-type method, known to be robust and efficient to solve this class of IOPs. Note that this approach can be viewed as an extension to the method proposed in [42] for the case of impenetrable scatterers. A number of methods have been proposed in recent years to solve elastic inverse problems numerically. In particular, Elchner *et al* proposed an optimization method in [46] with an objective functional-based approach depending on

a positive regularization parameter, together with a Gauss-Newton method. It is worth noting that our formulation coincides with their third objective functional. They also extend the method of Kirsch and Kress, based on an integral equation approach, to this IOP [47], and compare the results with their optimization method in [48]. At the same time, Monk and Selgas applied the Linear Sampling Method (LSM), introduced by Colton and Kirsch, to the inverse problem with far-field pattern data in [109] and near-field sampling-type methods in [110]. One advantage of the LSM over Newton method is that it avoids an iterative process, since the inverse problem can be formulated as an ill-posed first kind linear integral equation. Moreover, LSM allows to consider limited-aperture data and different boundary conditions without an a priori knowledge of the type of boundary conditions, so that it is independent of the geometry and physical properties of the scatterer. However, the main drawback of the LSM is that it requires to have the far-field pattern data corresponding to incident waves from many directions. In contrast, Newton method should deliver a good reconstruction using only a few incident directions and limited-aperture data. Therefore, even if Newton method requires an efficient direct solver, and a priori information, the method is conceptually simple, it is known to be more stable with respect to nonsmooth boundaries and more robust to the noise. Last, our methodology is interesting to reconstruct simultaneously both the shape and the material properties of the scatterer.

The solution of this IOP by a regularized Newton method incurs, at each iteration, the solution of a linear system whose entries are the Fréchet derivatives of the elasto-acoustic field with respect to the shape parameters. Moreover, ensuring the stability, fast convergence, and computational efficiency calls for computing these derivatives with a greater robustness and a higher level of accuracy than possible with finite differences. To this effect, following the approach used in [39] for the case of exterior Helmholtz problems, we have characterized in Chapter III the Fréchet derivative of the elasto-acoustic scattered field with respect to the shape of an elastic obstacle as the solution of a direct elasto-acoustic scattering problem which differs from the considered direct scattering problem only in the transmission conditions on the surface of the scatterer. Consequently, at each regularized Newton iteration, we can thus evaluate both the scattered field and the directional derivatives by solving a single system of equations with different right-hand sides. Observe that, in [46], the approach to characterize the directional derivative of the scattered field is based on the differentiation of the variational formulation of the boundary value problem, and the gradient for their optimization problem can be computed as the solution of the variational equation of the same transmission problem but with modified right-hand sides.

Clearly, the performance of the IOP solver depends mainly on the computational efficiency of the solution of the forward problems that arise at each Newton iteration. To this end, we propose to solve the direct scattering-type problems using a finite-element method based on discontinuous Galerkin

approximations, equipped with curved boundary edges, described in Chapter II. We present numerical results that illustrate the potential of the proposed solution methodology for retrieving the shape of scatterers with some singularities.

The remainder of the chapter is organized as follows. In Section IV.2, we recall the associated direct elasto-acoustic scattering problem. In Section IV.3, we outline the proposed solution methodology. We formulate the IOP of interest. We recall the important analytical characterization of the Fréchet derivatives of the far-field pattern with respect to the shape parameters established in Chapter III, and highlight its significance to the evaluation of the Jacobian matrices associated with the regularized Newton method. We also recall the discretization method proposed in Chapter II, and summarize the computational complexity of the proposed IOP solution methodology. In section IV.4, we illustrate the salient features of our proposed computational methodology for retrieving the shape of scatterers defined using three types of parametrization: a polygonal approximation, a star-like domain, and a quadratic B-spline representation. In Section IV.5, we conclude this chapter and give some perspectives.

IV.2 The corresponding direct elasto-acoustic scattering problem

The corresponding direct elasto-acoustic scattering problem consists in the scattering of time-harmonic acoustic waves by an elastic obstacle Ω^s embedded in a homogeneous medium Ω^f, as depicted on Figure IV.2.1. It can be formulated as follows:

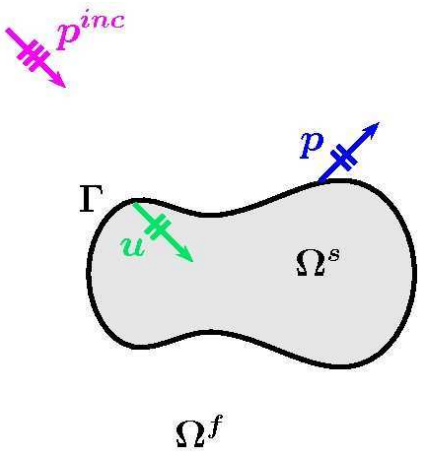

Figure IV.2.1 – Problem statement in the infinite domain.

$$\text{BVP (1)} \quad \begin{cases} \Delta p + k^2 p = 0 & \text{in } \Omega^f \quad \text{(IV.2.1)} \\ \nabla \cdot \sigma(u) + \omega^2 \rho_s u = 0 & \text{in } \Omega^s \quad \text{(IV.2.2)} \\ \omega^2 \rho_f u \cdot \nu = \dfrac{\partial p}{\partial \nu} + \dfrac{\partial g}{\partial \nu} & \text{on } \Gamma \quad \text{(IV.2.3)} \\ \tau(u) = -p\nu - g\nu & \text{on } \Gamma \quad \text{(IV.2.4)} \\ \lim\limits_{r \to +\infty} r^{(n-1)/2} \left(\dfrac{\partial p}{\partial r} - \mathrm{i}kp \right) = 0. & \quad \text{(IV.2.5)} \end{cases}$$

In practice, this is not the near field p which is measured, but the far-field pattern p_∞ of the solution p of the BVP (1) characterizing the asymptotic behavior of the acoustic scattered field [28]:

$$p(x) = \frac{e^{\mathrm{i}kr}}{r^{(n-1)/2}} \left(p_\infty \left(\frac{x}{r} \right) + O\left(\frac{x}{r} \right) \right) \quad , \quad r = \|x\|_2 \to +\infty. \tag{IV.2.6}$$

Hence, p_∞ is defined on the unit sphere S_1 , and admits the following representation in two dimensions:

$$p_\infty(\hat{x}) = \frac{e^{\mathrm{i}\pi/4}}{\sqrt{8\pi k}} \int_\Gamma \left(e^{\mathrm{i}k\hat{x}\cdot y} \frac{\partial p}{\partial \nu}(y) - \frac{\partial e^{\mathrm{i}k\hat{x}\cdot y}}{\partial \nu} p(y) \right) d\Gamma. \tag{IV.2.7}$$

This boundary value problem BVP (1) has been investigated mathematically and results pertaining to the existence, uniqueness and regularity can be found in [104] and the references therein, among others for sufficiently smooth domains, as well as in Chapter I when assuming the wet surface Γ to be only Lipschitz continuous, which is of more practical interest . More specifically, in Chapter I, we prove, under minimal condition on the fluid-structure interface Γ, (a) the existence of the solution of the BVP, (b) the uniqueness of the fluid pressure, and (c) the uniqueness of the structural displacement field modulo the so-called Jones frequencies [37, 92]. These frequencies may exist only for a particular class of elastic objects, such as spheres [37, 49, 79]. Therefore, it is worth noting that, although the fluid-structure problem may admits non-unique structural displacement solutions with the internal Jones resonance frequencies that can exist for certain geometries, the scattered field p and its far-field-pattern are always unique and depend continuously on the shape of the obstacle.

IV.3 Computational methodology

We propose a solution methodology based on a regularized Newton-type method for solving the IOP. The proposed method is an extension of the regularized Newton algorithm developed for solving the case where only Helmholtz equation is involved, that is the acoustic case by impenetrable scatterers [42].

IV.3.1 Formulation of the IOP

The direct elasto-acoustic scattering problem defines an operator $F : \Gamma \to p_\infty$ which maps the boundary Γ of the scatterer Ω^s onto the far-field pattern p_∞. Hence, given one or several measured far-field patterns $\tilde{p}_\infty(\hat{x})$, corresponding to one or several given directions d and wavenumbers k, one can formulate IOPs as follows:

$$\textit{Find a shape } \Gamma \textit{ such that} \quad F(\Gamma)(\hat{x}) = \tilde{p}_\infty(\hat{x}); \quad \hat{x} \in S^1. \tag{IV.3.1}$$

where the tilde notation designates a measured quantity.
Observe that the problem is nonlinear, because the solution of the direct problem depends nonlinearly on the boundary. Moreover, it is improperly ill-posed, since the far-field pattern is extremely smoothing due to the analyticity of the far-field pattern [28].

We recall next some theoretical results that were already mentioned in [42] and dealing with the case of the three dimensional exterior Helmholtz problem.

- When p_∞ is measured on the entire S_1 (full-aperture) and for an infinite number of incident waves characterized by distinct directions and the same wavenumber, the IOP (IV.3.1) admits a unique solution [28, 97].
- When some information about the size of the unknown scatterer is also provided, the IOP (IV.3.1) admits a unique solution even when the full-aperture far-field pattern data $p_\infty(\hat{x})$ are available only for a finite number of incident waves [28, 29]. In particular, when the scatterer can be embedded in a sphere of radius R and $kR < \pi$, it suffices to know the far-field pattern on the entire S_1 for a single incident wave to be able to determine uniquely the unknown shape [28].
- Because the far-field pattern p_∞ is an analytic function, it can be determined on the entire unit sphere S_1 from its knowledge on a subset of S_1. Hence, both theoretical results recalled above also hold when p_∞ is measured only on a subset of S_1 (limited-aperture).

In the case of the three dimensional exterior Helmholtz problem, numerical experiments (for example, see [39–42] in [42]) performed in the resonance region – that is, for a wavelength that is approximately equal to the diameter of the obstacle – tend to indicate that in practice, and at least for simple shapes, a unique and reasonably good solution of the IOP (IV.3.1) can often be computed:

- using only one incident wave and full-aperture far-field data,

- or using anywhere from 13 to 24 incident waves and limited-aperture far-field data as long as the aperture is larger than π. For smaller apertures, the reconstruction of Γ becomes more difficult and nearly impossible for apertures smaller than $\pi/4$.

Regarding the case of elastic scatterers, the question of the existence and the uniqueness of the solution to the inverse problem also arises, as well as the convergence of the Newton method (see, for e.g., [46, 110, 116] and the references therein). However, from a numerical viewpoint, one may expect to have similar results to the case of impenetrable scatterers, but with additional sensitivities due to the material properties of the scatterer.

IV.3.2 Parametrization

We assume that the fluid-structure interface Γ is Lipschitzian and can be represented by N shape parameters as follows:

$$\Gamma = \Gamma(s) \quad \text{where } s = [s_1, \cdots, s_N]^t \in \mathbb{R}^N.$$

Then, observe that $L^2(S_1)$ is the natural space for the far-field pattern p_∞ which is usually measured at a finite number of observation points x_j denoted by $N_{\hat{x}}$. Consequently, we project the IOP (IV.3.1) onto a finite-dimensional subspace of $L^2(S_1)$ and transform it into the following problem:

$$\textit{Find } s \in \mathbb{R}^N \textit{ such that} \quad F(\Gamma(s))(\hat{x}_j) = \widetilde{p}_\infty(\hat{x}_j); \quad \hat{x}_j \in S^1, j = 1, \cdots, N_{\hat{x}}. \tag{IV.3.2}$$

which can be solved by a suitable Newton-like method.
It is worth noting that the finite-dimensional IOP (IV.3.2) can also be formulated as an unconstrained optimization problem, and that its solution s can also be defined by:

$$s = arg \min_{t \in \mathbb{R}^N} \left\| \left[\begin{pmatrix} F(\Gamma(t))(\hat{x}_1) - \widetilde{p}_\infty(\hat{x}_1) \\ \cdot \\ \cdot \\ \cdot \\ F(\Gamma(t))(\hat{x}_{N_{\hat{x}}}) - \widetilde{p}_\infty(\hat{x}_{N_{\hat{x}}}) \end{pmatrix} \right] \right\|_2 \tag{IV.3.3}$$

where arg is used to denote that s is the minimizer of the considered vector function over $\mathbb{R}^N$.

IV.3.3 Linearization and regularization

The solution of the nonlinear IOP (IV.3.2) by the Newton method incurs at each iteration n the solution of a linearized problem of the form:

$$\sum_{l=1}^{N}[(F'_\Gamma(\Gamma^{(n)})h_l)(\hat{x_j})]\delta s_l^{(n)} = \tilde{p}_\infty(\hat{x_j}) - F(\Gamma^{(n)})(\hat{x_j}), \quad j = 1, \cdots, N_{\hat{x}}, \tag{IV.3.4}$$
$$\text{where } h_l = \frac{\partial \Gamma^{(n)}(s)}{\partial s_l} \quad \Gamma^{(n)} = \Gamma(s^{(n)}) \quad s^{n+1} = s^n + \delta s^n,$$

and $F'_\Gamma(\Gamma^{(n)})h_l$ is the Fréchet derivative of the FFP with respect to the shape of the obstacle in the direction of the parameter s_l.

Moreover, since in practice the number of observation points $N_{\hat{x}}$ is greater that the number of shape parameters N, the solution of the nonlinear IOP by the Newton method incurs at each iteration the solution of a linearized system of equations that is typically overdetermined. Therefore, the obtained system will be solved in a least-square sense as follows:

$$\sum_{l=1}^{N}\sum_{m=1}^{N_{\hat{x}}}\overline{[(F'_\Gamma(\Gamma^{(n)})h_j)}(\hat{x}_m)][(F'_\Gamma(\Gamma^{(n)})h_l)(\hat{x}_m)]\delta s_l^{(n)} \tag{IV.3.5}$$
$$= \sum_{m=1}^{N_{\hat{x}}}\overline{[(F'_\Gamma(\Gamma^{(n)})h_j)}(\hat{x}_m)](\tilde{p}_\infty(\hat{x}_m) - F(\Gamma^{(n)})(\hat{x}_m)), \quad j = 1, \cdots, N.$$

where the overline designates the complex conjugate.

Because F is a compact operator, each linear problem of the form given in (IV.3.4)– and a fortiori that given in (IV.3.5) – is ill-posed. Consequently, the discrete versions of problems (IV.3.4) and (IV.3.5) can be expected to be severely ill-conditioned. For this reason, the inversion must be done with a special treatment that must restore the stability to the equation. A stabilization technique such as Tikhonov's regularization is almost always used during the solution of (IV.3.5) to restore the stability. The standard Tikhonov's regularization technique consists in introducing a penalty term in (IV.3.2) and therefore replacing (IV.3.5) by the following problem:

$$\sum_{l=1}^{N}\sum_{m=1}^{N_{\hat{x}}}\overline{[(F'_\Gamma(\Gamma^{(n)})h_j)}(\hat{x}_m)][(F'_\Gamma(\Gamma^{(n)})h_l)(\hat{x}_m)]\delta s_l^{(n)} + \alpha\delta s_j^{(n)} \tag{IV.3.6}$$
$$= \sum_{m=1}^{N_{\hat{x}}}\overline{[(F'_\Gamma(\Gamma^{(n)})h_j)}(\hat{x}_m)](\tilde{p}_\infty(\hat{x}_m) - F(\Gamma^{(n)})(\hat{x}_m)), \quad j = 1, \cdots, N,$$

where $\alpha > 0$ is the regularization parameter. Numerical simulations reveal that the convergence of the Newton method is strongly dependent on the choice of α. Its determination could be done by

theoretical considerations such as Morozov's discrepancy principle [113, 114]. However, the mathematical foundation of this principle is limited to linear problems and incurs the solution of an auxiliary nonlinear problem. For these reasons, α is chosen simply by trial and error.

IV.3.4 Evaluation of the Jacobians

The solution of this IOP by a regularized Newton methods incurs, at each iteration, the solution of a linear system whose entries are the Fréchet derivatives of the elasto-acoustic field with respect to the shape parameters representing the surface of the scatterer. Furthermore, ensuring the stability, fast convergence, and computational efficiency of the regularized Newton method applied to the solution of this class of IOPs calls for computing these derivatives Fréchet derivatives arising during the Newton iterations with a greater robustness and a higher level of accuracy than possible with finite differences.

Using finite differencing for this purpose raises two issues pertaining to robustness and computational efficiency. Indeed, the estimation by finite differences of a Fréchet derivative $F'(\Gamma)h_j$ j may or may not strongly depend on the size of the perturbation of the parameter s_j, depending on the variation of the operator F with respect to that parameter. Furthermore, the evaluation by second-order central differencing of the N directional derivatives requires the solution at each regularized Newton iteration (IV.3.6) of $2N + 1$ distinct direct elasto-acoustic scattering problems. For these reasons, we consider here another approach for computing the Fréchet derivatives of the far-field pattern with respect to the shape parameters.

To this effect, following the ideas and the approach used in [39] for the case of exterior Helmholtz problems, we proved in Chapter III that the Fréchet derivative of the elasto-acoustic scattered field with respect to the shape of an elastic obstacle can be characterized as a solution of the same direct elasto-acoustic scattering problem which differs from the considered forward problem only in the transmission conditions on the surface of the scatterer.

We recall that the Fréchet derivative of the elasto-acoustic scattered field with respect to the shape of an obstacle in the direction of a parameter s_j, which we denote here by (p'_j, u'_j), is the solution of the following direct elasto-acoustic scattering problem :

$$\text{BVP (2)} \quad \begin{cases} \Delta p_j' + k^2 p_j' = 0 & \text{in } \Omega^f \quad \text{(IV.3.7)} \\ \nabla \cdot \sigma(u_j') + \omega^2 \rho_s u_j' = 0 & \text{in } \Omega^s \quad \text{(IV.3.8)} \\ \omega^2 \rho_f u_j' \cdot \nu = \dfrac{\partial p_j'}{\partial \nu} + G(u, p, h_j) & \text{on } \Gamma \quad \text{(IV.3.9)} \\ \tau(u_j') = -p_j' \nu + F(u, p, h_j) & \text{on } \Gamma \quad \text{(IV.3.10)} \\ \lim\limits_{r \to +\infty} r^{(n-1)/2} \left(\dfrac{\partial p_j'}{\partial r} - \mathrm{i}k p_j' \right) = 0. & \quad \text{(IV.3.11)} \end{cases}$$

where the functions F and G are given by:

$$F(u, p, h_j) = -{h_j}^t \nabla \sigma(u) \nu - \nabla p^T \cdot h_j \nu + \sigma(u)[h_j']^t \nu + p^T [h_j']^t \nu, \quad \text{(IV.3.12)}$$

$$G(u, p, h_j) = -(\omega^2 \rho_f \nabla u - \nabla(\nabla p^T)) h_j \cdot \nu + (\omega^2 \rho_f u - \nabla p^T) \cdot [h_j']^t \nu, \quad \text{(IV.3.13)}$$

and $p^T = p + p^{inc}$.
Here, the notation $h_j^t \nabla \sigma(u) \nu$ stands for $h_j^t \nabla \sigma(u) n = [h_j^t \nabla \sigma_l(u) \nu]_{l=1,\cdots,n}$, where σ_l is the row l of the matrix $\sigma(u)$.

The computational implication of this theoretical characterization is as follows. If the sought-after shape is represented by N parameters, then, at each regularized Newton iteration, the N directional derivatives needed for constructing the Jacobians can be computed by solving N direct elasto-acoustic scattering problems that differ only by their boundary conditions. Or, in algebraic terms, after FEM discretization, we can evaluate the scattered field and the N directional derivatives by solving a single system of equations with $N + 1$ right-hand sides. In contrast, evaluating the same N directional derivatives by a central differencing scheme, together with the scattered field, would require first choosing an arbitrary small parameter, then solving $2N + 1$ distinct forward problems.

IV.3.5 A multi-stage solution procedure

Even with the use of the regularization technique, the IOP remains difficult to solve, especially when the number of shape parameters is large. In order to accelerate the convergence of the specified method, we propose a multi-stage procedure for determining the sought-after shape as in [39].

Step 1 Initialize $s := s^{(0)}$ and construct $\Gamma^{(0)} = \Gamma(s^{(0)})$.

Step 2 Given a frequency ω and for a chosen α, solve the IOP (IV.3.2) by the regularized Newton method (IV.3.6) until convergence or stagnation of the residual $F(\Gamma(s^{(n)})) - \tilde{p}_\infty$.

- If convergence to a specified tolerance is achieved, stop.
- If not, go to Step 3.

Step 3 Switch to a lower regularization parameter α and/or a higher frequency ω, initialize the shape parameters with their final values in the previous step $s^{(0)} = s^{(n)}$, and repeat Step 2.

Note that it assumes that FFP data are also available for a higher wavenumber. Moreover, this procedure allows to recognize the influence of the wavenumber on the acoustic scattering observability of the small geometric features.

IV.3.6 Efficient solution of the direct elasto-acoustic scattering problems

For implementation purposes, we reformulate the BVP (1) in a bounded domain Ω_R^f in view of its discretization by the finite-element method and performing numerical simulations. The latter is accomplished by replacing the outgoing Sommerfeld condition in BVP (1) (IV.2.5) by some simple absorbing boundary condition. Consequently, as explained in Chapter II, the finite-element discretization of the direct elasto-acoustic scattering problem leads to the following algebraic problem:

$$\begin{pmatrix} \boldsymbol{A^f} + \boldsymbol{C} & \boldsymbol{B} \\ \boldsymbol{B^*} & \boldsymbol{A^s} \end{pmatrix} \begin{pmatrix} P \\ U \end{pmatrix} = \begin{pmatrix} F_1 \\ F_2 \end{pmatrix}. \tag{IV.3.14}$$

where A^f is a symmetric matrix given by:

$$\boldsymbol{A^f} = \frac{1}{\omega^2} \left(\boldsymbol{K^f} - k^2 \boldsymbol{M^f} - \boldsymbol{J^f} + \gamma_f \boldsymbol{S^f} \right), \tag{IV.3.15}$$

and

- $\boldsymbol{K^f}$ is the block diagonal stiffness matrix associated to the pressure field.
- $\boldsymbol{M^f}$ is the block diagonal mass matrix associated to the pressure field.
- $\boldsymbol{J^f}$ is the matrix that contains the jump terms. The entries of this matrix are defined over the interior edges.
- $\boldsymbol{S^f}$ is the mass-like matrix defined over the interior edges in the fluid resulting from the penalty term.

$\boldsymbol{C}$ is the complex-valued damping matrix. It is a mass-like matrix, whose entries are all zeros except for the elements located at the exterior boundary Γ_R. The matrix $\boldsymbol{A}^f + \boldsymbol{C}$ is symmetric, but non-hermitian, and thus non-positive-definite.
The symmetric matrix $\boldsymbol{A}^s$ is given by:

$$\boldsymbol{A}^s = \boldsymbol{K}^s - \omega^2 \rho_s \boldsymbol{M}^s - \boldsymbol{J}^s + \gamma_s \boldsymbol{S}^s, \tag{IV.3.16}$$

and

- $\boldsymbol{K}^s$ is the block diagonal elastic stiffness matrix related to the displacement field.
- $\boldsymbol{M}^s$ is the block diagonal mass matrix related to the displacement field.
- $\boldsymbol{J}^s$ is the matrix that contains the jump terms. The entries of this matrix are defined over the interior edges.
- $\boldsymbol{S}^s$ is the mass-like matrix defined over the interior edges in the solid resulting from the penalty term.

Note that the matrix $\boldsymbol{A}^s$ is positive-definite up to the Jones frequencies, thanks to the interior penalty term that compensates the weak ellipticity of the equation operator. $\boldsymbol{B}$ is a mass-like boundary matrix whose entries are defined on the interface edges only, whereas F_1 and F_2 are the source vectors. The vector P (resp. U) is the fluid pressure (resp. structural displacement) representation in the finite element basis.

Moreover, as mentioned in Section IV.3.4, the Fréchet derivative of the elasto-acoustic scattered field with respect to the shape parameter s_j can be evaluated by solving the same system of equations (IV.3.14) but with different right-hand sides $F_{1,j}, F_{2,j}$. Then, the corresponding far-field pattern – that is, the Fréchet derivative of the far-field pattern with respect to the shape parameter s_j – is obtained by post-processing the solution using (IV.2.6) on $\Gamma^{(n)}$.

In summary, adopting the nomenclature in [39], if the IOP (IV.3.1) employs a single incident wave, the iterative methodology for retrieving the shape of an elastic obstacle requires solving at each iteration n:

- one sparse system of equations associated with the discretization of the elasto-acoustic scattering problem but for $N + 1$ different right-hand sides (Problem P1),
- and one smaller-scale but full system of equations of size equal to N and of the form given in (IV.3.6) (Problem P2).

When the IOP (IV.3.1) is formulated using N_d incident waves characterized by the same wavenumber but N_d different incident directions, the same iterative procedure requires solving at each iteration n:

- one sparse system of equations associated with the discretization of the elasto-acoustic scattering problem but for $N_d(N+1)$ different right-hand sides (Problem P1),
- and one smaller-scale but full system of equations of size equal to $N_d N$ and of the form given in (IV.3.6) (Problem P2).

Clearly, the performance of the IOP solver outlined in this chapter depends essentially on the computational efficiency of the solution of the forward problems (Problem P1) that arise at each Newton iteration. To this effect, we propose to solve the direct scattering-type problems using a finite-element method based on high-order discontinuous Galerkin approximations equipped with curved boundary edges introduced in Chapter II.

Note that, the additional cost incurs by the computation of the Jacobian matrix is small compared with the solution of the initial forward problem. Indeed, the assembly and the LU factorization of the matrix is done only once for the evaluation of the scattered field (P, U), using MUMPS for instance. Then, the evaluation of the N Fréchet derivatives only require the construction of a multiple right-hand side, and the solution of a linear system already assembled and factorized.

Remark IV.3.6.1 *It is also possible to solve the IOP (IV.3.1) using the adjoint-state method based on the minimization of a cost functional under constraints, and combine it, for example, with a Quasi-Newton algorithm. This technique is a Lagrangian-type formulation. The advantage is that such approach is independent of the number of parameters, and the derivatives are expressed for all perturbations. This procedure requires the solution of one forward problem and one adjoint problem. However, the factorization of the system matrix carried out for the solution of the initial direct problem is in general not reusable for the solution of the adjoint system. Indeed, the system matrix is not only the transpose but also the conjugate of the matrix corresponding to the initial direct problem, owing to the presence of the complex-valued term associated with the absorbing boundary condition. It is expected that the cost associated with the factorization of such a system matrix is larger than the cost corresponding to the solution with a multiple right-hand side performed in our situation.*

IV.4 Applications

Numerical results are presented to illustrate the feasibility of the proposed solution methodology for retrieving the shape of an elastic scatterer from the measurement of several far-field patterns

$\tilde{p}_\infty(\hat{x})$, corresponding to one direction d and one wavenumber k.

Our objective is to retrieve the shape of the obstacle without finding its location. For this reason, as mentioned in [42], we exploit only the intensity of the measured far-field pattern –that is, the square of its amplitude, given by:

$$U(\Gamma)(\hat{x}) = [\overline{F(\Gamma)}(\hat{x})][F(\Gamma)(\hat{x})], \tag{IV.4.1}$$

which is invariant under any translation. This is a sound strategy not only for parametrization purposes, but also because the measurements of U are usually more accurate than the measurements of the phase of F. Note that, since we do not locate the object, we lose the uniqueness.
Consequently, the regularized Newton iteration (IV.3.6) becomes:

$$\begin{aligned} &\sum_{l=1}^{N}\sum_{m=1}^{N_{\hat{x}}}[\overline{(U'_\Gamma(\Gamma^{(n)})h_j)}(\hat{x}_m)][(U'_\Gamma(\Gamma^{(n)})h_l)(\hat{x}_m)]\delta s_l^{(n)} + \alpha\delta s_j^{(n)} \\ = &\sum_{m=1}^{N_{\hat{x}}}[\overline{(U'_\Gamma(\Gamma^{(n)})h_j)}(\hat{x}_m)](\overline{\tilde{p}_\infty(\hat{x}_m)}\tilde{p}_\infty(\hat{x}_m) - U(\Gamma^{(n)})(\hat{x}_m)), \quad j = 1, \cdots, N, \end{aligned}$$

and we deduce the Fréchet derivative of U from the Fréchet derivative of F as follows:

$$U'_\Gamma(\Gamma^{(n)})h_j)(\hat{x}_m) = 2Re\left([\overline{F(\Gamma^{(n)})}(\hat{x}_m)][F'_\Gamma(\Gamma^{(n)})h_j)(\hat{x}_m)]\right), \tag{IV.4.2}$$

In all numerical experiments, we choose to work with a single direction of incidence $d = (1, 0)$, and full-aperture far-field pattern data, that is 360 FFP data. Note that we use the same numerical method for generating the synthetic data and for solving the forward problems arising during the regularized Newton iterations. Therefore, in order to avoid the inverse crime, the synthetic far-field pattern data are generated by solving the direct elasto-acoustic scattering problem BVP (1) for the target obstacle on a fine mesh defined with about $N_{\lambda,data}$ elements per wavelength, whereas the forward problems arising at each Newton iteration are solved on meshes using N_λ elements per wavelength. At each iteration, the exterior boundary is updated and defined by a circle whose radius b is equal to R times the maximum of the shape parameters. This should avoid the adverse effect of domain truncation. The numerical experiments are performed using the same material properties as in Section II.5 of Chapter III, corresponding to an aluminum object immersed in water, and reported in Table IV.4.1.

We monitor the convergence of our IOP solver via the decay of the relative residual on the FFP intensity given by:

$$\frac{\|U(\Gamma^{(n)}) - \tilde{p}_\infty^*\tilde{p}_\infty\|_2}{\|\tilde{p}_\infty^*\tilde{p}_\infty\|_2}. \tag{IV.4.3}$$

Properties / Medium	Density ρ (kg/m^3)	Propagation velocity c_P (m/s)	c_S (m/s)
Water	1000	1500	–
Aluminum	2700	6198	3122

Table IV.4.1 – Material properties of the considered fluid-structure medium.

Remark IV.4.0.2 *The FFP computation via the integral formula (IV.2.7) on the surface Γ of the obstacle has been validated by means of the analytical series given for the unbounded problem in the case of Disk-shaped elastic scatterer problem (see Appendix C.1).*
Since the evaluation of the Fréchet derivative calls for the computation of second-order derivatives of u and p, we consider higher-order elements of degree 5 for the solution of the inverse problem. Let us consider an obstacle of radius a =0.01m, and compute 360 FFP data. We fix: $\omega = 1376017$, which corresponds to the dimensionless frequency $ka = 9.17$, and use 5 elements per wavelength.

- *First, we use the simplest condition that reads as:*

$$\frac{\partial p}{\partial n} - \mathrm{i}kp = 0 \qquad \text{on} \quad \Gamma_R. \tag{IV.4.4}$$

We report in Table IV.4.2 the error results on both fields p (over the entire computational fluid domain Ω_R^f) and p_∞ (over the unit sphere). These errors are evaluated with respect to the analytical series expressed in the infinite domain, that is without taking into account the low-order ABC in the series expansion, for different values of the radius b of the exterior circular-shaped boundary Σ.

b	b/a	p	p_∞
0.03	3	2.50	2.208
0.04	4	1.496	1.426
0.05	5	1.05	1.051
0.1	10	0.421	0.464

Table IV.4.2 – Disk-shaped elastic scatterer problem - Sensitivity of the L^2-relative errors (%) on p and p_∞ to different values of the the radius b of the exterior circular-shaped boundary Σ with the low-order CLA.

The following observations are noteworthy:

- *As we move away the exterior boundary, the approximate FFP, computed in the bounded configuration, tends to the analytical FFP expressed in the infinite domain.*
- *The error on the FFP p_∞ remains of the same order as the error on the solution p itself, which validates the FFP computation via the integral formula (IV.2.7).*

- *Second, a first-order condition, that is widely employed, is given by:*

$$\frac{\partial p}{\partial n} - \mathrm{i}kp + \frac{\kappa}{2}p = 0 \qquad \text{on} \quad \Gamma_R. \tag{IV.4.5}$$

where κ denotes the curvature of the external surface Γ_R.
Table IV.4.2 shows the error results on both fields p (over the entire computational fluid domain Ω_R^f) and p_∞ (over the unit sphere). The errors are evaluated with respect to the analytical series expressed in the infinite domain, that is without taking into account the first-order ABC in the series expansion, for different values of the radius b of the exterior circular-shaped boundary Σ.

b	b/a	p	p_∞
0.03	3	2.095	1.575
0.04	4	1.116	0.868
0.05	5	0.695	0.550
0.1	10	0.166	0.136

Table IV.4.3 – Disk-shaped elastic scatterer problem - Sensitivity of the L^2-relative errors (%) on p and p_∞ to different values of the the radius b of the exterior circular-shaped boundary Σ with the first-order CLA.

These results indicate the following:

- *When using the first-order ABC (IV.4.5) instead of (IV.4.4), the errors are halved. Thus using the curvature allows to improve the approximation.*
- *We observe that the more distant the exterior boundary is, the more the approximations are accurate.*
- *We notice that the relative L^2-error on the FFP remains of the same order as the error on the solution p itself, which once again validates the evaluation of the FFP with (IV.2.7).*

Remark IV.4.0.3 *The Fréchet derivative computation associated with BVP (2) has been validated via the analytical series given for the unbounded problem in the case of Disk-shaped elastic scatterer problem. The construction of the exact series for (p', u') is given in Appendix C.2.*
We report in Table IV.4.4 the error results on both fields (p, u) and (p', u') with respect to the analytical series expressed in the infinite domain, that is without taking into account the first-order ABC in the series expansion, for different values of the radius b of the exterior circular-shaped boundary Σ.

We observe the following:

- *Once again, the more the exterior boundary is far from the obstacle, the more the approximations are accurate.*

b	b/a	p	u_x	u_y	p'	u'_x	u'_y
0.03	3	2.095	0.698	0.646	2.366	0.634	0.580
0.04	4	1.116	0.387	0.357	1.284	0.309	0.216
0.05	5	0.695	0.257	0.237	0.813	0.185	0.170
0.1	10	0.166	6.185E-002	5.658E-002	0.199	4.642E-002	4.066E-002

Table IV.4.4 – Disk-shaped elastic scatterer problem - Sensitivity of the L^2-relative errors (%) on (p, u) and (p', u') to different values of the the radius b of the exterior circular-shaped boundary Σ with the first-order CLA.

- *The relative L^2-error on the Fréchet derivative remains of the same order as the error on the solution p itself, which tends to validate the evaluation of the Fréchet derivative with BVP (2).*

In the following numerical examples, we recover shapes defined with 10 parameters employing polygonal-shaped approximations, 9 parameters using the trigonometric parametrization in Fourier series, and 24 parameters using B-splines.

When the simulations are noise-free, we monitor the convergence of our IOP solver via the decay of the relative residual on the FFP intensity with a tolerance fixed to 1%, which corresponds to a tolerance of about 2%-5% on the FFP phase. We also assess the effect of the noise level on the reconstruction by using various noise levels. Note that we compute the synthetic data of the far-field pattern phase $\tilde{p}_\infty$, then we add the noise to these measurements $\tilde{p}_\infty$, and from them, we derive the intensity of FFP data $|\tilde{p}_\infty|$, which is used in the Newton algorithm. Given that, we monitor the decay of the relative residuals on the phase and the magnitude of the far-field pattern.

The choice of the regularization parameter is empirical and done by trial and error. In each experiment, we specify the dimensionless frequency ka, where $2a$ represents the diameter of the target scatterer, $a = \max_i s_i$ being the maximum of the shape parameters.

IV.4.1 Polygonal-shaped obstacles

IV.4.1.1 Parametrization

We want to recover a polygonal-shaped object of boundary Γ. To that effect, we parametrized the shape Γ by means of N vertices $X_j = r_j \begin{pmatrix} \cos\theta_j \\ \sin\theta_j \end{pmatrix}$, $j = 1, \cdots N$, uniformly distributed in the polar coordinate angle.

For each face S_j of the polygon, we use a linear interpolation as follows:

$$S_j(t) = (1-t)X_j + tX_{j+1}, \quad t \in [0,1],\ j = 1, \cdots, N \tag{IV.4.6}$$

with $X_{N+1} = X_1$.
This can be rewritten under the matricial form:

$$S_j(t) = \begin{bmatrix} t & 1 \end{bmatrix} \begin{pmatrix} -1 & 1 \\ 1 & 0 \end{pmatrix} \begin{bmatrix} X_j \\ X_{j+1} \end{bmatrix}.$$

Therefore, we have:

$$\Gamma = \{S_j(t), \quad t \in [0,1],\ j = 1, \cdots, N\}. \tag{IV.4.7}$$

The shape is entirely defined by the N radii r_j, $j = 1, \cdots N$, so that it can be written as follows:

$$\Gamma = \left\{ \sum_{j=1}^{N} r_j \phi_j(s) \begin{pmatrix} \cos\theta_j \\ \sin\theta_j \end{pmatrix}, \quad s \in [0, N] \right\} \tag{IV.4.8}$$

where, $t = s - j + 1$,

$$\phi_1(s) = \begin{cases} 1 - t & \text{if } 0 \leq s \leq 1, \\ t & \text{if } N - 1 \leq s \leq N, \\ 0 & \text{otherwise.} \end{cases} \tag{IV.4.9}$$

and for $j \neq 1$,

$$\phi_j(s) = \begin{cases} 1 - t & \text{if } j - 1 \leq s \leq j, \\ t & \text{if } j - 2 \leq s \leq j - 1, \\ 0 & \text{otherwise.} \end{cases} \tag{IV.4.10}$$

Then, the corresponding deformation directions with respect to the N shape parameters r_j are given by $h_j(s) = \phi_j(s) \begin{pmatrix} \cos\theta_j \\ \sin\theta_j \end{pmatrix}$.

IV.4.1.2 Square

We want to retrieve a square defined by using 8 parameters. We initialize the object with a larger shape, as reported in Table IV.4.5.

The number of elements per wavelength used to simulate the data on the sought-after shape is equal to $N_{\lambda,data} = 7$, whereas it is equal to $N_\lambda = 5$ for the meshes in the Newton iterations. Note that, in that experiment, we consider the exterior boundary for generating the far-field data at $R_{data} = 5$ and

Parameter	Target	Initial Guess
s_1	0.010607	0.0175
s_2	0.01	0.0175
s_3	0.010607	0.0175
s_4	0.01	0.0175
s_5	0.010607	0.0175
s_6	0.01	0.0175
s_7	0.010607	0.0175
s_8	0.01	0.0175

Table IV.4.5 – Shape parameters for the square-shaped target and the initial guess.

take $R = 4$ to define the exterior boundary during the Newton iterations. This is an argument to avoid the adverse effect of domain truncation.

Free noise results

The given frequency is $\omega = 150000$, which corresponds to $ka = 1.06$. The regularization parameter α is chosen equal to 1 in Step 2. At the fourth iteration, we go to Step 3, and the regularization parameter is decreased to 0.01 in order to accelerate the convergence.

The results are reported in Figures IV.4.1 and IV.4.2. The iterative shapes are depicted in Figure IV.4.1 and we plot in Figure IV.4.2 the convergence of the corresponding relative discrete residual on the far-field intensity. The Newton algorithm achieves the specified tolerance of 1% on the FFP intensity within 6 iterations. In Figure IV.4.2, we can observe the switch to the smaller regularization parameter highlighted by the jump in the error. Note that we can not expect the error to be reduced more. Indeed, the level of the order of $10^{-1}\%$ that is achieved corresponds to the error due to the difference between the exterior boundary radii R_{data} and R that are used for generating the data and along the Newton iterations.

Results with 5% of noise

In that experiment, the simulated FFP data $\tilde{p}_\infty$ are tainted with 5 % of noise, and we monitor the convergence of our IOP solver via the decay of the relative residuals on the phase and the intensity of the far-field pattern.

The given frequency is $\omega = 150000$, which corresponds to $ka = 1.06$. The regularization parameter α is chosen equal to 1 in Step 2. At the iteration 6, we go to Step 3, where we switch to a higher frequency $\omega = 200000$, corresponding to $ka = 1.41$, and the regularization parameter is decreased to

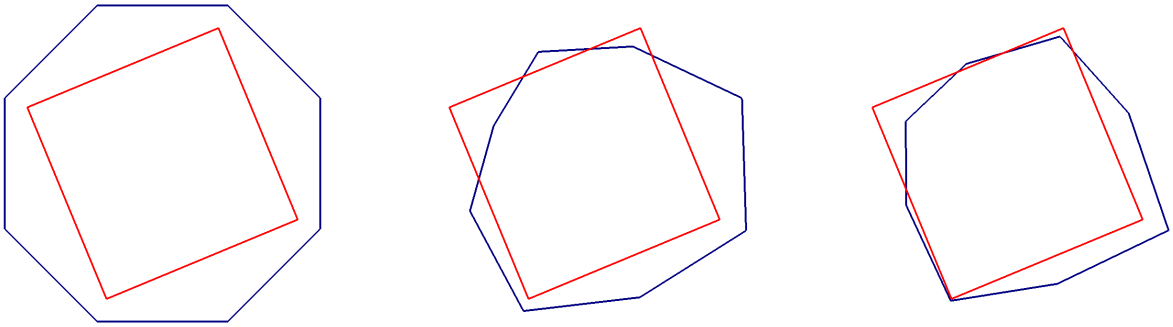

(a) Initial guess (b) Iter 1 (c) Iter 2

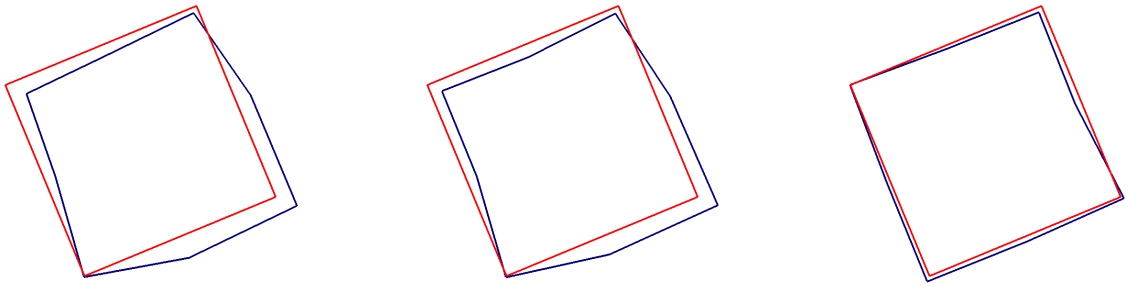

(d) Iter 3 (e) Iter 4 (f) Iter 5

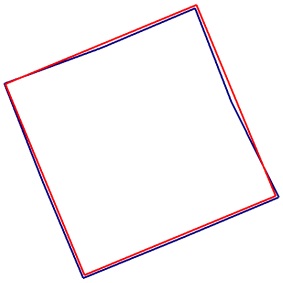

(g) Iter 6

Figure IV.4.1 – Iterative shapes for the square with noise-free data.

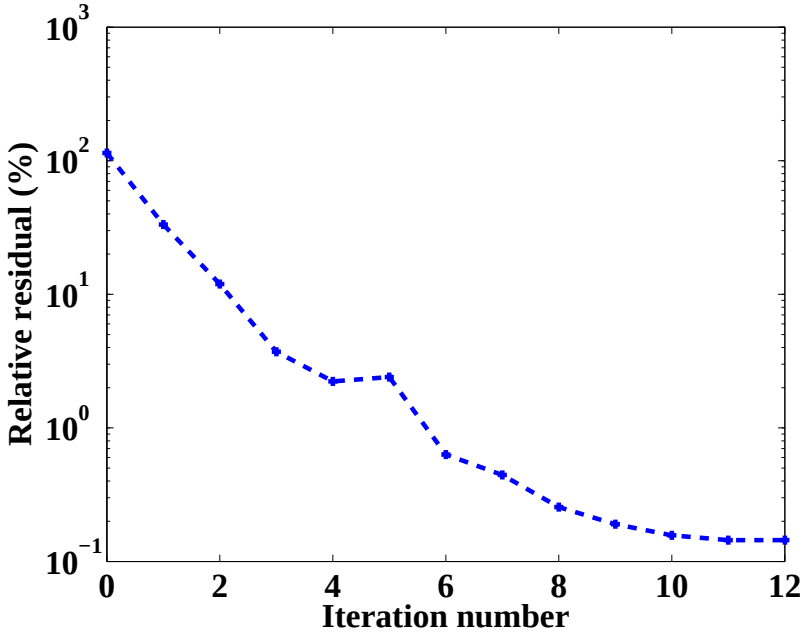

Figure IV.4.2 – Convergence history for the square with noise-free data.

0.01 in order to accelerate the convergence. We then initialize the shape parameters with their values at stagnation in the previous step, and solve again the IOP by the same regularized Newton method. The results are reported in Figures IV.4.3 and IV.4.4. They are similar to those obtained with noise-free data. In Figure IV.4.4, we compare the results to the previous ones obtained with noise-free data. In the case of tainted data, we also observe the convergence of the relative residuals on the FFP phase and FFP intensity. The Newton algorithm achieves a level of error of 6% on the FFP phase within 8 iterations, which is comparable to that of noise. The corresponding relative residual on the FFP intensity is of 1 %.

IV.4.1.3 A 4-point compass rose-like scatterer

We want to retrieve a 4-point compass rose-like obstacle obtained using 8 parameters. The initial guess is a larger square. The shape parameters are reported in Table IV.4.6.

The number of elements per wavelength and the definition of the exterior boundary are defined as in the previous experiment for the square scatterer.

Free noise results

Given the frequency $\omega = 150000$, which corresponds to $ka = 1.5$, the regularization parameter α is

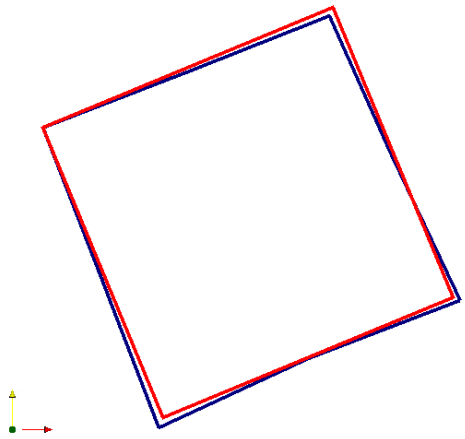

Figure IV.4.3 – Final shape for the square with data containing 5% of noise.

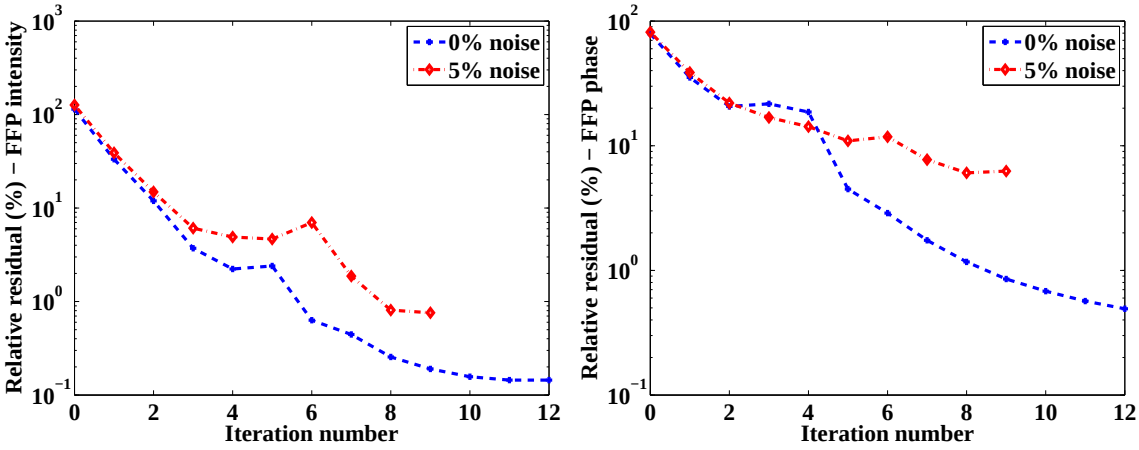

(a) FFP intensity (b) FFP phase

Figure IV.4.4 – Convergence history for the square.

Parameter	Target	Initial Guess
s_1	0.006	0.012374
s_2	0.015	0.0175
s_3	0.006	0.012374
s_4	0.015	0.0175
s_5	0.006	0.012374
s_6	0.015	0.0175
s_7	0.006	0.012374
s_8	0.015	0.0175

Table IV.4.6 – Shape parameters for the 4-point compass rose-shaped target and the initial guess.

chosen equal to 1. α is reduced to 0.1 at the 5^{th} iteration to accelerate the convergence in Step 3. The convergence to the specified tolerance of 1% on the FFP intensity is achieved within 7 iterations, as depicted in Figures IV.4.5 and IV.4.6. Similar comments to the previous example can be done. The method succeeds in recovering all corners of the shape.

Results with 2% of noise

In that case, we choose a level of 2% of noise to contaminate the data of the FFP phase $\tilde{p}_\infty$.
We consider again $\omega = 150000$, corresponding to $ka = 1.5$, and $\alpha = 1$. At iteration 4 and iteration 6, the regularization parameter α is decreased to 0.1 and 0.01 respectively, in order to accelerate the convergence.
The results are reported in Figures IV.4.7 and IV.4.8. In Figure IV.4.8, we compare the results to the previous ones obtained with noise-free data. The Newton algorithm converges within 11 iterations to a level of 3% of error on the FFP phase, which is a level comparable to that of noise. This is a slightly higher value than the noise level, but the corners of the target obstacle are recovered, as illustrated in Figure IV.4.7. The corresponding relative residual on the FFP intensity is also of the order of 3%.

IV.4.2 Star-like domains

IV.4.2.1 Parametrization

Now, we aim to retrieve the shape of curved scatterers. We choose to describe a class of star-like domains. Using polar coordinates, the shape (that we assume to be centered at the origin) can be

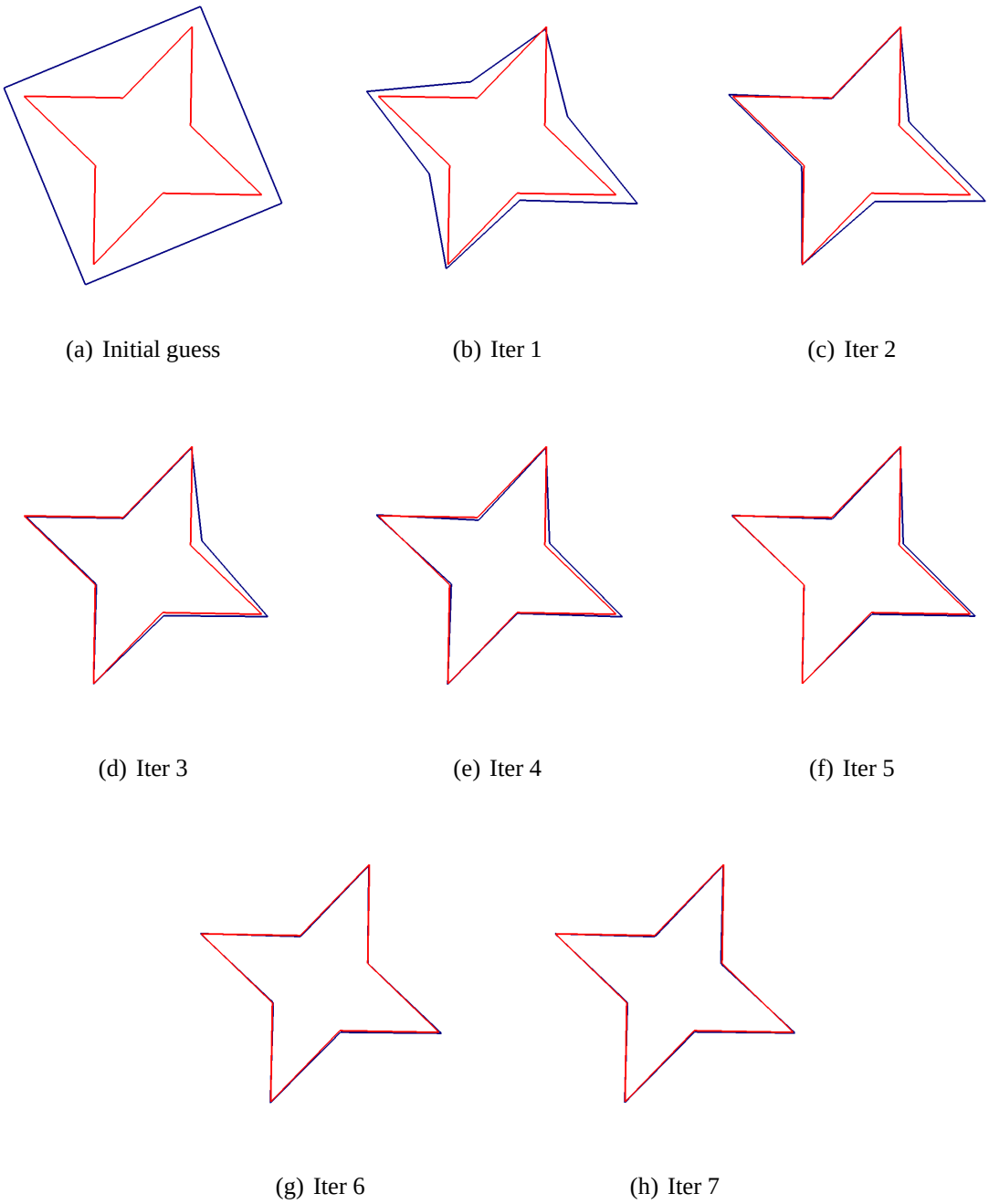

(a) Initial guess (b) Iter 1 (c) Iter 2

(d) Iter 3 (e) Iter 4 (f) Iter 5

(g) Iter 6 (h) Iter 7

Figure IV.4.5 – Iterative shapes for the 4-point compass rose-like scatterer.

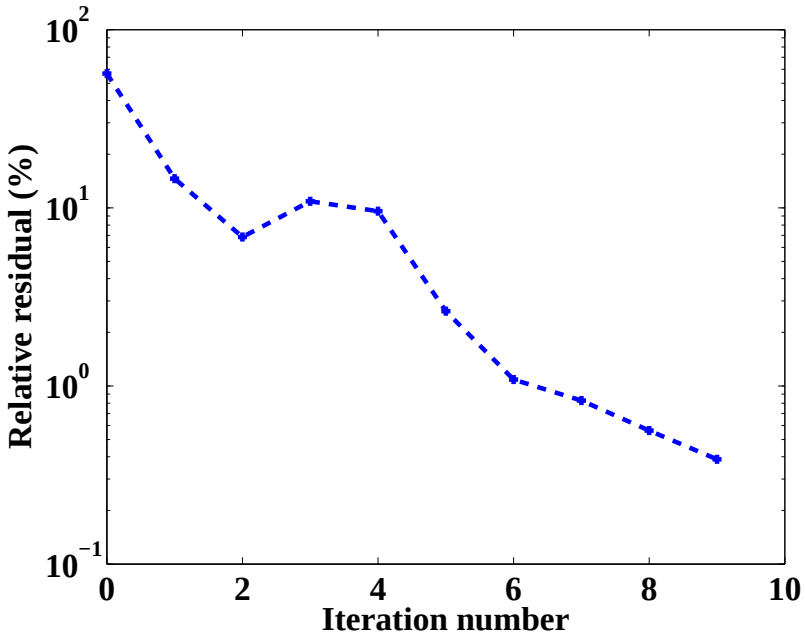

Figure IV.4.6 – Convergence history for the 4-point compass rose-like scatterer with noise-free data.

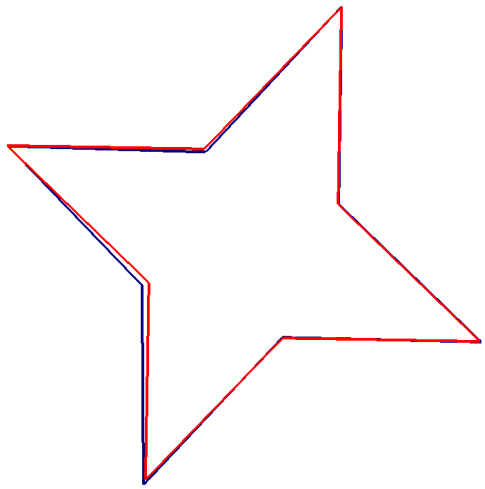

Figure IV.4.7 – Final shape for the 4-point compass rose-like scatterer with data containing 2% of noise.

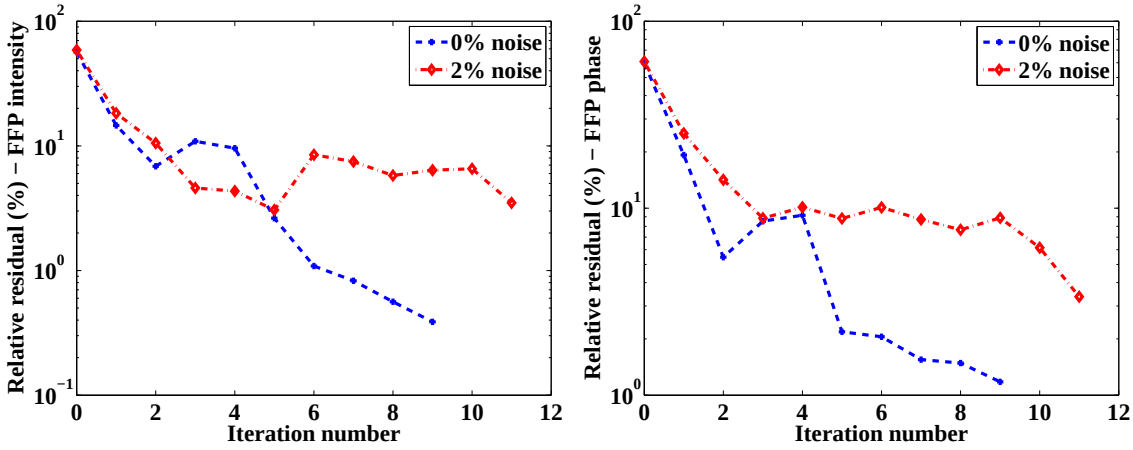

(a) FFP intensity (b) FFP phase

Figure IV.4.8 – Convergence history for the 4-point compass rose-like scatterer.

parametrized as follows:

$$\Gamma = \{r(\theta)\begin{pmatrix}\cos\theta\\ \sin\theta\end{pmatrix}, \quad \theta \in [0, 2\pi)\}, \tag{IV.4.11}$$

where r represent the polar radius. We approximate r by its truncated Fourier series as follows:

$$r^M(\theta) = a_0 + \sum_{k=1}^{M} b_k \cos(k\theta) + c_k \sin(k\theta). \tag{IV.4.12}$$

In this case, the shape is entirely defined by the $N = 2M + 1$ coefficients: a_0, b_j $j = 1, \cdots M$, and c_j, $j = 1, \cdots M$, so that we have:

$$\Gamma = \left\{\sum_{j=1}^{N} s_j \phi_j(\theta)\begin{pmatrix}\cos\theta\\ \sin\theta\end{pmatrix}, \quad \theta \in [0, 2\pi)\right\}, \tag{IV.4.13}$$

where $s_1 = a_0, s_{2k} = b_k, s_{2k+1} = c_k$ for $k = 1, \cdots, M$ and

$$\phi_1(\theta) = 1 \tag{IV.4.14}$$

$$\phi_{2k}(\theta) = \cos(k\theta), \tag{IV.4.15}$$

$$\phi_{2k+1}(\theta) = \sin(k\theta), \quad \text{for } k = 1, \cdots, M. \tag{IV.4.16}$$

Then, the associated deformation directions with respect to the N shape parameters are given by $h_j(\theta) = \phi_j(\theta) \begin{pmatrix} \cos\theta \\ \sin\theta \end{pmatrix}$, $j = 1, \cdots, N$.

IV.4.2.2 Circle

The Fourier series given by Eq. (IV.4.12) is truncated for $M = 0$, and we define a circular-shaped obstacle using the following shape parameter: $s_1 = 0.01$. The object is initialized with the larger circle of radius 0.015, so that $s_1 = 0.015$.

The number of elements per wavelength employed for generating the data with the target shape is equal to $N_{\lambda,data} = 5$, whereas it is equal to $N_\lambda = 3$ for the Newton iterations. Note that we consider the same definition of the exterior boundary for the far-field data generation and during the Newton iterations, i.e. $R_{data} = R = 4$.

The given frequency is equal to $\omega = 350000$, which corresponds to $ka = 2.33$. α is chosen equal to 0.1.
The convergence results are depicted in Figures IV.4.9 and IV.4.10. The Newton algorithm converges in 4 iterations to the specified tolerance of 1% on the intensity of the far-field pattern. Note that since we have taken the same values for R_{data} and R, the error can be reduced to a lower order. It requires 2 additional iterations within Step 2 to reduce the error to 5.10^{-4}.

When starting with a smaller radius of $s_1 = 0.005$ the algorithm requires 3 iterations. Nevertheless, note that the interest of this example do not rely on the fact to retrieve a circle since the problem only consists in determining one parameter. This example allows to observe the effect of the initial guess and wavenumber on the convergence algorithm. Indeed, assume that we start from the same frequency $\omega = 350000$ (corresponding to $ka = 2.33$) and a radius $s_1 = 0.02$. Then, the Newton algorithm fails to converge to the sought-after shape. The radius only reduces to 0.0196 in the first iteration and then stagnates. Once could think that we are located at a radius for which ω is a Jones frequency. However, according to the numerical study as in Chapter II, it seems that this is not the case for the first six modes. Then, it is necessary to switch to another higher frequency to "reset" the convergence.

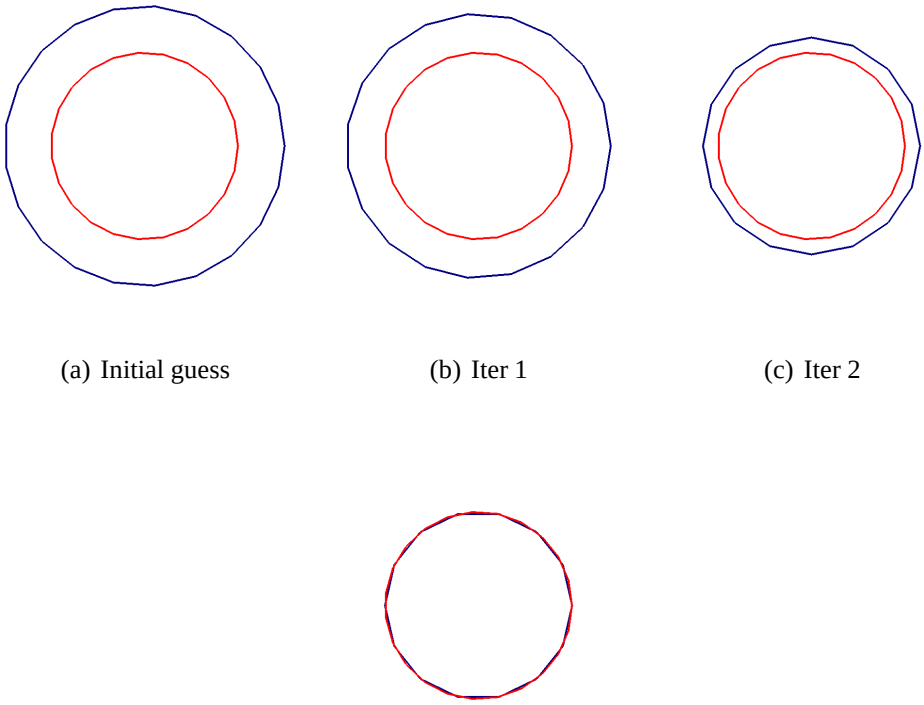

(a) Initial guess (b) Iter 1 (c) Iter 2

(d) Iter 3

Figure IV.4.9 – Iterative shapes for the circle.

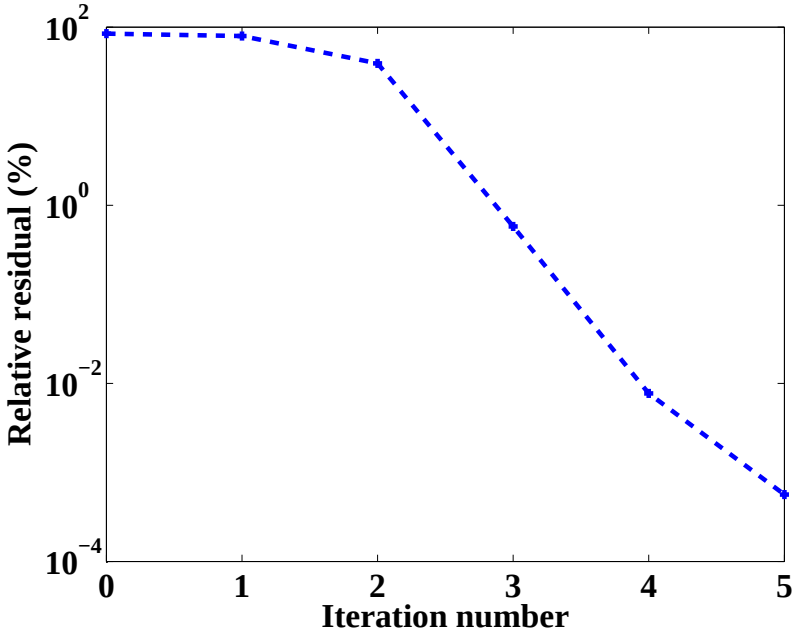

Figure IV.4.10 – Convergence history for the circle.

IV.4.2.3 Potato-like scatterer

The Fourier series given by Eq. (IV.4.12) is truncated for $M = 1$, and we define a potato-shaped obstacle by means of 3 shape parameters summarized in Table IV.4.7. The object is initialized with the circle of radius 0.0125.

Parameter	Target	Initial Guess
s_1	0.01	0.0125
s_2	0.007	0
s_3	0.0025	0

Table IV.4.7 – Shape parameters for the potato-shaped target and the initial guess.

We consider the same number of elements per wavelength and the same value for the radius of the exterior boundary as in the previous experiment.

Free noise results

The given frequency is $\omega = 1100000$, which corresponds to $ka = 7.33$, and the regularization parameter α is chosen equal to 50.

The convergence results obtained within the single Step 2 are depicted in Figures IV.4.11 and IV.4.12. We observe that the proposed method requires 7 iterations to achieve the prescribed tolerance of 1% on the FFP intensity.

Results with 5% of noise

In that case, we add 5% of noise to the FFP data $\tilde{p}_\infty$.

We keep the frequency $\omega = 1100000$, corresponding to $ka = 7.33$, and the regularization parameter $\alpha = 50$.

The results are reported in Figures IV.4.13 and IV.4.14. The shape reconstruction is similar to the one achieved with noise-free data. In Figure IV.4.14, we compare the convergence results to the previous ones obtained with noise-free data. The Newton algorithm converges within 6 iterations to a level of error of 6% on the FFP phase, which is a level comparable to that of noise. The corresponding error on the FFP intensity is of 3%.

IV.4.2.4 Peanut-like scatterer

The truncation of the series given by Eq. (IV.4.12) is done for $M = 2$, and we represent a peanut-shaped obstacle using 5 shape parameters indicated in Table IV.4.8 and we initialize the shape with the circle of radius 0.0125.

Parameter	Target	Initial Guess
s_1	0.01	0.0125
s_2	0.002	0
s_3	0.0005	0
s_4	0.004	0
s_5	0.001	0

Table IV.4.8 – Shape parameters for the peanut-shaped target and the initial guess.

We consider the same number of elements per wavelength and the same value for the radius of the exterior boundary as in the previous sets of experiments.

Free noise results

The circular frequency is given by $\omega = 700000$, which corresponds to $ka = 4.67$. The regularization parameter α is equal to 100.

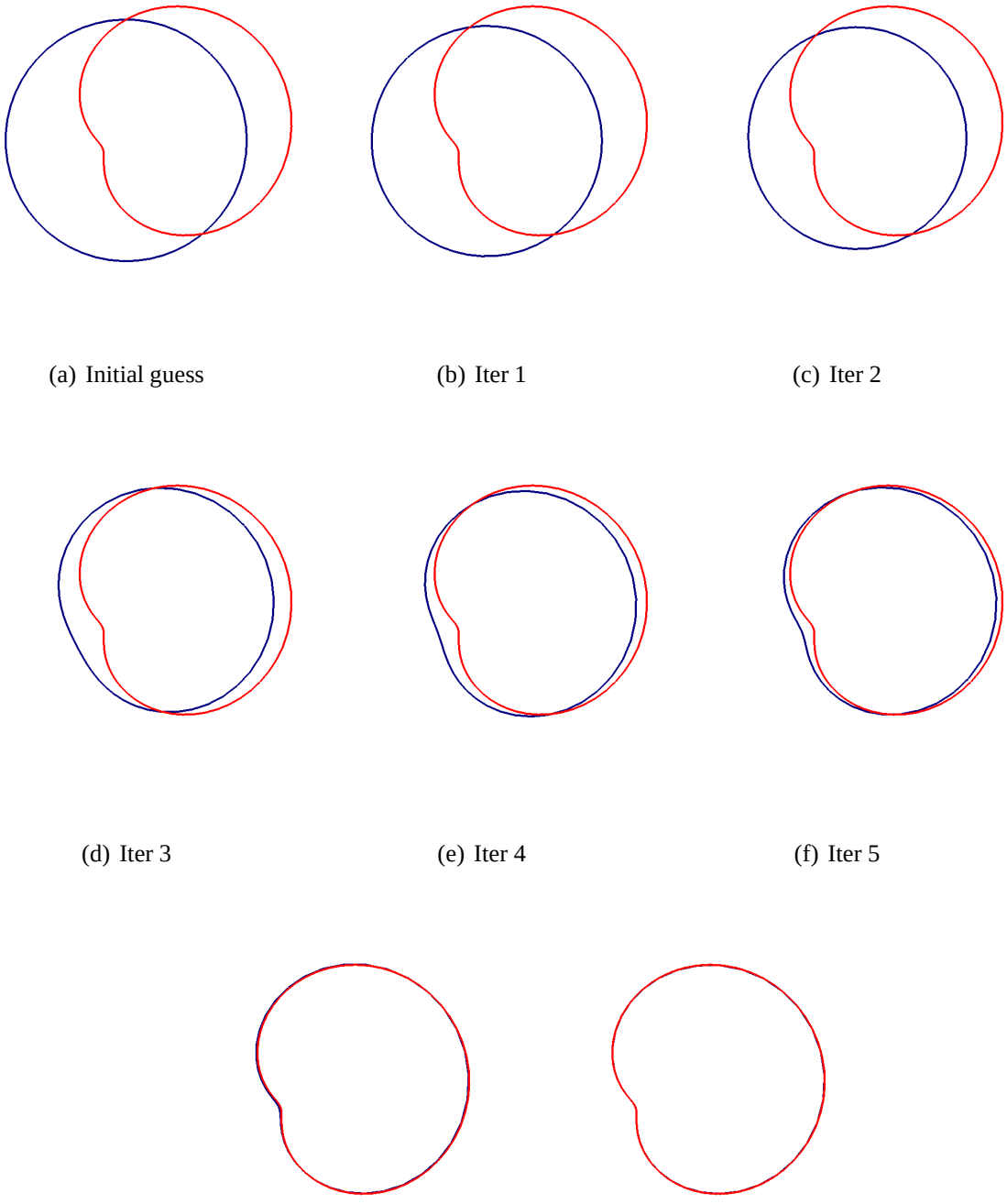

(a) Initial guess (b) Iter 1 (c) Iter 2

(d) Iter 3 (e) Iter 4 (f) Iter 5

(g) Iter 6 (h) Iter 7

Figure IV.4.11 – Iterative shapes for the potato-like scatterer.

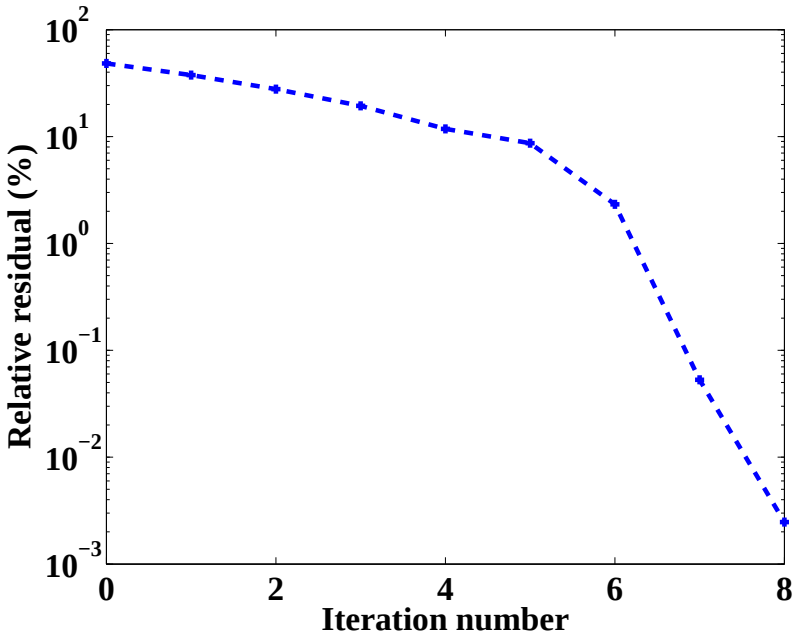

Figure IV.4.12 – Convergence history for the potato-like scatterer with noise-free data.

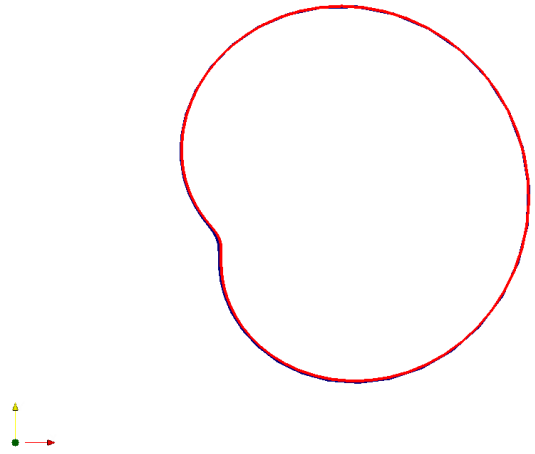

Figure IV.4.13 – Final shape for the potato with data containing 5 % of noise.

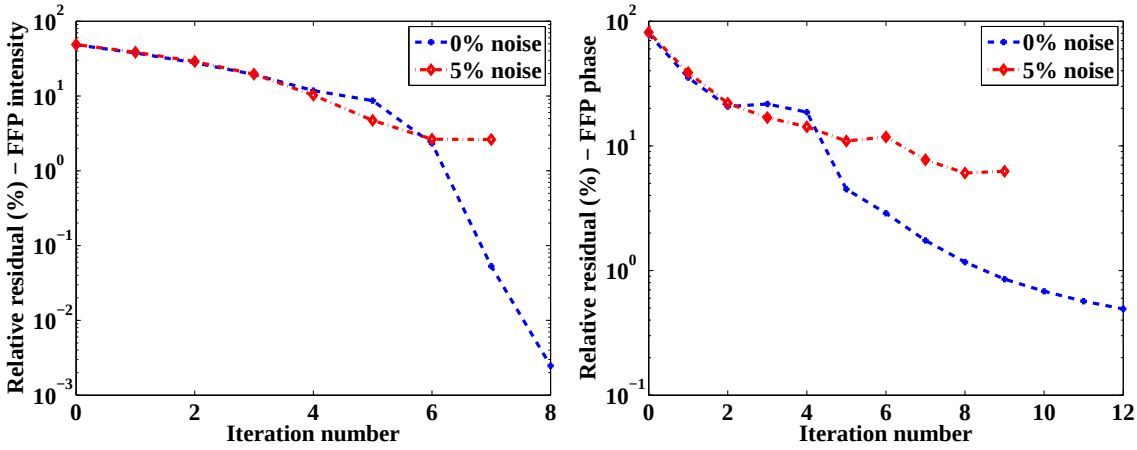

(a) FFP intensity (b) FFP phase

Figure IV.4.14 – Convergence history for the potato.

The iterative shapes are depicted in Figures IV.4.15 and IV.4.16 and we plot in Figure IV.4.17 the convergence of the corresponding relative discrete residual on the intensity of the far-field pattern during Step 2. The Newton algorithm converges in 12 iterations to the specified tolerance of 1% within a single step. It is worth noting that, once the tolerance of 1% is achieved, the algorithm requires some additional steps for reducing the relative residual associated with the FFP intensity to 10^{-2}.

Results with 5% of noise

In that case, the synthetic data of the FFP phase $\tilde{p}_\infty$ are tainted with 5% of noise.

Given the frequency $\omega = 700000$, corresponding to $ka = 4.67$, and for a regularization parameter $\alpha = 100$, the results are reported in Figures IV.4.18 and IV.4.19.

In Figure IV.4.19, we compare the convergence results to those obtained with noise-free data. In the case of tainted data, the Newton algorithm requires 15 iterations to reduce the relative residual on the FFP phase to a value of 6% comparable to the noise level. The corresponding error on the FFP intensity is of 5%.

IV.4.2.5 Ghost-like scatterer

The truncation of the series given by Eq. (IV.4.12) is done for $M = 3$, and we represent a ghost-shaped obstacle using 7 shape parameters, and the initial guess is the circle of radius 0.02, as reported in Table IV.4.9.

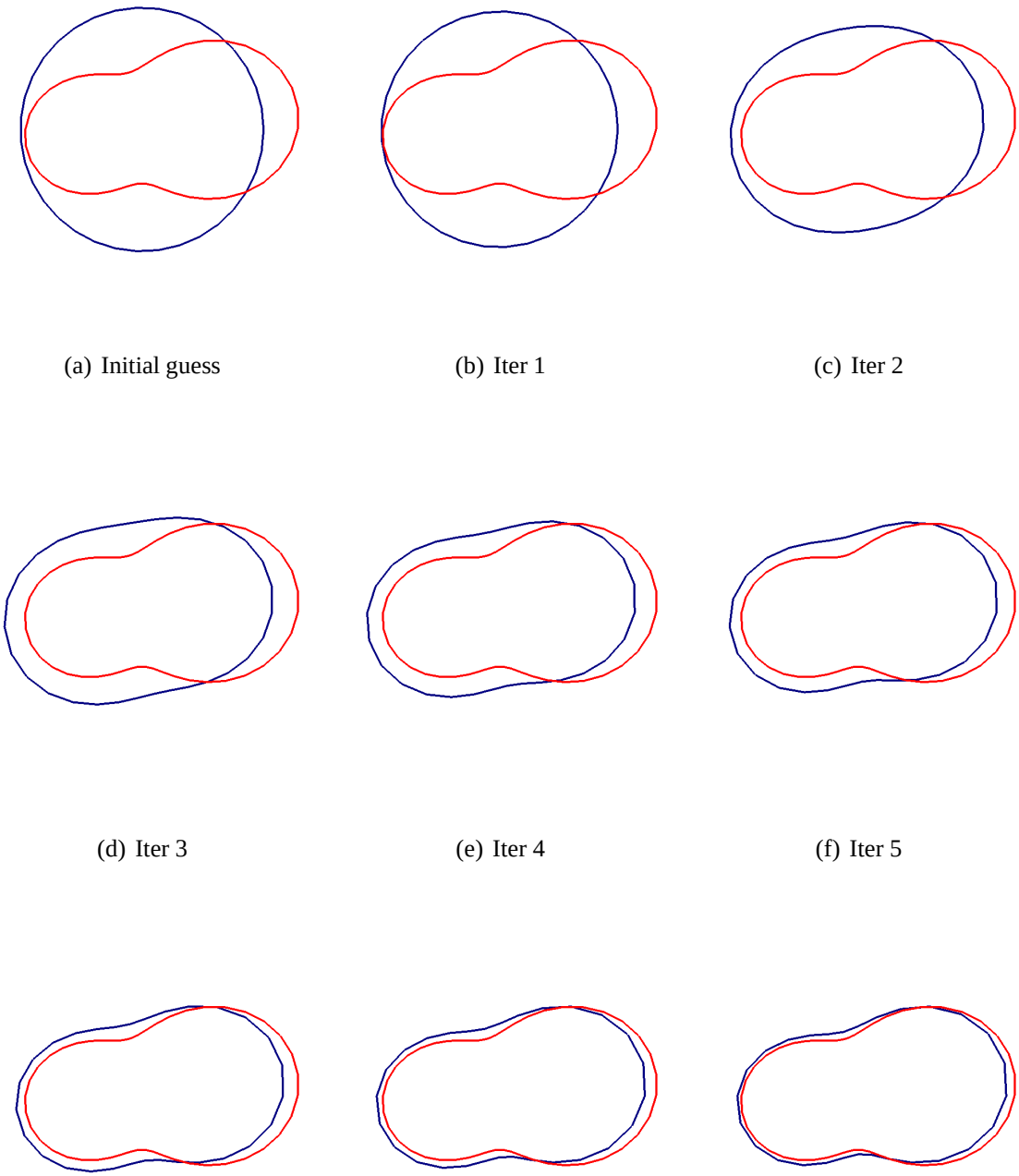

(a) Initial guess (b) Iter 1 (c) Iter 2

(d) Iter 3 (e) Iter 4 (f) Iter 5

(g) Iter 6 (h) Iter 7 (i) Iter 8

Figure IV.4.15 – Iterative shapes for the peanut-like scatterer.

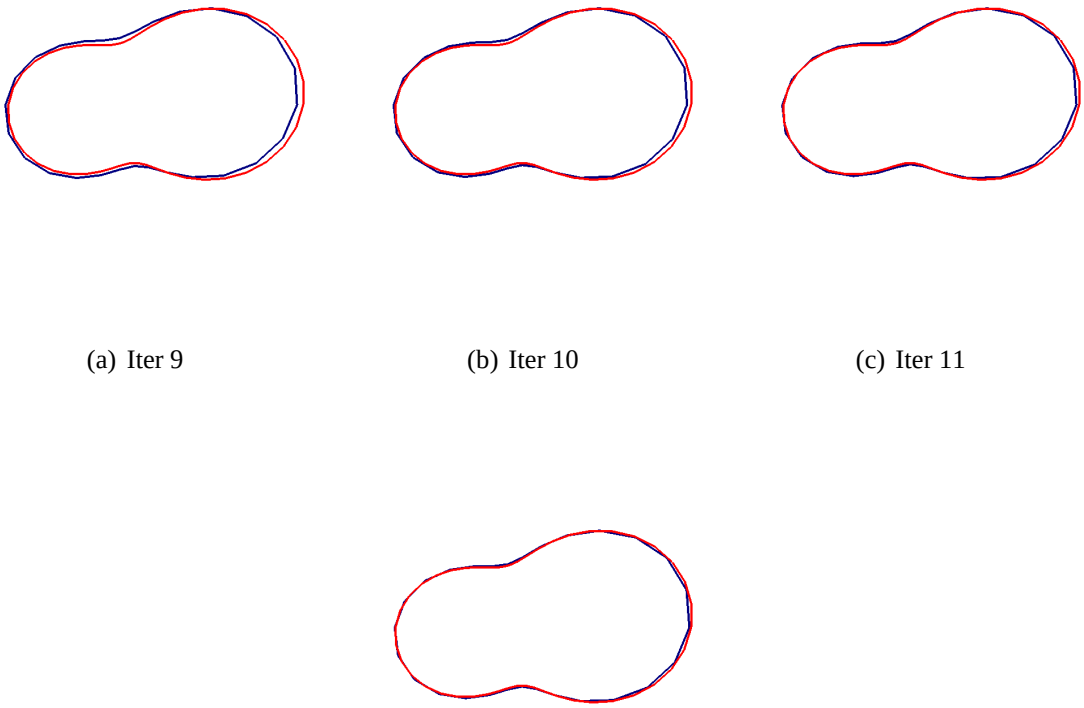

(a) Iter 9 (b) Iter 10 (c) Iter 11

(d) Iter 12

Figure IV.4.16 – Iterative shapes for the peanut-like scatterer.

Parameter	Target	Initial Guess
s_1	0.015	0.02
s_2	0.005	0
s_3	0.0015	0
s_4	0.007	0
s_5	0.0004	0
s_6	0.005	0
s_7	0.003	0

Table IV.4.9 – Shape parameters for the ghost-shaped target and the initial guess.

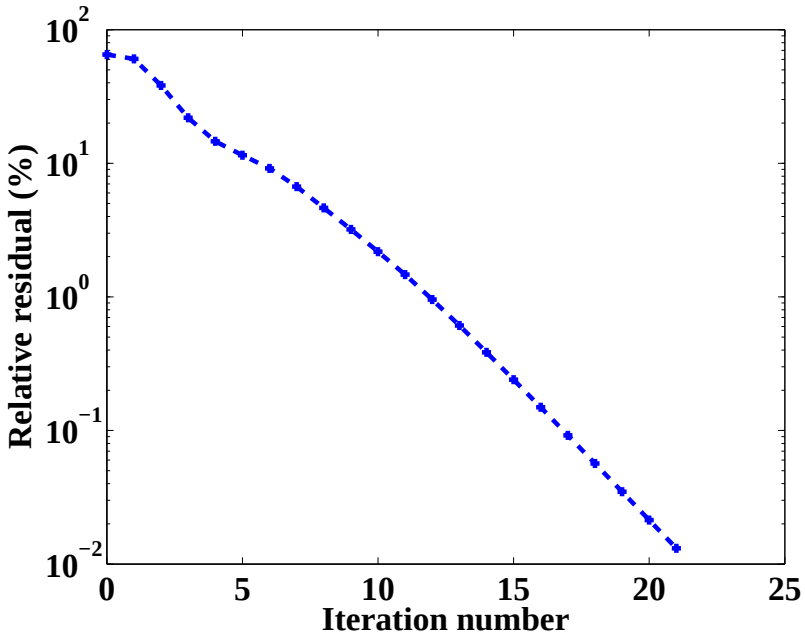

Figure IV.4.17 – Convergence history for the peanut-like scatterer with noise-free data.

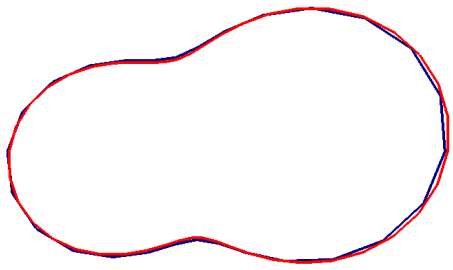

Figure IV.4.18 – Final shape for the peanut with data containing 5 % of noise.

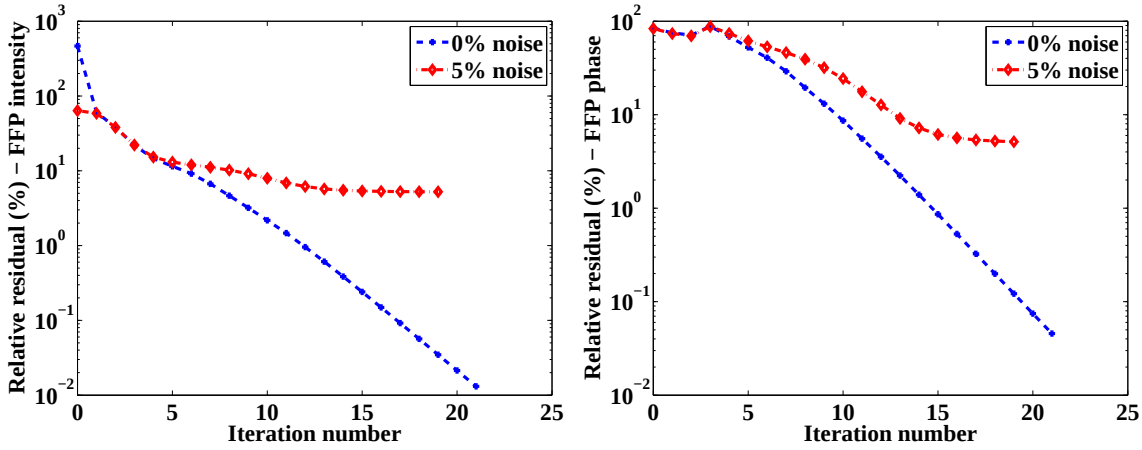

(a) FFP intensity (b) FFP phase

Figure IV.4.19 – Convergence history for the peanut.

We consider the same number of elements per wavelength and the same value for the radius of the exterior boundary as in the three previous experiments.

Free noise results

The given frequency is $\omega = 700000$, which corresponds to $ka = 7$, and the regularization parameter α is equal to 100.

The convergence results obtained within the single Step 2 are depicted in Figures IV.4.20 to IV.4.22 and IV.4.23. The convergence to the sought-after shape is quite slow in that case, and requires 18 iterations for the given tolerance of 1%.

Results with 5% of noise

Here, the measurements of the far-field pattern $\tilde{p}_\infty$ are tainted with 5 % of noise, and we monitor the errors on the phase and the intensity of the far-field pattern.

We keep $\omega = 700000$, corresponding to $ka = 7$, and $\alpha = 100$.

The results are reported in Figures IV.4.24 and IV.4.25. The final shape superimposed with the target depicted in Figure IV.4.24 illustrates a good reconstruction, all major features of the target obstacle are recovered. In comparison with the results obtained with noise-free data, we achieve convergence within 18 iterations, in which the relative residual on the FFP phase is reduced to a value of 7%, comparable to the noise level (see Figure IV.4.25). The corresponding relative residual on the FFP intensity is of 3%.

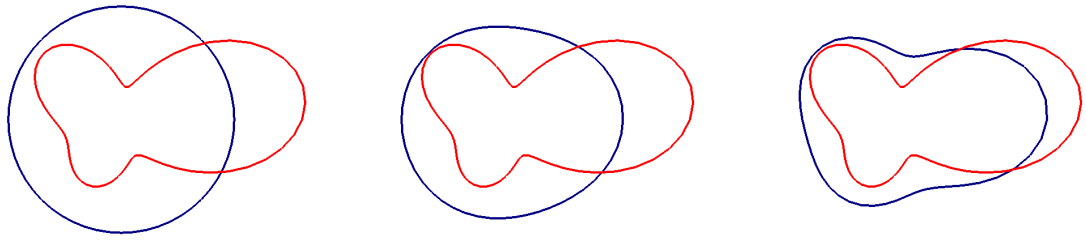

(a) Initial guess (b) Iter 1 (c) Iter 2

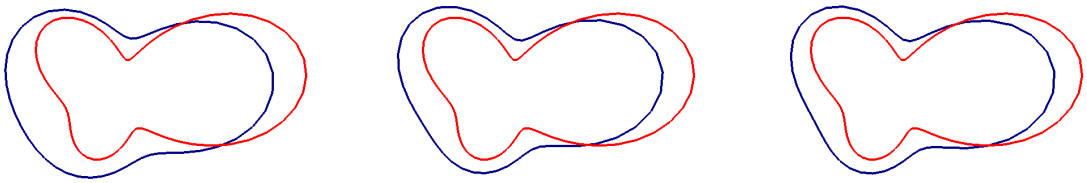

(d) Iter 3 (e) Iter 4 (f) Iter 5

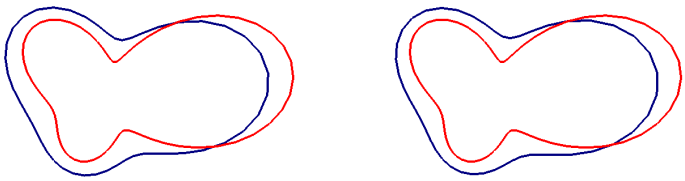

(g) Iter 6 (h) Iter 7

Figure IV.4.20 – Iterative shapes for the ghost scatterer.

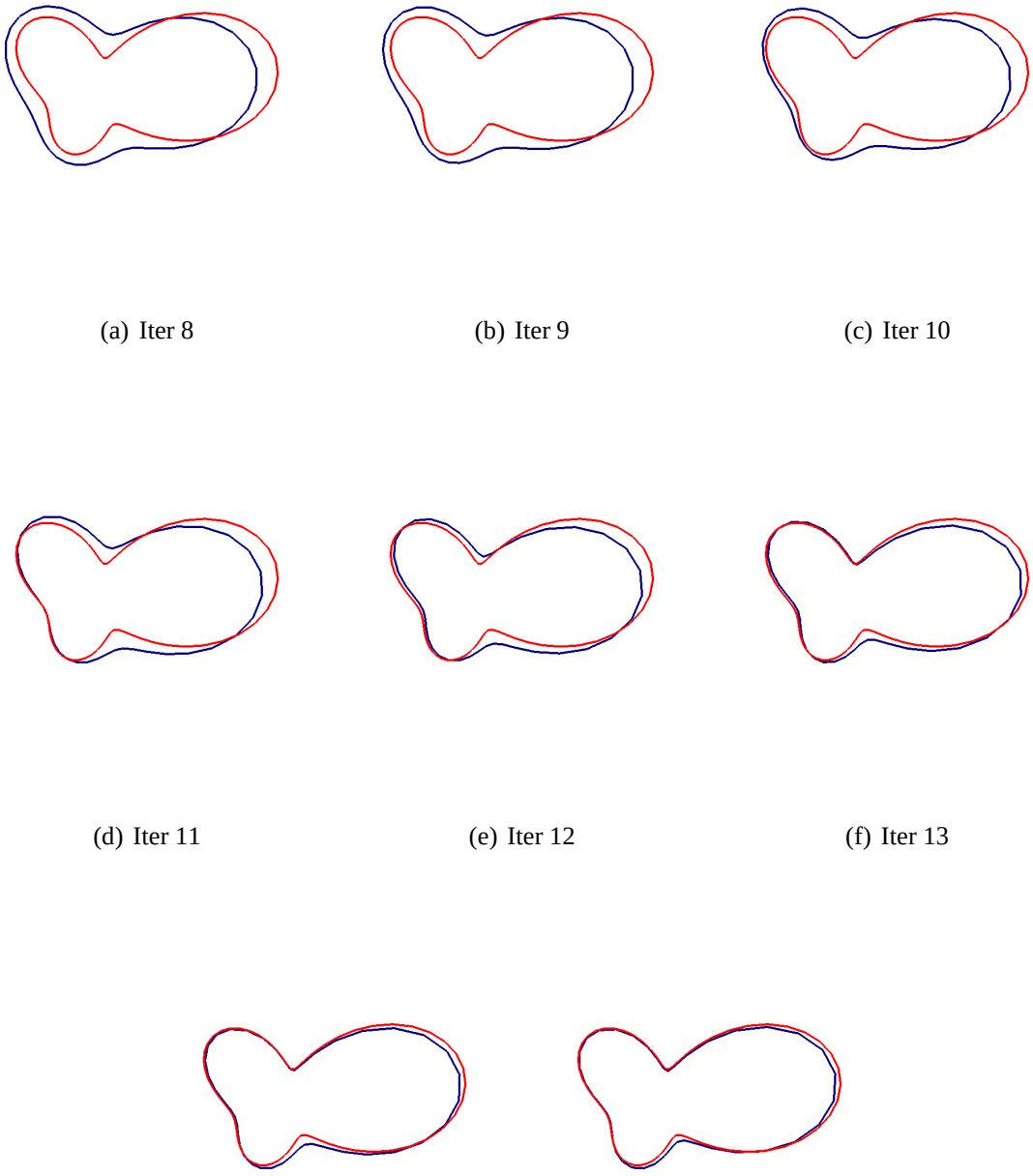

(a) Iter 8 (b) Iter 9 (c) Iter 10

(d) Iter 11 (e) Iter 12 (f) Iter 13

(g) Iter 14 (h) Iter 15

Figure IV.4.21 – Iterative shapes for the ghost scatterer.

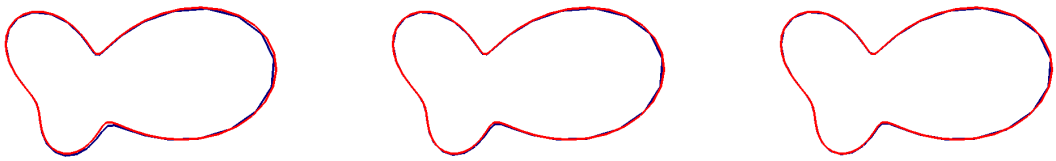

(a) Iter 16 (b) Iter 17 (c) Iter 18

Figure IV.4.22 – Iterative shapes for the ghost scatterer.

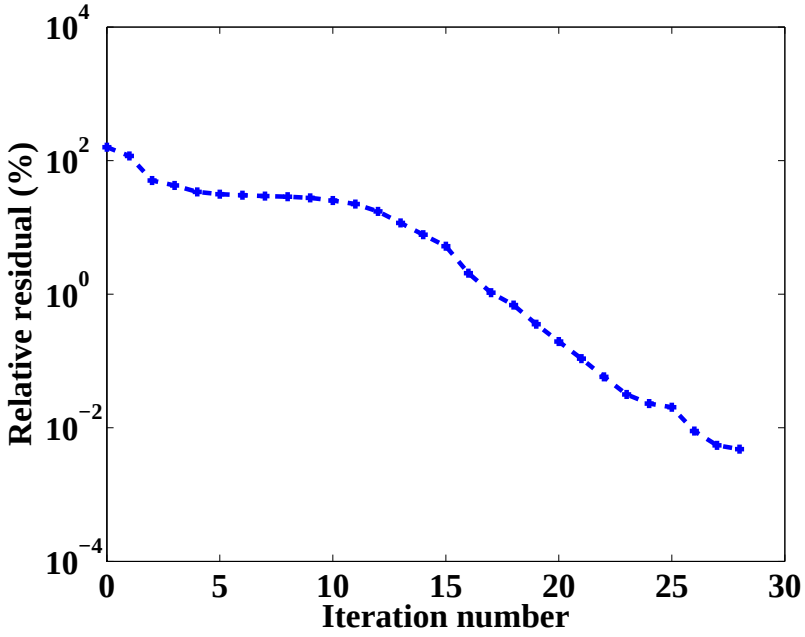

Figure IV.4.23 – Convergence history for the ghost scatterer with noise-free data.

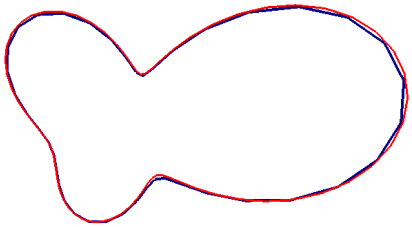

Figure IV.4.24 – Final shape for the ghost with data containing 5 % of noise.

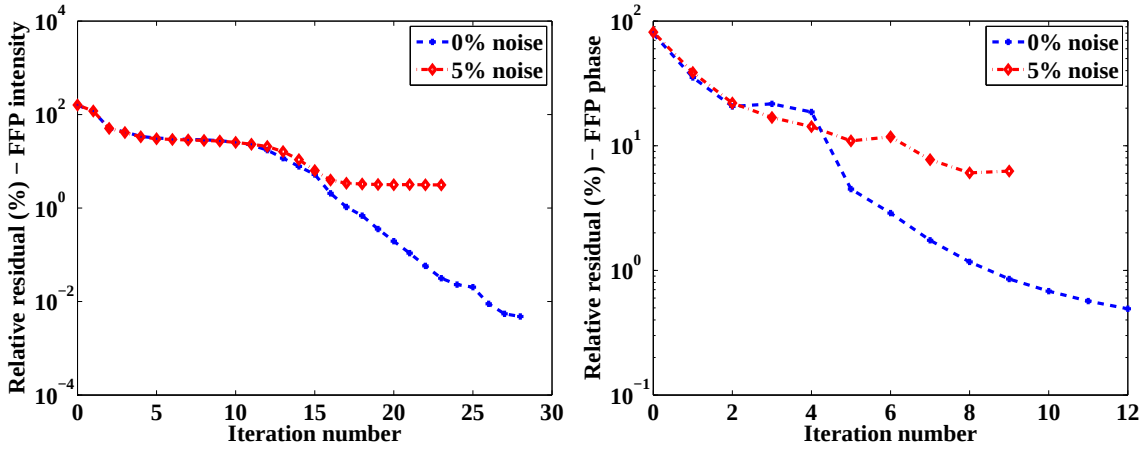

(a) FFP intensity (b) FFP phase

Figure IV.4.25 – Convergence history for the ghost.

IV.4.2.6 Mini-Submarine-like scatterer

Before being able to recover a real submarine, a first step can be to recover a smoother shape resembling a mini-submarine as in Figure IV.4.26. To that purpose, we truncate the trigonometric series for $M = 4$, and we represent a simplified fish-shaped scatterer using the 7 shape parameters summarized in Table IV.4.10. We initialize the shape with an oval initial guess, as indicated in Table IV.4.10.

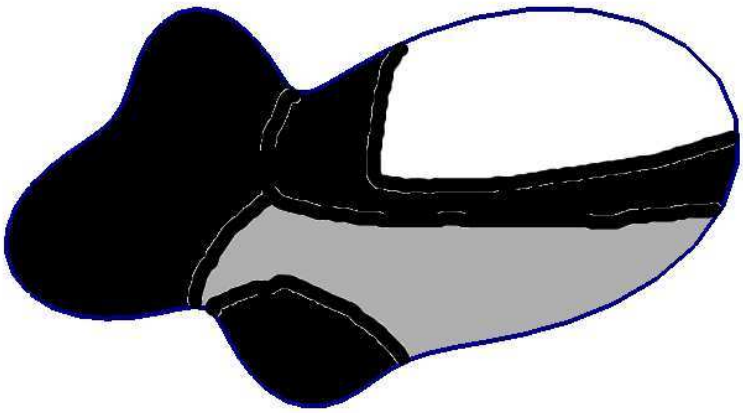

Figure IV.4.26 – Fictitious mini-submarine

Parameter	Target	Initial Guess
s_1	0.015	0.0175
s_2	0.005	0.006
s_3	0.0005	0
s_4	0.006	0.001
s_5	0.0001	0
s_6	0.002	0
s_7	0.001	0
s_8	0.002	0
s_9	0.003	0

Table IV.4.10 – Shape parameters for the mini-submarine-shaped target and the initial guess.

In that case, we increase the mesh resolution. The number of elements per wavelength used to simulate the data on the sought-after shape is equal to $N_{\lambda,data} = 8$, whereas it is equal to $N_\lambda = 6$ for the meshes during the Newton iterations. Note that, in that experiment, we consider the exterior boundary for the far-field pattern generation at $R_{data} = 5$ and still take $R = 4$ to define the exterior boundary

during the Newton iterations. This is an argument to avoid the adverse effect of domain truncation.

Free noise results

We consider $\omega = 350000$, which corresponds to $ka = 3.5$. The regularization parameter α is chosen equal to 100.

The iterative shapes and convergence results obtained within the single Step 2 are depicted in Figures IV.4.27 to IV.4.29. In the absence of noise, the Newton algorithm converges within 12 iterations to the prescribed tolerance of 1%. Unlike the previous experiments, the error can not be reduced more. Indeed, the level achieved of the order of 10^{-1}% corresponds to the error due to the difference between the exterior boundary radii R_{data} and R that are used for generating the synthetic data and along the Newton iterations.

Sensitivity to the noise level

The previous results were performed with noise-free data. In the following numerical example, we assess the performance of the algorithm when adding white noise to the synthetic data $\tilde{p}_\infty$. As previously, we monitor the convergence of the IOP solver via the decay of the discrete relative residuals on the phase and the intensity of the far-field pattern.

We keep $\omega = 350000$, corresponding to $ka = 3.5$, and $\alpha = 100$, and we vary the level of white noise between 0 and 20%.

The convergence results are depicted in Figure IV.4.30 and the corresponding relative errors obtained during Step 2 are summarized in Tables IV.4.11 and IV.4.12. For most cases where the FFP data are tainted by noise, the IOP solver converges in a few iterations within a single step. The initial relative residual on the FFP phase is reduced to a level comparable to that of the noise, as indicated in Table IV.4.11. Consequently, these results highlight the effect of noise on the recovery. Nevertheless, Figure IV.4.31 also illustrates that all major features of the target are recovered in all cases with a good overall accuracy, even when using 20% of noise. This is supported by Table IV.4.12. It is worth noting that once the relative residual is reduced to a level comparable to that of the noise, it stagnates during a few iterations but then diverges. This is particularly visible on the last experiment with 20% of noise, as shown in Figure IV.4.32 with 5 additional iterations in Step 2.

Remark IV.4.2.1 ***Sensitivity to the regularization parameter*** *- Note that we have considered a higher or smaller regularization parameter, such as $\alpha = 1000$ or $\alpha = 10$, but then the algorithm fails to converge when keeping the same parameters (initial guess, survey frequency, ...).*

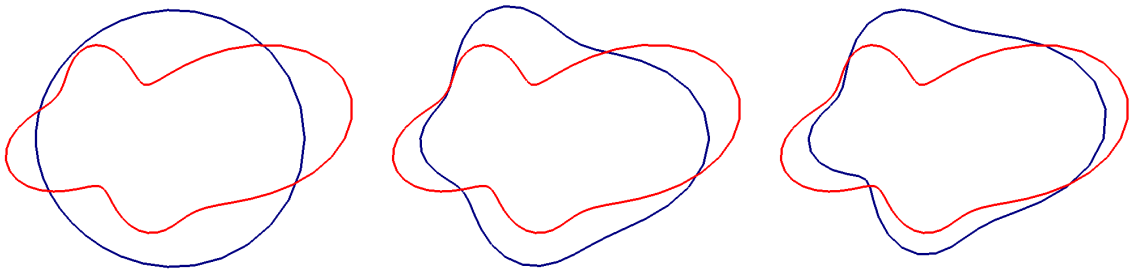

(a) Initial guess (b) Iter 1 (c) Iter 2

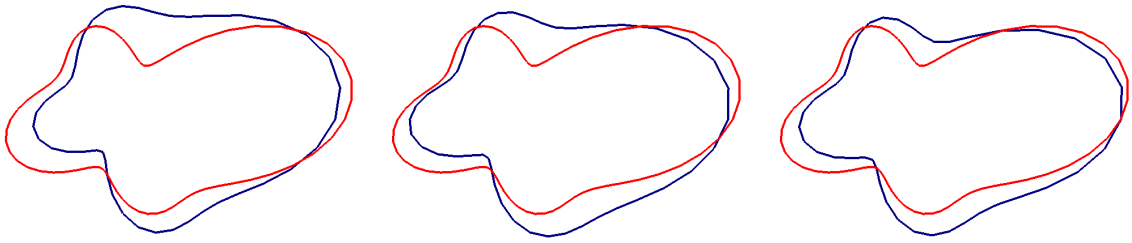

(d) Iter 3 (e) Iter 4 (f) Iter 5

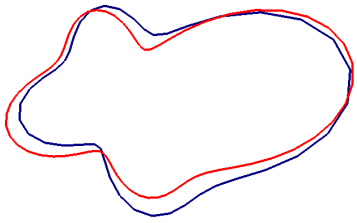

(g) Iter 6

Figure IV.4.27 – Iterative shapes for the mini-submarine-like scatterer.

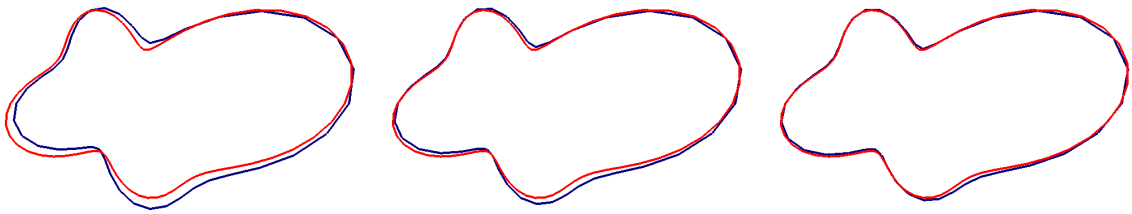

(a) Iter 7 (b) Iter 8 (c) Iter 9

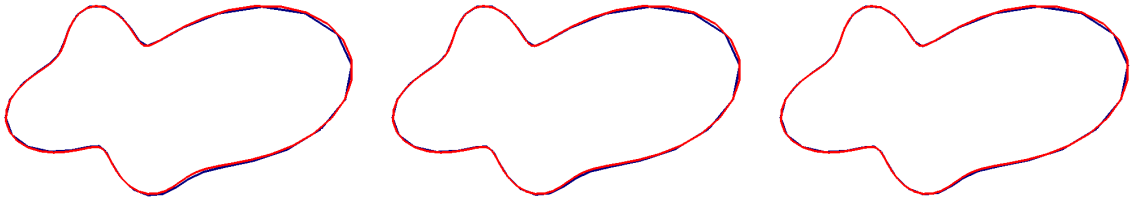

(d) Iter 10 (e) Iter 11 (f) Iter 12

Figure IV.4.28 – Iterative shapes for the mini-submarine-like scatterer.

Noise level	0	1	5	10	20
$\tilde{p}_\infty$	1.2	2	5.2	10.5	18.5
$\tilde{p}^*_\infty \tilde{p}_\infty$	0.3	0.8	3.4	5.9	11.8
Iter.	15	13	14	9	6

Table IV.4.11 – L^2-relative error on the reconstructed FFP: Sensitivity to the noise level.

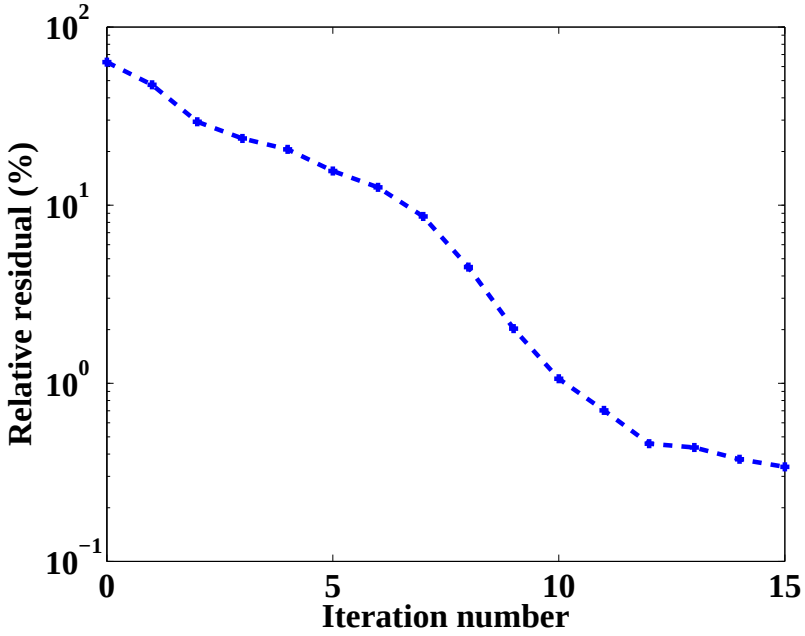

Figure IV.4.29 – Convergence history for the mini-submarine-like scatterer with noise-free data.

Noise level	0	1	5	10	20
L^1	0.5	1.4	1.6	2.8	7.6
L^2	0.5	1.1	1.6	2.9	6
L^∞	0.5	0.8	1.7	3.0	4.3
Iter.	15	13	14	9	6

Table IV.4.12 – Relative error on the shape parameters: Sensitivity to the noise level.

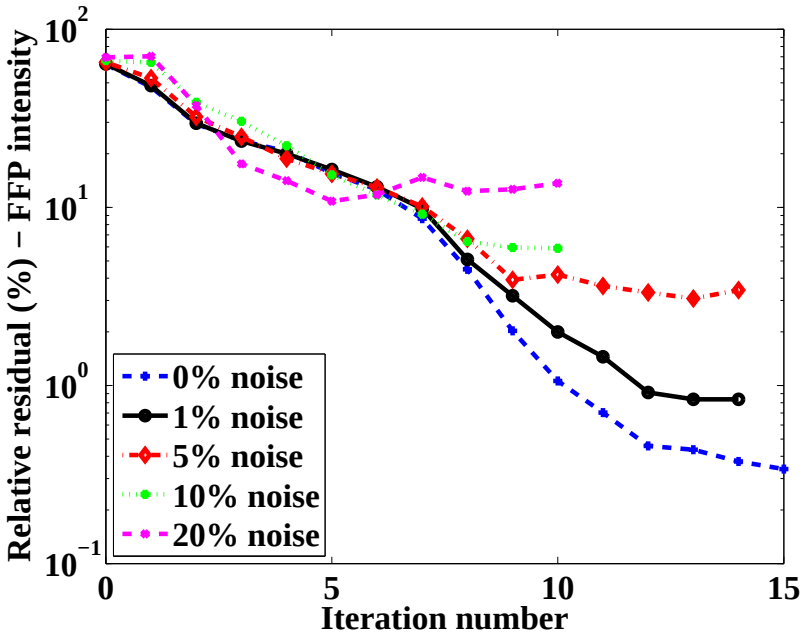

(a) FFP intensity

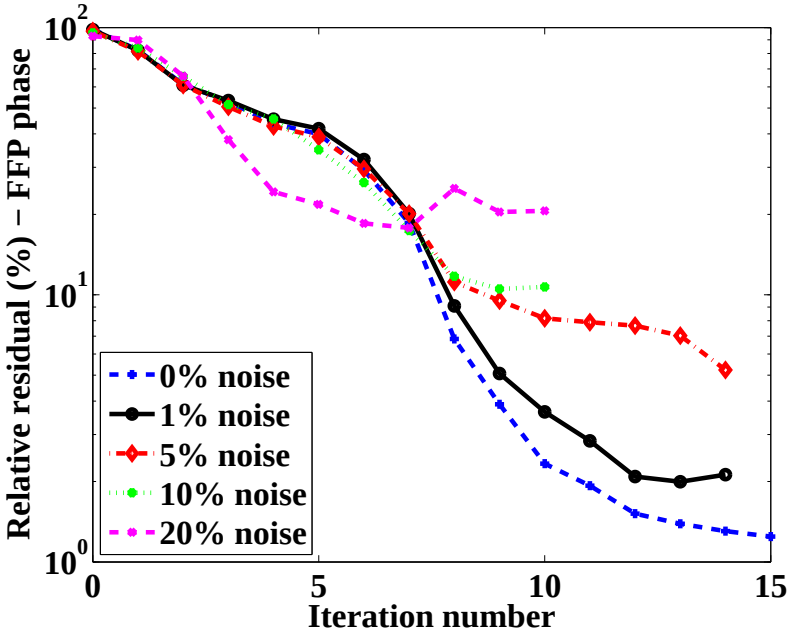

(b) FFP phase

Figure IV.4.30 – Convergence history : Sensitivity to the noise level.

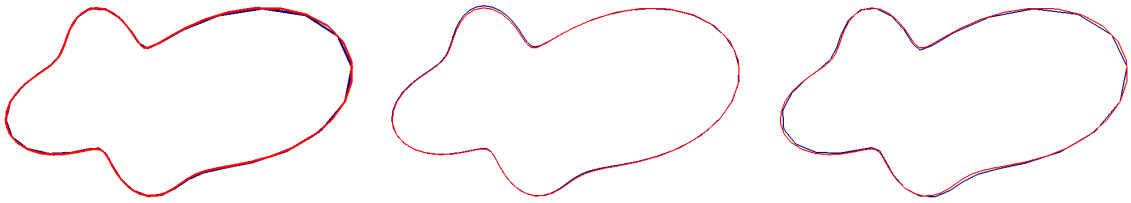

(a) 0 %noise (b) 1 %noise (c) 5 %noise

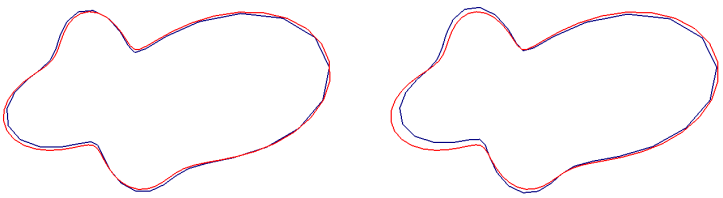

(d) 10 %noise (e) 20 %noise

Figure IV.4.31 – Effect of the noise level on the shape reconstruction: Computed (blue) vs Target (red).

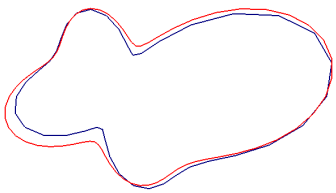

Figure IV.4.32 – Shape reconstruction: Computed (blue) vs Target (red) at iteration 11 of Step 2 using 20%

IV.4.3 B-spline representation

IV.4.3.1 Parametrization

We want to retrieve the shape of curved scatterers using uniform quadratic B-splines. To that effect, we define a set of N control points: $X_j = r_j \begin{pmatrix} \cos\theta_j \\ \sin\theta_j \end{pmatrix}$, $j = 1, \cdots N$, uniformly distributed in the polar coordinate angle.

Then, the j^{th} B-spline of degree 2 denoted by S_j is the parametric curve defined as follows:

$$S_j(t) = \frac{1}{2}\left[(t^2 - 2t + 1)X_{j-1} + (-2t^2 + 2t + 1)X_j + t^2 X_{j+1}\right], \quad t \in [0,1],\ j = 1, \cdots, N \tag{IV.4.17}$$

with $X_{N+1} = X_1$ and $X_0 = X_N$.

Put under matricial form, we have:

$$S_j(t) = \frac{1}{2}\begin{bmatrix} t^2 & t & 1 \end{bmatrix} \begin{pmatrix} 1 & -2 & 1 \\ -2 & 2 & 0 \\ 1 & 1 & 0 \end{pmatrix} \begin{bmatrix} X_{j-1} \\ X_j \\ X_{j+1} \end{bmatrix}.$$

Therefore, we get:

$$\Gamma = \{S_j(t), \quad t \in [0,1],\ j = 1, \cdots, N\}. \tag{IV.4.18}$$

The shape is entirely defined by the N radii r_j, $j = 1, \cdots N$, so that it can be written as follows:

$$\Gamma = \left\{ \sum_{j=1}^{N} r_j \phi_j(s) \begin{pmatrix} \cos\theta_j \\ \sin\theta_j \end{pmatrix}, \quad s \in [0, N] \right\} \tag{IV.4.19}$$

where, $t = s - j + 1$,

$$\phi_1(s) = \frac{1}{2} \begin{cases} t^2 - 2t + 1 & \text{if } 1 \le s \le 2, \\ -2t^2 + 2t + 1 & \text{if } 0 \le s \le 1, \\ t^2 & \text{if } N - 1 \le s \le N, \\ 0 & \text{otherwise.} \end{cases} \tag{IV.4.20}$$

$$\phi_N(s) = \frac{1}{2} \begin{cases} t^2 - 2t + 1 & \text{if } 0 \leq s \leq 1, \\ -2t^2 + 2t + 1 & \text{if } N-1 \leq s \leq N, \\ t^2 & \text{if } N-2 \leq s \leq N-1, \\ 0 & \text{otherwise.} \end{cases} \tag{IV.4.21}$$

and for $j = 2, \cdots, N-1$,

$$\phi_j(s) = \frac{1}{2} \begin{cases} t^2 - 2t + 1 & \text{if } j \leq s \leq j+1, \\ -2t^2 + 2t + 1 & \text{if } j-1 \leq s \leq j, \\ t^2 & \text{if } j-2 \leq s \leq j-1, \\ 0 & \text{otherwise.} \end{cases} \tag{IV.4.22}$$

Consequently, the deformation directions with respect to the N shape parameters r_j are given by $h_j(s) = \phi_j(s) \begin{pmatrix} \cos\theta_j \\ \sin\theta_j \end{pmatrix}$.

IV.4.3.2 Oval

We want to retrieve an oval-shaped obstacle parametrized with 4 shape parameters. We initialize the object with the larger shape given in Table IV.4.13.

Parameter	Target	Initial Guess
s_1	0.01	0.0175
s_2	0.015	0.0175
s_3	0.01	0.0175
s_4	0.015	0.0175

Table IV.4.13 – Shape parameters for the oval-shaped target and the initial guess.

The number of elements per wavelength used to simulate the data on the sought-after shape is equal to $N_{\lambda,data} = 5$, whereas it is equal to $N_\lambda = 3$ for the meshes in the Newton iterations. Here, we take $R_{data} = R = 4$.

Free noise results

The frequency is given by $\omega = 300000$, which corresponds to $ka = 3$. The regularization parameter α is equal to 1.

The Newton algorithm converges in only 3 iterations. The corresponding shapes and the convergence of the relative residual during Step 2 are depicted in Figures IV.4.33 and IV.4.34. It is worth noting that, once the tolerance of 1% is achieved, the algorithm requires five additional iterations for reducing the relative residual on the FFP intensity to 10^{-2}.

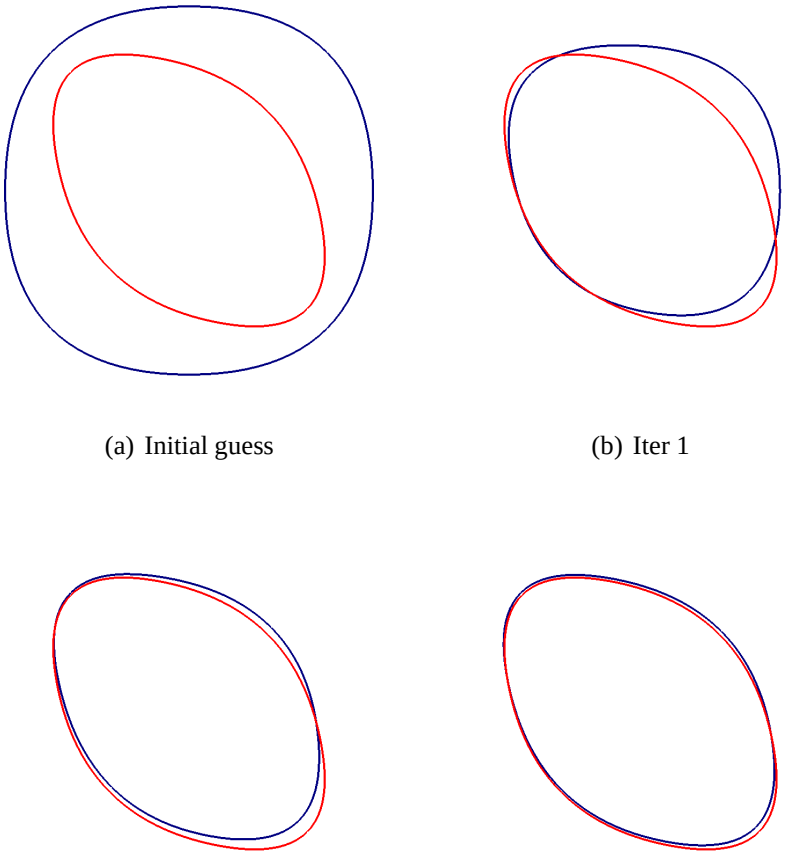

(a) Initial guess (b) Iter 1

(c) Iter 2 (d) Iter 3

Figure IV.4.33 – Iterative shapes for the oval scatterer.

Results with 5% of noise

In that case, the simulated FFP data $\tilde{p}_\infty$ are tainted with 5 % of noise, and we monitor the errors on

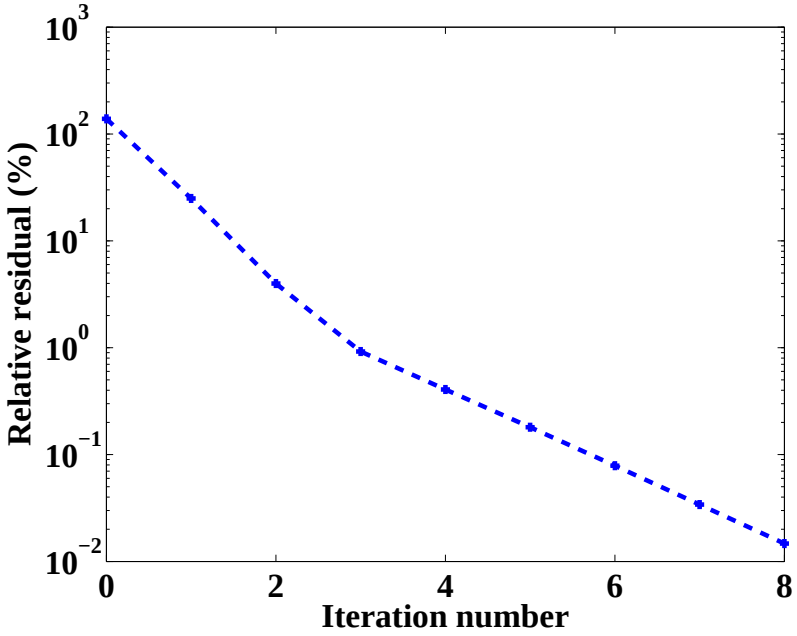

Figure IV.4.34 – Convergence history for the oval scatterer with noise-free data.

the phase and the intensity of the far-field pattern.
The frequency is given by $\omega = 300000$, corresponding to $ka = 3$ and we choose $\alpha = 50$. At the 4^{th} iteration, we switch to $\alpha = 5$.
The results are reported in Figures IV.4.35 and IV.4.36. In Figure IV.4.36, we compare the results to the previous ones obtained with noise-free data. In the case of tainted data, we also observe the convergence of the relative residuals. We achieve convergence within 5 iterations, in which the two relative residuals associated with the FFP phase and the FFP intensity are reduced to the noise level.

IV.4.3.3 A rounded square

We want to retrieve a rounded square target obtained using the 8 shape parameters reported in Table IV.4.14. We initialize the object with the larger shape given by $r_j = 0.0175$, for $j = 1, \cdots, 8$. Note that, in that experiment, we still take $N_{\lambda,data} = 5$ and $N_\lambda = 3$, but we consider the exterior boundary for generating the far-field pattern data at $R_{data} = 5$ and still take $R = 4$ to define the exterior boundary during the Newton iterations.

Free noise results
The frequency is given by $\omega = 150000$, which corresponds to $ka = 1.5$, and the regularization parameter α is equal to 1 in Step 2. At iteration 9, the regularization parameter is switched to 0.01

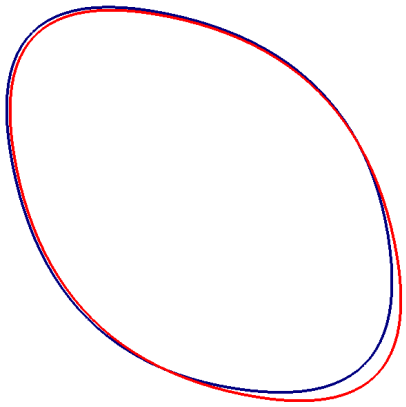

Figure IV.4.35 – Final shape for the oval-shaped scatterer with data containing 5 % of noise.

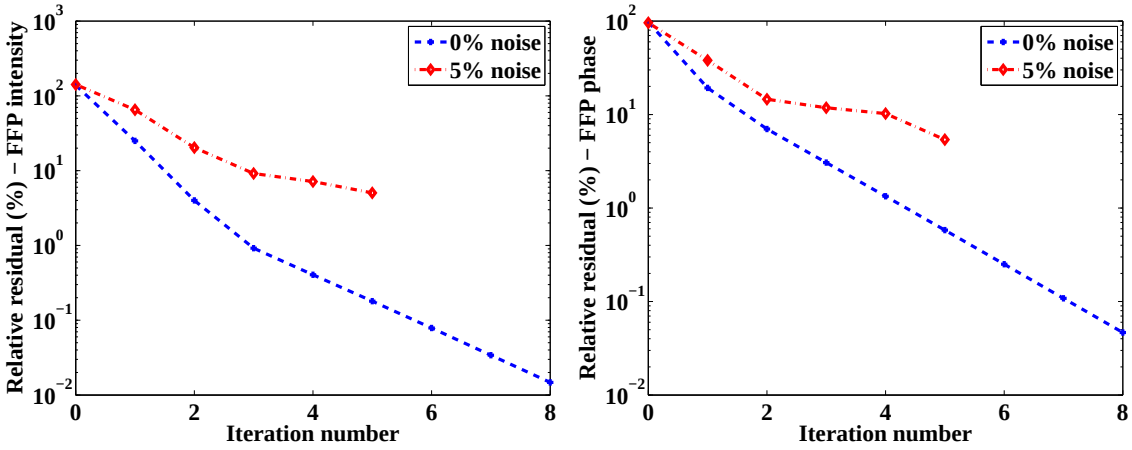

(a) FFP intensity (b) FFP phase

Figure IV.4.36 – Convergence history for the oval-shaped scatterer.

Parameter	Target	Initial Guess
s_1	0.01	0.0175
s_2	0.015	0.0175
s_3	0.01	0.0175
s_4	0.015	0.0175
s_5	0.01	0.0175
s_6	0.015	0.0175
s_7	0.01	0.0175
s_8	0.015	0.0175

Table IV.4.14 – Shape parameters for the rounded square-shaped target and the initial guess.

and 0.001 in two successive steps, whereas the wavenumber does not change.
The corresponding shapes and the relative residual convergence during the successive Step 2 and Step 3 are depicted in Figures IV.4.37 to IV.4.39. The Newton algorithm converges in 11 iterations. We can observe in Figure IV.4.39 the acceleration in the convergence due to the decrease of the regularization parameter.

Results with 5% of noise

Once again, we contaminate the synthetic data of the FFP phase with a noise level of 5%.
The frequency is given by $\omega = 150000$, corresponding to $ka = 1.5$, and we choose again $\alpha = 1$. At the 6^{th} iteration, we switch to $\omega = 200000$, which corresponds to $ka = 2$, and $\alpha = 5$.
The results are reported in Figures IV.4.40 and IV.4.41. Even when the data are tainted with white noise, the algorithm converges. It requires 10 iterations to reduce the two relative residuals associated with the FFP phase and the FFP intensity to a value of 4% slightly smaller than the noise level.

IV.4.3.4 Submarine-like scatterer

A parameter identification problem We want to recover a simplified submarine parametrized using 24 B-splines. The values of these 24 parameters corresponding to the target are specified in Table IV.4.15. For simplification purpose, we assume that we know the structure of the object, and we want to retrieve its real size. Therefore, we consider an initial guess which is the half of the object to be retrieved.

The mesh resolution is the same: $N_{\lambda,data} = 5$ and $N_\lambda = 3$. We again consider $R_{data} = 5$ and $R = 4$ to avoid the adverse effect of domain truncation.

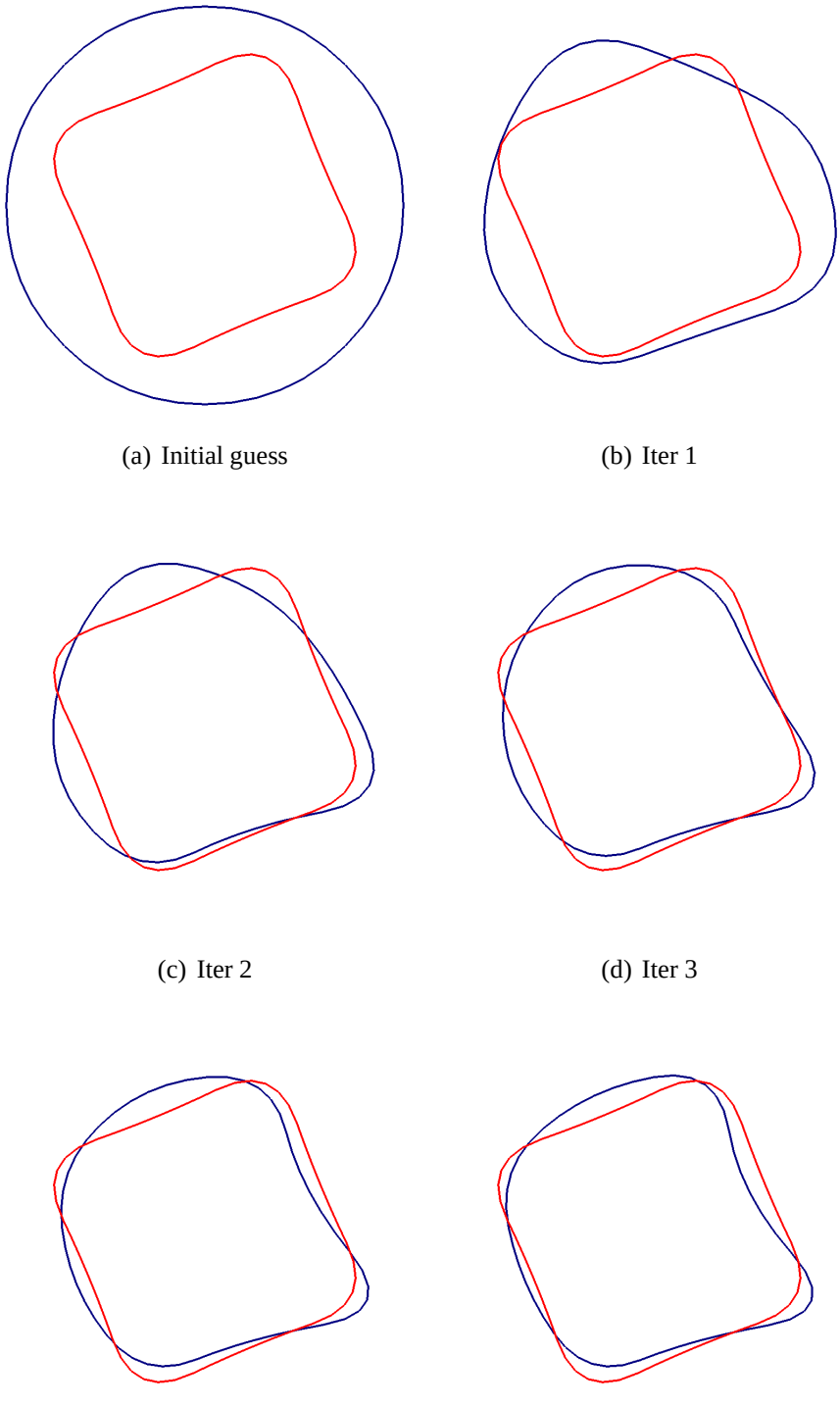

(a) Initial guess (b) Iter 1

(c) Iter 2 (d) Iter 3

(e) Iter 4 (f) Iter 5

Figure IV.4.37 – Iterative shapes for the rounded square.

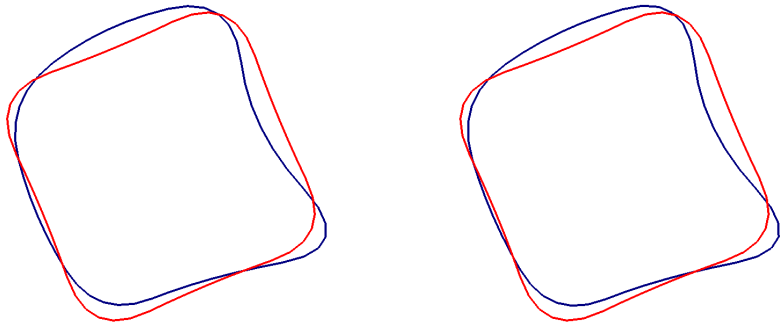

(a) Iter 6 (b) Iter 7

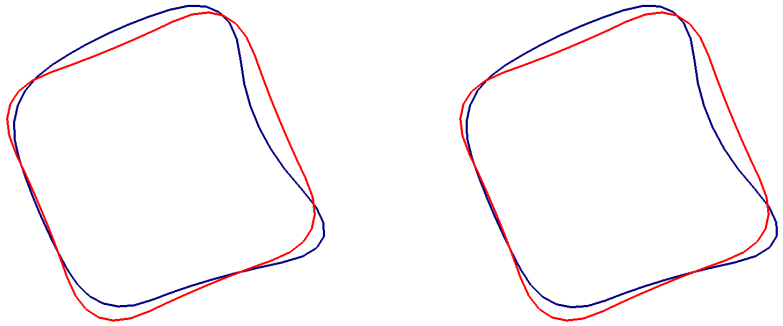

(c) Iter 8 (d) Iter 9

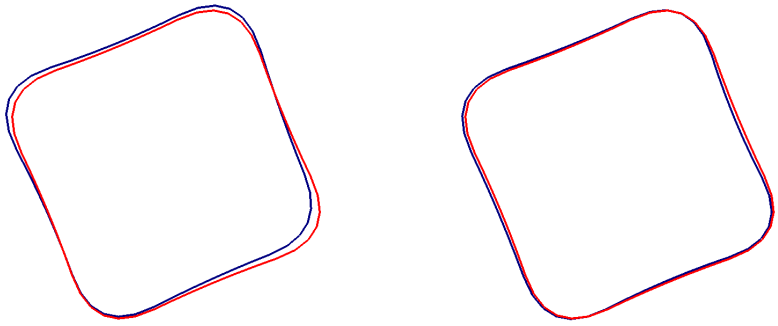

(e) Iter 10 (f) Iter 11

Figure IV.4.38 – Iterative shapes for the rounded square.

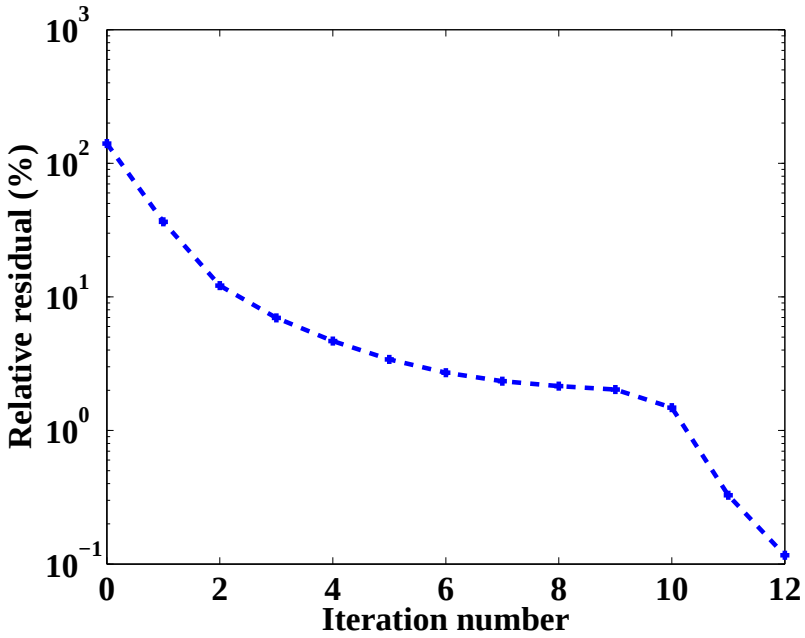

Figure IV.4.39 – Convergence history for the rounded square with noise-free data.

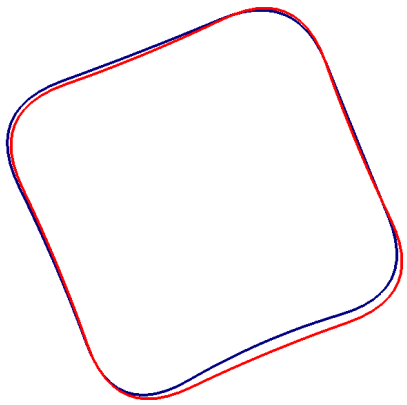

Figure IV.4.40 – Final shape for the rounded square with data containing 5 % of noise.

Parameter	Target	Initial Guess
s_1	0.018	0.009
s_2	0.017	0.0085
s_3	0.015	0.0075
s_4	0.012	0.006
s_5	0.01	0.005
s_6	0.014	0.007
s_7	0.015	0.0075
s_8	0.014	0.007
s_9	0.01	0.005
s_{10}	0.013	0.0065
s_{11}	0.018	0.009
s_{12}	0.027	0.0135
s_{13}	0.03	0.015
s_{14}	0.024	0.012
s_{15}	0.014	0.007
s_{16}	0.01	0.005
s_{17}	0.008	0.004
s_{18}	0.0075	0.00325
s_{19}	0.007	0.0035
s_{20}	0.0075	0.00375
s_{21}	0.008	0.004
s_{22}	0.01	0.005
s_{23}	0.013	0.0065
s_{24}	0.016	0.008

Table IV.4.15 – Shape parameters for the submarine-shaped target and the initial guess.

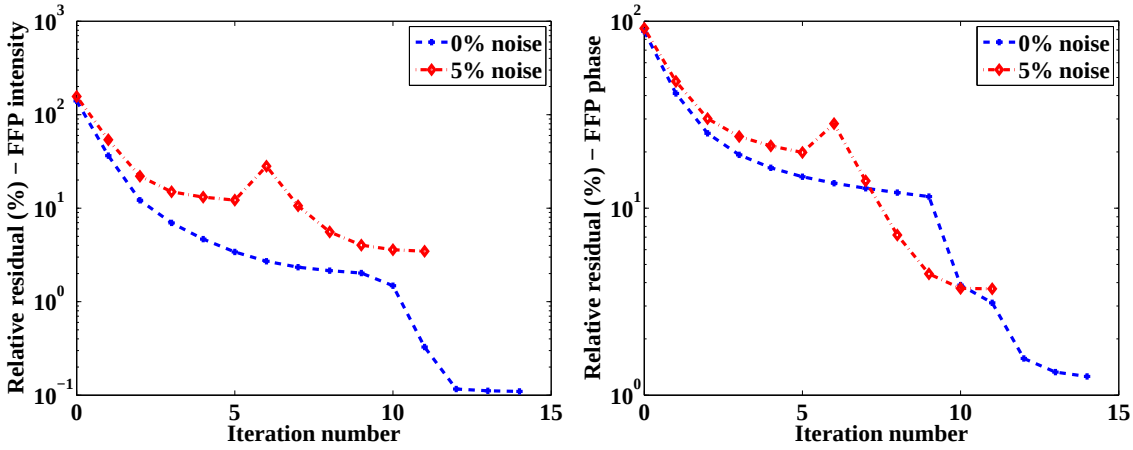

(a) FFP intensity (b) FFP phase

Figure IV.4.41 – Convergence history for the rounded square scatterer.

The frequency is given by $\omega = 100000$, which corresponds to $ka = 2$, and the regularization parameter is chosen equal to $\alpha = 0.5$. When the error stagnates in Step 2, we switch to $\omega = 200000$, corresponding to $ka = 4$ and $\alpha = 0.05$ at iteration 5. We then initialize the shape parameters with their values at stagnation in the previous step, and solve again the IOP by the same regularized Newton method. Next, at iteration 11, we switch to $\omega = 300000$, that is $ka = 6$, and $\alpha = 0.005$. Last, to improve the convergence results, we reduce α to 0.00005 at iteration 15.

The corresponding shapes and the relative residual convergence obtained during the successive Step 2 and Step 3 are depicted in Figures IV.4.42 to IV.4.44. The Newton algorithm requires 14 iterations to pass below the tolerance of 1% on the FFP intensity. The switches to a small regularization parameter and higher frequency allow to recover the global features.

Results with 2% of noise

Here, we choose a noise level of 2% to contaminate the data of the FFP phase $\tilde{p}_\infty$.

We consider the frequency $\omega = 100000$, which corresponds to $ka = 2$, to start in Step 2, with a regularization parameter $\alpha = 0.75$. When the error stagnates, we switch to $\omega = 200000$, that is $ka = 4$ and $\alpha = 0.1$ at iteration 6. Next, at iteration 11, we switch to $\omega = 300000$, corresponding to $ka = 6$, and keep $\alpha = 0.1$.

The results are depicted in Figure IV.4.45 and Figure IV.4.46. Figure IV.4.45 illustrates a good reconstruction where all major features of the target are recovered. In Figure IV.4.46, we observe the convergence within 14 iterations when the data are tainted with noise. The initial relative residual

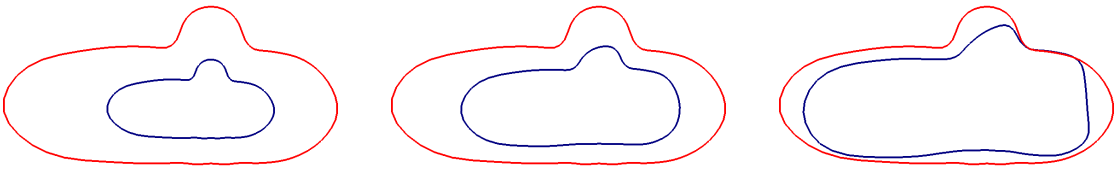

(a) Initial guess (b) Iter 1 (c) Iter 2

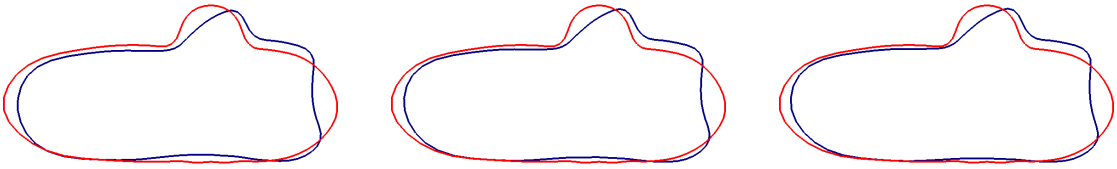

(d) Iter 3 (e) Iter 4 (f) Iter 5

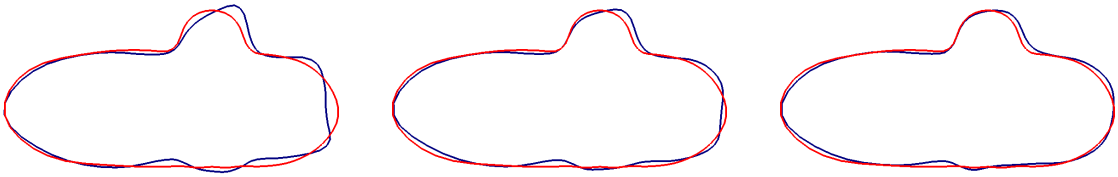

(g) Iter 6 (h) Iter 7 (i) Iter 8

Figure IV.4.42 – Iterative shapes for submarine-like scatterer.

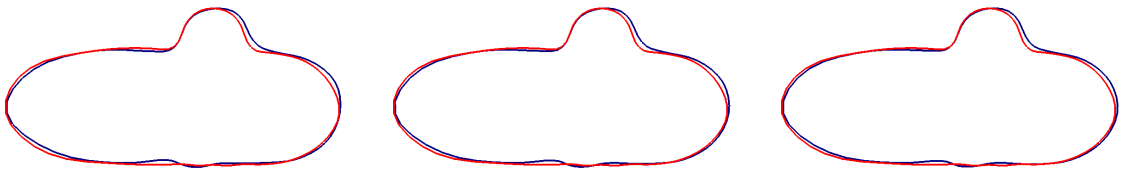

(a) Iter 9 (b) Iter 10 (c) Iter 11

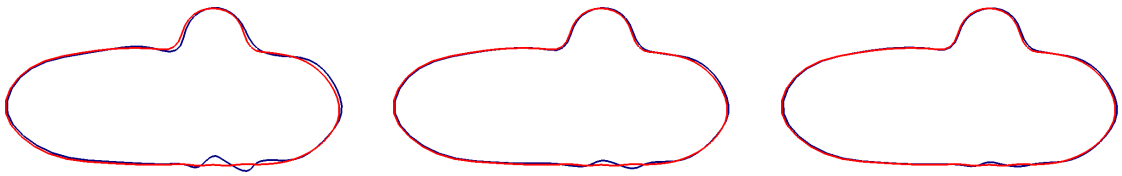

(d) Iter 12 (e) Iter 13 (f) Iter 14

Figure IV.4.43 – Iterative shapes for submarine-like scatterer.

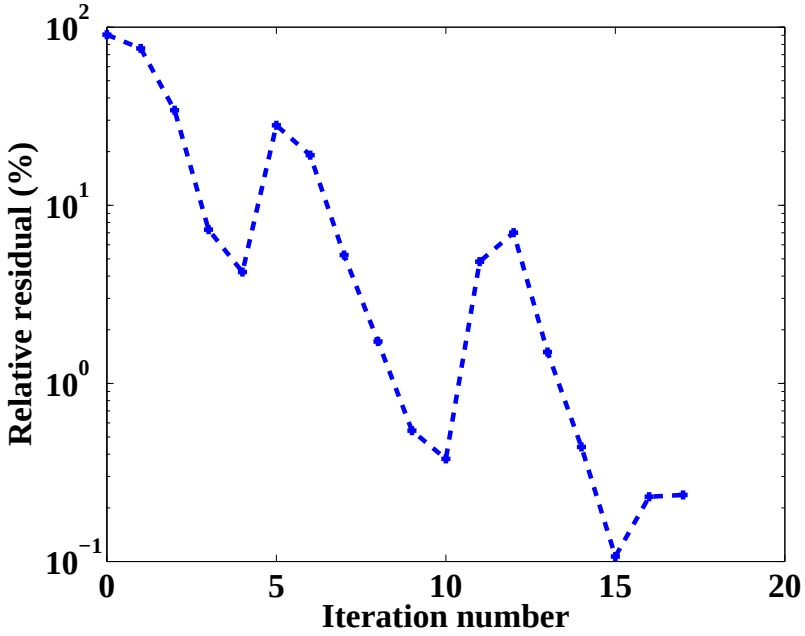

Figure IV.4.44 – Convergence history for the submarine-like scatterer with noise-free data.

on the FFP phase is reduced to a value of 4%, which is slightly higher than the noise level. The corresponding error on the FFP intensity is of 0.5%.

IV.5 Conclusions

On the given numerical examples, we have demonstrated the feasibility of the method. The numerical experiments that have been presented here are only preliminary results, but are promising results since they tend to illustrate the potential of the proposed solution methodology.

In particular, we have observed a sensitivity to various factors:

- the initial guess,
- the number of FFP data,
- the regularization parameter α,
- the wavenumber (or wavelength),
- the parametrization choice,
- the noise level,
- the number of quadrature points to evaluate the FFP,
- the direction of the incident wave,
- the distance of the exterior boundary,

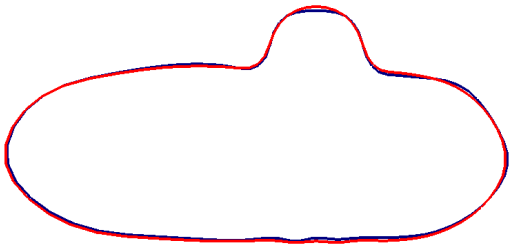

Figure IV.4.45 – Final shape for the submarine-like scatterer with data containing 2% of noise.

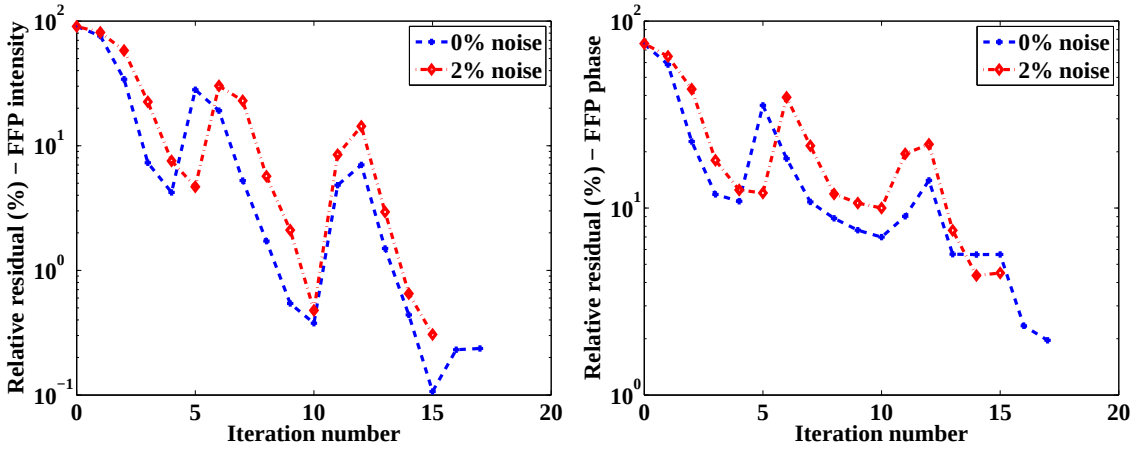

(a) FFP intensity (b) FFP phase

Figure IV.4.46 – Convergence history for the submarine-like scatterer.

- the order of the finite elements,
- the order of the curved boundary edges,
- ...

We now pursue the numerical investigation. To go further and in order to provide inverse problem solvers based on a regularized Newton method the robustness needed for realistic applications, some sensitivity analysis to the previous points should be addressed. For instance, the automatic initialization of the regularization parameter remains outstanding issues, as well as the choice of the initial guess. More specifically, the setting of the frequency seems to depend on the size of the scatterer to be found, on the complexity of the form and on the parametrization. The choice of the regularization parameter appears to be dependent on the survey wavenumber, on the complexity of the shape, and the noise level. It seems that the more we start with a high frequency, the more the regularization parameter has to be large. Moreover, the more there is noise, the more the problem must be regularized. Regarding the initial guess, its definition depends on the a priori informations, if available, that we can have on the obstacle.

A parallelization of the post-processing on the solution related to the evaluation of the far-field pattern should be done in order to accelerate and optimize the inverse solver.
Moreover, it would be relevant to study the behavior of the algorithm when considering a blind test problem, or a test problem with an imperfect parametrization, while adding different noise levels to the data and employing, for instance, B-splines.

We have used the same parametrization for the sought-after obstacle and the iterative shapes, and the number of shape parameters is a priori known. A procedure where the number of shape parameters is incremented all along the iterative process when the error stagnates could be considered. Moreover, we may mix polygonal and curved representations to retrieve the characteristics of a submarine for which we would have a priori information on the parameters to be identified.
In addition, we have used the intensity of the FFP, but we could observe the behavior of the method when considering FFP data to retrieve both the location and the shape of the scatterer.
Furthermore, it could be interesting to consider another type of regularization. An attempt to use the Levenberg-Marquardt algorithm, which also consists in a Tikhonov's regularization where the regularization term αI is replace with $\alpha\, diag(U^*U)$, has been quickly tried. A first observation is that the choice of the parameters for the simulation seems to be slightly different and no improvement has been achieved for the time being.

Another prospect consists in considering the Limited-Aperture Problem, employing multiple incident waves. Last, it would be interesting to retrieve both the shape and the material properties of the elastic scatterer.

Appendices

Appendix C

Appendices to the Chapter IV

C.1 Analytical far-field pattern for the disk-shaped elastic scatterer problem

In order to derive the analytical expression of the 2D far-field pattern p_∞, we proceed as in [28].

Recall that, in the infinite fluid domain, the outgoing scattered pressure field is expressed as follows: [16]:

$$p(r,\theta) = \sum_n A_n H_n^{(1)}(kr)\cos(n\theta). \tag{C.1.1}$$

where the complex-valued coefficients A_n thus satisfy:

$$A_n H_n^{(1)}(kr) = \int_{S_1} p(r\hat{x})\overline{\cos(n\theta)}d\hat{x}. \tag{C.1.2}$$

Moreover, for large radius [28] (p.66, Eq. (3.59)), we have the following asymptotic behavior of the Hankel function:

$$H_n^{(1)}(kr) \sim \sqrt{\frac{2}{k\pi r}} e^{\mathrm{i}(kr - n\pi/2 - \pi/4)}. \tag{C.1.3}$$

Nevertheless, in order to obtain the FFP of the pressure field, we cannot take the limit as $r \to +\infty$ because the asymptotic behavior (C.1.3) does not hold uniformly in n. However, according to Theorem 2.5 in Colton-Kress [28], the far-field pattern is an analytic function. This implies that p_∞ admits the following expansion:

$$p_\infty(\hat{x}) = \sum_n \tilde{A}_n \cos(n\theta). \tag{C.1.4}$$

where $\tilde{A_n}$ are complex-valued coefficients given by:

$$\tilde{A_n} = \int_{S_1} p_\infty(\hat{x})\overline{\cos(n\theta)}d\hat{x}. \tag{C.1.5}$$

From Eq. (IV.2.6), we have the following asymptotic behavior :

$$p_\infty(\hat{x}) = \lim_{r\to+\infty} \sqrt{r}e^{-ikr}p(r\hat{x}). \tag{C.1.6}$$

Therefore, substituting the latter equation (C.1.6) into Eq. (C.1.5) and using Eq. (C.1.2), we obtain:

$$\begin{aligned}
\tilde{A_n} &= \int_{S_1} \lim_{r\to+\infty} \sqrt{r}e^{-\mathrm{i}kr}p(r\hat{x})\overline{\cos(n\theta)}d\hat{x} \\
&= \lim_{r\to+\infty} \sqrt{r}e^{-\mathrm{i}kr}\int_{S_1} p(r\hat{x})\overline{\cos(n\theta)}d\hat{x} \\
&= \lim_{r\to+\infty} \sqrt{r}e^{-\mathrm{i}kr}A_n H_n^{(1)}(kr).
\end{aligned}$$

Then, we deduce that:

$$\tilde{A_n} = \sqrt{\frac{2}{k\pi}}\frac{e^{\mathrm{i}\pi/4}}{\mathrm{i}^{n+1}}A_n$$

Finally, we conclude that the far-field pattern can be expressed as follows:

$$p_\infty(\hat{x}) = \sum_n \sqrt{\frac{2}{k\pi}}\frac{e^{\mathrm{i}\pi/4}}{\mathrm{i}^{n+1}}A_n\cos(n\theta). \tag{C.1.7}$$

where the coefficients A_n are given by the series of the pressure field Eq. (C.1.1).

C.2 Analytical Fréchet derivative for the disk-shaped elastic scatterer problem

In this Appendix, we derive the analytical series of the Fréchet derivative in the disk-shaped configuration. In that case, the parametrization of circle with radius $r = a$ is given by:

$$\Gamma = \{x \in \mathbb{R}^2; x = a\begin{pmatrix}\cos\theta \\ \sin\theta\end{pmatrix};\ \theta \in [0, 2\pi)\}. \tag{C.2.1}$$

We denote by $(\vec{e}_r, \vec{e}_\theta)$ the polar basis vectors given by $\vec{e}_r = (\cos\theta,\ \sin\theta)^t$ and $\vec{e}_\theta = (-\sin\theta,\ \cos\theta)^t$. Then, we want to derive the expression of the Fréchet derivative (p', u') of the scattered field with

respect to r in the direction $h = \vec{e}_r$.

Let

$$\Gamma_t = \{x \in \mathbb{R}^2; \|x\| = a + t\}. \tag{C.2.2}$$

Then,

$$\Gamma_0 = \{x \in \mathbb{R}^2; \|x\| = a\}. \tag{C.2.3}$$

Let (p_t, u_t) (resp. $(p_0, u_0) = (p, u)$) be the scattered field corresponding to $\Omega_t^f \times \Omega_t^s$ (resp. $\Omega_0^f \times \Omega_0^s = \Omega^f \times \Omega^s$), where

$$\Omega_t^f = \{x \in \mathbb{R}^2; a + t < \|x\|\} \tag{C.2.4}$$

$$\Omega_t^s = \{x \in \mathbb{R}^2; 0 \leq \|x\| < a + t\}. \tag{C.2.5}$$

Therefore, in the infinite fluid domain, the outgoing scattered pressure field is expressed as follows [16]:

$$p_t(r, \theta) = \sum_{n=0}^{+\infty} A_n(t) H_n^{(1)}(kr) \cos(n\theta); \quad \forall\, r \leq a + t,\ \theta \in [0, 2\pi). \tag{C.2.6}$$

and

$$p(r, \theta) = \sum_{n=0}^{+\infty} A_n H_n^{(1)}(kr) \cos(n\theta); \quad \forall\, r \leq a,\ \theta \in [0, 2\pi). \tag{C.2.7}$$

In the solid obstacle, the scattered displacement field u_t (resp. u) is expressed using two displacement potentials ϕ and ψ [120]:

$$u_t = \nabla\phi_t + (-e_z) \times \nabla\psi_t \quad (\text{resp. } u = \nabla\phi + (-e_z) \times \nabla\psi, \tag{C.2.8}$$

where these two potentials are given by:

$$\begin{aligned} \phi_t(r, \theta) &= \sum_{n=0}^{+\infty} C_n(t) J_n(k_p r) \cos(n\theta), \\ \psi_t(r, \theta) &= \sum_{n=0}^{+\infty} D_n(t) J_n(k_s r) \sin(n\theta); \quad \forall\, 0 \leq r < a + t,\ \theta \in [0, 2\pi). \end{aligned} \tag{C.2.9}$$

$$\begin{aligned} &(\text{resp.} \\ \phi(r, \theta) &= \sum_{n=0}^{+\infty} C_n J_n(k_p r) \cos(n\theta), \\ \psi(r, \theta) &= \sum_{n=0}^{+\infty} D_n J_n(k_s r) \sin(n\theta); \quad \forall\, 0 \leq r < a,\ \theta \in [0, 2\pi)). \end{aligned} \tag{C.2.10}$$

Moreover, the complex coefficients $A_n(t)$, $C_n(t)$ and $D_n(t)$ satisfy a system of the following form (see [88] and Chapter II):

$$S_n(t)X_n(t) = b_n(t) \tag{C.2.11}$$

where $X_n(t) = (A_n(t), C_n(t), D_n(t))^t$ and $S_n(t)$ is a 3×3 matrix with complex-valued entries.

We set:

$$(q_t, v_t) = (p_t, u_t) \circ (I + t, I) = (p_t(r + t, \theta), u_t(r + t, \theta)). \tag{C.2.12}$$

let $\theta \in [0, 2\pi)$ be fixed. Therefore,

$$q_t(r, \theta) = \sum_{n=0}^{+\infty} A_n(t) H_n^{(1)}(k(r + t)) \cos(n\theta); \quad \forall\, r \leq a, \tag{C.2.13}$$

and

$$v_t = \nabla\phi_t(r + t, \theta) + (-e_z) \times \nabla\psi_t(r + t, \theta), \tag{C.2.14}$$

where:

$$\phi_t(r + t, \theta) = \sum_{n=0}^{+\infty} C_n(t) J_n(k_p(r + t)) \cos(n\theta), \tag{C.2.15}$$

$$\psi_t(r + t, \theta) = \sum_{n=0}^{+\infty} D_n(t) J_n(k_s(r + t)) \sin(n\theta); \quad \forall\, 0 \leq r < a. \tag{C.2.16}$$

Observe that:

$$\nabla p \cdot h = \left[\frac{\partial p}{\partial r} e_r + \frac{\partial p}{\partial r}\frac{\partial p}{\partial \theta} e_\theta\right] \cdot h \tag{C.2.17}$$

$$= \frac{\partial p}{\partial r} e_r \cdot e_r + \frac{\partial p}{\partial r}\frac{\partial p}{\partial \theta} e_\theta \cdot e_r \tag{C.2.18}$$

$$= \frac{\partial p}{\partial r}. \tag{C.2.19}$$

Then, we obtain:

$$\begin{aligned} p' &= \frac{\partial p_t}{\partial t}_{|t=0} \\ &= \frac{\partial q_t}{\partial t}_{|t=0} - \nabla p \cdot h \\ &= \frac{\partial q_t}{\partial t}_{|t=0} - \frac{\partial p}{\partial r} \end{aligned} \tag{C.2.20}$$

and similarly for the displacement field,

$$\begin{aligned} u' &= \frac{\partial u_t}{\partial t}_{|t=0} \\ &= \frac{\partial v_t}{\partial t}_{|t=0} - \frac{\partial u}{\partial r} \\ &= \nabla\phi' + (-e_z) \times \nabla\psi' \\ &= \nabla\left(\frac{\partial \phi_t(r+t,\theta)}{\partial t}_{|t=0}\right) + (-e_z) \times \nabla\left(\frac{\partial \psi_t}{\partial t}_{|t=0}\right) \\ &\quad -\nabla\left(\frac{\partial \phi}{\partial r}\right) + (-e_z) \times \nabla\left(\frac{\partial \psi}{\partial r}\right). \end{aligned} \tag{C.2.21}$$

Moreover, differentiating with respect to the perturbation radius t, we have:

$$\begin{aligned} \frac{\partial q_t}{\partial t}_{|t=0} &= \sum_{n=0}^{+\infty} \frac{d\, A_n(t)}{d\, t}_{|t=0} H_n^{(1)}(kr)\cos(n\theta) \\ &\quad + \sum_{n=0}^{+\infty} A_n k H^{(1)'}_n(kr)\cos(n\theta) \\ &= \sum_{n=0}^{+\infty} \frac{d\, A_n(t)}{d\, t}_{|t=0} H_n^{(1)}(kr)\cos(n\theta) \\ &\quad + \frac{\partial p}{\partial r}; \quad \forall\, a < r. \end{aligned} \tag{C.2.22}$$

and similarly for the displacement field,

$$\frac{\partial v_t}{\partial t}_{|t=0} = \nabla\left(\frac{\partial \phi_t(r+t,\theta)}{\partial t}_{|t=0}\right) + (-e_z) \times \nabla\left(\frac{\partial \psi_t}{\partial t}_{|t=0}\right). \tag{C.2.23}$$

where:

$$\begin{aligned} \frac{\partial \phi_t(r+t,\theta)}{\partial t}_{|t=0} &= \sum_{n=0}^{+\infty} \frac{d\, C_n(t)}{d\, t}_{|t=0} J_n(k_p r)\cos(n\theta) \\ &+ \sum_{n=0}^{+\infty} C_n k_p J_n{}'(k_p r)\cos(n\theta) \\ &= \sum_{n=0}^{+\infty} \frac{d\, C_n(t)}{d\, t}_{|t=0} J_n(k_p r)\cos(n\theta) \\ &+ \frac{\partial \phi}{\partial r}; \quad \forall\, 0 \le r < a \\ \frac{\partial \psi_t(r+t,\theta)}{\partial t}_{|t=0} &= \sum_{n=0}^{+\infty} \frac{d\, D_n(t)}{d\, t}_{|t=0} J_n(k_s r)\sin(n\theta) \end{aligned} \tag{C.2.24}$$

$$
\begin{aligned}
&+ \quad \sum_{n=0}^{+\infty} D_n k_s J_n{}'(k_s r)\cos(n\theta) \\
&= \quad \sum_{n=0}^{+\infty} \frac{d\,D_n(t)}{d\,t}_{|t=0} J_n(k_s r)\sin(n\theta) \\
&+ \quad \frac{\partial \psi}{\partial r}.; \quad \forall\, 0 \leq r < a. \qquad \text{(C.2.25)}
\end{aligned}
$$

Substituting Eqs.(C.2.22)-(C.2.25) into Eqs.(C.2.20)-(C.2.21), we deduce that:

$$p' = \sum_{n=0}^{+\infty} \frac{d\,A_n(t)}{d\,t}_{|t=0} H_n^{(1)}(kr)\cos(n\theta) \qquad \text{(C.2.26)}$$

and

$$u' = \nabla\phi' + (-e_z)\times\nabla\psi', \qquad \text{(C.2.27)}$$

where

$$\phi' = \sum_{n=0}^{+\infty} \frac{d\,C_n(t)}{d\,t}_{|t=0} J_n(k_p r)\cos(n\theta), \qquad \text{(C.2.28)}$$

$$\psi' = \sum_{n=0}^{+\infty} \frac{d\,D_n(t)}{d\,t}_{|t=0} J_n(k_s r)\sin(n\theta). \qquad \text{(C.2.29)}$$

Therefore, in order to compute (p', u'), we need to evaluate the complex coefficients $\frac{d\,A_n(t)}{d\,t}_{|t=0}$, $\frac{d\,C_n(t)}{d\,t}_{|t=0}$ and $\frac{d\,D_n(t)}{d\,t}_{|t=0}$. Since $X_n(t) = (A_n(t), C_n(t), D_n(t))^t$ satisfy Eq. (C.2.11), we have:

$$X_n(t) = [S_n(t)]^{-1} b_n(t). \qquad \text{(C.2.30)}$$

Then, differentiating with respect to t, it follows that:

$$\frac{d\,X_n(t)}{d\,t} = \frac{d\,[S_n(t)]^{-1}}{d\,t} b_n(t) + [S_n(t)]^{-1}\frac{d\,b_n(t)}{d\,t} \qquad \text{(C.2.31)}$$

$$= -[S_n(t)]^{-1}\frac{d\,S_n(t)}{d\,t}[S_n(t)]^{-1} b_n(t) + [S_n(t)]^{-1}\frac{d\,b_n(t)}{d\,t}, \qquad \text{(C.2.32)}$$

which concludes this Appendix.

General conclusions and perspectives

In this research work, we have proposed a solution methodology for retrieving the shape of an elastic bounded object immersed in an homogeneous fluid medium from some measurements of the far-field pattern, and assuming certain characteristics of the surface of the obstacle. Our approach for solving this inverse obstacle problem is based on a regularized Newton-type method.
Since the solution of this IOP mainly depends on the solution of the associated direct problem, the work accomplished here pertains to the mathematical and numerical analysis of both the direct elasto-acoustic scattering problem and of the inverse obstacle scattering problem.

First, we have examined the direct problem. On a theoretical viewpoint, we have revisited the question of the existence and uniqueness of the solution of the direct elasto-acoustic scattering problem (Chapter I). The proposed analysis distinguishes itself from previous studies by employing the DtN operator properties, and the Fredholm theory. We have then observed that the mathematical framework we propose is equivalent to set the problem in weighted Sobolev spaces. This approach allows the range of validity of the standard well-posed results to the case where the elastic scatterer is assumed to be only Lipschitz continuous, which is of more practical interest. Then, we have developed a numerical solution methodology for the direct problem, based on discontinuous Galerkin approximations (Chapter II). The proposed method possesses two distinctive features. First, it employs higher-order polynomial finite elements needed to address the high-frequency propagation regime. Second, it is equipped with curved boundary edges to provide a better modeling of the fluid-structure interaction. The designed solver reveals interesting performances. The numerical investigation demonstrates accurate approximations and a robustness to the resonance phenomenon. It also exhibits very little pollution effects, which highlights the potential of the proposed solution methodology for efficiently solving mid- to high-frequency elasto-acoustic scattering problems.

Second, we have focused our attention on the inverse problem. We have established the continuous Fréchet differentiability of the elasto-acoustic field with respect to Lipschitz continuous deformation of the shape of an elastic scatterer (Chapter III). In order to evaluate the Jacobian matrix that arises at each Newton iteration with more robustness and accuracy that possible with a finite difference scheme, we have established a characterization of the Fréchet of the elasto-acoustic scattered field. It is characterized as the solution to a particular direct elasto-acoustic scattering problem that differs only in the transmission conditions. Consequently, the direct solver we have developed has been used to solve the inverse two-dimensional elasto-acoustic obstacle problem into consideration by a regularized Newton-like method (Chapter IV). We have illustrated the feasibility of our approach using different types of parametrization of the scatterer, even when the data are tainted with noise.

As regards the main prospects to the works presented here, a theoretical analysis of the DG method applied to the fluid-structure interaction problem proposed in Chapter II would be interesting. Moreover, we keep in mind, in the long term, to apply this solver to configurations from geophysics by considering heterogeneous solids. We could then benefit from another interesting flexibility property of the DG method by combining different orders of polynomials. In addition, some theoretical issues related to the characterization of the Fréchet derivative in the framework of Lipschitz domains have been raised in Chapter III and remain open. Indeed, when the boundary is assumed to be only Lipschitz continuous, we have been faced with the absence of some regularity results to give a sense to the transmission conditions satisfied by the Fréchet derivative on the boundary Γ.
As regards the inverse problem, its ill-posed nature implies numerical difficulties, with a strong sensitivity and instabilities for its solution. We have presented preliminary results in Chapter IV. Its investigation is still pursued. In particular, the optimization of the code should be considered to speed up the computations. Some perspectives will consist, in the shorter or longer term, in considering more complex configurations, the determination of both the shape and the material properties of the elastic scatterer, and the limited aperture problem.

List of Figures

List of Tables

References

[1] a MUltifrontal Massively Parallel sparse direct Solver. *82*

[2] M. Abramowitz and I. A. Stegun. *Handbook of Mathematical Functions with Formulas, Graphs, and Mathematical Tables*. New York, Dover Publications Inc./Reprint of the 1972 edition, 1992. *21*, *31*, *49*, *50*, *51*, *52*, *111*, *169*, *170*

[3] R. A. Adams. *Sobolev spaces*. Academic Press, New-York, 1975. *16*, *35*, *67*, *208*

[4] M. Ainsworth, P. Monk, and W. Muniz. Dispersive and dissipative properties of discontinuous Galerkin finite element methods for the second-order wave equation. *J. Sc. Computing*, 27(1-3):5–40, 2006. *65*, *78*, *79*, *183*

[5] G. B. Alvarez, A. F. D. Loula, E. G. D. do Carmo, and F. A. Rochinha. A discontinuous finite element formulation for Helmholtz equation. *Comput. Methods Appl. Mech. Engrg.*, 195:4018–4035, 2006. *65*

[6] M. Amara, H. Calandra, R. Djellouli, and M. Grigoroscuta-Strugaru. A stable discontinuous Galerkin-type method for solving efficiently Helmholtz problems. *Computers and Structures*, 106-107:258–272, 2012. *64*

[7] X. Antoine, H. Barucq, and A Bendali. Bayliss–Turkel like radiation conditions on surfaces of arbitrary shape. *J. Math. Anal. Appl.*, 229:184–211, 1999. *61*

[8] F. Assous and P. Ciarlet Jr. Une caractérisation de l'orthogonal de $\Delta(H^2(\Omega) \cap H_0^1(\Omega))$ dans $L^2(\Omega)$. *C. R. Acad. Sci. Paris Sér. I Math.*, 325:605–610, 1997. *208*, *241*, *243*, *244*

[9] F. Assous, P. Ciarlet Jr, and E. Garcia. Singular electromagnetic fields: inductive approach. *C. R. Acad. Sci. Paris Sér. I Math.*, 341:605–610, 2005. *208*, *241*, *242*, *243*, *244*

[10] F. Assous, P. Ciarlet Jr, and E. Garcia. A characterization of singular electromagnetic fields by an inductive approach. *Int. J. Numer. Anal. Mod.*, 5:491–515, 2008. *208*, *241*, *244*

[11] I. M. Babuska and I. J. M. Melenk. The partition of Unity Method. *Int. J. Numer. Meth. Engng.*, 40:727–758, 1997. *64*

[12] I. M. Babuska and S. A. Sauter. Is the pollution effect of the FEM avoidable for the Helmholtz equation considering high wave numbers? *SIAM Review*, 42(3):451–484, 2000. *63*

[13] M. S. Berger. *Nonlinearity and Functional Analysis*. New York, 1977. *212*

[14] C. Bernardi, M. Dauge, and Y. Maday. Compatibilité de traces aux arêtes et coins d'un polyèdre. *C. R. Acad. Sci. Paris Sér. I Math.*, 331:679–684, 2000. *242*, *244*

[15] C. Bernardi, M. Dauge, and Y. Maday. Integral equation methods in inverse acoustic and electromagnetic scattering Boundary Integral Formulation for Inverse Analysis. Preprint IRMAR 07-14, Rennes, 2007. *244*

[16] J. J. Bowman, T. B. A. Senior, and P. L. E. Uslenghi. *Electromagnetic and acoustic scattering by simple shapes*. North-Holland Publishing company, Amsterdam, 1969. *110*, *169*, *317*, *319*

[17] H. Brezis. *Analyse fonctionnelle : Théorie et applications*. Paris, 1983. *12*

[18] A. Buffa. Trace Theorems on Non-Smooth Boundaries for Functional Spaces Related to Maxwell Equations: an Overview. *Computational Electromagnetics Lecture Notes in Computational Science and Engineering Volume*, 28:23–34, 2003. *28*

[19] A. Buffa and P. Ciarlet. On traces for functional spaces related to Maxwell's equations. Part I: An integration by parts formula in Lipschitz polyhedra. *Math. Comp.Math. Meth. Appl. Sc.*, 24:9–30, 2001. *218*, *220*

[20] A. Buffa, P. Ciarlet, and D. Sheen. On traces for $H(curl, \Omega)$ in Lipschitz domains. *J. Math. Anal. Appl.*, 276:845–876, 2002. *218*

[21] A. Buffa and G. Geymonat. On traces of functions in $W^{2,p}(\Omega)$ for Lipschitz domains in $\mathbb{R}^3$. *C. R. Acad. Sci. Paris Sér. I Math.*, 332:699–704, 2001. *244*, *245*, *246*, *247*

[22] D. S. Burnett and R. L. Holford. An ellipsoidal acoustic infinite element. *Comput. Meths. Appl. Mech. Engrg.*, 164:49–76, 1998. *46*

[23] D. S. Burnett and R. L. Holford. Prolate and oblate spheroidal acoustic infinite elements. *Comput. Meths. Appl. Mech. Engrg.*, 158:117–141, 1998. *46*

[24] O. Cessenat and B. Després. Application of an ultra-weak variational formulation of elliptic PDEs to the two-dimensional Helmholtz problems. *SIAM J. Numer. Anal.*, 35:255–299, 1998. *64*, *108*

[25] A. Charalambopoulos. On the Fréchet differentiability of boundary integral operators in the inverse elastic scattering problem. *Inverse Problems*, 11:1137–1161, 1995. *206*

[26] Z. S. Chen, G. Hofstetter, and H. A. Mang. A Galerkin-type BE-FE formulation for elasto-acoustic coupling. *Comput. Methods Appli. Mech. Eng.*, 152(1-2):147–155, 1998. *64*

[27] P. G. Ciarlet. *The Finite Element Method for Elliptic Problems*. Series Studies in Mathematics and its Applications, North-Holland, 1978. *67*

[28] D. Colton and R. Kress. *Inverse acoustic and electromagnetic scattering theory*. Berlin, 1992. *11*, *15*, *20*, *50*, *52*, *53*, *56*, *57*, *59*, *212*, *225*, *254*, *255*, *317*

[29] D. Colton and B. D. Sleeman. Uniqueness theorems for the inverse problem of acoustic scattering. *IMA J. Appl. Math.*, 31:253–259, 1983. *255*

[30] M. Costabel. Boundary Integral Operators on Lipschitz Domains: Elementary Results. *SIAM J. Math. Anal.*, 19(13):613–626, 1988. *28*, *33*, *37*, *218*, *220*, *235*, *239*

[31] M. Costabel. A remark on the regularity of solutions of Maxwell's equations on Lipschitz domains. *Math. Meth. Appl. Sc.*, 12:365–368, 1990. *245*

[32] M. Costabel, M. Dauge, and L. Demkowicz. Polynomial extension operators for H^1, $H(curl)$ and $H(div)$ - spaces on a cube. *Math. Comp.*, 77:1967–1999, 2008. *218*, *220*

[33] M. Costabel and F. Le Louër. Shape Derivatives of Boundary Integral Operators in Electromagnetic Scattering. Part I: Shape Differentiability of Pseudo-homogeneous Boundary Integral Operators. *Integral Equations and Operator Theory*, 72:509–535, 2012. *206*

[34] M. Costabel and F. Le Louër. Shape Derivatives of Boundary Integral Operators in Electromagnetic Scattering. Part II: Application to Scattering by a Homogeneous Dielectric Obstacle. *Integral Equations and Operator Theory*, 73:17–48, 2012. *206*

[35] M. Costabel and E. Stephan. Integral equations for transmission problems in elasticity. *J. Integral Equations and Applications*, 2:211–223, 1990. *28*, *33*, *218*, *220*, *235*, *239*

[36] B. E. J. Dahlberg, C. E. Kenig, and G.C. Verchota. Boundary value problems for the systems of elastostatics in Lipschitz domains. *Duke Math. J.*, 57(3):795–817, 1988. *29*, *221*

[37] A. G. Dallas. *Analysis of a Limiting-Amplitude Problem in Acousto-elastic Interactions*, volume I of *NRL Rept. 9172*. Washington, 1989. *12*, *42*, *254*

[38] W. Desmet, P. van Hal, P. Sas, and D. Vandepitte. A computationally efficient prediction technique for the steady-state dynamic analysis of coupled vibroacoustic systems. *Adv. Eng. Soft.*, 33:527–540, 2002. *64*

[39] R. Djellouli and C. Farhat. On the Characterization of the Fréchet Derivative with Respect to a Lipschitz Domain of the Acoustic Scattered Field. *J. Math. Anal. Appl.*, 238:259–276, 1999. *206*, *212*, *214*, *216*, *217*, *218*, *219*, *220*, *223*, *227*, *228*, *234*, *252*, *258*, *259*, *261*

[40] R. Djellouli, C. Farhat, A. Macedo, and R. Tezaur. Finite element solution of two-dimensional acoustic scattering problems using arbitrarily shaped convex artificial boundaries. *J. Comput. Acoust.*, 8:81–99, 2000. *46*

[41] R. Djellouli, C. Farhat, J. Mandel, and P. Vaněk. Continuous Fréchet Differentiability With Respect To Lipschitz Domain And A Stability Estimate For Direct Acoustic Scattering Problems. *IMA J. Appl. Math.*, 63:51–69, 1999. *206*, *212*, *225*

[42] R. Djellouli, C. Farhat, and R. Tezaur. On the solution of three-dimensional inverse obstacle acoustic scattering problems by a regularized Newton method. *Inverse Problems*, 18:1229–1246, 2002. *251*, *254*, *255*, *263*

[43] M. Durán and J. C. Nédélec. Un problème Spectral Issu d'un Couplage Elasto-Acoustique. *ESAIM: Mathematical Modelling and Numerical Analysis*, 34(04):835–857, 2000. *71*

[44] G. Duvaut and J. L. Lions. *Les inéquations en mécanique et en physique*. Paris, 1972. *36*

[45] A. El Kacimi and O. Laghrouche. Numerical modelling of elastic wave scattering in frequency domain by the partition of unity finite element method. *Int. J. Numer. Methods Engng.*, 77:1646–1669, 2009. *64*

[46] J. Elschner, G. Hsiao, and A. Rathsfeld. An inverse problem for fluid-solid interaction. *Inverse Problems and Imaging*, 2:83–119, 2007. *12*, *71*, *251*, *252*, *256*

[47] J. Elschner, G. Hsiao, and A. Rathsfeld. An optimization method in inverse acoustic scattering by an elastic obstacle. *SIAM J. Appl. Math.*, 70:168–187, 2009. *252*

[48] J. Elschner, G.C. Hsiao, and A. Rathsfeld. *Comparison of Numerical Methods for the Reconstruction of Elastic Obstacles from the Far-field Data of Scattered Acoustic Waves*. Preprint. WIAS, 2010. *252*

[49] A. C. Eringen and E. S. Suhubi. *Elastodynamics*, volume II of *Linear Theory*. New York, 1975. *12*, *42*, *254*

[50] C. Farhat, I. Harari, and U. Hetmaniuk. A discontinuous Galerkin method with Lagrange multipliers for the solution of Helmholtz problems in the mid-frequency regime. *Comput. Methods Appli. Mech. Eng.*, 192:1389–1419, 2003. *64*, *65*

[51] C. Farhat, I. Harari, and U. Hetmaniuk. The discontinuous enrichment method for multiscale analysis. *Comput. Methods Appli. Mech. Eng.*, 192:3195–3209, 2003. *65*

[52] C. Farhat, P. Massimi, and R. Tezaur. A Discontinuous Enrichment Method for Three-Dimensional Multiscale Harmonic Wave Propagation Problems in Multi-Fluid and Fluid-Solid Media. *Int. J. Numer. Meth. Engng.*, 76(3):400–425, 2008. *64*, *65*

[53] C. Farhat, R. Tezaur, and P. Wiedemann-Goiran. Higher-order extensions of a discontinuous Galerkin method for mid-frequency Helmholtz problems. *Int. J. Numer. Meth. Engng.*, 61:1938–1956, 2004. *64*, *65*

[54] C. Farhat, P. Wiedemann-Goiran, and R. Tezaur. A Discontinuous Galerkin method with plane waves and Lagrange multipliers for the solution of short wave exterior Helmholtz problems on unstructured meshes. *Wave Motion*, 39:307–317, 2004. *64*, *65*

[55] X. Feng and H. Wu. Discontinuous Galerkin Methods for the Helmholtz Equation with Large Wave Number. *SIAM J. Numer. Anal.*, 47(4):2872–2896, 2009. *64*, *65*

[56] X. Feng and H. Wu. hp-discontinuous Galerkin methods for the Helmholtz equation with large wave number. *Math. Comp.*, 80:1997–2024, 2011. *64*, *65*

[57] X. Feng and Y. Xing. Absolutely stable local discontinuous Galerkin methods for the Helmholtz equation with large wave number. *Math. Comp.*, 82:1269–1296, 2013. *64*

[58] M. Fischer and L. Gaul. Fast BEM-FEM mortar coupling for acousticâstructure interaction. *Int. J. Numer. Meth. Engng.*, 62(12):2137–2156, 2005. *64*

[59] L. Flax. High ka scattering of elastic cylinders and spheres. *J. Acoust. Soc. Am.*, 62(6):1502–1503, 1977. *108*

[60] A. Friedman. *Partial Differential Equations*. New York, 1969. *29*

[61] L. Gaul, D. Brunner, and M. Junge. *Simulation of Elastic Scattering with a Coupled* FMBE-FE *Approach*. Recent Advances in Boundary Element Methods, Springer, 2009. *64*

[62] B. V. Genechten, B. Bergen, D. Vandepitte, and W. Desmet. A Trefftz-based numerical modeling framework for Helmholtz problems with complex multiple-scatterer configurations. *J. Comput. Phys.*, 229:6623–6643, 2010. *64*

[63] G. Geymonat and F. Krasucki. On the existence of the Airy function in Lipschitz domains. Application to the traces of H^2. *C. R. Acad. Sci. Paris Sér. I Math.*, 330:355–360, 2000. *245*

[64] J. Giroire. *Etude de quelques problèmes aux limites extérieurs et résolution par équations intégrales* . PhD thesis, Université de Paris VI, 1987. *12*

[65] C. Gittelson, R. Hiptmair, and I. Perugia. Plane wave discontinuous Galerkin methods. *M2AN (Math. Model. Numer. Anal.)*, 43:297–331, 2009. *64*, *65*

[66] D. Givoli. Non-reflecting boundary conditions. *J. Comput. Phys.*, 94(1):1–29, 1991. *12*

[67] D. Givoli and J. B. Keller. A finite element method for large domains. *Comput. Meths. Appl. Mech. Engrg.*, 76:41–66, 1989. *45*, *46*

[68] R. Griesmaier and P. Monk. Discretization of the wave equation using continuous elements in time and a hybridizable discontinuous Galerkin method in space. *J. Sci. Comput.*, 2013. *65*

[69] M. Grigoroscuta-Strugaru. *Contribution à la résolution numérique des problèmes de* H*elmholtz*. PhD thesis, Université de Pau et des Pays de l'Adour, France, 2009. *64*, *108*

[70] P. Grisvard. *Elliptic Problems in Nonsmooth Domains*. London, 1985. 28, 33, 34, 208, 218, 220, 235, 237, 238, 239, 242, 243, 244

[71] P. Grisvard. *Singularities in Boundary Problems*. Paris, 1992. 235, 237, 238, 239, 242, 245

[72] M. Gröte, A. Schneebeli, and D. Schötzau. Discontinuous Galerkin Finite Element Method For The Wave Equation. *SIAM J. Num. Analysis*, 44:2408–2431, 2006. 65

[73] M. J. Grote and J. B. Keller. On nonreflecting boundary conditions. *J. Comput. Phys.*, 112(2):213–243, 1995. 12, 45

[74] W. Hackbusch. *Elliptic Partial Differential Equations, Theory and Numerical Treatment*. New York, 1992. 41

[75] H. Haddar and R. Kress. On the Fréchet derivative for Obstacle Scattering with an Impedance Boundary Condition. *Siam J. Appl. Math.*, 65(1):194–208, 2004. 206

[76] B. Hanouzet. Espaces de Sobolev avec poids. Application au problème de Dirichlet dans un demi-espace. *Rend. Sem. Mat. Univ. Padova*, 46:227–272, 1971. 12

[77] I. Harari and T. J. R. Hughes. Studies of domain-based formulations for computing exterior problems of acoustics. *Internat. J. Numer. Meths. Engrg.*, 37:2935–2950, 1994. 45

[78] I. Harari, M. Slavutin, and E. Turkel. Analytical and numerical studies of a finite element PML for the Helmholtz equation. *Journal of Computational Acoustic*, 8:121–137, 2000. 46

[79] T. Hargé. Valeurs propres d'un corps élastique. *C. R. Acad. Sci. Paris Sér. I Math.*, 311:857–859, 1990. 12, 40, 42, 71, 212, 220, 254

[80] F. Hettlich. Fréchet derivatives in inverse obstacle scattering. *Inverse Problems*, 11:371–382, 1995. 206

[81] R. Hiptmair, A. Moiola, and I. Perugia. Approximation by plane waves. Technical Report 2009-27, Seminar für Angewandte Mathematik, ETH Zürich, 2009. 64, 65

[82] R. Hiptmair, A. Moiola, and I. Perugia. Plane wave discontinuous Galerkin methods for the 2D Helmholtz equation: analysis of the p-version. *SIAM J. Num. Analysis*, 49:264–284, 2011. 64, 65

[83] T. Hohage. *Iterative Methods in Inverse Obstacle Scattering: Regularization Theory of Linear and Nonlinear Exponentially Ill-Posed Problems*. PhD thesis, PhD in Numerical analysis, University of Linz, 1999. 206

[84] R. H. W. Hoppe and N. S. Sharma. Convergence Analysis of an Adaptive Interior Penalty Discontinuous Galerkin Method for the Helmholtz Equation. *IMA J. Num. Anal.*, 33(3):898–921, 2012. 65

[85] G. C. Hsiao, R. E. Kleinman, and G. F. Roach. Weak Solutions of Fluid-Solid Interaction Problems. *Math. Nachr.*, 218:139–163, 2000. *11*, *12*, *15*, *71*

[86] G. C. Hsiao and N. Nigam. A transmission problem for fluid-structure interaction in the exterior of a thin domain. *Adv. Differential Equations*, 8(11):1281–1318, 2003. *42*

[87] G.C. Hsiao and W.L. Wendland. *Boundary Integral Equations*. Applied Mathematical Sciences. Springer, 2008. *29*, *38*, *71*

[88] T. Huttunen, J. Kaipio, and P. Monk. An ultra-weak method for acoustic fluid-solid interaction. *J. Comput. Appl. Math.*, 213:166–185, 2008. *64*, *66*, *108*, *110*, *111*, *112*, *113*, *114*, *116*, *129*, *130*, *131*, *141*, *169*, *171*, *320*

[89] F. Ihlenburg. *Finite Element Analysis of Acoustic Scattering*, volume 132. Appl. Math. Sci., Springer, 1998. *54*, *60*, *64*

[90] D. S. Jerison and C. E. Kenig. The Neumann problem on Lipschitz domains. *Bull. Amer. Math. Sot*, 4:203–207, 1981. *29*, *221*, *245*

[91] D. S. Jerison and C. E. Kenig. Boundary value problems on Lipschitz domains. *W L. Littman editor, Studies in P.D.E., MAA Stud. Math., Math. Assoc. America, Washington, D.C.*, 23:1–68, 1982. *245*

[92] D. S. Jones. Low-frequency scattering by a body in lubricated contact. *Quart. J. Mech. Appl. Math.*, 36:111–138, 1983. *11*, *12*, *42*, *71*, *212*, *220*, *254*

[93] M. C. Junger and D. Feit. *Sound, Structures, and Their Interaction*. The MIT Press, Cambridge, MA, 1972. *11*, *15*, *70*, *71*, *110*, *206*, *207*, *211*, *212*

[94] J. B. Keller and D. Givoli. Exact non-reflecting boundary conditions. *J. Comput. Phys.*, 82(1):172–192, 1989. *45*, *46*, *60*, *61*

[95] V. Khatskevich and D. Shoikhet. *Differentiable Operators and Nonlinear Equations*, volume 66 of *Operator Theory, Advances and Applications*. Basel, 1994. *214*

[96] A. Kirsch. The domain derivative and two applications in inverse scattering theory. *Inverse Problems*, 9:81–96, 1993. *206*

[97] P. D. Lax and R. S. Phillips. *Scattering theory*. Academic Press, 1989. *11*, *255*

[98] F. Le Louër. *Optimisation de formes dâantennes lentilles intégrées aux ondes millimétriques*. PhD thesis, PhD in Numerical analysis, University of Rennes 1, 2009. *206*

[99] N. N. Lebedev. *Special Functions and their Applications*. Englewood Cliffs, 1965. *51*, *52*

[100] P. Lesaint and P. A. Raviart. *On a finite element method for solving the neutron transport equation*. Mathematical Aspects of Finite Elements in Partial Differential Equations, de Boor C (ed.), Academic Press, New York, 1974. *65*

[101] J. L. Lions. *Problèmes aux limites dans les équations aux dérivées partielles*. Montreal, 1965. *34*, *218*, *220*, *235*, *239*

[102] J. L. Lions and E. Magenes. Problèmes aux limites non homogènes. *Ann. Inst. Fourier (Grenoble)*, II:137–178, 1961. *235*, *239*

[103] A. F. D. Loula, G. B. Alvarez, E. G. D. do Carmo, and F.A. Rochinha. A discontinuous finite element method a element level for Helmholtz equation. *Comput. Methods Appl. Mech. Engrg.*, 196:867–878, 2007. *65*

[104] C. J. Luke and P. A. Martin. Fluid-Solid Interaction: Acoustic Scattering by a Smooth Elastic Obstacle. *SIAM J. Appl. Math.*, 55:904–922, 1995. *11*, *12*, *15*, *40*, *42*, *71*, *212*, *220*, *254*

[105] M. Malhotra and P. M. Pinsky. A matrix-free interpretation of the non-local Dirichlet-to-Neumann radiation boundary condition. *Internat. J. Numer. Meths. Engrg.*, 39:3705–3713, 1996. *46*

[106] J. Mandel. An Iterative Substructuring Method for Coupled Fluid-Solid Acoustic Problems. *J. Comput. Phys.*, 177(1):95–116, 2002. *64*

[107] A. Marquez, S. Meddahi, and V. Selgas. A new BEM-FEM coupling strategy for two-dimensional fluid-solid interaction problems. *J. Comput. Phys.*, 199:205–220, 2004. *64*

[108] P. A. Martin. Scattering by Inclusions. *Analytical and Computational Methods in Scattering*, 8(11):209–216, 2010. *42*

[109] P. Monk and V. Selgas. An inverse fluid–solid interaction problem. *Inverse Problems and Imaging*, 3(2):173–198, 2009. *252*

[110] P. Monk and V. Selgas. Near field sampling type methods for the inverse fluid-solid interaction problem. *Inverse Problems and Imaging*, 5(2):465–483, 2011. *252*, *256*

[111] P. Monk and D. Q. Wang. A least-squares method for the Helmholtz equation. *Comput. Methods Appl. Mech. Eng.*, 175:121–136, 1999. *64*, *65*

[112] D. Moro, N. C. Nguyen, and J. Peraire. A hybridized discontinuous Petrov-Galerkin scheme for scalar conservation laws. *Int. J. Numer. Methods Engng.*, 91:950–970, 2012. *65*

[113] V. A. Morozov. On the solution of functional equations by the method of the regularization. *Dokl. Akad. Nauk*, 167:414–417, 1966. *258*

[114] V. A. Morozov. *Methods for Solving Incorrectly Posed Problems*. Berlin, 1984. *258*

[115] F. Murat and Simon J. Sur le contrôle par un domaine géométrique. Rapport du L.A., 1976. *208*, *210*, *227*, *229*, *232*

[116] D. Natroshvili, S. Kharibegashvili, and Z. Tediashvili. Direct and inverse fluidâstructure interaction problems. *Rendiconti di Matematica, Serie VII*, 20:57–92, 2000. *256*

[117] J. Nečas. *Les méthodes directes en théorie des équations elliptiques*. Paris, 1967. *217*, *218*, *219*, *220*, *235*, *239*

[118] J. C. Nédélec. *Acoustic and Electromagnetic Equations*. Springer-Verlag, New York, 2001. *11*, *15*, *16*, *20*, *57*, *209*

[119] O. A. Oleinik, A. S. Shamaev, and G. A. Yosifian. *Mathematical Problems in Elasticity and Homogenization*, volume 26 of *Studies in mathematics and its applications*. Amsterdam, 1992. *11*, *36*

[120] Y. H. Pao and C. C. Mow. *Diffraction of Elastic Waves and Dynamic Stress Concentrations*. Crane-Russak Inc, New York, 1973. *15*, *70*, *111*, *169*, *171*, *172*, *319*

[121] O. Popa. *Finite element solution of scattering in coupled fluid-solid systems*. PhD thesis, University of Colorado, Denver, 2002. *64*

[122] R. Potthast. Fréchet differentiability of boundary integral operators in inverse acoustic scattering. *Inverse Problems*, 10:431–447, 1994. *206*

[123] R. Potthast. Domain derivatives in electromagnetic scattering. *Math. Methods Appl. Sci.*, 19:1157–1175, 1996. *206*

[124] R. Potthast. Fréchet-differentiability of the solution to the acoustic Neumann scattering problem with respect to the domain. *J. Inverse Ill-Posed Probl.*, 4:67–84, 1996. *206*

[125] R. Rand. Torsional vibrations of elastic prolate spheroids. *J. Acoust.Soc.Amer.*, 44:749–751, 1968. *42*

[126] P. A. Raviart and J. M. Thomas. *Introduction à l'analyse numérique des équations aux dérivées partielles*, volume 6 of *Collection Mathématiques appliquées pour la maîtrise*. Paris, 1983. *12*

[127] W. H. Reed and T. R. Hill. Triangular mesh methods for the neutron transport equation. Technical report, Los Alamos Scientific Laboratory Report, LA-UR-73-479, Los Alamos, NM, 1973. *65*

[128] F. A. Rochinha, G. B. Alvarez, E. G. D. do Carmo, , and A. F. D. Loula. A locally discontinuous enriched finite element formulation for acoustics. *Commun. Numer. Meth. Engng.*, 23:623–637, 2007. *65*

[129] J. Sanchez-Hubert and E. Sanchez-Palencia. *Vibration and Coupling of Continuous Systems*. Springer Verlag, New York, 1989. *11*

[130] S. Sauter and C. Schwab. *Boundary Element Methods*. Springer Series in Computational Mathematics, 2011. *12*, *209*

[131] S. Schneider. FE/FMBE coupling to model fluid-structure interaction. *Int. J. Numer. Meth. Engng.*, 76(13):2137–2156, 2008. *64*

[132] L. Schwartz. *Théorie des Distributions*. Publications de l'Institut de Mathématique de l'Université de Strasbourg. Paris, 1966. No. IX-X Nouvelle édition, entièrement corrigée, refondue et augmentée. *50*

[133] J. Simon. Differentiation with respect to the domain in boundary value problems. *Numer. Funct. Anal. Optim.*, 2:649–687, 1980. *210*, *216*, *223*

[134] R. Tezaur, A. Macedo, C. Farhat, and R. Djellouli. Three-dimensional finite element calculations in acoustic scattering using arbitrarily shaped convex artificial boundaries. *Int. J. Numer. Methods Eng.*, 53(6):1461–1476, 2002. *46*, *64*

[135] S. Tordeux. *Méthodes Asymptotiques pour la Propagation des Ondes dans les Milieux Comportant des Fentes*. PhD thesis, Université de Versailles Saint-Quentin-en-Yvelines, 2004. *12*, *50*, *51*, *60*

[136] E. Turkel. Iterative methods for the exterior Helmholtz equation including absorbing boundary conditions. *Computational Methods for Acoustics Problems*, ed. F. Magoulès, Coburg Publ. UK:127–158, 2008. *46*

[137] D. Wang, R. Tezaur, J. Toivanen, and C. Farhat. Overview of the discontinuous enrichment method, the ultra-weak variational formulation, and the partition of unity method for acoustic scattering in the medium frequency regime and performance comparisons. *Int. J. Numer. Meth. Engng.*, 89:403–417, 2012. *64*, *141*

[138] G. N. Watson. Bessel functions and Kapteyn series. *Proc. London Math. Soc.*, 311:150–174, 1916. *50*

[139] C. H. Wilcox. *Scattering theory for the d'Alembert Equation in Exterior Domains*, volume 442 of *Lecture Notes in Mathematics*. Springer, 1975. *11*

[140] O. C. Zienkiewicz, R. L. Taylor, S. J. Sherwin, and J. Peiró. On discontinuous Galerkin methods. *Int. J. Numer. Meth. Engng.*, 58:1119–1148, 2003. *65*

[141] J. Zitelli, I. Muga, L. Demkowicz, J. Gopalakrishnan, D. Pardo, and V. Calo. A class of discontinuous Petrov-Galerkin methods. Part IV: Wave propagation. *J.Comput. Phys.*, 230:2406–2432, 2011. *65*

Contribution à l'analyse mathématique et à la résolution numérique d'un problème inverse de scattering élasto-acoustique

Résumé : La détermination de la forme d'un obstacle élastique immergé dans un milieu fluide à partir de mesures du champ d'onde diffracté est un problème d'un vif intérêt dans de nombreux domaines tels que le sonar, l'exploration géophysique et l'imagerie médicale. A cause de son caractère non-linéaire et mal posé, ce problème inverse de l'obstacle (IOP) est très difficile à résoudre, particulièrement d'un point de vue numérique. De plus, son étude requiert la compréhension de la théorie du problème de diffraction direct (DP) associé, et la maîtrise des méthodes de résolution correspondantes. Le travail accompli ici se rapporte à l'analyse mathématique et numérique du DP élasto-acoustique et de l'IOP. En particulier, nous avons développé un code de simulation numérique performant pour la propagation des ondes associée à ce type de milieux, basé sur une méthode de type DG qui emploie des éléments finis d'ordre supérieur et des éléments courbes à l'interface afin de mieux représenter l'interaction fluide-structure, et nous l'appliquons à la reconstruction d'objets par la mise en oeuvre d'une méthode de Newton régularisée.

Mots-clés : interaction fluide-solide, problème de diffraction, Fréquence de Jones, inégalité de Gårding, alternative de Fredholm, espace de Sobolev à poids, méthode de Galerkin discontinue, méthode élément fini, raffinement hp, effet de pollution, arêtes de frontière courbes, factorisation LU, différentiabilité au sens de Fréchet, dérivée de domaine, frontière Lipschitzienne, théorème des fonctions implicites, méthode de Newton, régularisation de Tikhonov, domaine étoilé, B-splines quadratiques.

Contribution to the mathematical analysis and to the numerical solution of an inverse elasto-acoustic scattering problem

Abstract : The determination of the shape of an elastic obstacle immersed in water from some measurements of the scattered field is an important problem in many technologies such as sonar, geophysical exploration, and medical imaging. This inverse obstacle problem (IOP) is very difficult to solve, especially from a numerical viewpoint, because of its nonlinear and ill-posed character. Moreover, its investigation requires the understanding of the theory for the associated direct scattering problem (DP), and the mastery of the corresponding numerical solution methods. The work accomplished here pertains to the mathematical and numerical analysis of the elasto-acoustic DP and of the IOP. More specifically, we have developed an efficient numerical simulation code for wave propagation associated to this type of media, based on a DG-type method using higher-order finite elements and curved edges at the interface to better represent the fluid-structure interaction, and we apply it to the reconstruction of objects with the implementation of a regularized Newton method.

Keywords : fluid-solid interaction, scattering problem, Jones frequency, Gårding's inequality, Fredholm alternative, weighted Sobolev space, Discontinuous Galerkin method, finite element method, hp-refinement, pollution effect, curved boundary edges, LU factorization, Fréchet differentiability, domain derivative, Lipschitz boundary, implicit function theorem, Newton method, Tikhonov regularization, star domain, quadratic B-splines.